Dynamic Modelling and Coordinated Control for Autonomous Path Tracking of Agricultural Wide-Span Implement Carriers

Xiaopeng Li

Thesis submitted to the University of Ottawa
in partial fulfillment of the requirements for the
Doctorate in Philosophy degree in Mechanical Engineering

Department of Mechanical Engineering
Faculty of Engineering
University of Ottawa

Abstract

Agricultural wide-span implement carriers (WSICs) are controlled traffic farming platforms that reduce soil compaction and improve field-operation efficiency through the coordinated motion of two supporting vehicles connected by a long-span truss. This research presents an original, applied systems-engineering integration of vehicle–truss dynamic modelling, control design, adjoint-curve-based leader–follower synchronization, simulation, and experimental evaluation for this configuration. A dynamic model was formulated for the supporting vehicles of the coupled vehicle–truss system, incorporating longitudinal and lateral motion, yaw dynamics, tire–ground interaction, and loads transmitted quasi-statically through the truss and implement. The model served as the basis for a combined control strategy using incremental model predictive control (MPC) for steering, with adaptive weighting evaluated in simulation, and proportional–integral–derivative (PID) control for longitudinal velocity. Inter-vehicle coordination was achieved through a follower synchronization controller based on offset-error regulation, with first-order error dynamics and a Lyapunov-based stability analysis. The strategy was evaluated through MATLAB/Simulink and CarSim co-simulations and experimentally validated on a small-scale WSIC platform equipped with real-time kinematic Global Positioning System (RTK-GPS) receivers, inertial measurement units, and wireless communication modules.

The dynamic-model-based strategy was compared with a kinematic approach under demanding simulated conditions, including curved and reverse motion, higher speeds, implement resistance, and initial offset errors, with differences assessed against sensor-based thresholds and application-specific error bounds. On curved paths, the strategy reduced steady-state lateral error from ± 0.20 m to ± 0.12 m, meeting the ± 0.15 m criterion, and reduced distance-based integral absolute error (IAE) for lateral tracking and offset by approximately 46% and 50%, respectively. In curved reverse motion, lateral-error IAE decreased by 34–36%. In straight-line simulations, the principal differences between the controllers were in offset regulation and recovery from a large initial offset. The combined MPC–PID strategy also reduced lateral-error IAE by about 28% relative to unified MPC during curved tracking. Small-scale experiments with fixed MPC weights demonstrated the strategy's feasibility: in two-vehicle cooperation, steady-state lateral errors were 0.02–0.03 m lower than those obtained with the kinematic controller. On sinusoidal paths, offset-error and separation-error IAEs decreased by 33–35%, while steady-state orientation error was approximately 0.02 rad larger. Experimental tracking errors exceeded simulated errors, owing mainly to the slower measured response of the follower velocity loop, together with unmodelled hardware nonlinearities, GPS fluctuations, and surface irregularities. Overall, incorporating vehicle dynamics, predictive steering, and explicit synchronization design provides an effective, experimentally validated foundation for WSIC guidance and future full-scale development.

Acknowledgements

First and foremost, I would like to express my deepest gratitude to Dr. Claude Laguë (P.Eng., ing. (à la retraite), FCAE, FEC; Dean and Professor Emeritus, Faculty of Engineering, University of Ottawa), whose unwavering guidance, insightful mentorship, and enduring belief in me have been pivotal throughout my Ph.D. journey. His patience and encouragement, particularly during the most challenging phases of my Ph.D. studies, sustained my motivation and perseverance.

I also extend my heartfelt gratitude to Dr. Thomas K. Uchida (P.Eng.; Associate Professor, Department of Mechanical Engineering, University of Ottawa). His meticulous feedback significantly refined my methodology and elevated the quality of this research.

My sincere thanks go to the current and previous members of my thesis committee: Dr. Eric Lanteigne (P.Eng.; Associate Professor, Department of Mechanical Engineering, and Associate Chair, Undergraduate Studies in Mechanical Engineering, University of Ottawa), Dr. Hashim Mohamed (P.Eng.; Assistant Professor, Department of Mechanical and Aerospace Engineering, Carleton University; SMIEEE), Dr. Steven Waslander (Professor, Institute for Aerospace Studies, and Director, Toronto Robotics and AI Laboratory, University of Toronto), Dr. Mojtaba Ahmadi (P.Eng.; Professor, Department of Mechanical and Aerospace Engineering, Carleton University), and Dr. Dan Necsulescu (P.Eng.; Professor, Department of Mechanical Engineering, University of Ottawa), for their insightful suggestions, constructive input, and support, which greatly strengthened this project.

I am particularly grateful to Dr. Colin Rennie (P.Eng.; Professor, Department of Civil Engineering, University of Ottawa) for generously granting me access to his laboratory's RTK-GPS equipment over extended periods, which was vital for my experiments.

Special thanks go to Dr. Chengming Luo (Lecturer, College of Engineering, Huazhong Agricultural University) for generously sharing his experience in the development of both the hardware and software of the WSIC platform. I am also deeply grateful to Kishita Pakhrani (AI/ML Engineer; Data Scientist) for her valuable assistance in developing the experimental WSIC platform and implementing software modifications. My sincere appreciation goes to Leo Denner (Lead Technologist, Laboratory Support, University of Ottawa) for his prompt and expert technical support in electronics, which proved invaluable throughout this project. I would also like to thank Dr. Eric Lanteigne for providing laboratory space for my experiments, and Line Campeau (Lead Officer, Administrative Support, University of Ottawa) for her support in equipment procurement.

I gratefully acknowledge the China Scholarship Council and the University of Ottawa for the scholarships that supported my Ph.D. studies, and the Natural Sciences and Engineering Research Council of Canada for funding this research.

I am especially grateful to my beloved partner, Fan Chen, whose unwavering support, love, and encouragement sustained me throughout this journey. Your encouragement during the most demanding times gave me the strength to persevere and ultimately complete this Ph.D.

Finally, I owe my deepest thanks to my parents for their unconditional love, patience, and tremendous sacrifices, and to my other family members and friends for their care, encouragement, and steady support.

Table of Contents

List of Figures

List of Tables

List of Abbreviations

2WS	Two-Wheel-Steering
4WD	Four-Wheel-Drive
4WS	Four-Wheel-Steering
BDS	BeiDou Navigation Satellite System
CG	Centre of Gravity
CTF	Controlled Traffic Farming
DC	Direct Current
DOF	Degrees of Freedom
FWS	Front-Wheel-Steering
GNSS	Global Navigation Satellite System
GPS	Global Positioning System
IAE	Integral Absolute Error
ICR	Instantaneous Centre of Rotation
IMU	Inertial Measurement Unit
INS	Inertial Navigation System
LiDAR	Light Detection and Ranging
LTV	Linear Time-Varying
MPC	Model Predictive Control
PI	Proportional–Integral
PID	Proportional–Integral–Derivative
RMSE	Root-Mean-Square Error
RPR	Rotary-Prismatic-Rotary
RTK	Real-Time Kinematic
RWD	Rear-Wheel-Drive
RWS	Rear-Wheel-Steering
SLAM	Simultaneous Localization and Mapping
SMC	Sliding Mode Control
WSIC	Wide-Span Implement Carrier
ZOH	Zero-Order Hold

List of Mathematical Symbols

${}^{i-1}{}_{i}T$: homogeneous transformation matrix from frame $\{O_{i-1}\}$ to frame $\{O_i\}$ (i = 1, 2, 3)

${}^{0}P$: position vector of the implement point P, expressed in frame $\{O_0\}$

a_{CG}: acceleration of a vehicle at point CG, m/s^2

a_{CG2}: acceleration of the follower vehicle at point CG$_2$, m/s^2

a_l, a_r: longitudinal and lateral acceleration of a vehicle, m/s^2

a_t, a_n: tangential and normal components of a_{CG} along $\mathbf{i}_m$ and $\mathbf{j}_m$, m/s^2

A_L, A_F: non-holonomic constraint matrices of the leader and follower vehicles

A_t, A_k: continuous-time and discrete-time state Jacobian

$\bar{A}$: augmented system matrix

b_a: acceleration bias of IMU, m/s^2

B: mass and inertia matrix of the vehicle, diag(m, m, I)

B_t, B_k: continuous-time and discrete-time input Jacobian

$\bar{B}$: augmented input matrix

C: wheel-force distribution matrix of the vehicle

C_k: output selection matrix

$\bar{C}$: augmented output matrix

C_0: geometric centre of vehicle 1

CG: centre of gravity of a vehicle

CG$_0$: centre of gravity (CG) of the vehicle 1

CG$_2$: CG of the follower vehicle

{CG; $\mathbf{i}_m$, $\mathbf{j}_m$}: moving frame attached to the leader vehicle

{CG$_2$; $\mathbf{i}_t$, $\mathbf{j}_t$}: moving frame attached to the follower vehicle

C_{Li}: cornering stiffness, N/rad

C_{Si}: longitudinal slip coefficient

d_0: distance between O_0 and O_1 along $\mathbf{k}_0$, $d_0 = d_1 + d_3$, m

d_1: fixed distance between the sliding joint's location on the truss and O_2 (centre of spherical joint 2), along $\mathbf{k}_1$, m. A geometric constant of the follower attachment hardware, not a joint variable (d_1 = 0 if spherical joint 2 is mounted directly at the slider)

d_2: distance between O_1 and O_2 along $\mathbf{j}_1$ (distance between the two vehicles' attachment points), m

$d_{2,\mathrm{ref}}$: desired inter-vehicle separation, m

d_3: distance between O_2 and O_3 along $\mathbf{k}_3$, m

d_4: position of the implement on the truss, measured from O_1 opposite to $\mathbf{j}_1$, m

d_5: vertical distance from the truss reference axis to the line of action of the resultant external (draft) force applied to the mobile carriage through the implement. The line of action generally lies at ground level, so d_5 depends on the implement in use and the agricultural operation; it is an implement-specific constant for a given operation and is treated as fixed in this study, m

d_{dist}: disturbance-injection term in the model-mismatch vector $d(k)$

ds: infinitesimal path length, m

ds_p: unit length of path, m

$\frac{dvp}{d\sigma p}$: derivative of velocity of the implement at point P^*, m/s^2

$d(k)$: model mismatch vector

$\bar{d}(k)$: augmented disturbance vector

D: truss-force vector expressed in the vehicle frame

e_v: difference between the target speed and current speed, m/s

e: difference between the curvilinear coordinates s_1 and s_2 of the two vehicles, m

e_d: separation error, m

e_f, e_r: horizontal distances of soil reaction to the centre of the front wheel / rear wheel, m

$\dot{e}$, $\ddot{e}$: first and second time derivatives of the offset error e, m/s, m/s^2

E: tracking error vector

$f(\cdot)$: nonlinear vehicle state function, $\xi = f(\xi, \delta)$

f_i: number of degrees of freedom of joint i

f_{GPS}: output frequency of GPS

F_{0X}: component of the external force exerted by the truss on the vehicle along the $\mathbf{i}_1$ axis of the truss coordinate frame, N

F_{0Y}: component of the external force exerted by the truss on the vehicle along the $\mathbf{j}_1$ axis of the truss coordinate frame, corresponding to the truss-span direction, N. For the follower vehicle, $F_{0Y} = 0$

F_{41i}, F_{41j}, F_{41k}: forces of carriage and implement on the truss, N

F_{Di}: forward force on the wheel, N

F_{external}: external load applied to the truss, opposing the direction of travel, N

F_f, F_r: gross tractive forces on the front wheel / rear wheel, N

F_{Li}: lateral force acting on wheel i, N

F_{nmp}: force of link n on link m (n, m = 0,1,2,3,4), in the p-axis direction (p= $\mathbf{i}$, $\mathbf{j}$, $\mathbf{k}$), N

F_{Wi}: wheel load, N

F_{dist}: occasional pulse disturbance force, N

$F_{\text{dist,max}}$: maximum value of disturbance force, N

g: gravitational acceleration, 9.81 m/s^2

G_1, G_2: truss-induced vertical loads on the leader and follower vehicles, N

h: distance from wheel centre to vehicle centreline ($\mathbf{i}_0$), m

H_f, H_r: horizontal forces of vehicle on the front wheel / rear wheel, N

I: identity matrix

I_n: inertia of the vehicle, N·m·s^2

J: MPC cost function

J_d: IAE of the separation error, m^2

J_e: IAE of the offset error, m^2

J_{FL}: geometric Jacobian of the follower vehicle with respect to the leader vehicle, $J_{FL}(\chi) \in \mathbb{R}^{3\times3}$

J_L: IAE of the lateral error, m^2

J_θ: IAE of the orientation error, rad·m

k_1, k_2: control gains of the kinematic-model-based path-tracking law (Luo, 2017)

k_{CG}: curvature of Γ_{CG} at point CG, m^{-1}

k_e: synchronization control gain, s^{-1}

k_{Op}: curvature of Γ_{Op} at point O_p, m^{-1}

k_{Om}: curvature of Γ_{Om} at O_m, m^{-1}

$\dot{k}_{\text{Om}}$: derivative of k_{Om} with respect to s, m^{-2}

k_{Om0}: reference-path curvature normalization constant, m^{-1}

k_{Om1}: curvature of the leader vehicle, m^{-1}

k_{Om2}: curvature of the follower vehicle, m^{-1}

k^+, k^-: value after and before the update at step k

K_d: coefficients for the derivative terms of a PID controller

K_i: coefficients for the integral terms of a PID controller

K_p: coefficients for the proportional terms of a PID controller

l_e: lateral error of a vehicle with respect to O_m, m

l_{e0}: normalization constant for lateral error, m

l_{e1}: lateral error of the leader vehicle with respect to CG_1, m

l_{e2}: lateral error of the follower vehicle with respect to CG_2, m

$l_{\text{e,max}}$: lateral-error allowance, m

l_f: length of CG to front, m

l_{pe}: lateral error of the implement with respect to O_P, m

l_r: length of CG to rear, m

$\dot{l}_e$, $\ddot{l}_e$: first and second derivatives of l_e with respect to s

$\dot{l}_{pe}$: derivative of l_{pe} with respect to s_p

L_c: characteristic travel distance used in the heading-tolerance estimate, m

L_{truss}: truss length, m

m: mass of the vehicle, kg

M_0: external moment exerted by the truss on the vehicle, N·m

M_{nmp}: moment of link n on link m (n, m = 0, 1, 2, 3, 4) about the p axis (p = $\mathbf{i}$, $\mathbf{j}$, $\mathbf{k}$), N·m

M_{dist}: occasional pulse disturbance moment, N·m

$M_{dist,max}$: maximum value of disturbance moment, N·m

N_c: the control horizon of an MPC

N_d: number of discrete steps

N_f, N_r: vertical forces of vehicle on the front wheel / rear wheel, N

N_{GPS}: update step size of GPS

N_{link}, N_{joint}: number of links and number of joints of the vehicle–truss mechanism

N_p: prediction horizon of an MPC

$N(\mu, \sigma^2)$: normal distribution with mean μ and variance σ^2

$\{O_0; \mathbf{i}_0, \mathbf{j}_0, \mathbf{k}_0\}$: moving frame attached to vehicle 1 (leader vehicle)

$\{O_1; \mathbf{i}_1, \mathbf{j}_1, \mathbf{k}_1\}$: moving frame attached to the truss at spherical joint 1 (leader end)

$\{O_2; \mathbf{i}_2, \mathbf{j}_2, \mathbf{k}_2\}$: moving frame attached to the sliding joint (follower attachment point)

$\{O_3; \mathbf{i}_3, \mathbf{j}_3, \mathbf{k}_3\}$: moving frame attached to vehicle 2 (follower vehicle)

$\{O_f; \mathbf{i}_f, \mathbf{j}_f, \mathbf{k}_f\}$: absolute (fixed) reference frame on the ground

O_m: reference point on Γ_{Om} that is closest to the point CG. The coordinate of O_m in the fixed frame is (x_{Omf}, y_{Omf})

$\{O_m; \boldsymbol{\alpha}, \boldsymbol{\beta}\}$: Frenet–Serret frame on the reference path

O_{m2}: reference point on Γ_{Om2}

O_P: closest reference point on Γ_{Op} to the point P^*. The coordinate of O_P in the fixed frame is (x_{Op}, y_{Op})

$\{O_p; \boldsymbol{\alpha}_p, \boldsymbol{\beta}_p\}$: a curve frame attached to the implement's reference path

q: self-weight of the truss per unit length, acting in the $-\mathbf{k}_1$ direction over the full truss length L_{truss}; its resultant acts at the truss mid-length, N/m

$q_Y(k)$: online-updated weight for lateral error

q_{Y0}: nominal baseline weight for lateral error

$q_\theta(k)$: online-updated weight for orientation error

$q_{\theta 0}$: nominal baseline weight for orientation error

[$q_{Y,\min}$, $q_{Y,\max}$], [$q_{\theta,\min}$, $q_{\theta,\max}$], [$r_{\delta,\min}$, $r_{\delta,\max}$]: saturation bounds of the adaptive weights

Q, R: weighting parameters of an MPC

$\bar{Q}$, $\bar{R}$: output weighting matrix and control weighting matrix

$Q_{\Delta\delta}$: quantization operator, corresponding to Δ_{δ}

$Q_{\Delta\theta}$: quantization operator, corresponding to resolution Δ_{θ}

r_f, r_r: rolling radii, defined as the vertical distances from the soil reactions to the centres of the front and rear wheels, respectively, m

r_i: rolling radius of wheel i, m

$r_{\delta}(k)$: online-updated weight for steering effort

$r_{\delta 0}$: nominal baseline weight for steering effort

$\mathbf{R}_{CG}$, $\mathbf{R}_{Om}$, $\mathbf{R}_{ICR}$, $\mathbf{R}_{P}$, $\mathbf{R}_{Op}$: position vectors of CG, O_m, ICR, P^* and O_P in the fixed frame, m

R_f, R_r: vertical parts of soil reaction on the front wheel / rear wheel, N

R_i: rotation matrix of the steering angle of wheel i

s: curvilinear coordinate of O_m, m

s_1, s_2: curvilinear coordinates of the leader and follower vehicles, m

s_p: curvilinear coordinate of point O_p, m

sat(·): saturation operator used to bound the adaptive weights within prescribed minimum and maximum values

T: sampling time, s

T_{acc}: accumulation matrix for converting steering increments to absolute steering angles

T_f, T_r: axle torques on the front wheel / rear wheel, N·m

TF_f, TF_r: horizontal parts of soil reaction on the front wheel / rear wheel, N

T_{GPS}: update period of GPS, s

T_L, T_F: poses of the leader and follower vehicles

T_{LF}, T_{FL}: the relative transformation from leader to follower, and transformation from follower to leader

$u(k)$: steering-angle control input at step k; u_{min}, u_{max}: its bounds

$u_v(t)$: output of the PID velocity controller

U_{act}: actuator output

U_{cmd}: steering angle and velocity command output by controllers

$U(k)$: stacked steering-angle sequence over the control horizon

U_{min}, U_{max}: lower and upper bounds of the steering-angle sequence

U_t: vector of the current steering angle used with T_{acc} to accumulate the increments

$\Delta u(k)$, $\Delta\delta(k)$: steering-angle increment at step k, $\delta(k) - \delta(k-1)$, rad

ΔU: stacked steering-increment vector over the control horizon

ΔU_{min}, ΔU_{max}: lower and upper bounds of the steering-increment vector

v_1, v_2: velocities of the leader and follower vehicles, m/s

v_{CG}: velocity of a vehicle at point CG, m/s

v_{CG2}: velocity of the follower vehicle at point CG_2, m/s

v_{ICR}: velocity of ICR, m/s

v_l: longitudinal velocity of a vehicle, m/s

v_{l0}: longitudinal velocity normalization constant, m/s

$\dot{v}_l$: longitudinal acceleration of a vehicle, m/s^2

v_p: velocity of the implement at point P^*, m/s

v_r: lateral velocity of a vehicle, m/s

$\dot{v}_r$: lateral acceleration of a vehicle, m/s^2

$v_{\mathrm{Target}}(k)$, $v_{\mathrm{Current}}(k)$: target and current vehicle speed at step k, m/s

v_{wi}: longitudinal velocity of wheel i, m/s; $v_{wi}*$: theoretical (no-slip) velocity of wheel i, $r_{\mathrm{i}}\omega_{w\mathrm{i}}$, m/s

$V(e)$, $\dot{V}(e)$: Lyapunov function candidate and its time derivative

V_L, V_F: planar twists of the leader and follower vehicles in their body frames

V_{FL}, w_{FL}, v_{FL}: relative twist of the follower with respect to the leader and its angular and linear parts

W_0: weight of the vehicle 1, N

W_f, W_r: weights of the front wheel / rear wheel, N

W_{vehicle}, W_{lane}: nominal vehicle width and traffic-lane (corridor) width, m

x_1, y_1: coordinates of the leader vehicle, m

x_2, y_2: coordinates of the follower vehicle, m

X, Y: position of the vehicle in the fixed coordinate system, m

$\dot{X}$, $\dot{Y}$: vehicle's velocities along the fixed axes, m/s

Γ_{CG}: actual path for CG of a vehicle

Γ_{CG2}: actual path for CG_2 of the follower vehicle

Γ_{Om}: reference path, which is the desired path for CG of a vehicle to follow

Γ_{Om2}: reference path for the CG_2 to follow

Γ_{Op}: reference path for the implement, which is the desired path for P^* to follow

Γ_P: actual path of P^*

γ_i: sideslip angle, rad

Δ_δ: resolution of the steering sensor rotation angle, deg

Δ_θ: resolution of IMU, deg

Δy_θ: heading-induced lateral displacement over L_{c}, m

δ_0, ξ_0: steering angle and state vector at the linearization point

δ_{act}: actual steering actuator rotation angle, rad

δ_f, δ_r: virtual front and rear steering angles, rad

δ_i: steering angle, rad

δ_{in}, δ_{out}: inner- and outer-wheel steering angles, rad

δ_L, δ_F: steering angles of the leader and follower vehicles, rad

$\delta_{\max}$, $\Delta\delta_{\max}$: maximum steering angle and maximum steering increment used to normalize $r_\delta(k)$, rad

δ_{meas}: measured steering angle, rad

ε_i: slip angle, rad

ε_M, $\varepsilon_{M,\max}$: slack variable and its maximum value, rad

ζ_m, ζ_I: standard normal random variables driving the mass and inertia perturbations

η: output vector for the steering angle controller

$\hat{\eta}$: stacked predicted output vector

$\hat{\eta}_{\mathrm{ref}}$: stacked reference output sequence

η_{buf}: measurement queue

η_d: delayed controller input

η_{meas}: measurement variable

ϖ_m, ϖ_I: slowly varying random perturbations

ϖ_{pos}: Gaussian white noise in the GPS position measurement, m

ϖ_{vel}: Gaussian white noise in the GPS velocity measurement, m/s

ϖ_δ: Gaussian white noise in the steering angle measurement, deg

ϖ_θ: Gaussian white noise in the IMU yaw angle measurement, deg

Θ: control influence matrix

θ: orientation of a vehicle with respect to $\mathbf{i}_f$ axis, rad

θ_1, θ_2: heading angles of the leader and follower vehicles, rad

θ_p: orientation error of a vehicle with respect to Γ_{Om}, $\theta_p = \theta - \theta_r$, rad

θ_{p0}: normalization constant for orientation error, rad

θ_{p1}: orientation error of the leader vehicle with respect to Γ_{Om1}, rad

θ_{p2}: orientation error of the follower vehicle with respect to Γ_{Om2}, rad

θ_{pe}: orientation error of the implement with respect to Γ_{Op}, rad

θ_{pr}: tangent of the reference path at point O_P with respect to $\mathbf{i}_0$ axis, rad

θ_r: tangent of the reference path at point O_m with respect to $\mathbf{i}_f$ axis, rad

θ_{r2}: tangent of the reference path at point O_{m2} with respect to $\mathbf{i}_f$ axis, rad

Λ: disturbance propagation matrix

$\lambda_d(k)$: forward/reverse direction factor

λ_i: the slip in the longitudinal direction of wheel i

μ: coefficient of friction between the vehicle's tires and the road surface

μ_{dY}: adaptation gain for motion-direction in $q_Y(k)$

$\mu_{d\theta}$: adaptation gain for motion-direction in $q_\theta(k)$

μ_{kY}: adaptation gain for path-curvature effect in $q_Y(k)$

$\mu_{k\theta}$: adaptation gain for path-curvature effect in $q_\theta(k)$

μ_l: adaptation gain for lateral-error magnitude

μ_v: adaptation gain for longitudinal velocity

μ_δ: adaptation gain for steering-angle magnitude

$\mu_{\Delta\delta}$: adaptation gain for steering-rate magnitude

μ_θ: adaptation gain for orientation-error magnitude

ξ: state vector of a vehicle

ρ: the radius of the actual path Γ_{CG} at point CG, m

ρ_2: radius of the actual path Γ_{CG2} at point CG_2, m

ρ_M: relaxation penalty coefficient

σ: the curvilinear coordinate of point CG, m

σ_{b0}, σ_b: the initial bias error and in-run bias stability of IMU, m/s^2

$\sigma_{\mathrm{gps,pos}}$: noise amplitude in the GPS position measurement, m

$\sigma_{\mathrm{gps,vel}}$: noise amplitude in the GPS velocity measurement, m/s

σ_{imu}: yaw angle noise amplitude of IMU, deg

σ_m, σ_I: amplitude values of uncertainties of mass m and moment of inertia I_n

σ_δ: noise amplitude of the steering sensor, deg

τ: pure loop delay considered in the delay analysis, s

τ_{act}: actuator delay, s

τ_{meas}: measurement delay for all sensors, s

τ_v: effective time constant of the follower velocity loop, s

Φ: stacked disturbance vector

φ: offset-error angle, which is the angular deviation between the line connecting the centres of gravity of the two vehicles and the lateral direction of the path

φ_{01}: yaw angle between $\mathbf{i}_0$ and $\mathbf{i}_1$, at spherical joint 1 (leader-end joint variable), rad

φ_{12}: yaw angle between $\mathbf{i}_1$ and $\mathbf{i}_2$, rad. In this study, $\varphi_{12} = 0$. Frames $\{O_1\}$ and $\{O_2\}$ share the same orientation ($\mathbf{i}_2 \parallel \mathbf{i}_1$, $\mathbf{j}_2 \parallel \mathbf{j}_1$, $\mathbf{k}_2 \parallel \mathbf{k}_1$); they differ only in position

φ_{23}: yaw angle between $\mathbf{i}_2$ and $\mathbf{i}_3$ at spherical joint 2 (follower-end joint variable), rad

φ_{03}: relative orientation between $\mathbf{i}_0$ and $\mathbf{i}_3$ (vehicle 1 and vehicle 2), $\varphi_{03} = \varphi_{01} + \varphi_{12} + \varphi_{23}$, rad

χ: joints between two vehicles, $\chi = [\varphi_{01}, d_2, \varphi_{23}]^T$

$\dot{\chi}$: joint rates

Ψ: free-response prediction matrix

ω: angular velocity of the vehicle, rad/s

ω_{wi}: angular velocity of wheel i, rad/s

$\dot{\omega}$: angular acceleration of the vehicle, rad/s^2

ω_1, ω_2: angular velocity of the leader and follower vehicles, rad/s

$\dot{\omega}_2$: angular acceleration of the follower vehicle, rad/s^2

ω_p: angular velocity of the implement, rad/s

$\dot{\omega}_p$: angular acceleration of the implement, rad/s^2

Chapter 1

Introduction

1.1 Context and Motivation

Agriculture and food production are fundamental to sustaining human life. However, current agricultural methods may struggle to meet global food demands by as early as 2050 (Xie et al., 2023). Autonomous machines and equipment are increasingly used for tasks such as weeding, fertilizing, and harvesting to enhance productivity and efficiency (Thomasson et al., 2019). Nevertheless, implementing autonomous control in agricultural machinery remains complex due to the highly variable nature of field environments, including crop diversity, field topography, soil load-bearing capacity, and the presence of obstacles.

One of the primary challenges in crop production is soil compaction caused by machinery traffic (Chamen and Cavalli, 1994). Agricultural wide-span implement carriers (WSICs) provide a platform for controlled traffic farming (CTF), with supporting vehicles travelling along permanent lanes and implements operating beneath a long-span truss (Laguë et al., 1997). The agricultural and machinery background is reviewed in Section 1.2. Figure 1.1 illustrates the prototype developed by Laguë et al. (1997) for cranberry production in stationary mode during harvesting.

Figure 1.1 Agricultural WSIC for cranberry production (Laguë et al., 1997)

The WSIC shown in Figure 1.1 can operate in two distinct modes: mobile and stationary (Figure 1.2). In mobile mode, the carriage supporting the implement is positioned at a specific location along the truss span, and the entire machine moves across the field perpendicular to the truss axis. The two supporting vehicles follow preplanned paths along the field length to ensure full coverage of the implement width. Deviations from the desired trajectories, caused by tracking errors at the supporting vehicle level, may result in overlaps or gaps between adjacent passes. In stationary mode, the entire machine stops at designated locations while the mobile carriage and implement travel along the truss. Once the implement reaches the end of the truss, the machine advances to the next position by a distance corresponding to the implement width.

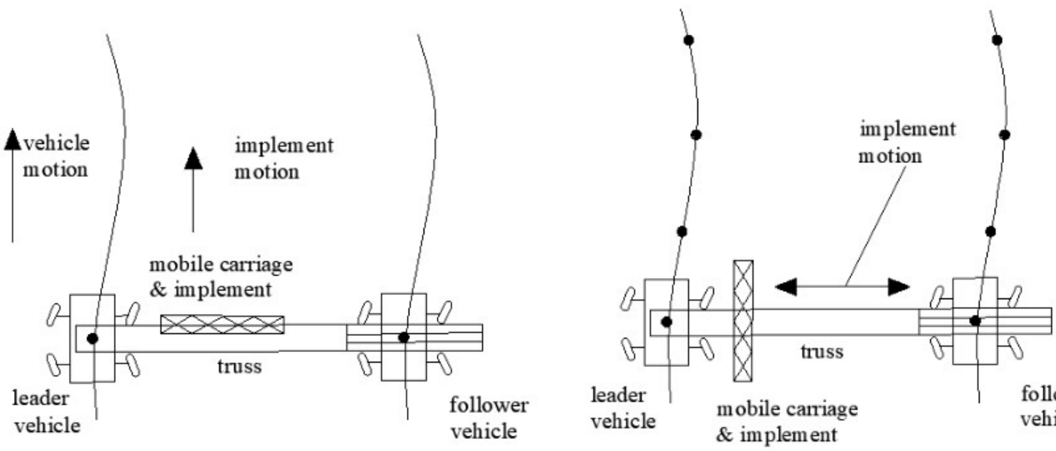

(a) (b)

Figure 1.2 Mobile (a) and stationary (b) operating modes of agricultural WSICs

Tracking and coordination become more demanding when wheel slip, acceleration, and implement forces affect the supporting vehicles. Luo (2017) developed kinematic WSIC guidance for mobile and stationary modes, assuming flat, firm paths and pure rolling without slip. Truss weight was treated as vertical loading whose effect on lateral stability was neglected. The work included curvilinear path following, curvature-dependent steering, and first-order offset regulation. Although an acceleration term was omitted from the steering derivation for normally constant forward speed, varying-speed simulations and experiments were also conducted. This work provides the WSIC-specific kinematic benchmark for the present research.

This thesis extends the WSIC modelling framework to represent tire–ground interaction and wheel slip, longitudinal and lateral motion, yaw dynamics, and truss-transmitted implement forces and moments. It integrates these effects with predictive steering, velocity regulation, and curvature-dependent path-coordinate synchronization. External implement-resistance effects are evaluated in simulation, while physical experiments assess tracking on a truss-connected small-scale platform. In contrast, Luo's (2017) experimental robots were not connected by a truss. The present model retains the flat-terrain assumption and does not represent vehicle pitch or terrain-induced attitude changes. Table 1.1 summarizes the comparison; Sections 2.1 and 2.3 review the broader coordination and control literature.

Table 1.1 Comparison of Luo's (2017) WSIC guidance framework with the present research

Aspect	Luo (2017)	Present research
Model basis	Bicycle kinematics for mobile and stationary modes.	Vehicle longitudinal, lateral and yaw dynamics with truss-transmitted force and moment terms.
Tires and terrain	Pure rolling without slip; flat, firm paths; roll and pitch ignored.	Tire–ground forces and slip represented; flat-terrain assumption retained.
Truss and implement loading	Truss weight treated as vertical loads; effects on lateral stability and truss dynamics neglected.	Implement-force and moment effects enter the coupled formulation; externally applied implement resistance is evaluated in simulation.
Speed and acceleration	Acceleration term omitted in the steering derivation; constant- and varying-speed cases tested.	Transient vehicle dynamics represented and tracking evaluated at different speeds.
Path geometry and synchronization	Curvilinear path following and curvature-dependent steering. Straight-path offset-rate model with first-order synchronization-error dynamics.	Adjoint-curve formulation with curvature-dependent path-coordinate progression integrated into the synchronization law.
Control architecture	Nonlinear feedback steering and follower-velocity adjustment for master–slave coordination.	Incremental MPC steering (adaptive weighting evaluated in simulation), PID velocity regulation and an explicit synchronization law.
Physical validation	Two unconnected robots; mobile- and stationary-mode tests on flat, firm ground at low speeds.	Truss-connected platform; straight-line and sinusoidal forward tracking without externally applied implement resistance.

Note: MPC = model predictive control; PID = proportional–integral–derivative. Chapter 3 develops the present model and control equations.

1.2 Controlled Traffic Farming and Wide-Span Systems

1.2.1 Controlled Traffic Farming

CTF confines machinery traffic to permanent lanes, separating traffic zones from crop-growing areas to reduce soil compaction. Field efficiency is the ratio of effective field capacity, the area actually worked per unit of field-operation time, to theoretical field capacity at the specified working width and travel speed, usually expressed as a percentage (Griffel et al., 2020). Turning, overlap, filling or unloading, and operational stops reduce the achieved capacity. Field efficiency therefore describes utilization of working width and operating time, rather than directly measuring fuel-use efficiency. Matching permanent lanes to machinery width and guidance requirements can reduce overlap and support more efficient field operations; the outcome also depends on field layout and operating conditions (Isbister et al., 2013). The wider agronomic, environmental, and engineering development of CTF is reviewed by Chamen et al. (2025).

Extensive research has established the agronomic benefits of CTF. By restricting wheel traffic to fixed paths, soil compaction is substantially reduced, which leads to improved soil structure, increased porosity, and enhanced root development. Studies on sugarcane production systems have shown that CTF improves soil compressibility characteristics and promotes stronger root systems compared with conventional farming practices (Souza et al., 2012). Similarly, research on grain production systems has demonstrated improvements in crop yield, water-use efficiency, and fertilizer utilization (Hussein et al., 2021). These findings are further supported by investigations into soil physical properties, which indicate reductions in bulk density and improvements in soil aeration under CTF practices (Bawatharani et al., 2026).

In addition to agronomic benefits, CTF provides substantial environmental advantages. Reduced soil disturbance enhances water infiltration and reduces surface runoff, while the preservation of soil structure contributes to lower greenhouse gas emissions. Studies have shown that CTF can reduce emissions of nitrous oxide and methane by maintaining soil integrity (Tullberg et al., 2018). Comprehensive reviews have also highlighted reductions in energy consumption and improvements in long-term soil sustainability (Antille et al., 2015; Gasso et al., 2013).

Practical implementation of CTF requires machinery matching and planning of traffic lanes and field operations (Isbister et al., 2013). In grass-silage production, Hargreaves et al. (2019) examined agronomic performance, system design, and economics. This connects the soil-management rationale to the machinery and operating choices required to implement CTF.

In recent years, commercial-scale implementations have demonstrated the practical viability of CTF. Wide-span controlled traffic systems, such as the NEXAT platform, employ large working widths (e.g., 15 m) to ensure that most of the field remains free from wheel traffic, thereby maximizing agronomic benefits (Chamen and McPhee, 2024; RealAgriculture, 2023). These systems integrate multiple field operations within a single carrier platform and incorporate coordinated implement integration and system-level optimization within a wide-span CTF framework (Chamen and McPhee, 2024). Similarly, autonomous power platforms such as OMNiPOWER enable interchangeable implement operation across multiple tasks and support fully autonomous field operations, reflecting a broader trend toward automation and interchangeable implement integration (Raven Industries, Inc., 2021, 2022). Collectively, these developments indicate a transition from experimental and research-oriented systems to commercially deployable, large-scale agricultural solutions.

CTF has been firmly established as an effective approach for improving soil health, productivity, and sustainability. However, its full implementation requires advanced machinery systems and coordinated control strategies that extend beyond traditional agricultural practices.

1.2.2 Wide-Span Systems

Wide-span vehicles, wide-span tractors, and WSICs represent a key technological advancement that enables the practical implementation of CTF. These systems operate on fixed traffic lanes while spanning large working widths, thereby minimizing soil compaction across the field. Reviews of wide-span self-propelled gantry-type machines have documented their effectiveness in reducing soil damage and improving work rate and cropped area (Önal, 2012). Additional studies have confirmed their suitability for large-scale agricultural operations (Kuvachov et al., 2024).

Mechanical and structural analyses of wide-span systems have provided important insights into their performance characteristics. These studies have examined load distribution, structural design, and adaptability to field conditions (Kuvachov et al., 2024). Investigations into vehicle stability emphasize the importance of maintaining dynamic balance and structural rigidity to ensure accurate motion under varying terrain conditions (Bulgakov et al., 2024). Furthermore, research on automated wide-span vehicles has demonstrated the feasibility of integrating automatic driving systems into these platforms (Bulgakov et al., 2017).

Related agricultural control studies address distinct operating problems. Maharlooei et al. (2024) evaluated affordable guidance for parallel movement in orchards, while Ma et al. (2022) considered grain-truck following under variable loads and control delay. These studies motivate attention to sensing, loading, and timing, but their vehicle arrangements differ from the two-support, implement-bearing truss considered here. The model and coordination requirements of the WSIC are therefore examined explicitly rather than inferred from single-vehicle or independently driven following systems.

Wide-span systems connect the soil-management benefits of CTF to machinery design. For autonomous WSIC operation, this structural arrangement also creates a coupled guidance problem involving vehicle tracking, implement loads, and coordination between the supports.

1.2.3 Comparative Analysis and Research Gaps

The reviewed CTF studies establish the agricultural motivation and machinery context for wide-span operation. The control problem addressed here is to maintain individual-vehicle tracking and coordinated support motion through a common implement-bearing truss. Luo (2017) provides a

WSIC-specific kinematic baseline; the modelling and validation extensions summarized in Table 1.1 define the starting point for this research.

Existing research addresses sensor disturbances and heading estimation (Harik, 2023), communication delay (Ploeg et al., 2011), model uncertainty and actuator limits in mechanically coupled tractor–trailer control (Kayacan et al., 2015), and shared-load robotic transport (Sugar and Kumar, 2002); none of these treats a mechanically coupled, side-by-side two-vehicle platform. Section 2.1.2 reviews these precedents.

The cranberry WSIC considered here (Figure 1.1) is based on the configuration of Laguë et al. (1997), in which a long-span truss straddles the bog and the support vehicles travel on the tops of the earthen dikes separating adjacent bogs, which serve as the permanent traffic lanes (minimum width 3.4 m). These dike tops are not paved: Laguë et al. (1997) reported that their soil condition ranged from very firm to very soft during a single harvesting season, depending on soil type and moisture, so the lane surface itself introduces variable rolling resistance and traction. The WSIC's mobile and stationary operating modes provide the machinery context for guidance and coordination. The present control development focuses on mobile-mode tracking; stationary-mode automation and mode transitions are not additional validation tasks in this study.

The resulting research program links dynamic modelling, predictive steering, longitudinal-velocity regulation, and path-coordinate synchronization to comparative simulation and physical implementation. Sections 1.3 and 1.4 state the objectives and contributions; Chapter 2 develops the navigation, positioning, and control rationale.

1.3 Research Objectives

The overall objective is to develop coordinated path-tracking control for an agricultural WSIC supported and propelled by two four-wheeled vehicles, accounting for wheel slip, externally applied implement resistance, and the sensing and actuation conditions considered in this study. External-load effects are represented in the model and evaluated through simulation. Physical experiments assess tracking on the truss-connected small-scale platform without externally applied implement resistance; additional load-dependent effects remain outside the experimental scope (Section 6.2).

The specific objectives are as follows:

- To develop a WSIC dynamic modelling framework that represents supporting-vehicle motion and the forces and moments transmitted through the connecting truss and implement carriage.

- To design control systems for the two supporting vehicles in mobile mode, using predictive steering and longitudinal-velocity regulation to improve path-tracking accuracy and inter-vehicle coordination.
- To formulate path-tracking control laws using model predictive control (MPC) for steering and proportional–integral–derivative (PID) control for longitudinal velocity, together with a synchronization strategy for coordinated leader–follower motion.
- To evaluate the proposed control approach through simulation and experimental tracking tests on a small-scale WSIC platform.
- To evaluate tracking and coordination under the selected operating conditions, compare the dynamic-model-based strategy with the kinematic approach of Luo (2017), and assess an additional unified-MPC benchmark in simulation.

1.4 Original Contributions

This research makes four applied systems-engineering contributions to autonomous WSIC path tracking, linking coupled modelling and coordinated control to simulation and physical implementation:

- A dynamic model of the WSIC vehicle–truss–vehicle configuration that incorporates tire–ground interaction, yaw dynamics, and the implement and truss loads transmitted to the vehicles through the connecting assembly, which is represented as a quasi-static load path. It extends the kinematic WSIC formulation of Luo (2017) to a force-based prediction framework for coordinated control. To the author's knowledge, this is the first dynamic model developed specifically for this WSIC structure.
- A WSIC-specific control architecture integrating incremental MPC steering with adaptive weighting and PID-based longitudinal-velocity regulation. The design coordinates tracking and speed control while representing the mechanical interaction transmitted through the implement-bearing truss.
- A leader–follower synchronization formulation within the adjoint-curve framework that uses curvature-dependent path-coordinate progression for coordinated WSIC motion. Building on Luo's (2017) first-order offset-regulation structure, it links tracking geometry to the follower-velocity command and provides a Lyapunov-based analysis of the resulting synchronization law.
- A comparative simulation and experimental evaluation of the developed system. Simulations compare the dynamic-model-based controller with the kinematic benchmark

across curved and reverse motion, external loading, and low-adhesion conditions, and include an additional unified-MPC benchmark. Physical experiments demonstrate connected-platform tracking on straight-line and sinusoidal forward paths with no externally applied implement resistance. The evaluation quantifies the tracking and formation-control improvements and the metric-specific trade-offs of the implemented designs.

1.5 Outline of the Thesis

This thesis is structured as follows:

Chapter 1 introduces the research context and motivation, reviews controlled traffic farming and wide-span systems, and states the research objectives and original contributions.

Chapter 2 reviews navigation and multi-vehicle cooperation, positioning, and motion control for agricultural and industrial vehicles, and relates the literature to the WSIC research contribution.

Chapter 3 details the methodology, including system modelling and control law design.

Chapter 4 describes the simulation setup and compares the proposed dynamic-model-based control strategy with the kinematic and unified-MPC benchmarks.

Chapter 5 presents the experimental setup and compares the dynamic-model-based and kinematic strategies on the connected small-scale platform.

Chapter 6 concludes the thesis by summarizing contributions, discussing limitations, and outlining directions for future research.

Chapter 2

Background and Literature Review

Autonomous agricultural machinery combines sensing, planning, and control to perform tasks such as planting, harvesting, and weeding. The resulting navigation systems must coordinate these functions under the sensing and operating conditions of agricultural work (Wu et al., 2025). The review below relates this technological foundation to the WSIC context introduced in Chapter 1.

The controlled traffic farming and wide-span background is presented in Section 1.2. This chapter reviews three technical areas relevant to autonomous WSIC operation: navigation and multi-vehicle cooperation, positioning, and motion control. Sections 2.1–2.3 examine these areas, and Section 2.4 identifies the contribution of the present work relative to the reviewed approaches.

2.1 Navigation System

A navigation system integrates localization, mapping, path planning, and motion control to guide a vehicle or robot toward a target. Sensor measurements and computational algorithms provide estimates of position and orientation, support the generation of feasible paths, and supply feedback for path following and obstacle avoidance (Alhmiedat et al., 2023; Yao et al., 2024). For agricultural machinery, these functions must also accommodate field geometry, crop arrangement, and the operational requirements of the attached implement.

2.1.1 Navigation Systems for Agricultural and Industrial Vehicles

Autonomous agricultural vehicles combine sensing, estimation, planning, and control to operate in semi-structured and unstructured field environments. Terrain variability, crop geometry, and changing environmental conditions influence both localization and vehicle motion. Reviews by Cheng et al. (2023), Yao et al. (2024), and Wu et al. (2025) describe the development of integrated navigation technologies for these conditions.

Global navigation satellite system (GNSS) positioning with real-time kinematic (RTK) corrections can provide centimetre-level accuracy in open-field conditions. Measurements from inertial measurement units (IMUs) complement satellite positioning, while machine vision and light detection and ranging (LiDAR) provide information for crop-row recognition, obstacle detection, and environmental mapping. The choice and fusion of these measurements depend on the operating environment: satellite signal interruptions, inertial drift, lighting changes, and occlusion affect the availability and quality of the navigation information (Wu et al., 2025).

Controlled traffic farming adds a requirement for repeatable guidance along permanent traffic lanes matched to machinery wheel tracks and implement spans, separating machinery traffic from the crop-growing area (Isbister et al., 2013).

Commercial developments also illustrate the integration of navigation and machine control. CNH Industrial (2022) announced driverless tillage and driver-assist harvesting technologies, including coordinated speed and path control of a tractor and grain cart alongside a combine during unloading. Such systems connect vehicle guidance to the timing and relative-position requirements of an agricultural operation.

Comparable machine-control technologies are established outside agriculture. Jeon et al. (2025) reviewed blade-mounted positioning arrangements, including GNSS sensors at both ends of a grader blade, and developed a system using two cab-mounted GNSS receivers with inertial and joint measurements. For a trial with a −2° target cross-slope, the estimated blade-height and cross-slope root-mean-square errors (RMSE) were 0.30 cm and 0.318°, respectively. These are blade-pose control metrics, not vehicle path-tracking errors or independently surveyed ground-level errors.

For an unmanned bulldozer, Peng et al. (2023) developed RTK-GNSS path tracking with proportional–integral (PI) control and reported mean position and heading deviations below 5 cm and 1° for the forward construction segment on a relatively flat site. The same study separately investigated fusion of GNSS with visual simultaneous localization and mapping (SLAM) and local map reloading for pose estimation when GNSS information was degraded or unavailable. Peng et al. (2025) subsequently combined GNSS, IMU, camera, and LiDAR measurements using factor-graph fusion for mine dumping operations. Data-withholding tests examined degraded sensing while retaining inertial measurements, and the motion-control design applied explicit output saturation.

Suzuki et al. (2021) developed a four-receiver, factor-graph-based estimator for the articulation of a six-wheeled dump truck, obtaining an articulation-angle RMSE of approximately 0.13° in post-processed open-sky field data. This is an articulation-estimation result rather than a closed-loop tracking error. Together, the cited industrial examples demonstrate positioning, complementary sensing, calibration, and mechanism-specific control. For the WSIC, these concerns are combined with coordinated motion of two independently propelled vehicles supporting a shared truss; the related multi-vehicle and mechanically coupled systems are reviewed in Section 2.1.2.

2.1.2 Multi-Vehicle Cooperation

The WSIC requires coordinated motion of two supporting vehicles while regulating longitudinal offset and separation. The truss carries the implement and transmits loads between the supports, while a sliding joint permits span adjustment within finite travel limits. Separation regulation keeps the support spacing within the usable range, and path-coordinate offset regulation synchronizes the vehicles' progress. In mobile mode both vehicles move together; in stationary mode they remain at prescribed positions while the implement moves laterally. These requirements connect individual-vehicle tracking to the geometry and motion of the shared structure.

Multi-vehicle coordination is an established research area encompassing formation control, platooning, cooperative transport, and agricultural operations. Dunbar and Murray (2006) developed distributed receding-horizon control for formation stabilization using dynamically uncoupled vehicle models, a coupled performance objective, and exchanged predicted trajectories. Velasco-Villa et al. (2024) formulated leader–follower coordination using non-inertial reference frames, with followers tracking delayed leader trajectories, and evaluated the method through simulations and real-time experiments. These approaches provide foundations for coordinating vehicle trajectories and relative motion.

Agricultural studies provide practical examples of multi-vehicle coordination. Zhang et al. (2016) developed a leader–follower system using two independently controlled robot tractors, including coordinated headland turns and fault-tolerant measures for Global Positioning System (GPS) and IMU disturbances; field experiments showed cooperative operation with an average lateral navigation error below 0.04 m. Harik (2023) investigated a heterogeneous system in which an autonomous mobile robot followed a manually driven tractor; to address unreliable IMU heading estimates, dual RTK-GNSS receivers were added to the follower, and the cooperation strategy was tested in the field.

Vision-based relative sensing provides another approach. Zhang et al. (2023) described a monocular-camera leader–follower system combining feedback steering with PID-based inter-vehicle distance regulation. Tests at an average leader speed of 0.30 m/s produced RMSE values of 6.5 to 16.4 cm across straight, turning, and zigzag paths; terrain effects were only partly considered: camera roll was compensated, vehicle pitch was not modelled, and undulating terrain was excluded from the experiments. This does not establish general terrain-noise rejection. The present WSIC likewise retains a flat-terrain model, while explicitly representing sensing disturbances and tire–ground interaction in simulation (Sections 1.1 and 4.1.4). For cooperative harvesting, Ma et al. (2024) developed supervised reinforcement learning for longitudinal coordination between a harvester and a grain vehicle, with a supervisor trained on driving data and a reward function addressing operational smoothness and unloading safety, evaluated through simulations and field unloading tests. These studies demonstrate different ways of combining relative sensing and control for task-specific agricultural cooperation.

Mechanically coupled cooperation also has established precedents. Sugar and Kumar (2002) developed coordinated control of mobile manipulators transporting a shared object. In agriculture, Kayacan et al. (2015) implemented robust tube-based decentralized nonlinear model predictive control for an articulated tractor–trailer system, with nonlinear moving-horizon estimation supplying state and slip-parameter estimates and a tube-based correction addressing discrepancies between the nominal model and the physical system; the controller was tested on a bumpy grass field. Physical coupling and practical model discrepancies are therefore existing research topics, although the system layouts and control objectives differ from those of a WSIC.

Practical implementation factors are also addressed explicitly in cooperative control. Ploeg et al. (2011) analyzed communication delay and string stability and experimentally evaluated cooperative adaptive cruise control. The agricultural and industrial studies above address sensor disturbances and heading drift (Harik, 2023; Zhang et al., 2016), uncertain parameters and model discrepancies (Kayacan et al., 2015), sensor-data losses and actuator-output limits (Peng et al., 2025), and mechanism calibration and vehicle inclination (Jeon et al., 2025). The present work represents relevant sensing, timing, actuation, and modelling effects in simulation (Section 4.1.4), and physically evaluates coordinated tracking on the connected small-scale platform.

The coupled vehicle–truss–vehicle configuration of the WSIC, with its side-by-side supporting vehicles, adjustable spacing, and path-coordinate synchronization, is the case addressed in the remainder of this thesis.

2.2 Positioning of Mobile Robots and Vehicles

Positioning, or localization, estimates a vehicle's position and orientation within a reference coordinate system and provides the state information required for path planning, tracking, and motion control. Agricultural vehicles must operate despite uneven terrain, vibration, wheel slip, and occasional degradation of satellite signals. Positioning accuracy and continuity are therefore important to autonomous field operation, as discussed by Qu et al. (2024) and Nijak et al. (2024).

Agricultural positioning and guidance employ GNSS, vision, LiDAR, inertial sensing, and combinations of these technologies. Vision-based approaches can exploit crop rows or nursery-bed geometry: Shi et al. (2023) reviewed row-detection methods, and Shabani et al. (2025) developed stereo-vision guidance for a ground vehicle in bareroot forest nurseries. The following discussion focuses on GNSS and its use with inertial measurements for the predefined-trajectory WSIC application, while retaining relevant comparisons with broader sensor-fusion approaches.

2.2.1 Global Navigation Satellite Systems

GNSS provides globally referenced positioning for agricultural guidance. Where an application requires greater accuracy than standalone positioning can provide, differential correction methods, particularly RTK-GNSS, are used. Radicioni et al. (2022) investigated multi-constellation network RTK for automatic guidance, while Esau et al. (2021) evaluated GNSS-based autosteer during low-speed wild blueberry harvesting on rough terrain. These studies connect positioning technology to practical machinery-guidance requirements.

GNSS performance depends on signal availability and measurement quality. Blockage, multipath, and interference can degrade positioning, motivating methods that improve the navigation estimate when satellite measurements become unreliable (Huang et al., 2022). The issue is therefore not simply nominal positioning accuracy, but also the continuity and consistency of the state information supplied to the controller.

One approach uses additional information without adding inertial sensors. Cui et al. (2024) combined dual-antenna RTK with a context-constrained Kalman filter, using straight-path geometry and tracking-error information as pseudo-measurements. Their method improved positioning under degraded RTK conditions without external sensors. This is a constraint-aided GNSS method, distinct from the GNSS–inertial integration considered below.

2.2.2 Integrated Global Navigation Satellite System–Inertial Positioning

Integrated GNSS–inertial positioning combines globally referenced satellite updates with high-rate gyroscope and accelerometer measurements for motion and attitude estimation. Inertial integration accumulates errors from sensor bias and noise, so the IMU is used here as a complementary sensing component, not as a standalone source of sustained absolute positioning. GNSS measurements update the navigation estimate and help constrain accumulated inertial error (Yin et al., 2023; Zhang et al., 2021).

Agricultural applications demonstrate this complementary use of sensors. Nagasaka et al. (2009) developed an autonomous rice transplanter guided by GPS and an IMU, while Vieira et al. (2022) combined an IMU with two RTK-GPS receivers for positioning and attitude determination. These examples establish the relevance of combined position and attitude information to agricultural guidance.

The estimation method determines how the available measurements and their uncertainties are combined. Li et al. (2021) proposed fuzzy adaptive finite impulse response Kalman filtering for GNSS/IMU-integrated agricultural navigation. In a vehicle-localization simulation study, Yin et al. (2023) combined an error-state Kalman filter with segmented Rauch–Tung–Striebel smoothing to assess localization under altered GNSS measurement errors. These studies illustrate distinct estimation strategies for combining position and attitude information.

Auxiliary information and operating conditions also affect performance. Zhang et al. (2021) evaluated low-end inertial sensing with RTK, non-holonomic constraints, and dual-antenna GNSS on wet and dry soils. During GNSS outages, the benefit of the motion constraints depended on the soil conditions, and dual-antenna aiding did not by itself eliminate position drift. This illustrates why integrated positioning must be assessed in relation to the available measurements and operating conditions, rather than assumed to retain its nominal accuracy throughout a satellite outage.

Further agricultural implementations connect integrated positioning to operational tasks. Huang et al. (2022) implemented Kalman-filter-based RTK-BeiDou Navigation Satellite System/inertial navigation system (RTK-BDS/INS) integration and evaluated it on routes with differing signal conditions. Jing et al. (2023) applied GNSS/INS positioning in an automatic navigation land levelling system. Liu and Nguyen (2024) compared an error-state Kalman filter combining RTK-GNSS, IMU, and wheel odometry with a LiDAR–inertial smoothing-and-mapping approach in unstructured farm environments. This comparison explicitly links the choice of sensors and estimator to localization performance and system cost.

Vision can also contribute directly to vehicle localization. Cremona et al. (2024) integrated GNSS measurements into a stereo-inertial SLAM framework for arable farming, demonstrating an alternative that combines global positioning with visual and inertial information. The appropriate architecture depends on the sensing requirements and the intended operating environment.

For the WSIC studied in this thesis, RTK-GPS and IMUs provide the position, attitude, and motion information required for tracking predefined paths and coordinating the supporting vehicles. This established sensing arrangement supports the development and experimental evaluation of the coupled vehicle–truss control strategy. The sensor specifications and implementation are described in Sections 4.1.4 and 5.1.2. Broader visual or LiDAR-based fusion remains a possible extension for operating conditions beyond the present study's scope.

2.3 Motion Control of Wheeled Mobile Robots and Vehicles

Motion control converts a reference path and speed command into steering and propulsion actions. For an agricultural vehicle, the design must account for the available actuators, the relationship between vehicle motion and implement loading, and the accuracy of the measured states. For a WSIC, it must also coordinate the two supporting vehicles through their shared truss. The relevant design question is therefore not which algorithm is universally best, but which combination of model, feedback law, and control architecture addresses these requirements.

These three choices should be distinguished. A kinematic or dynamic model describes the controlled motion; PID, sliding mode control (SMC), and MPC specify how control actions are generated; and a centralized or hierarchical architecture determines how the control tasks interact. MPC, for example, can use a kinematic model or a force-based dynamic model. Similarly, estimation and robustness mechanisms can be added to either model class (Graf Plessen and Bemporad, 2017; Kayacan et al., 2015). The following review separates steering configurations from control methods and then relates their advantages and limitations to the proposed WSIC strategy.

2.3.1 Steering and Drive Configurations

Front-wheel steering (FWS) provides directional control through the front axle, while rear-wheel drive (RWD) supplies propulsion through the rear axle. This conventional tractor arrangement offers a comparatively simple mechanical layout (Díaz Lankenau and Winter, 2019). Under the ideal rolling assumption, Ackermann steering geometry gives different inner- and outer-wheel angles consistent with a common instantaneous turning centre. It reduces the geometric incompatibility of wheel paths during a turn, but does not eliminate lateral tire deformation, slip, or soil-dependent steering forces (Rajamani, 2012).

Assigning steering and propulsion to different axles does not make their dynamics independent. Forward speed affects yaw response and lateral acceleration, while longitudinal tire forces and axle loading influence the lateral forces available for guidance. Pearson and Bevly (2007) modelled and validated the effect of hitch loading on tractor yaw dynamics, illustrating why an implement can alter steering behaviour. For a WSIC, the analogous control-design issue is the influence of forces transmitted through the truss. The choice of FWS/RWD therefore provides a practical actuation arrangement, not evidence that coupled dynamics can be omitted.

Four-wheel steering provides additional directional authority. Opposite-phase front and rear steering can reduce the turning radius at low speed, but requires coordination of additional actuators and wheel-angle measurements. Xu et al. (2021) developed an independently steered agricultural platform using electric linear actuators and a fuzzy PID controller. This illustrates the connection between steering-mechanism design and feedback control, rather than establishing that four-wheel steering is always preferable. Differential wheel forces offer another means of producing yaw motion; their usefulness depends on drive authority and tire–ground interaction, and they should not be treated as equivalent to a steerable-axle configuration (Rajamani, 2012).

The WSIC platform considered here uses FWS and RWD as its basic experimental configuration. Most simulation scenarios use front-wheel steering, while rear-wheel steering is used for the reverse-direction scenarios. Consequently, the controller must be formulated for the active steering axle and direction of travel. The configuration comparison motivates a manageable experimental platform; the comparison of feedback methods below addresses how its tracking and coordination objectives are achieved.

2.3.2 Path Following, Dynamic Modelling, and Control Strategies

2.3.2.1 Model Fidelity and Operating Conditions

A kinematic vehicle model relates position and heading changes to speed, steering angle, and vehicle geometry without resolving the underlying force balances. Its relatively small state and parameter set is attractive for low-speed guidance when the assumed rolling behaviour is adequate. A dynamic model adds effects such as yaw inertia, lateral velocity, and tire forces, allowing the controller to represent transient responses and external loading. This additional detail introduces identification and estimation requirements: uncertain tire characteristics or implement forces can reduce the benefit of a more elaborate prediction model. Model choice should therefore reflect both the operating regime and the information available for calibration, rather than a presumption that a dynamic formulation always improves tracking (Kong et al., 2015; Rajamani, 2012).

Kinematic control is not synonymous with ignoring all practical effects. Graf Plessen and Bemporad (2017) used a kinematic bicycle model within constrained linear time-varying (LTV) MPC for agricultural machines and discussed an extension for slip. For the present WSIC, the motivation for a dynamic model is more specific: to represent how vehicle motion and truss-transmitted forces interact during tracking and synchronization. Its value must be assessed through the model assumptions and the resulting closed-loop performance.

2.3.2.2 Geometric Path Following

Pure pursuit selects a point ahead on the reference path and commands the curvature of an arc connecting the vehicle to that point. The steering command depends on the wheelbase, look-ahead distance, and relative direction of the target, so the controller requires little online computation. Its main tuning trade-off is the look-ahead distance: a short distance gives a more responsive correction but can produce oscillatory steering, whereas a longer distance smooths the response but can increase corner cutting. The basic law does not explicitly predict tire-force transients or jointly enforce steering-magnitude and steering-rate constraints; these require additional compensation or limiting logic (Snider, 2009).

He et al. (2025) extended pure pursuit for automatic tractor navigation by incorporating drive-wheel lateral-deviation compensation. This provides a recent agricultural example of augmenting geometric tracking with a targeted correction mechanism. The added compensation is part of the controller and should be distinguished from the unmodified pure-pursuit law. Geometric control is therefore a useful low-complexity baseline for WSIC guidance, but a separate mechanism is still needed to regulate inter-vehicle synchronization.

2.3.2.3 Proportional–Integral–Derivative and Fuzzy Proportional–Integral–Derivative Control

PID control combines proportional action on the current error, integral action on accumulated error, and derivative action on its rate of change. Its low computational demand and directly tunable gains make it attractive for velocity regulation and actuator-level loops. Integral action can remove persistent error when the closed loop remains stable and sufficient actuation is available. However, fixed gains may not preserve the same response across changing loads and speeds; derivative action can amplify measurement noise, and saturation can cause integral windup. Filtering, gain selection, and saturation management are consequently implementation requirements rather than automatic properties of PID (Åström and Hägglund, 2001).

Practical applications can address these limitations without replacing PID entirely. Peng et al. (2023) used PI control with speed-dependent steering gain and control saturation for a tracked bulldozer. Xu et al. (2021) adjusted PID gains through fuzzy rules for agricultural steering and evaluated straight-line tracking experimentally on a flat road. Fuzzy adaptation provides a way to encode operating-dependent corrections, but introduces membership-function and rule-base choices; favourable performance in the tested regime does not establish stability for every combination of rules and operating conditions. These examples also distinguish path-level control from the lower-level actuator loop that executes a steering command.

2.3.2.4 Sliding Mode and Frequency-Domain Robust Control

SMC defines an error combination, or sliding variable, and drives the system towards the corresponding surface using a switching or higher-order control law. This provides a mechanism for rejecting disturbances that satisfy the controller's structural and boundedness assumptions. The associated difficulty is chattering: rapid control variation can interact with sampling, measurement noise, and actuator bandwidth. Increasing a switching gain is therefore not a cost-free improvement in robustness. Smoothing and higher-order formulations can reduce control oscillation, but alter the required assumptions and tuning. Matveev et al. (2013) explicitly considered sliding and control saturation in agricultural tractor guidance, demonstrating that constraints are not exclusive to MPC.

Ding et al. (2022) developed output-feedback SMC for agricultural path tracking with unknown bounded disturbances. A robust exact differentiator reconstructed the required states and estimated a lumped perturbation; a second-order controller based on a modified adding-a-power-integrator technique improved the error response and reduced chattering in simulation. The contribution is thus an estimator–controller combination with stated assumptions, not a general guarantee that any sliding mode law rejects arbitrary soil disturbances. For WSIC application, the available measurements, disturbance representation, and steering-rate limits would need to be matched to the chosen SMC formulation.

Frequency-domain robust control takes a different approach. H_2 design targets an energy-based performance measure, whereas H_∞ design limits the worst-case disturbance-to-performance gain of a specified model. Legrand et al. (2022) applied an H_2/H_∞ framework to an off-road vehicle with two steering axles on slippery, sloping soils. Such synthesis can move much of the design computation offline, but its guarantees depend on the selected model, uncertainty description, and weighting functions. Hard actuator-magnitude and rate limits need separate treatment when they are not included in the synthesis. These methods offer useful alternatives when disturbance attenuation is the primary objective; MPC instead makes finite-horizon tracking and explicit operating constraints central to the online calculation.

2.3.2.5 Predictive Control: Constraints, Computation, and Uncertainty

At each update, MPC predicts the response to a sequence of candidate inputs, minimizes a finite-horizon objective, and applies only the first input before repeating the calculation with new state information. Tracking-error weights determine the relative priority of lateral and orientation errors, while penalties on input magnitude or changes balance accuracy against control activity. Steering-angle and steering-rate limits can be imposed within the optimization rather than applied only after an unconstrained command has been calculated. This combination is particularly useful when rapid path correction would otherwise demand infeasible steering. A longer horizon permits earlier response to upcoming curvature but increases problem size. Sampling time sets the prediction resolution and, together with the horizon length, the physical preview interval; error scaling and weights determine the numerical balance between different tracking objectives (Rawlings et al., 2017).

The prediction model determines an important implementation trade-off. With linear time-varying models, quadratic objectives, and linear constraints, the optimization can be formulated as a quadratic program. Repeated linearization accommodates changing operating points, but local approximation errors can increase during large departures from the predicted motion. Nonlinear MPC retains nonlinear equations within the prediction, at the cost of a more demanding and generally non-convex optimization. Falcone et al. (2007) compared nonlinear and successive-linearization predictive steering designs, including slippery-road experiments. Graf Plessen and Bemporad (2017) combined reference-trajectory smoothing with constrained LTV-MPC for agricultural machines. Neither study implies that MPC must use a force-based dynamic model or that increasing model complexity necessarily improves a particular implementation.

Nominal MPC, adaptive MPC, and robust MPC also have different meanings. Updating weights changes the control priorities; updating model parameters changes the predicted response. Neither operation alone supplies a robustness guarantee. In tube-based MPC, a nominal prediction is combined with corrective feedback and constraint margins to account for bounded deviations. Kayacan et al. (2015) implemented a robust decentralized nonlinear MPC scheme with moving-horizon state and slip-parameter estimation on an articulated tractor–trailer. Their model remained kinematic, and experiments on a bumpy grass field demonstrated the combined estimation and control approach. The practical trade-off is the extra uncertainty characterization and constraint reserve required by robust design. Likewise, feasibility and stability of a nominal MPC require suitable formulation and assumptions, not simply the presence of a receding horizon (Rawlings et al., 2017).

2.3.2.6 Adaptive, Learning-Based, and Integrated Approaches

Data-based adaptation should be distinguished from force-based modelling. Zhang et al. (2024) developed model-free adaptive tractor control using preview heading deviation, with simulation comparisons against PID and pure pursuit and a real-vehicle comparison against PID. This reduces reliance on a prescribed physical prediction model, but the controller still requires suitable measurements and adaptation settings. For a truss-coupled WSIC, successful application to one tractor does not itself provide a representation of the shared-load interaction; the coordination problem must be formulated separately.

Learning MPC for iterative tasks addresses another problem. Rosolia and Borrelli (2018) used successful previous trajectories to construct a terminal safe set and a cost-to-go approximation, improving repeated-task performance under their assumptions. This is different from identifying a generic model-mismatch correction online. Repeated field operations could provide relevant experience for such a method, but changes in soil conditions, loading, or path geometry would require assessment of how the stored data and associated feasibility assumptions transfer.

Integration can occur at several levels. Lu et al. (2024) combined Hybrid A* planning with MPC-based tracking and evaluated the framework in simulations using farm datasets. This planning–tracking hierarchy should be distinguished from jointly optimizing lateral and longitudinal actuation. Falcone et al. (2008), for example, combined front steering and braking to address yaw and lateral stabilization. Joint actuation can coordinate competing demands on tire forces, but enlarges the control-design and optimization problem. A separated architecture instead offers modular tuning, while requiring the interactions between its loops to be represented or managed. These are alternative allocations of control tasks, not a universal ranking of integrated and separated control.

For WSIC design, the literature therefore supports comparison along four practical dimensions: the states and parameters required by the model; the treatment of disturbances and input limits; the online computational burden; and the mechanism for coordinating coupled motion. Table 2.1 condenses the preceding discussion along these dimensions, listing for each control approach its operating mechanism and principal advantage, the limitation that must be managed in implementation, and the resulting implication for a truss-coupled WSIC. The comparison is qualitative by design: published numerical errors should be interpreted within each study’s vehicle, path, speed, sensing, and validation conditions, rather than used to rank unrelated algorithms across experiments. Section 2.3.3 applies these distinctions to the control architecture selected for this thesis.

Table 2.1 Comparison of path-tracking control approaches and their implications for the WSIC

Approach	Mechanism and principal advantage	Principal limitation	Implication for the WSIC
Pure pursuit (geometric)	Look-ahead geometry gives a direct steering command with little computation.	Look-ahead distance trades responsiveness against smoothness; the basic law does not predict tire-force transients or jointly enforce steering-magnitude and steering-rate limits.	Useful low-complexity baseline; inter-vehicle synchronization and actuator-limit management remain separate tasks.
PID and fuzzy PID	Error feedback; integral action can remove persistent mismatch when stable and unsaturated; fuzzy rules adjust gains.	Sensitivity to loads and speed, derivative noise, possible windup under saturation, and rule-base tuning and stability requirements.	Practical velocity and actuator-level loop; not a complete formation-control law.
Sliding mode control	Drives an error combination to a sliding surface; rejects perturbations that satisfy its structural and boundedness assumptions.	Chattering interacts with sampling, noise, and actuator bandwidth; observer and measurement requirements; assumptions must hold for the plant.	A valid robust alternative if its disturbance representation and steering-limit treatment are matched to the WSIC plant.
$H_2/H\infty$ robust control	Offline frequency-domain shaping of performance and worst-case disturbance gain.	Guarantees depend on the selected model, uncertainty description, and weighting functions; hard magnitude and rate limits need separate treatment.	Emphasizes disturbance attenuation rather than online constrained prediction of steering.
LTV or nonlinear MPC	Predicts the multi-state response and optimizes tracking and inputs subject to explicit constraints.	Model fidelity, state estimates, horizon and weight selection, solver time, and feasibility.	Directly matches the steering-prediction and steering-magnitude/rate-limit requirements.
Robust or adaptive MPC	Feedback margins (tube) or updated model parameters or weights, addressing different design objectives.	Robust margins require uncertainty bounds; updating weights or parameters alone provides no robustness guarantee.	Keeps the adaptive weighting used in this thesis distinct from tube-based control and online identification.
Model-free adaptive control; learning MPC	Model-free adaptation uses measured input–output behaviour. Learning MPC retains a prediction model and uses successful trajectories for terminal safe sets and cost estimates.	Different measurement, model, adaptation, and stored-data requirements; applicability depends on each method’s assumptions.	Both require a WSIC coordination formulation; learning MPC is not model-free merely because it learns from prior runs.

2.3.3 Justification of the Proposed Control Strategy

The proposed WSIC architecture combines dynamic-model-based steering MPC, PID longitudinal-velocity regulation, and a path-coordinate synchronization law. This choice allocates prediction and explicit steering constraints to the lateral-control task, while retaining a direct feedback loop for velocity and a dedicated coordination mechanism between vehicles. It is motivated by the requirements of the coupled platform rather than by a claim that MPC–PID is inherently superior to every alternative.

Steering control must reduce lateral and orientation errors while respecting steering-angle and steering-rate limits. The incremental MPC formulation makes steering changes an explicit optimization variable and uses the vehicle model to predict their effect on the tracking states. Compared with a basic geometric or PID steering law, this permits the controller to balance several predicted error components and actuator limits in one calculation. The dynamic formulation additionally represents yaw and lateral-motion effects relevant to implement loading. Adaptive weighting changes the emphasis on lateral convergence and heading stabilization with operating condition and travel direction. Here, weight adaptation is a means of adjusting the objective, not a claim of online identification of tire parameters or robust constraint satisfaction under arbitrary uncertainty.

The longitudinal PID loop regulates velocity relative to the command supplied by the guidance and synchronization layers. Its integral component addresses persistent velocity mismatch, while its small number of gains allows the speed response to be tuned without adding a longitudinal input sequence to the steering optimization. This is a practical allocation when the required speeds and accelerations remain achievable. Its limitation is that it does not jointly optimize future steering and propulsion; saturation management remains a separate implementation consideration. The adequacy of the velocity loop must therefore be assessed together with the simulated actuator limits and measured tracking response, rather than inferred from its simplicity (Åström and Hägglund, 2001).

There are related precedents for this allocation of control tasks. Kayacan et al. (2015) combined predictive steering control with lower-level PI steering loops and cascaded PID speed control on their agricultural tractor–trailer platform. Chen et al. (2020) combined MPC steering with PID-generated longitudinal wheel torque and a friction-constrained speed profile, evaluating the design through simulation. These studies support the compatibility of predictive guidance and PID regulation, while using different vehicle models and coordination objectives from the WSIC.

Separating the control channels does not remove their physical coupling. Forward speed affects lateral motion, and the common truss transmits forces between the vehicles. Luo (2017) already used a path-coordinate offset and a first-order synchronization law based on straight-path progression. The present formulation uses curvature-dependent path-coordinate progression within the adjoint-curve framework and integrates the resulting follower-velocity command with predictive steering and PID regulation. Its first-order error dynamics and Lyapunov analysis concern the synchronization law, not a general proof for the complete constrained MPC–PID system.

A fully integrated nonlinear MPC could coordinate steering and propulsion when combined tire-force demands or large velocity changes dominate performance. Robust SMC or $H_2/H\infty$ control would emphasize disturbance rejection, while model-free adaptation or learning MPC would introduce different data and tuning requirements. The chosen architecture instead prioritizes constrained steering prediction, transparent speed-loop tuning, and explicit WSIC synchronization within an implementable framework. Its comparison with unified MPC in Chapter 4 evaluates the complete implementations: adaptive steering weights in the combined controller and fixed Q and R in the unified controller. The comparison therefore assesses the selected design as a whole, rather than isolating decoupling or presupposing a computational advantage. Together, the coupled model, incremental predictive steering, and synchronization design establish the system-specific basis for the simulation and experimental evaluation that follow.

2.4 Novelty Relative to Prior Art

The reviewed literature provides established methods for navigation, vehicle control, and multi-vehicle coordination. The contribution here is their WSIC-specific integration with a dynamic formulation of supporting-vehicle motion and truss-transmitted loads, followed by comparative simulations and connected-platform experiments.

Relative to Luo's (2017) kinematic WSIC framework, the present model explicitly represents tire–ground interaction, yaw dynamics, and implement-force and moment effects while retaining a flat-terrain assumption. Luo already considered curved path following and first-order synchronization; the extension concerns the curvature-dependent coordination formulation, its integration with dynamic-model-based MPC–PID control, and validation with a physical connecting truss. Table 1.1 summarizes the comparison. The unified-MPC benchmark additionally compares complete controller implementations with different weighting strategies, rather than isolating decoupling alone.

Formation and convoy methods such as those of Van Parys and Pipeleers (2017) and Cook et al. (2018) provide relevant coordination principles. Mechanically coupled systems are also established, including shared-object transport (Sugar and Kumar, 2002) and agricultural tractor–

trailer control (Kayacan et al., 2015). Adapting these ideas to a WSIC requires its side-by-side support geometry, shared implement loads, sliding-span limits, and synchronization relationships to be represented explicitly. The present work addresses these requirements through its integrated modelling and control design; Sections 1.4 and 2.3.3 state the contributions and design rationale.

Chapter 3

Methodology

This chapter develops the methodology for autonomous WSIC guidance by combining supporting-vehicle dynamics, truss-load transmission, path-tracking geometry, and steering, velocity, and synchronization control. Luo (2017) provides the WSIC-specific kinematic benchmark: his formulation includes path-coordinate tracking and first-order offset regulation, while his experimental robots operated without a connecting truss. Building on that work and the single-vehicle force formulation of Dai and Katupitiya (2014), the present research integrates tire–ground interaction and transmitted implement loads with coordinated control of the connected platform. The supporting vehicles retain their dynamic equations; the connecting truss, carriage, and implement are represented through quasi-static load transmission rather than independent inertial equations. The resulting framework enables the two supporting vehicles to follow their reference paths while regulating their relative motion.

3.1 Dynamic Model

3.1.1 Mechanism Analysis

The schematic diagram of the WSIC mechanism is shown in Figure 3.1.

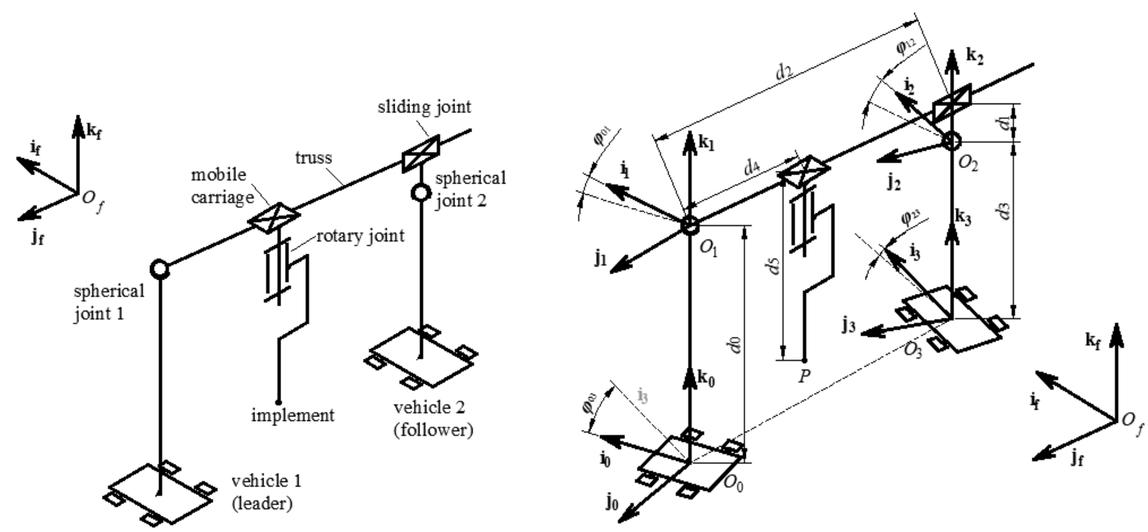

(a) (b)

Figure 3.1 Schematic diagram of the WSIC mechanism

A WSIC consists of two supporting vehicles connected by a truss. At the leader end, the truss is attached to vehicle 1 through a spherical joint (spherical joint 1), permitting free rotation about the vertical axis and restrained rotation about the two horizontal axes. At the follower end, a sliding joint allows the follower attachment point to translate along the truss, accommodating varying bog widths and the transport mode. A second spherical joint (spherical joint 2) connects that sliding point to vehicle 2, with the same rotational characteristics as spherical joint 1. A mobile carriage is mounted on the truss through an additional, separate sliding joint to carry the implement; it is a branch of the mechanism and does not affect the relative mobility of the two vehicles. The implement is attached to the mobile carriage through a revolute joint about the vertical axis, which keeps the implement facing the direction of travel of the path; this joint carries only the implement and transmits the external force and the associated moment from the implement to the truss through the carriage, so it does not alter the rotary-prismatic-rotary (RPR) analysis of the vehicle–truss–vehicle chain that follows.

On the physical prototype, the pitch and roll rotations at both spherical joints are spring-restrained to limit fore-and-aft and side-to-side tilting of the truss relative to each vehicle, while yaw rotation is unrestrained. This chapter develops the dynamic model of the WSIC mechanism, beginning with the kinematic description below; the kinematic description assumes flat-terrain operation and neglects pitch and roll displacement at both spherical joints. The force and moment assumptions for load transmission are stated separately in Section 3.1.3. Each reference frame is defined with its vertical (**k**) axis aligned with the global vertical, so $\mathbf{k}_0 = \mathbf{k}_1 = \mathbf{k}_2 = \mathbf{k}_3$. Under this assumption, each spherical joint reduces kinematically to a single revolute joint about the vertical axis, and the mechanism reduces to a planar chain. The frames and joint variables defined here are used both for the position and orientation relations in this section and for the free-body diagrams and moment-balance equations developed later in this chapter:

- $\{O_f; \mathbf{i}_f, \mathbf{j}_f, \mathbf{k}_f\}$: absolute (fixed) reference frame on the ground
- $\{O_0; \mathbf{i}_0, \mathbf{j}_0, \mathbf{k}_0\}$: moving frame attached to vehicle 1 (leader vehicle)
- $\{\mathrm{O}_1; \mathbf{i}_1, \mathbf{j}_1, \mathbf{k}_1\}$: moving frame attached to the truss at spherical joint 1 (leader end)
- $\{O_2; \mathbf{i}_2, \mathbf{j}_2, \mathbf{k}_2\}$: moving frame attached to the sliding joint (follower attachment point)
- $\{\mathrm{O}_3; \mathbf{i}_3, \mathbf{j}_3, \mathbf{k}_3\}$: moving frame attached to vehicle 2 (follower vehicle)
- φ_{01}: yaw angle between $\mathbf{i}_0$ and $\mathbf{i}_1$, at spherical joint 1 (leader-end joint variable), rad
- φ_{12}: yaw angle between $\mathbf{i}_1$ and $\mathbf{i}_2$, rad. In this study, $\varphi_{12} = 0$. Frames $\{O_1\}$ and $\{O_2\}$ share the same orientation ($\mathbf{i}_2 \parallel \mathbf{i}_1$, $\mathbf{j}_2 \parallel \mathbf{j}_1$, $\mathbf{k}_2 \parallel \mathbf{k}_1$); they differ only in position
- φ_{23}: yaw angle between $\mathbf{i}_2$ and $\mathbf{i}_3$ at spherical joint 2 (follower-end joint variable), rad

- φ_{03}: relative yaw orientation between vehicle 1 and vehicle 2, $\varphi_{03} = \varphi_{01} + \varphi_{12} + \varphi_{23}$, rad
- d_0: distance between O_0 and O_1 along $\mathbf{k}_0$, $d_0 = d_1 + d_3$, m
- d_1: fixed distance between the sliding joint's location on the truss and O_2 (centre of spherical joint 2), along $\mathbf{k}_1$, m. A geometric constant of the follower attachment hardware, not a joint variable ($d_1 = 0$ if spherical joint 2 is mounted directly at the slider)
- d_2: distance between O_1 and O_2 along $\mathbf{j}_1$ (distance between the two vehicles' attachment points), m
- d_3: distance between O_2 and O_3 along $\mathbf{k}_3$, m
- d_4: position of the implement on the truss, measured from O_1 opposite to $\mathbf{j}_1$, m
- d_5: vertical distance from the truss reference axis to the line of action of the resultant external (draft) force applied to the mobile carriage through the implement. The line of action generally lies at ground level, so d_5 depends on the implement in use and the agricultural operation; it is an implement-specific constant for a given operation and is treated as fixed in this study, m

Let ${}^{i-1}_{i}T$ (i = 1, 2, 3) denote the homogeneous transformation matrices between consecutive frames, given in

$$
\begin{aligned}
{}^{0}_{1}T &= \begin{bmatrix} \cos\varphi_{01} & -\sin\varphi_{01} & 0 & 0 \\ \sin\varphi_{01} & \cos\varphi_{01} & 0 & 0 \\ 0 & 0 & 1 & d_0 \\ 0 & 0 & 0 & 1 \end{bmatrix} \\
{}^{1}_{2}T &= \begin{bmatrix} 1 & 0 & 0 & 0 \\ 0 & 1 & 0 & -d_2 \\ 0 & 0 & 1 & -d_1 \\ 0 & 0 & 0 & 1 \end{bmatrix} \\
{}^{2}_{3}T &= \begin{bmatrix} \cos\varphi_{23} & -\sin\varphi_{23} & 0 & 0 \\ \sin\varphi_{23} & \cos\varphi_{23} & 0 & 0 \\ 0 & 0 & 1 & -d_3 \\ 0 & 0 & 0 & 1 \end{bmatrix}
\end{aligned}
\tag{1}
$$

The position of the implement expressed in the leader vehicle frame $\{O_0; \mathbf{i}_0, \mathbf{j}_0, \mathbf{k}_0\}$ can be obtained as follows:

$$
{}^{0}P = [d_4 \sin\varphi_{01} \quad -d_4\cos\varphi_{01} \quad d_0 - d_5 \quad 1]^T \tag{2}
$$

The mobility count below is made relative to vehicle 1, which is the reference link for the linkage analysis. It includes the carriage slide but excludes the separate implement-heading branch. The degrees of freedom (DOF) of the linkage are determined using the Grübler–Kutzbach criterion (Grübler, 1883; Kutzbach, 1929). Treating each spherical joint as a full 3-DOF joint and including the mobile carriage as an additional branch mounted on the truss through its own prismatic joint (the implement and its vertical-axis revolute joint on the carriage form a further branch whose single degree of freedom, the implement heading, does not enter the relative pose of the vehicles and is excluded from the count), the mechanism has $N_{\text{link}} = 5$ links (vehicle 1, truss, sliding block, vehicle 2, mobile carriage) and $N_{\text{joint}} = 4$ joints, spherical, prismatic, spherical, prismatic, with DOF of joint $f_1 = 3, f_2 = 1, f_3 = 3, f_4 = 1$. The DOF is then calculated as

$$\mathrm{DOF} = 6(N_{\text{link}} - 1) - \sum_{i=1}^{N_{\text{joint}}} (6 - f_i) = 6(5-1) - (3+5+3+5) = 8 \tag{3}$$

The DOF of the mechanism is 8. Under the flat-terrain assumption, each spherical joint reduces to a single revolute ($f = 1$), while the carriage's prismatic joint is unaffected, and the mechanism reduces to a planar chain with DOF = 4, matching the four joint variables φ_{01}, d_2, φ_{23} and d_4 used throughout the remainder of this chapter.

Vehicle 1 and vehicle 2 are the two supporting rigid bodies whose relative motion is of interest. The truss, span slider, and carriage are additional links included in the stated mobility count. The open-chain joint coordinates describe the follower pose relative to the leader, while the carriage coordinate locates the implement along the truss. Joint-travel limits restrict the usable range of motion. Wheel–ground rolling conditions are considered separately from this linkage count.

The mechanism admits three independent generalized coordinates governing the relative pose between the two vehicles, φ_{01}, d_2 and φ_{23}; the carriage position d_4 does not enter this relative pose, since it locates only the implement. Let the poses of the leader and follower vehicles be T_L, $T_F \in$ SE(2). The relative transformation is defined as $T_{FL} = T_L^{-1} T_F$. The RPR chain defines a nonlinear mapping between joint coordinates and relative pose. Because planar rotations in SO(2) commute, this nonlinearity does not arise from noncommutativity as in the general spatial case, but from the coupling between rotation and translation along the chain: each translational term depends on the sine and cosine of the upstream joint angles:

$$T_{FL} = T_{FL}(\chi), \quad \chi = [\varphi_{01}, d_2, \varphi_{23}]^T \tag{4}$$

Using the framework of screw theory (Murray et al., 1994), the relative twist of the follower vehicle with respect to the leader vehicle is

$$V_{FL} = \begin{bmatrix} w_{FL} \\ v_{FL} \end{bmatrix} \in \mathbb{R}^3 \tag{5}$$

The differential kinematics are as follows:

$$V_{FL} = J_{FL}(\chi)\dot{\chi} \tag{6}$$

where $J_{FL}(\chi) \in \mathbb{R}^{3\times3}$ is the geometric Jacobian and its columns are the joint screws expressed in a common reference frame. Its rank describes the local relationship between joint rates and relative vehicle motion. The number of joint coordinates alone does not establish the rank at every configuration. A kinematic singularity is characterized by loss of rank:

$$\det\left(J_{FL}(\chi)\right) = 0 \tag{7}$$

At a singular configuration, the mapping from joint rates to relative vehicle motion loses rank. This geometric condition concerns the local linkage mapping; it is distinct from a closed-loop stability or controllability result. The usable joint ranges and the actuation arrangement must therefore be considered when interpreting the mechanism analysis.

Under an ideal rolling assumption, each vehicle is subject to a constraint of the form

$$A_L V_L = 0, \quad A_F V_F = 0 \tag{8}$$

where V_L, $V_F \in \mathbb{R}^3$ are the planar twists of the leader and follower vehicles expressed in their respective body frames, and A_L, $A_F \in \mathbb{R}^{1\times3}$ are the corresponding non-holonomic constraint rows. When the vehicles are coupled through the RPR linkage, the vehicle twists V_L and V_F are no longer independent: the admissible motion must simultaneously satisfy the linkage's differential kinematics and each vehicle's rolling constraint:

$$V_{FL} = J_{FL}(\chi)\dot{\chi} \quad \text{and} \quad A_L, A_F \tag{9}$$

The linkage relations and ideal rolling conditions together describe compatible instantaneous motions under the corresponding assumptions. The force-based model in the following sections additionally represents wheel slip and transmitted loads. The mechanism analysis establishes the geometric context for coordination rather than a separate proof of closed-loop controllability.

The two supporting vehicles have separate steering and propulsion control loops, but they remain connected through the truss. The controller design must therefore address each vehicle's path tracking together with relative progress, support spacing, and the effects of transmitted loads. Separate control channels do not imply mechanical decoupling. The linkage analysis provides the physical context for the coordinated vehicle model and control architecture developed in the following sections.

3.1.2 Supporting Vehicles Modelling

The supporting vehicles are subjected to external forces and moments in both the horizontal and vertical planes, including lateral tire forces, tractive forces, soil reactions, rolling resistance, vertical wheel loads, and driving torques. In the WSIC system, the truss is additionally subjected to gravitational load and to loads transferred from the implement through the mobile carriage.

Luo (2017) modelled each supporting vehicle using a path-coordinate bicycle model with a virtual rear-wheel reference point. Figure 3.2, redrawn after Luo (2017) using the notation of the present study, illustrates this kinematic formulation and is included for comparison with the dynamic vehicle model adopted in this thesis. The wheelbase l and the rear-axle reference point are specific to the bicycle model; the remaining quantities (δ, θ, θ_p, θ_r, l_e, v_l, s, Γ_{Om}) are defined in Sections 3.1 and 3.2.

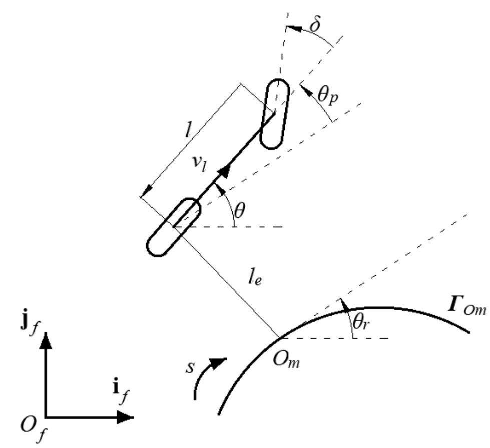

Figure 3.2 Path-coordinate bicycle model of Luo (2017), redrawn with the notation of this thesis

Dai and Katupitiya (2014) developed a force-based model of a four-wheel-steered, four-wheel-driven vehicle that relates wheel-force directions and slip to planar vehicle motion. This model provides the single-vehicle modelling basis adopted in the present study. The WSIC formulation extends this basis by incorporating the forces and moments transmitted between the connecting truss and each supporting vehicle. Because the two supporting vehicles have different truss attachments, the transmitted loads are determined according to the attachment arrangement of each vehicle rather than assumed to be identical at the two supports. The wheel-force model used for the present supporting vehicles is shown in Figure 3.3. Relative to Figure 3.2, the present model (Figure 3.3) replaces the virtual rear-wheel point by the vehicle centre of gravity, replaces the pure-rolling constraint by tire lateral and longitudinal slip, and adds the truss-transmitted forces and moments described in Section 3.1.3; the flat-terrain assumption is common to both.

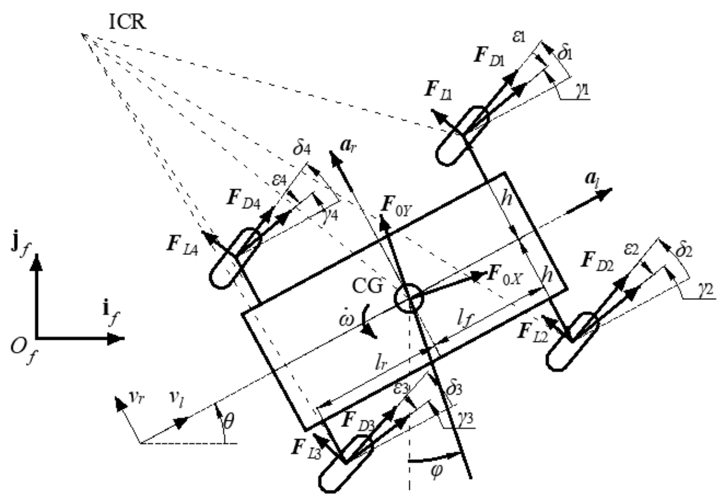

Figure 3.3 Dynamic model of a four-wheel vehicle in the horizontal $\mathbf{i}_f$-$\mathbf{j}_f$ plane

The relevant variables are defined as follows:

- F_{Li}: lateral force on the wheel, N
- F_{Di}: forward force on the wheel, N
- a_r: lateral acceleration, m/s^2
- a_l: longitudinal acceleration, m/s^2
- v_r: lateral velocity, m/s
- v_l: longitudinal velocity, m/s
- $\dot{\omega}$: angular acceleration of the vehicle, rad/s^2
- θ: orientation of the vehicle with respect to $\mathbf{i}_f$ axis, rad
- φ: offset-error angle measured with respect to the $\mathbf{j}_f$ axis, representing the angular deviation between the line connecting the centres of gravity of the two vehicles and the lateral direction of the path, rad.
- F_{0X}: component of the external force exerted by the truss on the vehicle along the $\mathbf{i}_1$ axis of the truss coordinate frame, N
- F_{0Y}: component of the external force exerted by the truss on the vehicle along the $\mathbf{j}_1$ axis of the truss coordinate frame, corresponding to the truss-span direction, N. For the follower vehicle, $F_{0Y} = 0$
- CG: centre of gravity of the vehicle
- l_f: length of CG to front axle, m
- l_r: length of CG to rear axle, m
- h: distance from wheel centre to vehicle centreline ($\mathbf{i}_0$), m

- δ_i: steering angle, rad
- ε_i: slip angle, rad
- γ_i: sideslip angle, rad

For vehicle 1, $F_{0X} = -F_{01i}$ and $F_{0Y} = -F_{01j}$; for vehicle 2, $F_{0X} = -F_{32i}$ and $F_{0Y} = 0$. The force balance for vehicle 1 in the horizontal plane is

$$\begin{cases} ma_l = \sum_{n=1}^{4} F_{Dn} \cos\delta_n - \sum_{n=1}^{4} F_{Ln} \sin\delta_n + F_{01i}\cos\varphi_{01} - F_{01j}\sin\varphi_{01} \\ ma_r = \sum_{n=1}^{4} F_{Dn} \sin\delta_n + \sum_{n=1}^{4} F_{Ln} \cos\delta_n + F_{01i}\sin\varphi_{01} + F_{01j}\cos\varphi_{01} \\ I_n\dot{\omega} = (-F_{D1}\cos\delta_1 + F_{D2}\cos\delta_2 + F_{D3}\cos\delta_3 - F_{D4}\cos\delta_4)h \\ \qquad + (F_{L1}\sin\delta_1 - F_{L2}\sin\delta_2 - F_{L3}\sin\delta_3 + F_{L4}\sin\delta_4)h \\ \qquad + (F_{D1}\sin\delta_1 + F_{D2}\sin\delta_2)l_f - (F_{D3}\sin\delta_3 + F_{D4}\sin\delta_4)l_r \\ \qquad + (F_{L1}\cos\delta_1 + F_{L2}\cos\delta_2)l_f - (F_{L3}\cos\delta_3 + F_{L4}\cos\delta_4)l_r \end{cases} \tag{10}$$

where m is the mass of the vehicle, kg, and I_n is the inertia of the vehicle, N·m·s^2.

The forces and moments for vehicle 1 in the vertical plane (**i**$_0$-**k**$_0$ plane) are shown in Figure 3.4.

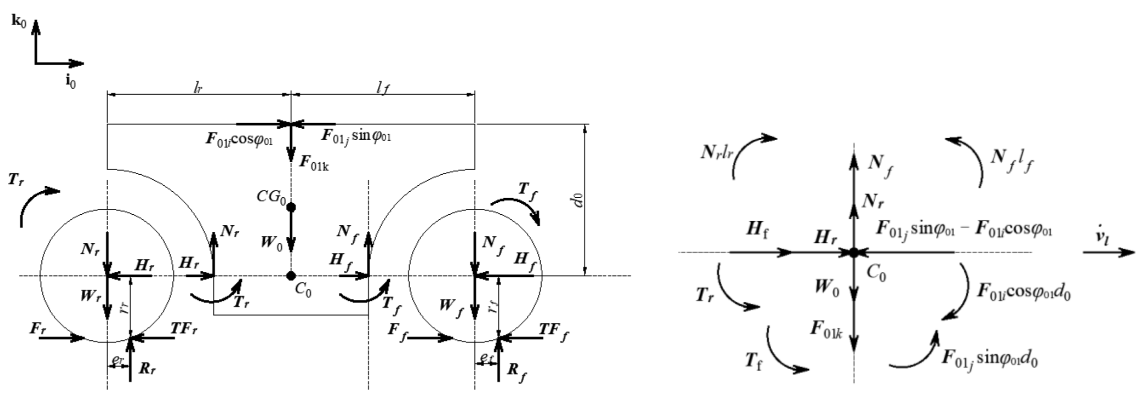

(a) (b)

Figure 3.4 Force and moment analysis for vehicle 1 in the **i**$_0$-**k**$_0$ plane at (a) wheels, (b) centre point C_0

The following variables are defined:

- R_f, R_r: vertical part of soil reaction on the front wheel / rear wheel, N
- TF_f, TF_r: horizontal part of soil reaction on the front wheel / rear wheel, N
- H_f, H_r: the horizontal force of vehicle on the front wheel / rear wheel, N; the horizontal force equals the forward force F_{Di} when the steering angle δ_i is 0
- N_f, N_r: the vertical force of vehicle on the front wheel / rear wheel, N

- W_f, W_r: the weights of the front wheel / rear wheel, N
- F_f, F_r: gross tractive force on the front wheel / rear wheel, N
- T_f, T_r: axle torque on the front wheel / rear wheel, N·m
- r_f, r_r: the rolling radii, defined as the vertical distances from the soil reactions to the centres of the front and rear wheels, respectively, m
- e_f, e_r: horizontal distance of soil reaction to the centre of the front wheel / rear wheel, m
- CG_0: centre of gravity (CG) of vehicle 1
- C_0: geometric centre of vehicle 1
- W_0: the weight of vehicle 1, N

Figure 3.4 shows only half of the force system for the vehicle in the vertical plane. To obtain the complete force analysis, the corresponding left and right wheel forces must be considered separately. For example, N_1, N_2, N_3 and N_4 replace the aggregate front and rear normal forces N_f and N_r, and T_1, T_2, T_3 and T_4 replace the aggregate axle torques T_f and T_r. The complete force balance for vehicle 1 in the vertical plane is therefore

$$\begin{cases} \sum_{n=1}^{4} H_n - F_{01i}\cos\varphi_{01} - F_{01j}\sin\varphi_{01} = m\dot{v}_l \\ W_0 + F_{01k} - \sum_{n=1}^{4} N_n = 0 \\ \sum_{n=1}^{4} T_n + (N_1+N_2)l_f - (N_3+N_4)l_r - F_{01i}\cos\varphi_{01}d_0 + F_{01j}\sin\varphi_{01}d_0 = 0 \end{cases} \tag{11}$$

Let v_{wi} denote the longitudinal velocity of wheel i, and let ω_{wi} denote its angular velocity. In the ideal rolling condition, $v_{wi} = \omega_{wi} r_i$, where r_i is the rolling radius of wheel i. However, because of longitudinal slip, the actual wheel velocity differs from the theoretical no-slip velocity v_{wi}^*. Let λ_i denote the longitudinal slip ratio of wheel i. Then

$$\lambda_i = \frac{v_{wi}^* - v_{wi}}{v_{wi}^*} = \frac{r_i\omega_{wi} - v_{wi}}{r_i\omega_{wi}} \tag{12}$$

The actual wheel velocity v_{wi} can be calculated by

$$\begin{aligned} v_{w1} &= \left(v_l - h\omega\right)\cos\gamma_1 + \left(v_r + l_f\omega\right)\sin\gamma_1 \\ v_{w2} &= \left(v_l + h\omega\right)\cos\gamma_2 + \left(v_r + l_f\omega\right)\sin\gamma_2 \\ v_{w3} &= \left(v_l + h\omega\right)\cos\gamma_3 + \left(v_r - l_r\omega\right)\sin\gamma_3 \\ v_{w4} &= \left(v_l - h\omega\right)\cos\gamma_4 + \left(v_r - l_r\omega\right)\sin\gamma_4 \end{aligned} \tag{13}$$

A lateral tire force develops whenever the wheel heading differs from the direction of travel of the wheel plane. This angular difference is referred to as the slip angle, ε_i. For small slip angles, the lateral force can be approximated by (Goering et al., 2003)

$$F_{Li} = -C_{Li}\varepsilon_i \tag{14}$$

where F_{Li} is the lateral force acting on wheel i, N, and C_{Li} is the cornering stiffness, N/rad.

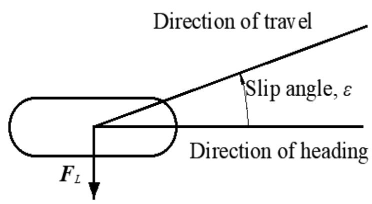

Figure 3.5 Lateral force generated by a slip angle

The cornering stiffness coefficient C_L is estimated under the assumption of small tire slip angles (Wang and Wang, 2013). A positive slip angle produces a negative lateral force, as illustrated in Figure 3.5. In this thesis, positive angles are defined as anticlockwise in the given plane, whereas negative angles are defined as clockwise.

Similarly, for small longitudinal slip, the longitudinal tire force can be approximated by (Rajamani, 2006)

$$\begin{aligned} F_{Di} &= \mu_{ri} F_{Wi} \\ \mu_{ri} &= C_{Si} \lambda_i \end{aligned} \tag{15}$$

where C_{Si} is the longitudinal slip coefficient. The wheel load F_{Wi} for each wheel in the model is calculated as

$$F_{W1} = F_{W2} = \frac{(mg + W_0)l_f}{2(l_f + l_r)}, \quad F_{W3} = F_{W4} = \frac{(mg + W_0)l_r}{2(l_f + l_r)} \tag{16}$$

These relations provide the force expressions required to derive the dynamic equations of the support vehicles under coupled WSIC operation.

3.1.3 Connecting Truss Modelling

As shown in Figure 3.1, the WSIC is represented by two supporting vehicles and the connecting truss–slider–carriage assembly. The vehicles are described dynamically, while the connecting assembly transfers self-weight and implement loads through the quasi-static relations below. No independent translational or rotational inertia of the truss, carriage, or implement is included in this load model. Figure 3.6 illustrates the assembly force analysis.

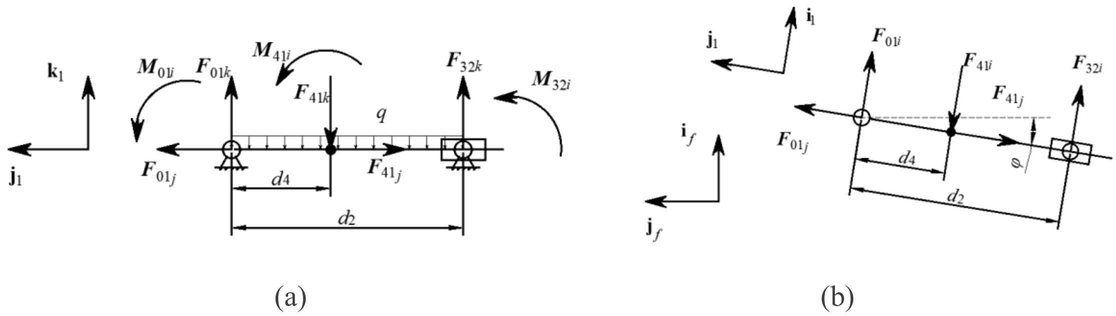

Figure 3.6 Force analysis for the RPR chain in (a) the $\mathbf{j}_1$-$\mathbf{k}_1$ plane, and (b) the $\mathbf{i}_1$-$\mathbf{j}_1$ plane

The variables associated with the truss force analysis are defined as follows:

- F_{nmp}: force of link n on link m (n, m = 0, 1, 2, 3, 4), in the p axis direction (p = $\mathbf{i}$, $\mathbf{j}$, $\mathbf{k}$), N
- M_{nmp}: moment of link n on link m (n, m = 0, 1, 2, 3, 4) about the p axis (p = $\mathbf{i}$, $\mathbf{j}$, $\mathbf{k}$), N·m
- q: self-weight of the truss per unit length, acting in the $-\mathbf{k}_1$ direction over the full truss length L_{truss}; its resultant acts at the truss mid-length, N/m
- F_{41i}, F_{41j}, F_{41k}: force of carriage and implement on the truss, N

The forces F_{41i}, F_{41j}, and F_{41k} represent the resultant of the implement's soil/crop interaction (draft resistance and vertical load, following the same draft/vertical-load distinction used for this platform by Laguë et al., 1997) as transmitted to the truss through the mobile carriage. The mobile carriage is mounted on the truss through its own sliding joint, held fixed at position d_4 in the mobile-mode operation considered in this study, and connects to the implement through a revolute joint about the vertical axis. This revolute joint keeps the implement oriented to the actual direction of travel regardless of the truss's own yaw angle relative to the vehicles; consequently, the implement's resistance force must be projected from the travel-aligned direction into the truss's own $\{O_1; \mathbf{i}_1, \mathbf{j}_1, \mathbf{k}_1\}$ frame, which is the projection carried out by the offset-error angle φ, shown in Figure 3.6.

During field operation, external forces act on the implement. In this study the external load is represented by a localized resistance force F_{external} directed opposite to the path direction and applied to the implement. Projected into the truss frame through the offset-error angle φ, it gives the truss forces F_{41i} and F_{41j}:

$$
\begin{aligned}
F_{41i} &= F_{\text{external}} \cos\varphi \\
F_{41j} &= F_{\text{external}} \sin\varphi
\end{aligned}
\tag{17}
$$

Because the implement's soil/crop-engaging point lies a vertical distance d_5 below the truss's reference axis ($\mathbf{k}_1 = 0$), representing this force at the truss's reference axis requires an additional couple alongside the point force, analogous to the hitch-height weight-transfer moment used to represent an offset drawbar pull in tractor-implement mechanics (Macmillan, 2002). Since the carriage-implement revolute joint is free only about the vertical axis, it still transmits moments about $\mathbf{i}_1$ and $\mathbf{j}_1$, so this couple, M_{41}, is transmitted to the truss along with the point force at d_4 and is given by Equation (18) and must be included in the force and moment balance of Equation (19):

$$M_{41i} = F_{41j} d_5, M_{41j} = -F_{41i} d_5 \tag{18}$$

This couple is applied at d_4 together with the point force and must be summed into the moment reactions M_{01i}, M_{01j}, M_{32i} and M_{32j} in the assembly balance accordingly. The force and moment balance for the RPR chain about O_1 is given by

$$\begin{cases} F_{01i} = -F_{41i} \dfrac{d_2 - d_4}{d_2}, F_{32i} = -F_{41i} \dfrac{d_4}{d_2} \\ F_{01j} = -F_{41j} \\ F_{01k} = F_{41k} \dfrac{d_4 - d_2}{d_2} + qL_{\text{truss}} \left(\dfrac{L_{\text{truss}}}{2d_2} - 1 \right), F_{32k} = -F_{41k} \dfrac{d_4}{d_2} - \dfrac{qL_{\text{truss}}^2}{2d_2} \\ M_{01i} + M_{32i} + M_{41i} + d_2 F_{32k} - d_4 F_{41k} - \dfrac{qL_{\text{truss}}^2}{2} = 0 \\ M_{01j} + M_{32j} + M_{41j} = 0 \end{cases} \tag{19}$$

Equation (19) is a single vector balance for the truss–slider–carriage assembly about O_1 and does not by itself separate M_{01} from M_{32}; the separation follows from the joint properties. Yaw is free at both spherical joints, so $M_{01k} = M_{32k} = 0$, and the $\mathbf{k}_1$ component of Equation (19) yields the $\mathbf{i}_1$ direction (travel-direction) reaction at the follower joint. Under the flat-terrain assumption the pitch restraint at the joints is neglected, so $M_{01i} = M_{32i} = 0$, and the $\mathbf{i}_1$ component yields the vertical reaction, the truss carrying vertical load as a simply supported beam. The $\mathbf{j}_1$ component is the torsional couple produced by the draft force acting below the truss axis; it is reacted by the roll restraints at the two joints, which is statically indeterminate, and is shared in proportion to their stiffnesses. With identical joint hardware at both ends, $M_{01j} = M_{32j} = M_{41j}/2$.

The truss model supplies the transmitted forces and moments required by the supporting-vehicle dynamic equations. It captures the effects of the applied load and its position within the adopted support assumptions, without modelling independent inertial motion or structural vibration of the connecting assembly. The consequences of that simplification for more demanding motion and field-scale loading are considered in the limitations; successful tracking on the small-scale platform is not, by itself, a quantitative estimate of omitted implement inertia.

3.1.4 Dynamic Equation

The wheel-force and planar rigid-body relations in this subsection are based on the single-vehicle formulation of Dai and Katupitiya (2014). The present derivation applies them to the WSIC supporting vehicles with the truss interaction terms described in Section 3.1.3. Using the wheel notation in Figure 3.3, the relationship among steering angle δ_i, the slip angle ε_i, and the sideslip angle γ_i is expressed as follows:

$$\delta_i = \gamma_i - \varepsilon_i \tag{20}$$

The sideslip angle can be obtained from the vehicle dynamic model in the horizontal $\mathbf{i}_f$-$\mathbf{j}_f$ plane

$$\begin{cases} \gamma_1 = \tan^{-1}\dfrac{\rho\sin\varphi + l_f}{\rho\cos\varphi - h} = \tan^{-1}\dfrac{v_r + \omega l_f}{v_l - \omega h} \\ \gamma_2 = \tan^{-1}\dfrac{\rho\sin\varphi + l_f}{\rho\cos\varphi + h} = \tan^{-1}\dfrac{v_r + \omega l_f}{v_l + \omega h} \\ \gamma_3 = \tan^{-1}\dfrac{\rho\sin\varphi - l_r}{\rho\cos\varphi + h} = \tan^{-1}\dfrac{v_r - \omega l_r}{v_l + \omega h} \\ \gamma_4 = \tan^{-1}\dfrac{\rho\sin\varphi - l_r}{\rho\cos\varphi - h} = \tan^{-1}\dfrac{v_r - \omega l_r}{v_l - \omega h} \end{cases} \tag{21}$$

Let R_i (i = 1, 2, 3, 4) denote the transformation matrix from the wheel frame to the moving frame {CG; $\mathbf{i}_m$, $\mathbf{j}_m$}, and F_{DLi} (i = 1, 2, 3, 4) denote the combined tractive and lateral force vector of each wheel, given in

$$R_i = \begin{bmatrix} \cos\delta_i & -\sin\delta_i \\ \sin\delta_i & \cos\delta_i \end{bmatrix} \tag{22}$$

$$F_{DLi} = \begin{bmatrix} F_{Di} \\ F_{Li} \end{bmatrix} \tag{23}$$

The dynamic equation of the vehicle can then be written as

$$\begin{bmatrix} \dot{v}_l \\ \dot{v}_r \\ \dot{\omega} \end{bmatrix} = B^{-1}C\begin{bmatrix} F_{DL1} \\ F_{DL2} \\ F_{DL3} \\ F_{DL4} \end{bmatrix} + B^{-1}D \tag{24}$$

$$B = \begin{bmatrix} m & & \\ & m & \\ & & I_n \end{bmatrix} \quad C = \begin{bmatrix} 1 & 0 & 1 & 0 & 1 & 0 & 1 & 0 \\ 0 & 1 & 0 & 1 & 0 & -1 & 0 & -1 \\ -h & l_f & h & l_f & h & l_r & -h & l_r \end{bmatrix} \begin{bmatrix} R_1 & & & \\ & R_2 & & \\ & & R_3 & \\ & & & R_4 \end{bmatrix}$$

$$D = \begin{bmatrix} F_{01i}\cos\varphi_{01} - F_{01j}\sin\varphi_{01} \\ F_{01i}\sin\varphi_{01} + F_{01j}\cos\varphi_{01} \\ 0 \end{bmatrix}$$

From Equation (19) the external forces exerted by the truss on each vehicle can be determined. By projecting these forces into the local coordinate system of the vehicle, the external interaction terms F_{01i} and F_{01j} can be obtained. Given the steering angles $[\delta_1, \delta_2, \delta_3, \delta_4]^T$, the accelerations $\dot{v}_r$, $\dot{v}_l$ and $\dot{\omega}$, Equation (24) can be expressed as a function of the forward forces $[F_{D1}, F_{D2}, F_{D3}, F_{D4}]^T$. Since the leader and follower vehicles have similar actuation structures, Equation (24) applies to both vehicles.

In this study, the supporting vehicles are modelled as four-wheel-steering (4WS) vehicles using equivalent steering angles defined on the longitudinal centreline of the vehicle. Specifically, the left and right front wheel steering angles are assumed to be represented by a single virtual front steering angle δ_f, and the left and right rear wheel steering angles are assumed to be represented by a single virtual rear steering angle δ_r. Both δ_f and δ_r are defined on the middle line of the vehicle and serve as equivalent steering inputs in the dynamic model. This assumption reduces the number of independent steering variables and simplifies the derivation of the vehicle dynamic equations and the design of the control system. However, it also introduces certain limitations, because it neglects possible steering differences between the left and right wheels, compliance in the steering and axle connections, and unequal tire slip characteristics during turning. Consequently, the model may not fully capture complex dynamic responses under aggressive manoeuvres or highly uneven terrain conditions. Nevertheless, under moderate operating conditions and representative agricultural guidance scenarios, this assumption provides a reasonable compromise between model accuracy and computational efficiency.

Because tire slip, traction, and friction are velocity dependent, incorporating the vehicle velocity components along the fixed axes, $\dot{X}$ and $\dot{Y}$, improves the realism of the dynamic equations and enhances prediction accuracy under acceleration and disturbance conditions. Accordingly, Equation (24) can be rewritten as

$$
\begin{aligned}
& m\dot{v}_r = -mv_l\omega + \left(F_{L1}+F_{L2}\right)\cos\delta_f + \left(F_{L3}+F_{L4}\right)\cos\delta_r + \left(F_{D1}+F_{D2}\right)\sin\delta_f \\
& \qquad + \left(F_{D3}+F_{D4}\right)\sin\delta_r + F_{01i}\sin\varphi_{01} + F_{01j}\cos\varphi_{01} \\
& m\dot{v}_l = mv_r\omega - \left(F_{L1}+F_{L2}\right)\sin\delta_f - \left(F_{L3}+F_{L4}\right)\sin\delta_r + \left(F_{D1}+F_{D2}\right)\cos\delta_f \\
& \qquad + \left(F_{D3}+F_{D4}\right)\cos\delta_r + F_{01i}\cos\varphi_{01} - F_{01j}\sin\varphi_{01} \\
& \dot{\theta} = \omega \\
& I_n\dot{\omega} = \left(F_{L1}-F_{L2}\right)h\sin\delta_f + \left(F_{L1}+F_{L2}\right)l_f\cos\delta_f + \left(F_{D1}+F_{D2}\right)l_f\sin\delta_f \\
& \quad - \left(F_{D1}-F_{D2}\right)h\cos\delta_f - \left(F_{L3}-F_{L4}\right)h\sin\delta_r - \left(F_{L3}+F_{L4}\right)l_r\cos\delta_r \\
& \quad - \left(F_{D3}+F_{D4}\right)l_r\sin\delta_r + \left(F_{D3}-F_{D4}\right)h\cos\delta_r \\
& \dot{X} = v_l\cos\theta - v_r\sin\theta \\
& \dot{Y} = v_l\sin\theta + v_r\cos\theta
\end{aligned}
\tag{25}
$$

For geometric completeness, the ideal Ackermann steering geometry distinguishes the inner- and outer-wheel steering angles from the equivalent centreline steering angle. For front-wheel steering with the rear wheels aligned, let δ_{in} and δ_{out} denote the inner-wheel and outer-wheel steering angles, respectively. For a nonzero equivalent front steering angle, the corresponding geometric relationships are

$$
\begin{cases}
\left|\delta_{\text{in}}\right| = \arctan\dfrac{l_f+l_r}{\dfrac{l_f+l_r}{\left|\tan\delta_f\right|}-h} \\
\left|\delta_{\text{out}}\right| = \arctan\dfrac{l_f+l_r}{\dfrac{l_f+l_r}{\left|\tan\delta_f\right|}+h}
\end{cases}
\tag{26}
$$

These relationships define the steering-angle magnitudes when the distance from the instantaneous centre of rotation (ICR) to the rear-axle midpoint exceeds h; they do not introduce a separate steering-sign convention. Both wheel angles approach zero as the equivalent steering angle approaches zero. For rear-wheel steering, the corresponding relationships are obtained by interchanging the steering and aligned axles. The Ackermann relationships are included only to clarify the geometric meaning of the equivalent centreline steering angle and are not substituted into Equations (24) to (29); in the simulations of Chapter 4, Section 4.1.2 uses them to reconstruct the individual wheel angles for the CarSim plant.

For the specific supporting vehicles considered in this study, the vehicle is treated as a two-wheel-steering (2WS) system under two possible operating modes: FWS and rear-wheel-steering (RWS). In FWS mode, the front axle provides the steering input, while the rear wheels remain aligned with the longitudinal axis of the vehicle. This condition is represented by setting the equivalent rear steering angle to zero. Therefore, by imposing $\delta_r = 0$, Equation (25) becomes

$$
\begin{aligned}
&m\dot{v}_r = -mv_l\omega + \left(F_{L1}+F_{L2}\right)\cos\delta_f + \left(F_{D1}+F_{D2}\right)\sin\delta_f + F_{01i}\sin\varphi_{01} + F_{01j}\cos\varphi_{01} \\
&m\dot{v}_l = mv_r\omega - \left(F_{L1}+F_{L2}\right)\sin\delta_f + \left(F_{D1}+F_{D2}\right)\cos\delta_f + F_{01i}\cos\varphi_{01} - F_{01j}\sin\varphi_{01} \\
&\dot{\theta} = \omega \\
&I_n\dot{\omega} = \left(F_{L1}-F_{L2}\right)h\sin\delta_f + \left(F_{L1}+F_{L2}\right)l_f\cos\delta_f + \left(F_{D1}+F_{D2}\right)l_f\sin\delta_f \\
&\qquad -\left(F_{D1}-F_{D2}\right)h\cos\delta_f \\
&\dot{X} = v_l\cos\theta - v_r\sin\theta \\
&\dot{Y} = v_l\sin\theta + v_r\cos\theta
\end{aligned}
\tag{27}
$$

In RWS mode, the rear axle provides the steering input, while the front wheels remain aligned with the longitudinal axis of the vehicle. This condition is represented by setting the equivalent front steering angle to zero. Therefore, by imposing $\delta_f = 0$, Equation (25) becomes

$$
\begin{aligned}
&m\dot{v}_r = -mv_l\omega + \left(F_{L3}+F_{L4}\right)\cos\delta_r + \left(F_{D3}+F_{D4}\right)\sin\delta_r + F_{01i}\sin\varphi_{01} + F_{01j}\cos\varphi_{01} \\
&m\dot{v}_l = mv_r\omega - \left(F_{L3}+F_{L4}\right)\sin\delta_r + \left(F_{D3}+F_{D4}\right)\cos\delta_r + F_{01i}\cos\varphi_{01} - F_{01j}\sin\varphi_{01} \\
&\dot{\theta} = \omega \\
&I_n\dot{\omega} = -\left(F_{L3}-F_{L4}\right)h\sin\delta_r - \left(F_{L3}+F_{L4}\right)l_r\cos\delta_r - \left(F_{D3}+F_{D4}\right)l_r\sin\delta_r \\
&\qquad +\left(F_{D3}-F_{D4}\right)h\cos\delta_r \\
&\dot{X} = v_l\cos\theta - v_r\sin\theta \\
&\dot{Y} = v_l\sin\theta + v_r\cos\theta
\end{aligned}
\tag{28}
$$

The FWS and RWS equations are special cases of the generalized steering representation obtained by setting the inactive axle's equivalent angle to zero. The physical experiments use front-wheel steering. Most simulation scenarios also use front-wheel steering, while rear-wheel steering is included for the reverse-direction scenarios. RWS is therefore part of the simulation formulation, not a second steering configuration validated on the physical platform.

The differential variables $\dot{v}_r$, $\dot{v}_l$, $\dot{\theta}$, $\dot{\omega}$, $\dot{X}$ and $\dot{Y}$ can then be expressed as functions of the kinematic parameters v_r, v_l, θ, ω, X, Y, and δ:

$$
(\dot{v}_r, \dot{v}_l, \dot{\theta}, \dot{\omega}, \dot{X}, \dot{Y}) = f(v_r, v_l, \theta, \omega, X, Y, \delta)
\tag{29}
$$

This dynamic formulation provides the state evolution model required for the steering and velocity controllers developed later in this chapter.

3.2 Kinematic Motion

3.2.1 Kinematic Description by an Adjoint Approach

The vehicle considered in this study is a four-wheel vehicle required to follow a prescribed reference path representing the desired trajectory of its centre of gravity. Ideally, the longitudinal velocity at the CG should be tangent to the reference path. In practice, however, lateral and orientation errors cause the vehicle trajectory to deviate from that path. In this framework, the reference path is treated as the original curve, whereas the actual vehicle trajectory is regarded as its adjoint curve.

Wang and Wang (2015) provide the differential-geometric framework for the adjoint-curve representation and moving-frame operations used in this section. The Frenet identities and the general representation are established methods. The contribution here is their application to the WSIC supporting vehicles and implement-support point, and the use of the resulting path-coordinate relations in coordinated control.

In this study, the adjoint-curve framework of Wang and Wang (2015) is applied to derive the kinematic error dynamics of the WSIC supporting vehicle. Based on this adjoint approach, as given by Equations (30) to (34), a kinematic description of the supporting vehicle with respect to the reference path is derived. The kinematic model of the leader vehicle is illustrated in Figure 3.7, and the relevant variables are defined as follows:

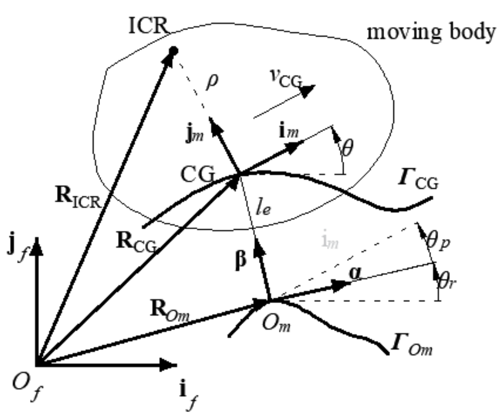

Figure 3.7 Kinematic model of the leader vehicle

- Γ_{Om}: reference path, which is the desired path for CG of the vehicle to follow
- Γ_{CG}: actual path for CG of the vehicle
- O_m: reference point on Γ_{Om} that is closest to the point CG. The coordinates of O_m in the fixed frame are (x_{Omf}, y_{Omf})
- θ_r: tangent of the reference path at point O_m with respect to $\mathbf{i}_f$ axis, rad
- θ_p: orientation error of the vehicle with respect to Γ_{Om}, $\theta_p = \theta - \theta_r$, rad
- l_e: lateral error of the vehicle with respect to O_m, m
- ρ: radius of the actual path Γ_{CG} at point CG, m
- v_{CG}: velocity of the vehicle at point CG, m/s
- a_{CG}: acceleration of the vehicle at point CG, m/s^2

- ω: angular velocity of the vehicle, rad /s

A curve frame $\{O_m; \boldsymbol{\alpha}, \boldsymbol{\beta}\}$ is defined along Γ_{Om} . The differential equations governing the Frenet–Serret frame $\{O_m; \boldsymbol{\alpha}, \boldsymbol{\beta}\}$ (Serret, 1851; Frenet, 1852) are

$$\frac{d\mathbf{R}_{Om}}{ds} = \boldsymbol{\alpha}, \frac{d\boldsymbol{\alpha}}{ds} = k_{Om}\boldsymbol{\beta}, \frac{d\boldsymbol{\beta}}{ds} = -k_{Om}\boldsymbol{\alpha} \tag{30}$$

where s is the curvilinear coordinate of O_m, ds denotes an infinitesimal arc length, and k_{Om} is the curvature of Γ_{Om} at O_m. The curvature k_{Om} is defined as

$$k_{Om} = \left(\frac{dx_{Omf}}{dt}\cdot\frac{d^2y_{Omf}}{dt^2} - \frac{dy_{Omf}}{dt}\cdot\frac{d^2x_{Omf}}{dt^2}\right) / \left[\left(\frac{dx_{Omf}}{dt}\right)^2 + \left(\frac{dy_{Omf}}{dt}\right)^2\right]^{\frac{3}{2}} \tag{31}$$

The first and second derivatives of s are given by

$$\frac{ds}{dt} = \sqrt{\left(\frac{dx_{Omf}}{dt}\right)^2 + \left(\frac{dy_{Omf}}{dt}\right)^2} \tag{32}$$

$$\frac{d^2s}{dt^2} = \left(\frac{dx_{Omf}}{dt}\cdot\frac{d^2x_{Omf}}{dt^2} + \frac{dy_{Omf}}{dt}\cdot\frac{d^2y_{Omf}}{dt^2}\right) / \left[\left(\frac{dx_{Omf}}{dt}\right)^2 + \left(\frac{dy_{Omf}}{dt}\right)^2\right]^{\frac{1}{2}} \tag{33}$$

The vectors $\boldsymbol{\alpha}$ and $\boldsymbol{\beta}$ can also be written as $\boldsymbol{\alpha} = \{\cos\theta_r, \sin\theta_r\}$, and $\boldsymbol{\beta} = \mathbf{k} \times \boldsymbol{\alpha} = \{-\sin\theta_r, \cos\theta_r\}$, where $\mathbf{k}$ is the unit vector normal to the plane. The derivative of $\boldsymbol{\alpha}$ with respect to s is

$$\frac{d\boldsymbol{\alpha}}{ds} = \frac{d\boldsymbol{\alpha}}{d\theta_r}\frac{d\theta_r}{ds} = \frac{d\theta_r}{ds}\{-\sin\theta_r, \cos\theta_r\} = \frac{d\theta_r}{ds}\boldsymbol{\beta} \tag{34}$$

Therefore, $k_{Om} = \frac{d\theta_r}{ds}$, which gives an equivalent expression for the curvature k_{Om}. Based on Equations (30) to (34), the relative motion of the moving body with respect to the reference curve can be derived (Wang and Wang, 2015).

In this study, the moving frame $\{CG; \mathbf{i}_m, \mathbf{j}_m\}$ is attached to the vehicle, with axis $\mathbf{i}_m$ aligned with the vehicle orientation. A new moving frame is then obtained as

$$\mathbf{i}_m = \frac{d\mathbf{R}_{\mathrm{CG}}}{d\sigma} = \frac{d\mathbf{R}_{\mathrm{CG}}}{ds}\frac{ds}{d\sigma} = \frac{ds}{d\sigma}\left[(1 - l_e \cdot k_{Om})\boldsymbol{\alpha} + \dot{l}_e\boldsymbol{\beta}\right] \tag{35}$$

$$\mathbf{j}_m = \mathbf{k} \times \mathbf{i}_m = \frac{ds}{d\sigma}\left[-\dot{l}_e\boldsymbol{\alpha} + (1 - l_e \cdot k_{Om})\boldsymbol{\beta}\right] \tag{36}$$

The vector $\mathbf{i}_m$ can also be expressed in the Frenet frame $\{O_m; \boldsymbol{\alpha}, \boldsymbol{\beta}\}$: $\mathbf{i}_m = \cos\theta_p \cdot \boldsymbol{\alpha} + \sin\theta_p \cdot \boldsymbol{\beta}$. Combining this expression with Equations (35) and (36) yields

$$\dot{l}_e = \tan\theta_p\left(1 - l_e \cdot k_{Om}\right) \tag{37}$$

The CG is selected as the reference point in the moving frame {CG; $\mathbf{i}_m$, $\mathbf{j}_m$}, and its trajectory is denoted by Γ_{CG}. Let σ be the curvilinear coordinate of the CG along this trajectory. The differential relation for σ is

$$\frac{d\sigma}{ds} = \sqrt{\left(1 - l_e \cdot k_{Om}\right)^2 + \left(\dot{l}_e\right)^2} = \frac{1 - l_e \cdot k_{Om}}{\cos\theta_p} \tag{38}$$

The trajectory Γ_{CG}, expressed in the fixed frame {O_f: $\mathbf{i}_f$, $\mathbf{j}_f$}, can be represented in the Frenet frame {O_m; $\boldsymbol{\alpha}$, $\boldsymbol{\beta}$} of Γ_{Om} as

$$\mathbf{R}_{\mathrm{CG}} = \mathbf{R}_{Om} + l_e \boldsymbol{\beta} \tag{39}$$

The curvature of Γ_{CG} at point CG is then

$$k_{\mathrm{CG}} = \frac{d\mathbf{i}_m}{ds} \cdot \mathbf{j}_m \cdot \frac{ds}{d\sigma} = \frac{\left(k_{Om} + \dot{\theta}_p\right)\cos\theta_p}{1 - l_e \cdot k_{Om}} \tag{40}$$

and the corresponding radius of curvature is

$$\rho = \frac{1}{k_{\mathrm{CG}}} = \frac{1 - l_e \cdot k_{Om}}{\left(k_{Om} + \dot{\theta}_p\right)\cos\theta_p} \tag{41}$$

At any instant, an ICR exists on the moving body. The position of the ICR can be expressed as

$$\mathbf{R}_{\mathrm{ICR}} = \mathbf{R}_{\mathrm{CG}} + \rho \mathbf{j}_m = \mathbf{R}_{Om} + \rho \sin\theta_p \boldsymbol{\alpha} + (l_e + \rho\cos\theta_p)\boldsymbol{\beta} \tag{42}$$

Let v_{ICR} denote the velocity of the ICR. This velocity must satisfy

$$v_{\mathrm{ICR}} = \frac{d\mathbf{R}_{\mathrm{ICR}}}{dt} = \frac{d\mathbf{R}_{\mathrm{ICR}}}{d\sigma}\frac{d\sigma}{dt} = \frac{d\rho}{d\sigma}\mathbf{j}_m \frac{d\sigma}{dt} = 0 \tag{43}$$

Hence,

$$\ddot{\theta}_p = \tan\theta_p \left(\dot{\theta}_p + k_{Om}\right)^2 - \left(2k_{Om}\tan\theta_p + \frac{\sin\theta_p}{\dot{l}_e}\frac{\dot{k}_{Om} l_e}{\cos\theta_p}\right)\left(\dot{\theta}_p + k_{Om}\right) - \dot{k}_{Om} \tag{44}$$

where

$$\begin{aligned}
\dot{k}_{Om} &= A_1 / \left(\frac{ds}{dt}\right)^4 - 3A_2 / \left(\frac{ds}{dt}\right)^6 \\
A_1 &= \frac{d^3 y_{Omf}}{dt^3} \cdot \frac{dx_{Omf}}{dt} - \frac{d^3 x_{Omf}}{dt^3} \cdot \frac{dy_{Omf}}{dt} \\
A_2 &= \left(\frac{dx_{Omf}}{dt} \cdot \frac{d^2 x_{Omf}}{dt^2} + \frac{dy_{Omf}}{dt} \cdot \frac{d^2 y_{Omf}}{dt^2}\right)\left(\frac{dx_{Omf}}{dt} \cdot \frac{d^2 y_{Omf}}{dt^2} - \frac{dy_{Omf}}{dt} \cdot \frac{d^2 x_{Omf}}{dt^2}\right)
\end{aligned} \tag{45}$$

The translational velocity at the CG, v_{CG}, and the angular velocity of the vehicle, ω, can be obtained from

$$\mathbf{v}_{\mathrm{CG}} = \frac{d\mathbf{R}_{\mathrm{CG}}}{dt} = \frac{d\mathbf{R}_{\mathrm{CG}}}{d\sigma}\frac{d\sigma}{dt} = \frac{ds}{dt}\frac{1-l_e \cdot k_{Om}}{\cos\theta_p}\mathbf{i}_m \tag{46}$$

$$\omega = \frac{d\theta}{dt} = \frac{ds}{dt}\frac{d(\theta_r+\theta_p)}{ds} = \frac{ds}{dt}(k_{Om}+\dot{\theta}_p) \tag{47}$$

The acceleration components are derived by differentiating Equations (46) and (47):

$$\begin{aligned} a_{\mathrm{CG}} &= \frac{dv_{\mathrm{CG}}}{dt} = a_t\mathbf{i}_m + a_n\mathbf{j}_m \\ a_t &= \frac{\dot{l}_e\left(\dot{\theta}_p - k_{Om}\right) - l_e\dot{k}_{Om}}{\cos\theta_p}\left(\frac{ds}{dt}\right)^2 + \frac{\dot{l}_e}{\sin\theta_p}\frac{d^2s}{dt^2} \\ a_n &= k_{\mathrm{CG}}\frac{\dot{l}_e^{\,2}}{\sin^2\theta_p}\left(\frac{ds}{dt}\right)^2 \end{aligned} \tag{48}$$

$$\dot{\omega} = (\dot{k}_{Om}+\ddot{\theta}_p)(\frac{ds}{dt})^2 + (k_{Om}+\dot{\theta}_p)\frac{d^2s}{dt^2} \tag{49}$$

Equations (30) to (49) describe the leader support vehicle relative to its reference path. The same derivation is applied to the follower with its own reference curve and tracking variables. The follower has a separate path-tracking controller, while the truss loads, finite support span, and synchronization objective maintain the connection between the two vehicle-control tasks. The kinematic model of the follower vehicle is illustrated in Figure 3.8, with the following variables:

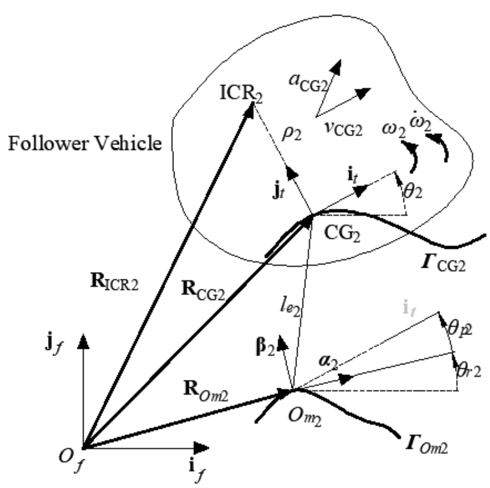

Figure 3.8 Kinematic model of the follower vehicle

- CG_2: CG of the follower vehicle
- Γ_{Om2}: reference path for the CG_2 to follow
- Γ_{CG2}: actual path for CG_2 of the follower vehicle

- O_{m2}: reference point on Γ_{Om2}
- θ_{r2}: tangent of the reference path at point O_{m2} with respect to $\mathbf{i}_f$ axis, rad
- θ_2: orientation of the follower vehicle with respect to $\mathbf{i}_f$ axis, rad
- θ_{p2}: orientation error of the follower vehicle with respect to Γ_{Om2}, $\theta_{p2} = \theta_2 - \theta_{r2}$, rad
- l_{e2}: lateral error of the follower vehicle with respect to O_{m2}, m
- ρ_2: radius of the actual path Γ_{CG2} at point CG_2, m
- v_{CG2}: velocity of the follower vehicle at point CG_2, m/s
- a_{CG2}: acceleration of the follower vehicle at point CG_2, m/s^2
- ω_2: angular velocity of the follower vehicle, rad/s
- $\dot{\omega}_2$: angular acceleration of the follower vehicle, rad/s^2

To describe the kinematic relationship among these parameters, a moving frame $\{CG_2; \mathbf{i}_t, \mathbf{j}_t\}$ is attached to the follower vehicle, with axis $\mathbf{i}_t$ aligned with its orientation. The frame $\{O_{m2}; \boldsymbol{\alpha}_2, \boldsymbol{\beta}_2\}$ is attached to the projected reference path Γ_{Om2}. By applying the same derivation procedure used for the leader vehicle, the follower motion can be described in an analogous manner, with its reference path obtained from the projected motion of the leader vehicle. This formulation provides a consistent basis for coordinated path tracking and synchronization control.

3.2.2 Implement Track Kinematic Description

To describe the implement trajectory in the $\mathbf{i}_0$-$\mathbf{j}_0$ plane, a common point P^* shared by the truss and implement is selected. The vehicle 1 frame is $\{O_0; \mathbf{i}_0, \mathbf{j}_0\}$, and a curve frame $\{O_p; \boldsymbol{\alpha}_p, \boldsymbol{\beta}_p\}$ is attached to the implement reference path Γ_{Op}, as shown in Figure 3.9.

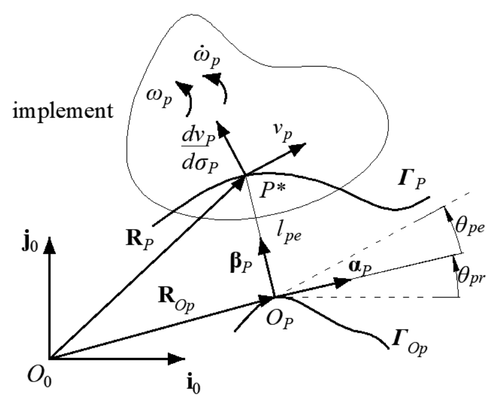

Figure 3.9 Kinematic model of the implement in the $\mathbf{i}_0$-$\mathbf{j}_0$ plane

The relevant variables are defined as follows:

- Γ_{Op}: reference path for the implement, which is the desired path for P^* to follow

- Γ_P: actual path of P^*
- O_P: closest reference point on Γ_{Op} to the point P^*. The coordinate of O_P in the fixed frame is (x_{Op}, y_{Op})
- θ_{pr}: tangent of the reference path at point O_P with respect to $\mathbf{i}_0$ axis, rad
- θ_{pe}: orientation error of the implement with respect to Γ_{Op}, rad
- l_{pe}: lateral error of the implement with respect to O_P, m
- v_P: velocity of the implement at point P^*, m/s
- $\frac{dv_p}{d_{\sigma p}}$: derivative of velocity of the implement at point P^*, m/s^2
- ω_p: angular velocity of the implement, rad/s
- $\dot{\omega}_p$: angular acceleration of the implement, rad/s^2

Let s_p be the curvilinear coordinate of point O_p, let ds_p denote an infinitesimal path length, and let k_{Op} denote the curvature of Γ_{Op} at point O_p. Using the same framework as Equations (30) to (49), the implement motion can be described by

$$k_{\mathrm{Op}} = \left(\frac{dx_{Op}}{dt}\cdot\frac{d^2y_{Op}}{dt^2} - \frac{dy_{Op}}{dt}\cdot\frac{d^2x_{Op}}{dt^2}\right) / \left[\left(\frac{dx_{Op}}{dt}\right)^2 + \left(\frac{dy_{Op}}{dt}\right)^2\right]^{\frac{3}{2}} = \frac{d\theta_{pr}}{ds_p} \tag{50}$$

$$\frac{ds_p}{dt} = \sqrt{\left(\frac{dx_{Op}}{dt}\right)^2 + \left(\frac{dy_{Op}}{dt}\right)^2} \tag{51}$$

$$\frac{d^2s_p}{dt^2} = \left(\frac{dx_{Op}}{dt}\cdot\frac{d^2x_{Op}}{dt^2} - \frac{dy_{Op}}{dt}\cdot\frac{d^2y_{Op}}{dt^2}\right) / \left[\left(\frac{dx_{Op}}{dt}\right)^2 + \left(\frac{dy_{Op}}{dt}\right)^2\right]^{\frac{1}{2}} \tag{52}$$

$$\dot{l}_{pe} = -\tan\theta_{pe}\left(1 - l_{pe}\cdot k_{Op}\right) \tag{53}$$

The adjoint curve Γ_P in the frame $\{O_0; \mathbf{i}_0, \mathbf{j}_0\}$ is

$$\begin{aligned}\mathbf{R}_P &= \mathbf{R}_{Op} + l_{pe}\boldsymbol{\beta}_P = x_{Op}\mathbf{i}_0 + \mathrm{y}_{Op}\mathbf{j}_0 + l_{pe}(-\sin\theta_{pr}\mathbf{i}_0 + \cos\theta_{pr}\mathbf{j}_0) \\ &= (x_{Op} - l_{pe}\sin\theta_{pr})\ \mathbf{i}_0 + (\mathrm{y}_{Op} + l_{pe}\cos\theta_{pr})\ \mathbf{j}_0\end{aligned} \tag{54}$$

The implement velocity v_p and angular velocity ω_p are obtained from

$$v_P = \frac{d\mathbf{R}_P}{dt} = -\frac{ds_P}{dt}\dot{l}_{pe}\left(\frac{1}{\tan\theta_{pe}}\boldsymbol{\alpha}_P - \boldsymbol{\beta}_P\right) \tag{55}$$

$$\omega_P = \frac{ds_P}{dt}\frac{d(\theta_{pr} - \theta_{pe})}{ds_P} = \frac{ds_P}{dt}(k_{Op} - \dot{\theta}_{pe}) \tag{56}$$

Using Equation (2), Equation (54) can also be rewritten as

$$\mathbf{R}_P = d_4 \sin\varphi_{01}\mathbf{i}_0 - d_4 \cos\varphi_{01}\mathbf{j}_0 \tag{57}$$

Thus,

$$\begin{aligned} d_4 \sin\varphi_{01} &= x_{Op} - l_{pe} \sin\theta_{pr} \\ -d_4 \cos\varphi_{01} &= \mathrm{y}_{Op} + l_{pe} \cos\theta_{pr} \end{aligned} \tag{58}$$

Finally, l_{pe} can be obtained as

$$\left| l_{pe} \right| = \sqrt{d_4^2 - \left(x_{Op} \cos\theta_{pr} + \mathrm{y}_{Op} \sin\theta_{pr} \right)^2} + x_{Op} \sin\theta_{pr} - \mathrm{y}_{Op} \cos\theta_{pr} \tag{59}$$

This application of the adjoint-curve framework relates the implement-support trajectory to the vehicle motion and truss geometry. It describes motion at the selected point and provides a basis for discussing implement-level guidance. It is a kinematic description and does not introduce an independent implement inertial model.

Equations (30) to (34) follow Wang and Wang (2015); Equations (35) to (59) apply that framework to the supporting-vehicle centre of gravity and to the implement-support point and are derived here.

3.2.3 Error Definitions

This section collects the lateral, orientation, offset, and separation errors used to describe tracking and synchronization of the WSIC. The offset and separation quantities serve different purposes: offset describes relative progress along the reference paths, whereas separation describes the actual distance between the two vehicle centres of gravity.

The leader tracks a prescribed reference path, and a virtual reference path is used for the follower. Luo (2017) formulated the vehicle path-following problem in path coordinates and used an offset error for synchronization, but did not explicitly formulate the curved-path synchronization offset as the difference between the curvilinear coordinates of the two reference paths. Figure 3.10 illustrates Luo's straight-path offset arrangement.

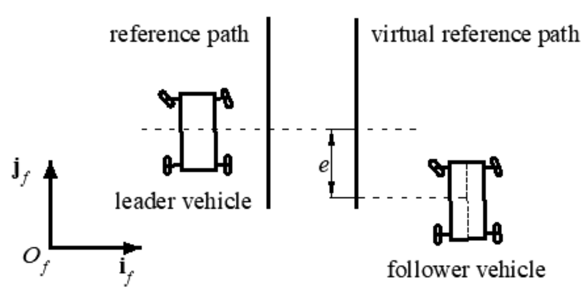

Figure 3.10 Offset error between two vehicles by Luo (2017)

This straight-path definition does not explicitly account for reference-path curvature. In the present study, the offset error e, also referred to as the synchronization error, is defined in path coordinates as the scalar difference between the curvilinear coordinates s_1 and s_2 of the two reference points, as illustrated in Figure 3.11. For each vehicle, the reference point is the point on its corresponding reference path closest to the vehicle centre of gravity, with the local path normal passing through the centre of gravity. This definition follows the path-coordinate formulation used in wheeled-mobile-robot path following (Soetanto et al., 2003). The present WSIC synchronization formulation further incorporates the curvature-dependent progression of these reference points.

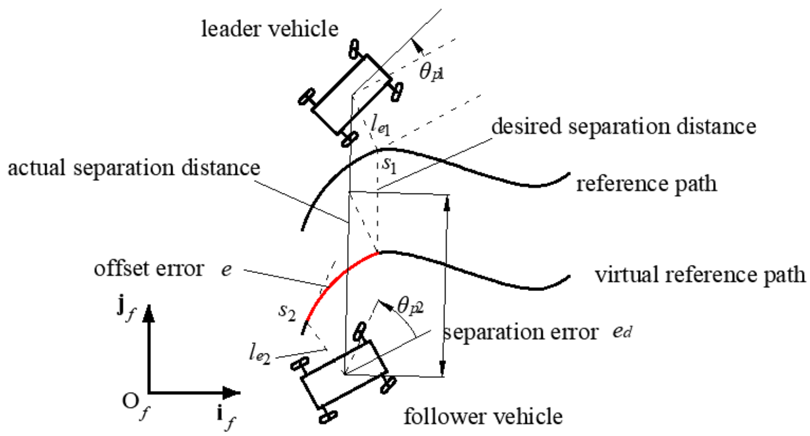

Figure 3.11 Error definitions in path coordinate

Figure 3.10 and Figure 3.11 illustrate the same offset-error concept under different path geometries rather than two different error quantities. Figure 3.10 shows the straight-path arrangement used in Luo's (2017) synchronization formulation, whereas Figure 3.11 illustrates the path-coordinate interpretation adopted in the present study for curved paths. Throughout the subsequent control development, the offset error (highlighted in red), also referred to as the synchronization error, is defined as the scalar quantity $e = s_1 - s_2$, where s_1 and s_2 are the curvilinear coordinates of the leader and follower reference points, respectively. The red curve in Figure 3.11 represents the path-coordinate interpretation of the offset error. For consistent interpretation of relative path progress, the coordinate origins of the two reference paths must be defined consistently.

From Equation (46), the derivative of the curvilinear coordinate s of point O_m along Γ_{Om} is obtained as

$$\frac{ds}{dt} = \frac{v_{\mathrm{CG}} \cos\theta_p}{1 - l_e \cdot k_{Om}} \tag{60}$$

Then, the derivative of the offset error e is obtained as

$$\dot{e} = \frac{ds_1}{dt} - \frac{ds_2}{dt} = \frac{v_1 \cos\theta_{p1}}{1 - l_{e1} \cdot k_{Om1}} - \frac{v_2 \cos\theta_{p2}}{1 - l_{e2} \cdot k_{Om2}} \tag{61}$$

As established in the published companion article (Li et al., 2026a), in the leader–follower WSIC system the leader tracks the main reference path while a virtual reference path is generated for the follower. The lateral errors, l_{e1} and l_{e2}, describe the distance between the centre of gravity of each vehicle and its reference path. The orientation errors, θ_{p1} and θ_{p2}, represent the difference between each vehicle's heading and the tangent of its reference path. The separation error, e_d, is defined as the actual inter-vehicle separation distance minus the desired separation distance. It therefore quantifies deviation from the prescribed vehicle spacing and is used to assess formation integrity and potential over-travel of the sliding joint on the truss, as illustrated in Figure 3.11.

The tire-force and wheel-motion relations in Equations (12) to (16) and (20) to (23), which are drawn from the literature, together with the original derivations in Equations (24) to (29), (44) to (49), (59), and (61) establish the theoretical basis for the tracking control strategies developed in this chapter. These strategies are formulated specifically for the WSIC supporting vehicles operating in mobile mode and provide the foundation for the coupled steering, velocity, and synchronization control laws described in the next section.

3.3 Control Law Design

3.3.1 Steering Angle Control

An incremental MPC strategy was developed for the steering control of each supporting vehicle. Steering MPC is established in vehicle guidance, including the studies of Tashiro (2013), Bao et al. (2020), and Falcone et al. (2007). The present contribution is the WSIC-specific formulation using the supporting-vehicle dynamic model, steering-angle increments, adaptive objective weights, and coordination with the velocity and synchronization loops. The finite-horizon objective balances heading and lateral-position tracking with steering effort, subject to the stated input constraints. The prediction and optimization matrices were assembled in MATLAB/Simulink, with quadprog used as the numerical solver; the MATLAB MPC Toolbox was not used, and the prediction, constraint and cost matrices of Equations (62) to (84) were coded directly in Simulink (Section 4.1.2). The contribution is the control formulation and its system integration rather than the solver itself.

3.3.1.1 State Definition

The state vector of the vehicle dynamic model was defined as

$$\xi(k) = [v_r(k), v_l(k), \theta(k), \omega(k), Y(k), X(k)]^T \tag{62}$$

where v_r is the lateral velocity in the vehicle body frame, v_l is the longitudinal velocity in the vehicle body frame, θ is the yaw angle, ω is the yaw rate, and Y and X are the global lateral and longitudinal positions, respectively.

The measured output vector contained only the yaw angle and lateral position, and was expressed as

$$\eta(k) = \begin{bmatrix} \theta(k) \\ Y(k) \end{bmatrix} = C_k \xi(k) \tag{63}$$

$$C_k = \begin{bmatrix} 0 & 0 & 1 & 0 & 0 & 0 \\ 0 & 0 & 0 & 0 & 1 & 0 \end{bmatrix}$$

Accordingly, the steering controller directly regulated vehicle heading and lateral position.

3.3.1.2 Linearized Discrete-Time Prediction Model

The steering prediction model was derived from the nonlinear dynamic model. In compact form, the continuous-time nonlinear model can be written as

$$\dot{\xi}(t) = f\left(\xi(t), \delta(t)\right) \tag{64}$$

where the nonlinear function $f(\cdot)$ contains the effects of tire lateral forces, longitudinal driving forces, vehicle inertia, and steering input.

Because the full vehicle dynamics are nonlinear, the model was linearized online at each sampling instant about the current operating point (ξ_0, δ_0). Using a first-order Taylor expansion, the linearized model was expressed as

$$\dot{\xi}(t) \approx A_t\left(\xi(t) - \xi_0\right) + B_t\left(\delta(t) - \delta_0\right) \tag{65}$$

$$A_t = \frac{\partial f\left(\xi(t), \delta(t)\right)}{\partial \xi}, \quad B_t = \frac{\partial f\left(\xi(t), \delta(t)\right)}{\partial \delta}$$

where A_t is the state Jacobian matrix and B_t is the input Jacobian vector, both evaluated at the current operating point.

The continuous-time linearized model was then converted into discrete-time form using the forward Euler method. With sampling period T, the discrete matrices were obtained as

$$\begin{aligned} A_k &= I + TA_t \\ B_k &= TB_t \end{aligned} \tag{66}$$

leading to the discrete-time model

$$\xi(k+1) = A_k \xi(k) + B_k \delta(k) + d(k) \tag{67}$$

where $d(k)$ is a mismatch term introduced to compensate for errors caused by model linearization, Euler discretization, and unmodelled disturbances. The mismatch term was defined as

$$d(k) = Td_{dist} + f(\xi_0, \delta_0) - A_k \xi_0 - B_k \delta_0 \tag{68}$$

where d_{dist} represents the disturbance-injection term associated with external lateral-force and yaw-moment effects. This term improved prediction accuracy and enhanced robustness in the presence of modelling uncertainty.

3.3.1.3 Incremental Augmented Model

To obtain an incremental MPC formulation, the previously applied steering angle was appended to the state vector, yielding the augmented state

$$\bar{\xi}(k) = \begin{bmatrix} \xi(k) \\ \delta(k-1) \end{bmatrix} \tag{69}$$

where $\delta(k-1)$ denotes the steering angle applied at the previous sampling instant.

The control input was defined as the steering angle increment

$$\Delta u(k) = \Delta\delta(k) = \delta(k) - \delta(k-1) \tag{70}$$

which served as the decision variable in the optimization problem.

The augmented state-space model was written as

$$\bar{\xi}(k+1) = \bar{A}\bar{\xi}(k) + \bar{B}\Delta u(k) + \bar{d}(k) \tag{71}$$

$$\bar{A} = \begin{bmatrix} A_k & B_k \\ 0 & 1 \end{bmatrix}, \quad \bar{B} = \begin{bmatrix} B_k \\ 1 \end{bmatrix}, \quad \bar{d}(k) = \begin{bmatrix} d(k) \\ 0 \end{bmatrix}$$

In this formulation, the previously applied steering angle was treated as an additional state, and the optimized variable became the steering angle increment rather than the absolute steering angle. The corresponding output equation can be written as

$$\eta(k) = \bar{C}\bar{\xi}(k) \tag{72}$$

$$\bar{C} = \begin{bmatrix} C_k & 0 \end{bmatrix}$$

At each sampling instant, a sequence of future reference points was generated along the desired path over the prediction horizon N_p. Using the augmented model, the stacked predicted output sequence was expressed as

$$\hat{\eta} = \Psi\bar{\xi}(k) + \Theta\Delta U + \Lambda\Phi \tag{73}$$

$$\hat{\eta} = \begin{bmatrix} \eta(k+1) \\ \vdots \\ \eta(k+N_p) \end{bmatrix}, \quad \Delta U = \begin{bmatrix} \Delta u(k) \\ \vdots \\ \Delta u(k+N_c-1) \end{bmatrix}, \quad \Psi = \begin{bmatrix} \bar{C}\bar{A} \\ \vdots \\ \bar{C}\bar{A}^{Np} \end{bmatrix}, \quad \Phi = \begin{bmatrix} \bar{d}(k) \\ \vdots \\ \bar{d}(k+N_p-1) \end{bmatrix}$$

$$\Lambda = \begin{bmatrix} \bar{C} & 0 & \cdots & 0 \\ \bar{C}\bar{A} & \bar{C} & \cdots & \vdots \\ \vdots & \vdots & \ddots & 0 \\ \bar{C}\bar{A}^{N_p-1} & \cdots & \bar{C}\bar{A} & \bar{C} \end{bmatrix}, \quad \Theta = \begin{bmatrix} \bar{C}\bar{B} & 0 & \cdots & 0 \\ \bar{C}\bar{A}\bar{B} & \bar{C}\bar{B} & \cdots & 0 \\ \vdots & \vdots & \ddots & \vdots \\ \bar{C}\bar{A}^{N_c-1}\bar{B} & \bar{C}\bar{A}^{N_c-2}\bar{B} & \cdots & \bar{C}\bar{B} \\ \vdots & \vdots & \ddots & \vdots \\ \bar{C}\bar{A}^{N_p-1}\bar{B} & \bar{C}\bar{A}^{N_p-2}\bar{B} & \cdots & \bar{C}\bar{A}^{N_p-N_c}\bar{B} \end{bmatrix}$$

where $\hat{\eta}$ is the stacked predicted output vector over the prediction horizon, Ψ is the free-response prediction matrix, Θ is the control-influence matrix, Λ is the disturbance-propagation matrix, ΔU is the stacked steering-increment vector, and Φ is the stacked disturbance vector. The matrix Ψ maps the current augmented state to the future outputs when no future control increment is applied. The matrix Θ captures the effect of future steering increments on the predicted outputs and has a lower block Toeplitz structure. The matrix Λ describes the propagation of the disturbance sequence over the prediction horizon. The vector ΔU contains all future steering increments over the control horizon N_c, and Φ contains the repeated or predicted disturbance terms used in the horizon-based prediction.

3.3.1.4 Objective Function and Constraints

The control objective function was formulated as

$$J = [\hat{\eta}_{\mathrm{ref}} - \hat{\eta}]^T \bar{Q} [\hat{\eta}_{\mathrm{ref}} - \hat{\eta}] + \Delta U^T \bar{R} \Delta U + \varepsilon_M^T \rho_M \varepsilon_M \tag{74}$$

$$\hat{\eta}_{\mathrm{ref}} = \begin{bmatrix} \eta_{\mathrm{ref}}(k+1) \\ \vdots \\ \eta_{\mathrm{ref}}(k+N_p) \end{bmatrix} \quad \bar{Q} = \begin{bmatrix} Q & 0 & 0 \\ 0 & \ddots & 0 \\ 0 & 0 & Q \end{bmatrix} \quad \bar{R} = \begin{bmatrix} R & 0 & 0 \\ 0 & \ddots & 0 \\ 0 & 0 & R \end{bmatrix}$$

where $\hat{\eta}_{\mathrm{ref}}$ is the stacked reference output sequence, Q is the block-diagonal output-weighting matrix, R is the control-weighting matrix, ρ_M is the relaxation-penalty coefficient, and ε_M is the slack variable. The matrix Q penalizes tracking errors in yaw angle and lateral position at each prediction step, whereas R penalizes excessive steering increments and therefore promotes smoother steering action. The scalar ρ_M determines the penalty associated with relaxing the optimization constraints through the slack variable ε_M.

The tracking error vector was defined as

$$E = \hat{\eta}_{\text{ref}} - \psi\bar{\xi}\left(k\right) - \Lambda\Phi \tag{75}$$

Accordingly, the MPC cost function in Equation (74) can be rewritten as

$$J = \Delta U^T \left(\Theta^T \bar{Q}\Theta + \bar{R}\right)\Delta U - 2E^T \bar{Q}\Theta\Delta U + E^T \bar{Q}E + \rho_M \varepsilon_M^2 \tag{76}$$

The predicted steering-angle sequence can be expressed as

$$U\left(k\right) = U_t + T_{\text{acc}}\Delta U\left(k\right) \tag{77}$$

$$U\left(k\right) = \begin{bmatrix} u\left(k\right) \\ \vdots \\ u\left(k+N_c-1\right) \end{bmatrix} \quad U_t = \begin{bmatrix} u\left(k-1\right) \\ \vdots \\ u\left(k-1\right) \end{bmatrix} \quad T_{\text{acc}} = \begin{bmatrix} I & 0 & \cdots & 0 \\ I & I & \cdots & \vdots \\ \vdots & \vdots & \ddots & 0 \\ I & I & \cdots & I \end{bmatrix}$$

The steering-magnitude constraint was expressed as

$$U_{\min} \le U_t + T_{\text{acc}}\Delta U\left(k\right) \le U_{\max} \tag{78}$$

$$U_{\min} = \begin{bmatrix} u_{\min} \\ \vdots \\ u_{\min} \end{bmatrix} \quad U_{\max} = \begin{bmatrix} u_{\max} \\ \vdots \\ u_{\max} \end{bmatrix}$$

The steering-increment constraint was given by

$$\begin{bmatrix} \Delta U_{\min} \\ 0 \end{bmatrix} \le \begin{bmatrix} \Delta U\left(k\right) \\ \varepsilon_M \end{bmatrix} \le \begin{bmatrix} \Delta U_{\max} \\ \varepsilon_{M,\max} \end{bmatrix} \tag{79}$$

where the limits $\Delta U_{\min}$ and $\Delta U_{\max}$ bound the rate of change of the steering command over the control horizon N_c, and $\varepsilon_{M,\max}$ is the maximum value of the slack variable. These bounds prevent unrealistically aggressive steering action and improve actuator feasibility.

By following the same procedure, the corresponding steering control law for the follower vehicle can be derived from Equations (62) to (79). This yields a consistent predictive steering framework for both supporting vehicles.

3.3.1.5 Adaptive Weighting Strategy

In the base controller, the tracking-weighting matrix Q and the control-weighting matrix R were constant. On straight-path segments with small tracking errors, the nominal weights were sufficient. However, on sharp curves or after disturbances, larger tracking errors could persist because the fixed cost function did not impose sufficient correction priority under all operating conditions. Increasing the weights only when the tracking condition became more demanding allowed the MPC controller to respond more aggressively without requiring manual retuning for different scenarios.

The adaptive weighting matrices $Q(k)$ and $R(k)$ were defined as

$$Q(k)=\begin{bmatrix} q_Y(k) & \\ & q_\theta(k) \end{bmatrix} \quad R(k)=r_\delta(k) \tag{80}$$

where $q_Y(k)$ is the lateral-error weight, $q_\theta(k)$ is the orientation-error weight, and $r_\delta(k)$ is the steering-effort weight.

To distinguish forward and reverse motion, a direction factor $\lambda_d(k)$ was defined as

$$\lambda_d(k)=\begin{cases} 0, & \text{forward} \\ 1, & \text{backward} \end{cases} \tag{81}$$

The weighting coefficients were updated online as bounded functions of the current operating condition. The lateral-error weight was updated as

$$q_Y(k)=\operatorname{sat}\left(q_{Y0}\left[1+\mu_l\frac{|l_e(k)|}{l_{e0}}+\mu_{kY}\frac{|k_{Om}(k)|}{k_{Om0}}+\mu_v\frac{|v_l(k)|}{v_{l0}}\right]\left[1+\mu_{dY}\left(1-\lambda_d(k)\right)\right]\right) \tag{82}$$

where q_{Y0} is the nominal baseline weight for lateral error, l_{e0} is the nominal lateral error, k_{Om0} is the nominal curvature, v_{l0} is the nominal longitudinal velocity, and μ_l, μ_{kY}, μ_v and μ_{dY} are the adaptation gains for lateral error, path curvature, longitudinal velocity, and motion direction in $q_Y(k)$, respectively. The operator sat(·) denotes saturation between prescribed lower and upper bounds.

The orientation-error weight was updated as

$$q_\theta(k)=\operatorname{sat}\left(q_{\theta0}\left[1+\mu_\theta\frac{|\theta_p(k)|}{\theta_{p0}}+\mu_{k\theta}\frac{|k_{Om}(k)|}{k_{Om0}}\right]\left[1+\mu_{d\theta}\lambda_d(k)\right]\right) \tag{83}$$

where $q_{\theta0}$ is the nominal baseline weight for orientation error, θ_{p0} is the nominal orientation error, and μ_θ, $\mu_{k\theta}$ and $\mu_{d\theta}$ are the adaptation gains associated with the magnitude of the orientation error, path curvature, and motion direction in $q_\theta(k)$, respectively.

The steering-effort weight was updated as

$$r_\delta(k)=\operatorname{sat}\left(r_{\delta0}\left[1+\mu_\delta\frac{|\delta(k-1)|}{\delta_{\max}}+\mu_{\Delta\delta}\frac{|\Delta\delta(k-1)|}{\Delta\delta_{\max}}\right]\right) \tag{84}$$

where $r_{\delta0}$ is the nominal baseline weight for steering effort, and μ_δ and $\mu_{\Delta\delta}$ are the adaptation gains associated with steering-angle magnitude and steering-rate magnitude, respectively.

Equation (82) increases the lateral-error penalty during forward motion when $\lambda_d(k) = 0$. Equation (83) increases the orientation-error penalty during reverse motion when $\lambda_d(k) = 1$. Equation (84) increases the steering-effort penalty when the steering angle or steering-angle increment becomes large. As a result, the controller places greater emphasis on lateral path convergence during forward travel, greater emphasis on heading alignment during backward travel, and greater emphasis on smooth and feasible steering action when steering demand becomes excessive. The adaptive weighting is evaluated in the simulations of Chapter 4; the experiments of Chapter 5 use the fixed weights of the base controller (Section 6.2).

3.3.2 Longitudinal Velocity Control

A PID controller is implemented to regulate the longitudinal velocity v_l. The positional form of the PID controller and its discrete representation are given by

$$u_v(t) = K_p e_v(t) + K_i \int_0^t e_v(\tau) d\tau + K_d \frac{de_v(t)}{dt} \tag{85}$$

$$u_v(k) = K_p e_v(k) + K_i \sum_{j=1}^{k} e_v(j)T + K_d \frac{e_v(k) - e_v(k-1)}{T} \tag{86}$$

where K_p, K_i and K_d denote the proportional, integral, and derivative gains, respectively, T is the sampling time, and $e_v(k)$ is the velocity tracking error at time step k.

The velocity form of the PID controller, which is commonly used in industrial applications because of its numerical convenience, is obtained by differentiating the positional form:

$$\begin{aligned} \Delta u_v &= u_v(k) - u_v(k-1) \\ &= K_p \left(e_v(k) - e_v(k-1) \right) + K_i e_v(k) T + K_d \frac{e_v(k) - 2e_v(k-1) + e_v(k-2)}{T} \end{aligned} \tag{87}$$

The error $e_v(k)$ is defined as the difference between the target speed and the current speed:

$$e_v(k) = v_{\text{Target}}(k) - v_{\text{Current}}(k) \tag{88}$$

This controller is used to regulate the longitudinal motion of each vehicle and provides the actuation channel required for both speed tracking and formation synchronization.

3.3.3 Synchronization Control

Synchronization is regulated through the same path-coordinate offset error e defined in Section 3.2.3. The steering controller makes the follower track its reference path, while the synchronization law supplies the follower's longitudinal-velocity command. Separation remains a distinct performance quantity. The analysis below concerns the scalar offset-error dynamics under the stated kinematic and command-tracking assumptions.

For the synchronous tracking problem defined by Equation (61), let

$$\frac{v_1 \cos\theta_{p1}}{1-l_{e1}\cdot k_{Om1}} - \frac{v_2 \cos\theta_{p2}}{1-l_{e2}\cdot k_{Om2}} = -k_e \cdot e \tag{89}$$

where $k_e > 0$ is a user-defined control gain. The control law for the follower longitudinal velocity can then be expressed as

$$v_2 = \left(\frac{v_1 \cos\theta_{p1}}{1-l_{e1}\cdot k_{Om1}} + k_e \cdot e\right)\cdot\frac{1-l_{e2}\cdot k_{Om2}}{\cos\theta_{p2}} \tag{90}$$

The resulting error dynamics are

$$\dot{e} + k_e \cdot e = 0 \tag{91}$$

This is a first-order linear system with eigenvalue $-k_e$, which is strictly negative when $k_e > 0$. Therefore, the synchronization error converges asymptotically to zero. A formal synchronization condition is thus given by

$$\lim_{s\to\infty} e(s) = 0 \tag{92}$$

which describes convergence of the scalar synchronization error under the modelled error dynamics. Together with individual-vehicle path tracking, offset regulation supports coordinated motion of the two vehicles.

The PID loop regulates longitudinal velocity, and the MPC loop regulates steering under the stated constraints. This allocation permits separate tuning of the two control tasks, while synchronization links the follower velocity command to the leader motion. The loops remain physically coupled through vehicle motion and the connecting truss; their practical tracking performance is assessed in the simulation and experimental chapters.

To characterize the stability of the synchronization law, consider the Lyapunov candidate function

$$V(e) = \frac{1}{2}e^2 \tag{93}$$

with derivative

$$\dot{V}(e) = e\dot{e} = -k_e e^2 \le 0 \tag{94}$$

Since $V(e)$ is positive definite and $\dot{V}(e)$ is negative definite for $k_e > 0$, $e = 0$ is asymptotically stable. The convergence statement applies to the nominal scalar error dynamics used in the derivation. It does not, by itself, establish a stability guarantee for the complete constrained MPC–PID system or zero offset under arbitrary persistent measurement and motion disturbances. The simulation and experimental results provide the corresponding performance assessment under the tested conditions.

3.3.4 Kinematic-Model-Based Control Laws

Luo (2017) developed the kinematic WSIC control system used as the baseline in this thesis. His method includes path-coordinate following and first-order synchronization rather than only Cartesian position regulation. Figure 3.2 shows his path-following bicycle model. The comparison evaluates the proposed dynamic-model-based strategy against this established WSIC approach, including the effects represented by the vehicle dynamics, tire slip, and transmitted truss loads.

The steering control law for both the leader and follower vehicles was defined by Luo (2017) as follows:

$$\delta = \tan^{-1}\left(l\left(-k_1 \tan\theta_p - k_2 \frac{l_e}{\cos\theta_p} + \frac{k_{Om}\cos\theta_p}{1 - l_e \cdot k_{Om}} \right)\right) \tag{95}$$

where k_1 and k_2 are positive control gains.

A PID controller was also used for velocity control. The velocity control law for the follower vehicle was given by Luo (2017) as

$$v_2 = \frac{v_1 \cos\theta_{p1} + k_e \cdot e}{\cos\theta_{p2}} \tag{96}$$

These control laws provide a useful baseline for comparison with the dynamic-model-based control approach proposed in this chapter.

3.3.5 A Unified Model Predictive Control Baseline

To provide a basis for comparison with the combined MPC–PID control architecture, a unified controller was constructed using a four-state kinematic bicycle model, where the state vector was defined as vehicle position, yaw angle, and longitudinal velocity, $[X, Y, \theta, v]$, and the control inputs were steering angle and acceleration, $[\delta, a]$, as established by Kong et al. (2015). At each sampling step, the nonlinear model was linearized about the current operating point to obtain a linear time-varying system, following the method of Pang et al. (2022). The corresponding constrained optimization problem was formulated as a quadratic program and solved within a receding-horizon MPC framework.

The unified baseline uses fixed Q and R, whereas the proposed steering MPC uses the adaptive weighting described in Section 3.3.1.5. The designs also differ in their prediction models and allocation of steering and longitudinal control. The Chapter 4 comparison therefore evaluates the complete controller implementations; it does not isolate the effect of separating the control loops alone.

3.4 Evaluation Parameters

3.4.1 Integral Absolute Error

To evaluate and compare the simulated and experimental results, the integral absolute error (IAE) was used to quantify the cumulative lateral, orientation, offset, and separation errors (Mousakazemi, 2021). In this study, the IAE was formulated with respect to the distance travelled by the vehicles; therefore, it represents accumulated absolute tracking error over the travelled path rather than an instantaneous deviation. As a cumulative index, the IAE increases with path length wherever the error is nonzero. Consequently, IAE values should be compared between cases with the same or closely comparable trajectory lengths. A lower IAE indicates smaller errors and/or reduced error persistence over the evaluated path. The lateral, orientation, offset, and separation errors are defined in Section 3.2.3. Here the integration distance is the non-decreasing distance travelled during the evaluated run, including reverse travel; it is distinguished from the oriented reference-path coordinates used for synchronization.

The IAE of lateral error, J_L (m^2), is defined as

$$J_L = \int_0^s \left| l_e(s) \right| ds \tag{97}$$

The IAE of orientation error, J_θ (rad·m), is defined as

$$J_\theta = \int_0^s \left| \theta_p(s) \right| ds \tag{98}$$

The IAE of offset error, J_e (m^2), is defined as

$$J_e = \int_0^s \left| e(s) \right| ds \tag{99}$$

The IAE of separation error, J_d (m^2), is defined as

$$J_d = \int_0^s \left| e_d(s) \right| ds \tag{100}$$

3.4.2 Instantaneous Error Bounds

Because the IAE is an accumulated measure, it was used to compare overall tracking quality over identical test paths. To complement this cumulative metric, instantaneous error bounds were specified as platform-level performance requirements. The following limits were adopted for the small-scale WSIC:

- Lateral error: within ± 0.15 m
- Orientation error: within ± 0.15 rad
- Offset error: within ± 0.30 m
- Separation error: within ± 0.30 m

The four criteria address complementary operating requirements: traffic-lane clearance, heading-induced lateral displacement, path-coordinate synchronization, and permissible inter-vehicle separation. Their numerical interpretation is based on the dimensions and intended operating configuration of the small-scale platform, with the supporting literature identified below.

3.4.2.1 Lateral Error

The lateral-error criterion was assessed against the clearance available within the intended permanent traffic corridor. Controlled traffic farming requires machinery wheel tracks to be matched to permanent traffic lanes (Isbister et al., 2013). For the WSIC configuration considered here, each supporting vehicle is assumed to operate within a corridor at least twice its width. This two-width corridor is a study-specific operating assumption rather than a universal lane-width rule. The corridor accommodates one complete supporting vehicle and is distinct from an individual tire-running strip.

Using the 0.54 m tread width and 0.05 m tire width in Table 4.1, and taking tread width as the distance between the left and right tire centrelines, the aligned outer-tire envelope provides a nominal vehicle-width measure of $W_{\text{vehicle}} = 0.54 + 0.05 = 0.59$ m. At the assumed minimum corridor width, $W_{\text{lane}} = 2W_{\text{vehicle}} = 1.18$ m, the lateral clearance for a centred, aligned vehicle is $(W_{\text{lane}} - W_{\text{vehicle}}) / 2 = 0.295$ m. The ± 0.15 m lateral-error limit therefore leaves $0.295 - 0.15 = 0.145$ m of nominal clearance on the displaced side. Equivalently, the basic aligned-vehicle condition is $W_{\text{lane}} \geq W_{\text{vehicle}} + 2l_{e,\max} = 0.89$ m, where $l_{e,\max} = 0.15$ m is the lateral-error allowance; the assumed 1.18 m corridor exceeds the corresponding 0.89 m minimum. Heading, steering, body overhang, and other clearance demands must be accommodated within the remaining allowance.

As supplementary industry context, AllyNav (2025) identifies ± 15 cm as its sub-metre agricultural GPS accuracy category. This supports the order of magnitude of the selected tolerance, but the WSIC requirement is justified by the platform-specific clearance calculation rather than treating GPS positioning accuracy as identical to maximum instantaneous tracking error.

3.4.2.2 Orientation Error

The orientation-error limit was related to the lateral displacement caused by heading misalignment over a characteristic travel distance. The no-slip path-tracking kinematics presented by Snider (2009) relate lateral-error growth to speed and the sine of heading error. For a locally straight path, negligible sideslip, and approximately constant heading error over a travelled distance L_c, the corresponding heading-only estimate is $\Delta y_\theta \approx L_c \sin \theta_p$.

Taking one vehicle wheelbase as the characteristic travel distance gives $L_c = l_f + l_r = 0.25 + 0.25 = 0.50$ m. At the selected orientation limit, $\Delta y_\theta \approx 0.50 \sin (0.15 \text{ rad}) = 0.075$ m. Thus, ± 0.15 rad corresponds to approximately 0.075 m of heading-induced lateral displacement over one wheelbase of travel, or half of the lateral-error allowance. This provides a physical interpretation of the selected heading tolerance. The characteristic length and tolerance are design choices for this study; Snider (2009) supports the kinematic relationship. The calculation is a local heading-only approximation, and traffic-lane clearance must accommodate lateral displacement and heading effects together.

3.4.2.3 Offset Error

The offset-error criterion limits the path-coordinate synchronization error, e, defined in Section 3.2.3. A tolerance of ± 0.30 m was selected to restrict the mismatch in the vehicles' path-coordinate progress to 12% of the nominal 2.5 m support span. This is a project-selected synchronization tolerance: it bounds how closely the vehicles progress together along their respective reference paths, separately from the actual-distance constraint used for separation error. On curved paths, the offset is evaluated from the path coordinates, not replaced by a Cartesian longitudinal displacement or a truss-skew angle.

3.4.2.4 Separation Error

The separation-error criterion was checked against the usable span of the truss-support arrangement. The permissible effective inter-vehicle separation, d_2, ranges from 2.0 m to 3.8 m with a desired separation of $d_{2,\text{ref}} = 2.5$ m. For $e_d = d_2 - d_{2,\text{ref}}$, these mechanical limits correspond to $-0.50 \leqslant e_d \leqslant 1.30$ m. The selected symmetric criterion, $|e_d| \leqslant 0.30$ m, restricts the accepted separation to $d_{2,\text{ref}} - 0.30 \leq d_2 \leq d_{2,\text{ref}} + 0.30$, which is 2.20 m $\leq d_2 \leq$ 2.80 m.

At the lower accepted separation, 0.20 m remains below the minimum-span limit; at the upper accepted separation, 1.00 m remains below the maximum-span limit. The ± 0.30 m criterion therefore maintains a minimum geometric reserve of 0.20 m while limiting deviation from the desired formation. This reserve concerns permissible support spacing and sliding travel, rather than allowable elastic deformation of the truss.

Together, these criteria provide a consistent basis for evaluating individual-vehicle tracking and cooperative WSIC control. The IAE quantifies accumulated performance over the complete evaluated path, while the instantaneous bounds assess operational deviations. Error histories or peak-error values must be checked over the stated evaluation interval to assess compliance; a lower IAE alone does not establish that an instantaneous bound was satisfied. Any initial-recovery interval considered separately from tracking operation should be identified explicitly.

3.5 Control Sequence

The control sequence for mobile mode is illustrated in Figure 3.12.

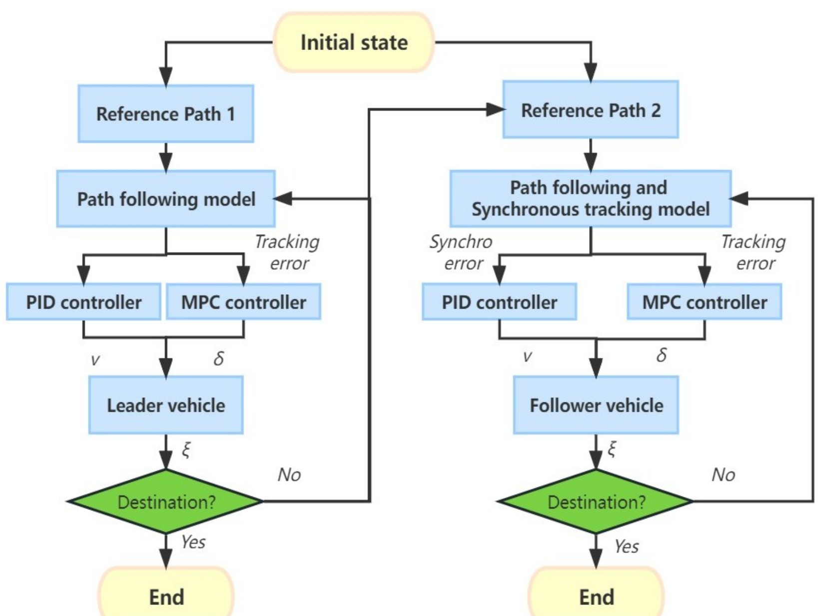

Figure 3.12 Control sequence for mobile mode

3.5.1 Initialization

Initial states were assigned to the leader and follower vehicles. All parameter initial values are defined as follows:

1. Leader vehicle:

- Position: $x_1(0)$, $y_1(0)$

- Heading angle: $\theta_1(0)$
- Lateral velocity: $v_{rL}(0)$
- Longitudinal velocity: $v_{lL}(0)$
- Angular velocity: $\omega_1(0)$
- Control inputs: steering angle $\delta_L(0)$, velocity $v_1(0)$

2. Follower vehicle:
   - Position: $x_2(0)$, $y_2(0)$
   - Heading angle: $\theta_2(0)$
   - Lateral velocity: $v_{rF}(0)$
   - Longitudinal velocity: $v_{lF}(0)$
   - Angular velocity: $\omega_2(0)$
   - Control inputs: steering angle $\delta_F(0)$, velocity $v_2(0)$
3. Reference path:
   - Reference state: (x_r, y_r, θ_r)

3.5.2 Control Process

At each time step, the control process proceeds as follows:

First, the leader vehicle performs path tracking using its own control law. The real-time leader state $\xi_L = (v_{rL}, v_{lL}, \theta_1, \omega_1, y_1, x_1)$ is sent to the controller. The controller then computes the path-tracking errors l_{e1} and θ_{p1} between the desired reference path and the current leader state, and uses these errors together with ξ_L to generate the control inputs $u_L = (\delta_L, v_1)$ using Equations (62) to (88). The leader vehicle updates its motion according to these inputs.

For the follower vehicle, a virtual reference state $(x_{rF}, y_{rF}, \theta_{rF})$ is generated from the path and the leader motion. The follower's own state ξ_F is compared with this virtual reference state by the controller, which computes the path-tracking errors l_{e2}, θ_{p2} and the offset error e. Using these errors together with Equations (62) to (88) and (90), the controller generates the follower control inputs $u_F = (\delta_F, v_2)$, after which the follower updates its motion.

The controller then waits for updated states from both vehicles before proceeding to the next control loop. This process is repeated in closed loop, allowing the trajectories of both vehicles to be corrected continuously to maintain path-tracking accuracy and coordination. This sequential control structure provides the practical implementation framework for the combined steering, velocity, and synchronization strategy proposed in this chapter.

Chapter 4

Simulations

Simulation is essential for testing and verifying the effectiveness of the designed control laws. In this research, MATLAB and CarSim were used to simulate the WSIC guidance model and control strategy.

4.1 Simulation Introduction

4.1.1 Simulation Setup

The WSIC consists of two supporting vehicles connected by a truss that carries an implement. The truss and any additional vertical implement load are supported by the two vehicles. The truss self-weight, its allocation between the vehicles, and the additional vertical-load design capacity are distinguished below. Schematic diagrams of the WSIC with dimensions are shown in Figure 4.1.

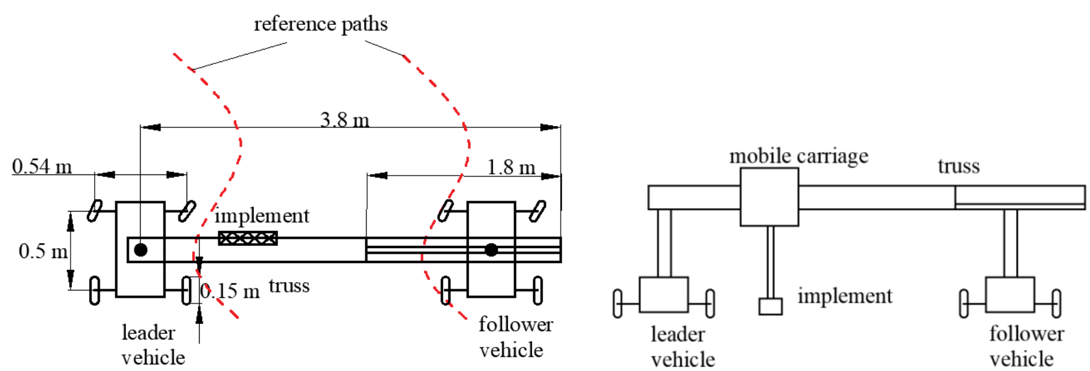

(a) horizontal plane (b) vertical plane

Figure 4.1 Schematic diagrams of WSIC with dimensions

For an actual WSIC system, the truss length between the two supporting vehicles could reach 61 m (Laguë et al., 1997). The follower vehicle can slide beneath one end of the truss over a range of 12.2 m to accommodate different field widths. The vehicle wheelbase is 3.2 m, and the tread width is 1.9 m. The truss weight is 53.5 kN, and its vertical load capacity is 11.1 kN. The field-scale leader and follower tractors weigh 35.6 kN and 24.4 kN, respectively. For experimental implementation, a small-scale platform was developed without imposing a single geometric scale factor on all components. The key physical parameters of the simulated vehicles and truss are listed in Table 4.1 and Table 4.2, and the mobile-mode operating scenarios are summarized in Table 4.3.

Table 4.1 Parameters of support vehicles

Description	Value
Length from centre to front wheel (l_f)	0.25 m
Length from centre to rear wheel (l_r)	0.25 m
Wheel diameter	0.15 m
Tire width	0.05 m
Tread width ($2h$)	0.54 m
Steering range (δ)	$\pm 32°$
Velocity constraint in the controller	± 4 m/s
Acceleration constraint in the controller	± 1 m/s^2

Table 4.2 Parameters of the connecting truss

Description	Value
Truss length	3.8 m
Sliding length under truss	1.8 m
Truss self-weight	120 N
Load capacity (excluding self-weight)	100 N

The truss self-weight is 120 N. The additional vertical-load design capacity of 100 N was calculated from the load-support capability of the vehicles and excludes the truss self-weight. The combined vertical weight would therefore be 220 N at the full additional-load allowance. This is a vehicle-based design allowance.

Table 4.3 Operating scenarios for mobile mode

Description	Value
Operating-speed range	1.5–3.5 m/s
Travel distance	40 m
Truss span range	2.5 m
Truss-induced vertical load on leader, G_1	0–120 N
Truss-induced vertical load on follower, G_2	120 N − G_1
Weight of each vehicle	280 N

The 0–120 N range describes the allocation of the fixed 120 N truss self-weight between the vehicles. Let G_1 and G_2 denote the downward truss-induced loads on the leader and follower, respectively. For flat-terrain operation without additional vertical payload, the simulation enforces

$G_1 + G_2 = 120$ N and $G_2 = 120$ N $- G_1$. The shares are complementary: a 0 N share on one vehicle corresponds to 120 N on the other, while equal sharing gives 60 N on each vehicle. The range specifies load-sharing bounds, rather than a variation in total truss weight or a claim that every distribution was tested. These loads are additional to each vehicle's 280 N self-weight; any additional vertical payload is accounted for separately.

4.1.1.1 Dimensional Scale-Ratio Mismatch Between the Field-Scale and Small-Scale Platforms

The dimensional ratios between the field-scale WSIC platform and the small-scale WSIC prototype used in this study are listed in Table 4.4.

Table 4.4 Dimensional ratios between the field-scale and small-scale WSIC prototypes[a]

Description	Dimensional ratios for field-scale platform	Dimensional ratios for small-scale platform
Wheelbase to tread width	1.7	0.93
Wheel diameter to wheelbase	0.35	0.30
Wheel diameter to tread width	0.59	0.28
Tire width to wheelbase	0.17	0.10
Tire width to tread width	0.29	0.093
Length of connecting truss to wheelbase	19.1	7.6
Length of connecting truss to tread width	32.1	7.0

[a] Field-scale ratios involving tire width or wheel diameter use approximate dimensions inferred from the reported tire designation and manufacturer specifications, rather than direct measurements of the original field-scale tires. See the tire-dimension discussion below. Ratios calculated from the small-scale dimensions are rounded independently.

The dimensional ratios of the connecting truss to the vehicle wheelbase and tread width in Table 4.4 are computed using the truss length consistently at both scales: 61 m for the field-scale platform (Laguë et al., 1997) and 3.8 m for the small-scale platform (Table 4.2).

Using the truss length as the reference dimension gives a field-to-small-scale length ratio of 61/3.8 = 16.05. Applying this factor to the field-scale tractor wheelbase and tread width (3.2 m and 1.9 m, respectively; Laguë et al., 1997) would give approximately 0.20 m and 0.12 m. The vehicles used in this study instead have a 0.50 m wheelbase and a 0.54 m tread width (Table 4.1), approximately 2.5 and 4.5 times these uniformly scaled dimensions. The truss-to-wheelbase and truss-to-tread-width ratios are 19.1 and 32.1 for the field-scale platform, compared with 7.6 and 7.0

for the small-scale platform. Thus, the small-scale vehicles occupy a proportionally larger fraction of the truss span.

The platform was sized component by component to accommodate the hardware required for autonomous operation. The connecting truss is a passive structural link, whereas each support vehicle houses its drivetrain and FWS hardware, RTK-GPS receiver, IMU, XBee radio, and onboard computer. These requirements set practical lower bounds on vehicle size. This component-based design retained the vehicle–truss–vehicle configuration while providing the sensing, communication, and actuation needed for experimental controller implementation.

The relative weight distribution also differs between the two platforms. The field-scale leader and follower weigh 35.6 kN and 24.4 kN, respectively, and the truss weighs 53.5 kN (Laguë et al., 1997). Each small-scale vehicle weighs 280 N, and its truss weighs 120 N (Tables 4.2 and 4.3). The ratio of truss weight to total supporting-vehicle weight is therefore approximately 53,500 / (35,600 + 24,400) = 0.892 at field scale, compared with 120 / (280 + 280) = 0.214 at small scale. The leader-to-follower weight ratio is approximately 1.46 at field scale and 1.00 at small scale. Thus, the small-scale load distribution is explicitly defined, but its normalized truss loading is not proportional to that of the field-scale system.

These comparisons establish the role of the prototype as a small-scale experimental validation platform rather than a dynamically similar miniature. The importance of matched dynamic parameters in scaled-vehicle testing is discussed by Lapapong et al. (2009). Here, geometric and relative-weight ratios were not matched, so dynamic similarity has not been established. Consequently, quantitative field-scale response cannot be predicted by applying a single scale factor to the small-scale results.

The platform nevertheless provides a direct experimental link between control development and physical WSIC operation: the proposed controller was implemented on two vehicles mechanically connected by a truss, and coordinated tracking was evaluated with the actual sensing, communication, and control hardware. The model formulation and control architecture provide a foundation for field-scale implementation. Because geometry and mass distribution affect the predicted vehicle and coupled-system responses, that implementation requires identification or verification of the field-scale model parameters; reassessment of actuator constraints and operating conditions, including separate response delays for the hydraulic steering and engine-transmission drive systems of a field-scale tractor in place of the common 0.04 s actuator delay used for the electric drives of the small-scale platform (Section 4.1.4); and review and retuning of the MPC weights, prediction horizon, sampling interval, and PID gains as appropriate. These steps extend the small-scale control design to the target configuration while accounting explicitly for the scale-dependent dynamics.

Using identical 280 N leader and follower vehicles was consistent with the independently actuated experimental design. In the field-scale configuration described by Laguë et al. (1997), the leader carries the shared hydraulic power unit. In the present platform, each vehicle has its own motor, battery, steering actuation, and onboard computer. This arrangement supports autonomous operation of both vehicles without a shared power unit. The different leader–follower weight distribution of a field-scale system must be represented when adapting the model and controller to that configuration.

The field-scale tire dimensions in Table 4.4 are approximate. Laguë et al. (1997) report the designation "21.5-16 low profile," from which the nominal 21.5 in section width is taken as approximately 0.546 m. The overall diameter is estimated as 44.3 in (approximately 1.12 m), using the mean of two 21.5L-16.1 specifications: Carlisle Farm Specialist I-1 (44.5 in) and Firestone Turf and Field R3 (44.1 in). These manufacturer specifications are used as dimensional proxies for the reported tires; the resulting ratios are estimates rather than direct measurements or a verified equivalence between the designations.

4.1.2 Software and Simulink Model

This research used a co-simulation platform integrating MATLAB/Simulink and CarSim to develop and implement the control algorithms (Corke, 2021; Li et al., 2019). CarSim is an industry-standard vehicle dynamics simulation tool that provides a high-fidelity environment for the development and evaluation of controllers, particularly for autonomous vehicle path tracking. Although CarSim can operate as a standalone application, it can also be interfaced with MATLAB/Simulink for direct controller design and testing.

In this co-simulation architecture, CarSim supplied the high-fidelity vehicle and terrain dynamics used as the simulated plant, superseding the simplified dynamic model of Section 3.1 in that role. The Section 3.1 dynamic model was retained as the internal predictive model used by the MPC steering controller (Section 3.3.1) to compute the control action at each step; it was not used to represent the plant being controlled once CarSim was introduced. The MPC controller itself, including the incremental formulation, adaptive weighting, and constraint handling described in Section 3.3.1, was implemented directly in MATLAB/Simulink rather than through the built-in MATLAB MPC Toolbox, so that these features could be specified explicitly.

Figure 4.2 summarizes this architecture and its relation to the control design of Chapter 3. The plant, simulated in CarSim through the Simulink interface, comprises the leader and follower vehicles, represented by force-based dynamic models with wheel slip, inertia, and yaw dynamics, and the truss and implement, through which the truss-transmitted forces and moments and the external load act on the vehicles. Sensor models matched to the experimental hardware of Section 5.1.2 (RTK-GPS position and speed, IMU yaw, and the steering-angle sensor) supply the state estimate; no state is assumed to be known perfectly. The controller-internal model is the reduced dynamic model with the adjoint-curve leader–follower description, adapted and extended from Wang and Wang (2015) with the instantaneous-centre-of-rotation kinematics and the offset-error state, and it drives three control laws: the incremental MPC steering controller with adaptive direction-sensitive weighting, the velocity-form PID longitudinal controller, and the Lyapunov-stable synchronization law that sets the follower velocity from the offset error. The kinematic model of Luo (2017) is retained only as a comparison baseline. Actuator commands act on the plant through the steering actuator and drive motors, closing the loop. The mismatch between the high-fidelity plant and the reduced controller-internal model is therefore deliberate: the controllers are evaluated against dynamics they do not represent exactly, as they would be in the field.

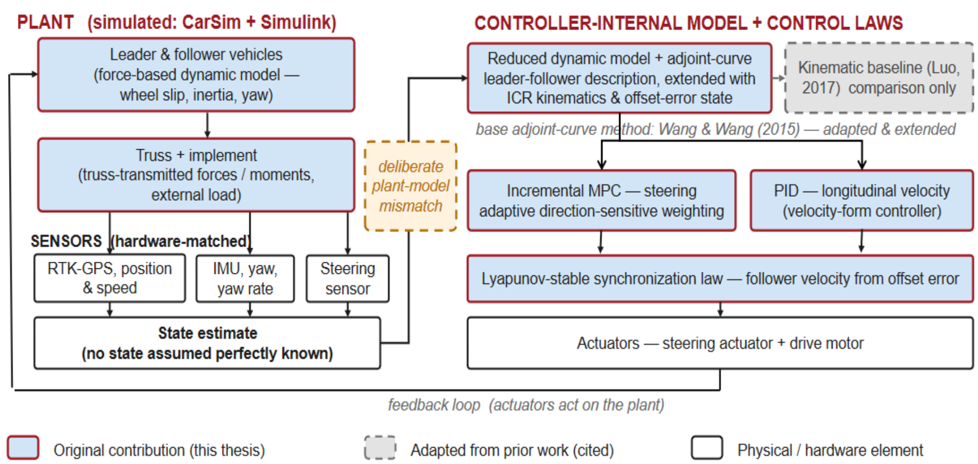

Figure 4.2 Architecture of the CarSim–Simulink co-simulation: plant, sensors, and state estimate (left); controller-internal model and control laws (right)

The vehicle model in CarSim is a 4WS-4WD vehicle, which can switch to FWS or RWS mode. In this study, the two steering wheels were simplified as a single virtual wheel located at the centre of the steered axle (front axle for FWS, rear axle for RWS). This is the standard two-axle bicycle-model simplification: the vehicle has two axles, and the pair of physical wheels on the steered axle is represented by one virtual wheel at that axle's centre; no third axle is implied. The steering angles δ_1 and δ_2 of the FWS vehicle can be obtained via Ackermann geometry during turning (Ackermann and Sienel, 1993)

$$
\begin{aligned}
\delta_1 &= \begin{cases} \arctan\dfrac{(l_f+l_r)\tan\delta}{l_f+l_r+h\cdot\tan\delta}, \delta<0 \\ \arctan\dfrac{(l_f+l_r)\tan\delta}{l_f+l_r-h\cdot\tan\delta}, \delta\geq 0 \end{cases} \\
\delta_2 &= \begin{cases} \arctan\dfrac{(l_f+l_r)\tan\delta}{l_f+l_r-h\cdot\tan\delta}, \delta<0 \\ \arctan\dfrac{(l_f+l_r)\tan\delta}{l_f+l_r+h\cdot\tan\delta}, \delta\geq 0 \end{cases}
\end{aligned}
\tag{101}
$$

The steering angles δ_3 and δ_4 of the RWS vehicle can be obtained as follows:

$$
\begin{aligned}
\delta_3 &= \begin{cases} \arctan\dfrac{(l_f+l_r)\tan\delta}{l_f+l_r+h\cdot\tan\delta}, \delta<0 \\ \arctan\dfrac{(l_f+l_r)\tan\delta}{l_f+l_r-h\cdot\tan\delta}, \delta\geq 0 \end{cases} \\
\delta_4 &= \begin{cases} \arctan\dfrac{(l_f+l_r)\tan\delta}{l_f+l_r-h\cdot\tan\delta}, \delta<0 \\ \arctan\dfrac{(l_f+l_r)\tan\delta}{l_f+l_r+h\cdot\tan\delta}, \delta\geq 0 \end{cases}
\end{aligned}
\tag{102}
$$

After the steering controller calculated the desired steering angle of the virtual steering wheel δ, Equations (101) and (102) were used to output the actual steering angles to the steering actuator.

The co-simulation procedure involved three main stages.

- Path and model definition: The vehicle model, reference paths, and operating environment were defined in CarSim. The modelling and environment setup interface is shown in Figure 4.3.

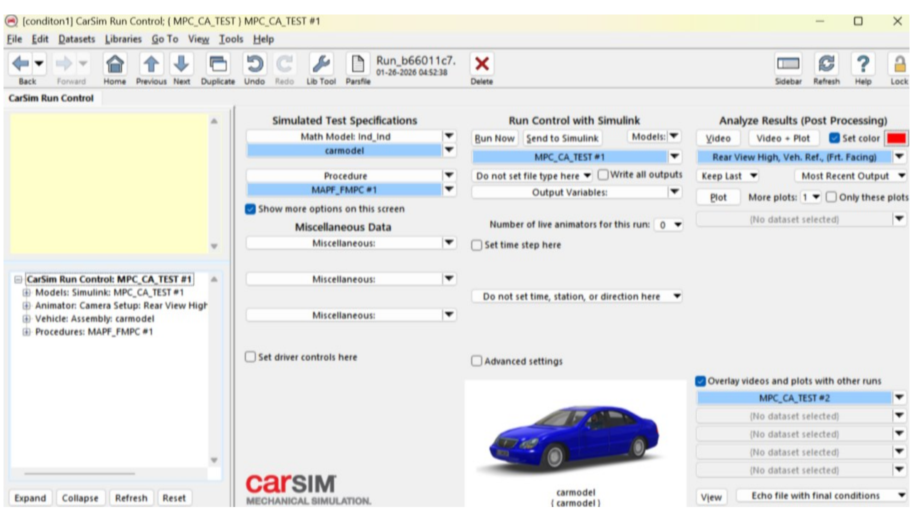

Figure 4.3 Vehicle modelling and environment setup interface in CarSim

- Controller design: The control algorithms were developed in Simulink to generate steering and velocity commands. The Simulink model also incorporated the application of external forces and transmitted command signals to the CarSim vehicle model. The established control system is shown in Figure 4.4.

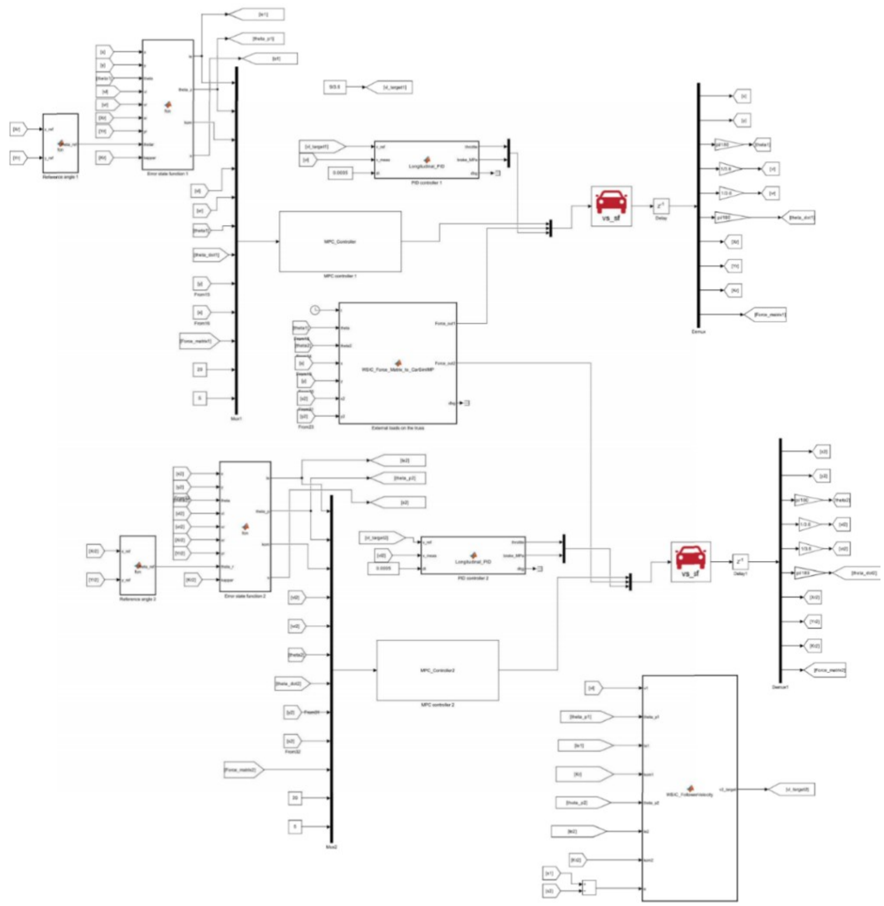

Figure 4.4 Control system modelling in Simulink

- Co-simulation execution: CarSim handled the high-fidelity vehicle and environment model, while Simulink executed the controller, with data exchanged in real time.

4.1.3 Simulation Test Scenarios

To validate the tracking performance of the control strategy under realistic agricultural operating conditions, the simulation study employed combined test scenarios. These scenarios were constructed by varying key operational parameters, including motion direction, path geometry, surface condition, speed, external load, implement position, and initial condition.

The simulation test matrix included the following factors.

1. Vehicle motion: Forward and reverse motion.

2. Path geometry: Straight-line and S-shaped curved reference paths. The S-shaped path was defined by Equation (103).

$$
\begin{aligned}
y_L &= \begin{cases} 2.5, & x_L < 8 \\ 0.5\cos\left(\dfrac{x_L-8}{4}\pi\right) - 0.25\cos\left(\dfrac{x_L-8}{6}\pi\right) + 2.25, & 8 <= x_L <= 32 \\ 2.5, & x_L > 32 \end{cases} \\
y_F &= \begin{cases} 0, & x_F < 8 \\ 0.5\cos\left(\dfrac{x_F-8}{4}\pi\right) - 0.25\cos\left(\dfrac{x_F-8}{6}\pi\right) - 0.25, & 8 <= x_F <= 32 \\ 0, & x_F > 32 \end{cases}
\end{aligned} \tag{103}
$$

3. Surface adhesion: Three pathway conditions representing different terrains, including high-adhesion concrete pavement (μ = 1.0), medium-adhesion earth road (μ = 0.75), and low-adhesion grass (μ = 0.5).

4. Target speeds: Most agricultural operations are conducted at low speeds (typically no more than 15 km/h). Based on representative operating speeds for off-road agricultural vehicles (Grisso et al., 2019), three target speeds were selected: 1.5 m/s for low-speed precision operation, 2.5 m/s for general operation, and 3.5 m/s for higher-speed transport or field operation. The ±4 m/s velocity range listed in Table 4.1 represents the speed limit for agricultural field operation, consistent with the typical agricultural operating-speed ceiling of approximately 15 km/h noted above. The 3.5 m/s maximum tested target speed was set below this limit, leaving margin for closed-loop speed control.

5. External load: A force opposing the direction of travel, applied to the truss at magnitudes of F_{external} = 50 N or 200 N.

6. Implement position: The implement was mounted on the truss at lateral offsets of d_4 = 0.8 m and 1.5 m, measured from the leader vehicle.

7. Initial condition: The initial offset error between the two vehicles was set to e = 0 m, 0.5 m, or 1 m.

4.1.4 Real-World Environment Setup

To improve the realism of the simulation, environmental factors including sensor noise, system delay, external disturbance, and model uncertainty were injected into the control loop. The sampling period was set to T = 0.02 s, corresponding to a control frequency of 50 Hz. To ensure repeatability of the stochastic processes, a fixed random seed was used. The numerical values adopted for each of these factors are justified where they are introduced, on the basis of the platform hardware described in Section 5.1.2, the responses logged during the platform experiments, or the literature.

4.1.4.1 Sensor Noise

1. GPS-RTK measurements (position and velocity):

In real-time systems, GPS-RTK typically provides position and velocity measurements at a relatively low output frequency. In this study, GPS measurements were modelled at 10 Hz. Because the controller operated at 50 Hz, a low-frequency update mechanism with zero-order hold (ZOH) was used to simulate the GPS output sequence. The update period is given by Equation (104).

$$T_{\mathrm{GPS}} = \frac{1}{f_{\mathrm{GPS}}}, \quad f_{\mathrm{GPS}} = 10 \quad \mathrm{Hz} \tag{104}$$

Under the control period $T = 0.02$ s, the corresponding update step size is given by Equation (105).

$$N_{\mathrm{GPS}} = \mathrm{round}\left(\frac{T_{\mathrm{GPS}}}{T}\right) = \mathrm{round}\left(\frac{0.1}{0.02}\right) = 5 \tag{105}$$

Therefore, GPS measurements were updated once every N_{GPS} control steps and retained their previous value between updates. Let k denote the control step index. When $k \equiv 0 \pmod{N_{\mathrm{GPS}}}$, the GPS measurements were updated according to Equation (106).

$$\begin{aligned} \tilde{x}(k) &= x(k) + \varpi_{\mathrm{pos}}(k) \\ \tilde{y}(k) &= y(k) + \varpi_{\mathrm{pos}}(k) \\ \tilde{v}(k) &= v(k) + \varpi_{\mathrm{vel}}(k) \end{aligned} \tag{106}$$

Otherwise, they were updated according to Equation (107).

$$\begin{aligned} \tilde{x}(k) &= \tilde{x}(k-1) \\ \tilde{y}(k) &= \tilde{y}(k-1) \\ \tilde{v}(k) &= \tilde{v}(k-1) \end{aligned} \tag{107}$$

where ϖ_{pos} and ϖ_{vel} represent Gaussian white noise in the GPS position and velocity measurements, respectively, as defined in Equation (108).

$$\varpi_{\mathrm{pos}}(k) \sim N(0, \sigma^2_{\mathrm{gps,pos}}), \quad \varpi_{\mathrm{vel}}(k) \sim N(0, \sigma^2_{\mathrm{gps,vel}}) \tag{108}$$

The corresponding noise amplitudes of the GPS position and velocity measurements were set to $\sigma_{\mathrm{gps,pos}}$ = 0.01 m and $\sigma_{\mathrm{gps,vel}}$ = 0.02 m/s, respectively. These amplitudes correspond to the specification of the NovAtel FlexPak6 receivers used on the platform (Section 5.1.2), which report a horizontal RTK accuracy of 1 cm + 1 ppm and a velocity accuracy of 0.03 m/s (root mean square). The position amplitude $\sigma_{\mathrm{gps,pos}}$ = 0.01 m is the 1 cm term at the short baselines of the test area. The velocity amplitude $\sigma_{\mathrm{gps,vel}}$ = 0.02 m/s lies within the 0.03 m/s specification and was set toward its lower end so that the injected noise represents the receiver operating within specification without dominating the tracking performance being evaluated; the sensitivity of the controllers to measurement noise is therefore assessed at a representative rather than a worst-case level. The 10 Hz update rate is the output rate of the rover receivers in the experiments.

2. IMU measurements (attitude and acceleration):

IMU attitude measurements were represented by Euler angles. In the simulation, emphasis was placed on modelling the yaw angle measurement error θ. To avoid discontinuities at $\pm\pi$, angle wrapping was first applied, as shown in Equation (109).

$$\theta \leftarrow \mathrm{wrap}(\theta) \in [-\pi,\ \ \pi] \tag{109}$$

Gaussian noise and quantization were then introduced to account for measurement accuracy and sensor resolution. The IMU yaw measurement model is given by Equation (110).

$$\tilde{\theta}(k) = Q_{\Delta\theta}(\theta(k) + \varpi_{\theta}(k)) \tag{110}$$

where ϖ_θ denotes Gaussian white noise and $Q_{\Delta\theta}$ is the quantization operator corresponding to the resolution Δ_θ, as defined in Equation (111).

$$Q_{\Delta\theta}(f) = \Delta_{\theta} \cdot \mathrm{round}(\frac{f}{\Delta_{\theta}}), \quad \Delta_{\theta} = 0.1° \tag{111}$$

The yaw angle noise ϖ_θ and noise amplitude σ_{imu} were specified in Equations (112) and (113).

$$\varpi_{\theta}(k) \sim N(0, \sigma_{\text{imu}}^{2}) \tag{112}$$

$$\sigma_{\text{imu}} = 0.5° \tag{113}$$

After quantization, the wrap operation was applied again to maintain output continuity. The yaw noise amplitude $\sigma_{\text{imu}} = 0.5°$ and the resolution $\Delta\theta = 0.1°$ are the manufacturer values for the LORD MicroStrain 3DM-GX3-25 used on each vehicle: the static attitude accuracy of $\pm 0.5°$ and the attitude resolution of less than 0.1°. The dynamic attitude accuracy of $\pm 2.0°$ quoted in Section 5.1.2 applies to cyclic motion and arbitrary angles; the static value was used because the yaw measurement in the low-speed field operations considered here is closer to the static condition and because the complementary filter of the sensor suppresses the dynamic error over the control horizon.

For IMU acceleration measurements, both bias stability and initial bias error were modelled using a stochastic bias process. Let $b_a(k)$ denote the acceleration bias. The adopted model is given by Equations (114) and (115).

$$b_{a}(0) \sim N(0, \sigma_{b0}^{2}), \quad \sigma_{b0} = 0.002g \tag{114}$$

$$b_a(k+1) = b_a(k) + \varpi_b(k), \quad \varpi_b(k) \sim N(0, \sigma_b^2), \quad \sigma_b = 0.00004g \tag{115}$$

where g = 9.81 m/s^2, and σ_{b0} and σ_b denote the initial bias error and in-run bias stability, respectively. The values $\sigma_{b0} = 0.002g$ and $\sigma_b = 0.00004g$ are the accelerometer initial bias error ($\pm 0.002g$) and in-run bias stability ($\pm 0.00004g$) specified for the 3DM-GX3-25.

3. Steering sensor measurements:

The steering angle measurement used the actual actuator rotation angle $\delta_{\text{act}}(k)$ as the true value. The steering sensor reading $\delta_{\text{meas}}(k)$ was obtained by superimposing measurement noise and quantization error, as expressed in Equation (116).

$$\delta_{\text{meas}}(k) = Q_{\Delta\delta}(\delta_{\text{act}}(k) + \varpi_\delta(k)) \tag{116}$$

where ϖ_δ denotes Gaussian white noise in the steering angle measurement, and $Q_{\Delta\delta}$ is the quantization operator associated with the steering angle resolution Δ_δ, as given in Equation (117).

$$\varpi_\delta(k) \sim N(0, \sigma_\delta^2), \quad \sigma_\delta = 0.05°, \quad \Delta_\delta = 0.01° \tag{117}$$

The steering-angle sensor on the platform is a Honeywell 308 conductive-plastic potentiometer read by the 10-bit analog-to-digital converter of the ATmega2560 microcontroller (Section 5.1.2). With a 295° electrical travel, one converter count corresponds to approximately 0.29°. The simulation values $\sigma_\delta = 0.05°$ and $\Delta\delta = 0.01°$ are therefore finer than the hardware quantization and represent an optimistic steering-sensor model. They were retained because this case was intended to isolate the effect of steering feedback noise on the MPC steering law rather than to reproduce the platform converter, and because the $\pm 32°$ steering range spans about 220 converter counts, so the coarser hardware quantization affects the reported resolution rather than the controller structure. This difference is identified as a limitation in Chapter 6.

The steering sensor reading was then used directly as the control input from the previous time step, as shown in Equation (118).

$$\delta(k-1) \triangleq \delta_{\text{meas}}(k) \tag{118}$$

4.1.4.2 System Delay

System delay was modelled as the combined effect of measurement or communication delay and actuator dynamic response delay. Measurement delay was implemented using a discrete buffer queue. Let the measurement delay be τ_{meas}, corresponding to the number of discrete steps defined by Equation (119).

$$N_d = \max\left(0, \quad \text{round}\left(\frac{\tau_{\text{meas}}}{T}\right)\right) \tag{119}$$

In the simulation, $\tau_{\text{meas}} = 0.02$ s was assumed, giving $N_d = 1$. For any measured variable $\eta_{\text{meas}}(k)$, the delayed controller input is given by Equation (120), and the equivalent queue implementation is expressed in Equation (121).

$$\eta_d(k) = \eta_{\text{meas}}(k - N_d) \tag{120}$$

$$\eta_{\text{buf}}(k) = [\eta_{\text{meas}}(k), \eta_{\text{meas}}(k-1), \ldots]^T, \quad \eta_d(k) = \eta_{\text{buf}}^{N_d+1}(k) \tag{121}$$

The value $\tau_{\text{meas}} = 0.02$ s represents the communication path between the two vehicles rather than the sensors themselves, since the 10 Hz GPS output is already represented by the zero-order hold. The inter-vehicle link uses XBee-PRO S2B ZigBee modules (Section 5.1.2) with a 115,200 bps serial interface. Experimental measurements on the closely related XBee S2C module at this baud rate report a one-hop round-trip latency of 0.028 s for 10-byte packets, increasing linearly to 0.040 s for 60-byte packets without encryption (Haque et al., 2022), that is, a one-way delay of 14 to 20 ms for the short synchronization packets exchanged here. One control step is therefore a representative value.

The actuator dynamic response delay was modelled as a first-order inertia element. Let $U_{\text{cmd}}(k)$ be the steering angle and velocity command generated by the controllers. The actuator output U_{act} satisfies Equation (122):

$$U_{\text{act}}(k+1) = U_{\text{act}}(k) + \frac{T}{\tau_{\text{act}} + T}(U_{\text{cmd}}(k) - U_{\text{act}}(k)) \tag{122}$$

where the actuator delay was set to $\tau_{\text{act}} = 0.04$ s. Both the control output and the feedback loop used U_{act}, thereby forming a complete command-actuator-sensor-controller loop.

The value $\tau_{\text{act}} = 0.04$ s is the first-order envelope of the steering-angle and wheel-speed responses logged during the platform experiments. It is consistent with the motor data: the Parvalux PBL60-70 24 V motors used for propulsion have a rotor inertia of 7.28×10^{-5} kg·m^2, a phase resistance of 0.12 Ω, a torque constant of 0.06 N·m/A, and a speed–torque gradient of 1121.9 rpm/(N·m), which give a motor-only electromechanical time constant of 2.6 to 8.6 ms depending on whether the phase resistance or the speed–torque gradient is used. The 40 ms value is five to fifteen times this figure, which accounts for the gearbox, the reflected inertia of the vehicle and steering linkage, and the current-loop update of the motor drivers. The steering channel is driven by a separate Shayangye 24 V DC gear motor for which no manufacturer time constant is available; the same 0.04 s was applied to both channels because the logged steering-angle response fell within the same envelope as the wheel-speed response. On field-scale tractors the steering (hydraulic) and drive (engine and transmission) systems respond at different rates, and separate delays would be required; this is noted with the other scale-transfer limitations in Section 4.1.1.1. The velocity and acceleration values of Table 4.1 (±4 m/s and ±1 m/s²) are constraints applied to the commanded velocity within the controllers, in the constraint set of the unified MPC formulation and as bounds on the velocity setpoint supplied to the PID loop; they are not limits of the CarSim plant. The plant's start-up acceleration in the co-simulation was governed by the drive torque, the first-order actuator response, and the tractive limit at the tire–ground contact, and was not constrained separately, so the vehicle speed can rise faster at the start of a run than the controller-side bound would suggest.

4.1.4.3 Model and Perturbation Uncertainty

To account for uncertainty in vehicle parameters and unmodelled disturbances, random perturbations in mass m and moment of inertia I_n were introduced, together with nonsmooth lateral disturbance forces and yaw moments. Parameter perturbations were expressed as relative disturbances, as shown in Equation (123).

$$\tilde{m} = m(1+\varpi_m), \quad \tilde{I}_n = I_n(1+\varpi_I) \tag{123}$$

where ϖ_m and ϖ_I represent slowly varying random processes. The initial disturbance was generated by a Gaussian distribution according to Equation (124).

$$\varpi_m(0) \sim N\left(0, \sigma_m^2\right), \quad \varpi_I(0) \sim N\left(0, \sigma_I^2\right) \tag{124}$$

The amplitudes were set to σ_m = 0.02 and σ_I = 0.03. To avoid abrupt parameter variations within each sampling period, low-frequency updating and a first-order filtered random walk updated every 0.5 s were used, as described by Equations (125) and (126).

$$\varpi_m\left(k^+\right) = 0.97\varpi_m\left(k^-\right) + 0.03\sigma_m\zeta_m, \quad \zeta_m \sim N(0,1) \tag{125}$$

$$\varpi_I\left(k^+\right) = 0.97\varpi_I\left(k^-\right) + 0.03\sigma_I\zeta_I, \quad \zeta_I \sim N(0,1) \tag{126}$$

The relative perturbations σ_m = 0.02 and σ_I = 0.03 are design choices for this platform. They are small compared with the ranges used in robustness studies of road vehicles, where mass is typically varied by ±30% and yaw inertia by ±10% to represent passenger and cargo loading (Yeneneh and Sufe, 2026) and the model parameters by 10% to 30% (Wang et al., 2025), because the mass and inertia of the small-scale vehicles are known from direct weighing (Table 4.1) and do not vary with payload during a test. The values represent the residual uncertainty from battery state and the sliding length of the truss. The 0.5 s update interval, 25 control steps, was chosen so that the perturbation drifts over a time scale much longer than the control step, as a real parameter change would, rather than changing at every step.

To simulate nonsmooth external lateral disturbances during vehicle operation, occasional pulse disturbance forces F_{dist} and moments M_{dist} were applied, as defined in Equations (127) and (128).

$$F_{\text{dist}}(k) = \begin{cases} \pm F_{\text{dist,max}}, & \text{with prob. } p = \text{pulse rate} \cdot T \\ 0, & \text{otherwise} \end{cases} \tag{127}$$

$$M_{\text{dist}}(k) = \begin{cases} \pm M_{\text{dist,max}}, & \text{with prob. } p = \text{pulse rate} \cdot T \\ 0, & \text{otherwise} \end{cases} \tag{128}$$

In the simulation, $F_{\text{dist,max}} = 120$ N, $M_{\text{dist,max}} = 50$ N·m, and the pulse rate was 0.08 Hz. These pulses represent implement-resistance events such as sudden changes in soil or crop resistance. The force amplitude $F_{\text{dist,max}} = 120$ N lies within the 50 to 200 N range of the external load applied in the test scenarios of Section 4.1.3, and the moment amplitude is not an independent choice: it is the same force acting at the implement engagement depth d_5 defined in Section 3.1.3, which is 0.42 m for the small-scale implement, $M_{\text{dist,max}} = F_{\text{dist,max}}\, d_5 = 120 \text{ N} \times 0.42 \text{ m} \approx 50$ N·m. The pulse rate of 0.08 Hz, a mean interval of 12.5 s, was chosen relative to the 40 m test path: at the target speeds of 1.5, 2.5, and 3.5 m/s a run lasts approximately 27, 16, and 11 s, so each run contains on the order of one to two pulses. The disturbances are therefore sporadic, as intended, and their effect can be observed as isolated events rather than as a continuous disturbance that would change the character of the test.

In the error dynamics, these disturbances were modelled as equivalent linear and angular accelerations within the system bias term. This approach ensured that the system followed the nominal model for most of the simulation while being subjected to sporadic random disturbances. As a result, the robustness assessment was more realistic and better reflected engineering feasibility.

4.1.5 Control Gains Tuning

Control gains were determined through a structured simulation-based tuning and validation procedure designed to balance tracking accuracy, control effort, actuator feasibility, and robustness over a range of operating conditions. The evaluation criteria included the integral absolute errors of lateral, orientation, offset, and separation errors, together with satisfaction of steering-angle and steering-rate limits. The tuning scenarios included straight and curved paths, different initial lateral offsets, variations in path geometry, changes in implement position and external load, and both forward and reverse motion over a range of velocities.

For the dynamic model, the steering controller was tuned using the adaptive MPC formulation described in Section 3.3.1. Unlike the initial fixed-weight design, the final controller employed constant prediction and control horizons together with online-updated weighting coefficients. The tuning process therefore consisted of three steps. First, the prediction horizon N_p, control horizon N_c, and the nominal baseline weights q_{Y0}, $q_{\theta 0}$, and $r_{\delta 0}$ were selected to provide satisfactory nominal tracking performance while maintaining real-time computational feasibility. Second, the adaptive parameters governing the online variation of $q_Y(k)$, $q_\theta(k)$, and $r_\delta(k)$ were tuned iteratively in simulation. The adaptation gains were adjusted so that the controller placed greater emphasis on lateral-error reduction during forward motion, greater emphasis on orientation stabilization during reverse motion, and greater emphasis on suppressing excessive steering activity when steering demand became large. Third, lower and upper saturation bounds were assigned to the adaptive weights to prevent excessive variation and to preserve numerical stability of the optimization problem. This approach reduced the need for separate manual retuning under different operating conditions and allowed a single MPC framework to accommodate both forward and reverse manoeuvres.

Table 4.5 is the single set of adaptive MPC tuning parameters for all simulation scenarios.

Table 4.5 Adaptive MPC tuning parameters for the dynamic model

Parameter	Description	Tuned value
N_p	Prediction horizon	20
N_c	Control horizon	10
q_{Y0}	Nominal baseline weight for lateral error	10
$q_{\theta 0}$	Nominal baseline weight for orientation error	10
$r_{\delta 0}$	Nominal baseline weight for steering effort	1000
μ_l	Adaptation gain for lateral-error magnitude	0.25
μ_{kY}	Adaptation gain for path curvature in $q_Y(k)$	0.45
$\mu_{k\theta}$	Adaptation gain for path curvature in $q_\theta(k)$	20
μ_v	Adaptation gain for longitudinal velocity	0.25
μ_{dY}	Adaptation gain for motion direction in $q_Y(k)$	1800
$\mu_{d\theta}$	Adaptation gain for motion direction in $q_\theta(k)$	5.25
μ_θ	Adaptation gain for orientation-error magnitude	9
μ_δ	Adaptation gain for steering-angle magnitude	2
$\mu_{\Delta\delta}$	Adaptation gain for steering-rate magnitude	5
$[q_{Y,\min}, q_{Y,\max}]$	Saturation bounds for $q_Y(k)$	[5, 30000]
$[q_{\theta,\min}, q_{\theta,\max}]$	Saturation bounds for $q_\theta(k)$	[5, 20000]
$[r_{\delta,\min}, r_{\delta,\max}]$	Saturation bounds for $r_\delta(k)$	[5, 10000]

The horizons were re-tuned together with the weights when the adaptive weighting was introduced, because the prediction horizon, the control horizon, and the weighting coefficients are interacting tuning parameters (Garriga and Soroush, 2010), and the values selected for the fixed-weight cost function do not carry over to the adaptive formulation; the scenario-dependent horizons of the initial submission ($N_p = 23$, $N_c = 10$ on straight paths; $N_p = 32$, $N_c = 15$ on curved paths) were retained in the experiments of Chapter 5.

The PID controller for longitudinal velocity was tuned independently using conventional simulation-based procedures and was not adaptively updated. The proportional gain was first increased to obtain a sufficiently fast response, the integral gain was then introduced to remove steady-state error, and the derivative gain was finally adjusted to suppress oscillation and improve damping. The final velocity-control gains were

- $K_p = 0.25$, $K_i = 0.1$ and $K_d = 0.025$

The synchronous tracking gain was also tuned independently and remained constant throughout the simulations. Its value was selected by minimizing the integral absolute error of the offset error while preserving coordinated motion between the two supporting vehicles. The final synchronous tracking gain was

- $k_e = 2.5\ \mathrm{s}^{-1}$

For the kinematic model, the gains for the steering controller were tuned separately because that controller did not use adaptive weighting. The initial values were selected from the analytical relationship $k_1 = 2\sqrt{k_2}$, which provides exponential convergence under ideal kinematic assumptions, and were then refined through simulation using the same IAE-based criteria applied to the dynamic model. Because the kinematic model neglects inertial and tire-dynamic effects, its gains could be tuned more aggressively in forward motion than in reverse motion. The final forward-motion gains were

- $k_1 = 3.6$, $k_2 = 3.24$

whereas the reverse-motion gains were

- $k_1 = 3.6$, $k_2 = 0.5$

Overall, the tuning results showed that the adaptive MPC formulation enabled a single steering-control structure to respond appropriately to different tracking conditions by adjusting its weighting priorities online. In contrast, the PID velocity controller, the synchronous tracking controller, and the kinematic path-tracking controller retained fixed gains throughout the simulations.

4.1.6 Activity of the Steering Constraints

The steering-increment constraint of Equation (79) bounds the change of the steering command over the control horizon by $\Delta U_{\min}$ and $\Delta U_{\max}$ and admits a bounded slack variable $\varepsilon_M \leq \varepsilon_{M,\max}$, and the adaptive weighting of Equations (82) to (84) saturates the weighting coefficients. Both are hard nonlinearities added to an otherwise linear time-varying MPC formulation, and their effect on closed-loop performance and stability depends on how often they become active: a constraint that is never active leaves the controller equivalent to the unconstrained linear design, whereas one that is active for sustained periods changes the closed-loop behaviour and can degrade convergence. To establish which case applies, the curved-trajectory scenario, the forward scenario with the greatest steering activity, was run with the steering angle and the steering angle rate logged at every control step. The steering angle rate bound used in this study is ± 0.523 rad/s (30°/s), which at the control period $T = 0.02$ s corresponds to a steering-increment bound of $\Delta U_{\max} = -\Delta U_{\min} = 0.0105$ rad per step; the steering angle itself is bounded by the $\pm 32°$ (± 0.559 rad) steering range of Table 4.1.

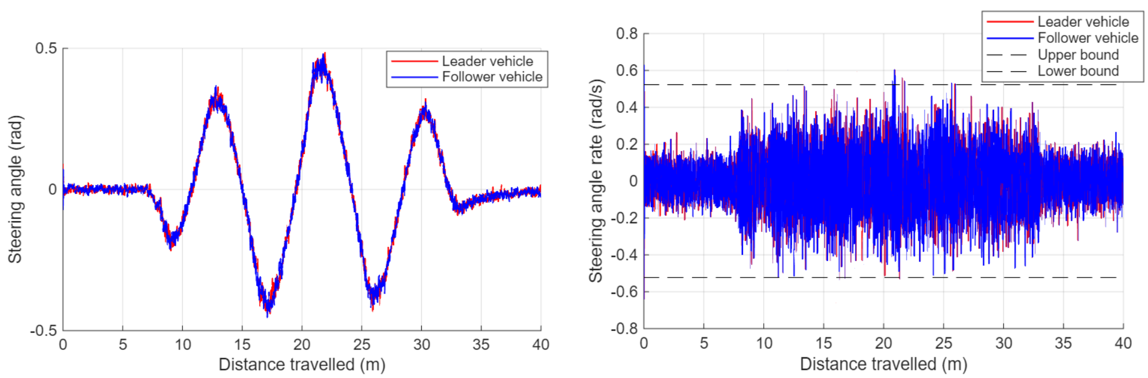

(a) (b)

Figure 4.5 Steering control responses of the leader and follower vehicles: (a) steering angle and (b) steering angle rate with allowable rate limits

Figure 4.5 presents the steering angle and steering angle rate of the leader and follower vehicles against distance travelled. The steering angles varied continuously throughout the manoeuvre, with the two vehicles exhibiting closely matched responses. Steering activity was concentrated on the curved portion of the path, between about 7.5 m and 33 m, where the steering angle reached peaks of approximately ± 0.45 rad, within the ± 0.559 rad steering range, so the steering-angle magnitude constraint was never active. On the straight sections the steering angles remained close to zero.

The steering angle rate in Figure 4.5 is the time derivative of the actuator steering angle, and it is compared with the ± 0.523 rad/s bounds imposed on the commanded increment through

Equation (79). It remained within the bounds for nearly the entire run. On the straight sections it fluctuated within a band of about ± 0.2 rad/s; this is the rate noise produced by differentiating a steering signal that carries the sensor noise and quantization, which feeds back into the command through Equation (118), and not commanded steering action. On the curved portion the rate stayed mostly within about ± 0.45 rad/s and reached or exceeded the bound only at isolated samples, approximately 0.065% of the total. Because a first-order actuator cannot move faster than its rate-limited command, the isolated excursions of the plotted rate beyond the dashed lines, to about ± 0.6 rad/s, are the noise band superimposed on a command that was itself at the bound, or on the small additional increment permitted by the slack variable; the slack variable was not logged in this run, so its individual contribution cannot be separated, but the optimization remained feasible at every control step, as the slack formulation guarantees, and the excursions are of the same magnitude as the noise band. Sustained steering-rate saturation did not occur.

These observations answer the question of the constraints' consequences for this scenario. The steering-increment constraint acted as a rarely active saturation, engaged for about one sample in about fifteen hundred without loss of feasibility, so the closed loop behaved as the linear time-varying MPC design for more than 99.9% of the run. Because the scenario examined is the forward case with the largest steering activity, the constraint is expected to be at least as inactive in the other forward scenarios; in the curved reverse scenario, where steering demand is higher, the constraint is likely to be active more often and its effect on performance is part of the larger tracking errors reported there. This assessment is empirical for the scenarios simulated and does not constitute a stability proof for the constrained controller; likewise, the saturation of the adaptive weighting coefficients in Equations (82) to (84) was not analyzed formally. Both points are recorded as limitations in Chapter 6.

4.2 Simulation Results

This section presents the simulation results obtained from the CarSim−Simulink co-simulation platform. To organize the analysis of the extensive parameter space described in Section 4.1.3 and avoid redundancy, one condition set was designated as the nominal, or general, case. Performance under this baseline condition was then compared with the results obtained by varying one key parameter at a time across the different test scenarios.

Before comparing scenarios, sensor-based thresholds are defined to distinguish numerical differences from practically meaningful improvements. Based on the sensor specifications in Sections 4.1.4 and 5.1.2, the lateral-error threshold is the RTK-GPS horizontal accuracy of 0.01 m.

The orientation-error threshold is the IMU static heading accuracy of 0.5° (0.0087 rad). For offset and separation errors, a threshold of $\sqrt{2} \times 0.01\ \text{m} \approx 0.014\ \text{m}$ is adopted using an equal-accuracy, uncorrelated-position-error approximation.

For the distance-integrated IAE metrics, each comparison threshold represents the accumulated absolute error produced by a constant error at the corresponding sensor-based threshold over the 40 m test path (Table 4.3). Using 0.01 m, 0.0087 rad, and 0.014 m gives IAE thresholds of 0.40 m^2 for lateral error, 0.35 rad·m for orientation error, and 0.56 m^2 for offset and separation errors. These values are engineering comparison thresholds rather than statistical detection limits.

Differences below the adopted thresholds are retained in the tables but are not used to rank the controllers for the corresponding metric. Differences exceeding the thresholds are evaluated alongside the corresponding instantaneous errors relative to the bounds in Section 3.4: ± 0.15 m for lateral error, ± 0.15 rad for orientation error, and ± 0.30 m for offset and separation errors. An improvement is considered practically meaningful only when it exceeds the relevant comparison threshold and contributes to meeting or maintaining these application-specific bounds. A lower IAE alone does not establish compliance with an instantaneous error bound.

4.2.1 General Case

This subsection presents the general case, which was designed to validate the control strategy and provide a benchmark for the specialized scenarios that follow. The baseline test conditions were as follows:

1. Forward motion.
2. Straight trajectory.
3. Medium-adhesion earth road ($\mu = 0.75$).
4. Target speed of the support vehicles: 2.5 m/s.
5. External loads on truss (opposite to the path direction): $F_{\text{external}} = 50$ N.
6. Implement position on the truss: $d_4 = 0.8$ m.
7. Initial offset error: $e = 0$ m.

The key simulation results for the dynamic model are shown in Figure 4.6 to Figure 4.10, while the supplementary results are provided in Appendix A.

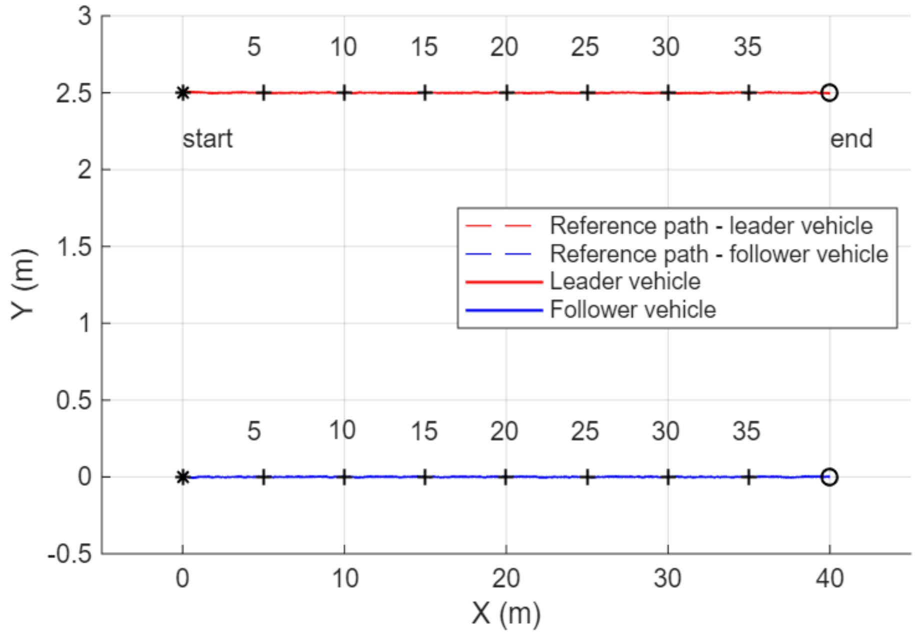

Figure 4.6 Reference and actual paths using the dynamic model in the general case. Asterisks: start of motion; circles: end of motion; plus symbols: increments of 5 m along reference path

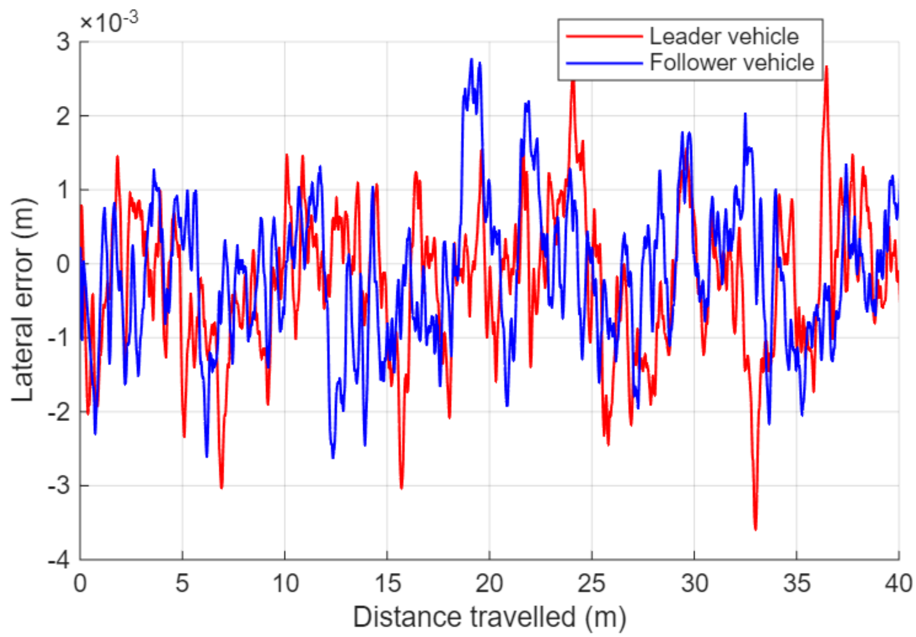

Figure 4.7 Lateral error using the dynamic model in the general case

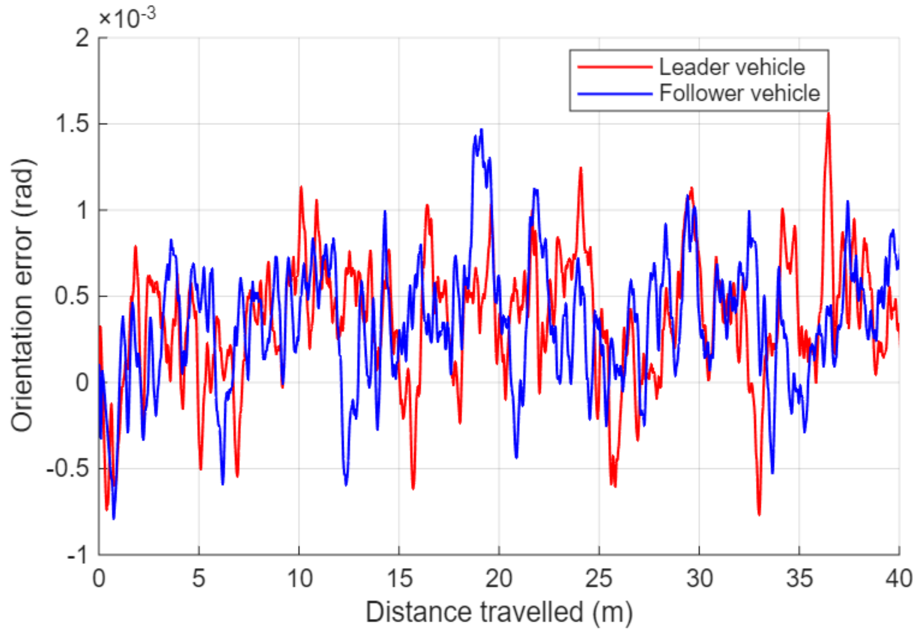

Figure 4.8 Orientation error using the dynamic model in the general case

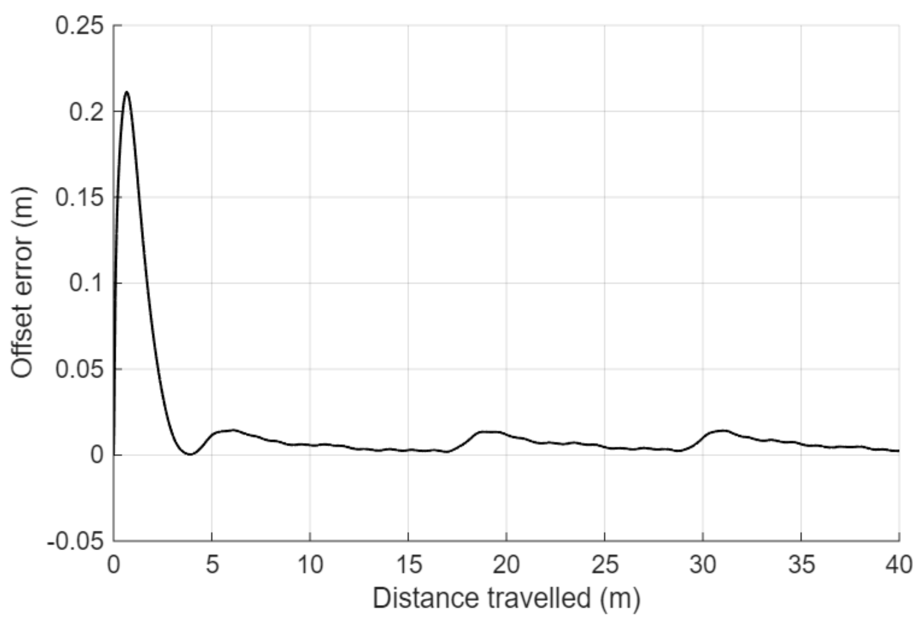

Figure 4.9 Offset error using the dynamic model in the general case

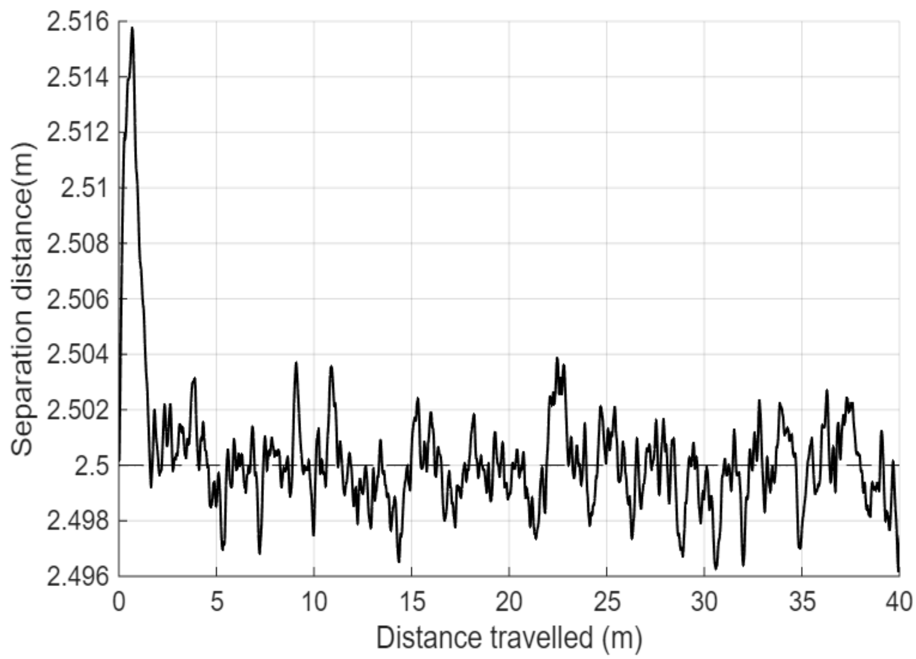

Figure 4.10 Distance between the two support vehicles using the dynamic model in the general case

After the start-up transient, the offset error returns to within 0.01 m of zero at about 4 m of travel and thereafter remains within ± 0.014 m, at the 0.014 m threshold of Section 4.2, with no periodic component (Figure 4.9). The three transient rises visible in Figure 4.9 coincide with the three momentary reductions of the follower velocity in Figure A.2, that is with the injected disturbance events of Section 4.1.4; each is corrected within about 5 m. The steady-state lateral errors of the leader and follower remain within ± 0.0036 m and ± 0.0028 m, the orientation errors within ± 0.0016 rad and ± 0.0015 rad, and the separation error within ± 0.0039 m (Table 4.6), all below the practical-significance thresholds of Section 4.2, and the steering commands carry the injected measurement noise without saturating. These values are the net effect of the noise, delays, and disturbances of Section 4.1.4 on the steady-state tracking of the dynamic-model controller. The absence of a periodic component is consistent with the synchronization loop being over-damped when it is closed through the 0.04 s actuator response assumed in Section 4.1.4.

The key simulation results for the kinematic model are shown in Figure 4.11 to Figure 4.15, while the supplementary results are provided in Appendix A.

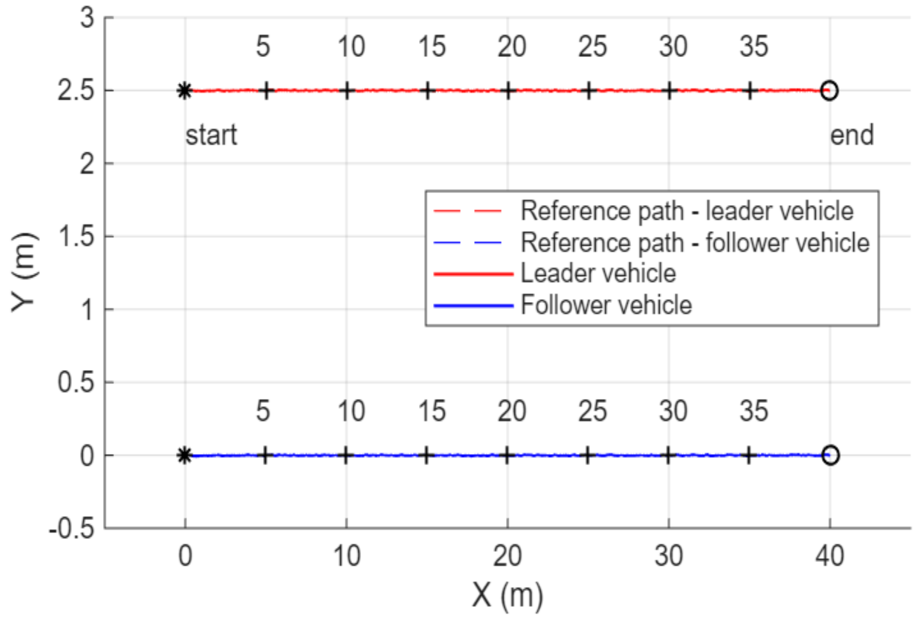

Figure 4.11 Reference and actual paths using the kinematic model in the general case

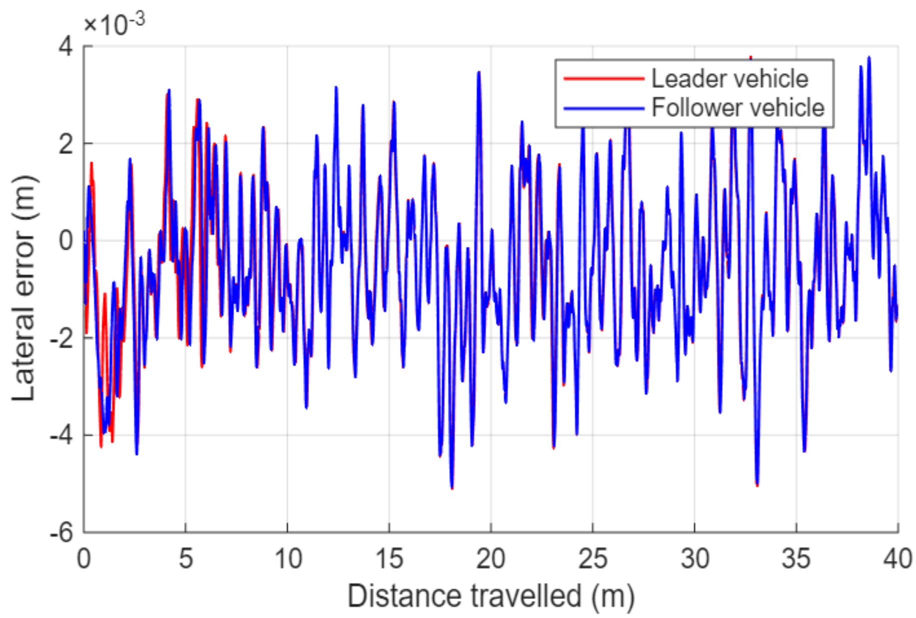

Figure 4.12 Lateral error using the kinematic model in the general case

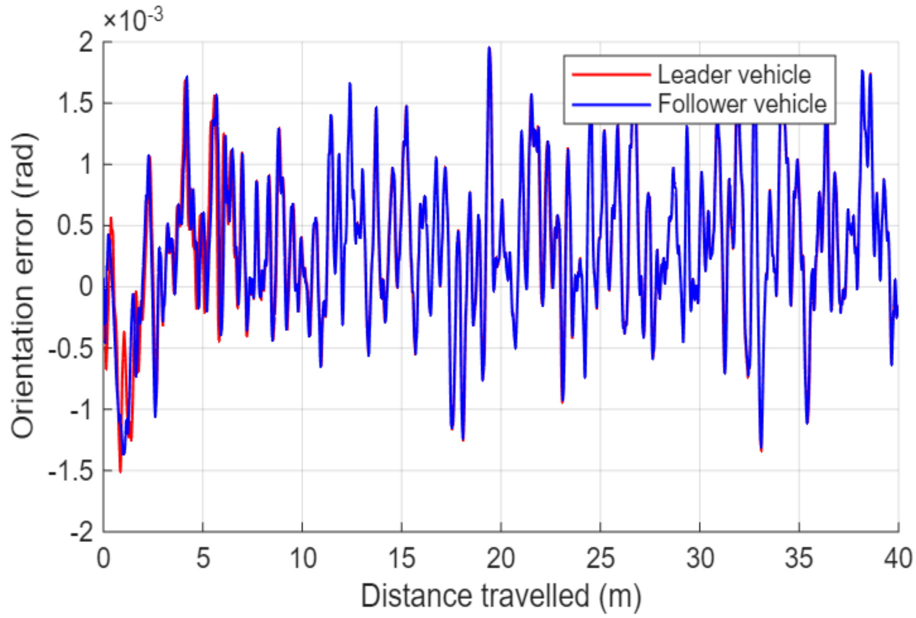

Figure 4.13 Orientation error using the kinematic model in the general case

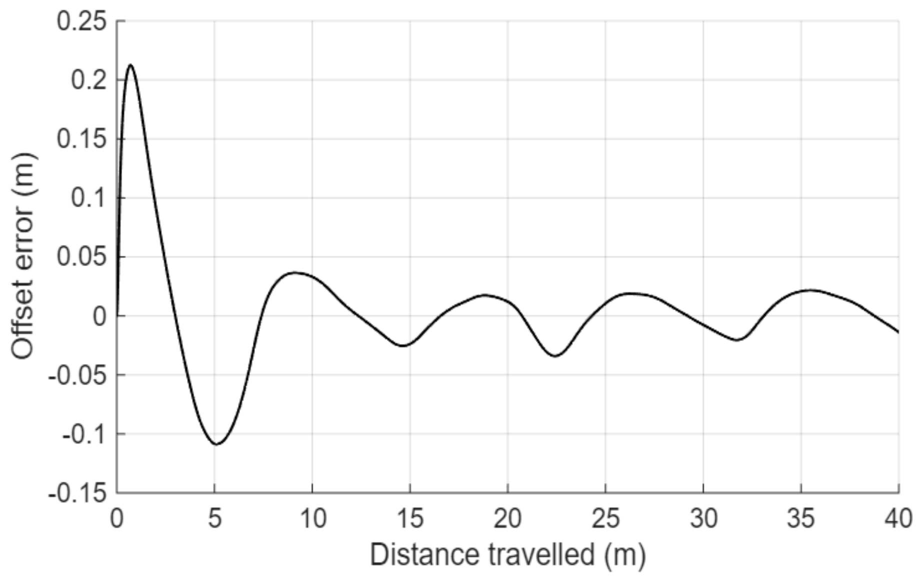

Figure 4.14 Offset error using the kinematic model in the general case

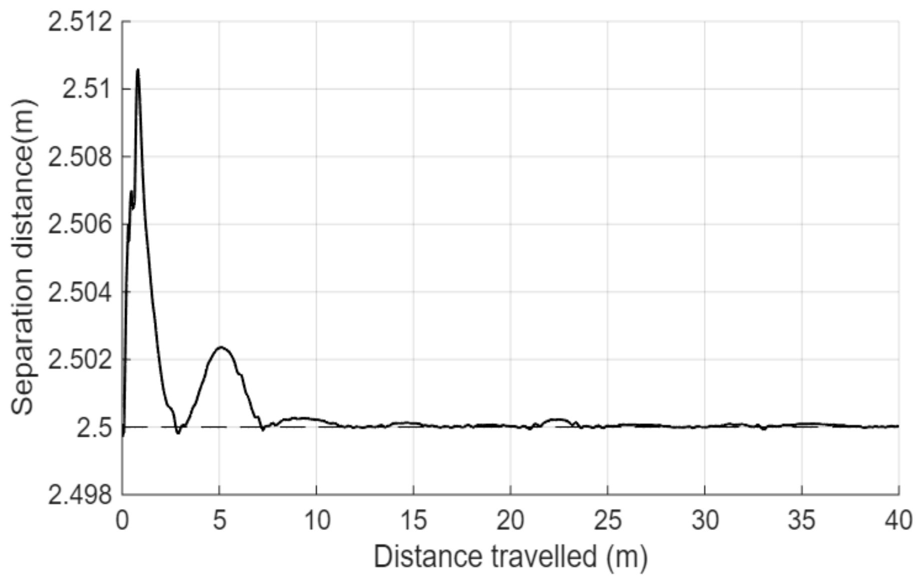

Figure 4.15 Distance between the two support vehicles using the kinematic model in the general case

The steady-state and IAE performance metrics for the general case are summarized in Table 4.6.

Table 4.6 Steady-state and IAE performance metrics for the general case[a]

		Dynamic	Kinematic
Leader vehicle	Steady-state velocity (m/s)	2.50	2.47
	Steady-state lateral error (m)	**±0.0036**	±0.0051
	Steady-state orientation error (rad)	**±0.0016**	±0.0020
	Lateral error IAE (m^2)	**0.0317**	0.0553
	Orientation error IAE (rad·m)	**0.0172**	0.0218
Follower vehicle	Steady-state velocity (m/s)	2.50	2.47
	Steady-state lateral error (m)	**±0.0028**	±0.0051
	Steady-state orientation error (rad)	**±0.0015**	±0.0020
	Lateral error IAE (m^2)	**0.0315**	0.0551
	Orientation error IAE (rad·m)	**0.0168**	0.0218
Steady-state offset error (m)		**±0.014**	±0.034
Steady-state separation error (m)		±0.0039	±0.00023
Offset error IAE (m^2)		**0.583**	1.16
Separation error IAE (m^2)		0.0547	0.0185

[a] Boldface: notably better than the other model.

Based on the simulation results in Table 4.6, both controllers achieved high accuracy in straight-line tracking under the general conditions. The steady-state lateral and orientation errors of both models were below the sensor resolution (millimetres and milliradians), and the differences between them in these metrics and in the lateral and orientation IAE values are within measurement resolution; no ranking of the controllers is drawn from them. The dynamic model reduced the offset error IAE from 1.16 m² to 0.583 m², a difference of 0.58 m² that just reaches the 0.56 m² offset threshold and is therefore reported as marginal, and the steady-state offset error from $\pm$0.034 m to $\pm$0.014 m, a difference of 0.02 m above the 0.014 m threshold. The kinematic model showed a smaller separation error IAE, 0.0185 m² compared with 0.0547 m² for the dynamic model, a difference within measurement resolution. Under the general conditions the two models are therefore indistinguishable at the sensor level in individual-vehicle tracking, and differ resolvably only in offset regulation, which favoured the dynamic model. This case is the reference against which each of the following scenarios is compared.

4.2.2 Curved Trajectory

A curved trajectory tracking test was conducted to evaluate control system performance and stability under more complex conditions. In this test, the support vehicles tracked a path defined by Equation (103), representing a continuously varying trajectory. The test scenario was as follows:

1. Forward motion.
2. Curved trajectory.
3. Medium-adhesion earth road ($\mu = 0.75$).
4. Target speed of the support vehicles: 2.5 m/s.
5. External loads on truss (opposite to the path direction): $F_{\text{external}} = 50$ N.
6. Implement position on the truss: $d_4 = 0.8$ m.
7. Initial offset error: $e = 0$ m.

The key simulation results for the dynamic model are shown in Figure 4.16 to Figure 4.20.

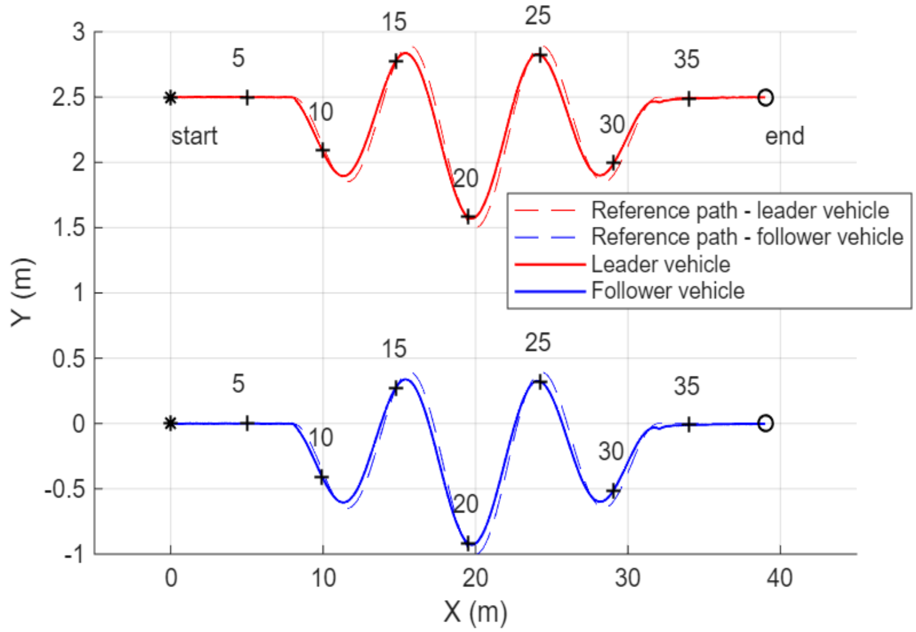

Figure 4.16 Reference and actual paths using the dynamic model for curved-trajectory tracking

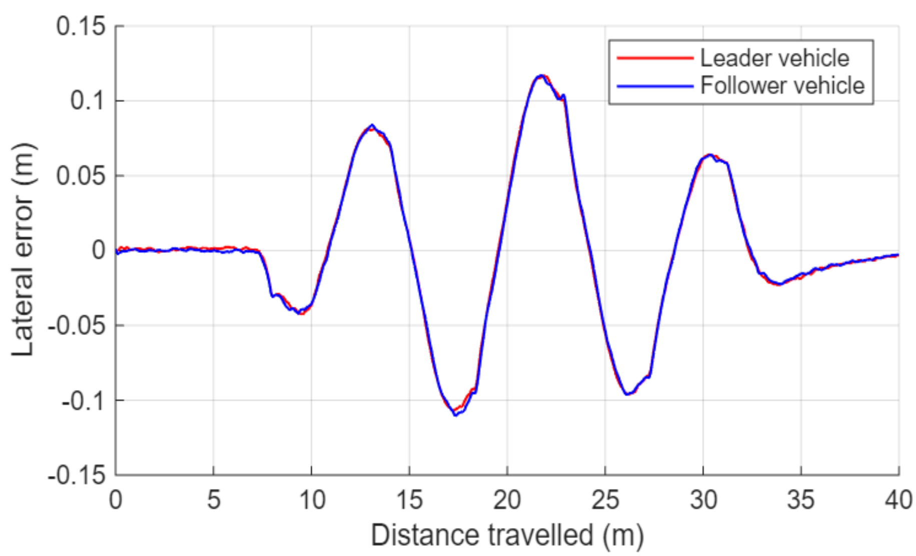

Figure 4.17 Lateral error using the dynamic model for curved-trajectory tracking

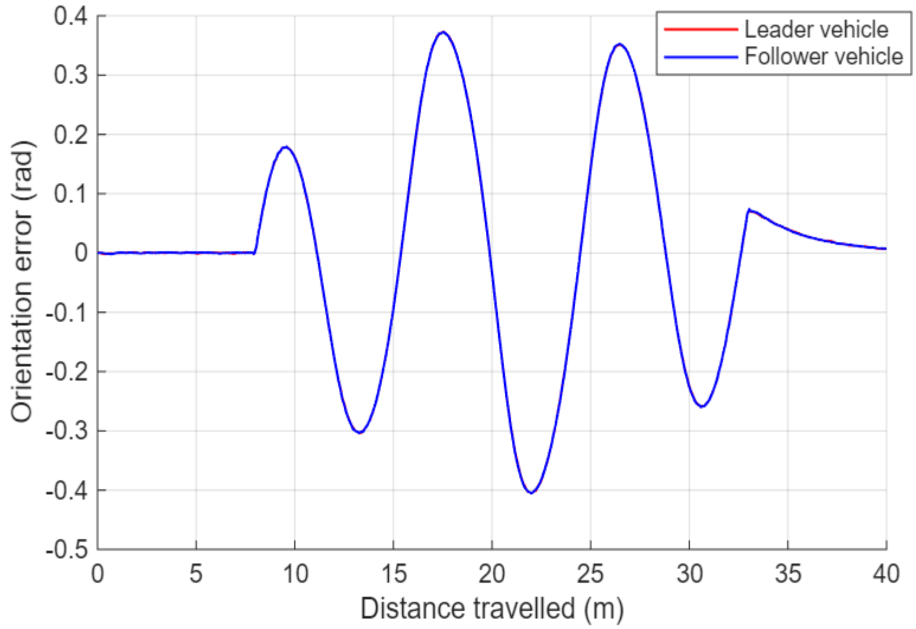

Figure 4.18 Orientation error using the dynamic model for curved-trajectory tracking

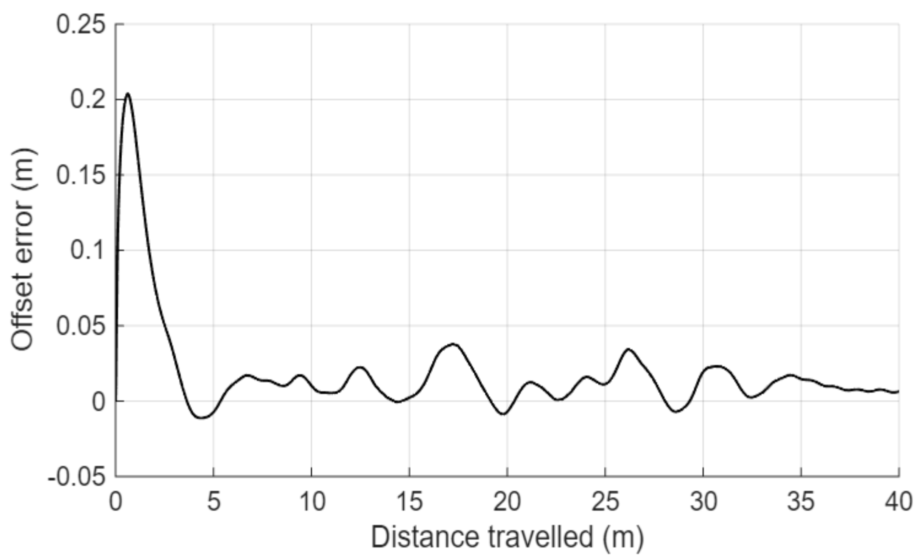

Figure 4.19 Offset error using the dynamic model for curved-trajectory tracking

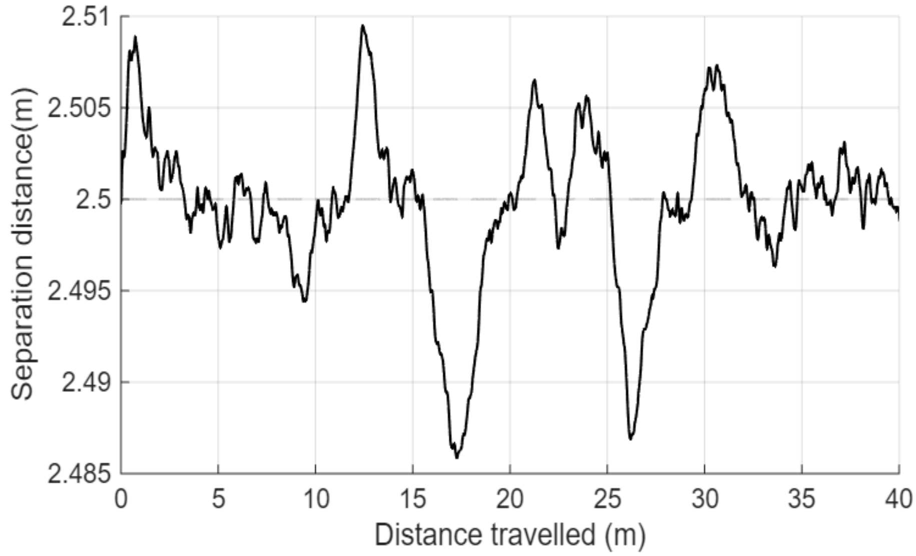

Figure 4.20 Distance between the two support vehicles using the dynamic model for curved-trajectory tracking

The key simulation results for the kinematic model are shown in Figure 4.21 to Figure 4.25.

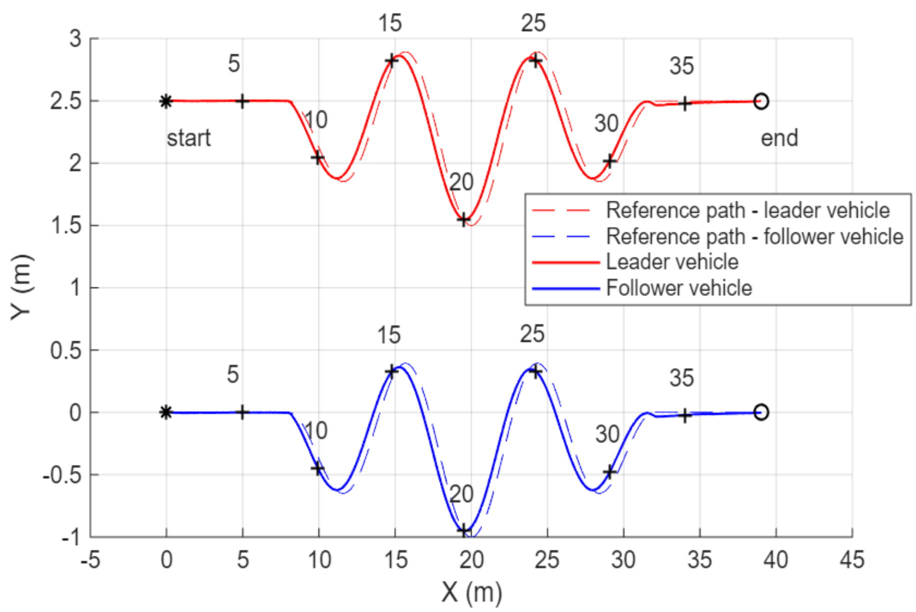

Figure 4.21 Reference and actual paths using the kinematic model for curved-trajectory tracking

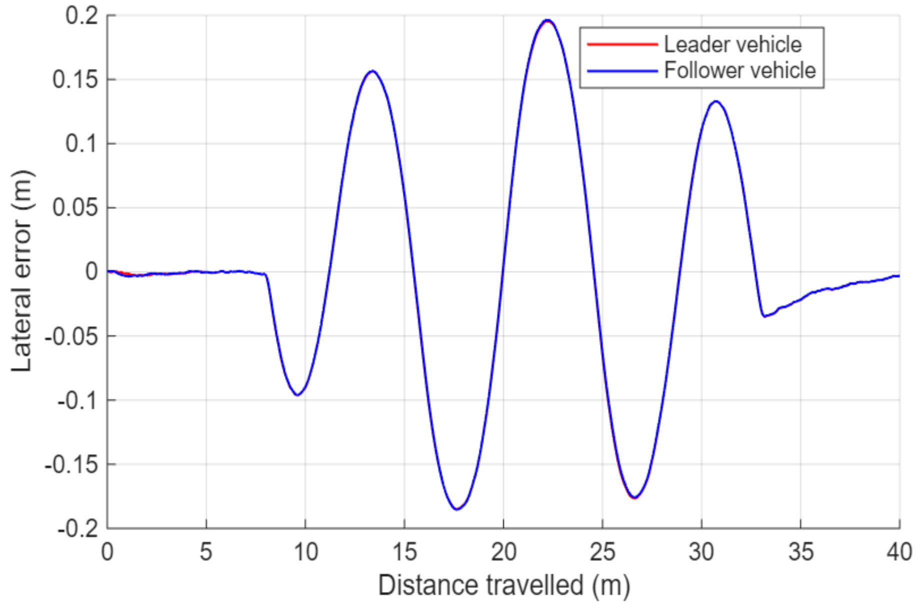

Figure 4.22 Lateral error using the kinematic model for curved-trajectory tracking

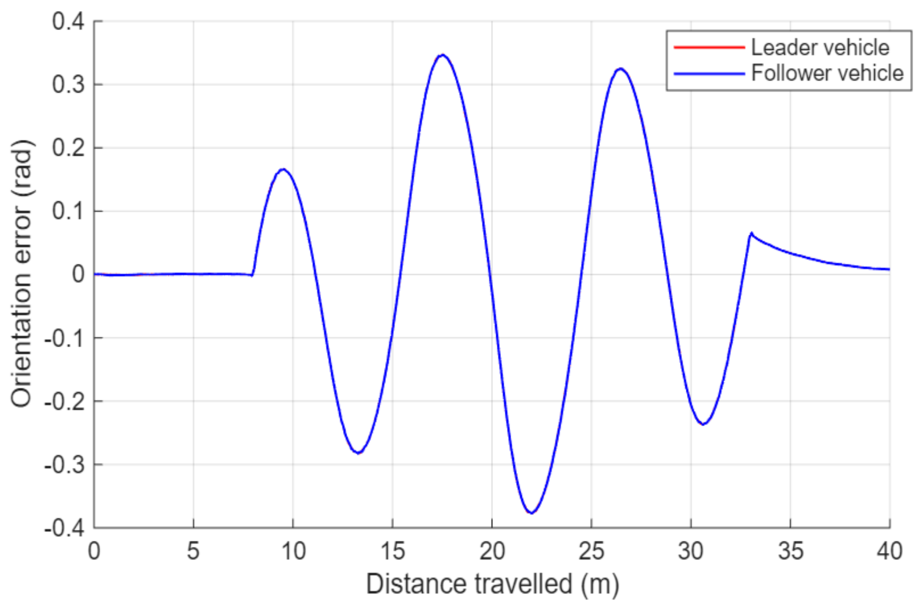

Figure 4.23 Orientation error using the kinematic model for curved-trajectory tracking

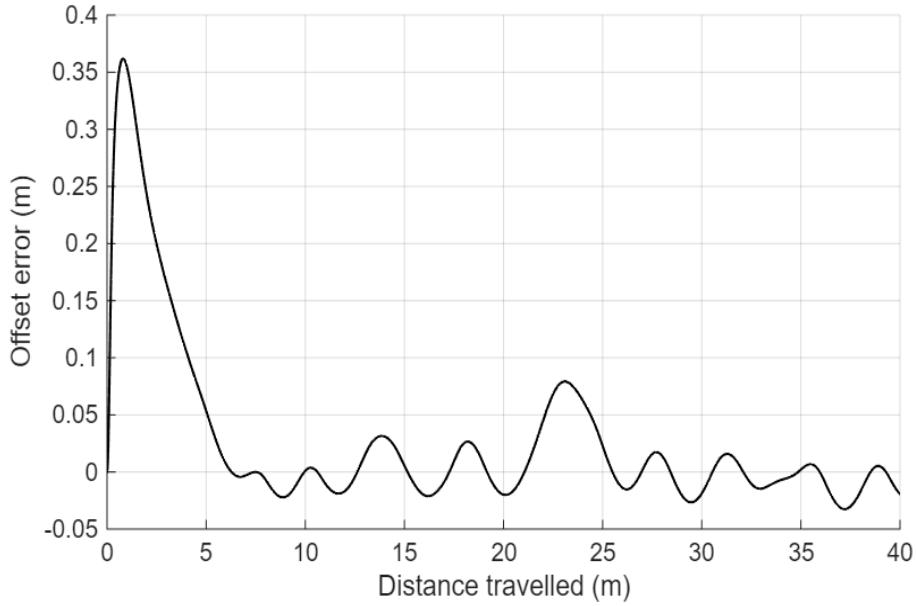

Figure 4.24 Offset error using the kinematic model for curved-trajectory tracking

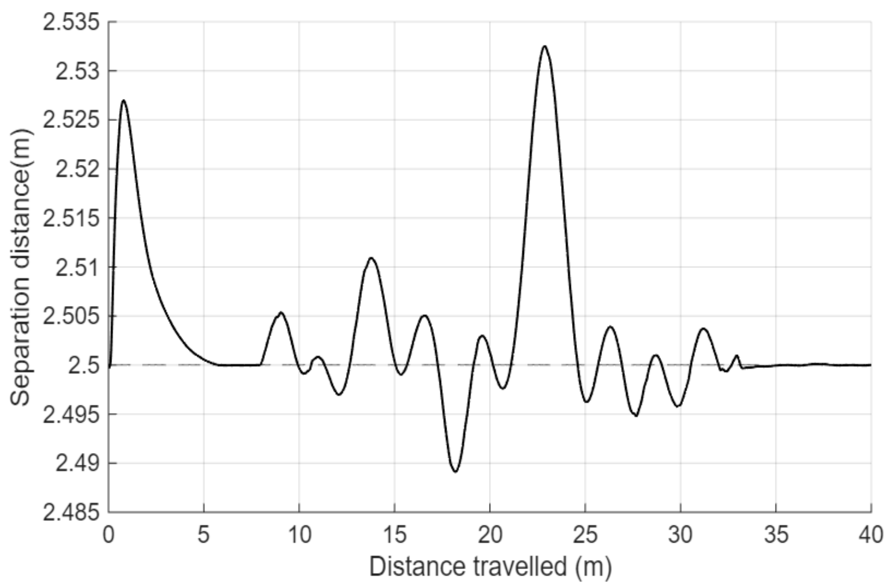

Figure 4.25 Distance between the two support vehicles using the kinematic model for curved-trajectory tracking

The steady-state and IAE performance metrics for curved trajectory tracking are summarized in Table 4.7.

Table 4.7 Steady-state and IAE performance metrics for curved-trajectory tracking[a]

		Dynamic	Kinematic
Leader vehicle	Steady-state velocity (m/s)	2.50	2.47
	Steady-state lateral error (m)	**±0.12**	±0.20
	Steady-state orientation error (rad)	±0.41	±0.38
	Lateral error IAE (m^2)	**1.47**	2.73
	Orientation error IAE (rad·m)	5.32	4.88
Follower vehicle	Steady-state velocity (m/s)	2.50	2.47
	Steady-state lateral error (m)	**±0.12**	±0.20
	Steady-state orientation error (rad)	±0.41	±0.38
	Lateral error IAE (m^2)	**1.48**	2.73
	Orientation error IAE (rad·m)	5.32	4.88
Steady-state offset error (m)		**±0.038**	±0.079
Steady-state separation error (m)		**±0.014**	±0.032
Offset error IAE (m^2)		**0.794**	1.59
Separation error IAE (m^2)		**0.120**	0.178

[a] Boldface: notably better than the other model.

Based on the simulation results from Sections 4.2.1 and 4.2.2 and Tables 4.6 and 4.7, several key findings can be identified. The curved trajectory scenario provided the more demanding evaluation of the two control strategies, and it is the scenario in which the differences between them exceed the practical-significance thresholds. For both the leader and follower vehicles, the dynamic model reduced the steady-state lateral error from ±0.20 m to ±0.12 m compared with the kinematic model, a difference of 0.08 m that is well above the 0.01 m resolution threshold and, more importantly, moves the response from outside to inside the ±0.15 m lateral bound of Section 3.4. The improvement was also reflected in the lateral error IAE, which decreased from 2.73 m^2 to 1.47 m^2 for the leader vehicle and from 2.73 m^2 to 1.48 m^2 for the follower vehicle, reductions of approximately 46.2% and 45.8% that far exceed the 0.4 m^2 IAE threshold. These results indicate that the dynamic model provided practically meaningful lateral path-tracking accuracy under curved motion, where lateral inertia, tire slip, and vehicle-terrain interaction have greater influence on vehicle response.

The formation-control results showed a similar advantage for the dynamic model during curved trajectory tracking. The steady-state offset error decreased from ±0.079 m with the kinematic model to ±0.038 m with the dynamic model, and the offset error IAE from 1.59 m^2 to 0.794 m^2; both differences exceed the offset thresholds (0.014 m and 0.56 m^2). The steady-state separation error decreased from ± 0.032 m to ± 0.014 m, a difference at the 0.014 m threshold, while the reduction in separation error IAE from 0.178 m^2 to 0.120 m^2 is within measurement resolution. The orientation error results showed the opposite trend: the dynamic model produced a larger steady-state orientation error of ± 0.41 rad compared with ± 0.38 rad for the kinematic model, and a higher orientation error IAE of 5.32 rad·m compared with 4.88 rad·m. Both differences are resolvable, and both controllers exceeded the ± 0.15 rad orientation bound on this path, so heading regulation on curved paths is a limitation shared by the two models rather than an advantage of either. The practically meaningful advantage of the dynamic model in curved tracking was therefore improved lateral accuracy and offset regulation, not orientation error reduction.

In both the general case and the curved case, the offset error rises from zero over the first few metres of travel before the synchronization law brings it back (Figures 4.9, 4.14, 4.19 and 4.24). This initial rise is a start-up effect of the velocity loop rather than a path-tracking error. Both vehicles start from rest, and the synchronization law of Section 3.3.3 commands the follower to match the leader's measured speed plus the offset error multiplied by the synchronization gain, 2.5 s^{-1} in this study. At the start of the run the leader accelerates towards its 2.5 m/s target while the follower's command still reflects the leader's earlier, lower speed through the measurement and actuator delays of Section 4.1.4; the follower's tractive demand saturates at the drive limit during this acceleration, and on the medium-adhesion surface the resulting longitudinal slip means that the follower's speed builds up more slowly than the leader's. The follower therefore falls behind and the offset grows, until the growing offset raises the commanded increment enough for the follower to catch up. The offset peaks near the beginning of travel, then decreases and settles through a damped overshoot once the follower's speed exceeds the leader's. The mechanism is the same as in the large-initial-offset case of Section 4.2.8.1, where a commanded increment of 2.5 m/s saturates the velocity loop from the first control step and produces a rise of much larger amplitude. The rise is bounded and followed by convergence, so it contributes to the transient part of the offset IAE but not to the steady-state values in Tables 4.6 and 4.7. The rise is larger with the kinematic model because it does not represent the slip that limits the follower under a saturated tractive demand, whereas the dynamic model's steering and state prediction account for it and produce a follower response that follows the command more closely.

4.2.3 Backward Motion

The WSIC is a large agricultural implement carrier platform designed to span the full width of the field, with its supporting vehicles travelling on permanent traffic lanes rather than on the cultivated area. This differs from smaller agricultural vehicles that manoeuvre directly on the field.

Consequently, when the WSIC operates in mobile mode to complete adjacent passes along the field length, the supporting vehicles are expected to switch from forward to backward motion without turning around. Simulating control performance in reverse is therefore essential for verifying system behaviour under this practical operating requirement.

In the backward motion evaluation, the two supporting vehicles reversed along the linear trajectory from Section 4.2.1 and the curved trajectory from Section 4.2.2 without turning around, thereby retracing the forward paths in reverse. During this phase, the vehicles operated in RWS mode. The steering angles of the rear wheels δ_3 and δ_4 were used, while the front-wheel steering angles were set to zero ($\delta_1 = \delta_2 = 0$).

4.2.3.1 Straight-Line Reverse

The test conditions were as follows:

1. Backward motion.
2. Straight trajectory.
3. Medium-adhesion earth road ($\mu = 0.75$).
4. Target speed of the support vehicles: 2.5 m/s.
5. External loads on truss (opposite to the path direction): $F_{\text{external}} = 50$ N.
6. Implement position on the truss: $d_4 = 0.8$ m.
7. Initial offset error: $e = 0$ m.
8. Initial state of the vehicles: The initial state of the leader vehicle was defined as $x_1(0) = 40$ m, $y_1(0) = 2.5$ m, $\theta_1(0) = \pi$ rad, $\delta_L(0) = 0$ rad, and $v_1(0) = 0$ m/s. The initial state of the follower vehicle was defined as $x_2(0) = 40$ m, $y_2(0) = 0$ m, $\theta_2(0) = \pi$ rad, $\delta_F(0) = 0$ rad, and $v_2(0) = 0$ m/s. The steering angles and longitudinal velocities, δ_L, δ_F, v_1, and v_2, were defined in the vehicle-fixed coordinate systems, whereas the position and heading variables were defined in the global coordinate system.

The key simulation results for the dynamic model are shown in Figure 4.26 to Figure 4.30.

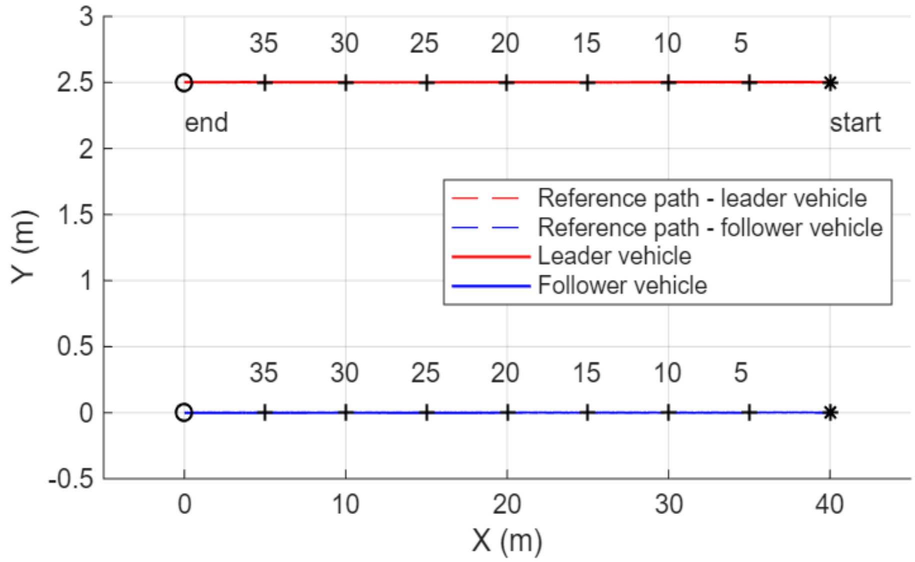

Figure 4.26 Reference and actual paths using the dynamic model in straight-line reverse tracking

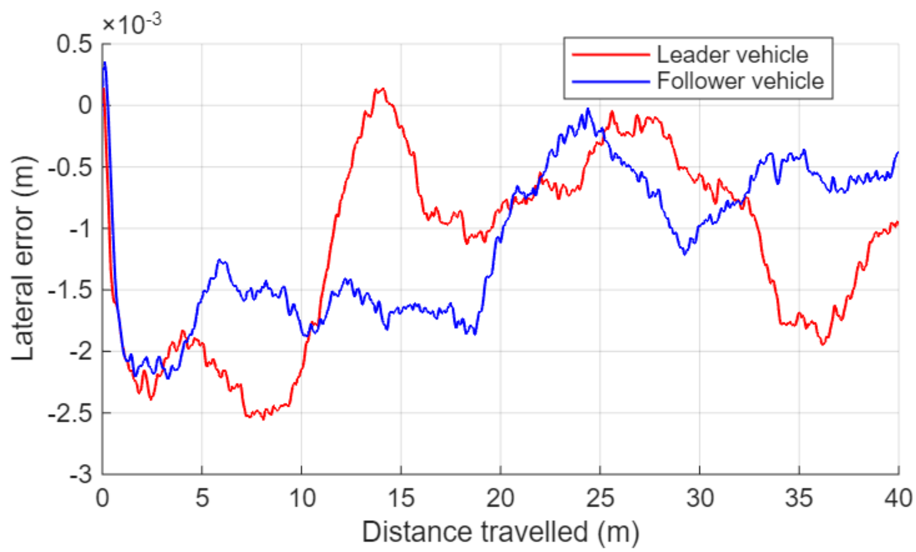

Figure 4.27 Lateral error using the dynamic model in straight-line reverse tracking

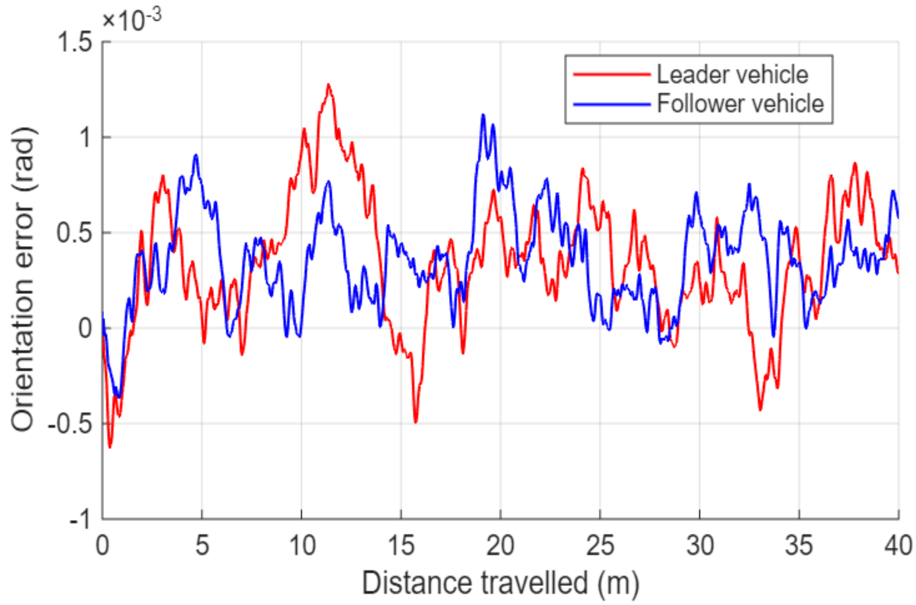

Figure 4.28 Orientation error using the dynamic model in straight-line reverse tracking

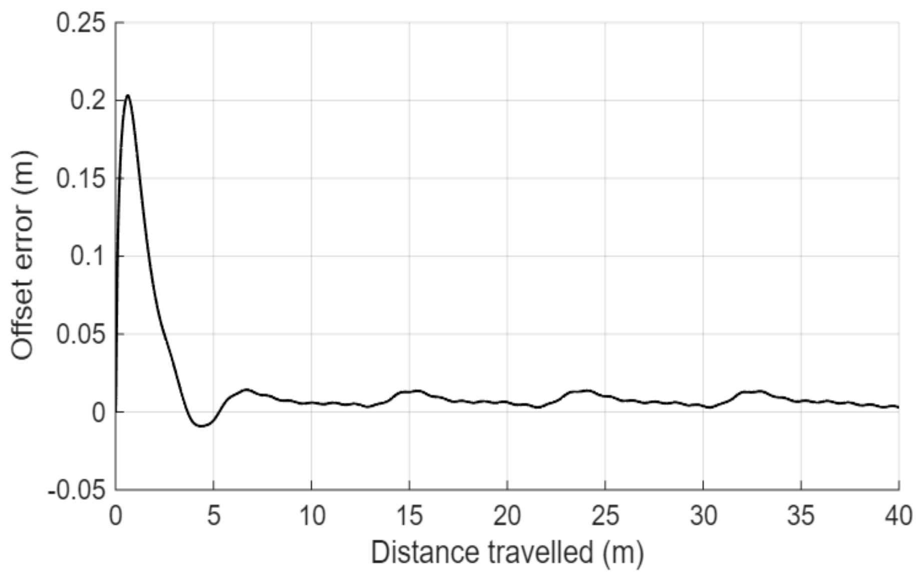

Figure 4.29 Offset error using the dynamic model in straight-line reverse tracking

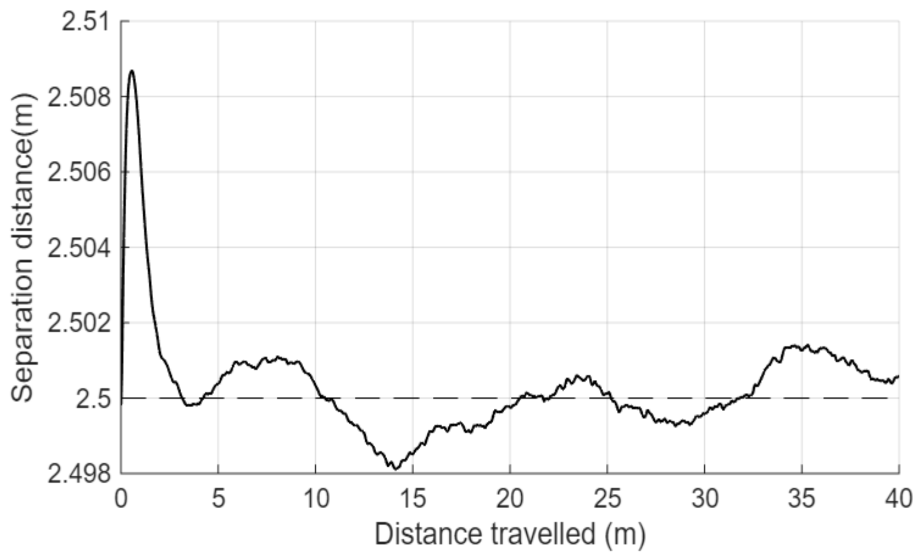

Figure 4.30 Distance between the two support vehicles using the dynamic model in straight-line reverse tracking

The key simulation results for the kinematic model are shown in Figure 4.31 to Figure 4.35.

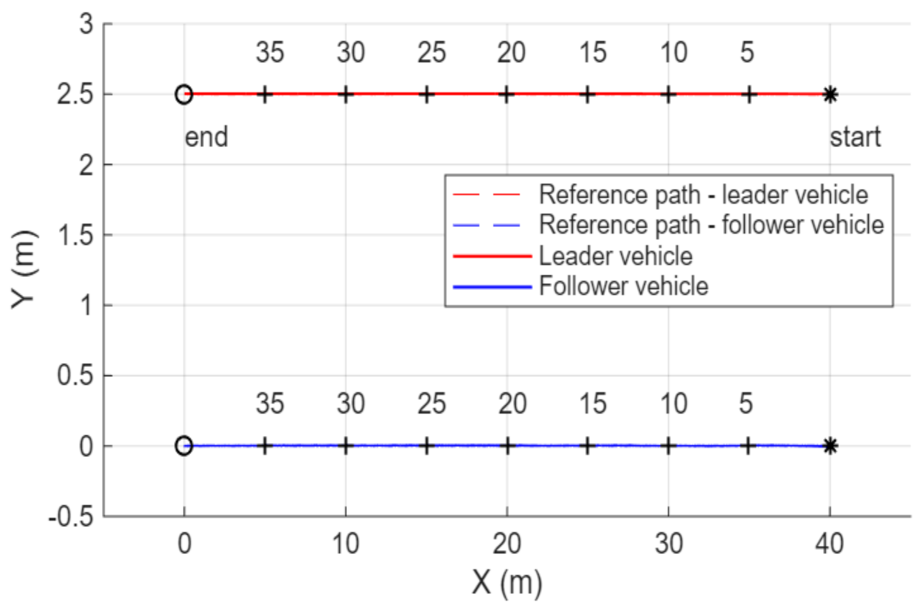

Figure 4.31 Reference and actual paths using the kinematic model in straight-line reverse tracking

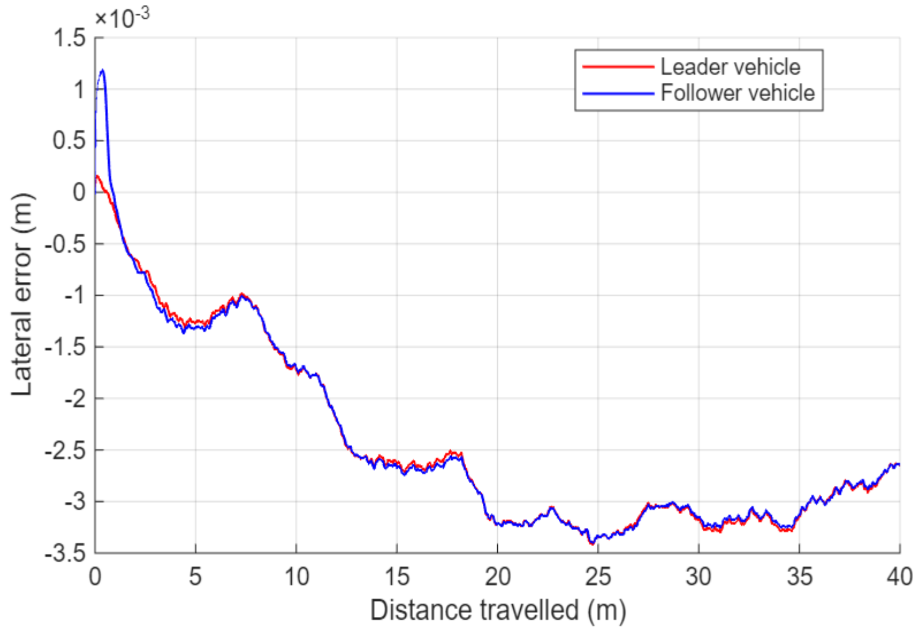

Figure 4.32 Lateral error using the kinematic model in straight-line reverse tracking

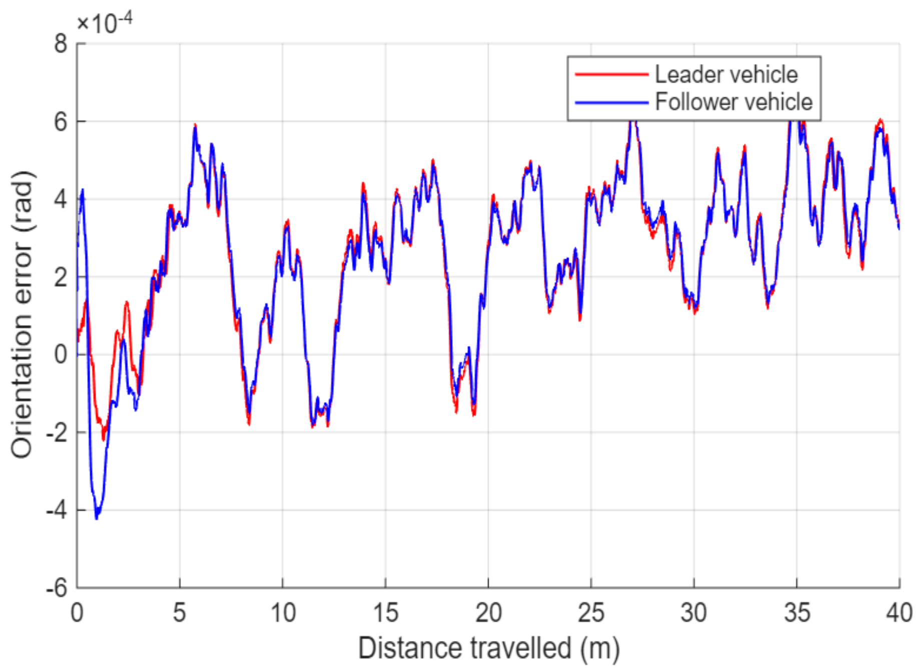

Figure 4.33 Orientation error using the kinematic model in straight-line reverse tracking

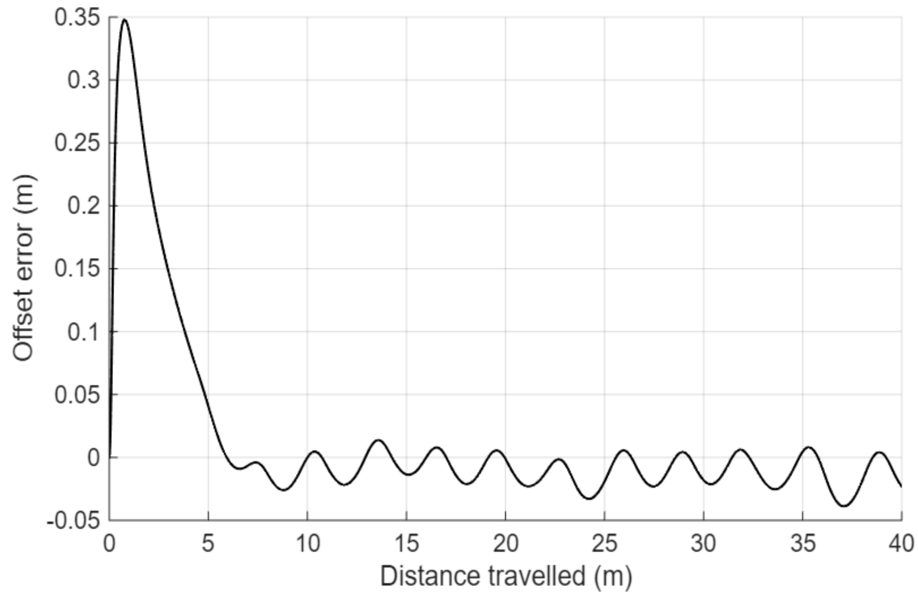

Figure 4.34 Offset error using the kinematic model in straight-line reverse tracking

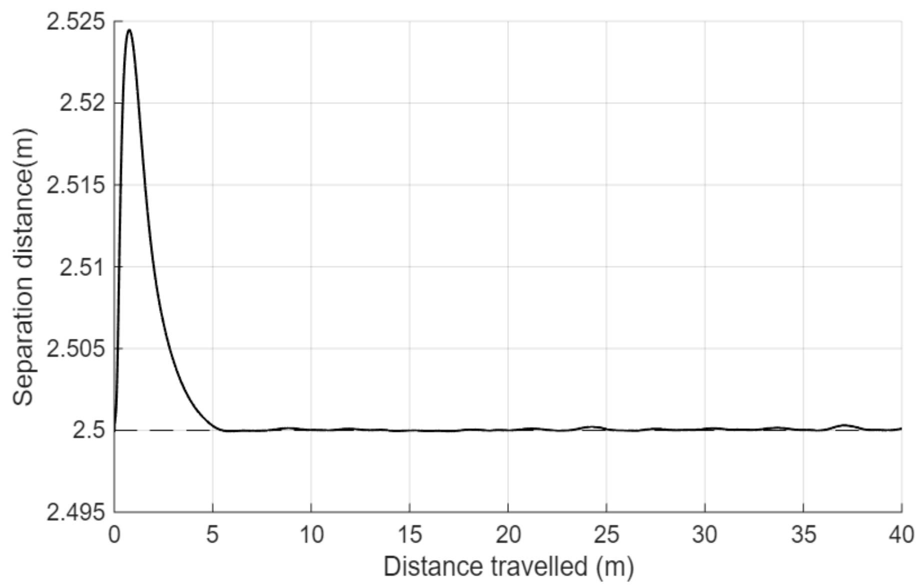

Figure 4.35 Distance between the two support vehicles using the kinematic model in straight-line reverse tracking

The steady-state and IAE performance metrics for straight-line reverse tracking are summarized in Table 4.8.

Table 4.8 Steady-state and IAE performance metrics in the straight-line reverse tracking[a]

		Dynamic	Kinematic
Leader vehicle	Steady-state velocity (m/s)	2.50	2.47
	Steady-state lateral error (m)	**±0.0022**	±0.0034
	Steady-state orientation error (rad)	±0.0013	±0.00069
	Lateral error IAE (m^2)	**0.0483**	0.0973
	Orientation error IAE (rad·m)	0.0157	0.0117
Follower vehicle	Steady-state velocity (m/s)	2.50	2.47
	Steady-state lateral error (m)	**±0.0020**	±0.0034
	Steady-state orientation error (rad)	±0.0011	±0.00066
	Lateral error IAE (m^2)	**0.0466**	0.0983
	Orientation error IAE (rad·m)	0.0146	0.0120
Steady-state offset error (m)		**±0.014**	±0.039
Steady-state separation error (m)		±0.0019	±0.00030
Offset error IAE (m^2)		**0.628**	1.36
Separation error IAE (m^2)		**0.0367**	0.0459

[a] Boldface: notably better than the other model.

Based on the simulation results from Sections 4.2.1 and 4.2.3 and Table 4.6 and Table 4.8, both controllers achieved accurate straight-line tracking in forward and reverse motion. The steady-state lateral errors remained very small in all cases: in reverse motion ±0.0022 m for the leader vehicle and ±0.0020 m for the follower vehicle with the dynamic model, compared with ±0.0034 m for both vehicles with the kinematic model, and in forward motion ±0.0036 m and ±0.0028 m compared with ±0.0051 m. All of these values, and the differences between them, lie below the 0.01 m resolution threshold. The lateral error IAE values were likewise small, 0.0483 m² and 0.0466 m² for the leader and follower vehicles with the dynamic model in reverse motion compared with 0.0973 m² and 0.0983 m² with the kinematic model, with similar values in forward motion; the differences, although large in relative terms (approximately 50.4%, 52.6%, and 42.7%), are an order of magnitude below the 0.4 m² IAE threshold and are within measurement resolution. These results therefore indicate that both models tracked straight-line paths in either travel direction to an accuracy that the platform sensors cannot distinguish, not that one model outperformed the other.

The orientation error results were of the same character. In forward motion the dynamic model produced slightly lower steady-state orientation errors and orientation error IAE values than the kinematic model, and in reverse motion the kinematic model produced the lower values, with orientation error IAE of 0.0117 rad·m for the leader and 0.0120 rad·m for the follower compared with 0.0157 rad·m and 0.0146 rad·m for the dynamic model. All of these differences are far below the 0.35 rad·m threshold, and the steady-state values are below the 0.0087 rad IMU threshold, so neither travel direction reveals a practically meaningful difference in heading regulation under straight-line motion.

The synchronous tracking results are where the two models differ at a resolvable level. In reverse motion, the offset error IAE decreased from 1.36 m^2 with the kinematic model to 0.628 m^2 with the dynamic model, a difference of 0.73 m^2 that exceeds the 0.56 m^2 offset threshold; in forward motion it decreased from 1.16 m^2 to 0.583 m^2, a difference that just reaches the threshold. These reductions indicate that the dynamic model provided more stable relative-position control between the two supporting vehicles. Separation control showed no resolvable difference: the separation error IAE was 0.0367 m^2 compared with 0.0459 m^2 in reverse motion and 0.0547 m^2 compared with 0.0185 m^2 in forward motion, all within measurement resolution. Overall, straight-line forward and reverse tracking were not challenging for either controller; the only practically meaningful distinction in this scenario is the offset regulation of the dynamic model, which is clearer in reverse motion.

4.2.3.2 Curved Trajectory Reverse

The test conditions were as follows:

1. Backward motion.
2. Curved trajectory.
3. Medium-adhesion earth road ($\mu = 0.75$).
4. Target speed of the support vehicles: 2.5 m/s.
5. External loads on truss (opposite to the path direction): $F_{\text{external}} = 50$ N.
6. Implement position on the truss: $d_4 = 0.8$ m.
7. Initial offset error: $e = 0$ m.
8. The initial states of the vehicles in the curved trajectory reverse simulation were the same as those defined in Section 4.2.3.1.

The key simulation results for the dynamic model are shown in Figure 4.36 to Figure 4.40.

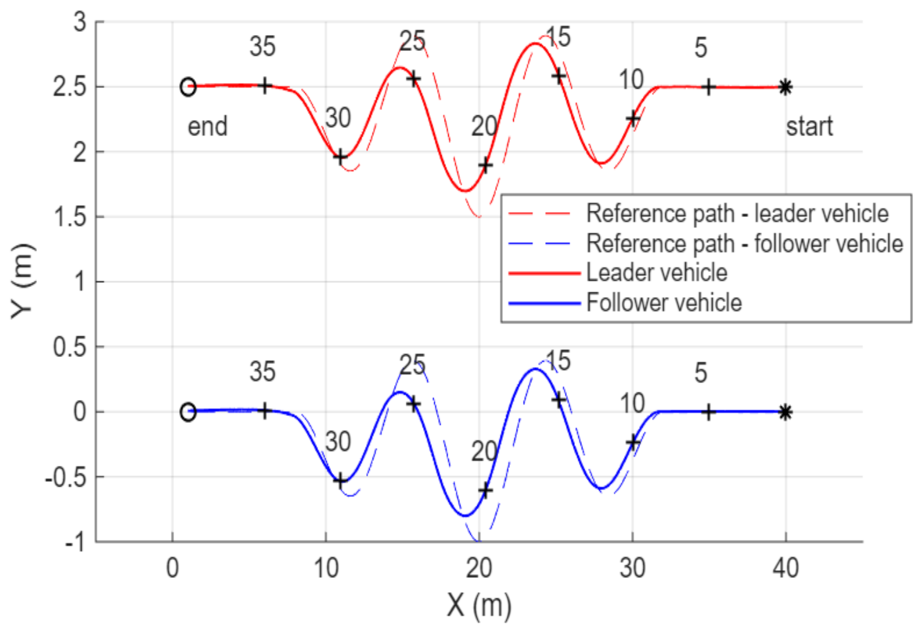

Figure 4.36 Reference and actual paths using the dynamic model for reverse curved-trajectory tracking

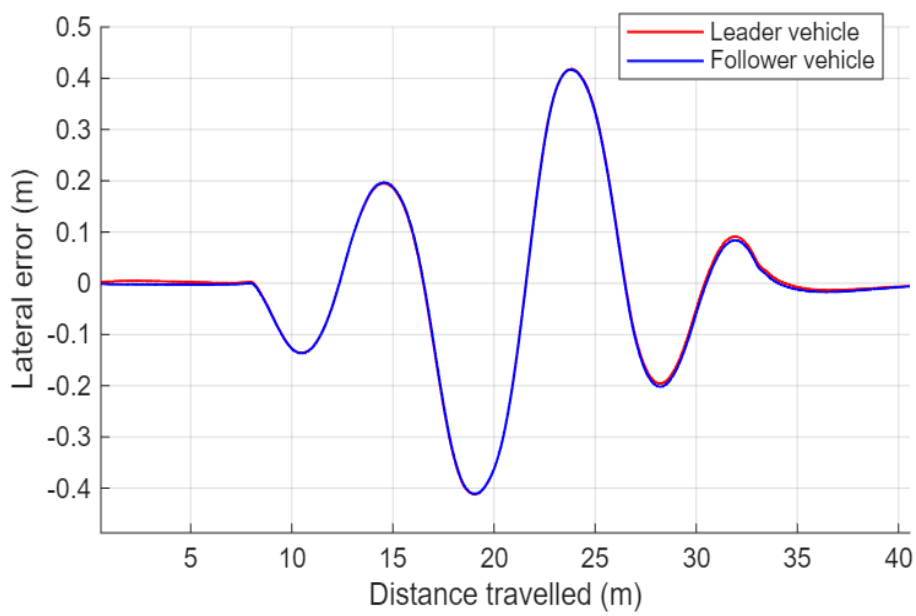

Figure 4.37 Lateral error using the dynamic model for reverse curved-trajectory tracking

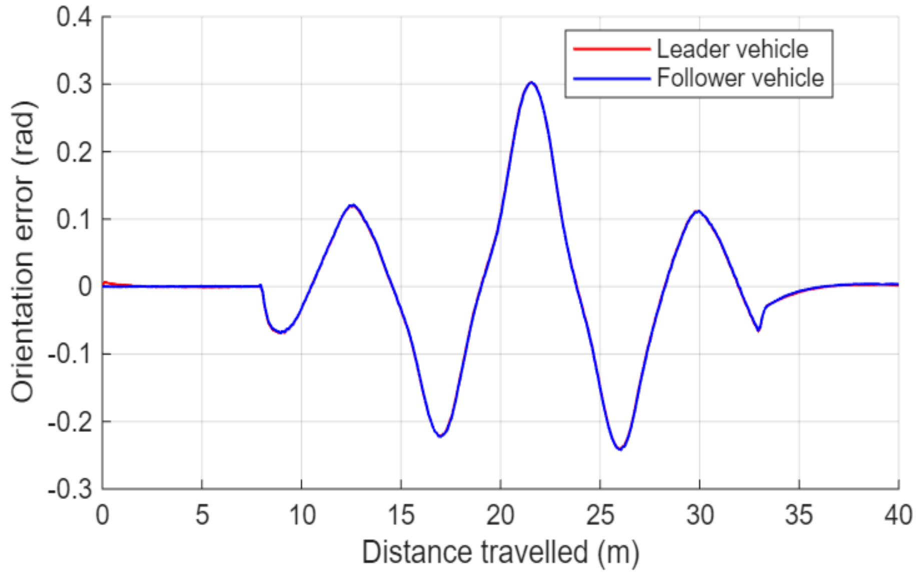

Figure 4.38 Orientation error using the dynamic model for reverse curved-trajectory tracking

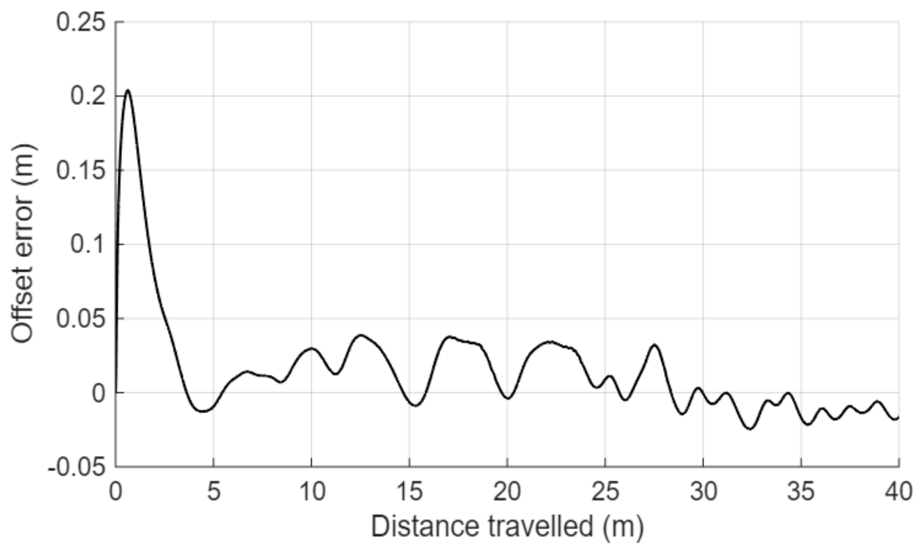

Figure 4.39 Offset error using the dynamic model for reverse curved-trajectory tracking

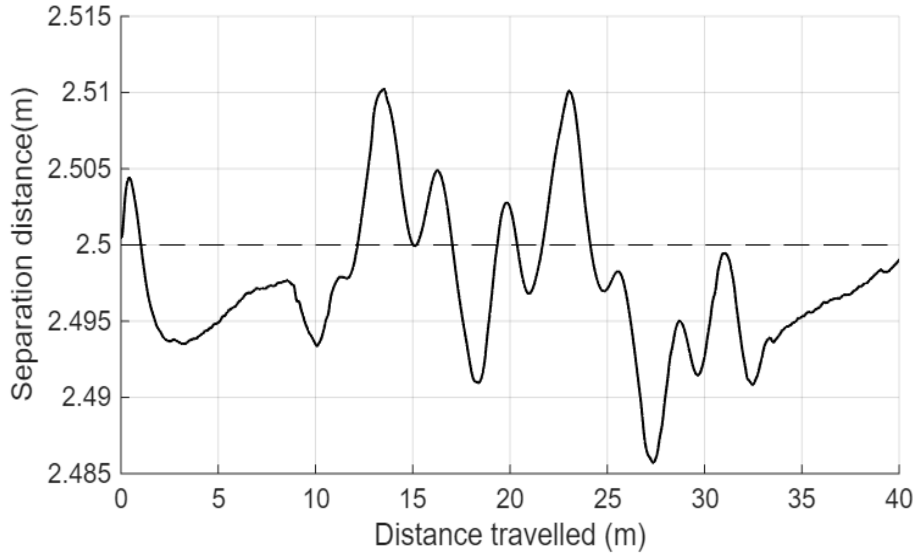

Figure 4.40 Distance between the two support vehicles using the dynamic model for reverse curved-trajectory tracking

The key simulation results for the kinematic model are shown in Figure 4.41 to Figure 4.45.

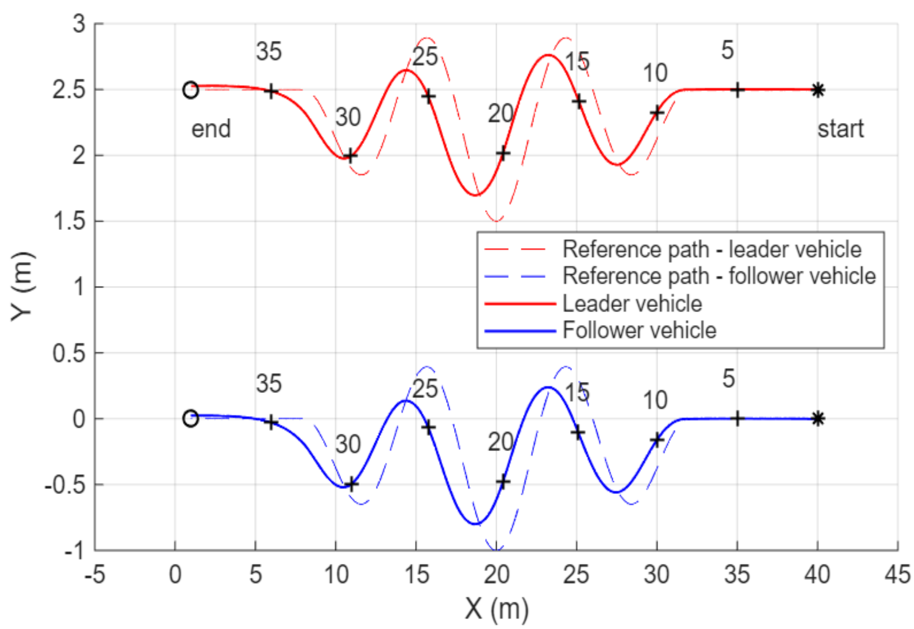

Figure 4.41 Reference and actual paths using the kinematic model for reverse curved-trajectory tracking

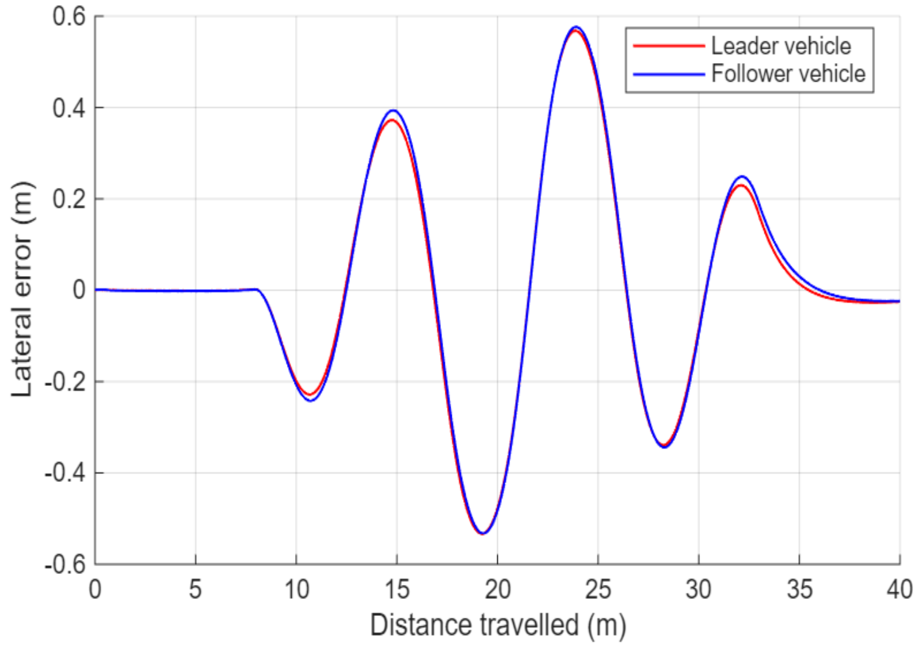

Figure 4.42 Lateral error using the kinematic model for reverse curved-trajectory tracking

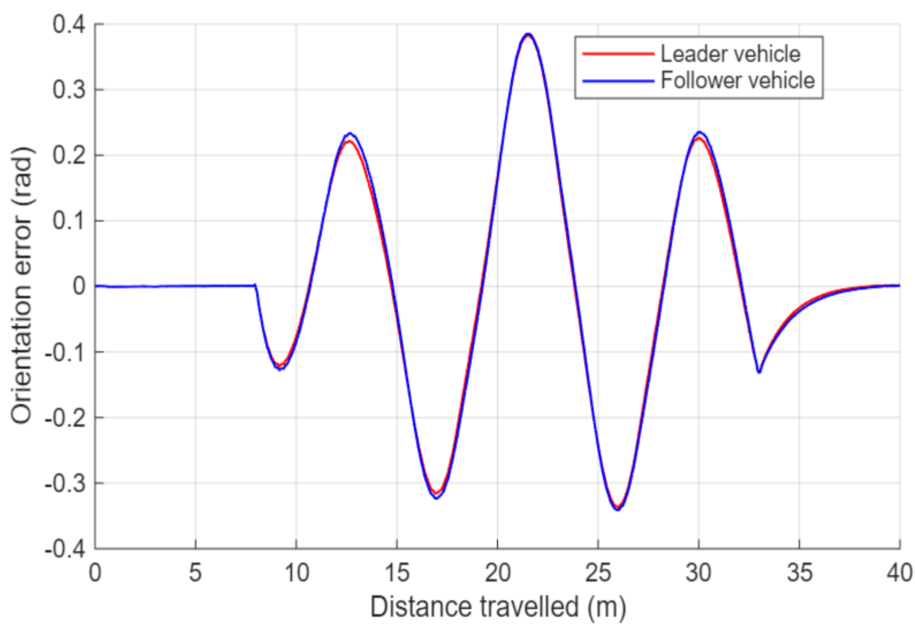

Figure 4.43 Orientation error using the kinematic model for reverse curved-trajectory tracking

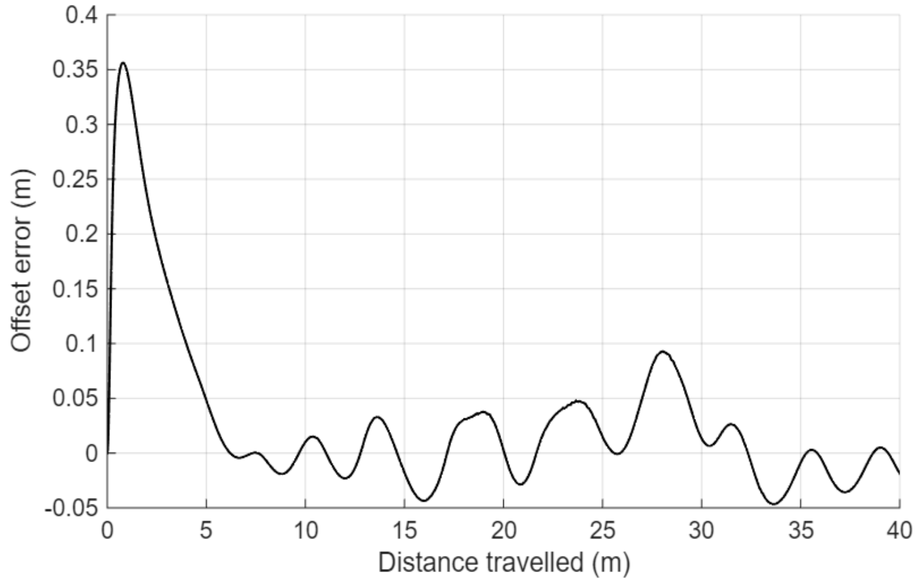

Figure 4.44 Offset error using the kinematic model for reverse curved-trajectory tracking

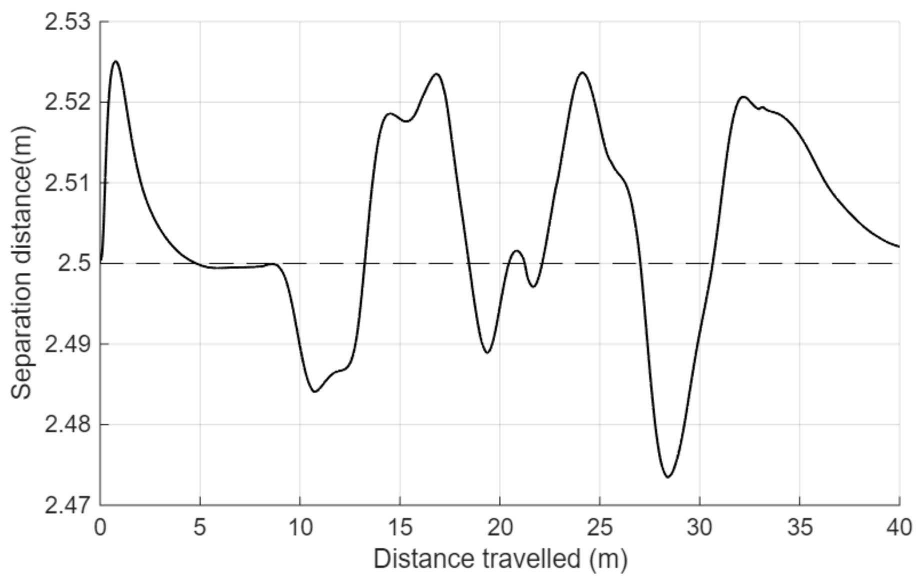

Figure 4.45 Distance between the two support vehicles using the kinematic model for reverse curved-trajectory tracking

The steady-state and IAE performance metrics for curved reverse tracking are summarized in Table 4.9.

Table 4.9 Steady-state and IAE performance metrics for reverse curved-trajectory tracking[a]

		Dynamic	Kinematic
Leader vehicle	Steady-state velocity (m/s)	2.43	2.43
	Steady-state lateral error (m)	**±0.42**	±0.57
	Steady-state orientation error (rad)	**±0.30**	±0.38
	Lateral error IAE (m^2)	**4.40**	6.67
	Orientation error IAE (rad·m)	**2.64**	4.34
Follower vehicle	Steady-state velocity (m/s)	2.43	2.43
	Steady-state lateral error (m)	**±0.42**	±0.58
	Steady-state orientation error (rad)	**±0.30**	±0.39
	Lateral error IAE (m^2)	**4.41**	6.85
	Orientation error IAE (rad·m)	**2.64**	4.49
Steady-state offset error (m)		**±0.040**	±0.093
Steady-state separation error (m)		**±0.014**	±0.027
Offset error IAE (m^2)		**0.926**	1.79
Separation error IAE (m^2)		**0.182**	0.420

[a] Boldface: notably better than the other model.

Based on the simulation results from Sections 4.2.2 and 4.2.3, and from Table 4.7 and Table 4.9, curved reverse tracking was considerably more demanding than curved forward tracking for both controllers. For the leader vehicle, the steady-state lateral error of the dynamic model increased from ±0.12 m in forward motion to ±0.42 m in reverse motion, while the kinematic model increased from ±0.20 m to ±0.57 m. A similar trend was observed for the follower vehicle, where the reverse-motion lateral errors were ±0.42 m for the dynamic model and ±0.58 m for the kinematic model. The lateral error IAE also increased substantially in reverse motion. However, the dynamic model remained consistently more accurate than the kinematic model. In reverse motion, the dynamic model reduced the lateral error IAE from 6.67 m^2 to 4.40 m^2 for the leader vehicle and from 6.85 m^2 to 4.41 m^2 for the follower vehicle, corresponding to reductions of approximately 34.0% and 35.6%, respectively.

The orientation error results showed that the dynamic model performed more favourably in reverse curved tracking than in forward curved tracking. In reverse motion, the dynamic model achieved lower steady-state orientation errors, ±0.30 rad for both vehicles, compared with ±0.38 rad for the leader and ±0.39 rad for the follower using the kinematic model. The orientation error IAE was also lower with the dynamic model, decreasing from 4.34 rad·m to 2.64 rad·m for the leader vehicle and from 4.49 rad·m to 2.64 rad·m for the follower vehicle. This differs from the forward curved case, where the dynamic model improved lateral tracking but produced a slightly higher orientation error IAE than the kinematic model. Therefore, under reverse curved tracking, the dynamic model provided improvements in both lateral and orientation tracking accuracy.

The formation-control metrics further confirm the advantage of the dynamic model under curved reverse motion. The steady-state offset error decreased from ± 0.093 m with the kinematic model to ± 0.040 m with the dynamic model, and the offset error IAE from 1.79 m^2 to 0.926 m^2; both differences exceed the offset thresholds. The separation error also decreased, from ± 0.027 m to ± 0.014 m in steady state and from 0.420 m^2 to 0.182 m^2 in IAE, but these differences (0.013 m and 0.24 m^2) are within measurement resolution and are reported as indicative only. Compared with forward curved motion, reverse curved motion increased the offset and separation IAE values for both controllers, indicating that travel direction has a stronger influence when path curvature is present. These results show that curved reverse tracking is one of the more demanding operating conditions. Note also that both controllers exceeded the ± 0.15 m lateral and ± 0.15 rad orientation bounds of Section 3.4 in this scenario, so the dynamic model reduced but did not eliminate the tracking deficit of the 2WS support vehicles in curved reverse motion. Within that limitation, the dynamic model maintained resolvably better lateral tracking, orientation regulation, and offset control than the kinematic model, supporting its suitability for WSIC operation under complex curved and reverse manoeuvres.

Overall, the forward and reverse motion comparisons show that travel direction had limited influence under straight-line tracking but became critical under curved trajectory tracking. In the straight-line case, both controllers maintained lateral and orientation errors below the sensor resolution in both directions, indicating that reverse operation can be controlled effectively when path curvature is absent. In contrast, reverse motion along curved paths substantially increased lateral errors and IAE values for both controllers, beyond the Section 3.4 bounds, showing that reverse tracking becomes more difficult when steering action, vehicle orientation, and curvature effects are coupled.

Across the reverse-tracking scenarios, the dynamic model provided resolvably better offset regulation in both path geometries and better lateral and orientation tracking under curved reverse motion; under straight-line reverse motion the two models could not be distinguished at the sensor level. These results indicate that reverse operation should be evaluated together with path geometry, particularly for WSIC mobile-mode operation, where reverse motion along curved paths represents the most demanding condition. Although the simulated results show that the 2WS support vehicles can complete successive forward and reverse displacements, the curved reverse errors exceeded the performance bounds for both models, and a 4WS configuration would be more appropriate for practical WSIC operation because it can provide greater manoeuvrability and improved bidirectional tracking capability.

4.2.4 Different Pathways

The preceding cases were conducted on a medium-adhesion earth road (μ = 0.75). To verify robustness, the simulation was extended to include a high-adhesion concrete pavement (μ = 1) and a low-adhesion grass surface (μ = 0.5).

4.2.4.1 High-Adhesion Pathway

The test scenario was as follows:

1. Forward motion.
2. Straight trajectory.
3. High-adhesion concrete pavement (μ = 1).
4. Target speed of the support vehicles: 2.5 m/s.
5. External loads on truss (opposite to the path direction): F_{external} = 50 N.
6. Implement position on the truss: d_4 = 0.8 m.
7. Initial offset error: e = 0 m.

The key simulation results for the dynamic model are shown in Figure 4.46 to Figure 4.50.

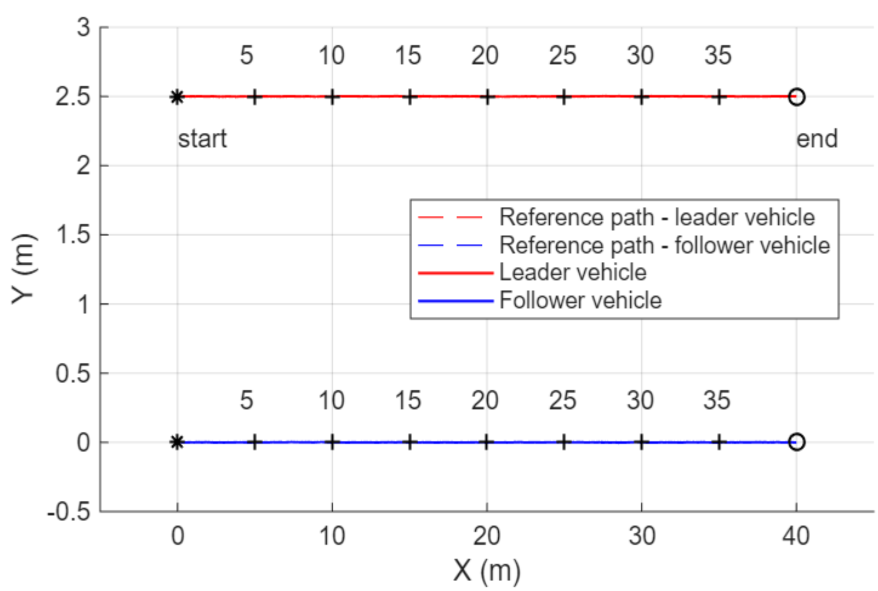

Figure 4.46 Reference and actual paths using the dynamic model on high-adhesion pathway

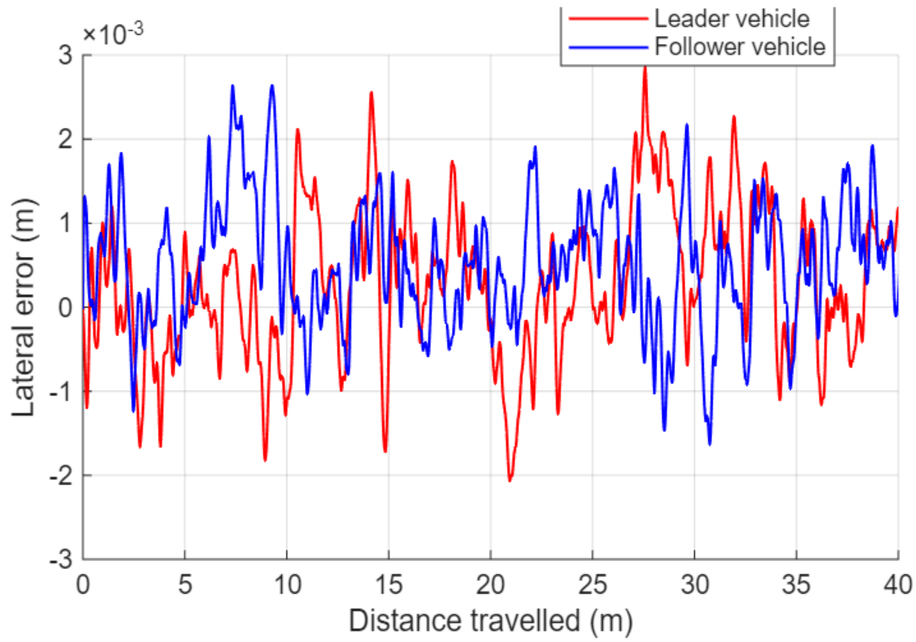

Figure 4.47 Lateral error using the dynamic model on high-adhesion pathway

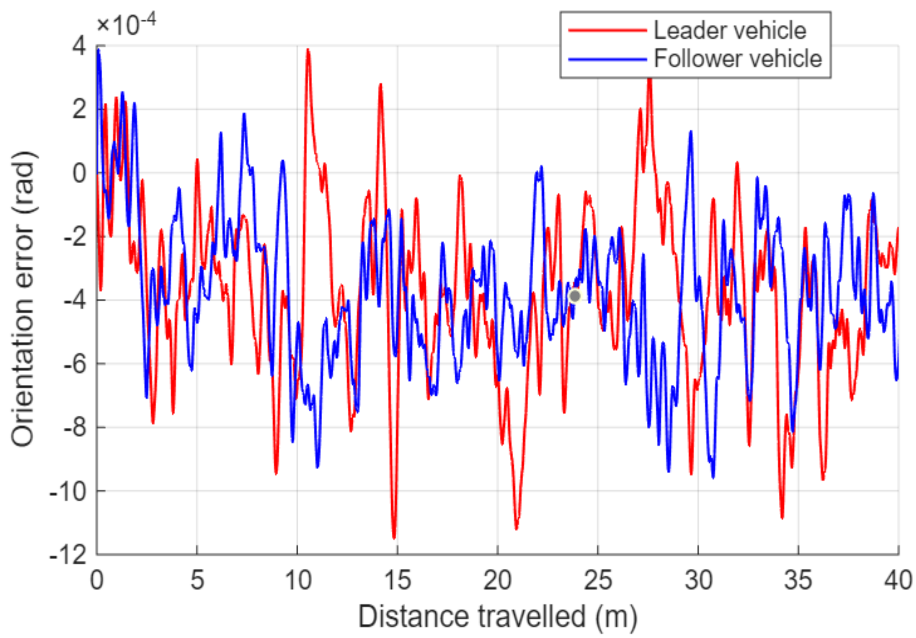

Figure 4.48 Orientation error using the dynamic model on high-adhesion pathway

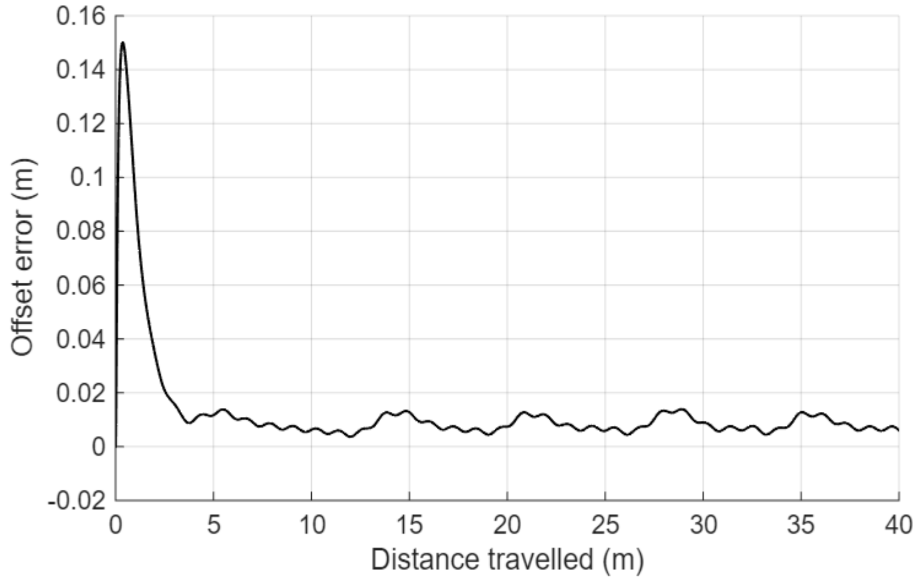

Figure 4.49 Offset error using the dynamic model on high-adhesion pathway

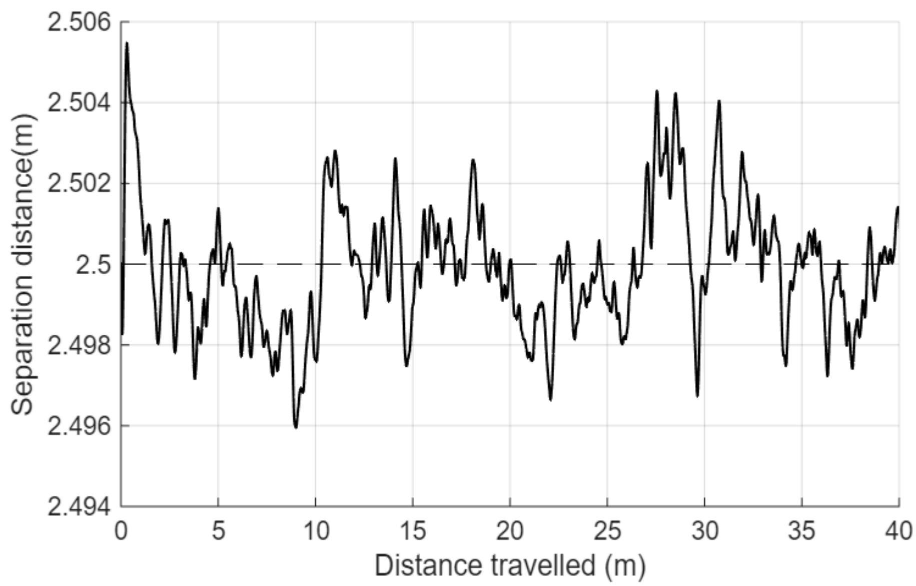

Figure 4.50 Distance between the two support vehicles using the dynamic model on high-adhesion pathway

The key simulation results for the kinematic model are shown in Figure 4.51 to Figure 4.55.

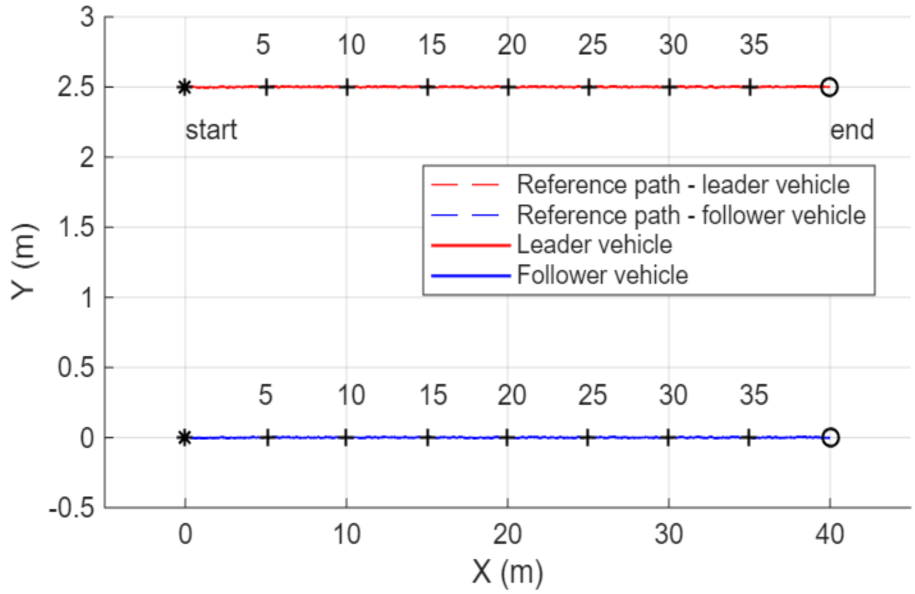

Figure 4.51 Reference and actual paths using the kinematic model on high-adhesion pathway

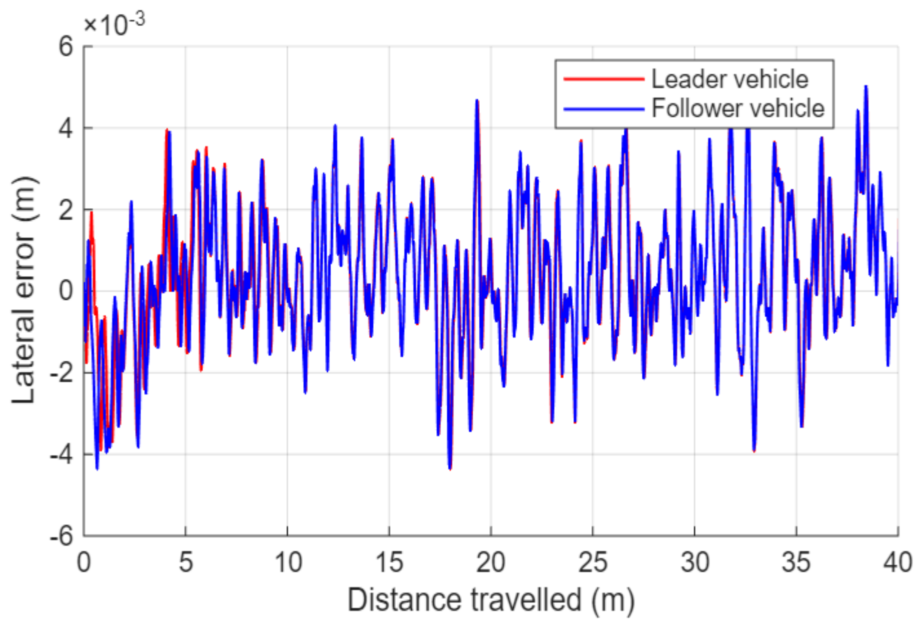

Figure 4.52 Lateral error using the kinematic model on high-adhesion pathway

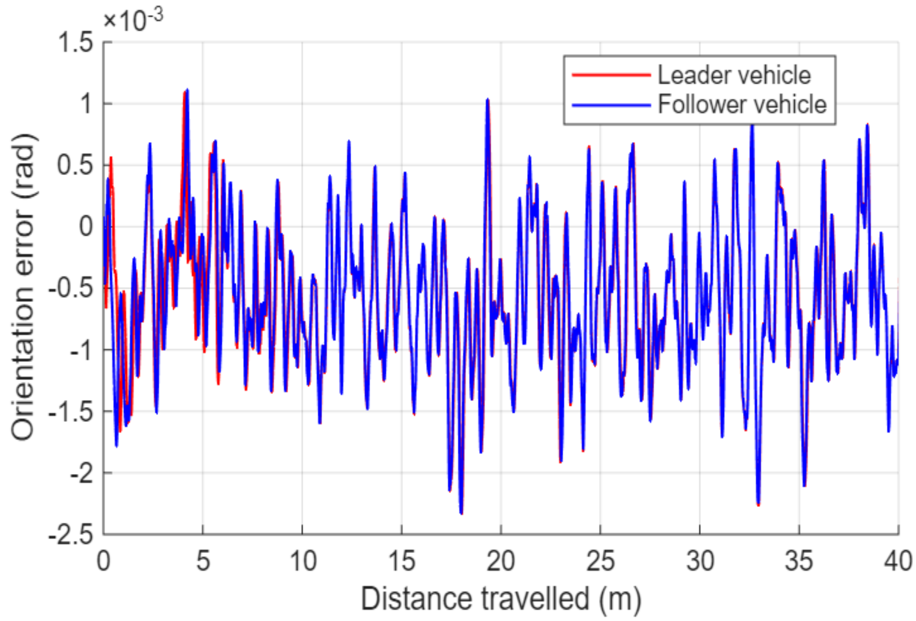

Figure 4.53 Orientation error using the kinematic model on high-adhesion pathway

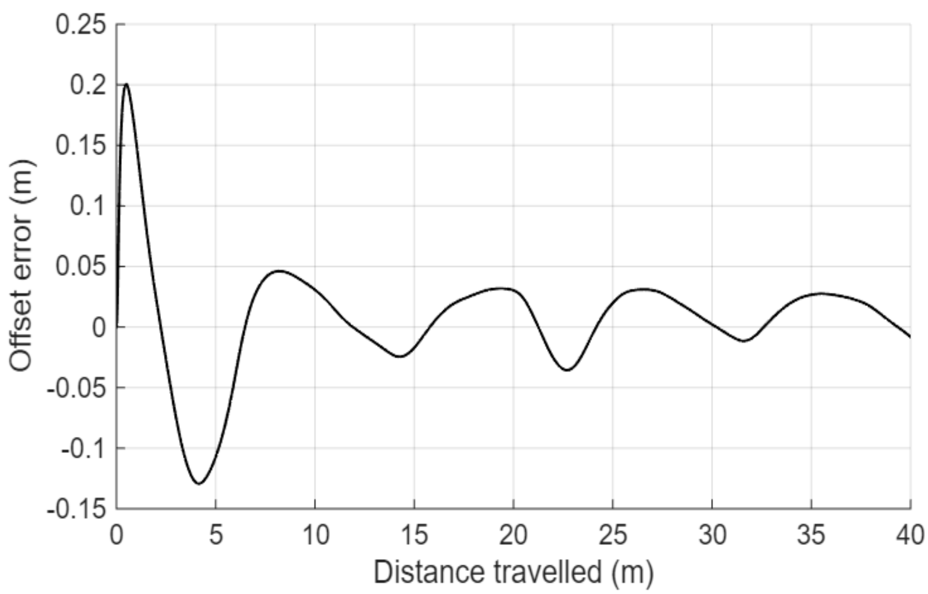

Figure 4.54 Offset error using the kinematic model on high-adhesion pathway

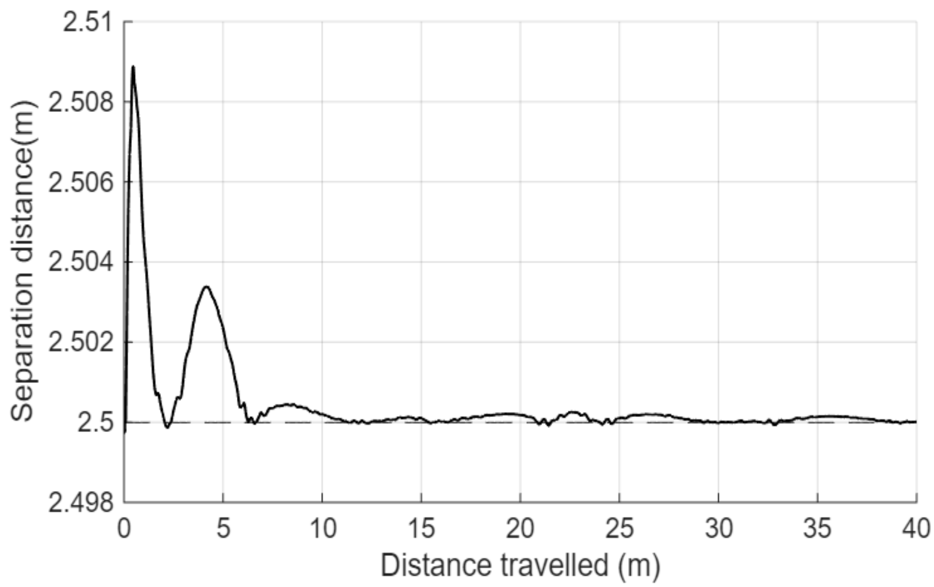

Figure 4.55 Distance between the two support vehicles using the kinematic model on high-adhesion pathway

The steady-state and IAE performance metrics for the high-adhesion pathway are summarized in Table 4.10.

Table 4.10 Steady-state and IAE performance metrics for the high-adhesion pathway[a]

		Dynamic	Kinematic
Leader vehicle	Steady-state velocity (m/s)	2.50	2.46
	Steady-state lateral error (m)	**±0.0029**	±0.0050
	Steady-state orientation error (rad)	**±0.0011**	±0.0023
	Lateral error IAE (m^2)	**0.0296**	0.0537
	Orientation error IAE (rad·m)	**0.0158**	0.0271
Follower vehicle	Steady-state velocity (m/s)	2.50	2.47
	Steady-state lateral error (m)	**±0.0022**	±0.0050
	Steady-state orientation error (rad)	**±0.0010**	±0.0023
	Lateral error IAE (m^2)	**0.0289**	0.0540
	Orientation error IAE (rad·m)	**0.0154**	0.0272
Steady-state offset error (m)		**±0.014**	±0.036
Steady-state separation error (m)		±0.0041	±0.00026
Offset error IAE (m^2)		**0.514**	1.25
Separation error IAE (m^2)		0.0462	0.0185

[a] Boldface: notably better than the other model.

Based on the simulation results of Sections 4.2.1 and 4.2.4.1 and Tables 4.6 and 4.10, both models tracked the straight path within sensor resolution on the high-adhesion pavement, as they did on the medium-adhesion earth road. The lateral error IAE of the dynamic model was 0.0296 m^2 for the leader vehicle and 0.0289 m^2 for the follower vehicle, compared with 0.0537 m^2 and 0.0540 m^2 for the kinematic model, against 0.0317 m^2 and 0.0315 m^2, and 0.0553 m^2 and 0.0551 m^2, in the general case; the orientation error IAE was 0.0158 rad·m and 0.0154 rad·m for the dynamic model and 0.0271 rad·m and 0.0272 rad·m for the kinematic model. All steady-state lateral and orientation errors are below the 0.01 m and 0.0087 rad thresholds, and all IAE differences, between the models and between the two surfaces, are far below the 0.4 m^2 and 0.35 rad·m thresholds, so no practically meaningful difference in individual-vehicle tracking is claimed; the higher adhesion changed the tracking metrics of both models only marginally relative to the general case.

The formation-control results show the only resolvable difference. The offset error IAE was 0.514 m^2 with the dynamic model and 1.25 m^2 with the kinematic model, a difference of 0.74 m^2 that exceeds the 0.56 m^2 threshold, compared with 0.583 m^2 and 1.16 m^2 (a difference of 0.58 m^2) in the general case; the steady-state offset error was ± 0.014 m against ± 0.036 m, a difference of 0.022 m above the 0.014 m threshold. The kinematic model produced the smaller separation error IAE, 0.0185 m^2 against 0.0462 m^2, but both steady-state separation errors are below the 0.014 m threshold and the IAE difference is within resolution. On the high-adhesion pavement the dynamic model therefore maintained practically better offset regulation, with a margin slightly larger than in the general case.

4.2.4.2 Low-Adhesion Pathway

The test scenario was as follows:

1. Forward motion.
2. Straight trajectory.
3. Low-adhesion grass pathway ($\mu = 0.5$).
4. Target speed of the support vehicles: 2.5 m/s.
5. External loads on truss (opposite to the path direction): $F_{\text{external}} = 50$ N.
6. Implement position on the truss: $d_4 = 0.8$ m.
7. Initial offset error: $e = 0$ m.

The key simulation results for the dynamic model are shown in Figure 4.56 to Figure 4.60.

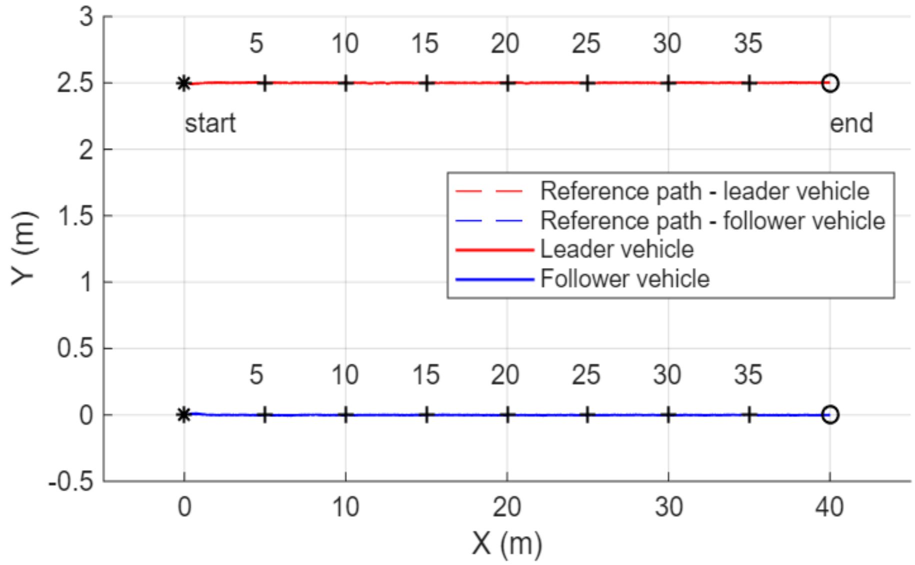

Figure 4.56 Reference and actual paths using the dynamic model on low-adhesion pathway

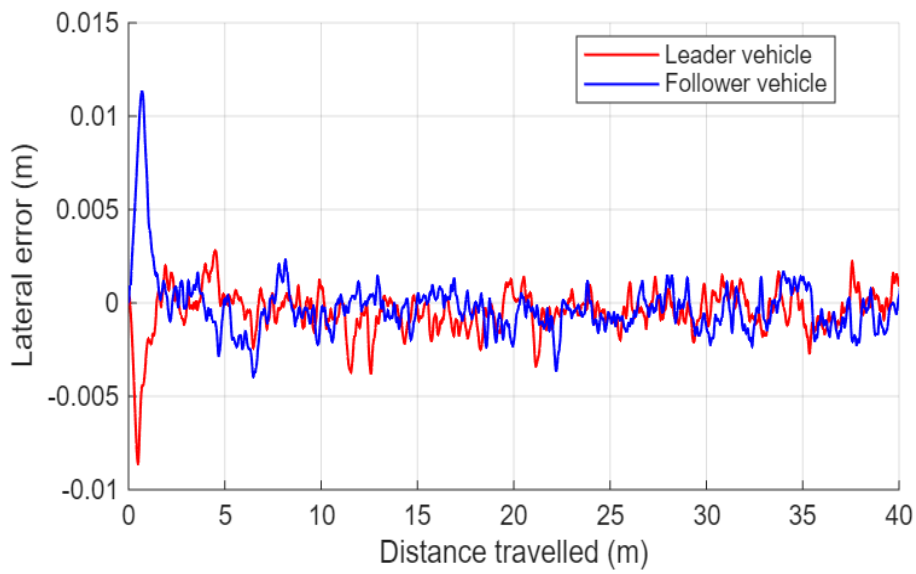

Figure 4.57 Lateral error using the dynamic model on low-adhesion pathway

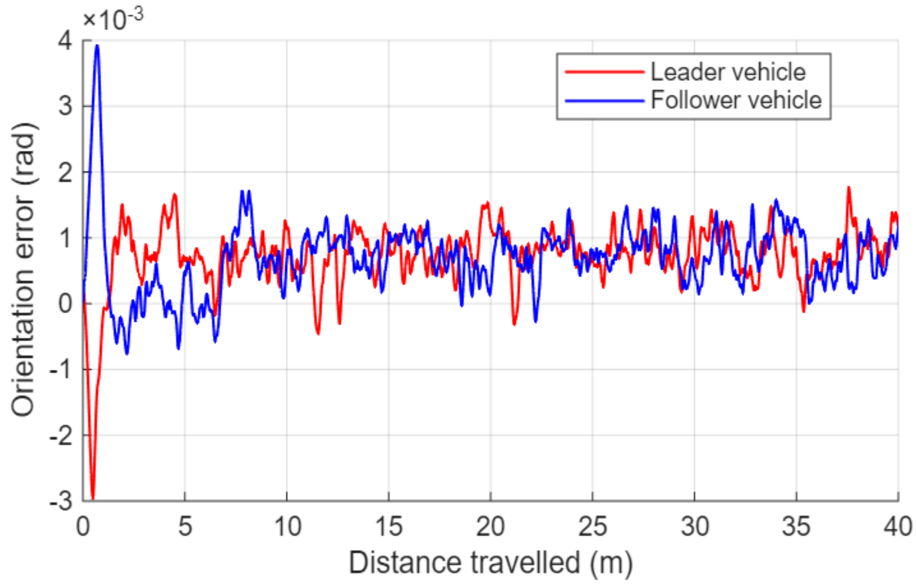

Figure 4.58 Orientation error using the dynamic model on low-adhesion pathway

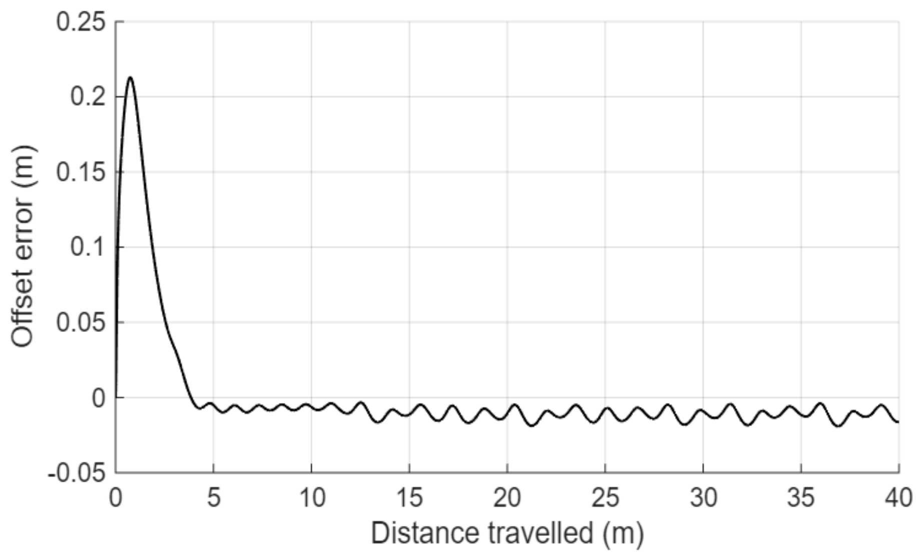

Figure 4.59 Offset error using the dynamic model on low-adhesion pathway

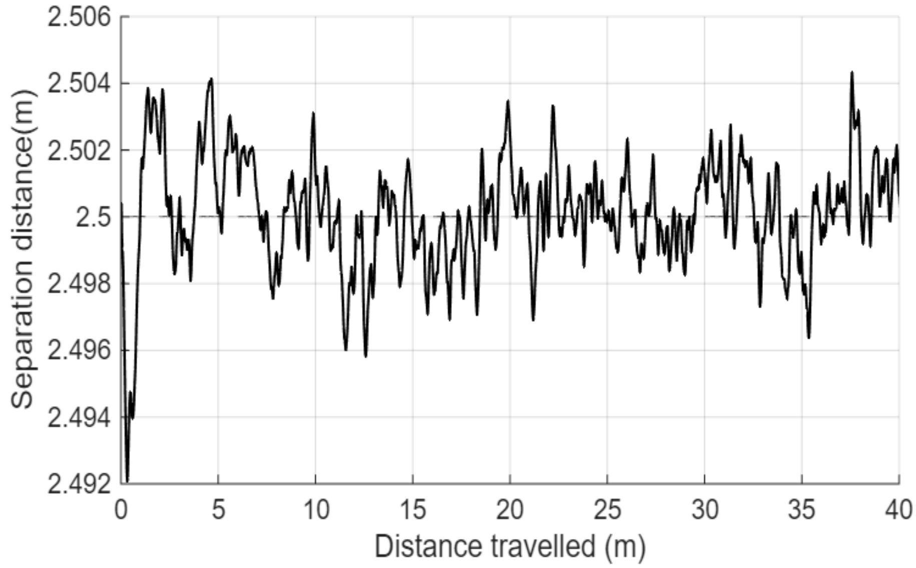

Figure 4.60 Distance between the two support vehicles using the dynamic model on low-adhesion pathway

The key simulation results for the kinematic model are shown in Figure 4.61 to Figure 4.65.

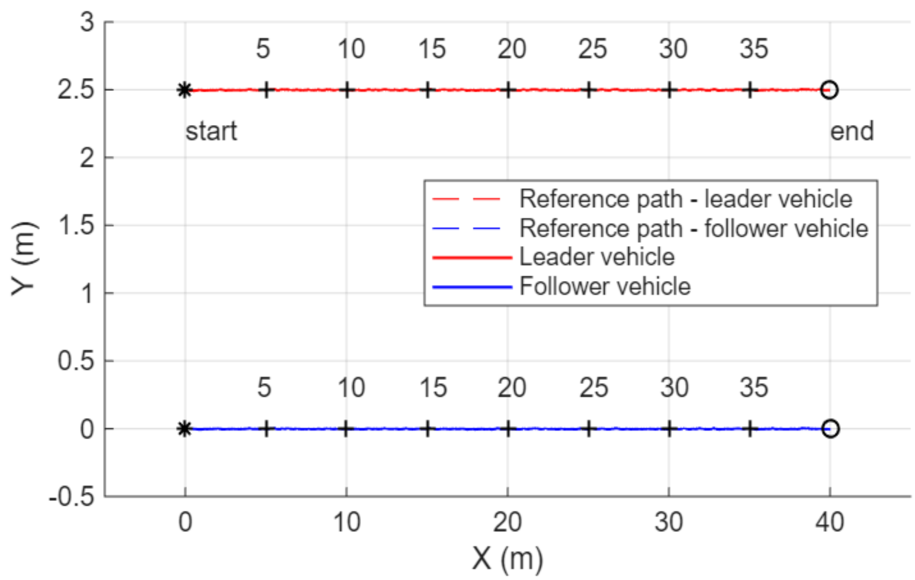

Figure 4.61 Reference and actual paths using the kinematic model on low-adhesion pathway

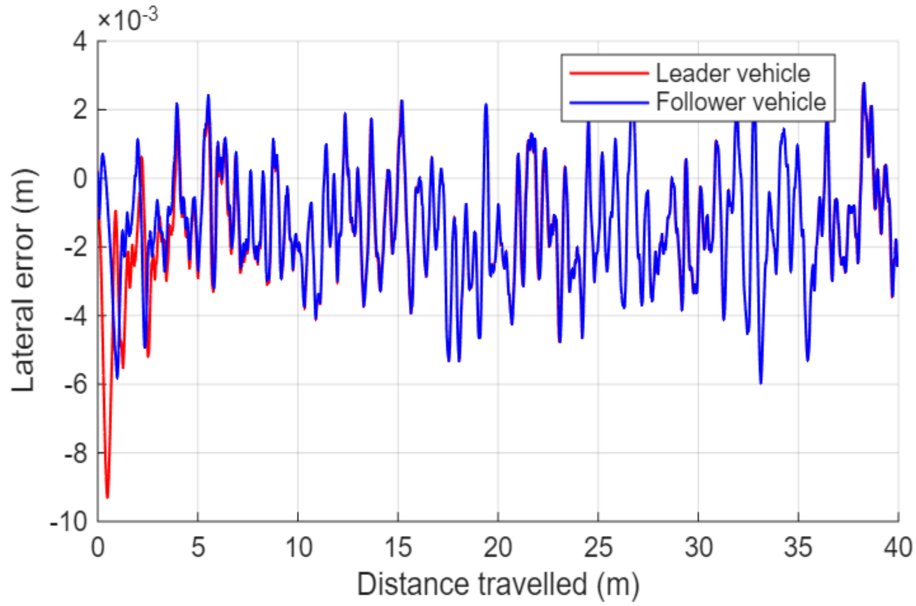

Figure 4.62 Lateral error using the kinematic model on low-adhesion pathway

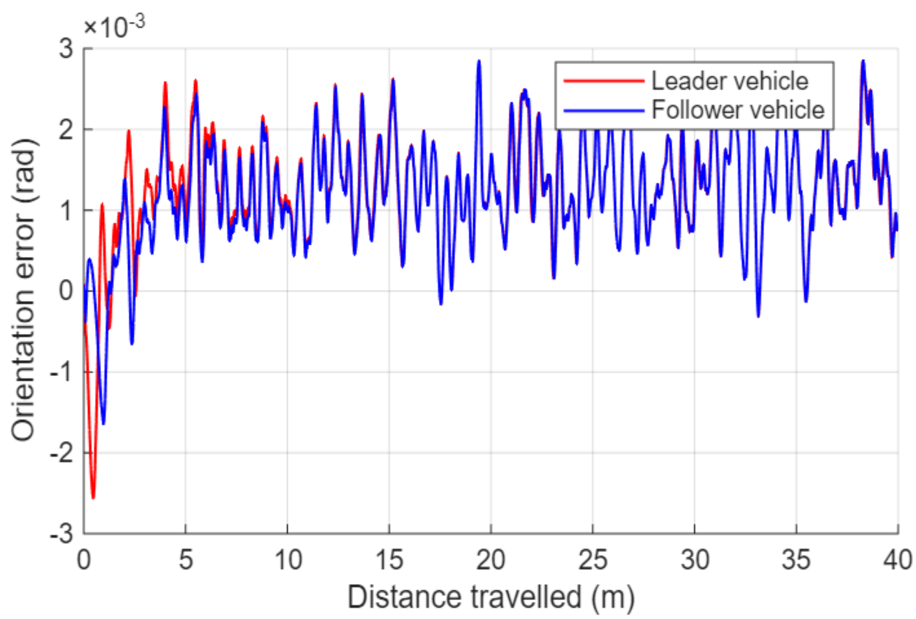

Figure 4.63 Orientation error using the kinematic model on low-adhesion pathway

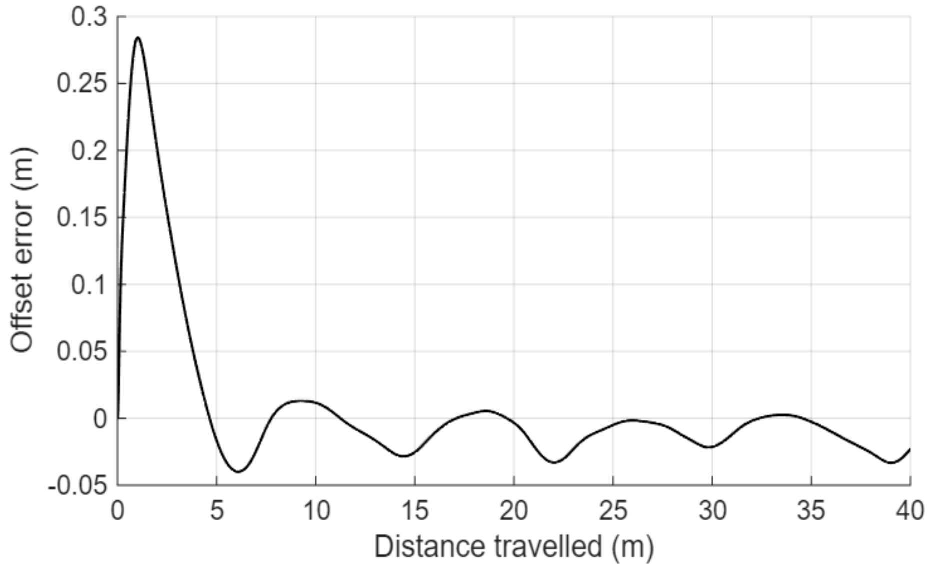

Figure 4.64 Offset error using the kinematic model on low-adhesion pathway

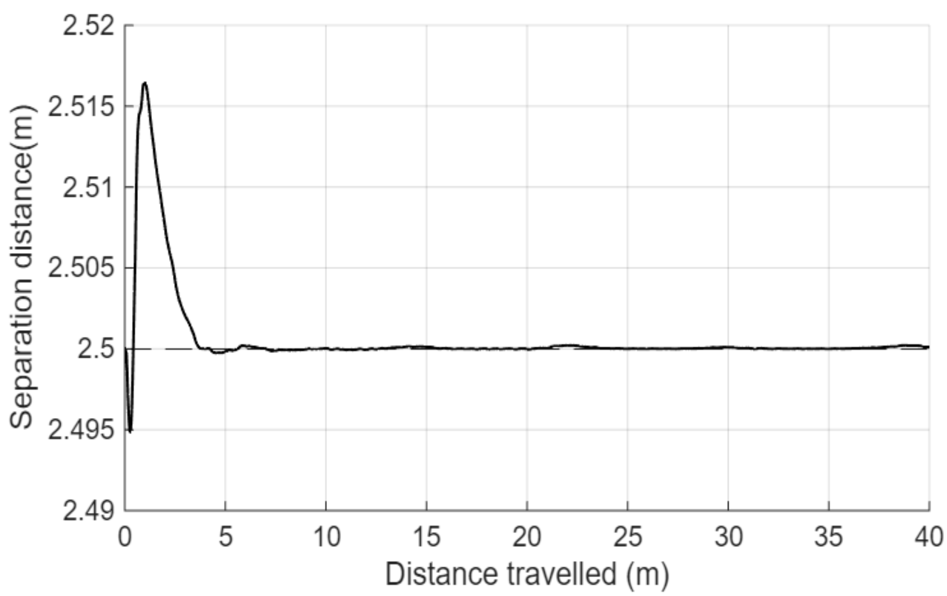

Figure 4.65 Distance between the two support vehicles using the kinematic model on low-adhesion pathway

The steady-state and IAE performance metrics for the low-adhesion pathway are summarized in Table 4.11.

Table 4.11 Steady-state and IAE performance metrics for the low-adhesion pathway[a]

		Dynamic	Kinematic
Leader vehicle	Steady-state velocity (m/s)	2.50	2.48
	Steady-state lateral error (m)	**±0.0038**	±0.0060
	Steady-state orientation error (rad)	**±0.0018**	±0.0029
	Lateral error IAE (m^2)	**0.0353**	0.0749
	Orientation error IAE (rad·m)	**0.0319**	0.0538
Follower vehicle	Steady-state velocity (m/s)	2.50	2.48
	Steady-state lateral error (m)	**±0.0037**	±0.0060
	Steady-state orientation error (rad)	**±0.0016**	±0.0029
	Lateral error IAE (m^2)	**0.0414**	0.0700
	Orientation error IAE (rad·m)	**0.0298**	0.0513
Steady-state offset error (m)		**±0.019**	±0.033
Steady-state separation error (m)		±0.0043	±0.00022
Offset error IAE (m^2)		**0.751**	1.16
Separation error IAE (m^2)		0.0493	0.0274

[a] Boldface: notably better than the other model.

Based on the simulation results of Sections 4.2.1 and 4.2.4.2 and Tables 4.6 and 4.11, both models still tracked the straight path within sensor resolution on the low-adhesion grass surface. The lateral error IAE of the dynamic model rose from 0.0317 m^2 (leader vehicle) and 0.0315 m^2 (follower vehicle) in the general case to 0.0353 m^2 and 0.0414 m^2, whereas the kinematic model rose from 0.0553 m^2 and 0.0551 m^2 to 0.0749 m^2 and 0.0700 m^2; the orientation error IAE rose to 0.0319 rad·m and 0.0298 rad·m for the dynamic model and to 0.0538 rad·m and 0.0513 rad·m for the kinematic model. All steady-state values remain below the 0.01 m and 0.0087 rad thresholds and all differences are well below the 0.4 m^2 and 0.35 rad·m thresholds, so no practically meaningful difference in individual-vehicle tracking is claimed. In relative terms the reduced adhesion degraded the kinematic model more in leader lateral error IAE (an increase of about 35% against 11%) and in both orientation error IAE values (about 147% and 135% against 85% and 77%), while the follower lateral error IAE increased by a similar proportion for both models; the direction of this trend is consistent with the dynamic model accounting for tire slip, although at these magnitudes it is indicative only.

For formation control, the offset error IAE of the dynamic model rose from 0.583 m^2 in the general case to 0.751 m^2, while that of the kinematic model remained at 1.16 m^2. The difference of 0.41 m^2 is below the 0.56 m^2 threshold, so, unlike the general case, no practically meaningful advantage in offset regulation is claimed under low adhesion, although the steady-state offset error of ± 0.019 m against ± 0.033 m, a difference of 0.014 m at the threshold, still favoured the dynamic model. The separation errors of both models remained below the 0.014 m threshold, and the separation error IAE difference (0.0493 m² against 0.0274 m²) is within resolution. Low adhesion therefore affected offset regulation more than individual tracking, and narrowed the dynamic model's advantage from resolvable in the general case to marginal.

4.2.5 Different Target Speeds

The robustness of the control strategy was further assessed with respect to vehicle speed. The simulation was expanded to include two additional operating points: high-speed travel at 3.5 m/s and low-speed travel at 1.5 m/s.

4.2.5.1 High Speed

The test scenario was as follows:

1. Forward motion.
2. Straight trajectory.
3. Medium-adhesion earth road ($\mu = 0.75$).
4. Target speed of the support vehicles: 3.5 m/s.
5. External loads on truss (opposite to the path direction): $F_{\text{external}} = 50$ N.
6. Implement position on the truss: $d_4 = 0.8$ m.
7. Initial offset error: $e = 0$ m.

The key simulation results for the dynamic model are shown in Figure 4.66 to Figure 4.70.

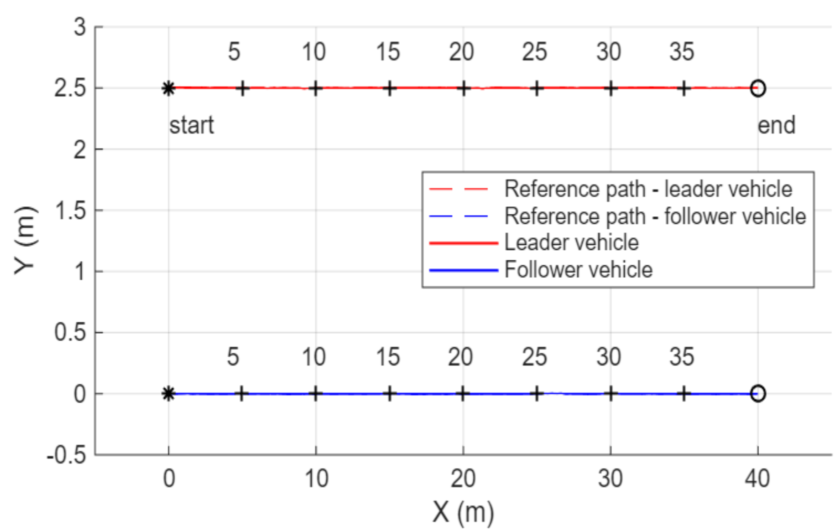

Figure 4.66 Reference and actual paths using the dynamic model at high speed

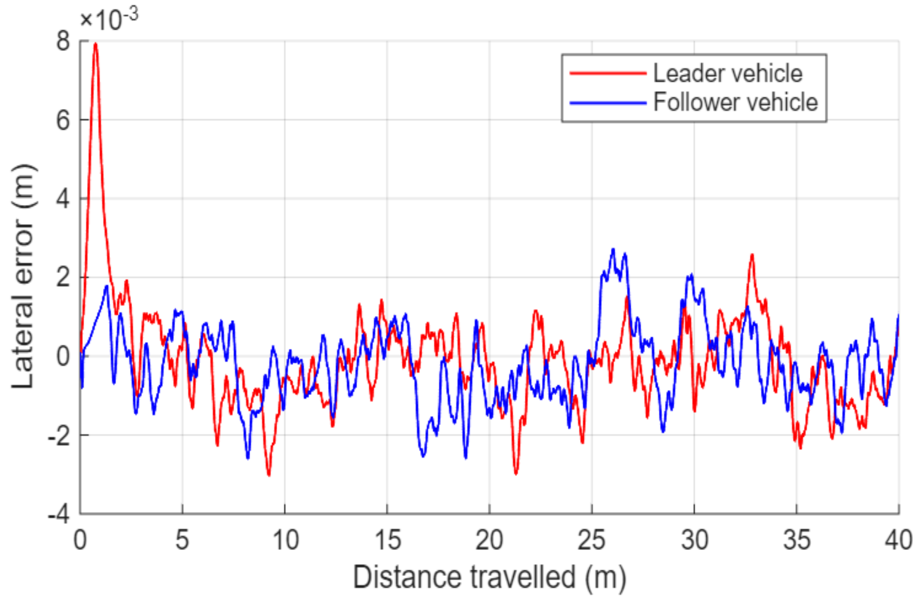

Figure 4.67 Lateral error using the dynamic model at high speed

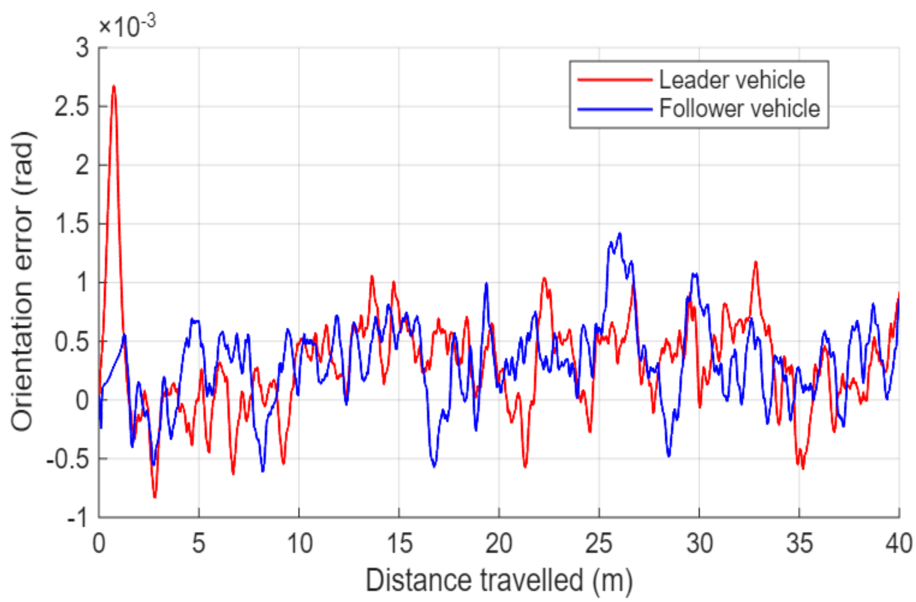

Figure 4.68 Orientation error using the dynamic model at high speed

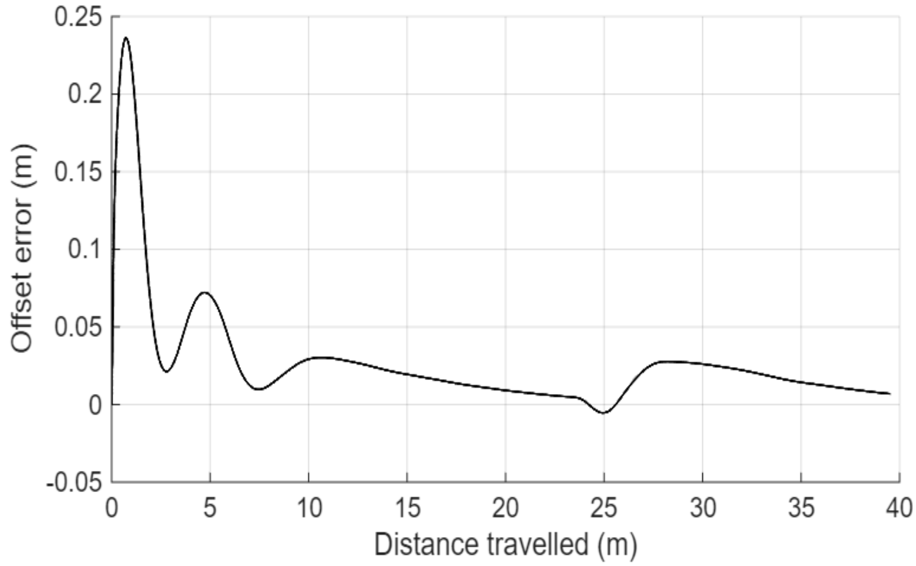

Figure 4.69 Offset error using the dynamic model at high speed

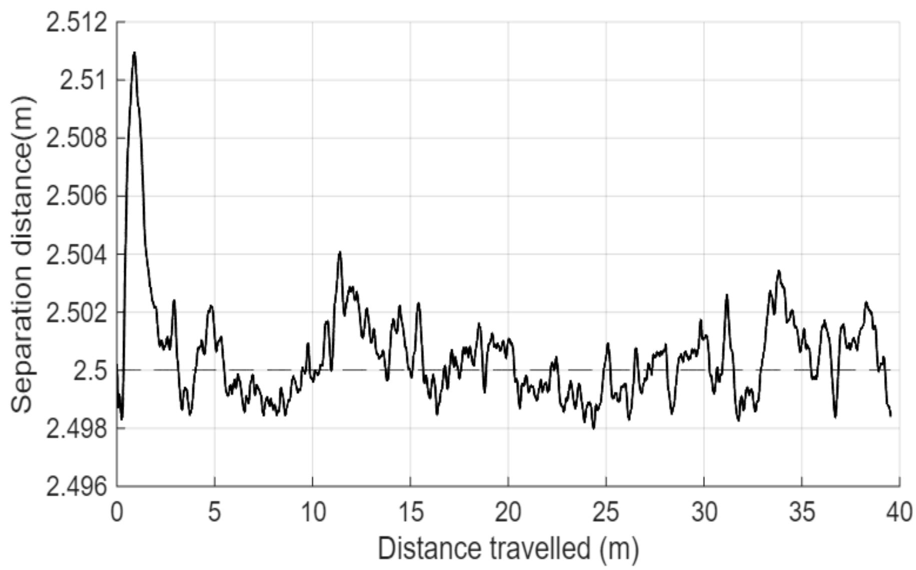

Figure 4.70 Distance between the two support vehicles using the dynamic model at high speed

The key simulation results for the kinematic model are shown in Figure 4.71 to Figure 4.75.

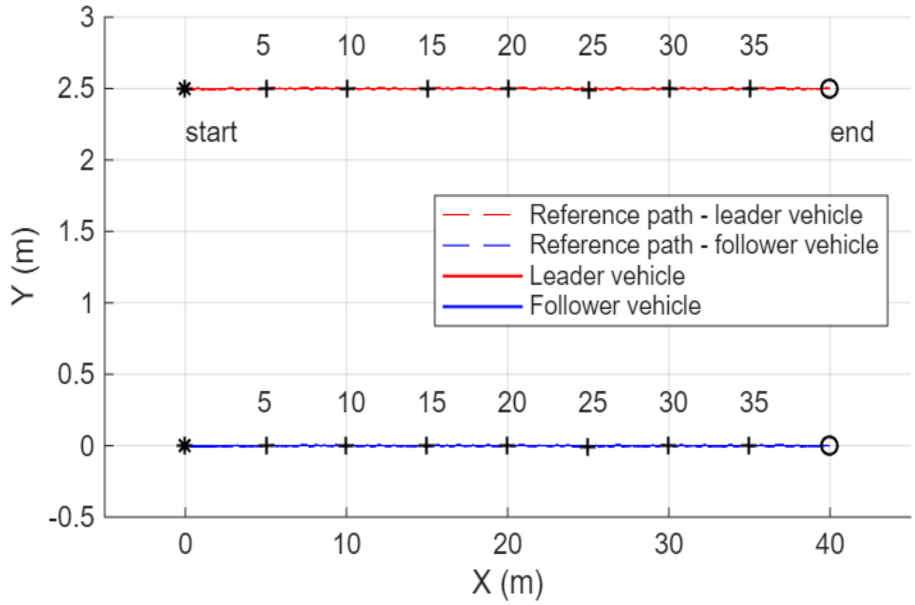

Figure 4.71 Reference and actual paths using the kinematic model at high speed

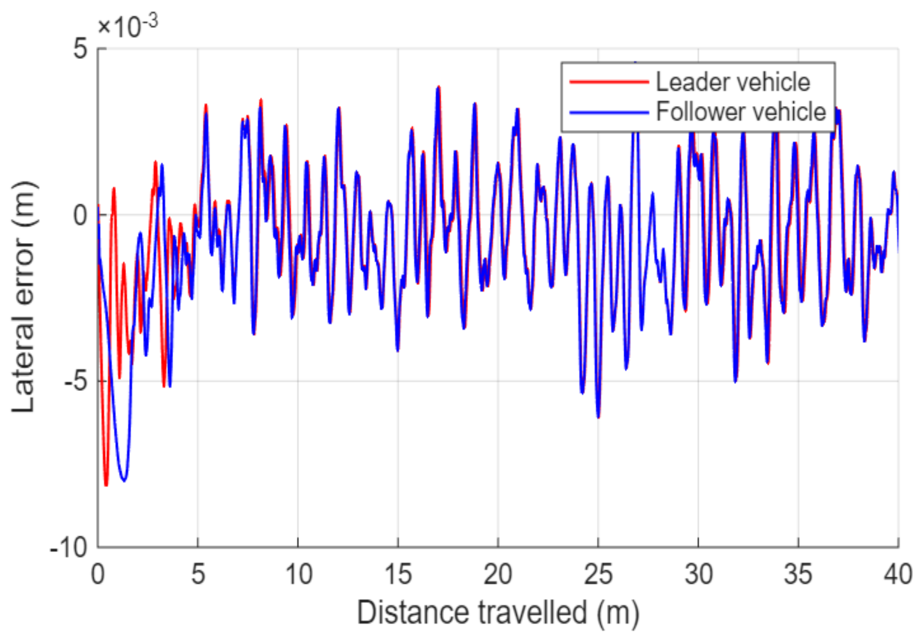

Figure 4.72 Lateral error using the kinematic model at high speed

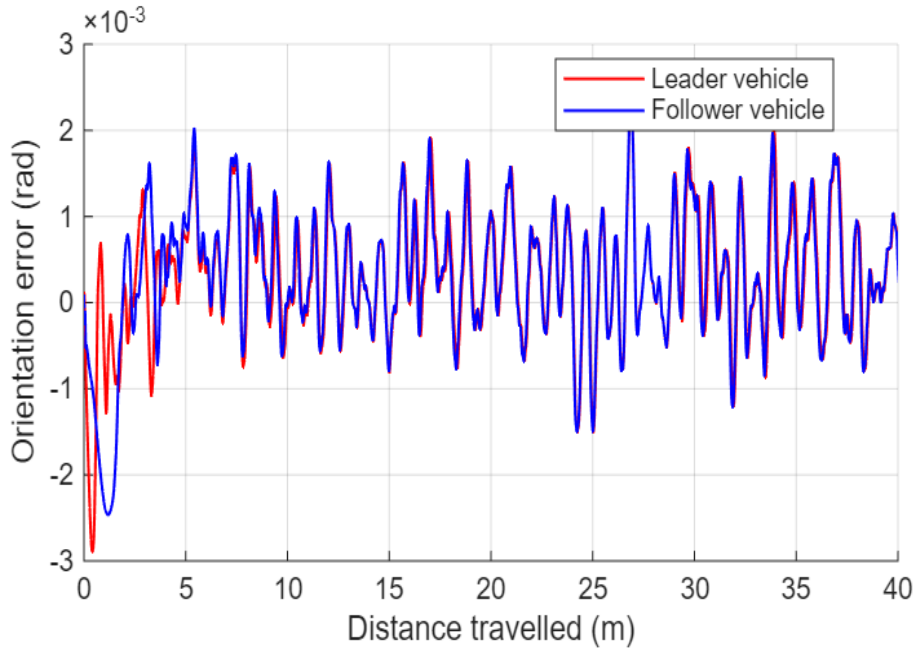

Figure 4.73 Orientation error using the kinematic model at high speed

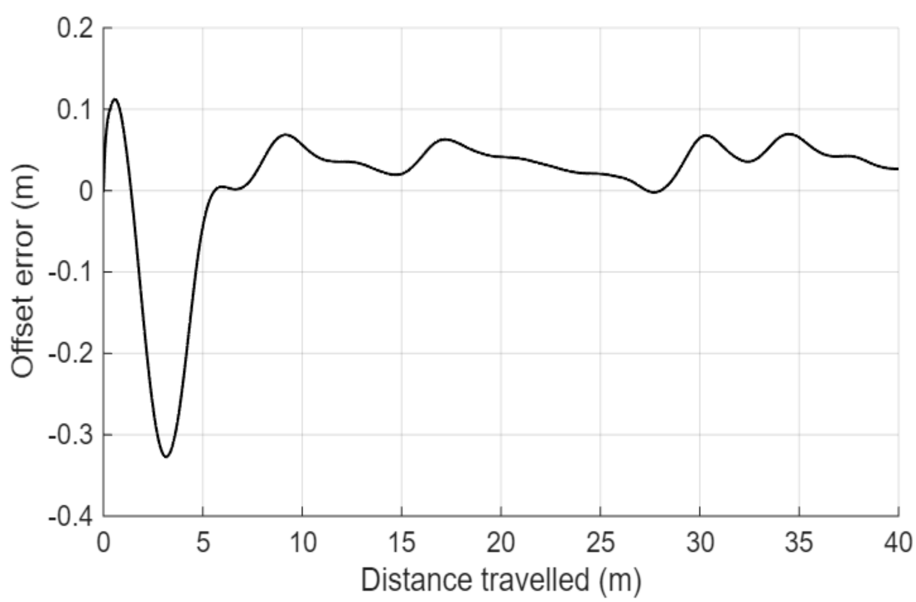

Figure 4.74 Offset error using the kinematic model at high speed

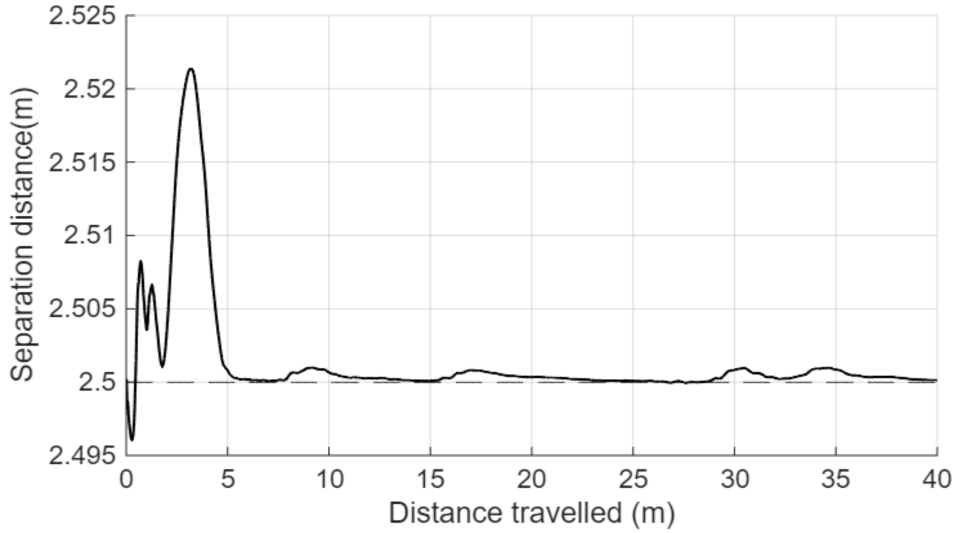

Figure 4.75 Distance between the two support vehicles using the kinematic model at high speed

The steady-state and IAE performance metrics for the high-speed simulation are summarized in Table 4.12.

Table 4.12 Steady-state and IAE performance metrics for the high-speed simulation[a]

		Dynamic	Kinematic
Leader vehicle	Steady-state velocity (m/s)	3.45	3.44
	Steady-state lateral error (m)	**±0.0030**	±0.0061
	Steady-state orientation error (rad)	**±0.0012**	±0.0024
	Lateral error IAE (m^2)	**0.0369**	0.0671
	Orientation error IAE (rad·m)	**0.0163**	0.0249
Follower vehicle	Steady-state velocity (m/s)	3.45	3.44
	Steady-state lateral error (m)	**±0.0027**	±0.0061
	Steady-state orientation error (rad)	**±0.0014**	±0.0024
	Lateral error IAE (m^2)	**0.0319**	0.0705
	Orientation error IAE (rad·m)	**0.0157**	0.0265
Steady-state offset error (m)		**±0.030**	±0.069
Steady-state separation error (m)		±0.0041	±0.00098
Offset error IAE (m^2)		**1.09**	2.12
Separation error IAE (m^2)		0.0463	0.0572

[a] Boldface: notably better than the other model.

Based on the simulation results of Sections 4.2.1 and 4.2.5.1 and Tables 4.6 and 4.12, both models tracked the straight path within sensor resolution at the 3.5 m/s target speed. The lateral error IAE of the dynamic model was 0.0369 m^2 for the leader vehicle and 0.0319 m^2 for the follower vehicle, compared with 0.0671 m^2 and 0.0705 m^2 for the kinematic model, against 0.0317 m^2 and 0.0315 m^2, and 0.0553 m^2 and 0.0551 m^2, at the 2.5 m/s target speed of the general case; the orientation error IAE was 0.0163 rad·m and 0.0157 rad·m for the dynamic model and 0.0249 rad·m and 0.0265 rad·m for the kinematic model. Steady-state lateral and orientation errors remained below the 0.01 m and 0.0087 rad thresholds and all IAE differences are far below the 0.4 m^2 and 0.35 rad·m thresholds, so no practically meaningful difference in individual-vehicle tracking is claimed. The higher speed raised the kinematic model's lateral error IAE by about 21% (leader) and 28% (follower) relative to the general case, against about 16% and 1% for the dynamic model, an indicative trend consistent with the dynamic model representing speed-dependent effects.

The formation-control results show the resolvable effect of speed. The offset error IAE increased from 0.583 m^2 in the general case to 1.09 m^2 with the dynamic model and from 1.16 m^2 to 2.12 m^2 with the kinematic model; the difference between the models, 1.03 m^2, exceeds the 0.56 m^2 threshold, and the kinematic model's increase relative to the general case (0.96 m^2) exceeds it as well, whereas the dynamic model's increase (0.51 m^2) does not. The steady-state offset error rose from $\pm$0.014 m to $\pm$0.030 m with the dynamic model and from $\pm$0.034 m to $\pm$0.069 m with the kinematic model, a difference between the models of 0.039 m against the 0.014 m threshold. The separation errors of both models stayed below the 0.014 m threshold and the separation error IAE difference (0.0463 m^2 against 0.0572 m^2) is within resolution. Higher speed therefore made relative-position coordination harder for both controllers, and the dynamic model retained a practically meaningful advantage in offset regulation that was larger than in the general case.

4.2.5.2 Low Speed

The test scenario was as follows:

1. Forward motion.
2. Straight trajectory.
3. Medium-adhesion earth road (μ = 0.75).
4. Target speed of the support vehicles: 1.5 m/s.
5. External loads on truss (opposite to the path direction): F_{external} = 50 N.
6. Implement position on the truss: d_4 = 0.8 m.
7. Initial offset error: e = 0 m.

The key simulation results for the dynamic model are shown in Figure 4.76 to Figure 4.80.

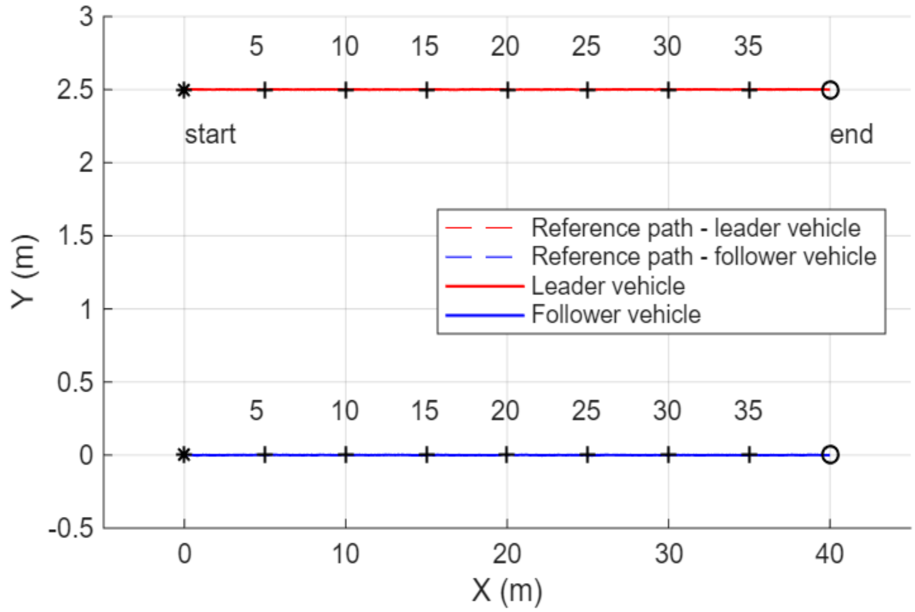

Figure 4.76 Reference and actual paths using the dynamic model at low speed

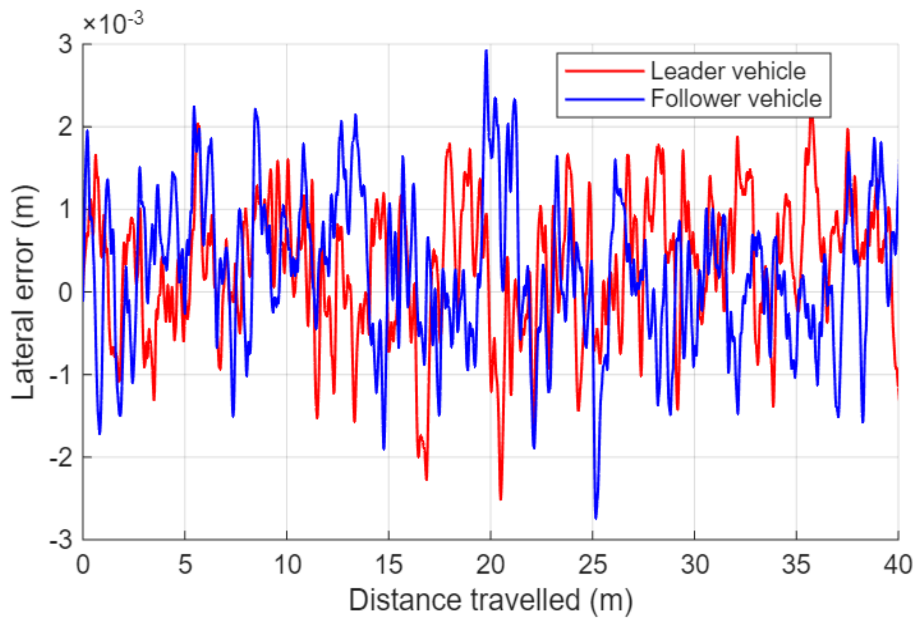

Figure 4.77 Lateral error using the dynamic model at low speed

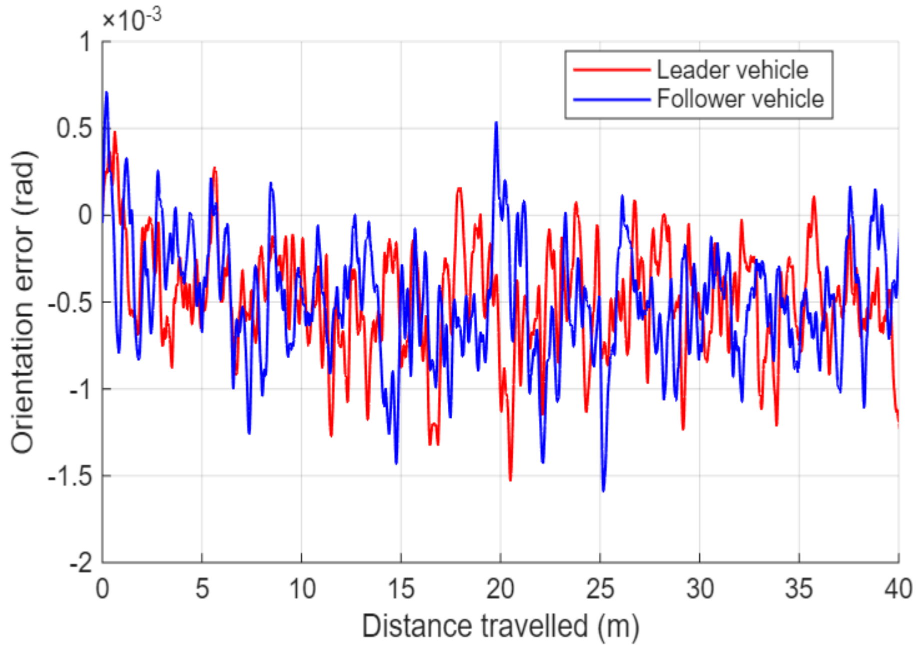

Figure 4.78 Orientation error using the dynamic model at low speed

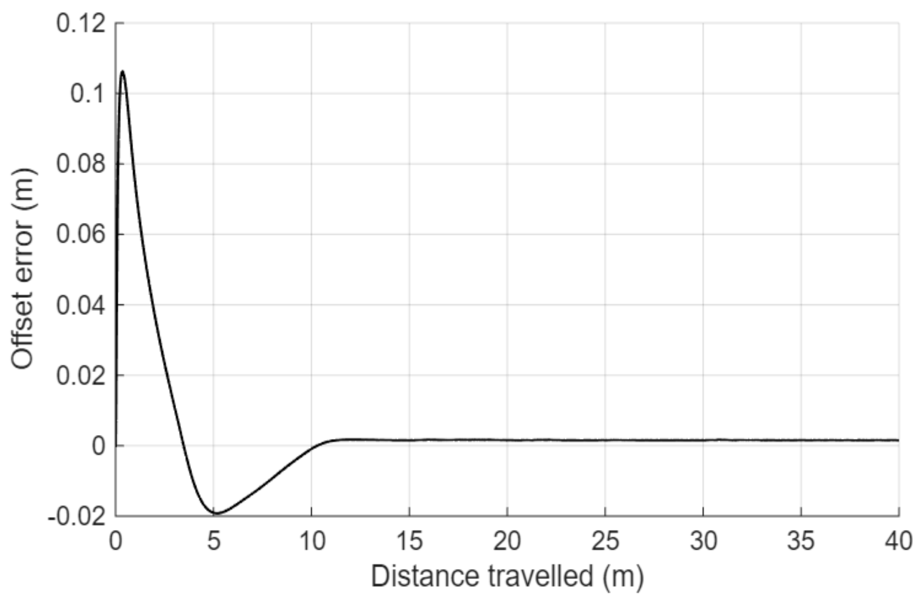

Figure 4.79 Offset error using the dynamic model at low speed

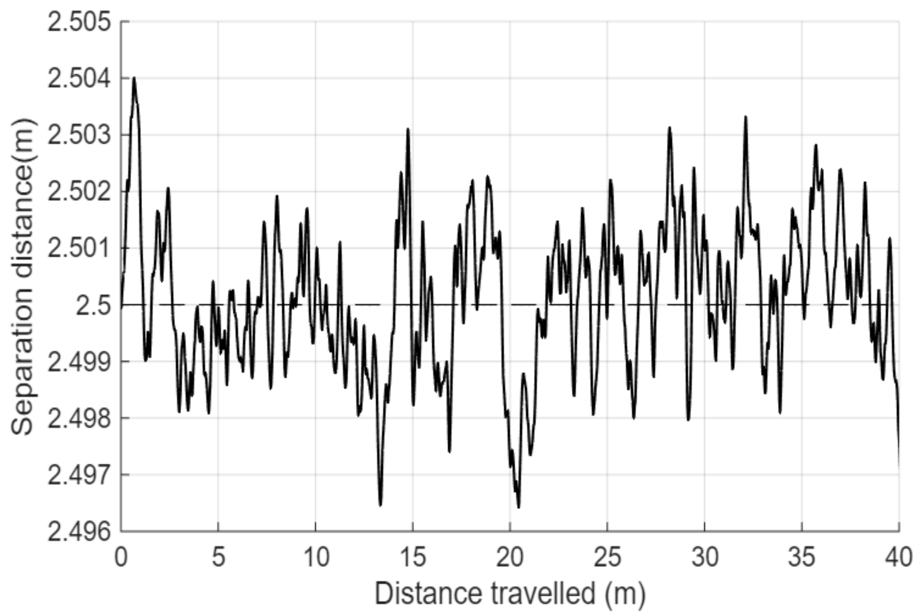

Figure 4.80 Distance between the two support vehicles using the dynamic model at low speed

The key simulation results for the kinematic model are shown in Figure 4.81 to Figure 4.85.

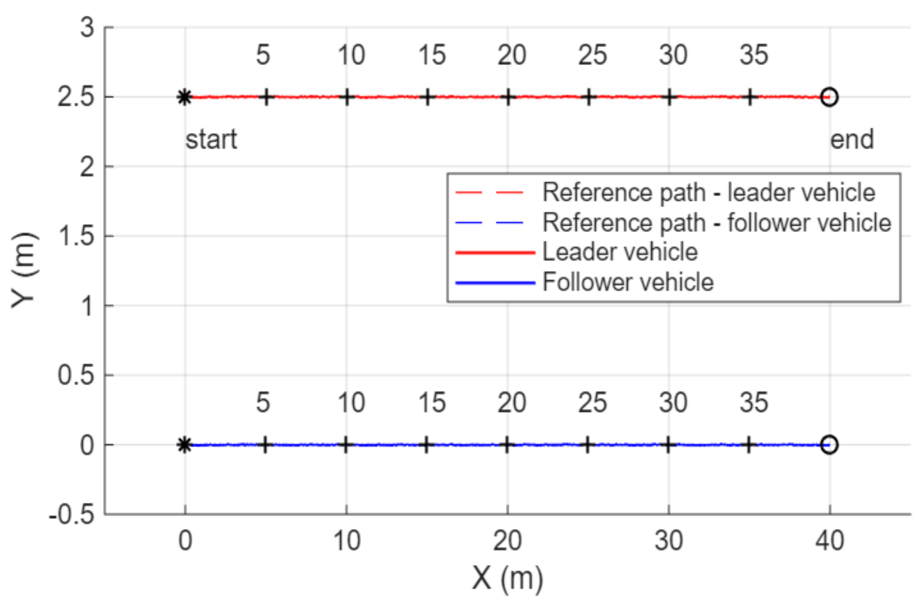

Figure 4.81 Reference and actual paths using the kinematic model at low speed

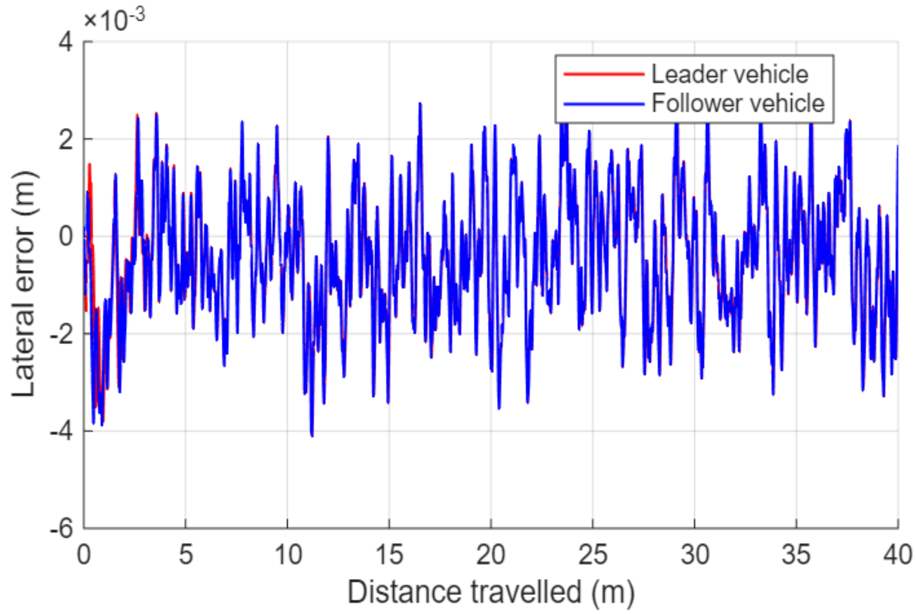

Figure 4.82 Lateral error using the kinematic model at low speed

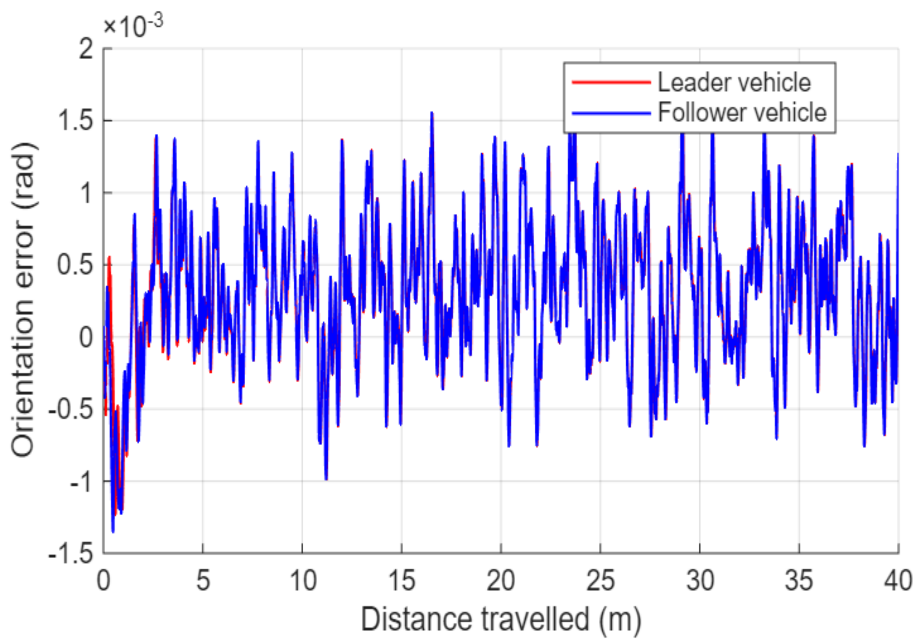

Figure 4.83 Orientation error using the kinematic model at low speed

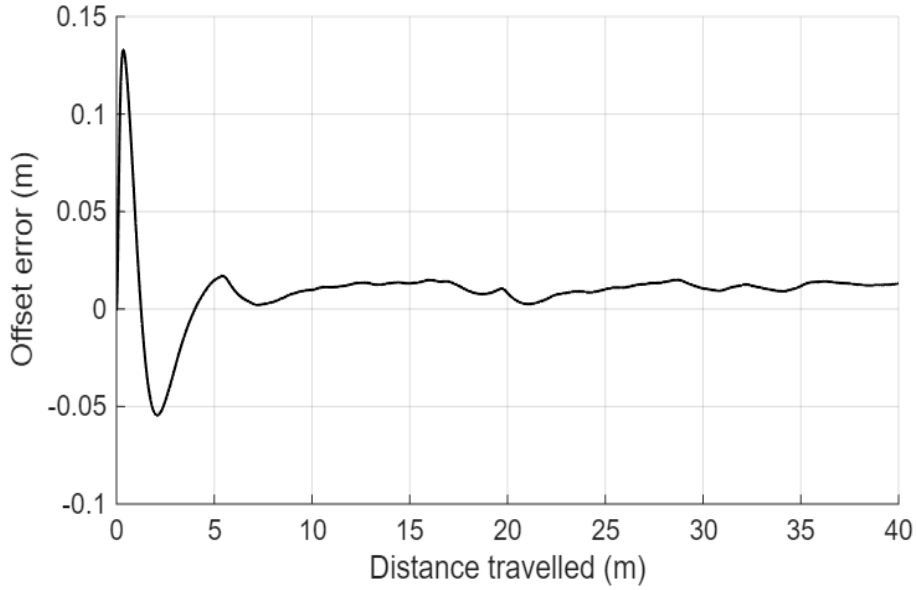

Figure 4.84 Offset error using the kinematic model at low speed

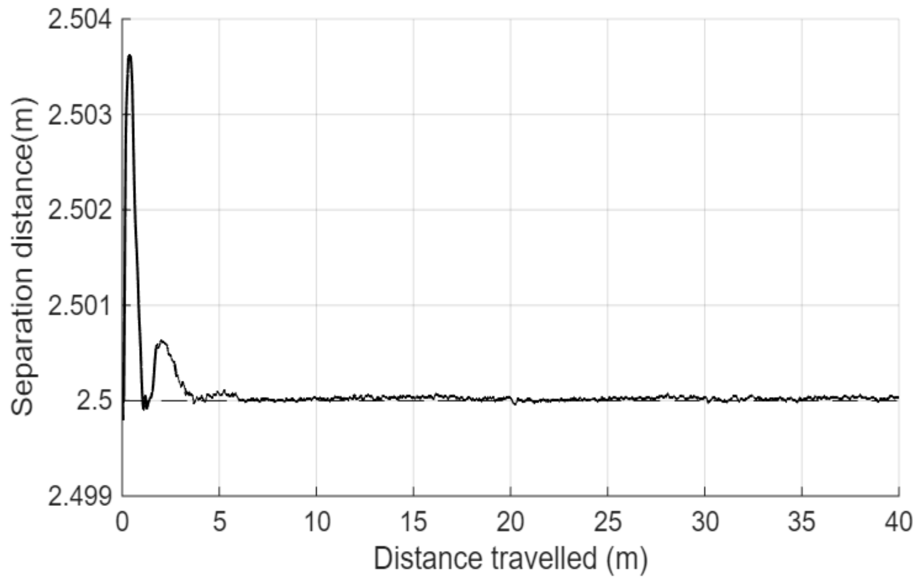

Figure 4.85 Distance between the two support vehicles using the kinematic model at low speed

The steady-state and IAE performance metrics for the low-speed simulation are summarized in Table 4.13.

Table 4.13 Steady-state and IAE performance metrics for the low-speed simulation[a]

		Dynamic	Kinematic
Leader vehicle	Steady-state velocity (m/s)	1.51	1.50
	Steady-state lateral error (m)	**±0.0025**	±0.0041
	Steady-state orientation error (rad)	±0.0015	±0.0018
	Lateral error IAE (m^2)	**0.0287**	0.0443
	Orientation error IAE (rad·m)	0.0200	0.0188
Follower vehicle	Steady-state velocity (m/s)	1.51	1.50
	Steady-state lateral error (m)	**±0.0029**	±0.0041
	Steady-state orientation error (rad)	±0.0016	±0.0018
	Lateral error IAE (m^2)	**0.0295**	0.0446
	Orientation error IAE (rad·m)	0.0206	0.0190
Steady-state offset error (m)		**±0.0017**	±0.015
Steady-state separation error (m)		±0.0036	±0.000071
Offset error IAE (m^2)		**0.289**	0.560
Separation error IAE (m^2)		0.0418	0.00368

[a] Boldface: notably better than the other model.

Based on the simulation results of Sections 4.2.1 and 4.2.5.2 and Tables 4.6 and 4.13, both models tracked the straight path within sensor resolution at the 1.5 m/s target speed, with slightly smaller lateral errors than in the general case: the lateral error IAE was 0.0287 m² for the leader vehicle and 0.0295 m² for the follower vehicle with the dynamic model, against 0.0443 m² and 0.0446 m² with the kinematic model. The orientation error IAE was 0.0200 rad·m and 0.0206 rad·m for the dynamic model and 0.0188 rad·m and 0.0190 rad·m for the kinematic model, so at low speed the kinematic model produced the slightly lower heading values, the reverse of the general case. All of these differences are far below the 0.4 m² and 0.35 rad·m thresholds and the steady-state values are below the sensor resolution, so no practically meaningful difference in individual-vehicle tracking is claimed.

Formation control was easier at low speed for both models: the offset error IAE fell from 0.583 m² in the general case to 0.289 m² with the dynamic model and from 1.16 m² to 0.560 m² with the kinematic model, and the steady-state offset errors to ±0.0017 m and ±0.015 m. The difference between the models, 0.27 m², is below the 0.56 m² threshold, so, unlike the general case, no practically meaningful advantage in offset regulation is claimed at low speed, although the steady-state offset difference of 0.013 m is at the 0.014 m threshold. The kinematic model produced the smaller separation error IAE (0.00368 m² against 0.0418 m²), with both steady-state separation errors below the 0.014 m threshold and the difference within resolution. At low speed the two controllers were therefore equivalent at the sensor level in every metric except a marginal offset-regulation advantage for the dynamic model.

4.2.6 External Load on Truss

In the preceding cases, the truss was subjected to an external load of 50 N applied opposite to the path direction. To verify robustness under changing loads, the external load was increased to 200 N, thereby testing the control strategy under a substantially larger external force.

The test scenario was as follows:

1. Forward motion.
2. Straight trajectory.
3. Medium-adhesion earth road ($\mu = 0.75$).
4. Target speed of the support vehicles: 2.5 m/s.
5. External loads on truss (opposite to the path direction): $F_{\text{external}} = 200$ N.
6. Implement position on the truss: $d_4 = 0.8$ m.
7. Initial offset error: $e = 0$ m.

The key simulation results for the dynamic model are shown in Figure 4.86 to Figure 4.90.

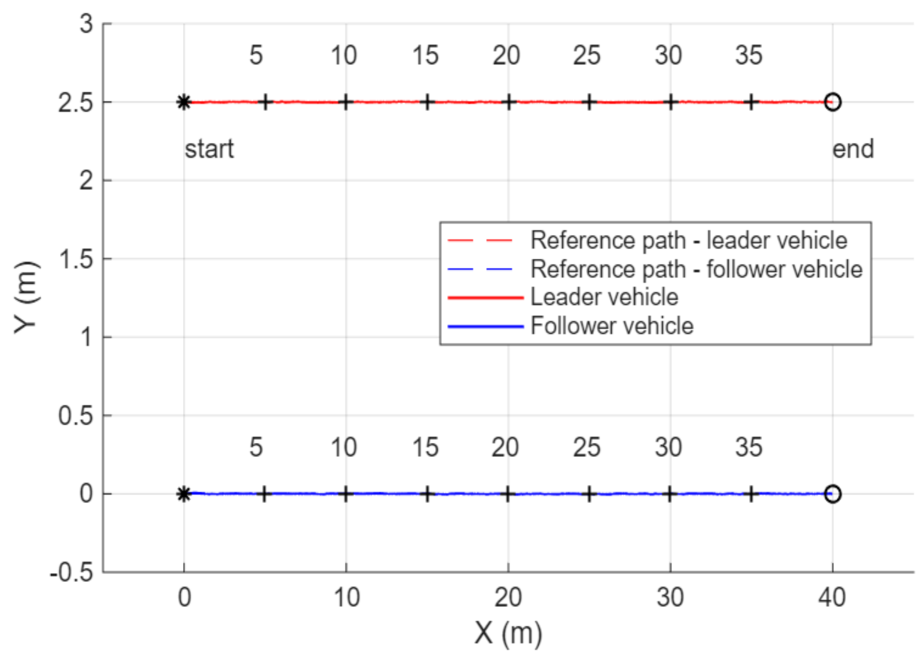

Figure 4.86 Reference and actual paths using the dynamic model with a large external load

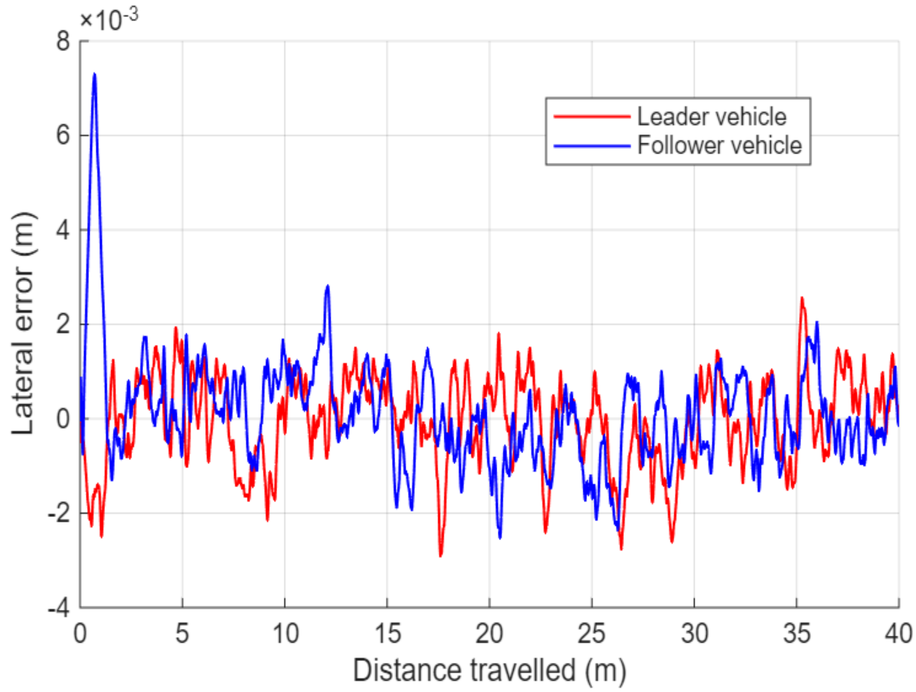

Figure 4.87 Lateral error using the dynamic model with a large external load

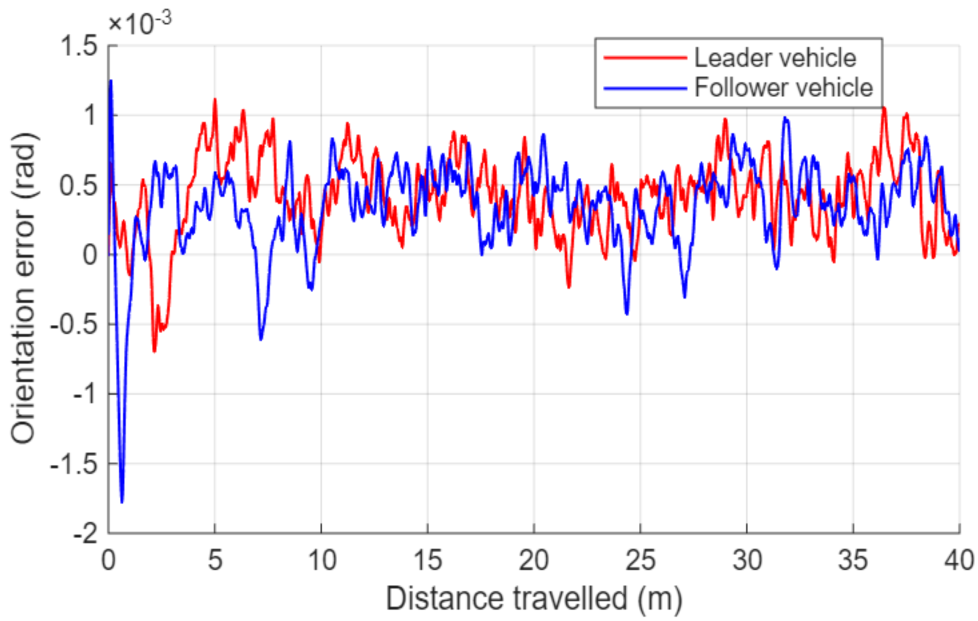

Figure 4.88 Orientation error using the dynamic model with a large external load

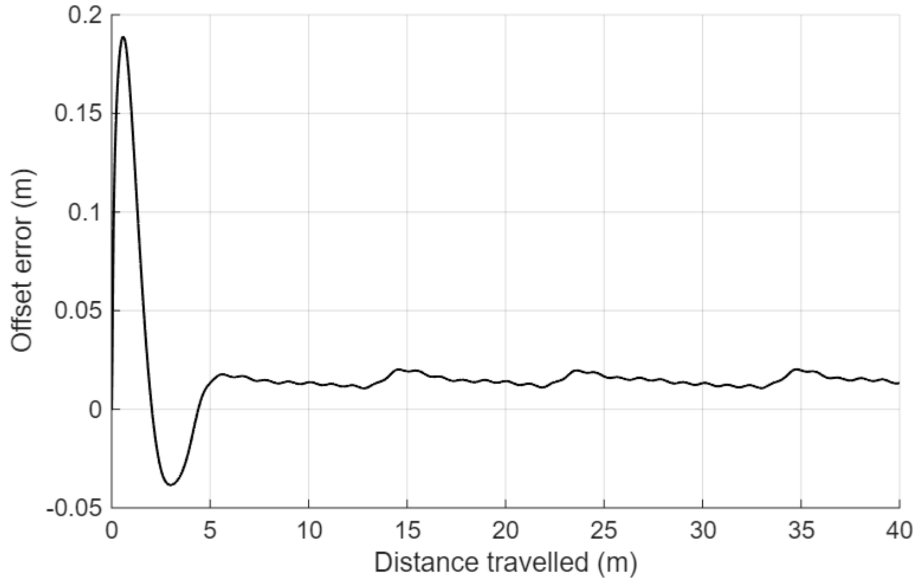

Figure 4.89 Offset error using the dynamic model with a large external load

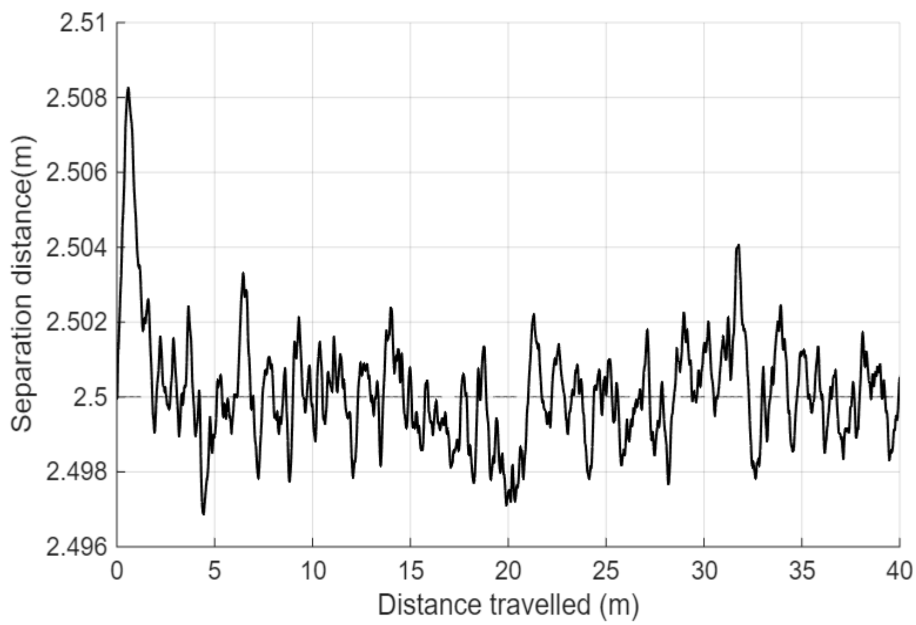

Figure 4.90 Distance between the two support vehicles using the dynamic model with a large external load

The key simulation results for the kinematic model are shown in Figure 4.91 to Figure 4.95.

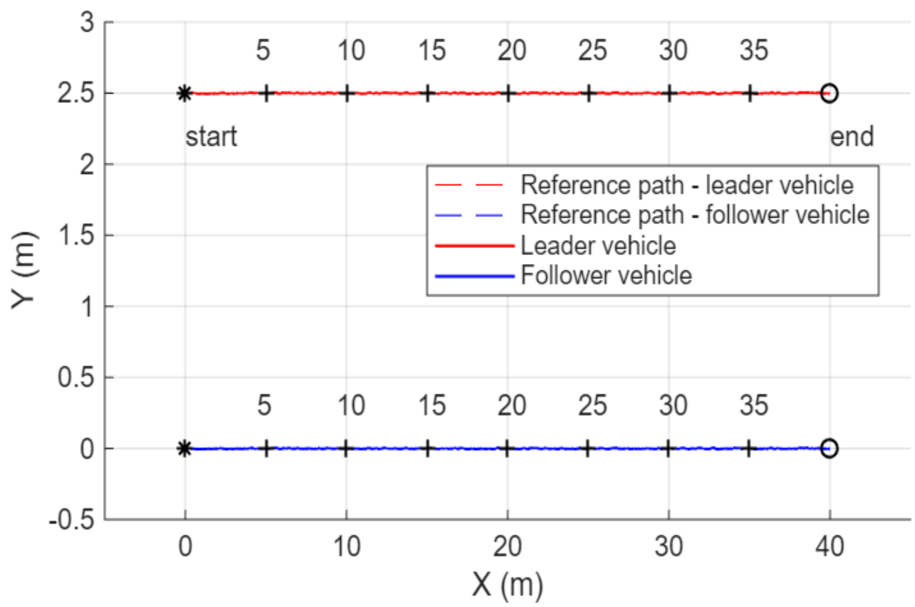

Figure 4.91 Reference and actual paths using the kinematic model with a large external load

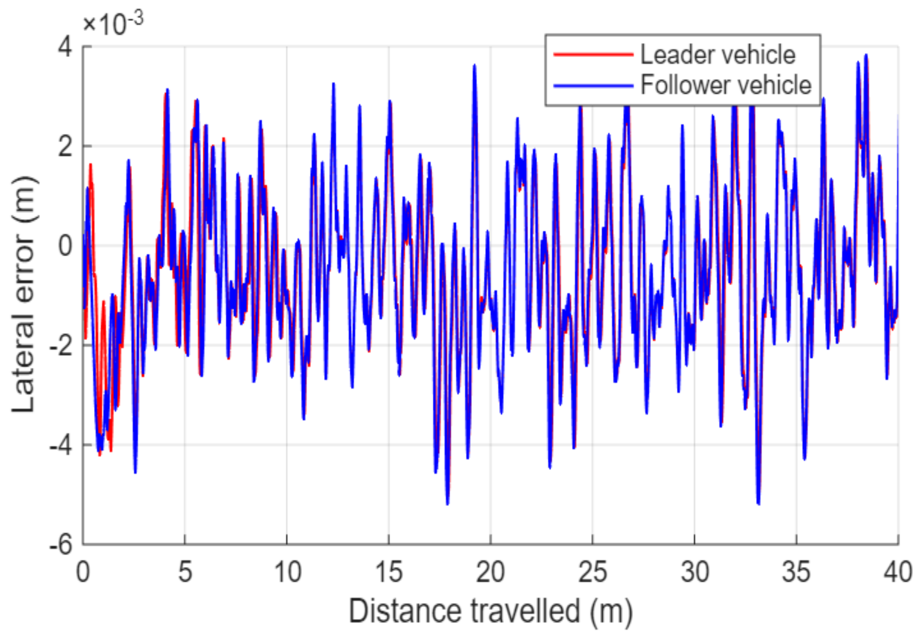

Figure 4.92 Lateral error using the kinematic model with a large external load

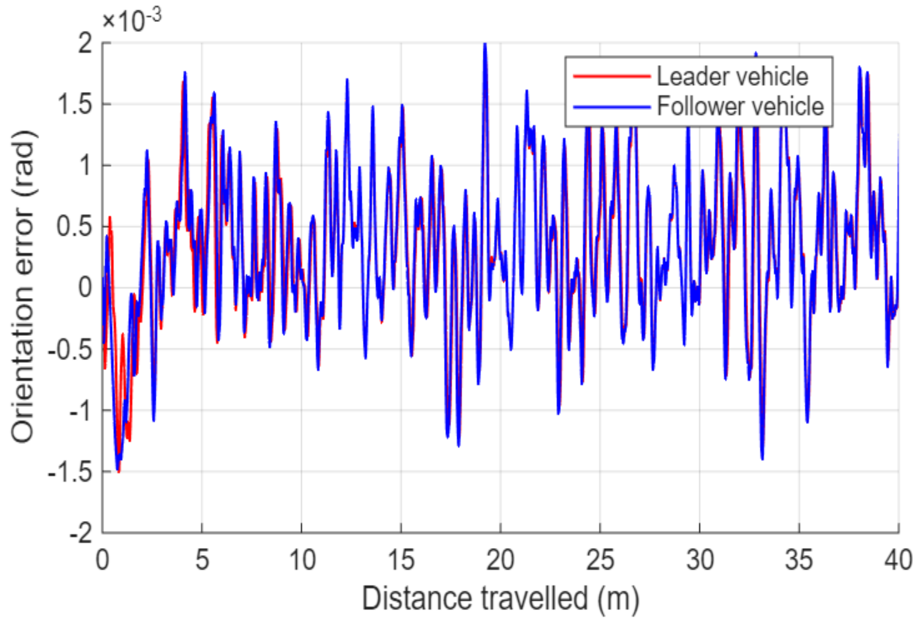

Figure 4.93 Orientation error using the kinematic model with a large external load

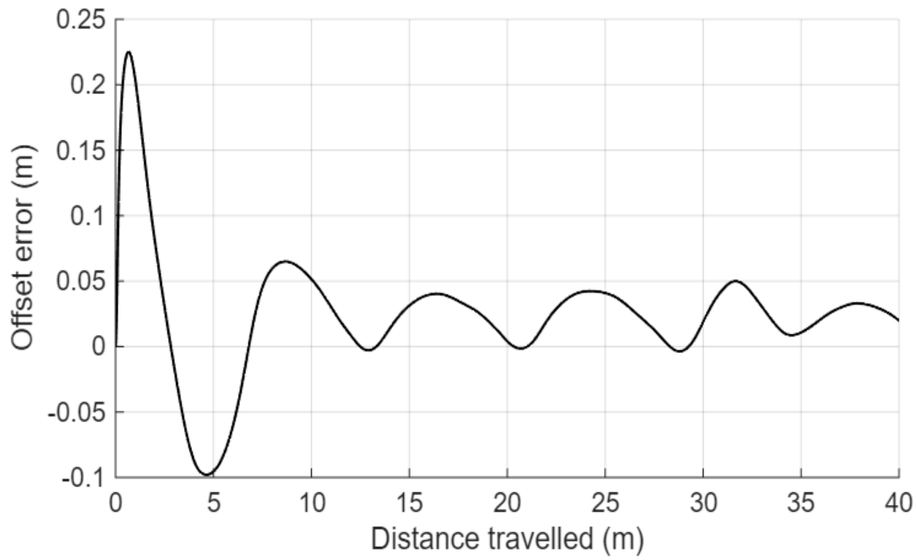

Figure 4.94 Offset error using the kinematic model with a large external load

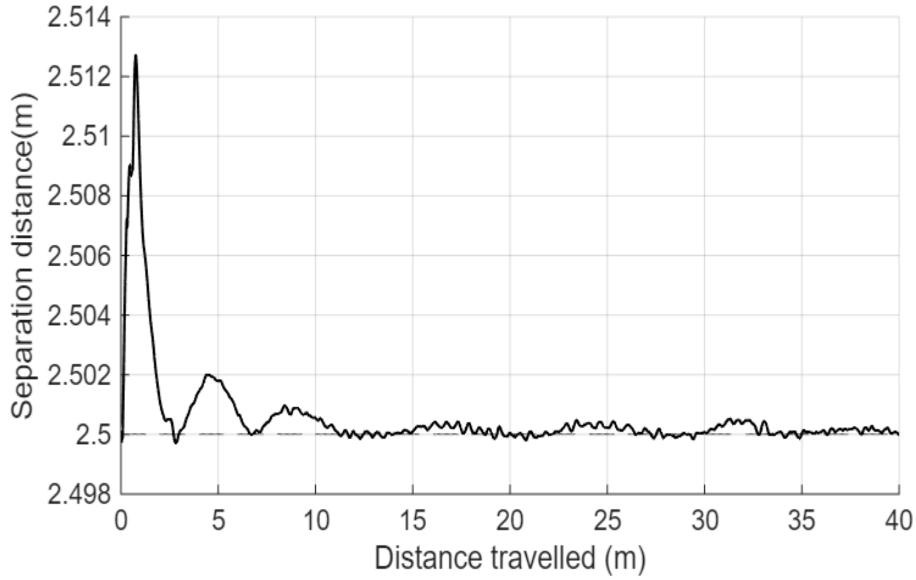

Figure 4.95 Distance between the two support vehicles using the kinematic model with a large external load

The steady-state and IAE performance metrics for the large external load case are summarized in Table 4.14.

Table 4.14 Steady-state and IAE performance metrics for the large external load simulation[a]

		Dynamic	Kinematic
Leader vehicle	Steady-state velocity (m/s)	2.50	2.46
	Steady-state lateral error (m)	**±0.0028**	±0.0050
	Steady-state orientation error (rad)	**±0.0011**	±0.0019
	Lateral error IAE (m^2)	**0.0309**	0.0552
	Orientation error IAE (rad·m)	**0.0179**	0.0217
Follower vehicle	Steady-state velocity (m/s)	2.50	2.46
	Steady-state lateral error (m)	**±0.0030**	±0.0052
	Steady-state orientation error (rad)	**±0.0010**	±0.0020
	Lateral error IAE (m^2)	**0.0311**	0.0568
	Orientation error IAE (rad·m)	**0.0165**	0.0224
Steady-state offset error (m)		**±0.020**	±0.052
Steady-state separation error (m)		±0.0041	±0.00057
Offset error IAE (m^2)		**0.812**	1.51
Separation error IAE (m^2)		0.0426	0.0232

[a] Boldface: notably better than the other model.

Based on the simulation results from Section 4.2.1 and Section 4.2.6, and Table 4.6 and Table 4.14, both models tracked the straight path within sensor resolution under both external load conditions. When the external load increased to 200 N, the dynamic model produced steady-state lateral errors of ± 0.0028 m for the leader vehicle and ± 0.0030 m for the follower vehicle, compared with ± 0.0050 m and ± 0.0052 m for the kinematic model, and lateral error IAE values of 0.0309 m² and 0.0311 m² compared with 0.0552 m² and 0.0568 m². These values and their differences are below the 0.01 m and 0.4 m² thresholds, as they were under the 50 N load, so no practically meaningful difference in lateral tracking is claimed; both models absorbed the fourfold increase in external load without a resolvable change in lateral accuracy.

The orientation error results were also within resolution. Under the 200 N condition the orientation error IAE was 0.0179 rad·m for the leader vehicle and 0.0165 rad·m for the follower vehicle with the dynamic model, and 0.0217 rad·m and 0.0224 rad·m with the kinematic model, with similar values under the 50 N load; all differences are far below the 0.35 rad·m threshold. Heading regulation was therefore insensitive to the external load for both models at the sensor level.

The formation-control results show the resolvable effect of the external load. When it increased from 50 N to 200 N, the offset error IAE increased from 0.583 m² to 0.812 m² for the dynamic model and from 1.16 m² to 1.51 m² for the kinematic model. The difference between the models, 0.58 m² at 50 N and 0.70 m² at 200 N, reaches the 0.56 m² threshold in both cases, so the dynamic model maintained practically better offset regulation under both loads, and its advantage grew with the load. The kinematic model produced lower separation error IAE values under both loads, but the steady-state separation errors of both models were below the 0.014 m threshold and the IAE differences are within resolution. Overall, the external load affected formation synchronization rather than individual-vehicle tracking, and the dynamic model was the more robust of the two in the metric where the load had a resolvable effect, which is the relevant robustness for WSIC operation under variable implement resistance.

4.2.7 Position of Implement on the Truss

In the preceding cases, the implement was positioned at $d_4 = 0.8$ m, representing a leader-proximal configuration. To investigate robustness with respect to changes in the load application point, the configuration was changed to a follower-proximal arrangement, with the implement placed at $d_4 = 1.5$ m.

The test scenario was as follows:

1. Forward motion.
2. Straight trajectory.

3. Medium-adhesion earth road ($\mu = 0.75$).

4. Target speed of the support vehicles: 2.5 m/s.

5. External loads on truss (opposite to the path direction): $F_{external} = 50$ N.

6. Implement position on the truss: $d_4 = 1.5$ m.

7. Initial offset error: $e = 0$ m.

The key simulation results for the dynamic model are shown in Figure 4.96 to Figure 4.100.

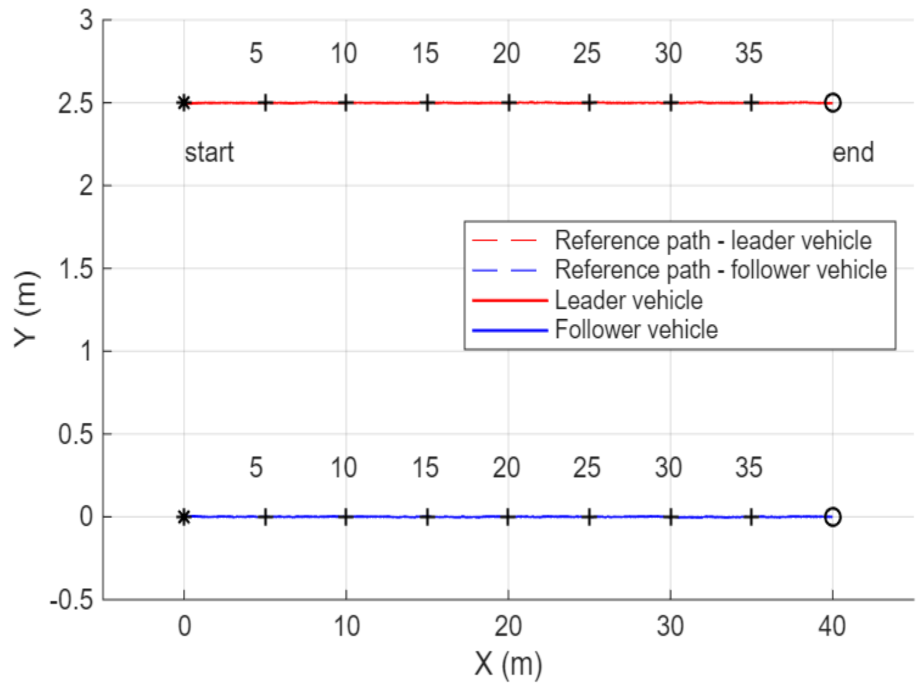

Figure 4.96 Reference and actual paths using the dynamic model for the follower-proximal configuration

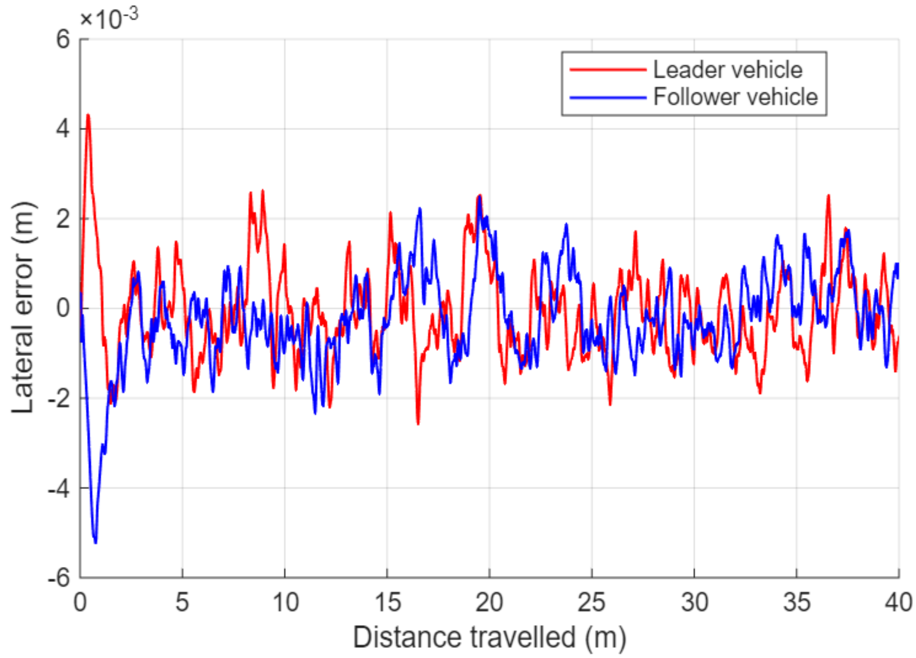

Figure 4.97 Lateral error using the dynamic model for the follower-proximal configuration

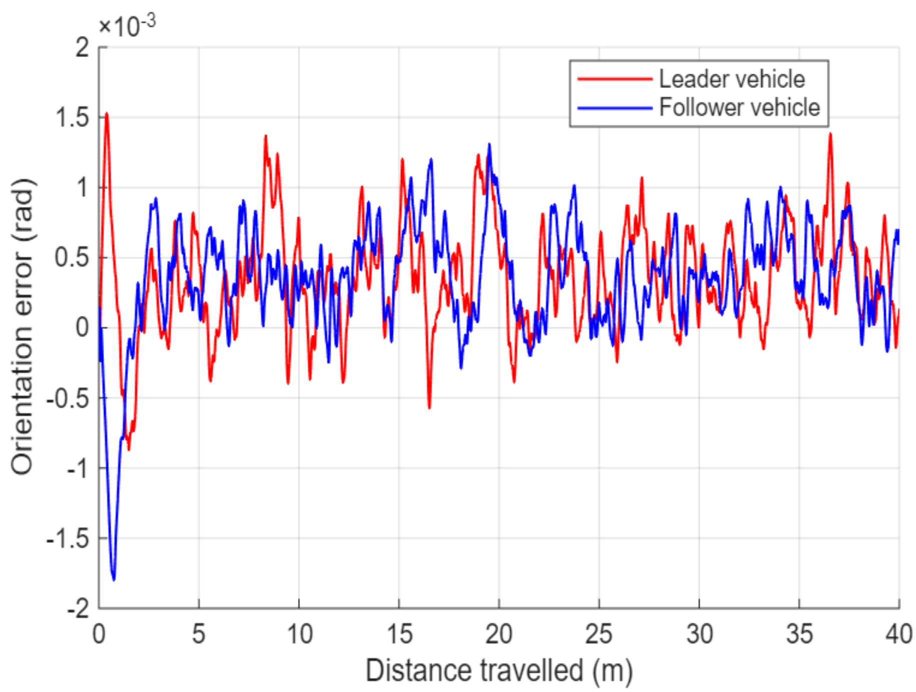

Figure 4.98 Orientation error using the dynamic model for the follower-proximal configuration

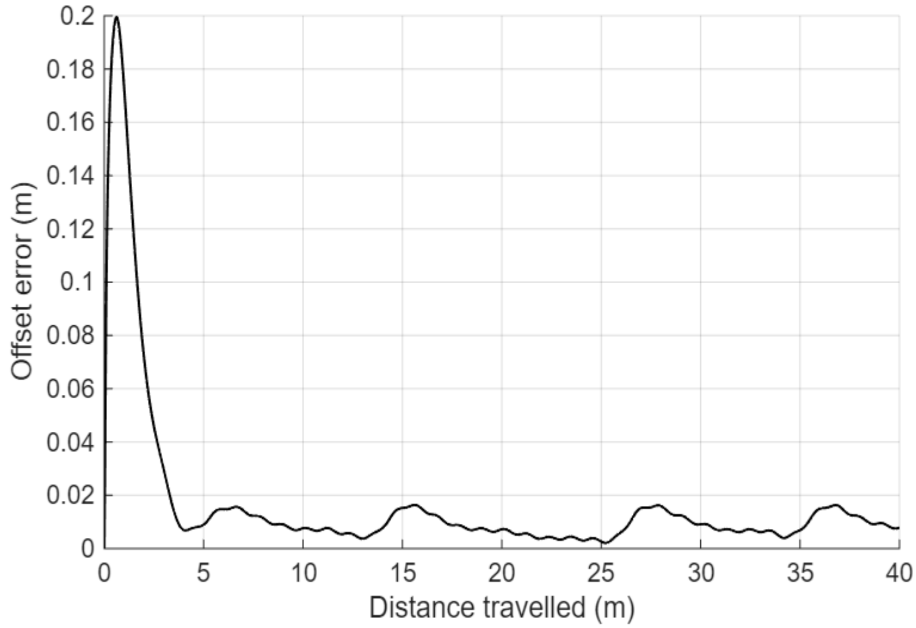

Figure 4.99 Offset error using the dynamic model for the follower-proximal configuration

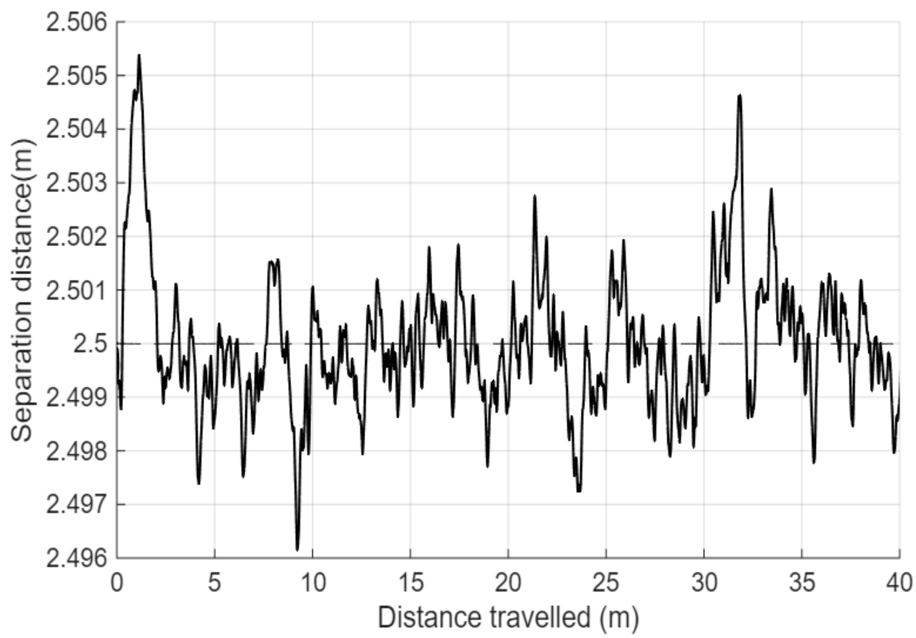

Figure 4.100 Distance between the two support vehicles using the dynamic model for the follower-proximal configuration

The key simulation results for the kinematic model are shown in Figure 4.101 to Figure 4.105.

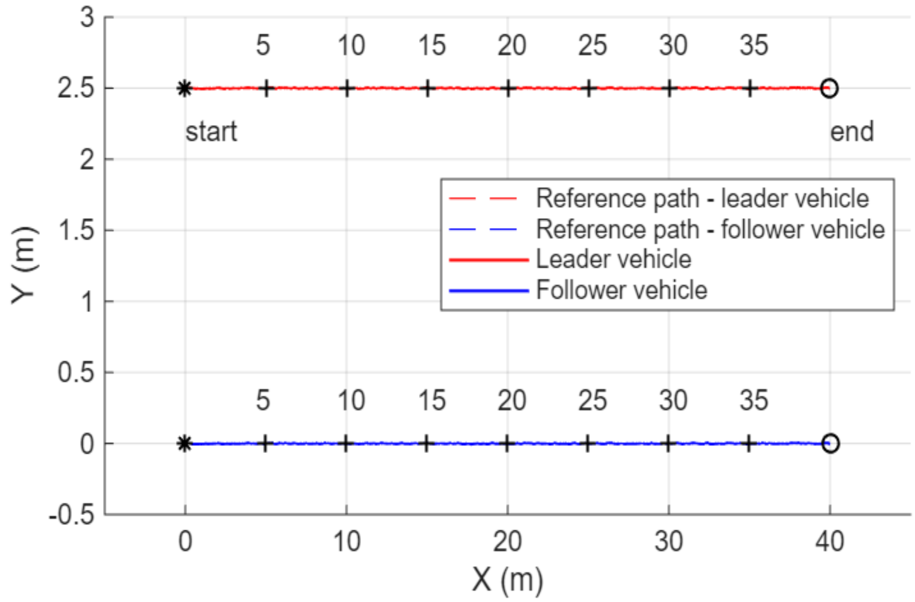

Figure 4.101 Reference and actual paths using the kinematic model for the follower-proximal configuration

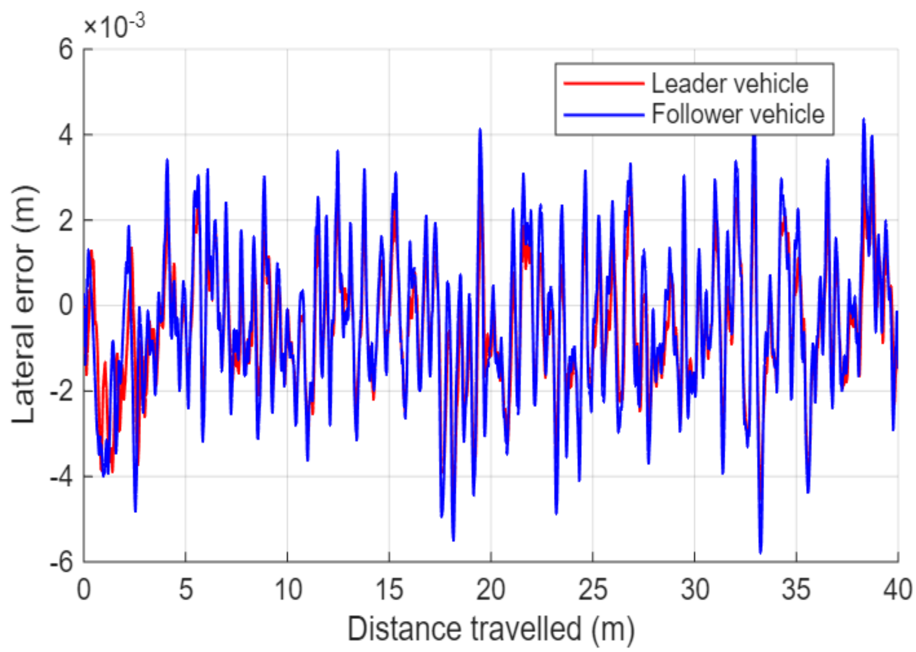

Figure 4.102 Lateral error using the kinematic model for the follower-proximal configuration

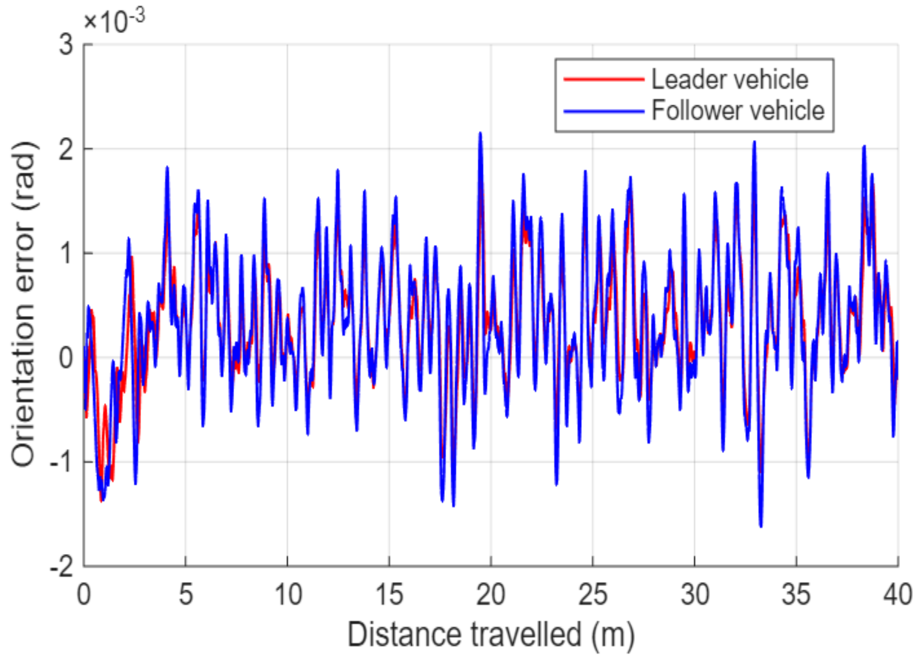

Figure 4.103 Orientation error using the kinematic model for the follower-proximal configuration

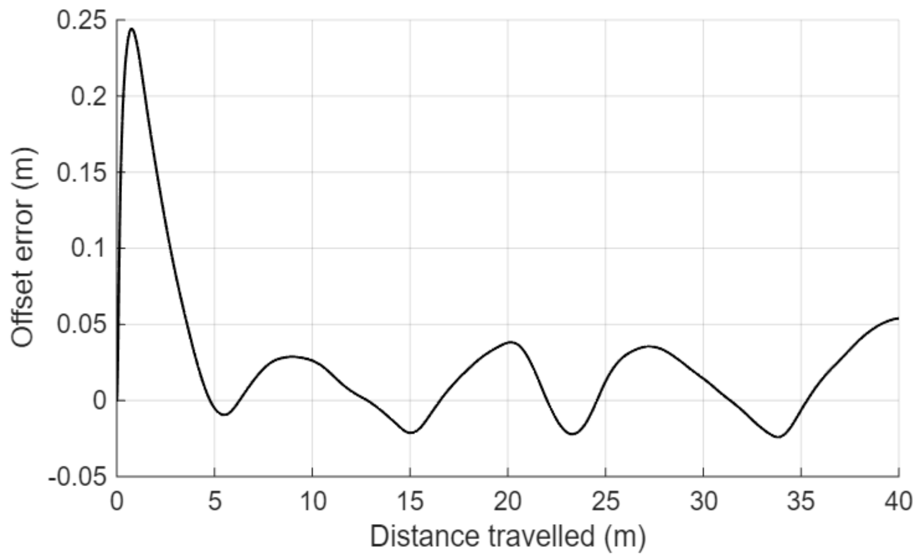

Figure 4.104 Offset error using the kinematic model for the follower-proximal configuration

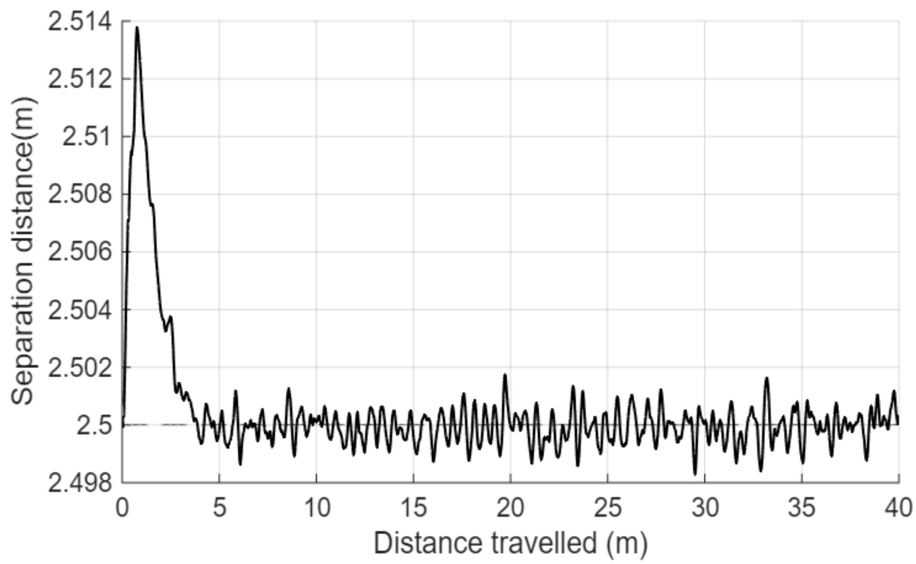

Figure 4.105 Distance between the two support vehicles using the kinematic model for the follower-proximal configuration

The steady-state and IAE performance metrics for the follower-proximal configuration are summarized in Table 4.15.

Table 4.15 Steady-state and IAE performance metrics for the follower-proximal implement configuration [a]

		Dynamic	Kinematic
Leader vehicle	Steady-state velocity (m/s)	2.50	2.48
	Steady-state lateral error (m)	**±0.0026**	±0.0048
	Steady-state orientation error (rad)	**±0.0014**	±0.0018
	Lateral error IAE (m^2)	**0.0319**	0.0508
	Orientation error IAE (rad·m)	**0.0166**	0.0203
Follower vehicle	Steady-state velocity (m/s)	2.50	2.48
	Steady-state lateral error (m)	**±0.0025**	±0.0058
	Steady-state orientation error (rad)	**±0.0013**	±0.0021
	Lateral error IAE (m^2)	**0.0322**	0.0605
	Orientation error IAE (rad·m)	**0.0175**	0.0237
Steady-state offset error (m)		**±0.016**	±0.054
Steady-state separation error (m)		±0.0046	±0.0017
Offset error IAE (m^2)		**0.668**	1.26
Separation error IAE (m^2)		0.0372	0.0357

[a] Boldface: notably better than the other model.

Based on the simulation results from Section 4.2.1 and Section 4.2.7, and Table 4.6 and Table 4.15, both models tracked the straight path within sensor resolution under both implement configurations. For the leader vehicle, the lateral error IAE values of the dynamic model were 0.0319 m^2 in the follower-proximal configuration and 0.0317 m^2 in the leader-proximal configuration, compared with 0.0508 m^2 and 0.0553 m^2 for the kinematic model; for the follower vehicle they were 0.0322 m^2 and 0.0315 m^2, while the kinematic model increased from 0.0551 m^2 in the leader-proximal case to 0.0605 m^2 in the follower-proximal case. All differences are below the 0.4 m^2 threshold. The implement position therefore had no practically meaningful effect on individual-vehicle lateral tracking for either model; the slightly larger change shown by the kinematic model when the implement was near the follower vehicle is indicative only.

The orientation error results were likewise within resolution. The dynamic model orientation error IAE ranged from 0.0166 to 0.0175 rad·m across both configurations, and the kinematic model reached 0.0237 rad·m for the follower vehicle in the follower-proximal configuration; these values and their differences are far below the 0.35 rad·m threshold.

The formation-control results are where the implement position had a resolvable effect. The offset error IAE of the dynamic model was 0.668 m^2 in the follower-proximal configuration and 0.583 m^2 in the leader-proximal configuration, compared with 1.26 m^2 and 1.16 m^2 for the kinematic model; both differences (0.59 m^2 and 0.58 m^2) reach the 0.56 m^2 threshold. The kinematic model also showed a resolvable increase in steady-state offset error when the implement was moved near the follower vehicle, from $\pm$0.034 m to $\pm$0.054 m, a change of 0.02 m against the 0.014 m threshold, whereas the dynamic model did not. For separation error, the kinematic model produced smaller IAE values in both configurations, but the differences are within resolution. Overall, the implement position affected formation synchronization rather than individual-vehicle tracking, and the dynamic model maintained practically better offset regulation in both configurations and was less sensitive to the implement position.

4.2.8 Initial Offset Error

The system response to initial positioning error was investigated. Whereas previous simulations assumed zero initial offset between the two vehicles, two new scenarios were introduced: one with a 1.0 m initial offset error and another with a 0.5 m initial offset error. These cases were used to test the recovery performance of the algorithm.

4.2.8.1 Large Initial Offset Error

The test scenario was as follows:

1. Forward motion.

2. Straight trajectory.

3. Medium-adhesion earth road ($\mu = 0.75$).

4. Target speed of the support vehicles: 2.5 m/s.

5. External loads on truss (opposite to the path direction): $F_{\text{external}} = 50$ N.

6. Implement position on the truss: $d_4 = 0.8$ m.

7. Initial offset error: $e = 1$ m.

The key simulation results for the dynamic model are shown in Figure 4.106 to Figure 4.110.

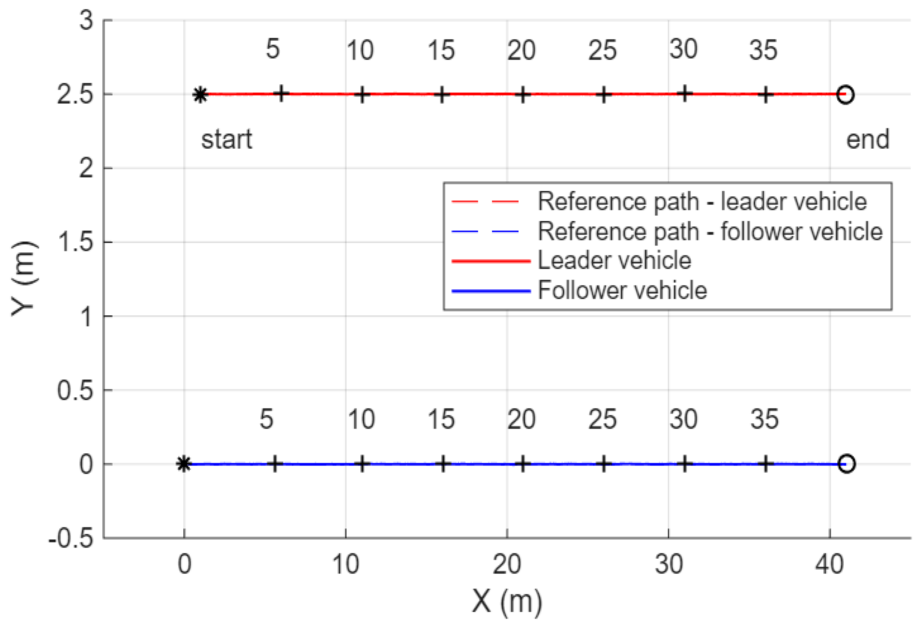

Figure 4.106 Reference and actual paths using the dynamic model with a large initial offset error

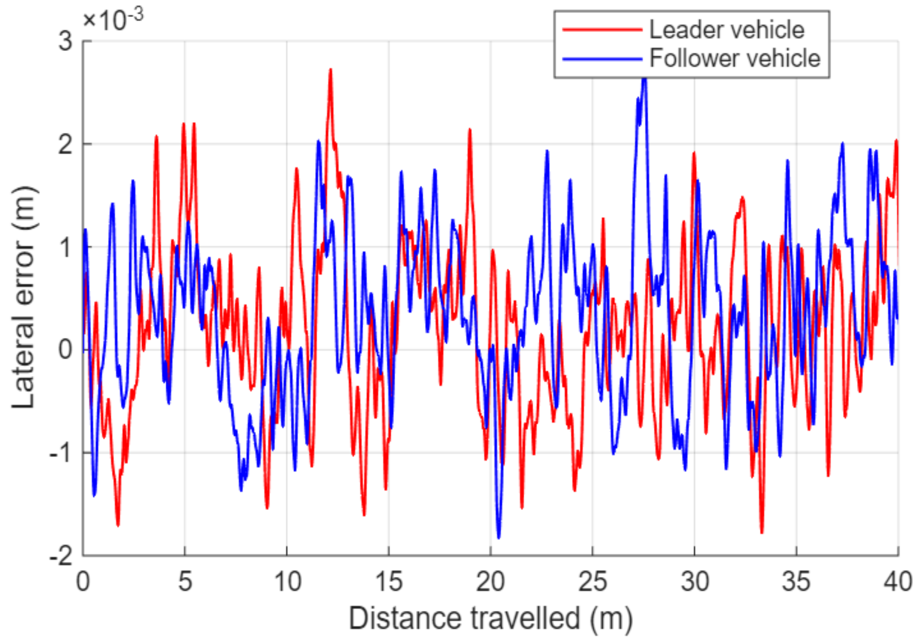

Figure 4.107 Lateral error using the dynamic model with a large initial offset error

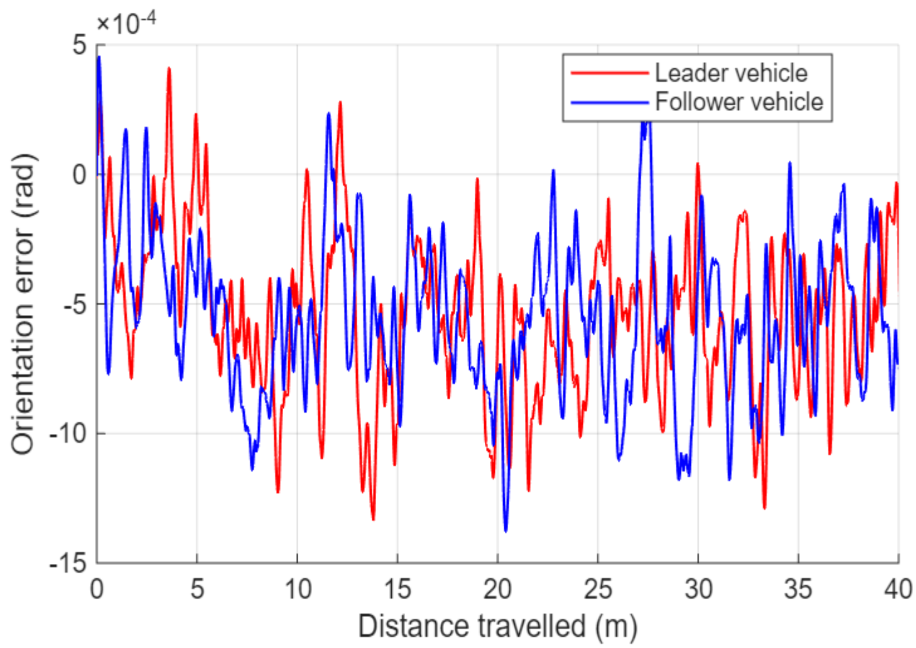

Figure 4.108 Orientation error using the dynamic model with a large initial offset error

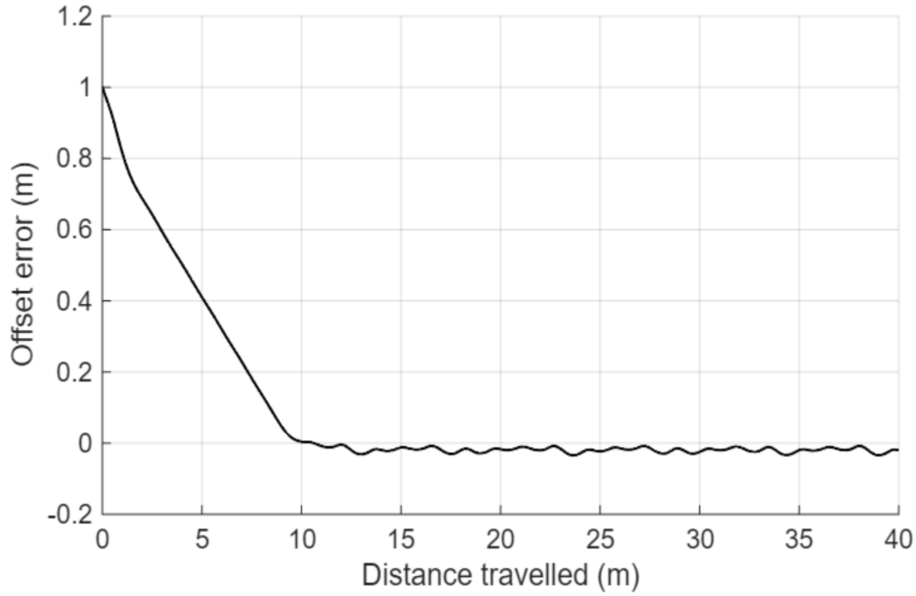

Figure 4.109 Offset error using the dynamic model with a large initial offset error

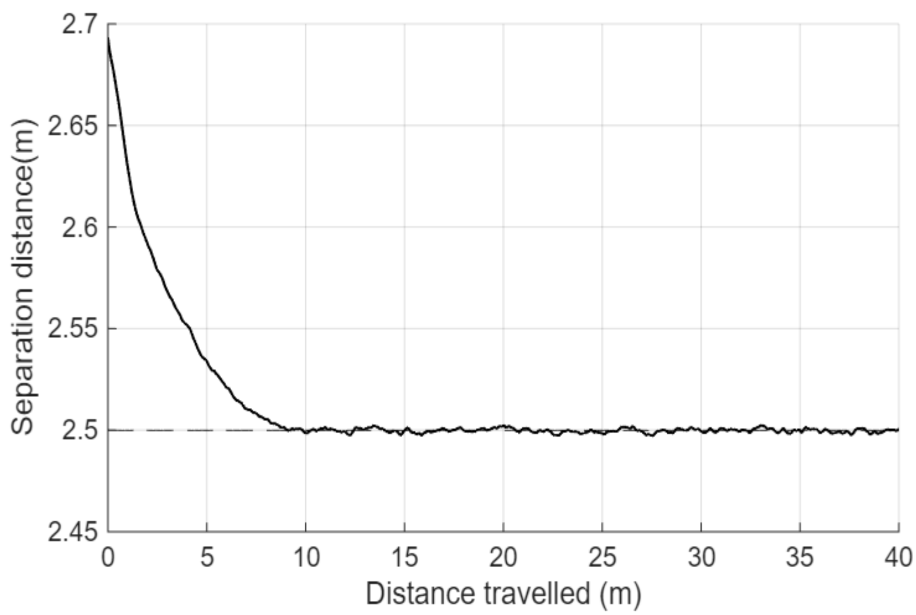

Figure 4.110 Distance between the two support vehicles using the dynamic model with a large initial offset error

The key simulation results for the kinematic model are shown in Figure 4.111 to Figure 4.115.

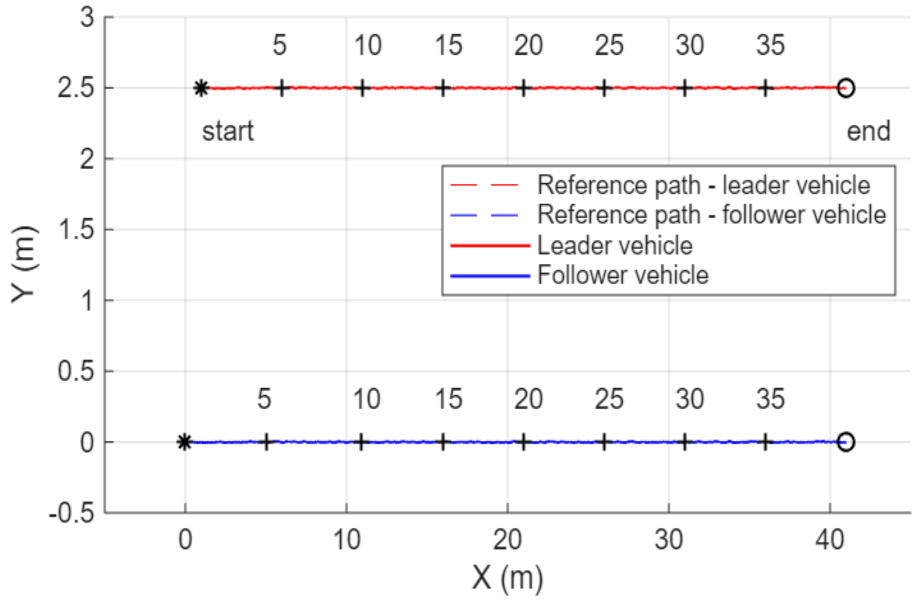

Figure 4.111 Reference and actual paths using the kinematic model with a large initial offset error

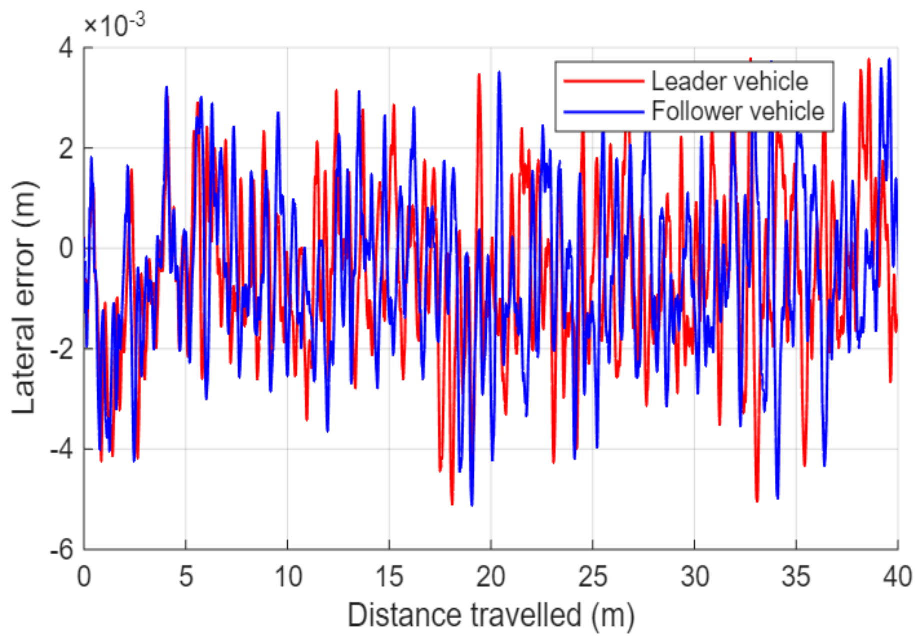

Figure 4.112 Lateral error using the kinematic model with a large initial offset error

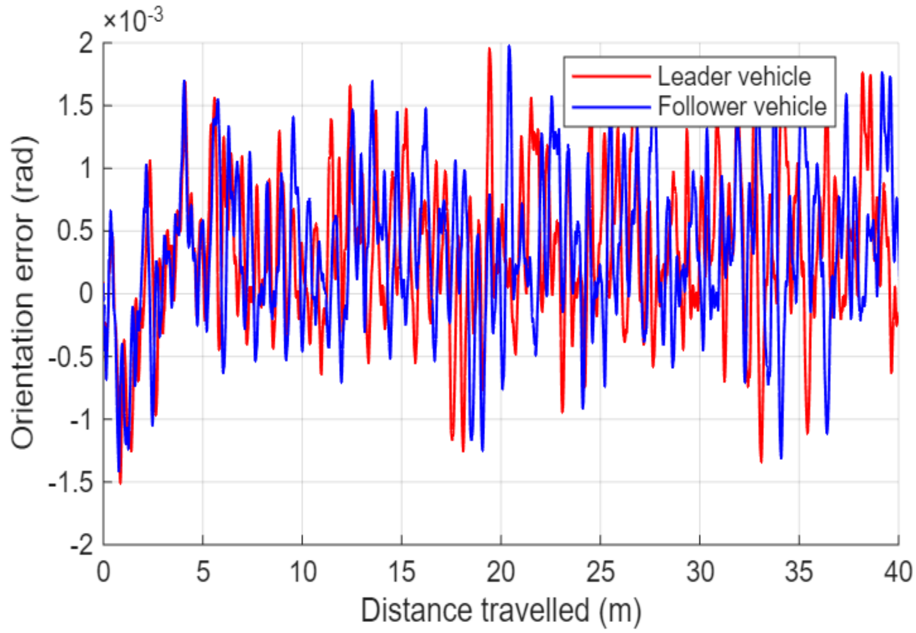

Figure 4.113 Orientation error using the kinematic model with a large initial offset error

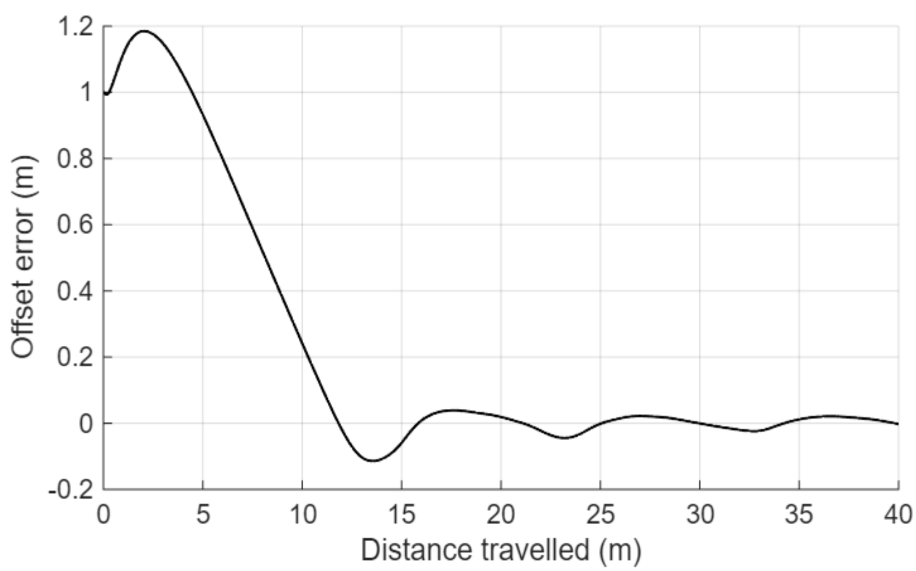

Figure 4.114 Offset error using the kinematic model with a large initial offset error

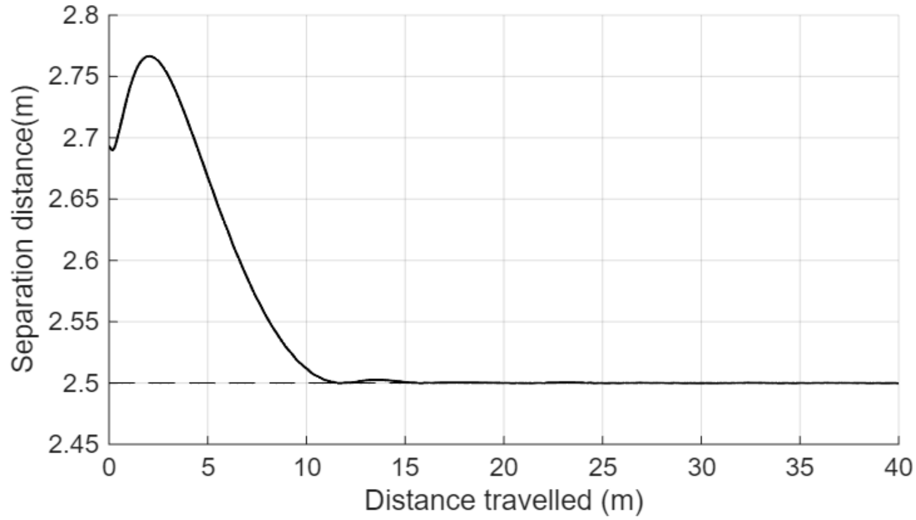

Figure 4.115 Distance between the two support vehicles using the kinematic model with a large initial offset error

The steady-state and IAE performance metrics for the large initial offset error case are summarized in Table 4.16.

Table 4.16 Steady-state and IAE performance metrics for the large initial offset error simulation[a]

		Dynamic	Kinematic
Leader vehicle	Steady-state velocity (m/s)	2.50	2.47
	Steady-state lateral error (m)	**±0.0027**	±0.0051
	Steady-state orientation error (rad)	**±0.0013**	±0.0020
	Lateral error IAE (m^2)	**0.0269**	0.0553
	Orientation error IAE (rad·m)	0.0218	0.0218
Follower vehicle	Steady-state velocity (m/s)	2.50	2.48
	Steady-state lateral error (m)	**±0.0028**	±0.0051
	Steady-state orientation error (rad)	**±0.0014**	±0.0020
	Lateral error IAE (m^2)	**0.0286**	0.0570
	Orientation error IAE (rad·m)	0.0235	0.0224
Steady-state offset error (m)		**±0.034**	±0.12
Steady-state separation error (m)		±0.0028	±0.0029
Offset error IAE (m^2)		**4.31**	9.37
Separation error IAE (m^2)		**0.467**	1.54

[a] Boldface: notably better than the other model.

The offset error in Figure 4.114 rises from its initial value of 1 m before it decreases, a behaviour that, among the initial-offset scenarios, occurred with the kinematic model at the large initial offset only. The longitudinal velocities of the two vehicles in this run (Figure A.44) show the cause. The synchronization law of Section 3.3.3 commands the follower to exceed the leader's speed by the offset error multiplied by the synchronization gain, 2.5 s^{-1} in this study, the same value used in the dynamic-model runs; for a 1 m offset this increment is 2.5 m/s on top of the leader's speed of about 2.5 m/s, so the commanded follower speed of about 5 m/s exceeds the ± 4 m/s velocity range of Table 4.1 and, more restrictively, the speed the drive can actually deliver on this surface (about 2.85 m/s in Figure A.44); the follower's velocity loop therefore saturates from the first control step. Over the first two metres the follower's speed builds up more gradually than the leader's, because a saturated tractive demand on the medium-adhesion surface produces longitudinal wheel slip that limits the speed the follower can actually reach; the follower is slower than the leader during this interval and the offset grows. From about 2.5 m the follower runs faster than the leader, holding about 2.85 m/s against about 2.45 m/s for some 9 m, which closes the offset at the largest speed differential the drive can sustain rather than at the commanded one. As the offset approaches zero the command falls to the leader's speed, the follower slows below the leader, and the offset overshoots and settles through damped oscillations by about 30 m. For the small initial offset the increment is 1.25 m/s, giving a commanded follower speed of about 3.75 m/s that lies within the ± 4 m/s range, and because the offset shrinks from the outset the command falls toward the leader's speed; the follower's speed therefore builds up with the leader's and the offset decreases from the outset. The velocity gains were identical in the dynamic-model run at the same offset (Figure 4.109), which shows no rise; the difference lies in the model used for steering and state prediction, which in the dynamic case represents the tire slip and lateral dynamics during start-up and produces a follower response that follows the command more closely, whereas the kinematic model does not represent the slip that limits the follower under a saturated demand. The rise is bounded and followed by convergence, so it affects the transient IAE rather than stability; tire relaxation is excluded by the zero relaxation lengths of the tire model, and the individual contributions were not isolated by re-running the scenario.

Based on the simulation results of Sections 4.2.1 and 4.2.8.1 and Tables 4.6 and 4.16, the 1.0 m initial offset had no practically meaningful effect on individual-vehicle tracking: both models converged to steady-state lateral and orientation errors below the sensor resolution, and the lateral error IAE values, 0.0269 m^2 and 0.0286 m^2 for the dynamic model and 0.0553 m^2 and 0.0570 m^2 for the kinematic model, are essentially those of the general case. The orientation error IAE differences, which slightly favoured the kinematic model for the follower vehicle (0.0224 rad·m against 0.0235 rad·m), are within resolution.

The effect of the large initial offset appears in the synchronous tracking metrics. The offset error IAE increased from 0.583 m² in the general case to 4.31 m² with the dynamic model and from 1.16 m² to 9.37 m² with the kinematic model; the difference between the models, 5.06 m², is nine times the 0.56 m² threshold. The steady-state offset error, evaluated after the recovery transient, was $\pm$0.034 m with the dynamic model against $\pm$0.12 m with the kinematic model, a difference of 0.086 m that is six times the 0.014 m threshold, compared with $\pm$0.014 m against $\pm$0.034 m in the general case. The separation error IAE also differed resolvably, 0.467 m² against 1.54 m², a difference of 1.07 m² above the 0.56 m² threshold, whereas in the general case the separation metrics were within resolution. The dynamic model therefore recovered the formation from a large initial misalignment with practically better transient behaviour and offset regulation, consistent with the start-up analysis above: the kinematic model's follower could not follow the saturated velocity command, whereas the dynamic model's prediction of slip and lateral dynamics produced a response closer to the command.

4.2.8.2 Small Initial Offset Error

The test scenario was as follows:

1. Forward motion.
2. Straight trajectory.
3. Medium-adhesion earth road (μ = 0.75).
4. Target speed of the support vehicles: 2.5 m/s.
5. External loads on truss (opposite to the path direction): F_{external} = 50 N.
6. Implement position on the truss: d_4 = 0.8 m.
7. Initial offset error: e = 0.5 m.

The key simulation results for the dynamic model are shown in Figure 4.116 to Figure 4.120.

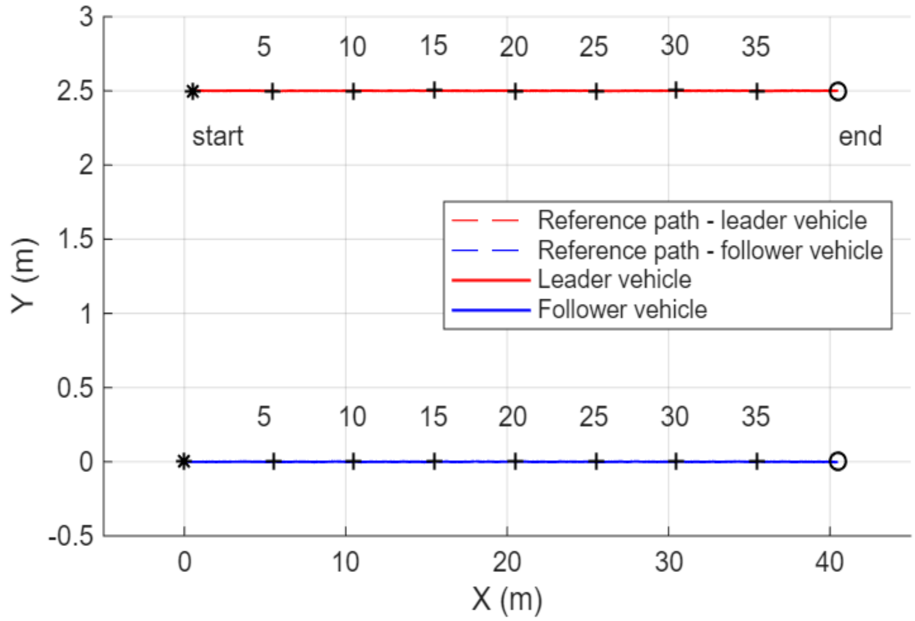

Figure 4.116 Reference and actual paths using the dynamic model with a small initial offset error

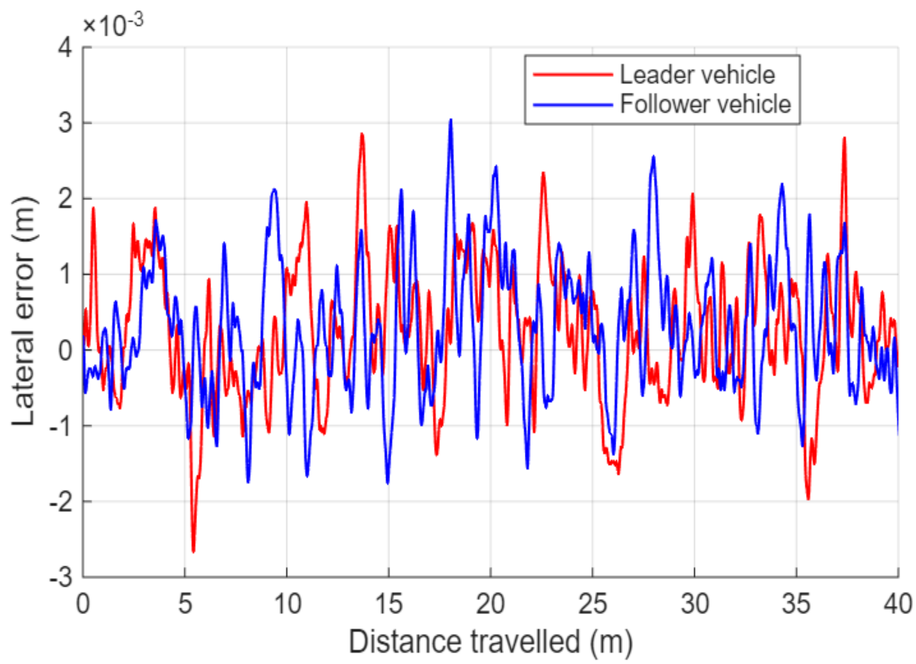

Figure 4.117 Lateral error using the dynamic model with a small initial offset error

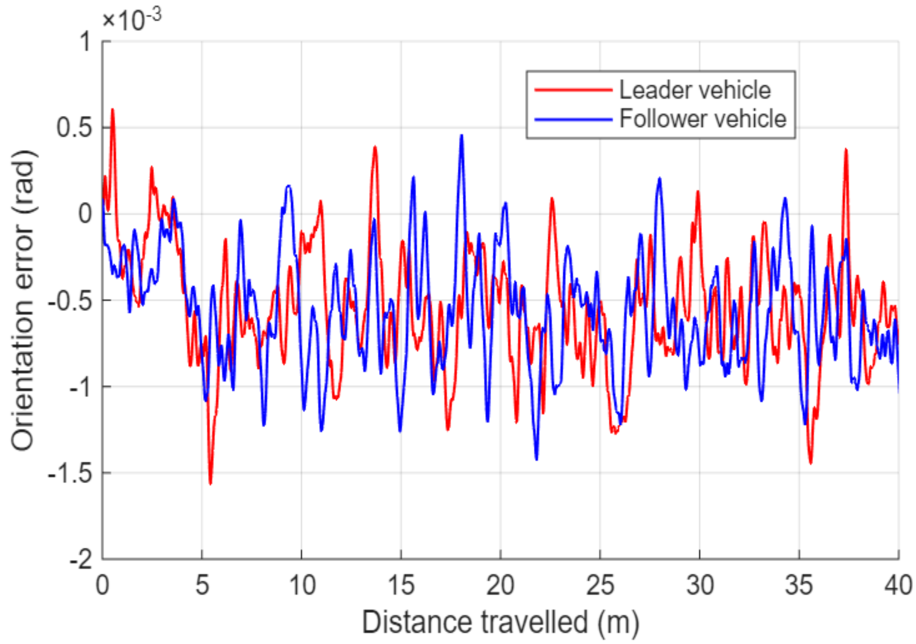

Figure 4.118 Orientation error using the dynamic model with a small initial offset error

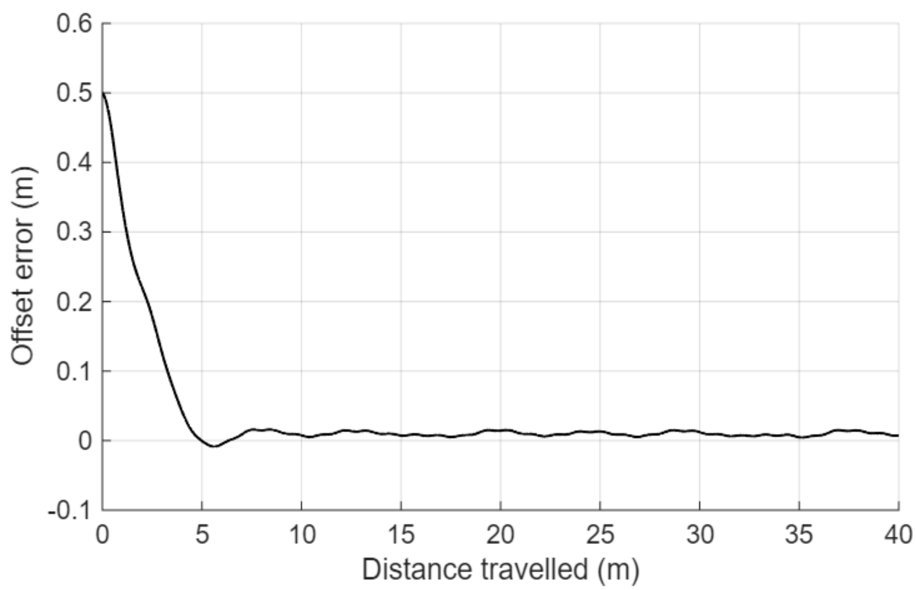

Figure 4.119 Offset error using the dynamic model with a small initial offset error

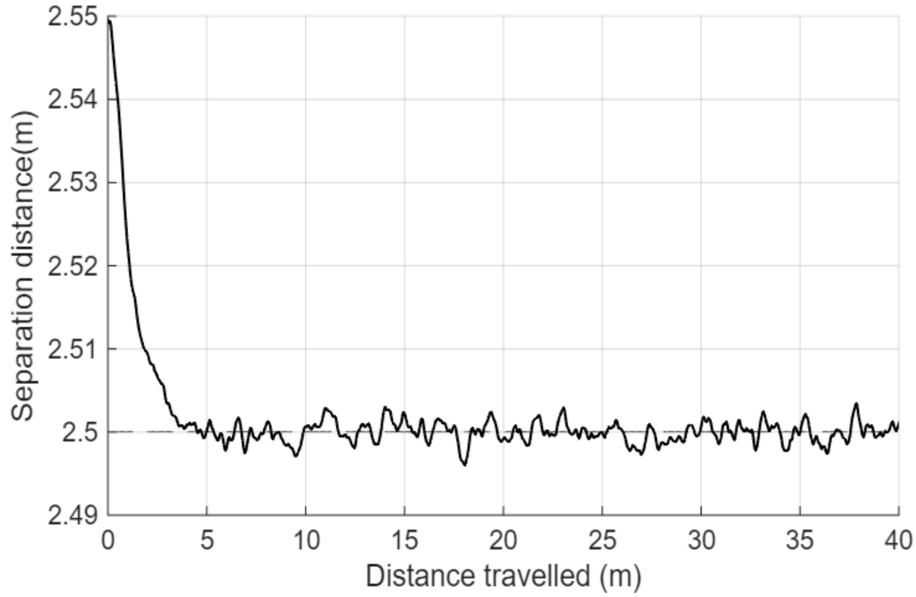

Figure 4.120 Distance between the two support vehicles using the dynamic model with a small initial offset error

The key simulation results for the kinematic model are shown in Figure 4.121 to Figure 4.125.

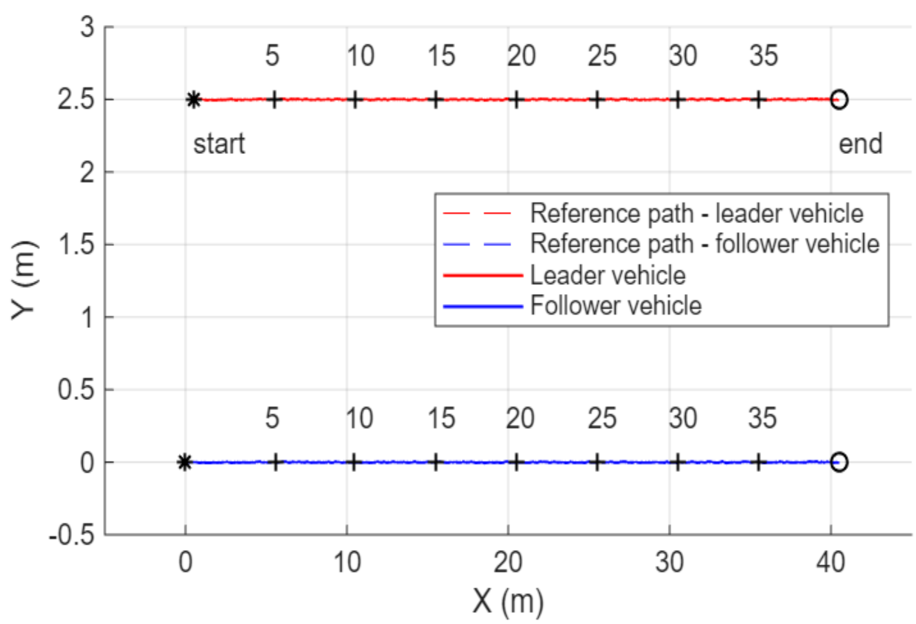

Figure 4.121 Reference and actual paths using the kinematic model with a small initial offset error

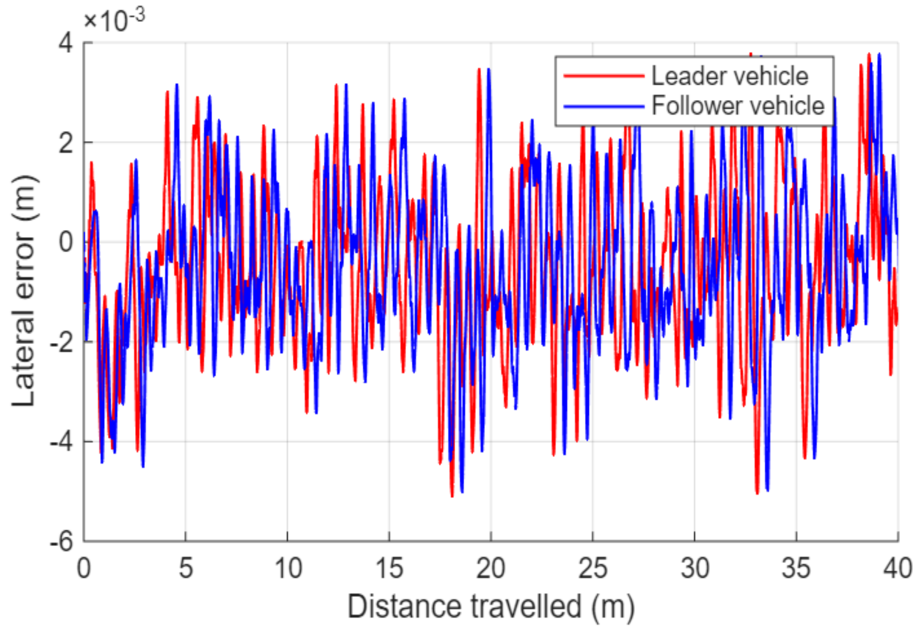

Figure 4.122 Lateral error using the kinematic model with a small initial offset error

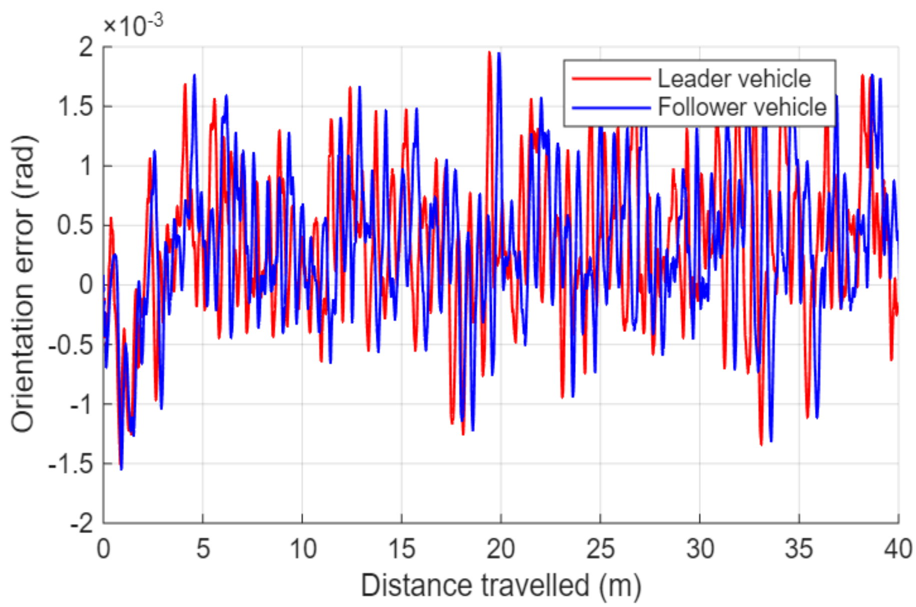

Figure 4.123 Orientation error using the kinematic model with a small initial offset error

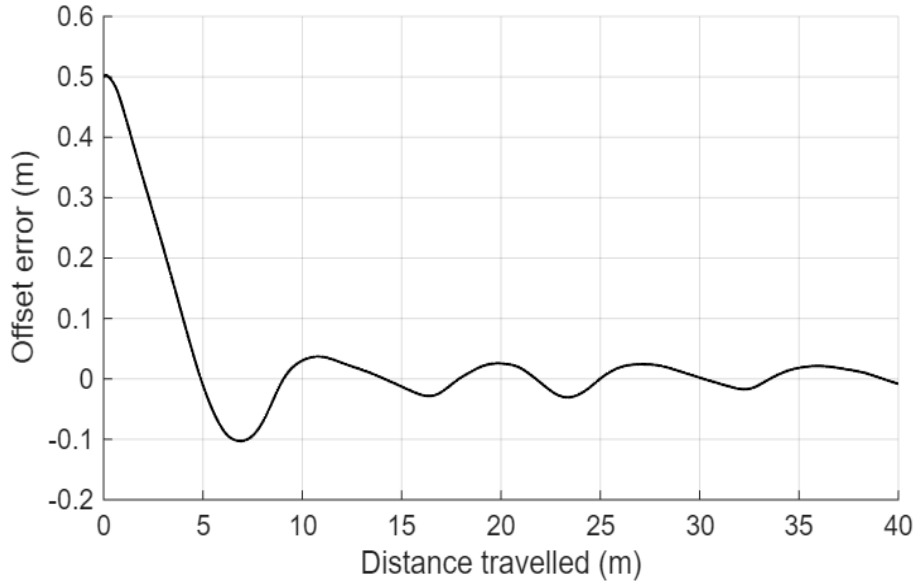

Figure 4.124 Offset error using the kinematic model with a small initial offset error

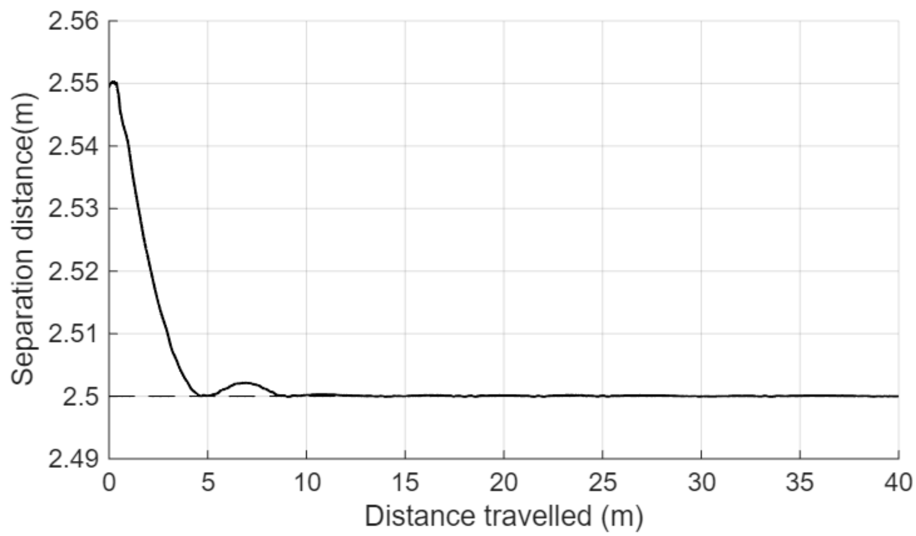

Figure 4.125 Distance between the two support vehicles using the kinematic model with a small initial offset error

The steady-state and IAE performance metrics for the small initial offset error case are summarized in Table 4.17.

Table 4.17 Steady-state and IAE performance metrics for the small initial offset error simulation[a]

		Dynamic	Kinematic
Leader vehicle	Steady-state velocity (m/s)	2.50	2.47
	Steady-state lateral error (m)	**±0.0029**	±0.0051
	Steady-state orientation error (rad)	**±0.0014**	±0.0020
	Lateral error IAE (m^2)	**0.0290**	0.0553
	Orientation error IAE (rad·m)	0.0225	0.0218
Follower vehicle	Steady-state velocity (m/s)	2.50	2.47
	Steady-state lateral error (m)	**±0.0030**	±0.0050
	Steady-state orientation error (rad)	**±0.0015**	±0.0019
	Lateral error IAE (m^2)	**0.0292**	0.0560
	Orientation error IAE (rad·m)	0.0234	0.0222
Steady-state offset error (m)		**±0.015**	±0.037
Steady-state separation error (m)		±0.0040	±0.00027
Offset error IAE (m^2)		**1.19**	2.13
Separation error IAE (m^2)		**0.0882**	0.105

[a] Boldface: notably better than the other model.

Based on the simulation results of Sections 4.2.1 and 4.2.8.2 and Tables 4.6 and 4.17, the 0.5 m initial offset likewise left individual-vehicle tracking within sensor resolution: the lateral error IAE values, 0.0290 m² and 0.0292 m² for the dynamic model and 0.0553 m² and 0.0560 m² for the kinematic model, and the orientation error IAE values, 0.0225 rad·m and 0.0234 rad·m against 0.0218 rad·m and 0.0222 rad·m, slightly favouring the kinematic model, differ from the general case and from each other by far less than the 0.4 m² and 0.35 rad·m thresholds.

For formation control, the offset error IAE rose from 0.583 m² in the general case to 1.19 m² with the dynamic model and from 1.16 m² to 2.13 m² with the kinematic model; the difference between the models, 0.94 m², exceeds the 0.56 m² threshold, so the dynamic model retained a practically meaningful advantage in offset regulation, larger than the 0.58 m² margin of the general case. The steady-state offset errors, ±0.015 m against ±0.037 m, a difference of 0.022 m, also favoured the dynamic model resolvably. The separation error IAE (0.0882 m² against 0.105 m²) and the steady-state separation errors were within resolution. Because the commanded velocity increment of 1.25 m/s remained within the drive’s capability, the offset decreased from the outset for both models; the small initial offset acted as a moderate formation disturbance from which both controllers recovered, the dynamic model with resolvably less accumulated offset error.

4.2.9 Analysis of Simulation Results

This section draws together the comparisons of Sections 4.2.1 to 4.2.8, in which each scenario was assessed against the general case of Section 4.2.1 and the dynamic-model-based and kinematic-model-based control strategies were compared against the practical-significance thresholds defined at the start of Section 4.2.

For individual-vehicle path tracking, the two strategies could not be distinguished at the sensor level on straight paths under any of the tested conditions. Forward and reverse motion, high, medium and low adhesion, target speeds of 1.5, 2.5 and 3.5 m/s, external loads of 50 N and 200 N, both implement positions, and initial offsets of 0, 0.5 and 1.0 m all produced steady-state lateral and orientation errors below the 0.01 m and 0.0087 rad thresholds and IAE differences below the 0.4 m² and 0.35 rad·m thresholds. The differences that do exist have a consistent direction: the kinematic model's lateral and orientation error IAE values grew more, in relative terms, as adhesion decreased and as speed increased, which is consistent with the dynamic model accounting for tire slip and speed-dependent lateral dynamics, but at the magnitudes reached on the 40 m straight path these trends are indicative only. The strategies separate on curved paths. In forward curved tracking the dynamic model reduced the steady-state lateral error from ±0.20 m to ±0.12 m, bringing the response inside the ±0.15 m bound of Section 3.4, and reduced the lateral error IAE by about 46%; in curved reverse tracking it reduced the steady-state lateral error from ±0.57 m to ±0.42 m and the orientation error from ±0.38 rad to ±0.30 rad, although both strategies exceeded the Section 3.4 bounds in that scenario. The one metric on which the kinematic model was resolvably better was the orientation error in forward curved tracking (±0.38 rad against ±0.41 rad), where both strategies exceeded the ±0.15 rad bound; heading regulation on curved paths is therefore a limitation shared by the two strategies rather than an advantage of either.

Formation control is where the advantage of the dynamic model was consistent. Its offset error IAE was lower than that of the kinematic model in every scenario, and the difference reached or exceeded the 0.56 m² threshold in the general case (0.58 m²), forward and reverse curved tracking (0.80 m² and 0.86 m²), straight-line reverse motion (0.73 m²), high and medium adhesion (0.74 m² and 0.58 m²), medium and high speed (0.58 m² and 1.03 m²), both external loads (0.58 m² and 0.70 m²), both implement positions (0.59 m² and 0.58 m²), and both initial offsets (0.94 m² and 5.06 m²); only on the low-adhesion surface (0.41 m²) and at low speed (0.27 m²) did it fall below the threshold. The steady-state offset errors showed the same pattern. The scenarios that most stressed coordination, the high target speed, the initial offsets and the curved paths, were also those in which the advantage of the dynamic model was largest, and the absolute margin between the two strategies widened as speed, load or initial offset increased. Steady-state separation error, which is bounded by the travel of the sliding joint, remained below the 0.014 m threshold for both strategies on the straight paths; on the curved paths the kinematic model's value exceeded it ($\pm$0.032 m forward, $\pm$0.027 m reverse) while the dynamic model's did not, and the separation error IAE differed resolvably only at the large initial offset (0.467 m^2 against 1.54 m^2); where the kinematic model produced the smaller separation error IAE, the differences were within resolution.

Overall, the simulation results support selecting the dynamic-model-based strategy on the basis of its curved-path tracking and its formation control rather than its straight-line tracking, where the two strategies are indistinguishable at the sensor level. The dynamic-model-based strategy met the Section 3.4 lateral and offset bounds in every forward scenario, whereas the kinematic strategy exceeded the lateral bound on the forward curved path; neither strategy met the orientation bound on curved paths nor the lateral bound in curved reverse motion, which identifies curved and reverse operation as the conditions requiring further development. The resolvable improvements are concentrated in the conditions that matter for WSIC operation: curved passes, higher speeds, heavier implement loads and recovery from initial misalignment.

4.3 Simulation Results for the Unified Baseline

The weighting matrices of the unified MPC controller were initially determined using the same procedure described in Section 4.1.5. The final tuning values represented a balance between tracking performance and real-time implementation feasibility, i.e., keeping the per-step optimization solve time comfortably below the 0.02 s control period (50 Hz) so that the controller could execute within each sampling interval.

- Weighting parameters: Q = diag [1, 500,100,1], R = diag [1,5]
- Prediction horizon and control horizon: N_p = 20, N_c = 10

In this section, only a selected set of challenging scenarios was examined for the unified MPC controller in order to compare its performance with that of the proposed controller.

4.3.1 Curved Trajectory

The test scenario was identical to that described in Section 4.2.2. The main simulation results for the unified MPC controller are shown in Figure 4.126 to Figure 4.130, while the supplementary results are provided in Appendix A.9.

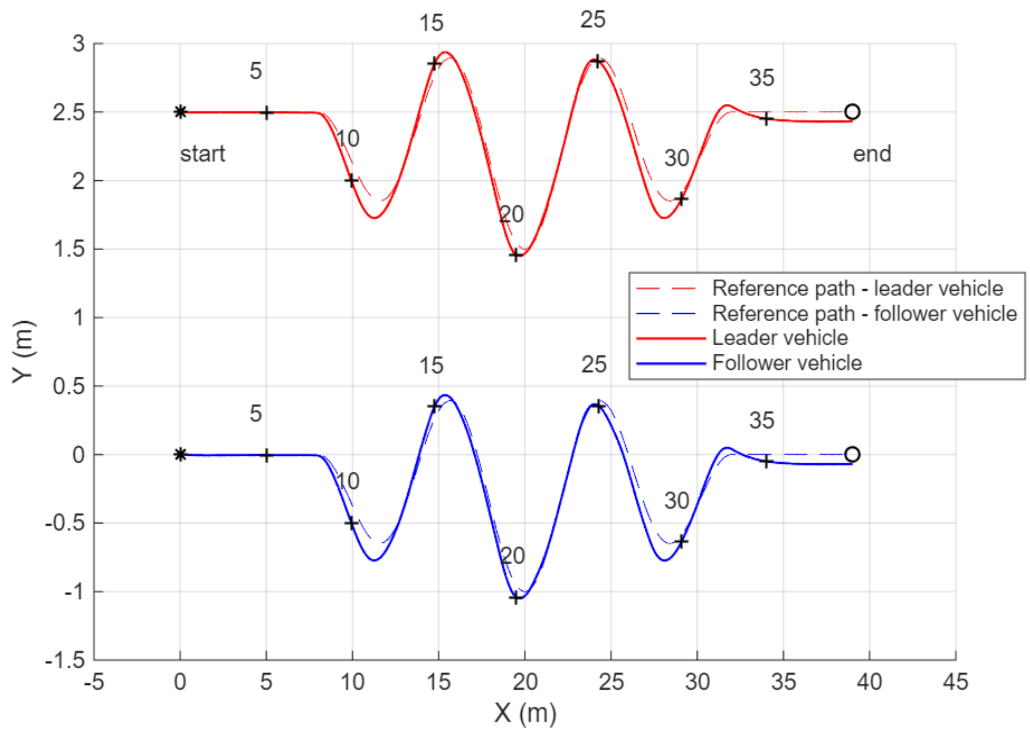

Figure 4.126 Reference and actual paths using the unified MPC controller for curved-trajectory tracking

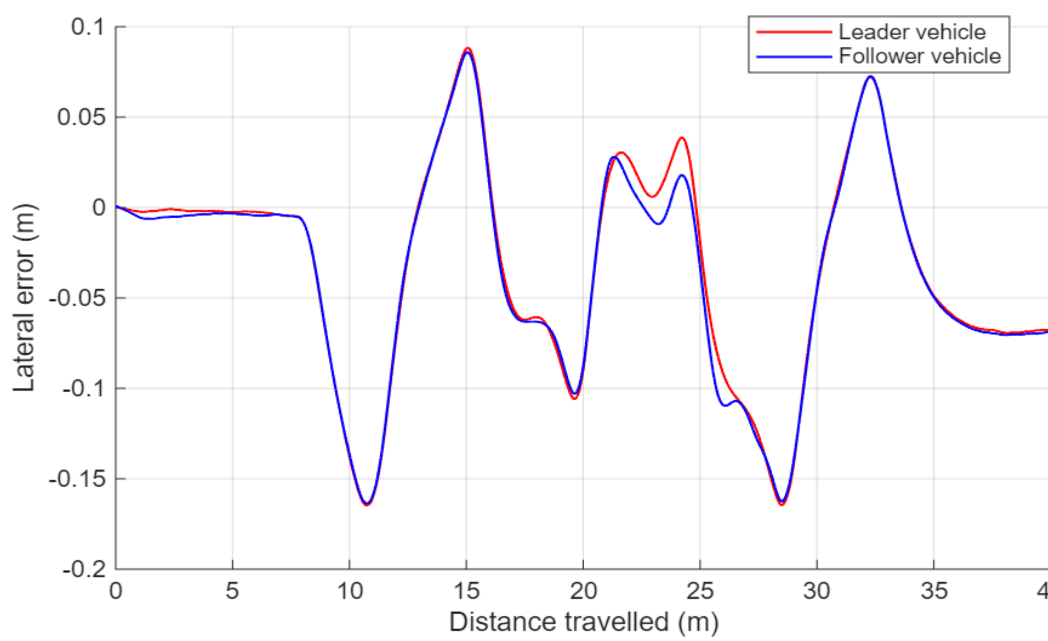

Figure 4.127 Lateral error using the unified MPC controller for curved-trajectory tracking

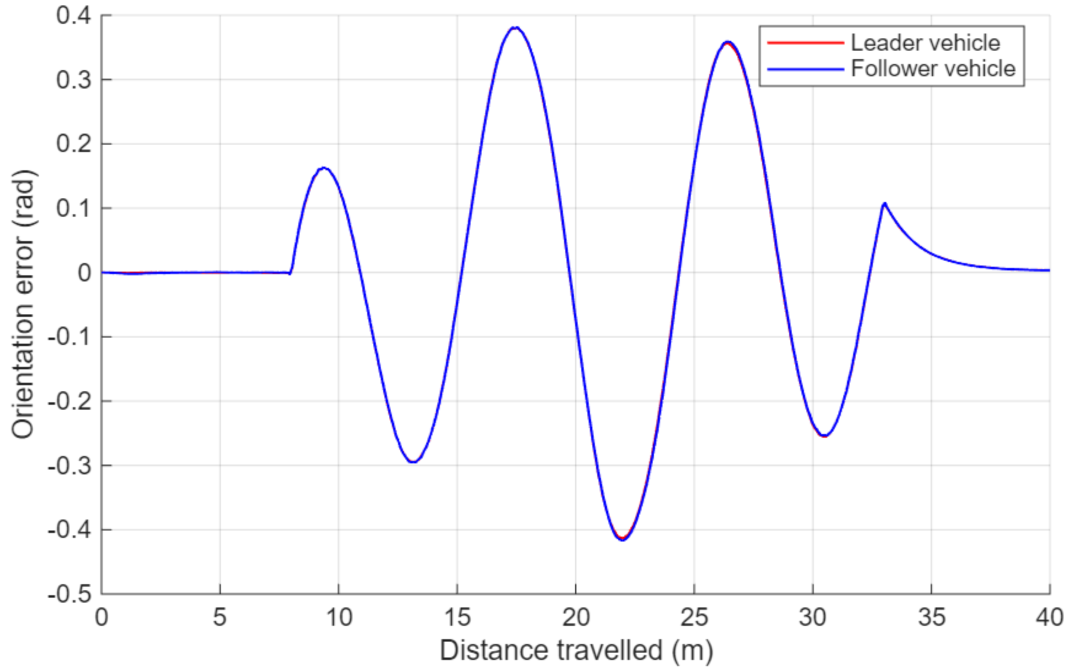

Figure 4.128 Orientation error using the unified MPC controller for curved-trajectory tracking

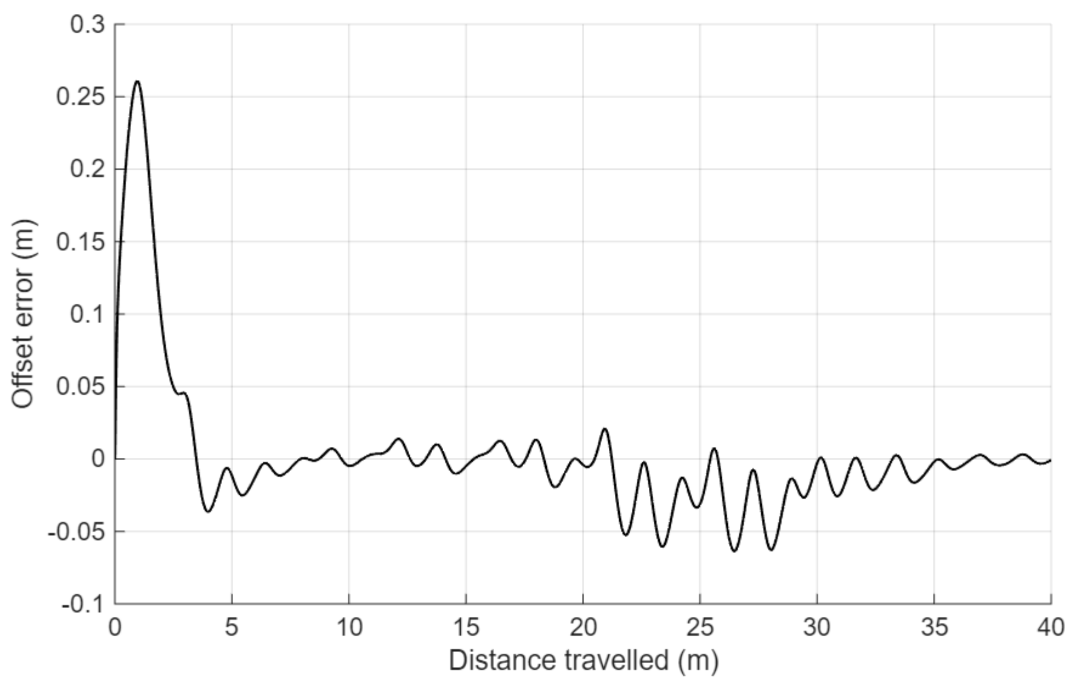

Figure 4.129 Offset error using the unified MPC controller for curved-trajectory tracking

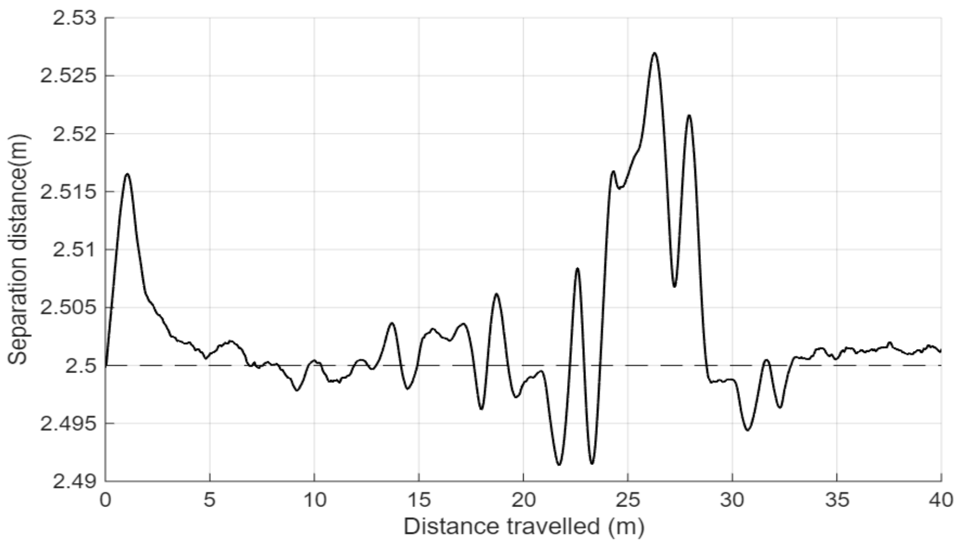

Figure 4.130 Distance between the two support vehicles using the unified MPC controller for curved-trajectory tracking

The steady-state and IAE performance metrics for curved trajectory tracking using the combined MPC and unified MPC controllers are summarized in Table 4.18.

Table 4.18 Steady-state and IAE performance metrics for curved-trajectory tracking using the combined MPC and unified MPC controllers[a]

		MPC–PID	Unified MPC
Leader vehicle	Steady-state velocity (m/s)	2.50	2.48
	Steady-state lateral error (m)	**±0.12**	±0.16
	Steady-state orientation error (rad)	±0.41	±0.41
	Lateral error IAE (m^2)	**1.47**	2.04
	Orientation error IAE (rad·m)	5.32	5.22
Follower vehicle	Steady-state velocity (m/s)	2.50	2.48
	Steady-state lateral error (m)	**±0.12**	±0.16
	Steady-state orientation error (rad)	±0.41	±0.42
	Lateral error IAE (m^2)	**1.48**	2.04
	Orientation error IAE (rad·m)	5.32	5.23
Steady-state offset error (m)		**±0.038**	±0.064
Steady-state separation error (m)		**±0.014**	±0.027
Offset error IAE (m^2)		**0.794**	0.921
Separation error IAE (m^2)		**0.120**	0.163

[a] Boldface: notably better than the other model.

Based on the simulation results from Sections 4.2.2 and 4.3.1 and Tables 4.7 and 4.18, the combined MPC–PID controller achieved practically better lateral tracking than the unified MPC controller during curved trajectory tracking. For both the leader and follower vehicles, the steady-state lateral error decreased from ± 0.16 m with the unified MPC controller to ± 0.12 m with the combined MPC–PID controller, a difference of 0.04 m that is well above the 0.01 m threshold and moves the response from outside to inside the ± 0.15 m lateral bound of Section 3.4. The lateral error IAE decreased from 2.04 m^2 to 1.47 m^2 for the leader vehicle and from 2.04 m^2 to 1.48 m^2 for the follower vehicle, reductions of approximately 27.9% and 27.5% that exceed the 0.4 m^2 threshold. These results indicate that the combined MPC–PID structure provided more effective lateral path correction during curved motion.

The orientation error results showed no resolvable difference between the two controllers. For the leader vehicle, both produced a steady-state orientation error of approximately ± 0.41 rad, and the follower vehicle showed ± 0.41 rad with the combined MPC–PID controller and ± 0.42 rad with the unified MPC controller. The unified MPC controller produced slightly lower orientation error IAE values, 5.22 rad·m for the leader and 5.23 rad·m for the follower compared with 5.32 rad·m for both vehicles under the combined MPC–PID controller, a difference of 0.1 rad·m that is below the 0.35 rad·m threshold. As noted in Section 4.2.2, both controllers exceeded the ± 0.15 rad orientation bound on this path.

The formation-control metrics show one further resolvable advantage of the combined MPC–PID controller: the steady-state offset error decreased from ± 0.064 m with the unified MPC controller to ± 0.038 m, a difference of 0.026 m that exceeds the 0.014 m threshold. The remaining formation metrics differ by less than the thresholds: the offset error IAE was 0.794 m^2 compared with 0.921 m^2, the steady-state separation error ± 0.014 m compared with ± 0.027 m, and the separation error IAE 0.120 m^2 compared with 0.163 m^2. Overall, the combined MPC–PID controller provided practically better lateral tracking and steady-state offset regulation during curved trajectory tracking, with the other metrics equivalent at the sensor level; on this evidence it is the more reliable control strategy for curved-path WSIC operation.

4.3.2 High Speed

The test scenario was identical to that described in Section 4.2.5.1. The main simulation results for the unified MPC controller are shown in Figure 4.131 to Figure 4.135.

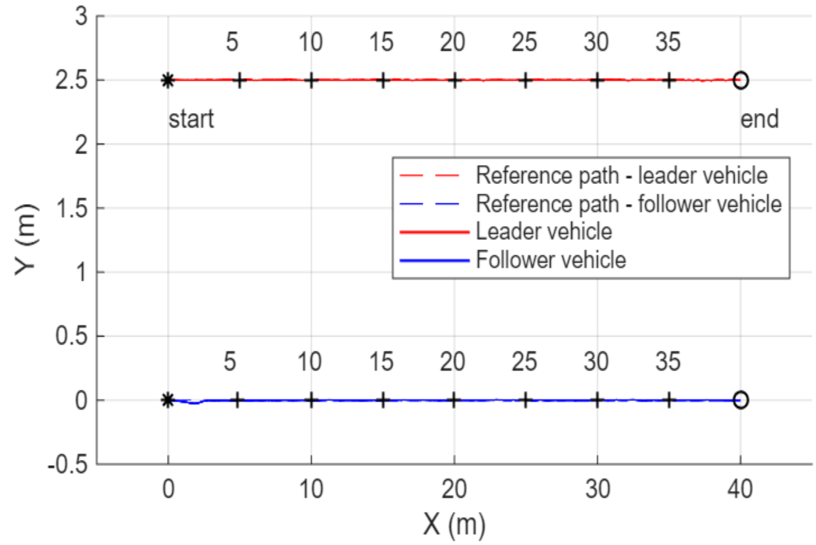

Figure 4.131 Reference and actual paths using the unified MPC controller at high speed

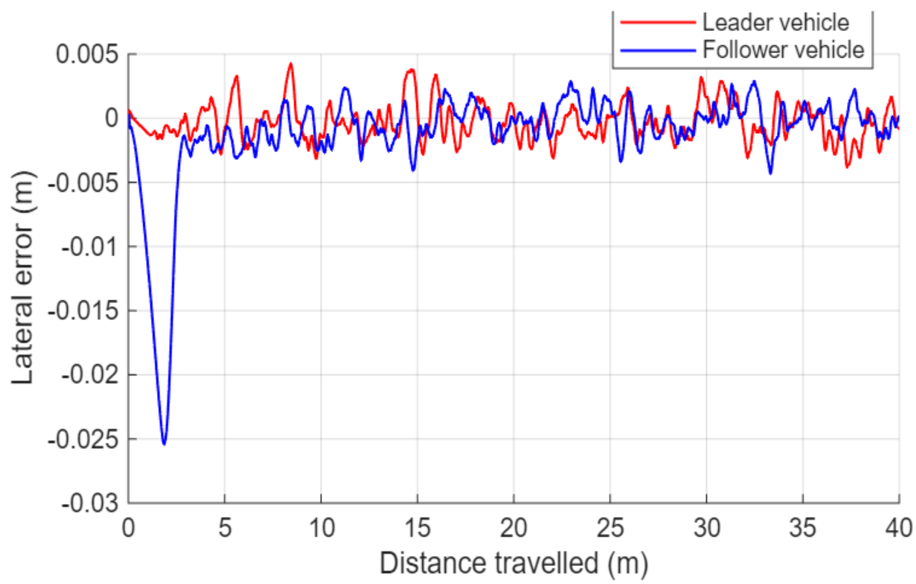

Figure 4.132 Lateral error using the unified MPC controller at high speed

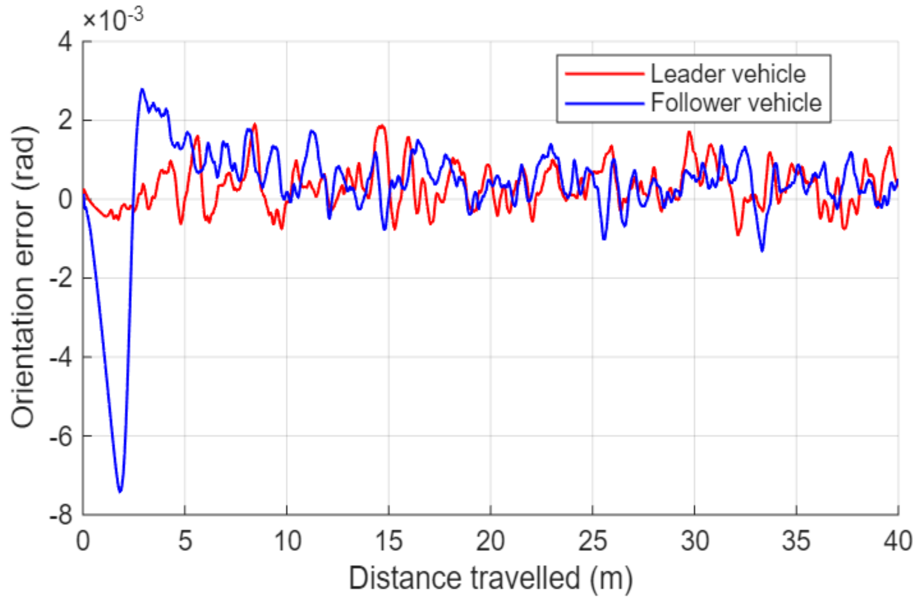

Figure 4.133 Orientation error using the unified MPC controller at high speed

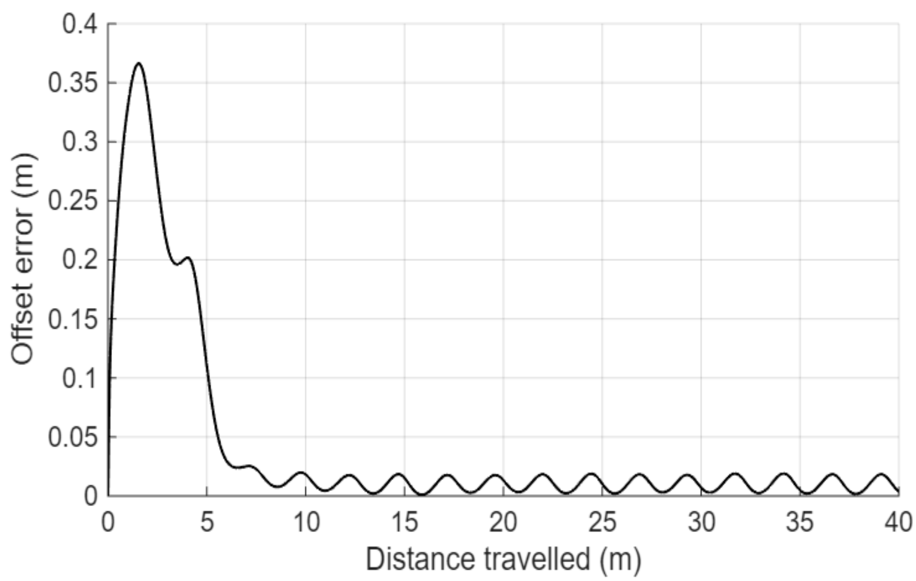

Figure 4.134 Offset error using the unified MPC controller at high speed

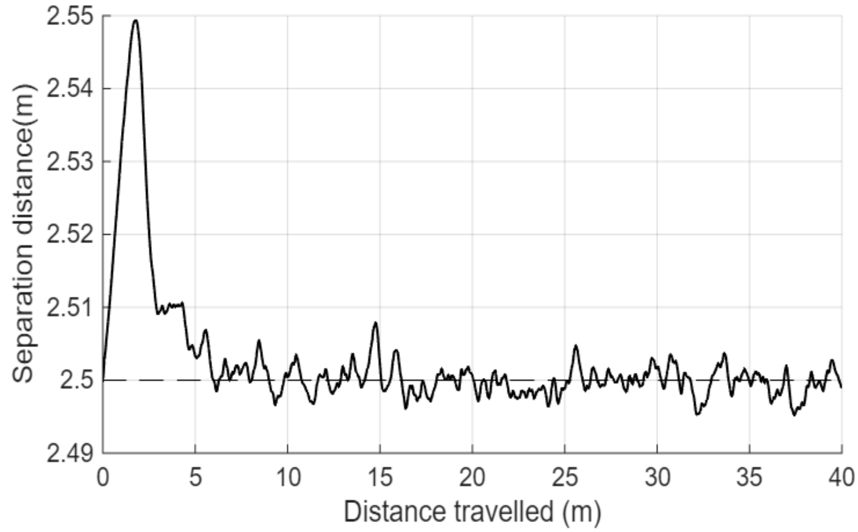

Figure 4.135 Distance between the two support vehicles using the unified MPC controller at high speed

The steady-state and IAE performance metrics for the high-speed simulation using the combined MPC and unified MPC are summarized in Table 4.19.

Table 4.19 Steady-state and IAE performance metrics for the high-speed simulation using the combined MPC and unified MPC[a]

		Combined MPC	Unified MPC
Leader vehicle	Steady-state velocity (m/s)	3.45	3.49
	Steady-state lateral error (m)	**±0.0030**	±0.0038
	Steady-state orientation error (rad)	**±0.0012**	±0.0019
	Lateral error IAE (m^2)	**0.0369**	0.0476
	Orientation error IAE (rad·m)	**0.0163**	0.0194
Follower vehicle	Steady-state velocity (m/s)	3.45	3.50
	Steady-state lateral error (m)	**±0.0027**	±0.0043
	Steady-state orientation error (rad)	**±0.0014**	±0.0017
	Lateral error IAE (m^2)	**0.0319**	0.0766
	Orientation error IAE (rad·m)	**0.0157**	0.0347
Steady-state offset error (m)		±0.030	±0.019
Steady-state separation error (m)		**±0.0041**	±0.0079
Offset error IAE (m^2)		**1.09**	1.65
Separation error IAE (m^2)		**0.0463**	0.153

[a] Boldface: notably better than the other model.

The follower lateral error in Figure 4.132 starts at zero, grows rapidly during the first part of the run, and then converges. This start-up transient is present in every high-speed run, including those with the combined MPC–PID controller, but it is largest with the unified MPC controller, which points to the mechanism. At the start of the run both vehicles accelerate from rest toward the 3.5 m/s target, the highest speed tested. During this phase the follower's reference is the virtual path generated from the leader's actual state, so the leader's own start-up steering and speed transient moves the follower's reference while the follower is still gaining speed, and the leader's motion is transmitted to the follower directly through the truss coupling forces of Section 3.1.3 before the follower controller has developed steering authority. The unified MPC controller optimizes steering and longitudinal velocity jointly with the fixed weighting matrices of Section 4.3; while the velocity error is large the velocity term dominates the cost, lateral correction is under-weighted, and the lateral error is allowed to grow before it is corrected. The combined controller assigns speed regulation to the PID loop and applies adaptive steering weights, which is why its transient is smaller under the same conditions. Two other candidate causes were considered and set aside. Tire relaxation dynamics are excluded because the tire model has zero relaxation lengths, so the tire forces respond without lag. Integrator windup in the PID velocity loop cannot be the primary cause, because the largest transient occurs with the unified MPC controller, which has no PID loop. The transient decays without oscillation and the error converges to the steady-state value in Table 4.19; it is a start-up effect of the coupled formation rather than a stability problem, and it is captured by the IAE values, which is why the follower lateral error IAE of the unified MPC controller is more than twice that of the combined controller in this scenario.

Based on the simulation results from Sections 4.2.5.1 and 4.3.2 and Tables 4.12 and 4.19, both controllers tracked the high-speed straight path within sensor resolution. For the leader vehicle, the steady-state lateral error was ± 0.0030 m with the combined MPC controller and ± 0.0038 m with the unified MPC controller, and the lateral error IAE 0.0369 m² compared with 0.0476 m²; for the follower vehicle, the lateral error IAE was 0.0319 m² compared with 0.0766 m². Although the relative reductions are large (approximately 22.5% and 58.4%), the absolute differences are below the 0.01 m and 0.4 m² thresholds, and no practically meaningful difference in lateral tracking is claimed. The larger relative reduction for the follower vehicle, which is the vehicle more exposed to synchronization effects, is indicative of the direction in which the two designs differ.

The orientation error results were likewise within resolution. For the leader vehicle, the orientation error IAE was 0.0163 rad·m with the combined MPC controller and 0.0194 rad·m with the unified MPC controller; for the follower vehicle it was 0.0157 rad·m compared with 0.0347 rad·m. Both differences are far below the 0.35 rad·m threshold, and the steady-state orientation errors of both controllers were below the IMU resolution.

The formation-control results contain the only high-speed difference that approaches the thresholds. The unified MPC controller produced a smaller steady-state offset error, ±0.019 m compared with ±0.030 m for the combined MPC controller, a difference of 0.011 m that is below the 0.014 m threshold, while its offset error IAE was larger, 1.65 m^2 compared with 1.09 m^2, a difference of 0.56 m^2 that is at the 0.56 m^2 threshold and is reported as marginal. This indicates that the unified MPC controller reached a comparable final offset but accumulated more formation deviation during the manoeuvre. The separation error differences, ±0.0041 m compared with ±0.0079 m in steady state and 0.0463 m^2 compared with 0.153 m^2 in IAE, are within resolution. Overall, the high-speed scenario does not separate the two controllers at a practically meaningful level; the evidence for the combined MPC–PID design rests on the curved-path scenario.

4.3.3 Analysis of Simulation Results for the Unified Baseline

The unified MPC comparison provides an additional engineering benchmark for the proposed WSIC control strategy. Whereas unified MPC jointly optimizes steering and longitudinal velocity, the combined controller uses MPC for predictive steering and PID for longitudinal-velocity regulation. Comparing these designs complements the kinematic benchmark by testing the proposed controller against an alternative predictive-control architecture and quantifying its tracking and formation-control performance.

The combined design offers three practical features relevant to interpreting these results. First, the steering-MPC weights and longitudinal-PID gains can be tuned separately to address path tracking and speed regulation. Second, steering optimization is formulated directly in terms of steering control, with steering-angle and steering-rate constraints, while velocity regulation is assigned to the PID loop. Third, the steering MPC uses the adaptive weighting strategy described in Section 4.1.5 and Table 4.5, whereas unified MPC uses the fixed Q and R matrices specified in Section 4.3. Adaptive weighting enables the combined controller to adjust lateral-error, orientation-error, and steering-effort priorities according to operating conditions. These features provide a practical rationale for the design and plausible contributors to its performance; their individual effects were not isolated in this comparison.

Sections 4.3.1 and 4.3.2 compare the achieved closed-loop responses of the implemented designs. Because both architecture and weighting strategy differ, the gains characterize the combined design as a whole rather than decoupling alone. Assessed against the practical-significance thresholds of Section 4.2, the combined MPC–PID design provided resolvable improvements in the curved-path scenario, in steady-state lateral error (bringing the response within the ± 0.15 m bound), lateral error IAE, and steady-state offset error, whereas in the high-speed straight-path scenario the two designs were equivalent at the sensor level with a marginal advantage in accumulated offset error. This is the appropriate reading of the benchmark: the proposed design is not distinguishable from unified MPC on undemanding paths, and is practically better where curvature makes the tracking problem demanding. This additional benchmark extends the evaluation presented in the related WSIC control studies of Li et al. (2026a, 2026b).

Chapter 5

Experiments

This chapter presents the experimental validation of the proposed guidance and control strategy using a scaled-down WSIC platform. The experiments were conducted to evaluate the applicability of the dynamic model and control strategy developed in Chapter 3 under physical operating conditions and to compare their performance with the kinematic model proposed by Luo (2017).

The experimental program included single-vehicle path-following tests, which are reported in Appendix B.1, and the cooperative two-vehicle tests reported in this chapter. Straight-line and sinusoidal trajectories were used to assess controller performance under constant-curvature and varying-curvature motion. In all experiments, the dynamic-model-based controller and Luo's kinematic-model-based controller were implemented and tested separately under the same conditions.

The experimental platform was developed from two heavy-duty mobile vehicles and integrated into a scaled-down WSIC system for real-time validation. The development of the physical platform, the candidate's contributions, the hardware and instrumentation, the experimental procedures, and the experimental results analysis are described in the following sections.

5.1 Experimental Setup

5.1.1 Platform Development

The experimental WSIC platform was developed by modifying two existing heavy-duty mobile vehicles into a physically connected two-vehicle system. The original vehicles, developed by Luo (2017), were intended for independent operation and therefore did not include the mechanical coupling system, upgraded propulsion transmission, RTK-GPS base-station configuration, and model-based real-time control implementation required for the present study.

To satisfy the requirements of the present study, the candidate undertook the principal modifications necessary to transform the original vehicles into a scaled-down WSIC platform. The first major development was the design and construction of the mechanical connecting system that physically coupled the two vehicles. This system comprised two rotary joints supported by large bearings, a truss with a functional length of 3.8 m assembled from eight 2 m T-slot structural members, and a sliding joint formed from four L-shaped components fastened with screws and nuts. Together, these elements provided the structural linkage and constrained relative motion necessary for WSIC operation.

The candidate also designed and developed a new propulsion transmission system for the upgraded brushless drive motor. A gear-chain transmission was introduced to transfer motor output to the drive mechanism and to ensure compatibility between the new motor and the propulsion requirements of the scaled-down platform.

In addition, the RTK-GPS positioning infrastructure was upgraded by replacing the original base receiver and assembling a new RTK-GPS base station for the experiments. This modification improved the positioning capability required for real-time vehicle guidance and synchronization.

A new electrical circuit system was also developed to accommodate the newly integrated devices and batteries. This system included safety switches for the main power bus and GPS receiver circuits, connection ports for integrating devices into the power bus, and an additional braking circuit for the drive motor.

Finally, the candidate implemented the real-time experimental control system by hard-coding the dynamic model and control strategy developed in Chapter 3 into the onboard control system. This implementation enabled direct experimental evaluation of the proposed dynamic-model-based controller.

The chassis, steering system, IMU modules, and XBee modules from the original vehicle design were retained (Luo, 2017). Other onboard components, including the drive motors, motor controllers, batteries, potentiometers, Arduino boards, and gears, were replaced and reorganized during platform development. Kishita Pakhrani, a co-op student at the University of Ottawa, assisted with the platform's development across two co-op terms under the candidate's direct supervision: an initial term (May 1–August 31, 2023; 525 hours) during which she assisted with the early stages of platform assembly, which was not completed during that term, and a second term (September 4–December 1, 2023; 455 hours) during which she assisted with testing and reorganizing newly integrated devices; the hardware upgrade was 75% completed by the end of her second term, and the candidate completed the remaining work independently afterwards. In total, her assistance spanned approximately 980 hours across the two terms, directed toward hardware assembly, device testing, and Arduino code modification for steering and drive-motor actuation, a minority of the overall platform-development and experimental effort. The candidate was independently responsible for the mechanical connecting system, propulsion transmission, and electrical system design; the RTK-GPS upgrade; completion of the remaining hardware integration; the final WSIC integration; all model-based control implementation used in the experimental study; and all experiments described in this chapter.

5.1.2 Hardware and Instrumentation

The vehicle dimensions and loads are given in Table 4.1 and Table 4.3. The experiments were conducted on a pavement/concrete road that provided unobstructed vehicle motion and adequate satellite reception for RTK-GPS measurements. This surface corresponds only to the firm end of the range of dike-top conditions reported by Laguë et al. (1997) for the full-scale WSIC; the softer, lower-adhesion conditions are addressed by the low-adhesion simulations of Chapter 4 rather than by the experiments. Figure 5.1 shows the experimental WSIC platform and the dimensions of the testing area.

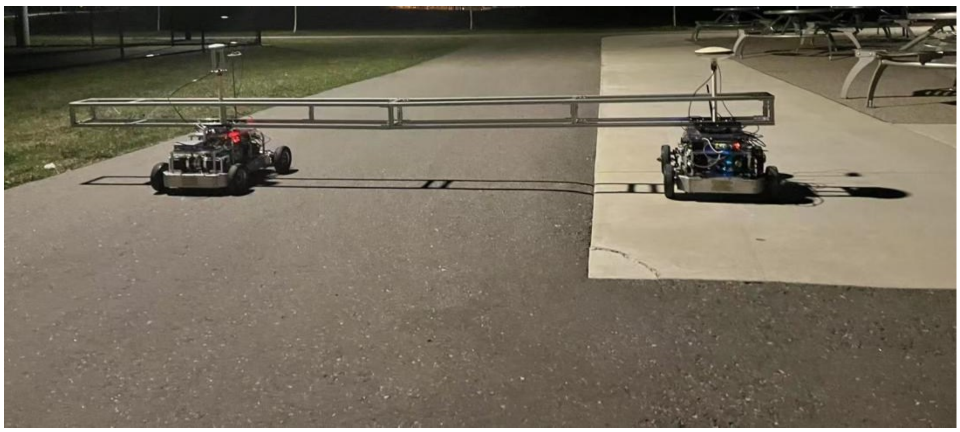

(a)

(b)

Figure 5.1 (a) Experimental WSIC on the pavement/concrete test surface (b) Dimensions of the testing area.

All experiments in this chapter were carried out at the same outdoor site on the pavement/concrete surface shown in Figure 5.1. Sessions were run in the evening and at night, when the site was free of pedestrians and vehicles. No weather instruments were deployed; conditions were recorded by observation at the time of each session.

The final experimental platform consisted of two support vehicles connected by a 3.8 m truss. Each vehicle was configured with two rear drive wheels and two front steerable wheels. The platform incorporated a dual-rover RTK-GPS system for real-time position tracking, two IMUs for orientation measurement, two XBee-PRO modules for wireless communication, two onboard mini-computers for high-level computation, and two microcontrollers for low-level actuation and communication.

Each vehicle was driven by two Parvalux PBL60-70 24 V brushless direct current gear motors for rear-wheel propulsion (157 W nominal power, 3000 rpm nominal speed, 0.5 N·m nominal continuous torque) and one Shayangye 24 V direct current gear motor for FWS. Steering angles were measured using Honeywell 308N5K conductive-plastic rotary potentiometers (295° electrical travel), read by the 10-bit analog-to-digital converter of an Arduino Mega (ATmega2560) board on each vehicle, which gives an angular resolution of approximately 0.29° per count. Each vehicle was powered by a 24 V, 30 Ah Li-ion battery for motor actuation and a 12 V, 9.6 Ah $LiFePO_4$ battery for the remaining onboard electronics.

A base RTK-GPS receiver and two rover receivers were used to provide real-time positioning data for vehicle guidance and synchronization. Table 5.1 lists the RTK-GPS equipment used in the experiments. The rover receivers output positioning data at 10 Hz; the datasheet specifies a horizontal RTK accuracy of 1 cm + 1 ppm and a velocity accuracy of 0.03 m/s (root mean square).

Table 5.1 RTK-GPS equipment

Equipment	Model	Quantity	Brand
Base receiver	PW7700-GDN-NZN-NNN	1	NovAtel
Rover receiver	FlexPak6	2	NovAtel
Base antenna	GPS-702-GG	1	NovAtel
Rover antenna	GPS-600-LB	1	NovAtel
Rover antenna	G5Ant-3AT1	1	Antcom
Radio modem	n920-ENC	3	Microhard

Each vehicle was also equipped with a 3DM-GX3-25 IMU from LORD MicroStrain. This sensor includes tri-axial accelerometers, gyroscopes, magnetometers, temperature sensors, and an onboard processor for static and dynamic inertial measurements. The IMU provides dynamic Euler angles, including pitch, roll, and heading, with a static attitude accuracy of 0.5° and a dynamic accuracy of 2°, a resolution better than 0.1°, an in-run bias stability of 0.00004*g*, and an initial bias error of 0.002*g* for acceleration measurement.

Wireless communication between the two vehicles was achieved using XBee-PRO S2B modules from Digi International Inc. These modules operate at 2.4 GHz, support a data rate of 250 kbps, and provide an outdoor line-of-sight range of up to 3.2 km, which was sufficient for real-time exchange of control and synchronization data between the vehicles.

Each vehicle was equipped with a Beelink EQ12 N100 onboard computer with built-in serial communication capability for interfacing with external devices. During the experiments, MATLAB was used to provide the graphical user interface, read and parse data from the GPS and IMU modules, support bidirectional communication through the XBee modules and Arduino boards, and execute the real-time control algorithms.

5.1.3 Experimental Procedures

The experiments were conducted to evaluate both individual vehicle path tracking and cooperative WSIC path tracking under real operating conditions. Two trajectory types were considered: straight-line paths and sinusoidal paths. These trajectories were selected to assess controller performance under both simple and varying-curvature motion.

The experimental procedure began with the initialization of the RTK-GPS base station, rover receivers, IMUs, onboard computers, and wireless communication modules. After communication and sensor initialization were completed successfully, the control software running in MATLAB acquired real-time position and orientation data, computed the required steering and velocity commands, and transmitted control signals to the Arduino-based actuation system. At each control step, the follower vehicle received the leader vehicle's state information and executed the synchronization controller in addition to the path-following controller.

Single-vehicle experiments were first performed to evaluate the path-tracking capability of each support vehicle independently (Appendix B.1). Cooperative experiments were then conducted using the fully connected WSIC platform to evaluate the coordinated motion of the leader and follower vehicles. In all experiments, the dynamic model developed in Chapter 3 and the kinematic model proposed by Luo (2017) were tested separately under the same trajectory conditions. Their performance was compared in terms of path-tracking behaviour, synchronization capability, and overall control stability.

5.2 Two-Vehicle Cooperation

To validate the cooperative tracking performance of the WSIC, two vehicles connected by a truss were tested on both straight-line and sinusoidal trajectories. Each condition, defined by the trajectory type and model type, was repeated twice to assess repeatability and reduce the effect of anomalous runs. The two-vehicle experiments were conducted from June 6 to June 8, 2025. Due to space limitations, one representative trial for each condition is presented here, while duplicate trials and supplementary results are included in Appendix B. The RTK-GPS solution remained in fixed mode throughout all recorded runs. Cloud cover, haze, and darkness do not attenuate GNSS signals appreciably, and the tropospheric and ionospheric delays that do affect positioning are removed by the short-baseline differential correction of the RTK system, with the base station located within the test area, so satellite signal quality was not a limiting factor on any of the test days. The conditions observed at each session are noted with the corresponding experiment below.

5.2.1 Straight-Line Tracking

Table 5.2 presents the initial and steady-state performance values for the leader and follower vehicles.

Table 5.2 Performance variables for two-vehicle straight-line tracking[a]

	Description	Initial value	Steady-state value (Dynamic model)	Steady-state value (Kinematic model)
Leader vehicle	Longitudinal velocity (m/s)	0	0.96	0.96
	Lateral error (m)	0.015	**±0.043**	±0.072
	Orientation error (rad)	0.010	±0.13	±0.11
	Steering angle (rad)	0	–	–
Follower vehicle	Longitudinal velocity (m/s)	0	0.96	0.97
	Lateral error (m)	−0.024	**±0.055**	±0.081
	Orientation error (rad)	−0.027	±0.080	±0.080
	Steering angle (rad)	0	–	–
	Offset error (m)	1.1	±0.14	**±0.11**
	Separation error (m)	0.25	**±0.077**	±0.084

[a] Boldface: notably better than the other model.

The vehicles followed the straight-line reference path defined as

$$\begin{aligned} y_1 &= -1.6 \\ y_2 &= -4.1 \end{aligned} \tag{129}$$

The initial conditions were: $x_1(0) = -7.67$ m, $y_1(0) = -1.58$ m, $\theta_1(0) = 0.010$ rad, $x_2(0) = -8.73$ m, $y_2(0) = -4.12$ m, $\theta_2(0) = -0.027$ rad.

5.2.1.1 Dynamic Model

This experiment was conducted on June 6, 2025. The session was run in dry conditions with light wind; no precipitation occurred during testing, and the pavement was dry and free of debris. Regional wildfire smoke reduced visibility across the Greater Toronto Area on this day; it had no bearing on the test, which relies on RTK-GPS and IMU measurements rather than vision.

The control gains were configured as follows:

- Weighting parameters: $Q = [20\ 0;\ 0\ 42]$, $R = 30$
- Prediction horizon and control horizon: $N_p = 23$, $N_c = 10$
- Control gain: $k_e = 1.3\ \mathrm{s}^{-1}$

The results are shown in Figure 5.2 to Figure 5.6.

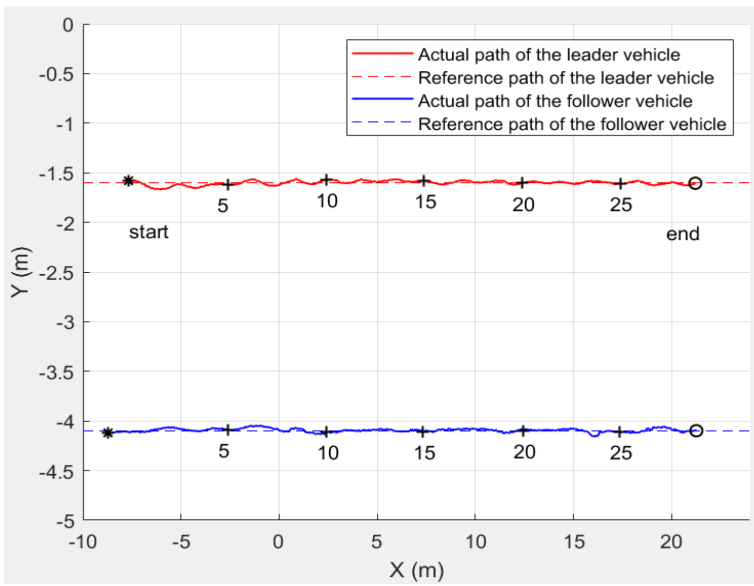

Figure 5.2 Reference and actual paths for two-vehicle straight-line tracking using the dynamic model

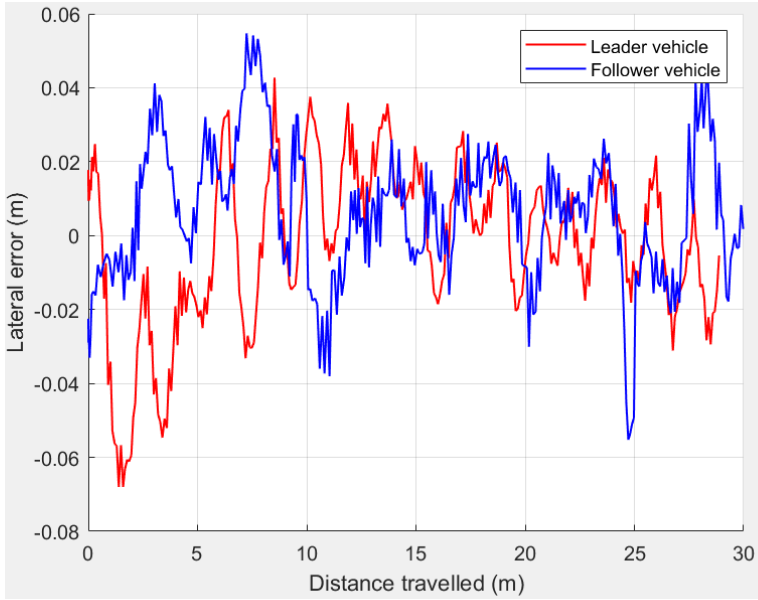

Figure 5.3 Lateral error for two-vehicle straight-line tracking using the dynamic model

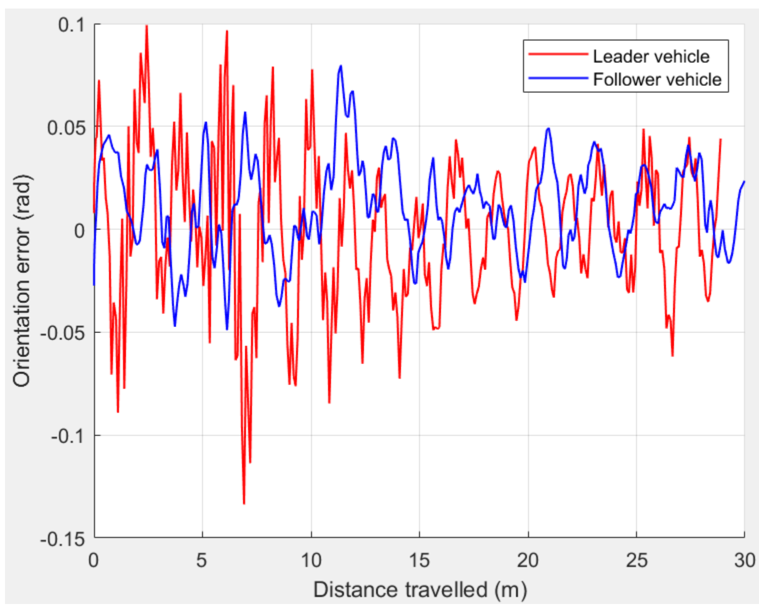

Figure 5.4 Orientation error for two-vehicle straight-line tracking using the dynamic model

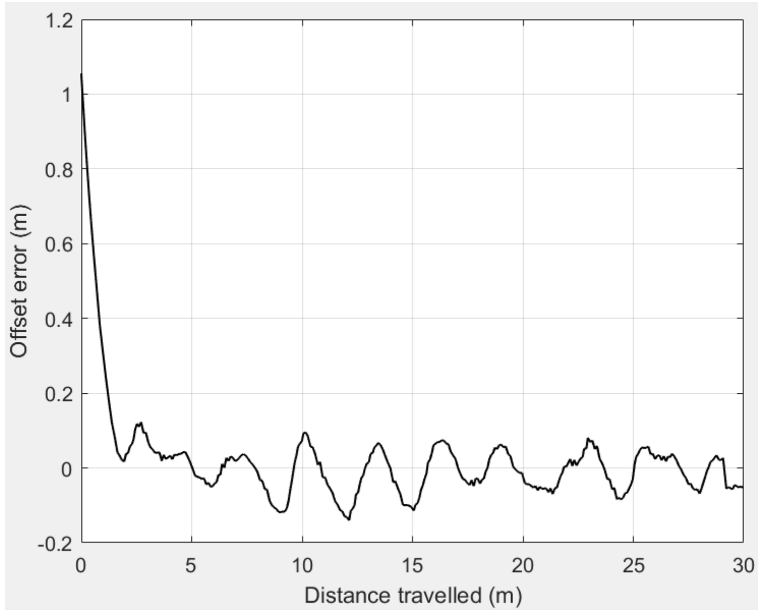

Figure 5.5 Offset error for two-vehicle straight-line tracking using the dynamic model

The periodic component visible in Figure 5.5 after the initial transient is analyzed in Section 5.2.1.3.

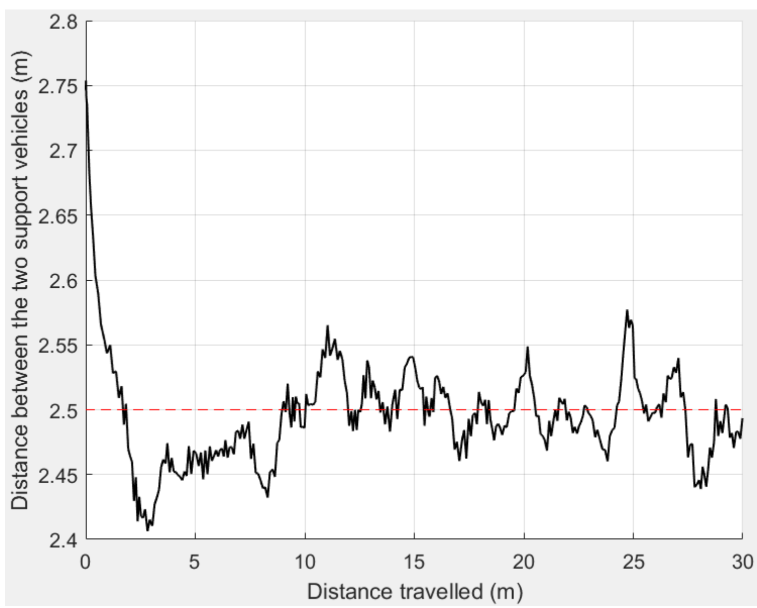

Figure 5.6 Distance between the two support vehicles for two-vehicle straight-line tracking using the dynamic model

The allowable distance between the two support vehicles is 2.0 m to 3.8 m. Figure 5.6 shows that the measured distance ranged from 2.4 m to 2.75 m, which remained within the allowable range throughout the experiment.

The IAE values were as follows:

- Lateral error $J_L^{\text{leader}} = 0.496\ \text{m}^2$, $J_L^{\text{follower}} = 0.467\ \text{m}^2$.
- Orientation error $J_\theta^{\text{leader}} = 0.842$ rad·m, $J_\theta^{\text{follower}} = 0.611$ rad·m.
- Offset error $J_e = 2.05\ \text{m}^2$.
- Separation error $J_d = 0.847\ \text{m}^2$.

5.2.1.2 Kinematic Model

This experiment was conducted on June 6, 2025. The session was run under the same conditions as the dynamic-model test above: dry pavement, light wind, no precipitation, and regional wildfire smoke that did not affect the RTK-GPS and IMU measurements.

The control gains were configured as follows:

- Control gains: $k_1 = 2.2$, $k_2 = 1.21$, $k_e = 1.3\ \text{s}^{-1}$

The results are shown in Figure 5.7 to Figure 5.11.

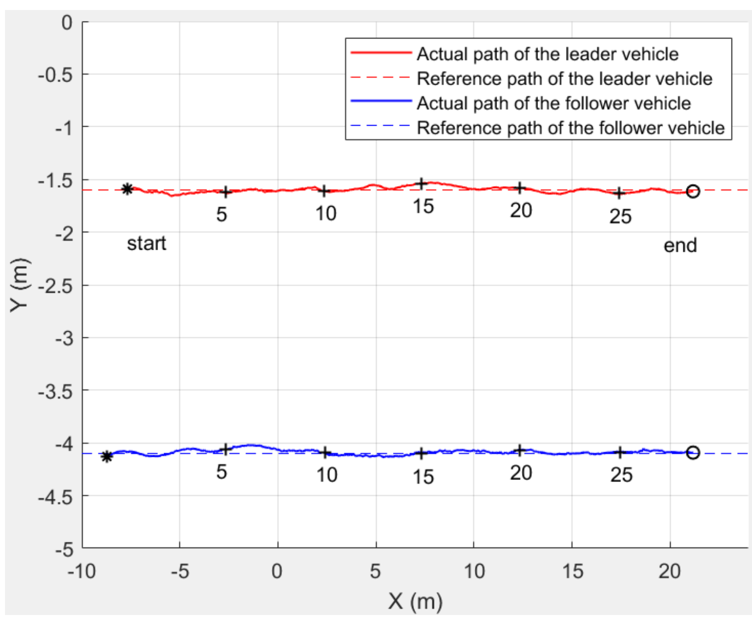

Figure 5.7 Reference and actual paths for two-vehicle straight-line tracking using the kinematic model

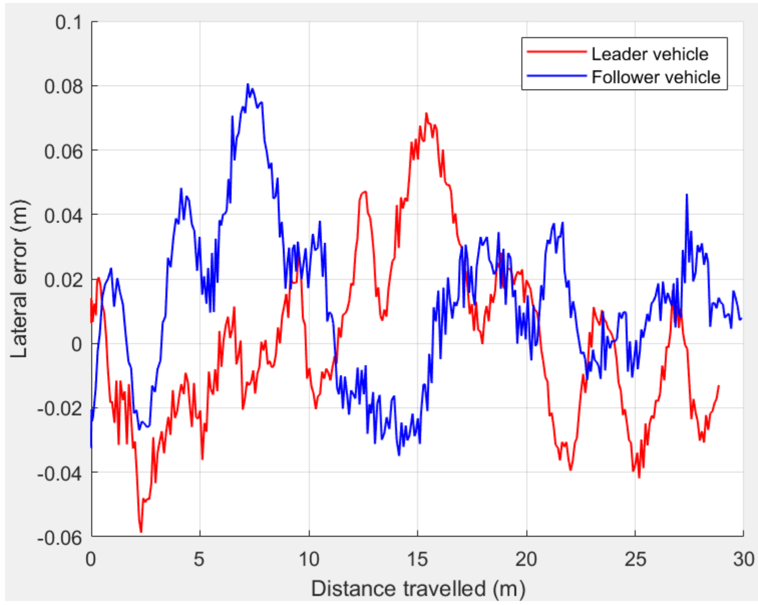

Figure 5.8 Lateral error for two-vehicle straight-line tracking using the kinematic model

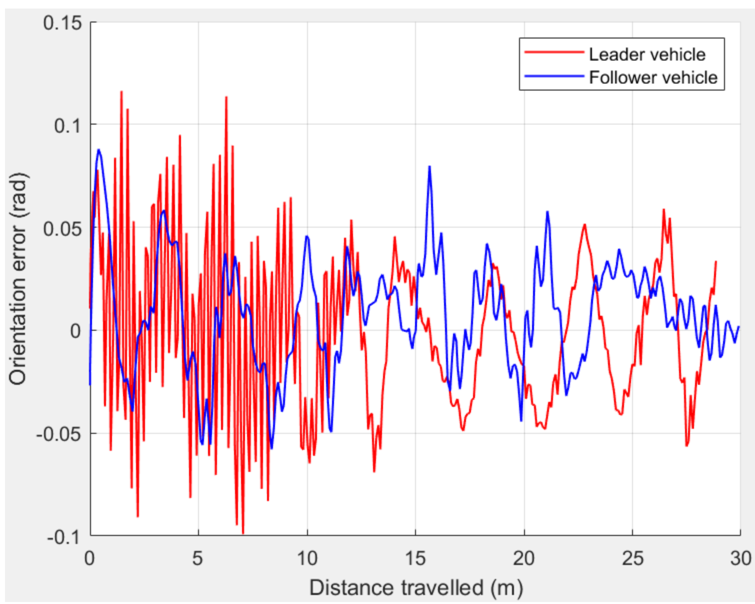

Figure 5.9 Orientation error for two-vehicle straight-line tracking using the kinematic model

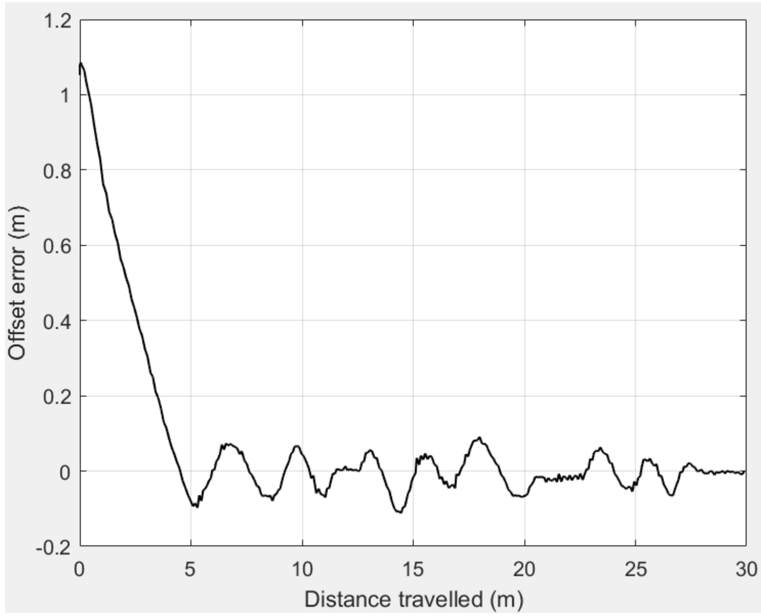

Figure 5.10 Offset error for two-vehicle straight-line tracking using the kinematic model

The offset error in Figure 5.10 contains a periodic component similar to that in the dynamic-model run; both are analyzed in Section 5.2.1.3.

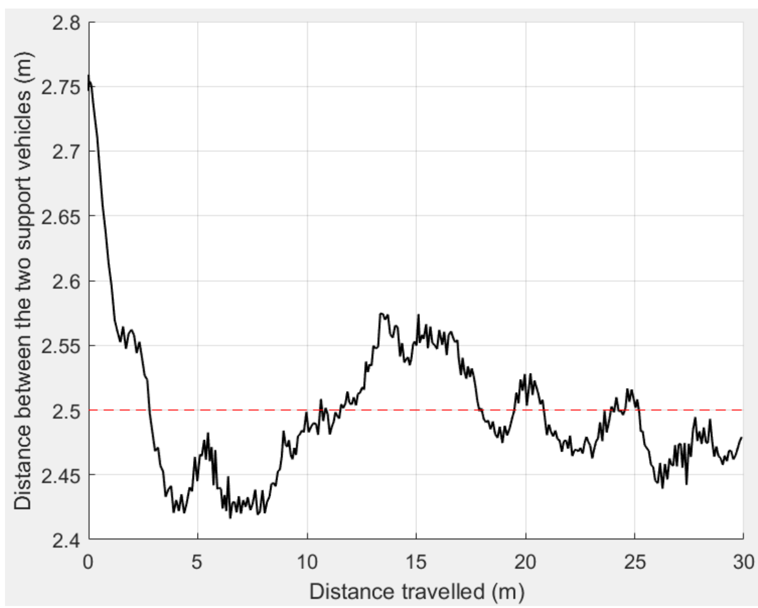

Figure 5.11 Distance between the two support vehicles for two-vehicle straight-line tracking using the kinematic model

Figure 5.11 shows that the distance between the two support vehicles ranged from 2.4 m to 2.75 m, which was also within the allowable range of 2.0 m to 3.8 m.

The IAE values were as follows:

- Lateral error $J_L^{\text{leader}} = 0.619\ \text{m}^2$, $J_L^{\text{follower}} = 0.657\ \text{m}^2$.
- Orientation error $J_\theta^{\text{leader}} = 0.924$ rad·m, $J_\theta^{\text{follower}} = 0.657$ rad·m.
- Offset error $J_e = 3.14\ \text{m}^2$.
- Separation error $J_d = 1.21\ \text{m}^2$.

5.2.1.3 Periodic Component of the Offset Error

The offset error in both straight-line runs contains a periodic component after the initial transient (Figures 5.5 and 5.10). Table 5.3 characterizes it over the steady-state segment, defined as leader distance greater than 5 m. With the dynamic-model controller, the component has a dominant frequency of 0.31 Hz, a period of 3.25 s or 3.1 m of travel at 0.96 m/s, and an amplitude of ±0.078 m; with the kinematic-model controller it has a frequency of 0.36 Hz, a period of 2.77 s or 2.7 m, and an amplitude of ±0.064 m. In both runs the component decays slowly over the 30 m path but does not disappear.

Table 5.3 Periodic component of the offset error in the two-vehicle straight-line experiments (steady-state segment, leader distance greater than 5 m)

Quantity	Dynamic model	Kinematic model
Steady-state segment (m)	5.0–28.9	5.0–28.8
Standard deviation (m)	0.054	0.042
Mean peak (m)	+0.064	+0.056
Mean trough (m)	−0.092	−0.071
Amplitude (m)	±0.078	±0.064
Dominant frequency (Hz)	0.31	0.36
Period (s)	3.25	2.77
Spatial period (m)	3.1	2.7
Follower velocity: dominant frequency (Hz)	0.31	0.36
Follower velocity: standard deviation (m/s)	0.13	0.13
Leader velocity: standard deviation (m/s)	0.047 (no low-frequency peak)	0.053 (no low-frequency peak)
Cross-correlation	0.71	0.62
Offset error vs follower velocity	offset leads by 0.7 s	offset leads by 0.5 s

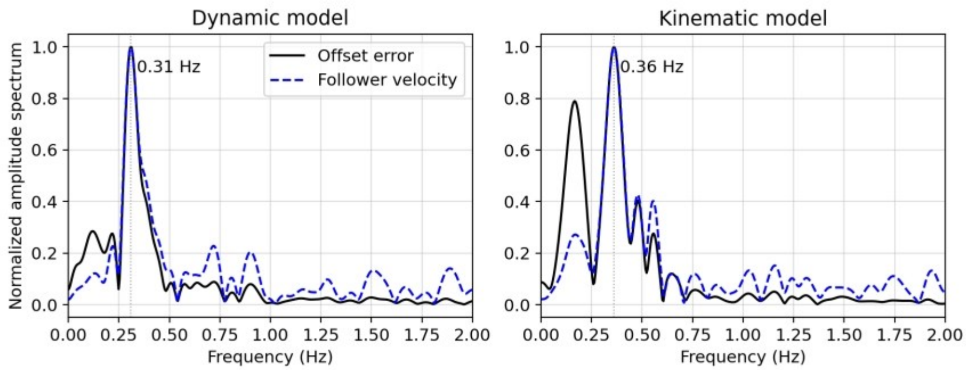

Figure 5.12 Normalized amplitude spectra of the offset error and follower velocity for both models

Figure 5.12 shows that the follower velocity carries the same component at the same frequency in each run. Over the two runs the follower velocity ranged from 0.52 to 1.38 m/s about the 1 m/s commanded velocity (0.65 to 1.29 m/s in the dynamic-model run, 0.52 to 1.38 m/s in the kinematic-model run); the mean measured velocity of both vehicles was 0.96 m/s (Table 5.2). The leader velocity has no low-frequency component and a standard deviation of only 0.047 m/s, which is the GPS speed noise. The cross-correlation between the offset error and the follower velocity peaks at 0.71 with the offset error leading by 0.7 s and by 0.5 s in the kinematic-model run, close to a quarter of the period, which is the phase relation expected between the error of a loop and the velocity that corrects it. The steering angles of both vehicles have a standard deviation of 0.04 to 0.05 rad and no spectral peak at the offset frequency. The component therefore originates in the interaction between the synchronization law and the follower velocity loop and not in the steering controller.

The mechanism can be examined with a first-order representation of the follower velocity loop. The synchronization law, Equation (90), commands the follower velocity v_2 so that its rate of progress along the path equals that of the leader plus $k_e \cdot e$; the offset error therefore obeys $\dot{e} = -k_e \cdot e$ when the follower velocity loop follows its command instantly. On the straight path ($k_{Om} = 0$) with the small heading errors of the experiments ($\cos\theta_p > 0.99$), the commanded velocity reduces to $v_2 \approx v_1 + k_e \cdot e$. If the follower velocity loop, that is the fixed-gain velocity PID, the drive and the 10 Hz GPS speed measurement, responds to its command as a first-order element with time constant τ_v, the closed offset dynamics are $\tau_v \cdot \ddot{e} + \dot{e} + k_e \cdot e = 0$, with natural frequency $\sqrt{k_e/\tau_v}$ and damping ratio $1/(2\sqrt{k_e \cdot \tau_v})$. This representation cannot reproduce the measurement exactly: for $k_e = 1.3\ \text{s}^{-1}$ the damped frequency of a first-order loop cannot exceed 1.3 rad/s (0.21 Hz), whereas 0.31 Hz (1.95 rad/s) was measured, and the loop would decay rather than persist. The measured frequency and the persistence of the component over the 30 m path therefore require additional phase lag in the follower velocity loop beyond a first-order response, such as the integral action of the velocity PID, the drive nonlinearity at low speed, and the 10 Hz update of the speed measurement. Matching the natural frequency alone, $\sqrt{k_e/\tau_v}$ = 1.95 rad/s, gives $\tau_v \approx 0.35$ s as an order-of-magnitude estimate of the effective response of the loop, an order of magnitude slower than the 0.04 s actuator response assumed in Section 4.1.4. Consistently, the amplitude of the follower velocity component, about 0.17 m/s after the GPS noise is removed, exceeds the amplitude of the correction term of the synchronization command, $k_e \times 0.078$ m ≈ 0.10 m/s, so the velocity loop amplifies the command near 0.3 Hz.

Delay is not the cause. The communication delay (0.02 s) and the actuator response (0.04 s) identified in Section 4.1.4 total 0.06 s. A pure delay τ around the synchronization loop can sustain an oscillation only when $k_e \cdot \tau \geq \pi/2$, that is $\tau \geq 1.2$ s for $k_e = 1.3$ s^{-1}, and the oscillation would then have a period of about 4τ; the measured period of 3.25 s would require $\tau \approx 0.8$ s.

The same loop model explains why the simulations show no periodic component. In the general case of Section 4.2.1 the offset error returns from its start-up peak without oscillation and remains within ± 0.014 m (Figure 4.9), because the simulated velocity loop responds within the 0.04 s actuator time constant: with $k_e = 2.5$ s^{-1} and $\tau_v = 0.04$ s the damping ratio is 1.6, so the loop is over-damped, whereas on the platform the slower and more lagged velocity loop places the same loop in the under-damped region, with the natural frequency matched at 0.31 Hz. The difference between the simulated and the experimental behaviour is therefore the difference between the assumed and the actual response of the velocity loop; the 0.04 s value used in Chapter 4 represents the actuator alone, whereas the closed velocity loop of the platform, which includes the velocity PID and the 10 Hz GPS speed measurement, responds an order of magnitude more slowly; this is recorded as a limitation in Section 6.2.

The component is present with both controllers at similar frequency and amplitude, so it does not affect the comparison of the dynamic-model and kinematic-model controllers in Section 5.3, although it contributes to the offset IAE of both. Because it is set by k_e and τ_v, it can be removed by reducing the synchronization gain or by increasing the bandwidth of the follower velocity loop; identifying the velocity-loop response of the supporting vehicles and retuning k_e and the velocity PID gains together is listed in Section 6.3.

5.2.2 Sinusoidal Trajectory Tracking

Table 5.4 presents the initial and steady-state performance values for sinusoidal cooperative tracking.

Table 5.4 Performance variables for two-vehicle sinusoidal trajectory tracking[a]

	Description	Initial value	Steady-state value (Dynamic model)	Steady-state value (Kinematic model)
Leader vehicle	Longitudinal velocity (m/s)	0	0.96	0.96
	Lateral error (m)	0.059	**±0.11**	±0.14
	Orientation error (rad)	−0.095	±0.11	**±0.089**
	Steering angle (rad)	0	−	−
Follower vehicle	Longitudinal velocity (m/s)	0	0.97	0.97
	Lateral error (m)	0.11	**±0.089**	±0.11
	Orientation error (rad)	−0.073	±0.12	**±0.098**
	Steering angle (rad)	0	−	−
	Offset error (m)	0.97	**±0.18**	±0.21
	Separation error (m)	0.44	±0.16	±0.15

[a] Boldface: notably better than the other model.

The vehicles followed the sinusoidal reference path defined as

$$
\begin{aligned}
y_1 &= 0.5 \cdot \sin \frac{\pi}{4} x_1 - 1.6 \\
y_2 &= 0.5 \cdot \sin \frac{\pi}{4} x_2 - 4.1
\end{aligned}
\tag{130}
$$

The initial conditions were: $x_1(0) = -7.61$ m, $y_1(0) = -1.39$ m, $\theta_1(0) = 0.263$ rad, $x_2(0) = -8.53$ m, $y_2(0) = -4.18$ m, $\theta_2(0) = 0.276$ rad.

5.2.2.1 Dynamic Model

This experiment was conducted on June 7, 2025. The session was run in dry conditions with light wind; no precipitation occurred during testing, and the pavement was dry and free of debris.

The control gains were configured as follows:

- Weighting parameters: $Q = [27\ 0;\ 0\ 36]$, $R = 100$
- Prediction horizon and control horizon: $N_p = 32$, $N_c = 15$
- Control gain: $k_e = 1.3\ \mathrm{s}^{-1}$

The results are shown in Figure 5.13 to Figure 5.17.

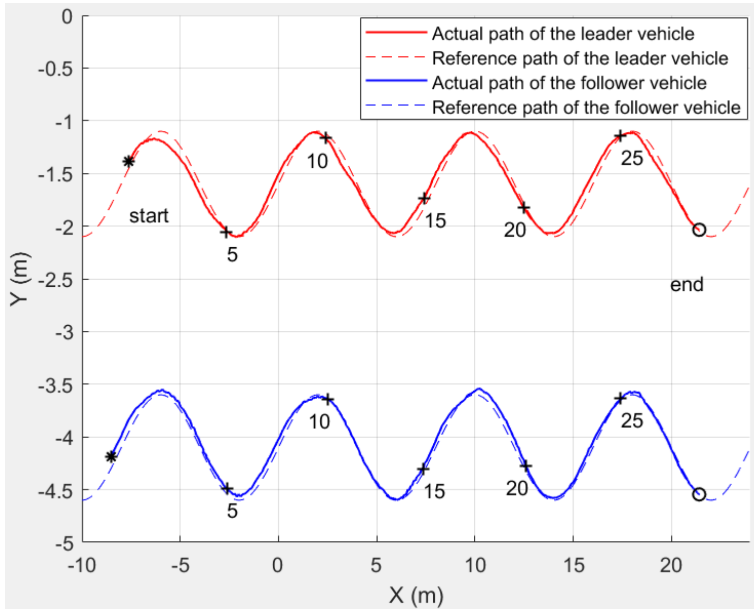

Figure 5.13 Reference and actual paths for two-vehicle sinusoidal trajectory tracking using the dynamic model

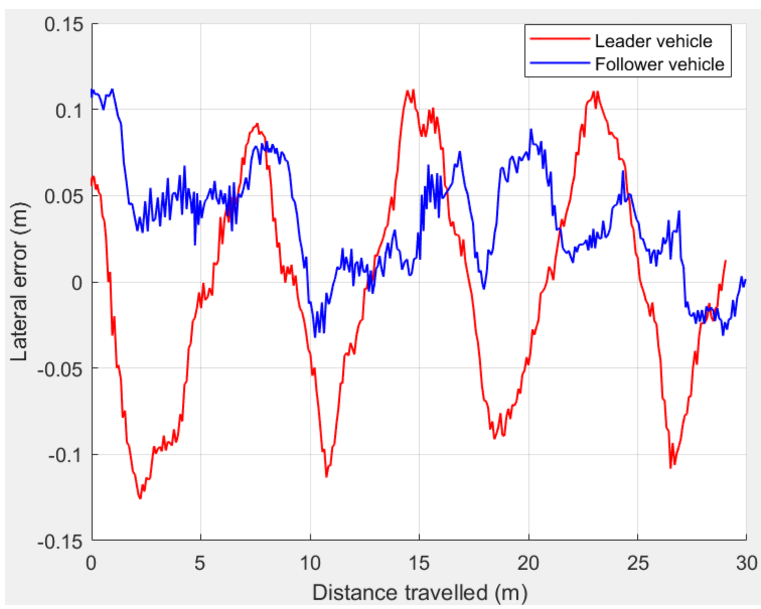

Figure 5.14 Lateral error for two-vehicle sinusoidal trajectory tracking using the dynamic model

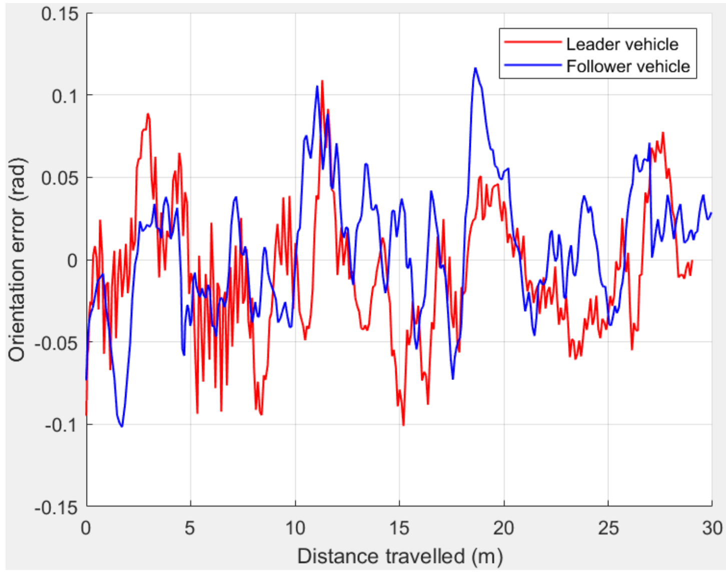

Figure 5.15 Orientation error for two-vehicle sinusoidal trajectory tracking using the dynamic model

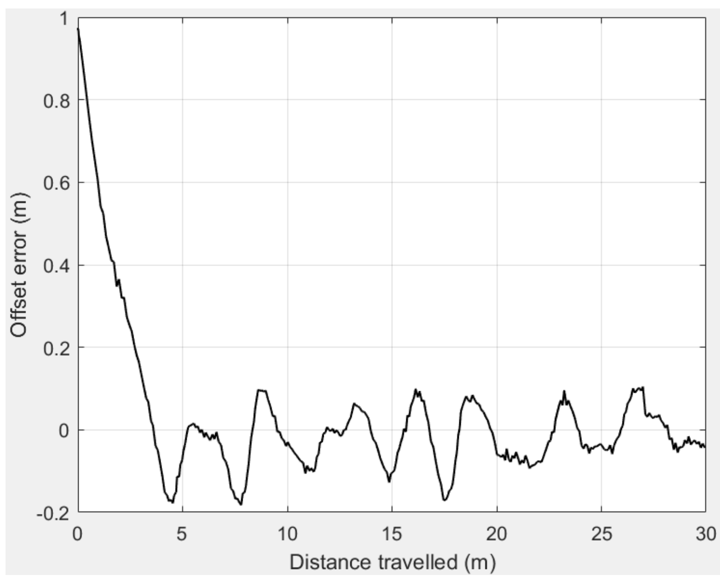

Figure 5.16 Offset error for two-vehicle sinusoidal trajectory tracking using the dynamic model

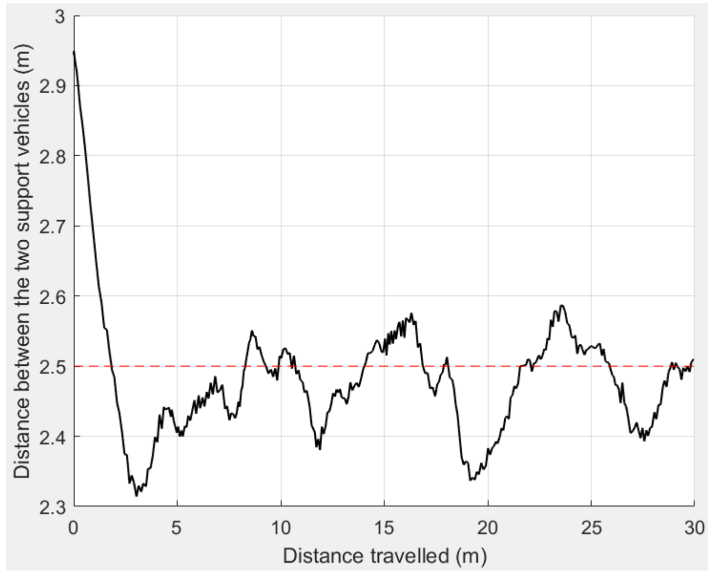

Figure 5.17 Distance between the two support vehicles for two-vehicle sinusoidal trajectory tracking using the dynamic model

Figure 5.17 shows that the distance between the two support vehicles ranged from 2.3 m to 2.95 m, which remained within the allowable range of 2.0 m to 3.8 m.

The IAE values were as follows:

- Lateral error $J_L^{\text{leader}} = 1.60\ \text{m}^2$, $J_L^{\text{follower}} = 1.18\ \text{m}^2$.
- Orientation error $J_\theta^{\text{leader}} = 0.969$ rad·m, $J_\theta^{\text{follower}} = 0.972$ rad·m.
- Offset error $J_e = 3.02\ \text{m}^2$.
- Separation error $J_d = 1.91\ \text{m}^2$.

5.2.2.2 Kinematic Model

This experiment was conducted on June 8, 2025. The session was run in dry conditions with light wind; no precipitation occurred during testing, and the pavement was dry and free of debris.

The control gains were configured as follows:

- Control gains: $k_1 = 1.8$, $k_2 = 0.81$, $k_e = 1.3\ \text{s}^{-1}$

The results are shown in Figure 5.18 to Figure 5.22.

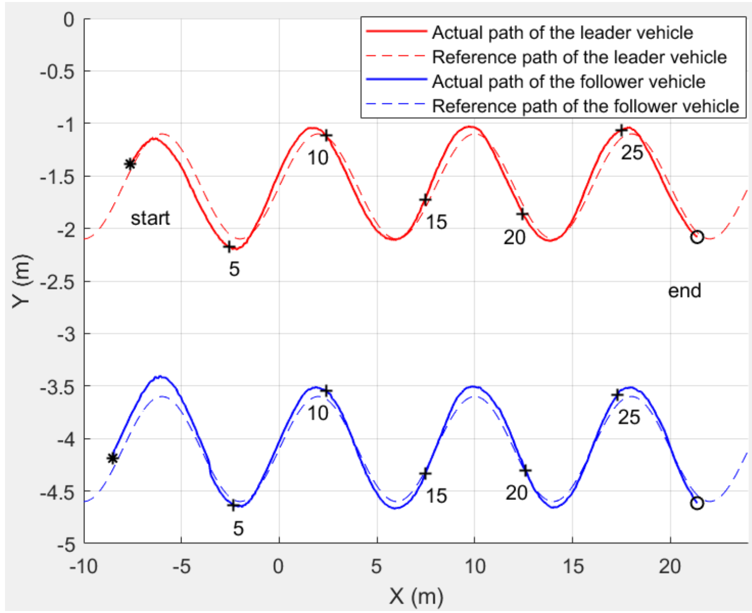

Figure 5.18 Reference and actual paths for two-vehicle sinusoidal trajectory tracking using the kinematic model

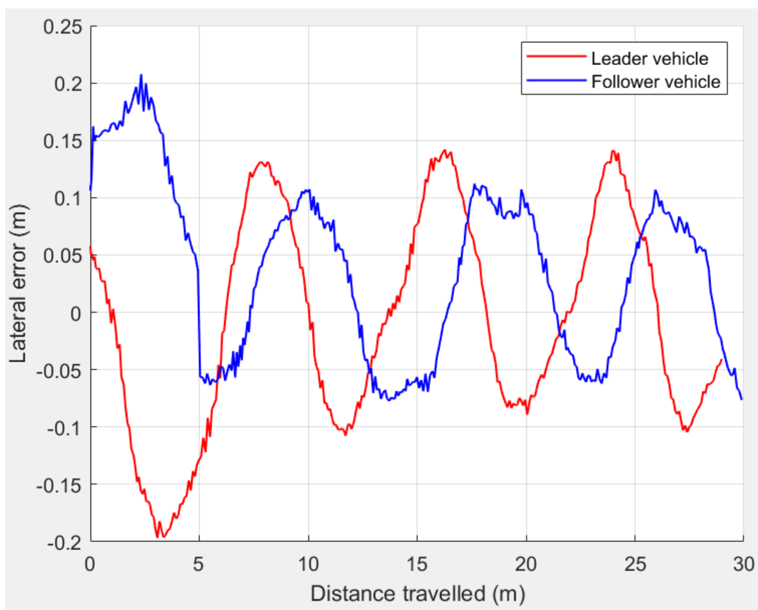

Figure 5.19 Lateral error for two-vehicle sinusoidal trajectory tracking using the kinematic model

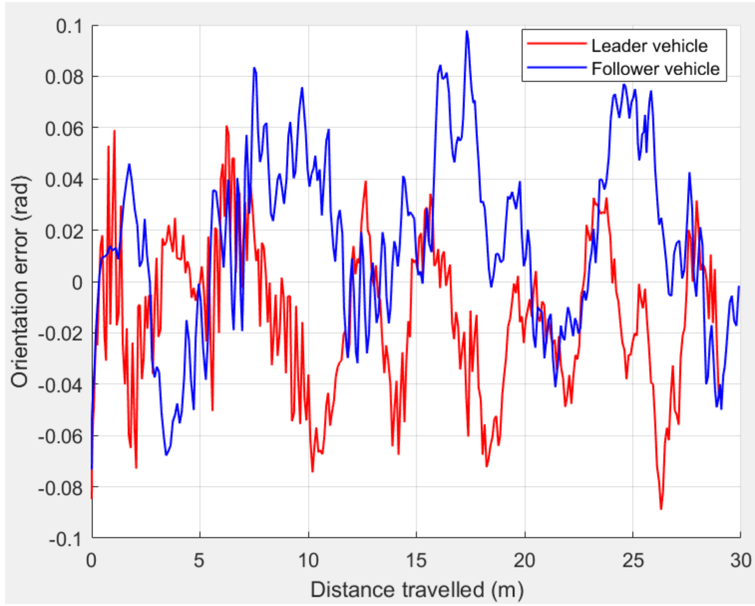

Figure 5.20 Orientation error for two-vehicle sinusoidal trajectory tracking using the kinematic model

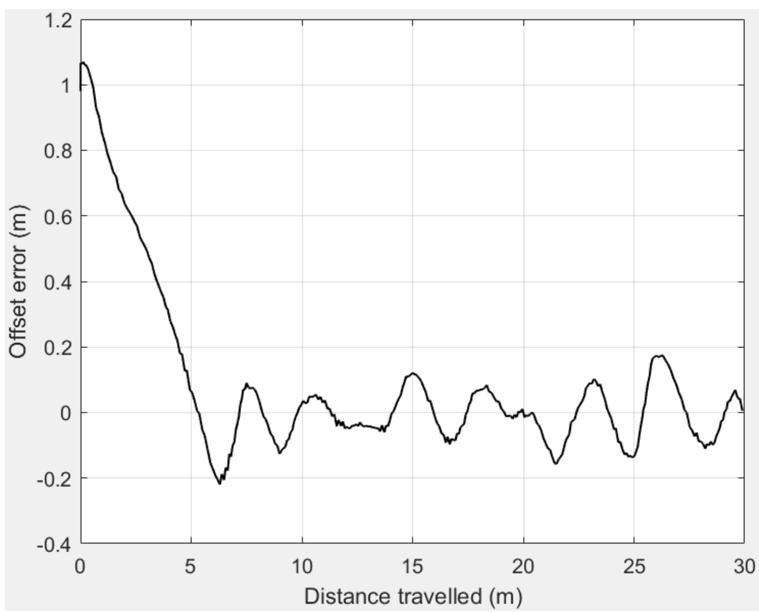

Figure 5.21 Offset error for two-vehicle sinusoidal trajectory tracking using the kinematic model

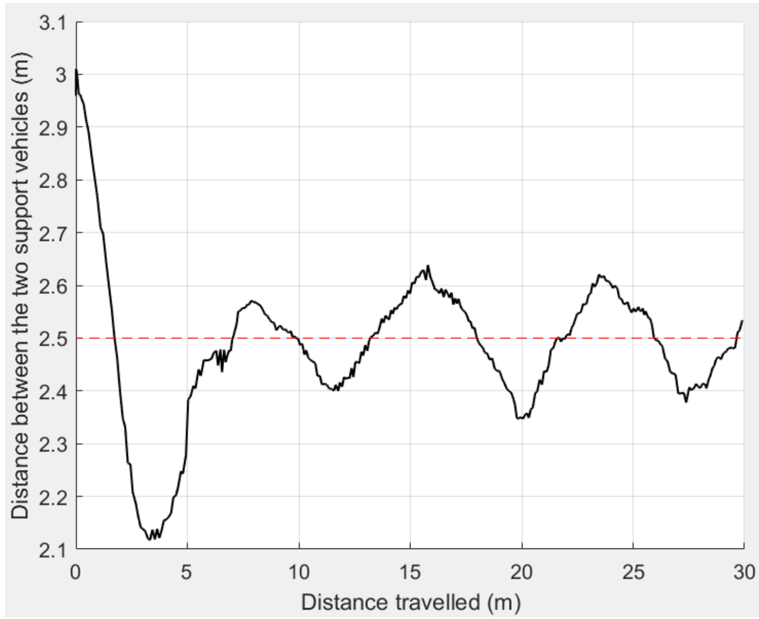

Figure 5.22 Distance between the two support vehicles for two-vehicle sinusoidal trajectory tracking using the kinematic model

Figure 5.22 shows that the distance between the two support vehicles ranged from 2.1 m to 3.0 m, which was within the allowable range of 2.0 m to 3.8 m.

The IAE values were as follows:

- Lateral error $J_L^{\text{leader}} = 2.32\ \text{m}^2$, $J_L^{\text{follower}} = 2.17\ \text{m}^2$.
- Orientation error $J_\theta^{\text{leader}} = 0.759$ rad·m, $J_\theta^{\text{follower}} = 0.944$ rad·m.
- Offset error $J_e = 4.51\ \text{m}^2$.
- Separation error $J_d = 2.92\ \text{m}^2$.

5.3 Experimental Results Comparison

The experimental results highlight the differences between the dynamic and kinematic models in terms of tracking accuracy and cooperative stability. The comparison covers two-vehicle cooperative tracking on straight-line and sinusoidal trajectories; the single-vehicle comparison is given in Appendix B.1. Differences between the two models are assessed against the practical-significance thresholds defined in Section 4.2: 0.01 m for lateral error, 0.0087 rad for orientation error, and 0.014 m for offset and separation error in steady state, and, for the IAE metrics, the IAE that a constant error equal to the sensor accuracy would accumulate over the 30 m experimental path, that is, 0.30 m² for lateral error, 0.26 rad·m for orientation error, and 0.42 m² for offset and separation error. Differences smaller than these thresholds are within the resolution of the RTK-

GPS and IMU that measured them and are reported as such; differences larger than the thresholds are compared with the instantaneous error bounds of Section 3.4.

5.3.1 Two-Vehicle Cooperation

5.3.1.1 Straight Line

The experimental trajectories for two-vehicle straight-line tracking using the dynamic and kinematic models are shown in Figure 5.23.

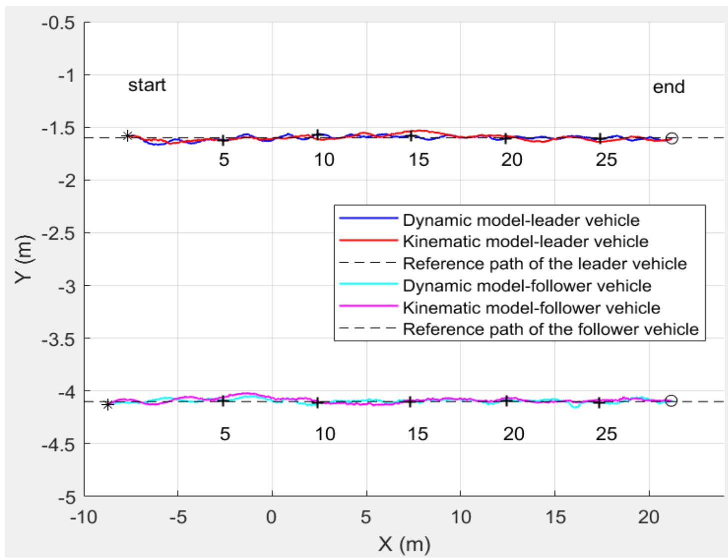

Figure 5.23 Experimental trajectories based on dynamic and kinematic models of the two-vehicle straight-line tracking

Based on Section 5.2.1, Table 5.2 and Figure 5.23, the dynamic model provided practically better lateral tracking than the kinematic model for both the leader and follower vehicles, at the cost of a resolvable increase in leader heading error. For the leader vehicle, the steady-state lateral error was 40% smaller with the dynamic model ($\pm$0.043 m vs. $\pm$0.072 m), a difference of 0.029 m that is well above the 0.01 m threshold. The steady-state orientation error was larger for the dynamic model ($\pm$0.13 rad vs. $\pm$0.11 rad); the 0.02 rad difference exceeds the 0.0087 rad accuracy and is therefore a real trade-off, although both values remain within the $\pm$0.15 rad bound. The dynamic model also produced 20% lower lateral error IAE (0.496 vs. 0.619 m^2) and 9% lower orientation error IAE (0.842 vs. 0.924 rad·m); these differences, 0.12 m^2 and 0.082 rad·m, are below the 0.30 m^2 and 0.26 rad·m IAE thresholds and are within measurement resolution, so the leader comparison rests on the steady-state lateral error.

Similar trends were observed for the follower vehicle. The steady-state lateral error was 32% smaller with the dynamic model ($\pm$0.055 m vs. $\pm$0.081 m), a resolvable difference of 0.026 m. The steady-state orientation error was identical for both models ($\pm$0.080 rad). The dynamic model reduced lateral error IAE by 29% (0.467 vs. 0.657 m²), but the difference of 0.19 m² is below the 0.30 m² threshold, and the 7% reduction in orientation error IAE (0.611 vs. 0.657 rad·m, a difference of 0.046 rad·m) is likewise within measurement resolution; as for the leader, the resolvable evidence is the steady-state lateral error.

The offset and separation errors decreased from their initial values to steady-state values within the $\pm$0.30 m bounds for both models. In steady state the kinematic model held the smaller offset error ($\pm$0.11 m vs. $\pm$0.14 m), a resolvable difference of 0.03 m, while the separation errors ($\pm$0.077 m vs. $\pm$0.084 m) differ by less than the 0.014 m threshold. Over the whole run, however, the dynamic model produced substantially lower accumulated errors: offset error IAE was 35% lower (2.05 vs. 3.14 m²), a difference of 1.09 m² that is well above the 0.42 m² formation IAE threshold, whereas the 30% lower separation error IAE (0.847 vs. 1.21 m², a difference of 0.36 m²) falls just below it and is reported as indicative. The dynamic model therefore reached the formation with smaller offset deviations during the manoeuvre but settled to a slightly larger residual offset. Overall, the straight-line experiments showed that the dynamic model improved steady-state lateral tracking by 32 to 40% and accumulated offset error by 35%, with a resolvable trade-off in leader heading error and residual offset.

These differences follow from what each controller represents. The dynamic-model-based steering MPC predicts the lateral and yaw response of the vehicle, including tire slip, so its steering corrections anticipate the vehicle's response and the lateral error settles closer to the path; the kinematic controller corrects only the geometric error and settles with a larger residual. The larger leader heading error with the dynamic model is the counterpart of this behaviour: the fixed weighting matrices used in the experiments were set to emphasize lateral error reduction, so the controller accepts a slightly larger heading deviation in order to hold the path more tightly. In formation control, the lower accumulated offset error of the dynamic model reflects the follower's closer tracking of its velocity command during the approach to the formation, the same behaviour observed in simulation under an initial offset (Section 4.2.8), whereas the smaller residual offset of the kinematic model in steady state is a difference of 0.03 m at the limit of what the experiment resolves.

5.3.1.2 Sinusoidal Trajectory

The experimental trajectories for two-vehicle sinusoidal tracking using the dynamic and kinematic models are shown in Figure 5.24.

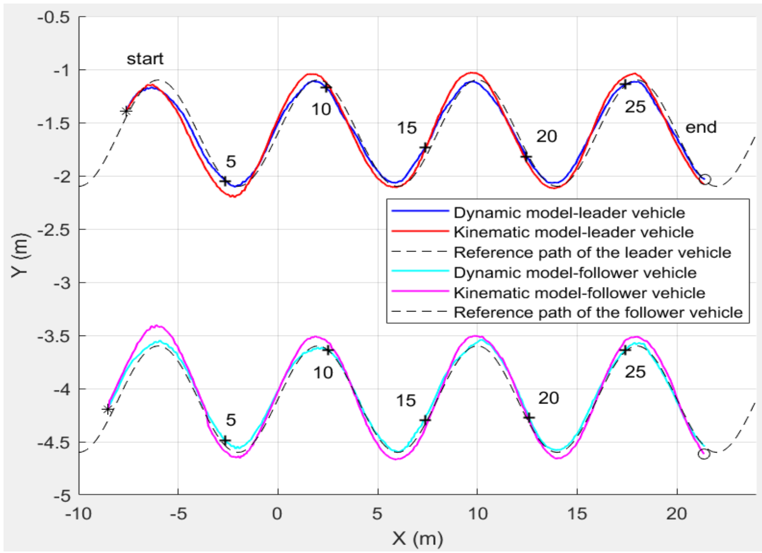

Figure 5.24 Experimental trajectories based on dynamic and kinematic models of the two-vehicle sinusoidal trajectory

Based on Section 5.2.2, Table 5.4 and Figure 5.24, the dynamic model again achieved practically lower lateral errors for both the leader and follower vehicles than the kinematic model. For the leader, the steady-state lateral error was 21% lower (± 0.11 m vs. ± 0.14 m), and for the follower 19% lower (± 0.089 m vs. ± 0.11 m); both differences (0.03 m and 0.021 m) exceed the 0.01 m threshold, and the kinematic leader value of ± 0.14 m approaches the ± 0.15 m bound while the dynamic values stay clear of it. Lateral error IAE improved by 31% for the leader (1.60 vs. 2.32 m^2) and 46% for the follower (1.18 vs. 2.17 m^2), differences of 0.72 m^2 and 0.99 m^2 that are far above the lateral IAE threshold.

However, in sinusoidal tracking, the steady-state orientation error was larger for the dynamic model for both the leader (± 0.11 vs. ± 0.089 rad, a 24% increase) and the follower (± 0.12 vs. ± 0.098 rad, a 22% increase); both differences, 0.021 and 0.022 rad, exceed the 0.0087 rad threshold and are therefore real, although all four values remain within the ± 0.15 rad bound. The orientation error IAE also increased for the dynamic model, for the leader from 0.759 to 0.969 rad·m (a 28% increase) and for the follower from 0.944 to 0.972 rad·m (a 3% increase); both differences (0.21 and 0.028 rad·m) are below the 0.26 rad·m threshold, so the resolvable part of the trade-off is the steady-state heading error. This trade-off resulted from the control gains, which emphasized lateral error reduction and therefore improved path adherence at the expense of some orientation accuracy. Such a trade-off may be acceptable or even desirable depending on the operational objective, provided the orientation bound is respected, as it was here.

Despite this difference in orientation error, the dynamic model yielded lower formation errors. In steady state its offset error was ± 0.18 m against ± 0.21 m for the kinematic model, a resolvable difference of 0.03 m, with both within the ± 0.30 m bound; the steady-state separation errors (± 0.16 m vs. ± 0.15 m) differ by less than the 0.014 m threshold. The accumulated errors favoured the dynamic model clearly: offset error IAE was 33% lower (3.02 vs. 4.51 m^2) and separation error IAE 35% lower (1.91 vs. 2.92 m^2), differences of 1.49 m^2 and 1.01 m^2 that are far above the 0.42 m^2 formation IAE threshold. These results indicate that the dynamic model provided practically better cooperative tracking on the sinusoidal path, particularly in maintaining formation integrity during curved motion, with formation IAE improvements exceeding 30% even though orientation errors increased by a resolvable but bounded amount.

On the sinusoidal path the mechanism is the same but its effect is larger. The continuously changing curvature keeps the lateral dynamics excited, so the anticipatory steering of the dynamic model reduces both the steady-state lateral error and the lateral error IAE by resolvable margins, and the follower, which tracks a virtual path generated from the leader's motion, benefits most (46% lower lateral error IAE). The heading trade-off is also larger, for the same reason as on the straight path, and remains within the ± 0.15 rad bound. The formation IAE improvements of 33 to 35% show that the tighter lateral tracking of both vehicles translates into a more consistent relative position during curved motion, which is the condition under which the sliding joint is most exercised.

5.3.2 Analysis of Experimental Results

Taken together, the experiments reproduce the pattern found in simulation. On the straight path the two controllers differ resolvably in steady-state lateral error, with a resolvable but bounded increase in leader heading error for the dynamic model, and not in lateral error IAE for either vehicle; on the sinusoidal path the dynamic-model-based controller is resolvably better in lateral tracking and formation control for both vehicles, and the kinematic controller's leader lateral error approaches the ± 0.15 m bound. The experimental advantage of the dynamic model in lateral tracking (steady-state lateral error 19 to 40% lower; sinusoidal lateral error IAE 31 to 46% lower) is of the same order as its curved-path advantage in simulation (Section 4.2.9), and the orientation trade-off observed in simulation on curved paths (Section 4.2.2) is likewise observed experimentally, which supports the conclusion that the simulations captured the behaviour of the two controllers on the physical platform. The comparison with Chapter 4 is qualitative, because the experimental steering MPC used fixed weights whereas the simulated controller used the adaptive weighting of Section 3.3.1.5 (tuned in Section 4.1.5); the experiments therefore validate the dynamic-model-based MPC–PID structure, not the adaptive weighting strategy itself.

The results also indicate when each controller is preferable. Where the path is straight and the initial alignment is good, the kinematic controller is adequate: its errors stay within the Section 3.4 bounds and its heading regulation is marginally better, so its simpler tuning and lower computational demand could justify its use for straight passes. Where the path curves, where the vehicles must recover a formation, or where lateral accuracy relative to the traffic lane is the binding requirement, the dynamic-model-based controller is preferable: it holds the lateral error further from the bound and accumulates 33 to 35% less formation error, at the cost of a bounded increase in heading error that could be traded back through the weighting if heading were the priority.

Three qualifications apply. The experiments also retain the scenario-dependent horizons of the fixed-weight design ($N_p = 23$, $N_c = 10$ on straight paths; $N_p = 32$, $N_c = 15$ on curved paths), which differ from the single set used in simulation for the reason given in Section 4.1.5. All experimental differences are evaluated against the sensor accuracies of Section 5.1.2, and heading differences below the static accuracy of the IMU are not claimed; the periodic component of the offset error analyzed in Section 5.2.1.3 is present with both controllers (0.31 and 0.36 Hz, ± 0.078 and ± 0.064 m) and does not affect the comparison; it originates in the follower velocity loop, whose effective response is of the order of 0.35 s and carries more phase lag than the 0.04 s first-order actuator response assumed in the simulations, and it is one reason why the experimental offset IAE values exceed the simulated ones. The experiments cover forward motion on a dry pavement without externally applied implement resistance, so the loaded, low-adhesion and reverse conditions compared in Chapter 4 remain simulation results, as discussed in Section 6.2.

Chapter 6

Conclusion

6.1 Summary of Contributions

This research presents an applied, systems-engineering integration of dynamic modelling, control design, simulation, and experimental validation for the supporting vehicles of a WSIC platform. The key original contributions are summarized as follows.

1. Development of a dynamic model for the WSIC

A dynamic model of the WSIC supporting vehicles was developed, with the connecting truss and mobile carriage represented as a quasi-static load path that transmits their self-weight and the implement loads to the vehicles. The model explicitly incorporated longitudinal and lateral dynamics, yaw motion, and tire–ground interaction forces, as formulated through the force balance and Equations (10), (11), (19), and (24) to (29).

In contrast to the kinematic formulation of Luo (2017), which neglected inertial and force effects, the proposed model accounted for velocity-dependent dynamics, yaw-rate evolution, and coupling between translational and rotational motion. This established a force-based prediction framework for analyzing transient WSIC motion and designing the control strategy under varying operating conditions. Building on established tire-force and yaw-dynamics formulations, the research extended dynamic vehicle modelling to the coupled WSIC configuration. To the author's knowledge, this is the first dynamic model developed specifically for the WSIC vehicle–truss–vehicle structure. Its contribution is the explicit representation of the supporting-vehicle dynamics, together with the loads transmitted through the connecting assembly, that coordinated control requires; the inertia of the truss, carriage and implement is not represented (Section 6.2).

2. Derivation of the theoretical motions of the supporting vehicles

The theoretical motion relationships of the two supporting vehicles were derived within a differential geometric framework tailored to the WSIC configuration. The leader trajectory was defined as an adjoint curve of the reference path, while the follower trajectory was generated as a function of the leader's instantaneous state. The formulation was supported by the equations of motion for the supporting vehicles and the implement trajectory, as described in Equations (35) to (59), while the longitudinal offset relationship between the two vehicles was defined in Equations (60) and (61). Together, these derivations establish a consistent description of WSIC motion in curvilinear coordinates and connect the reference-path geometry to the required vehicle trajectories.

The adjoint-curve method was used to derive the kinematic error dynamics of a four-wheeled agricultural support vehicle following a curved path. Combining this formulation with ICR kinematics related path geometry to vehicle velocities and accelerations. The single-vehicle formulation was then extended to the WSIC leader–follower configuration, providing the mathematical basis for coordinated path tracking with adjustable inter-vehicle separation.

Synchronization between the supporting vehicles is quantified by the path-coordinate offset error. Luo (2017) had defined this offset and regulated it with a first-order law for straight-path progression; the present formulation extends it to curvature-dependent path-coordinate progression within the adjoint-curve framework, giving an explicit state-dependent relationship between leader and follower motion on curved paths rather than treating their trajectories as independent path-following problems. The resulting formulation makes coordinated motion and formation-error regulation part of the WSIC guidance problem and provides the basis for the synchronization controller.

3. Control strategy design for the supporting vehicles of the WSIC

A combined guidance and control strategy was designed for the supporting vehicles of the WSIC. It integrates incremental MPC-based steering, direction-sensitive adaptive weighting, PID-based longitudinal-velocity regulation, and offset-error-based synchronization. This WSIC-specific control design addresses individual-vehicle tracking and inter-vehicle coordination within a single implementable architecture.

For steering control, an incremental MPC formulation was developed using lateral and longitudinal velocities, yaw angle, yaw rate, and global position. The controller was implemented directly in MATLAB/Simulink rather than through the built-in MATLAB MPC Toolbox, allowing the prediction model, steering constraints, and adaptive weighting logic to be specified explicitly (Section 4.1.2). Optimizing the steering-angle increment subject to magnitude and rate constraints provided direct regulation of steering changes within actuator limits. The adaptive weighting strategy adjusted control priorities online according to operating condition and direction of travel, emphasizing lateral path convergence during forward motion and heading stabilization during reverse motion.

For inter-vehicle coordination, a synchronization control law was derived from the offset-error formulation. The derivation yielded first-order closed-loop synchronization-error dynamics and an explicit Lyapunov-based stability analysis. The follower combined this synchronization law with the MPC-based steering strategy, incorporating formation regulation directly into the control design. This linked the coordinated-motion derivation to a closed-loop control law for the physically coupled WSIC.

Together, these developments established an integrated control approach combining predictive steering, adaptive tracking priorities, longitudinal speed regulation, and synchronization. Its implementation and evaluation connected the theoretical design to autonomous operation of the experimental platform. Distance-integrated absolute error metrics for lateral tracking, orientation, longitudinal offset, and inter-vehicle separation provided a quantitative assessment of both individual-vehicle tracking and cooperative performance.

4. Simulation validation of the dynamic-model-based control strategy

The proposed control strategy was validated through a systematic MATLAB/Simulink and CarSim simulation study. Sensor noise, system delays, and model uncertainties were explicitly incorporated into the control loop using reproducible random sequences. FWS was used for most scenarios, while RWS was used for the reverse-direction tests, extending the evaluation to bidirectional WSIC motion.

A metric-based comparison with the kinematic control approach of Luo (2017) quantified the performance benefits of the dynamic-model-based strategy. The comparison covered concrete, earth-road, and grass surfaces; different speeds; externally applied loads and attachment configurations; straight and curved trajectories; forward and reverse motion; and cases with and without initial offset error. This scenario-based evaluation established how the proposed control strategy performed across the range of simulated operating conditions.

The simulation results, assessed against the sensor-based practical-significance thresholds defined in Section 4.2, demonstrated resolvable improvements in lateral tracking and formation control relative to the kinematic benchmark in the demanding scenarios. During curved-trajectory tracking, the dynamic-model-based controller reduced the steady-state lateral error from ± 0.20 m, outside the ± 0.15 m bound, to ± 0.12 m, inside it, and reduced lateral-error IAE by approximately 46.2% for the leader and 45.8% for the follower and offset-error IAE by 50.1%. During curved reverse tracking, lateral-error IAE decreased by approximately 34.0% for the leader and 35.6% for the follower, and offset-error IAE from 1.79 to 0.926 m^2. These results demonstrate improved coordinated tracking when path curvature and reverse motion were combined in simulation, while both controllers exceeded the orientation bound on curved paths and both bounds in curved reverse motion, which motivates the four-wheel-steering configuration recommended in Section 4.2.3.2

Across the straight-line scenarios, which varied ground adhesion, target speed, implement resistance, implement position, and initial formation error, both controllers tracked the path to within the resolution of the platform sensors, and the differences between them in lateral and orientation error were not practically meaningful; the resolvable effect of these conditions was on formation regulation. The dynamic-model-based controller maintained lower offset-error IAE at medium and high speed (0.583 vs. 1.16 m^2 and 1.09 vs. 2.12 m^2), under 50 N and 200 N path-opposing implement resistance (0.583 vs. 1.16 m^2 and 0.812 vs. 1.51 m^2), and in both implement configurations (0.668 vs. 1.26 m^2 for the follower-proximal case), and with a large initial offset error it reduced offset-error IAE from 9.37 to 4.31 m^2 and separation-error IAE from 1.54 to 0.467 m^2, demonstrating improved recovery from a non-ideal initial formation. The kinematic controller also showed the larger relative degradation with decreasing adhesion and increasing speed, a trend that is indicative of its omitted slip and speed dependence although the absolute differences remained below the thresholds on the straight path.

An additional comparison against unified MPC showed the advantage of the combined design where the tracking problem is demanding. During curved tracking, MPC–PID reduced the steady-state lateral error from ± 0.16 m, outside the ± 0.15 m bound, to ± 0.12 m, inside it; reduced lateral-error IAE from 2.04 to 1.47 m^2 for the leader and from 2.04 to 1.48 m^2 for the follower; and reduced the steady-state offset error from ± 0.064 m to ± 0.038 m. Under high-speed straight-line operation the two designs were equivalent at the sensor level, with a marginal advantage in accumulated offset error for the combined design. These gains characterize the complete combined controller, including its adaptive steering weights, relative to the fixed-weight unified MPC. The orientation-error and steady-state-offset trade-offs, together with the achieved-speed differences, are discussed in Section 4.3.

Overall, the simulation study demonstrated the value of incorporating vehicle dynamics into coordinated WSIC control in the conditions where it matters: curved and reverse motion, higher speed, implement loading, and recovery from initial formation errors. It quantified improvements in lateral tracking and offset regulation against thresholds derived from the sensor accuracy of the platform, and it identified the conditions, straight-line tracking at low speed on firm ground, in which the simpler kinematic controller is equivalent at the sensor level. The evaluation complements the physical experiments and provides a systematic basis for further controller development and field evaluation.

5. Experimental validation on a scaled WSIC platform

The proposed control strategy was implemented and experimentally validated on a physically connected small-scale WSIC platform equipped with RTK-GPS, an IMU, wireless communication modules, and embedded controllers. The connecting truss retained the mechanical interaction between the two supporting vehicles, extending the evaluation from numerical simulation to closed-loop operation of the coupled system. Both vehicles used FWS, and the experiments included straight-line and sinusoidal forward trajectories on a relatively flat pavement/concrete surface, with no externally applied implement resistance. The tests therefore exercised the controller with the actual truss self-weight, physical coupling, and experimental hardware.

The physical experiments, assessed against the same thresholds, demonstrated resolvable improvements in lateral tracking relative to the kinematic controller during two-vehicle cooperation, with steady-state lateral errors 0.02 to 0.03 m lower and all values within the ± 0.15 m bound:

- On straight-line paths, steady-state lateral error was reduced by 40% for the leader and 32% for the follower; the accompanying lateral-error IAE reductions of 20% and 29% were within measurement resolution.
- On sinusoidal paths, steady-state lateral error was reduced by 21% for the leader and 19% for the follower, and lateral-error IAE by 31% and 46%.

The dynamic-model-based controller also improved formation regulation:

- Offset-error IAE was reduced by 35% on straight-line paths; the 30% reduction in separation-error IAE was just below the measurement-resolution threshold.
- On sinusoidal paths, offset-error and separation-error IAE were reduced by 33% and 35%.

These experiments established an experimental basis for improved tracking and formation control on the physically coupled small-scale WSIC. The improvement came with a resolvable trade-off: the dynamic-model-based controller produced steady-state orientation errors about 0.02 rad larger than the kinematic controller (for the leader on the straight-line path and for both vehicles on the sinusoidal path), and a slightly larger residual offset on the straight-line path, all within the Section 3.4 bounds. The results show that the advantages of the dynamic-model-based controller extended beyond simulation to operation with real sensing, communication, and control hardware. Together, the modelling, coordinated-motion derivations, controller implementation, comparative simulations, and physical experiments form an integrated contribution to autonomous WSIC control. The scope for extending this validation to additional implement loading, reverse operation, and field-scale conditions is set out in Sections 6.2 and 6.3.

Publications

Portions of this research have been peer-reviewed and published as follows:

- Li, X., Laguë, C., & Uchida, T. (2023). Integration of model predictive control and proportional–integral–derivative strategies for the autonomous path tracking of agricultural wide-span implement carriers. Proceedings of the 2023 IEEE International

Symposium on Robotic and Sensors Environments (ROSE) (pp. 1-7). IEEE. https://doi.org/10.1109/ROSE60297.2023.10410680

- Li, X., Laguë, C., & Uchida, T. (2026a). Autonomous control of agricultural wide-span implement carriers (WSIC), Part 1: Development and validation of a hybrid dynamic control strategy. Applied Engineering in Agriculture, 42(4), 367-376. https://doi.org/10.13031/aea.16553
- Li, X., Laguë, C., & Uchida, T. (2026b). Autonomous control of agricultural wide-span implement carriers (WSIC), Part 2: Dynamic vs. kinematic control strategies. Applied Engineering in Agriculture, 42(4), 377-386. https://doi.org/10.13031/aea.16571

6.2 Limitations

The simulations and physical experiments demonstrated the effectiveness of the proposed control strategy for the scenarios examined. The following modelling, experimental, and scale-related limitations define the conditions for extending these results to broader WSIC operation.

1. Modelling assumptions

The dynamic model used equivalent front and rear steering angles on the vehicle centreline to represent the left and right wheels, simplifying the analytical derivation and controller design. The active steering axle depended on the scenario: FWS was used in most simulations and all physical experiments, and RWS in the reverse-direction simulations. Individual wheel angles were reconstructed in simulation using Ackermann steering geometry. Steering compliance, axle or linkage flexibility, and unequal left–right tire-slip behaviour were not fully represented in the analytical model, which may affect prediction accuracy during aggressive manoeuvres or severe wheel slip. The connecting truss, slider and carriage were modelled as a quasi-static load path (Section 3.1.3): their self-weight and the implement loads enter the vehicle equations through the force and moment balance, but the inertia of the truss, carriage and implement was not represented, so dynamic loads arising from acceleration of the connecting assembly are outside the model. The flat-terrain formulation also omitted vehicle pitch and the additional force and moment components associated with sloped or undulating ground. The steering-increment constraint and the saturation of the adaptive weighting coefficients introduce nonlinearities whose effect on closed-loop stability was assessed empirically for the most demanding forward scenario (Section 4.1.6) and not analyzed formally.

2. Experimental environment and scenario constraints

Experimental validation covered straight-line and sinusoidal forward tracking on a relatively flat pavement/concrete surface using front-wheel steering. The vehicles were physically connected by the truss, so the tests included its self-weight and the mechanical interaction between the vehicles. No externally applied implement resistance was imposed because the connecting truss, assembled from bolted T-slot aluminum structural members, was sized for the platform's own weight and normal operating forces and had not been analyzed or tested for additional applied load. Before implement-loading experiments, the truss, connections, and vehicle support arrangement require structural assessment for the intended forces and load distributions. The predicted changes in coupling forces and formation errors under externally applied implement loads have not yet been experimentally validated. Gravel and grass surfaces were not tested because the small-diameter, narrow (0.05 m) tires of the platform do not provide sufficient traction or ground clearance on loose or soft surfaces; testing on such surfaces requires the vehicles to be refitted with off-road wheels. Reverse motion, low-adhesion surfaces, and variable externally applied implement loads were likewise outside the physical test program. These scenarios, together with uneven terrain, soil deformation, and variable traction, define the next stage of experimental evaluation under agricultural field conditions.

3. Limitations of the scaled-down platform

The small-scale platform provided experimental validation of the coupled control strategy, but its geometry, truss-to-vehicle weight ratio, and leader–follower weight distribution differ from the field-scale configuration (Section 4.1.1.1). Dynamic similarity has not been established. Full-scale performance therefore requires model reparameterization, appropriate controller retuning and constraint reassessment, and validation on the target platform. The small-scale results establish the demonstrated tracking and formation-control capabilities; they are not quantitative predictions or guaranteed conservative bounds for field-scale response. The follower velocity loop of the platform, a fixed-gain PID with 10 Hz GPS speed feedback, responds an order of magnitude more slowly than the 0.04 s actuator response assumed in the simulations and with more phase lag than a first-order element, and its interaction with the synchronization law produces the 0.3 Hz periodic component of the offset error (± 0.06 to ± 0.08 m) observed in the two-vehicle experiments (Section 5.2.1.3); the simulations are over-damped in this loop and show no such component.

4. Resolution of the controller comparison

The steering-sensor noise and resolution used in the simulations (0.05° and 0.01°) are finer than the 0.29° quantization of the 10-bit converter on the experimental platform; the simulated steering feedback is therefore optimistic relative to the hardware, and a hardware-matched steering-sensor model should be used in future simulation studies. The comparison between the dynamic and kinematic controllers was assessed against thresholds derived from the accuracy of the platform sensors (Section 4.2). In the straight-line simulation scenarios, both controllers tracked the path to within that resolution, so the simulation results distinguish the controllers only in the demanding scenarios (curved and reverse motion, higher speed, implement loading, and initial formation error) and in the formation metrics. The physical experiments produced steady-state lateral differences of 0.02 to 0.03 m, two to three times the RTK-GPS accuracy, but the thresholds themselves rest on manufacturer specifications rather than on a measured repeatability of the platform; repeated trials with a statistical treatment of run-to-run variability would allow the practical-significance thresholds to be set from the data.

5. Experimental validation of the adaptive weighting strategy

The adaptive weighting strategy of the steering MPC (Section 3.3.1.5) was introduced after the physical experiments had been completed, so all experiments used fixed weighting matrices. Its benefits, the reduced curved-path lateral error and the direction-sensitive emphasis on lateral convergence or heading stabilization, are therefore demonstrated in simulation only, and the experimental results validate the dynamic-model-based MPC–PID structure rather than the adaptive weighting itself. Repeating the two-vehicle experiments with the adaptive weighting enabled is the first step in extending the experimental validation.

6.3 Recommendations for Future Work

The modelling framework, integrated controller, and small-scale experimental results establish a foundation for further development of autonomous WSICs. Future work should build on these contributions through model refinement, expanded field experiments, full-scale implementation, and evaluation against agricultural performance requirements.

1. Model refinement

The analytical model can be extended by incorporating wheel-specific steering behaviour, steering compliance, and more detailed tire-slip effects. These developments would complement the existing Ackermann-based wheel-angle reconstruction and extend the model to operating conditions in which steering flexibility and unequal wheel behaviour become important. The velocity loop of the supporting vehicles should be represented by its identified command-to-measured-speed response rather than by the actuator response alone, and the synchronization gain and the velocity PID gains should be retuned together so that the periodic component of the offset error identified in Section 5.2.1.3 is removed.

2. Field experiments and expanded scenarios

Future experiments should extend the established straight-line and sinusoidal tracking tests to representative implement loading and agricultural field conditions. Additional vertical payload and path-opposing implement resistance should be specified separately, with structural assessment of the truss, its connections, and the supporting vehicles completed for the intended loading cases. Tracking and formation errors should be compared with the simulation predictions, and coupling forces and structural deflection should be measured when those quantities are evaluated. Expanded scenarios should include reverse motion, uneven terrain, variable traction, low-adhesion surfaces, variable implement loads, and nonzero initial offset errors. The two-vehicle tests should also be repeated with the adaptive weighting strategy enabled so that its simulated benefit can be confirmed on the platform. Refitting the vehicles with off-road wheels would allow the straight-line and sinusoidal tests to be repeated on gravel and grass, providing an experimental counterpart to the low-adhesion simulations of Section 4.2.4.2.

3. Full-scale WSIC implementation

The next development stage is implementation and evaluation of the control strategy on a field-scale WSIC. This requires identification or verification of the target model parameters, representation of the field-scale truss-to-vehicle weight and leader–follower weight distribution, and adaptation of actuator constraints and controller settings. The MPC weights, prediction horizon, sampling interval, and PID gains should be reviewed and retuned as appropriate. Integrating high-precision localization, communication, and actuation systems with the developed control architecture would extend the small-scale implementation to the intended field-operating environment.

4. Additional field-scale performance criteria

Future evaluation should connect tracking and formation-control performance to agricultural operating requirements. The achieved lateral-error margins should be compared with the traffic-path widths of the target field-scale system, extending the small-scale corridor assessment of Section 3.4.2.1, to define allowable tracking errors, and computation time should be assessed relative to the control period on field-deployable hardware. Energy or fuel use and field-coverage efficiency, measured by overlap and gaps, would provide complementary indicators of practical performance. A further combined MPC–PID/unified-MPC benchmark with comparable weighting strategies, tuning procedures, constraints, prediction horizons, sampling intervals, and reference conditions, together with achieved-speed and computation-time reporting, would quantify the separate contributions of the design choices and guide further controller development.

References

Ackermann, J., & Sienel, W. (1993). Robust yaw damping of cars with front and rear wheel steering. IEEE Transactions on Control Systems Technology, 1(1), 15-20.

Alhmiedat, T., Marei, A. M., Messoudi, W., Albelwi, S., Bushnag, A., Bassfar, Z., Alnajjar, F., & Elfaki, A. O. (2023). A SLAM-based localization and navigation system for social robots: The pepper robot case. Machines, 11(2), 158. https://doi.org/10.3390/machines11020158

AllyNav. (2025). Precision agriculture GPS: Complete guide to smart farming technology in 2026. Retrieved from https://www.allynav.com/blog/precision-agriculture-gps/

Antille, D. L., Imhoff, S. C., Alesso, C. A., Chamen, W. C. T., & Tullberg, J. N. (2015). Potential to increase productivity and sustainability in argentinean agriculture with controlled traffic farming: a short discussion. Acta Technologica Agriculturae, 18(3), 83-87. https://doi.org/10.1515/ata-2015-0016

Åström, K. J., & Hägglund, T. (2001). The future of PID control. Control Engineering Practice, 9(11), 1163-1175. https://doi.org/10.1016/S0967-0661(01)00062-4

Bao, C., Feng, J., Wu, J., Liu, S., Xu, G., & Xu, H. (2020). Model predictive control of steering torque in shared driving of autonomous vehicles. Science Progress, 103(3). https://doi.org/10.1177/0036850420950138

Bawatharani, R., Grafton, M., Jeyakumar, P., Bishop, P., & Davies, C. (2026). An investigation of the impacts of controlled traffic farming on soil properties. AgriEngineering, 8(2), 54. https://doi.org/10.3390/agriengineering8020054

Bulgakov, V., Aboltins, A., Adamchuk, V., Kuvachov, V., Pascuzzi, S., Kyurchev, V., Rucins, A., & Nesvidomin, V. (2024). Investigation of wide span vehicle technological part movement stability. Engineering for Rural Development, 23, 522-530. https://doi.org/10.22616/ERDev.2024.23.TF099

Bulgakov, V., Adamchuk, V., Kuvachov, V., Arak, M., & Olt, J. (2017). Study into movement of wide span tractors (vehicles) used in controlled traffic farming. In Annals of DAAAM & Proceedings (Vol. 28, pp. 199-208). DAAAM International Vienna. https://doi.org/10.2507/28th.daaam.proceedings.027

Chamen, W. C. T., & Cavalli, R. (1994). The effect of soil compaction on mole plough draught. Soil and Tillage Research, 32(4), 303-311.

Chamen, W. C. T., & McPhee, J. E. (2024). Unlocking potentials: Advantages of widespan controlled traffic farming compared to standard CTF. Retrieved from https://www.nexat.de/en/advantages-of-widespan-controlled-traffic-farming-compared-to-standard-ctf/

Chamen, W. C. T., McPhee, J. E., Pedersen, H. H., & Carter, L. M. (2025). Developments in controlled traffic farming (CTF) in precision agriculture. In Precision Agriculture for Sustainability (2nd ed., Vol. 1, pp. 327-368). Burleigh Dodds Science Publishing. https://doi.org/10.1201/9781003767428-14

Chen, S.-P., Xiong, G.-M., Chen, H.-Y., & Negrut, D. (2020). MPC-based path tracking with PID speed control for high-speed autonomous vehicles considering time-optimal travel. Journal of Central South University, 27, 3702-3720. https://doi.org/10.1007/s11771-020-4561-1

Cheng, C., Fu, J., Su, H., & Ren, L. (2023). Recent advancements in agriculture robots: Benefits and challenges. Machines, 11(1), 48.

CNH Industrial. (2022). CNH Industrial adds new automation and autonomy solutions to ag tech portfolio. CNH Industrial. Retrieved from https://www.cnh.com/media/press_releases/2022/december/CNH-Industrial-adds-new-Automation-and-Autonomy-Solutions-to-Ag-Tech-portfolio

Cook, J. T., Ray, L. E., & Lever, J. H. (2018). Dynamics modeling and robotic-assist, leader-follower control of tractor convoys. Journal of Terramechanics, 75, 57-72. https://doi.org/10.1016/j.jterra.2017.05.002

Corke, P. (2021). Robotics and control: fundamental algorithms in MATLAB® (Vol. 141). Switzerland: Springer Cham.

Cremona, J., Civera, J., Kofman, E., & Pire, T. (2024). GNSS-stereo-inertial SLAM for arable farming. Journal of Field Robotics, 41(7), 2215-2225. https://doi.org/10.1002/rob.22232

Cui, B., Zhang, J., Wei, X., Cui, X., Sun, Z., Zhao, Y., & Liu, Y. (2024). Improved information fusion for agricultural machinery navigation based on context-constrained Kalman filter and dual-antenna RTK. Actuators, 13(5), 160. https://doi.org/10.3390/act13050160

Dai, P., & Katupitiya, J. (2014). Path planning and tracking of a 4WD4WS vehicle to be driven under force control. IEEE International Conference on Mechatronics and Automation, Tianjin, China, pp. 1709-1715. https://doi.org/10.1109/ICMA.2014.6885958

Díaz Lankenau, G. F., & Winter, A. G. (2019). An engineering review of the farm tractor's evolution to a dominant design. Journal of Mechanical Design, 141(3), 031107. https://doi.org/10.1115/1.4042338

Ding, C., Ding, S., Wei, X., & Mei, K. (2022). Output feedback sliding mode control for path-tracking of autonomous agricultural vehicles. Nonlinear Dynamics, 110(3), 2429-2445. https://doi.org/10.1007/s11071-022-07739-2

Dunbar, W. B., & Murray, R. M. (2006). Distributed receding horizon control for multi-vehicle formation stabilization. Automatica, 42(4), 549-558. https://doi.org/10.1016/j.automatica.2005.12.008

Esau, T. J., MacEachern, C. B., Farooque, A. A., & Zaman, Q. U. (2021). Evaluation of Autosteer in Rough Terrain at Low Ground Speed for Commercial Wild Blueberry Harvesting. Agronomy 2021, 11, 384. https://doi.org/10.3390/agronomy11020384

Falcone, P., Borrelli, F., Asgari, J., Tseng, H. E., & Hrovat, D. (2007). Predictive active steering control for autonomous vehicle systems. IEEE Transactions on Control Systems Technology, 15(3), 566-580. https://doi.org/10.1109/TCST.2007.894653

Falcone, P., Eric Tseng, H., Borrelli, F., Asgari, J., & Hrovat, D. (2008). MPC-based yaw and lateral stabilisation via active front steering and braking. Vehicle System Dynamics, 46(sup1), 611-628. https://doi.org/10.1080/00423110802018297

Frenet, F. (1852). Sur les courbes à double courbure. Journal de mathématiques pures et appliquées, 17, 437-447.

Garriga, J. L., & Soroush, M. (2010). Model predictive control tuning methods: A review. Industrial & Engineering Chemistry Research, 49(8), 3505-3515. https://doi.org/10.1021/ie900323c

Gasso, V., Sørensen, C. A. G., Oudshoorn, F. W., & Green, O. (2013). Controlled traffic farming: A review of the environmental impacts. European Journal of Agronomy, 48, 66-73. https://doi.org/10.1016/j.eja.2013.02.002

Goering, C. E., Stone, M. L., Smith, D. W., & Turnquist, P. K. (2003). Traction and transport devices. Off-Road Vehicle Engineering Principles, St. Joseph, Michigan: ASAE, pp. 351-382.

Graf Plessen, M. M., & Bemporad, A. (2017). Reference trajectory planning under constraints and path tracking using linear time-varying model predictive control for agricultural machines. Biosystems Engineering, 153, 28-41. https://doi.org/10.1016/j.biosystemseng.2016.10.019

Griffel, L. M., Vazhnik, V., Hartley, D. S., Hansen, J. K., & Roni, M. (2020). Agricultural field shape descriptors as predictors of field efficiency for perennial grass harvesting: An empirical proof. Computers and Electronics in Agriculture, 168(C), 105088. https://doi.org/10.1016/j.compag.2019.105088

Grisso, R., Helsel, Z. R., & Grubinger, V. (2019). Selecting engine and travel speeds for optimal fuel efficiency. Farm Energy. Retrieved from https://farm-energy.extension.org/selecting-engine-and-travel-speeds-for-optimal-fuel-efficiency/

Grübler, M. (1883). Allgemeine Eigenschaften der zwangläufigen ebenen kinematischen Ketten. Der Civilingenieur, 29, 167-200.

Haque, K. F., Abdelgawad, A., & Yelamarthi, K. (2022). Comprehensive performance analysis of Zigbee communication: An experimental approach with XBee S2C module. Sensors, 22(9), 3245. https://doi.org/10.3390/s22093245

Hargreaves, P. R., Peets, S., Chamen, W. C. T., White, D. R., Misiewicz, P. A., & Godwin, R. J. (2019). Improving grass silage production with controlled traffic farming (CTF): agronomics, system design and economics. Precision Agriculture, 20(2), 260-277. https://doi.org/10.1007/s11119-018-09633-7

Harik, E. H. C. (2023). Tractor-robot cooperation: A heterogeneous leader-follower approach. Robotics, 12(2), 57. https://doi.org/10.3390/robotics12020057

He, J., Zeng, H., Li, M., He, J., Mo, J., Wang, P., & Zhao, R. (2025). Improved pure pursuit path tracking control method for automatic navigation tractor based on drive wheel lateral deviation compensation. Transactions of the Chinese Society for Agricultural Machinery, 56(2), 28-37. https://doi.org/10.6041/j.issn.1000-1298.2025.02.003

Huang, Y., Fu, J., Xu, S., Han, T., & Liu, Y. (2022). Research on integrated navigation system of agricultural machinery based on RTK-BDS/INS. Agriculture, 12(8), 1169. https://doi.org/10.3390/agriculture12081169

Hussein, M. A., Antille, D. L., Kodur, S., Chen, G., & Tullberg, J. N. (2021). Controlled traffic farming effects on productivity of grain sorghum, rainfall and fertiliser nitrogen use efficiency. Journal of Agriculture and Food Research, 3(1-2), 100111.

Isbister, B., Blackwell, P., Riethmuller, G., Davies, S., Whitlock, A., & Neale, T. (2013). Controlled traffic farming technical manual. NACC, Perth. Report. https://library.dpird.wa.gov.au/fc_publishedrpts/14

Jeon, J., Bae, J., Kwon, O., Ko, Y., Kim, C., Won, S., Shin, W., & Hong, D. (2025). Automating motor grader leveling operations: Kinematic analysis for blade pose control. Automation in Construction, 175, 106199. https://doi.org/10.1016/j.autcon.2025.106199

Jing, Y., Li, Q., Ye, W., & Liu, G. (2023). Development of a GNSS/INS-based automatic navigation land levelling system. Computers and Electronics in Agriculture, 213, 108187. https://doi.org/10.1016/j.compag.2023.108187

Kayacan, E., Kayacan, E., Ramon, H., & Saeys, W. (2015). Robust tube-based decentralized nonlinear model predictive control of an autonomous tractor-trailer system. IEEE/ASME Transactions on Mechatronics, 20(1), 447-456. https://doi.org/10.1109/TMECH.2014.2334612

Kong, J., Pfeiffer, M., Schildbach, G., & Borrelli, F. (2015). Kinematic and dynamic vehicle models for autonomous driving control design. 2015 IEEE Intelligent Vehicles Symposium (IV), 1094-1099. https://doi.org/10.1109/IVS.2015.7225830

Kutzbach, K. (1929). Mechanische Leistungsverzweigung, ihre Gesetze und Anwendungen. Maschinenbau, Der Betrieb, 8(21), 710-716.

Kuvachov, V., Ihnatiev, Y., Mitkov, V., Boltianskyi, B., & Sharova, T. (2024). Research on the properties of wide span vehicle in controlled traffic farming. E3S Web of Conferences, 508, 08005. https://doi.org/10.1051/e3sconf/202450808005

Laguë, C., Roy, P.-M., & Savard, P. (1997). Wide-Span Implement Carrier (WSIC) for cranberry production. Applied Engineering in Agriculture, 13(3), 309-317.

Lapapong, S., Gupta, V., Callejas, E., & Brennan, S. (2009). Fidelity of using scaled vehicles for chassis dynamic studies. Vehicle System Dynamics, 47(11), 1401-1437. https://doi.org/10.1080/00423110802687604

Legrand, R., Claveau, F., Chevrel, P., Rancinangue, B., & Dollet, A. (2022). $H_2/H\infty$ robust lateral control of an off-road two-steering-axle vehicle on slippery sloping soils. IFAC-PapersOnLine, 55(25), 187-192. https://doi.org/10.1016/j.ifacol.2022.09.345

Li, S., Zhang, M., Ji, Y., Zhang, Z., Cao, R., Chen, B., Li, H., & Yin, Y. (2021). Agricultural machinery GNSS/IMU-integrated navigation based on fuzzy adaptive finite impulse response Kalman filtering algorithm. Computers and Electronics in Agriculture, 191, 106524. https://doi.org/10.1016/j.compag.2021.106524

Li, X., Laguë, C., & Uchida, T. (2023). Integration of model predictive control and proportional-integral-derivative strategies for the autonomous path tracking of agricultural wide-span implement carriers. Proceedings of the 2023 IEEE International Symposium on Robotic and Sensors Environments (ROSE) (pp. 1-7). IEEE. https://doi.org/10.1109/ROSE60297.2023.10410680

Li, X., Laguë, C., & Uchida, T. (2026a). Autonomous control of agricultural wide-span implement carriers (WSIC), Part 1: Development and validation of a hybrid dynamic control strategy. Applied Engineering in Agriculture, 42(4), 367-376. https://doi.org/10.13031/aea.16553

Li, X., Laguë, C., & Uchida, T. (2026b). Autonomous control of agricultural wide-span implement carriers (WSIC), Part 2: Dynamic vs. kinematic control strategies. Applied Engineering in Agriculture, 42(4), 377-386. https://doi.org/10.13031/aea.16571

Li, Y., Deng, H., Xu, X., & Wang, W. (2019). Modelling and testing of in-wheel motor drive intelligent electric vehicles based on co-simulation with Carsim/Simulink. IET Intelligent Transport Systems, 13(1), 115-123. https://doi.org/10.1049/iet-its.2018.5047

Liu, C., & Nguyen, B. K. (2024). Low-cost real-time localisation for agricultural robots in unstructured farm environments. Machines, 12(9), 612. https://doi.org/10.3390/machines12090612

Lu, M., Gao, H., Dai, H., Lei, Q., & Liu, C. (2024). Path tracking Hybrid A* for autonomous agricultural vehicles (Version 1) [Preprint]. arXiv. https://arxiv.org/abs/2411.14086v1

Luo, C. (2017). Automatic guidance of agricultural Wide-Span Implement Carrier (WSIC) (Doctoral dissertation, Université d'Ottawa/University of Ottawa).

Ma, Z., Chong, K., Ma, S., Fu, W., Yin, Y., Yu, H., & Zhao, C. (2022). Control strategy of grain truck following operation considering variable loads and control delay. Agriculture (Basel), 12(10), Article 1545. https://doi.org/10.3390/agriculture12101545

Ma, Z., Zhang, C., Wang, W., Wang, H., Yu, H., & Zhao, C. (2024). Supervised reinforcement learning-based collaborative master-slave harvest control study in wheat. Agronomy, 14(11), 2577.

Macmillan, R. H. (2002). The mechanics of tractor-implement performance: Theory and worked examples: A textbook for students and engineers. https://hdl.handle.net/11343/33718

Maharlooei, M., Toudeshki, A., Steenwyk, R. V., & Ehsani, R. (2024). Assessing the performance of an affordable guidance systems for parallel movement in orchards. 2024 ASABE Annual International Meeting (Paper No. 2401270). Anaheim, California July 28-31, 2024.

Matveev, A. S., Hoy, M., Katupitiya, J., & Savkin, A. V. (2013). Nonlinear sliding mode control of an unmanned agricultural tractor in the presence of sliding and control saturation. Robotics and Autonomous Systems, 61(9), 973-987. https://doi.org/10.1016/j.robot.2013.05.003

Mousakazemi, S. M. H. (2021). Comparison of the error-integral performance indexes in a GA-tuned PID controlling system of a PWR-type nuclear reactor point-kinetics model. Progress in Nuclear Energy, 132, 103604.

Murray, R. M., Li, Z., & Sastry, S. S. (1994). A Mathematical Introduction to Robotic Manipulation (1st ed.). CRC Press. https://doi.org/10.1201/9781315136370

Nagasaka, Y., Saito, H., Tamaki, K., Seki, M., Kobayashi, K., & Taniwaki, K. (2009). An autonomous rice transplanter guided by global positioning system and inertial measurement unit. Journal of Field Robotics, 26(6-7), 537-548. https://doi.org/10.1002/rob.20294

Nijak, M., Skrzypczyński, P., Ćwian, K., Zawada, M., Szymczyk, S., & Wojciechowski, J. (2024). On the importance of precise positioning in robotised agriculture. Remote Sensing, 16(6), 985. https://doi.org/10.3390/rs16060985

Önal, İ. (2012). Controlled traffic farming and wide span tractors. Journal of Agricultural Machinery Science, 8(4), 353-364.

Pang, H., Liu, N., Hu, C., & Xu, Z. (2022). A practical trajectory tracking control of autonomous vehicles using linear time-varying MPC method. Proceedings of the Institution of Mechanical Engineers. Part D, Journal of Automobile Engineering, 236(4), 709-723. https://doi.org/10.1177/09544070211022904

Pearson, P., & Bevly, D. M. (2007). Modeling and validation of hitch loading effects on tractor yaw dynamics. Journal of Terramechanics, 44(6), 439-450. https://doi.org/10.1016/j.jterra.2008.03.001

Peng, G., Duan, H., Tan, Z., Zhou, Y., Li, J., Hu, B., & Zhou, C. (2023). Construction path tracking and pose estimation of unmanned bulldozer. Automation in Construction, 154, 105015. https://doi.org/10.1016/j.autcon.2023.105015

Peng, G., Gao, Q., Liu, X., Zhou, Y., Duan, H., Wu, Z., Hu, B., Zhu, X., & Xu, D. (2025). An integrated intelligent autonomous driving bulldozer system: Pose estimation, object detection, and work planning for dumping operations. Journal of Field Robotics, 42(6), 2740-2763. https://doi.org/10.1002/rob.22542

Ploeg, J., Scheepers, B. T. M., van Nunen, E., van de Wouw, N., & Nijmeijer, H. (2011). Design and experimental evaluation of cooperative adaptive cruise control. In 2011 14th International IEEE Conference on Intelligent Transportation Systems (ITSC) (pp. 260-265). IEEE. https://doi.org/10.1109/ITSC.2011.6082981

Qu, J., Zhang, Z., Qin, Z., Guo, K., & Li, D. (2024). Applications of autonomous navigation technologies for unmanned agricultural tractors: A review. Machines, 12(4), 218. https://doi.org/10.3390/machines12040218

Radicioni, F., Stoppini, A., Tosi, G., & Marconi, L. (2022). Multi-constellation network rtk for automatic guidance in precision agriculture. In 2022 IEEE Workshop on Metrology for Agriculture and Forestry (MetroAgriFor), Perugia, Italy (pp. 260-265). https://doi.org/10.1109/MetroAgriFor55389.2022.9965046

Rajamani, R. (2006). Vehicle dynamics and control. Springer. https://doi.org/10.1007/0-387-28823-6

Rajamani, R. (2012). Vehicle dynamics and control (2nd ed.). Springer. https://doi.org/10.1007/978-1-4614-1433-9

Raven Industries, Inc. (2021, May 12). Raven Industries launches the OMNi brand. Business Wire. Retrieved from https://www.businesswire.com/news/home/20210512005126/en

Raven Industries, Inc. (2022). Raven Industries unveils upgraded OMNiPOWER™ 3200 model at Commodity Classic. Business Wire. Retrieved from https://www.businesswire.com/news/home/20220310005025/en

Rawlings, J. B., Mayne, D. Q., & Diehl, M. (2017). Model predictive control: Theory, computation, and design (2nd ed.). Santa Barbara, CA: Nob Hill Publishing.

RealAgriculture. (2023). All-encompassing controlled traffic machine, the NEXAT, makes debut. Retrieved from https://www.realagriculture.com/2023/08/all-encompassing-controlled-traffic-machine-the-nexat-makes-debut

Rosolia, U., & Borrelli, F. (2018). Learning model predictive control for iterative tasks. A data-driven control framework. IEEE Transactions on Automatic Control, 63(7), 1883-1896. https://doi.org/10.1109/TAC.2017.2753460

Serret, J. A. (1851). Sur quelques formules relatives à la théorie des courbes à double courbure. Journal de mathématiques pures et appliquées, 16, 193-207.

Shabani, S., Mulaka, A. R., Stokes, T. A., Rehman, T. U., & Bao, Y. (2025). Development of a stereo vision-based UGV guidance system for bareroot forest nurseries. Smart Agricultural Technology, 11, 100990. https://doi.org/10.1016/j.atech.2025.100990

Shi, J., Bai, Y., Diao, Z., Zhou, J., Yao, X., & Zhang, B. (2023). Row detection based navigation and guidance for agricultural robots and autonomous vehicles in row-crop fields: Methods and applications. Agronomy, 13(7), 1780. https://doi.org/10.3390/agronomy13071780

Snider, J. M. (2009). Automatic steering methods for autonomous automobile path tracking (Tech. Rep. CMU-RI-TR-09-08). Robotics Institute, Carnegie Mellon University. https://publications.ri.cmu.edu/automatic-steering-methods-for-autonomous-automobile-path-tracking

Soetanto, D., Lapierre, L., & Pascoal, A. (2003). Adaptive, non-singular path-following control of dynamic wheeled robots. In Proceedings of the 42nd IEEE Conference on Decision and Control (Vol. 2, pp. 1765–1770). IEEE. https://doi.org/10.1109/CDC.2003.1272868

Souza, G. S., Souza, Z. M., Silva, R. B., Araújo, F. S., & Barbosa, R. S. (2012). Soil compressibility and root system of sugarcane with and without controlled-traffic farming. Pesquisa Agropecuária Brasileira, 47(4), 603-612.

Sugar, T. G., & Kumar, V. (2002). Control of cooperating mobile manipulators. IEEE Transactions on Robotics and Automation, 18(1), 94-103. https://doi.org/10.1109/70.988979

Suzuki, T., Ohno, K., Kojima, S., Miyamoto, N., Suzuki, T., Komatsu, T., Shibata, Y., Asano, K., & Nagatani, K. (2021). Estimation of articulated angle in six-wheeled dump trucks using multiple GNSS receivers for autonomous driving. Advanced Robotics, 35(23), 1376-1387. https://doi.org/10.1080/01691864.2021.1974942

Tashiro, T. (2013). Vehicle steering control with MPC for target trajectory tracking of autonomous reverse parking. 2013 IEEE International Conference on Control Applications (CCA), Hyderabad, India (pp. 247-251). https://doi.org/10.1109/CCA.2013.6662766

Thomasson, J. A., Baillie, C. P., Antille, D. L., Lobsey, C. R., & McCarthy, C. L. (2019). Autonomous technologies in agricultural equipment: A review of the state of the art. 2019 Agricultural Equipment Technology Conference, St. Joseph, Michigan, (40), 20.

Tullberg, J., Antille, D. L., Bluett, C., Eberhard, J., & Scheer, C. (2018). Controlled traffic farming effects on soil emissions of nitrous oxide and methane. Soil & Tillage Research, 176, 18-25. https://doi.org/10.1016/j.still.2017.09.014

Van Parys, R., & Pipeleers, G. (2017). Distributed MPC for multi-vehicle systems moving in formation. Robotics and Autonomous Systems, 97, 144-152. https://doi.org/10.1016/j.robot.2017.08.009

Velasco-Villa, M., Rodriguez-Angeles, A., Maruri-López, I. Z., Báez-Hernández, J. A., & Cruz Morales, R. D. (2024). Leader–follower formation control based on non-inertial frames for non–holonomic mobile robots. PLOS ONE, 19(1), e0297061. https://doi.org/10.1371/journal.pone.0297061

Vieira, D., Orjuela, R., Spisser, M., & Basset, M. (2022). Positioning and attitude determination for precision agriculture robots based on IMU and two RTK GPSs sensor fusion. IFAC-PapersOnLine, 55(32), 60-65. https://doi.org/10.1016/j.ifacol.2022.11.115

Wang, D., & Wang, W. (2015). Kinematic differential geometry and saddle synthesis of linkages. Singapore: John Wiley & Sons.

Wang, R., & Wang, J. (2013). Tire–road friction coefficient and tire cornering stiffness estimation based on longitudinal tire force difference generation. Control Engineering Practice, 21(1), 65-75.

Wang, X., Dou, G., Chen, T., & Lu, J. (2025). Improved robust model predictive trajectory tracking control for intelligent vehicles based on multi-cell hyperbody vertex modelling and double-layer optimization. Sensors, 25(21), 6537. https://doi.org/10.3390/s25216537

Wu, H., Wang, X., Chen, X., Zhang, Y., & Zhang, Y. (2025). Review on key technologies for autonomous navigation in field agricultural machinery. Agriculture, 15(12), 1297. https://doi.org/10.3390/agriculture15121297

Xie, B., Jin, Y., Faheem, M., Gao, W., Liu, J., Jiang, H., Cai, L., & Li, Y. (2023). Research progress of autonomous navigation technology for multi-agricultural scenes. Computers and Electronics in Agriculture, 211, 107963.

Xu, Q., Li, H., Wang, Q., & Wang, C. (2021). Wheel deflection control of agricultural vehicles with four-wheel independent omnidirectional steering. Actuators, 10(12), 334. https://doi.org/10.3390/act10120334

Yao, Z., Zhao, C., & Zhang, T. (2024). Agricultural machinery automatic navigation technology. iScience, 27(2), 108714. https://doi.org/10.1016/j.isci.2023.108714

Yeneneh, K., & Sufe, G. (2026). AutoDyn: Robust model predictive control design for trajectory tracking under varying vehicle dynamics. Scientific Reports, 16, 25130. https://doi.org/10.1038/s41598-026-56118-z

Yin, Y., Zhang, J., Guo, M., Ning, X., Wang, Y., & Lu, J. (2023). Sensor fusion of GNSS and IMU data for robust localization via smoothed error state Kalman filter. Sensors, 23(7), 3676. https://doi.org/10.3390/s23073676

Zhang, B., Cheng, J., Zhang, Y., Zhang, C., & Shen, G. (2024). Path tracking of autonomous tractor based on model-free adaptive control. Proceedings of the Institution of Mechanical Engineers, Part D: Journal of Automobile Engineering, 238(4), 749-759. https://doi.org/10.1177/09544070221135389

Zhang, C., Noguchi, N., & Yang, L. (2016). Leader–follower system using two robot tractors to improve work efficiency. Computers and Electronics in Agriculture, 121, 269-281.

Zhang, L., Ahamed, T., Zhang, Y., Gao, P., & Takigawa, T. (2023). Vision-based leader vehicle trajectory tracking for multiple agricultural vehicles. In T. Ahamed (Ed.), IoT and AI in agriculture: Self-sufficiency in food production to achieve Society 5.0 and SDG's globally (pp. 311–333). Springer. https://doi.org/10.1007/978-981-19-8113-5_16

Zhang, Q., Chen, Q., Xu, Z., Zhang, T., & Niu, X. (2021). Evaluating the navigation performance of multi-information integration based on low-end inertial sensors for precision agriculture. Precision Agriculture, 22(3), 627-646. https://doi.org/10.1007/s11119-020-09747-x

Appendix A

Additional Simulation Results

A.1 General Case

A.1.1 Dynamic Model

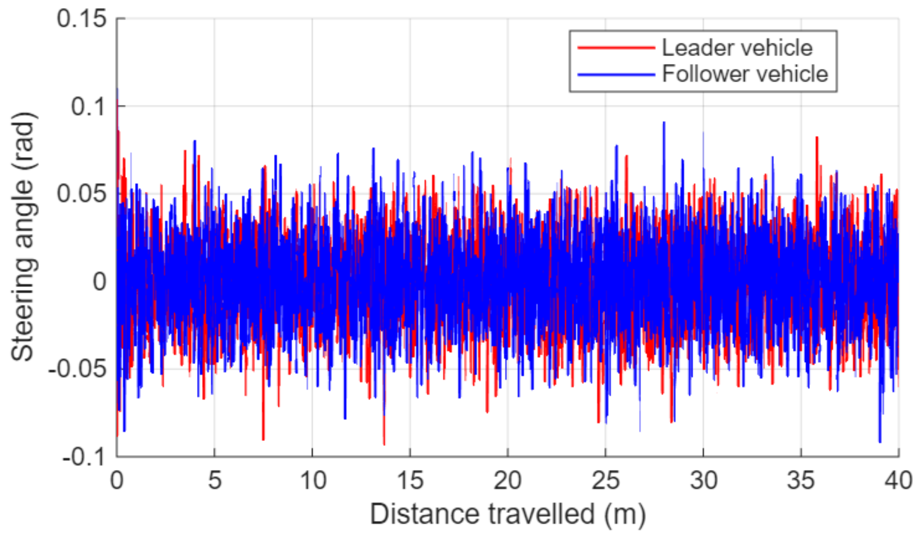

Figure A.1 Steering angle using the dynamic model in the general case

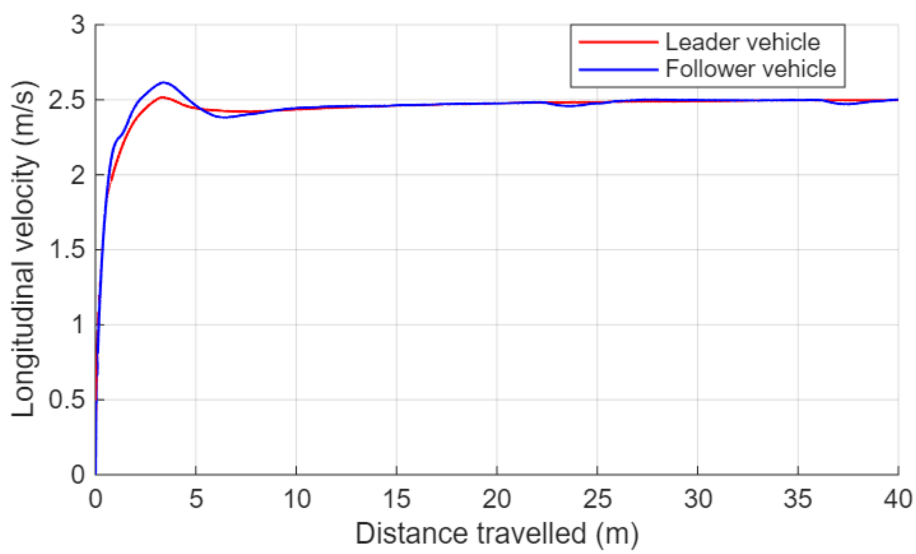

Figure A.2 Longitudinal velocity using the dynamic model in the general case

A.1.2 Kinematic Model

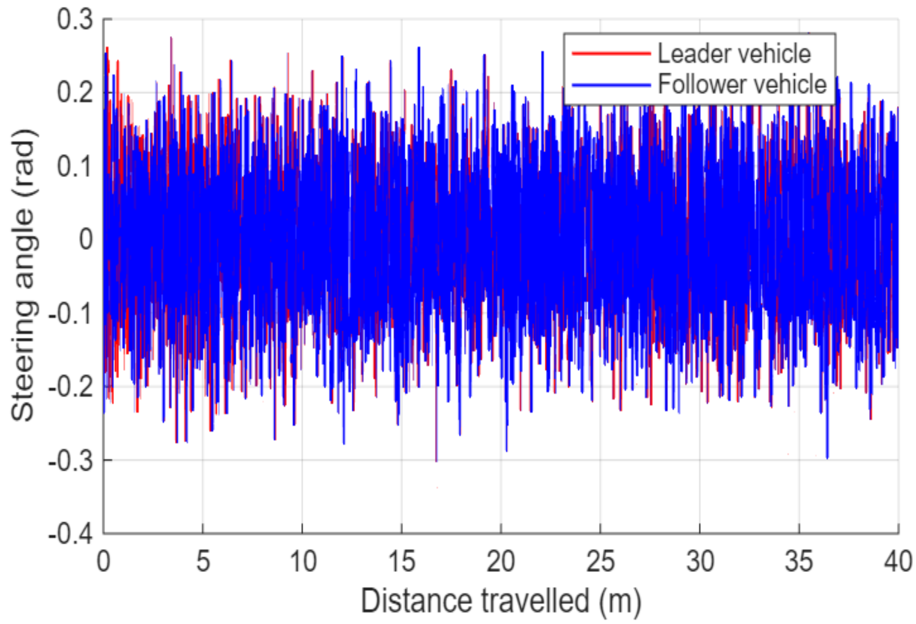

Figure A.3 Steering angle using the kinematic model in the general case

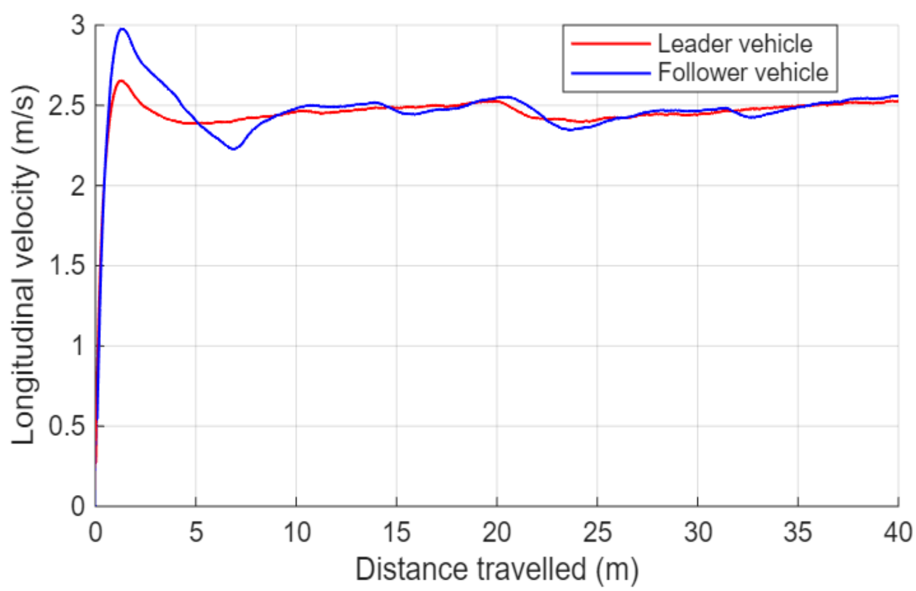

Figure A.4 Longitudinal velocity using the kinematic model in the general case

A.2 Curved Trajectory

A.2.1 Dynamic Model

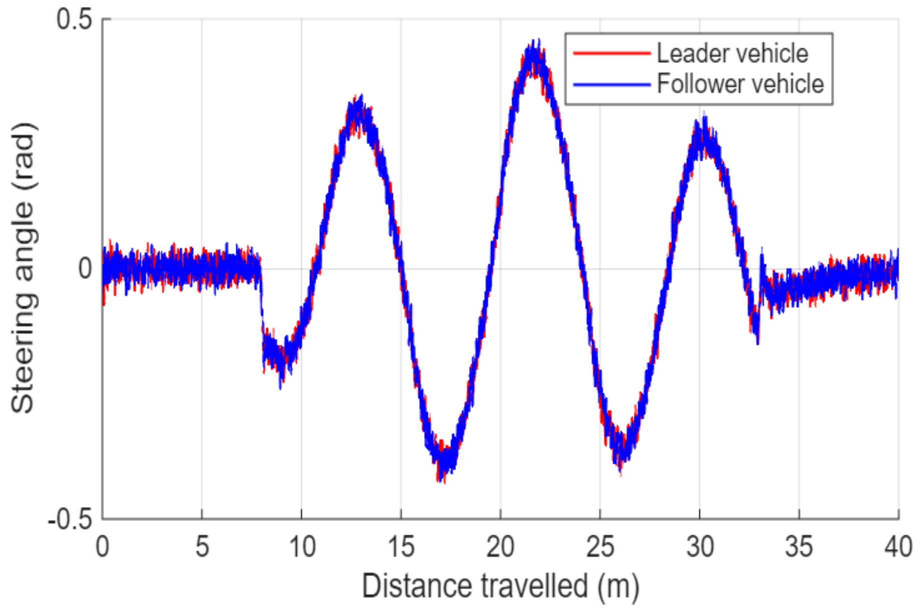

Figure A.5 Steering angle using the dynamic model for curved-trajectory tracking

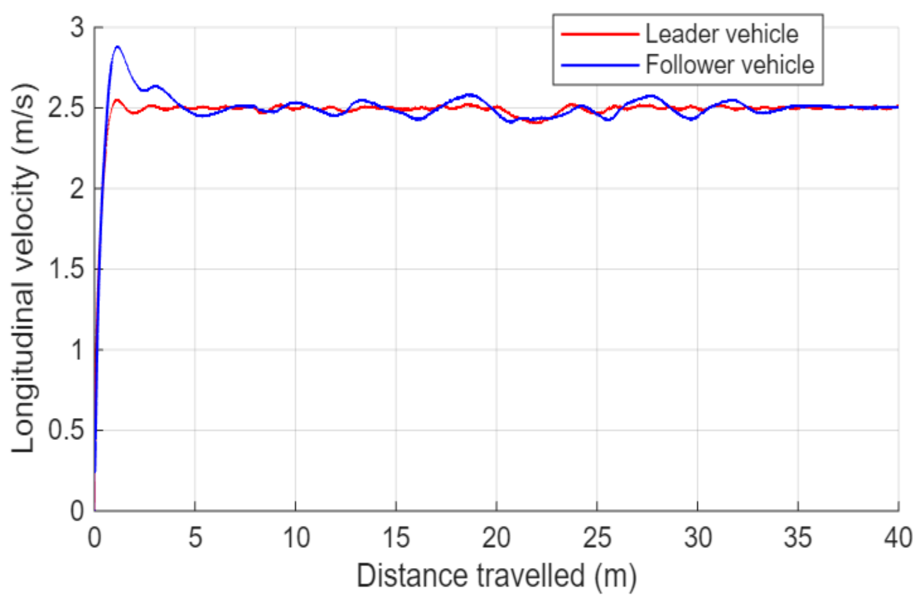

Figure A.6 Longitudinal velocity using the dynamic model for curved-trajectory tracking

A.2.2 Kinematic Model

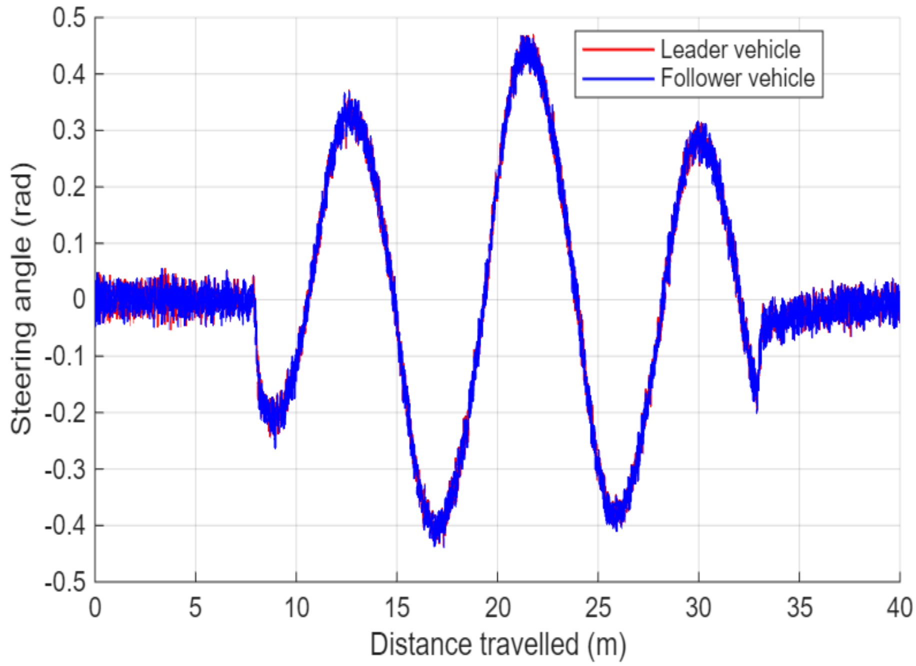

Figure A.7 Steering angle using the kinematic model for curved-trajectory tracking

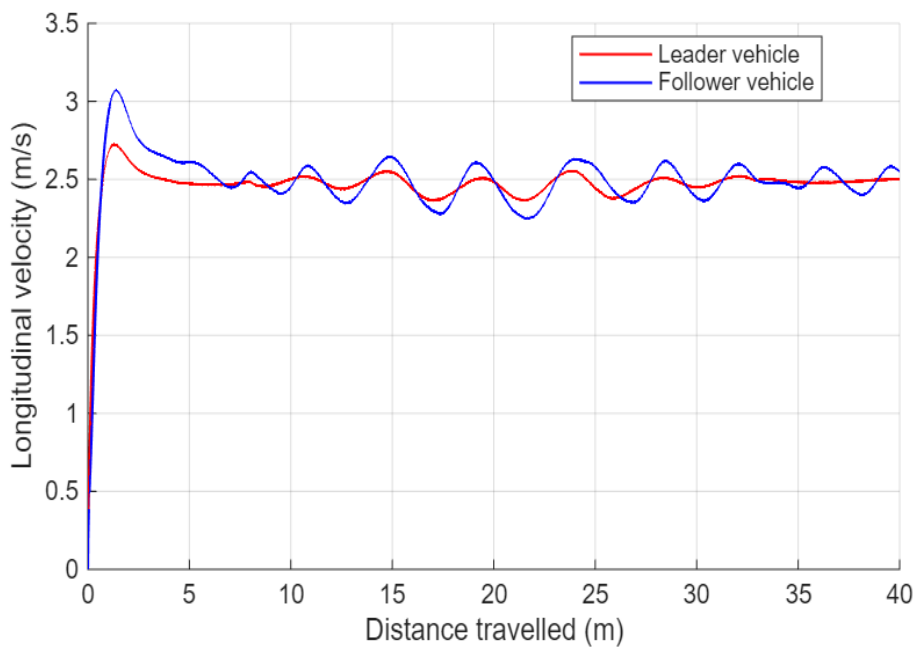

Figure A.8 Longitudinal velocity using the kinematic model for curved-trajectory tracking

A.3 Backward Motion

A.3.1 Straight-Line Reverse

A.3.1.1 Dynamic Model

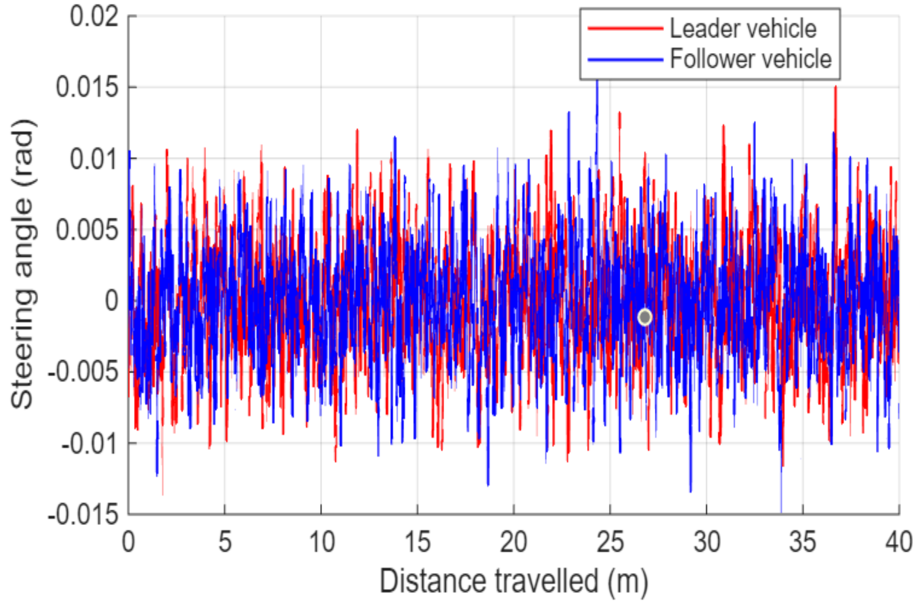

Figure A.9 Steering angle using the dynamic model in straight-line reverse tracking

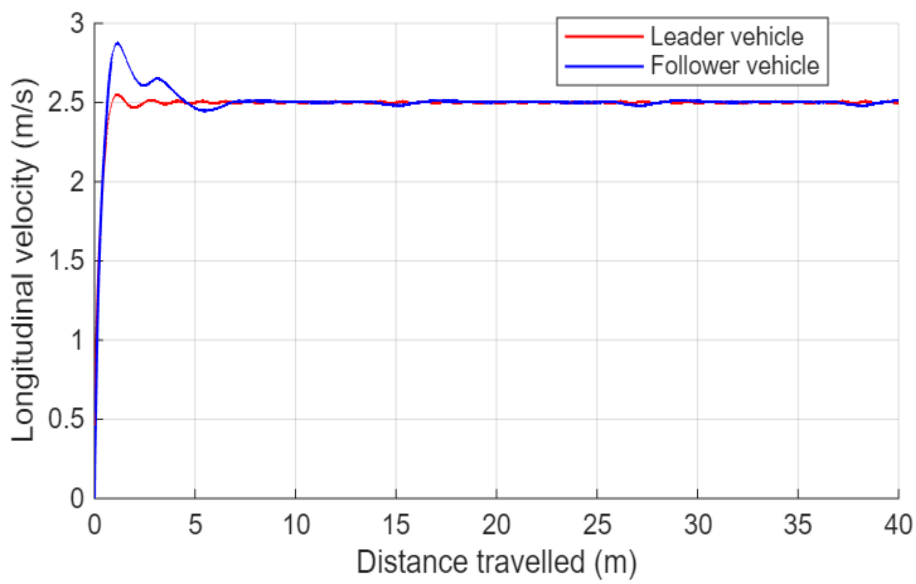

Figure A.10 Longitudinal velocity using the dynamic model in straight-line reverse tracking

A.3.1.2 Kinematic Model

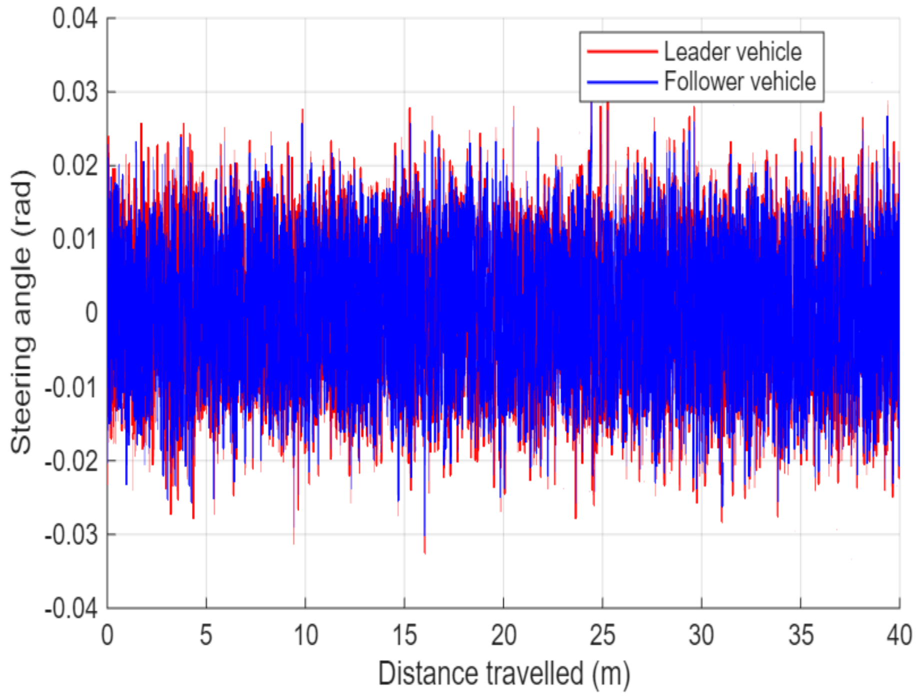

Figure A.11 Steering angle using the kinematic model in straight-line reverse tracking

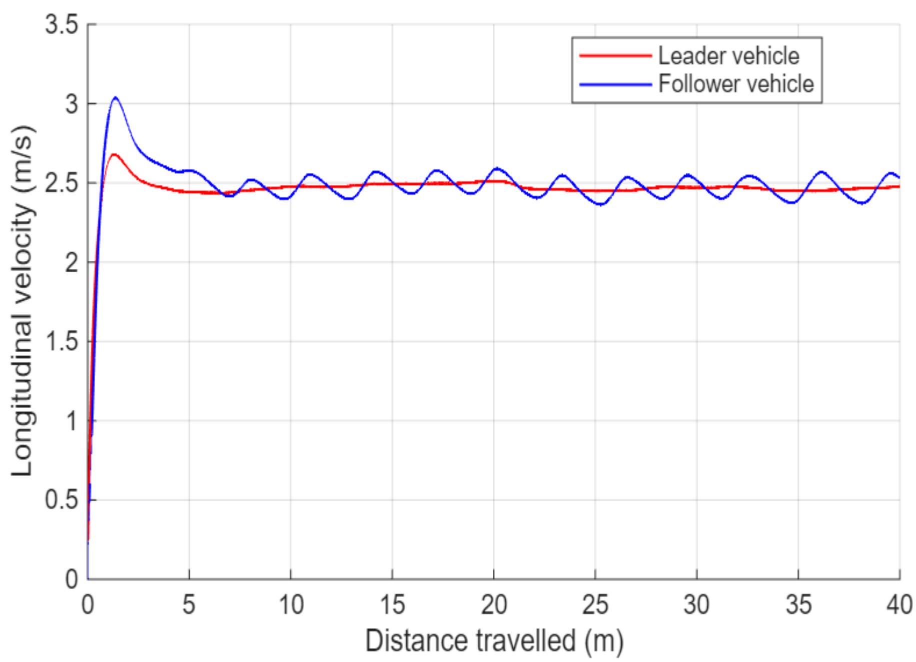

Figure A.12 Longitudinal velocity using the kinematic model in straight-line reverse tracking

A.3.2 Curved Trajectory Reverse

A.3.2.1 Dynamic Model

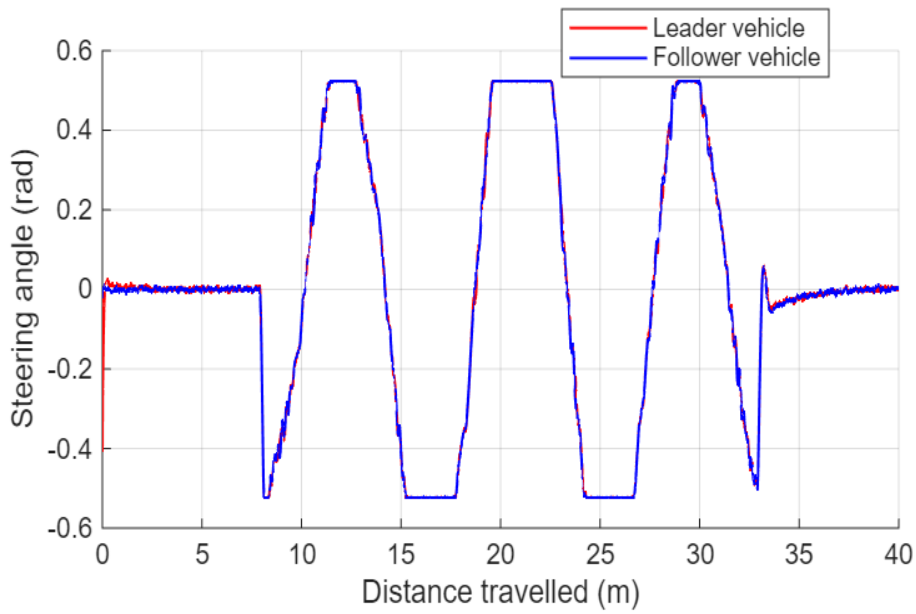

Figure A.13 Steering angle using the dynamic model for reverse curved-trajectory tracking

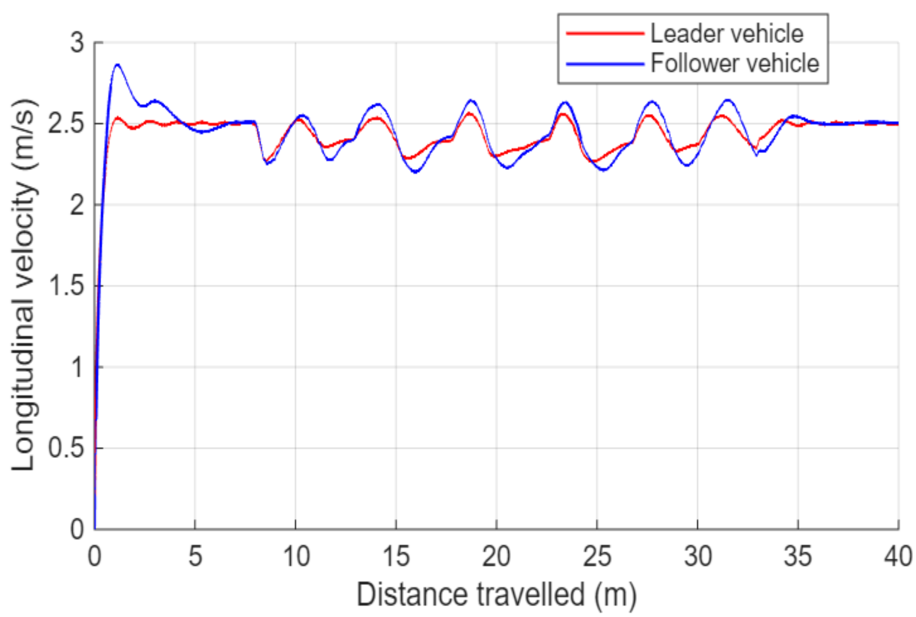

Figure A.14 Longitudinal velocity using the dynamic model for reverse curved-trajectory tracking

A.3.2.2 Kinematic Model

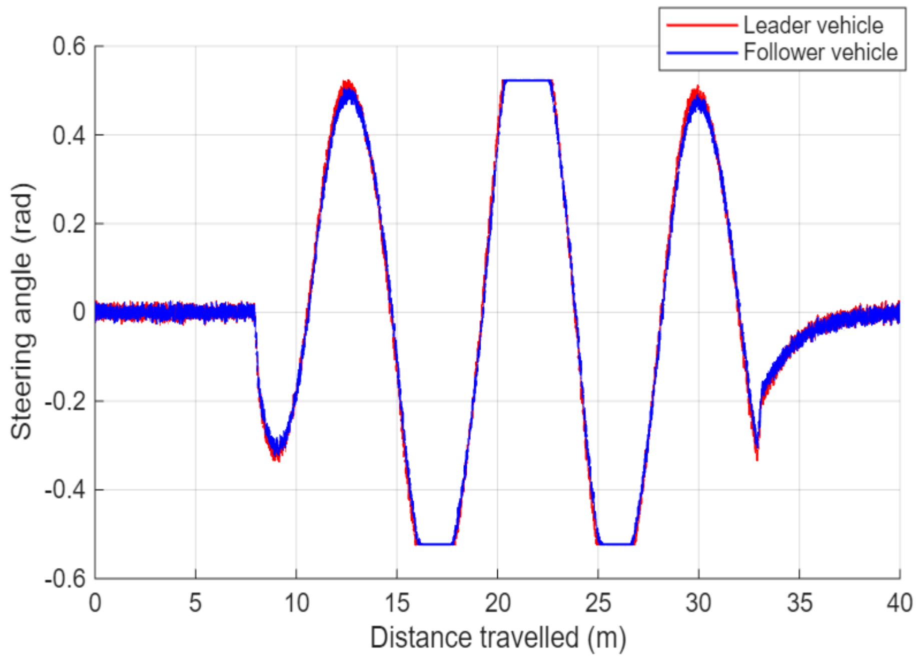

Figure A.15 Steering angle using the kinematic model for reverse curved-trajectory tracking

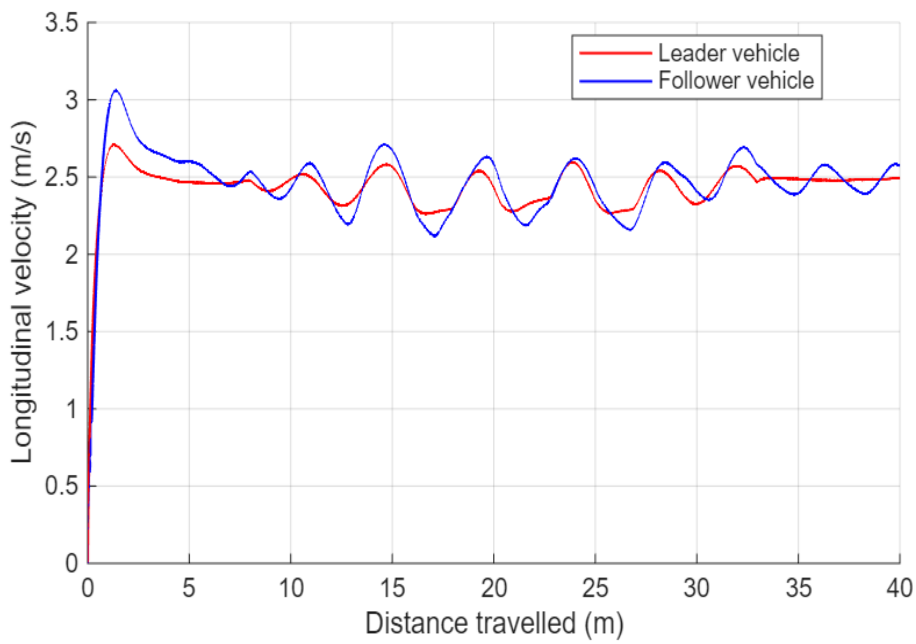

Figure A.16 Longitudinal velocity using the kinematic model for reverse curved-trajectory tracking

A.4 Different Pathways

A.4.1 High-Adhesion Pathway

A.4.1.1 Dynamic Model

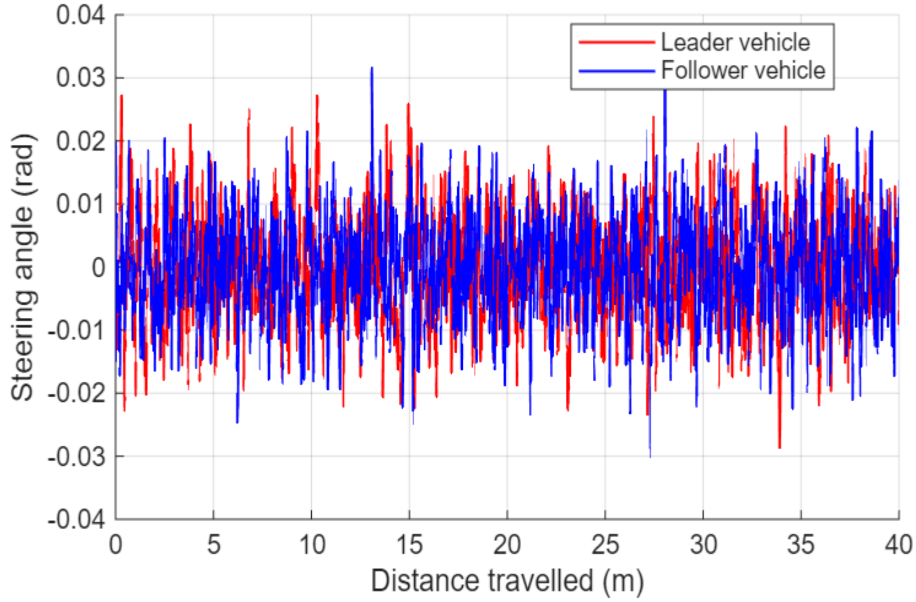

Figure A.17 Steering angle using the dynamic model on high-adhesion pathway

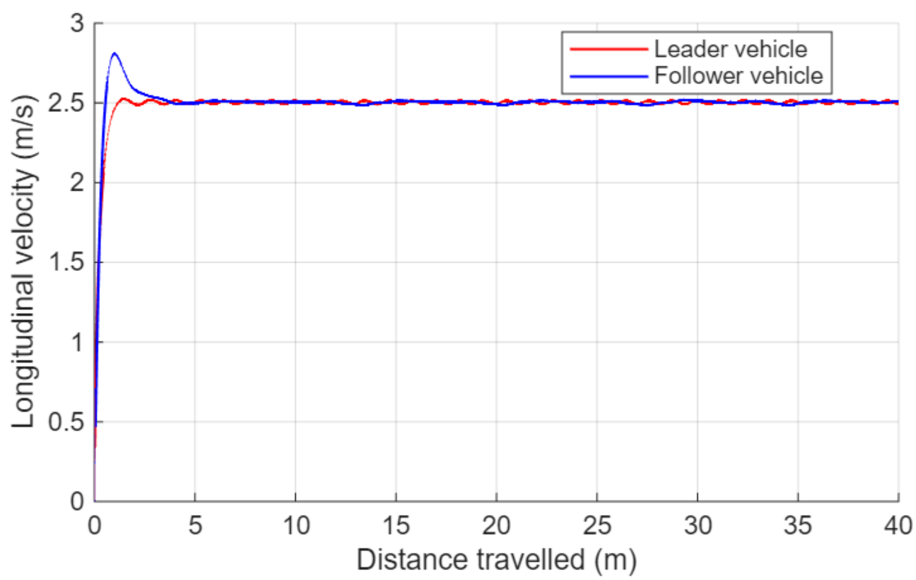

Figure A.18 Longitudinal velocity using the dynamic model on high-adhesion pathway

A.4.1.2 Kinematic Model

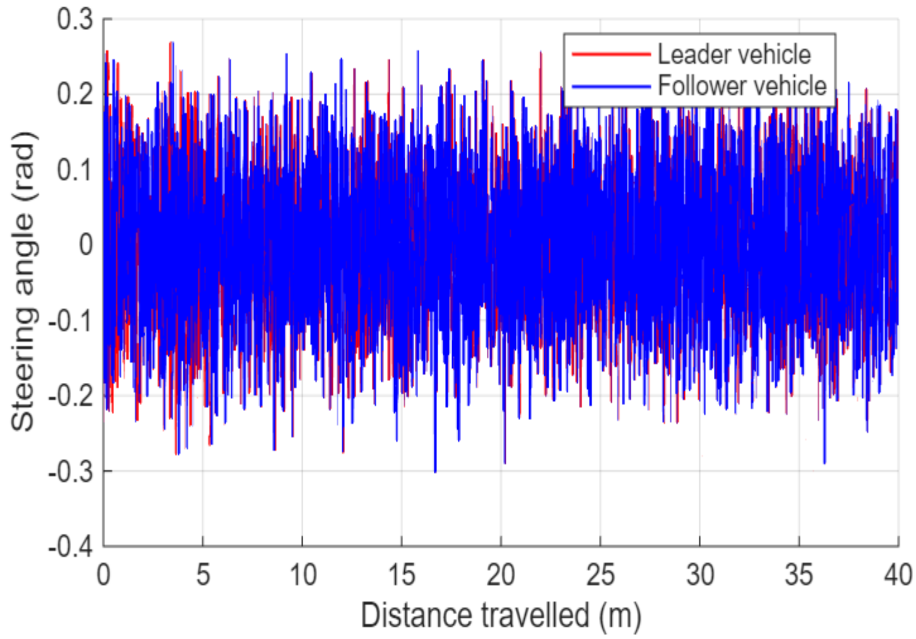

Figure A.19 Steering angle using the kinematic model on high-adhesion pathway

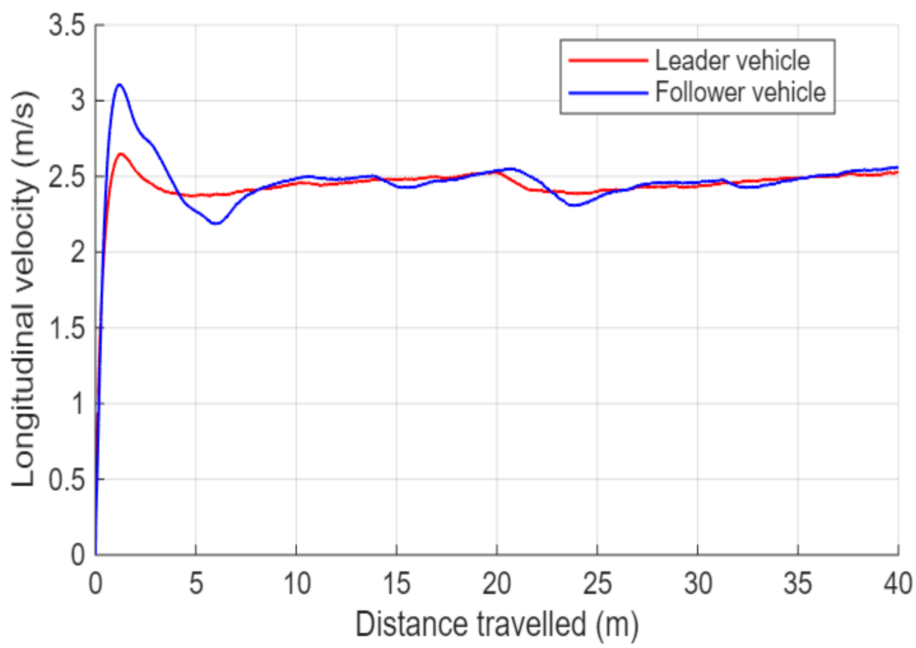

Figure A.20 Longitudinal velocity using the kinematic model on high-adhesion pathway

A.4.2 Low-Adhesion Pathway

A.4.2.1 Dynamic Model

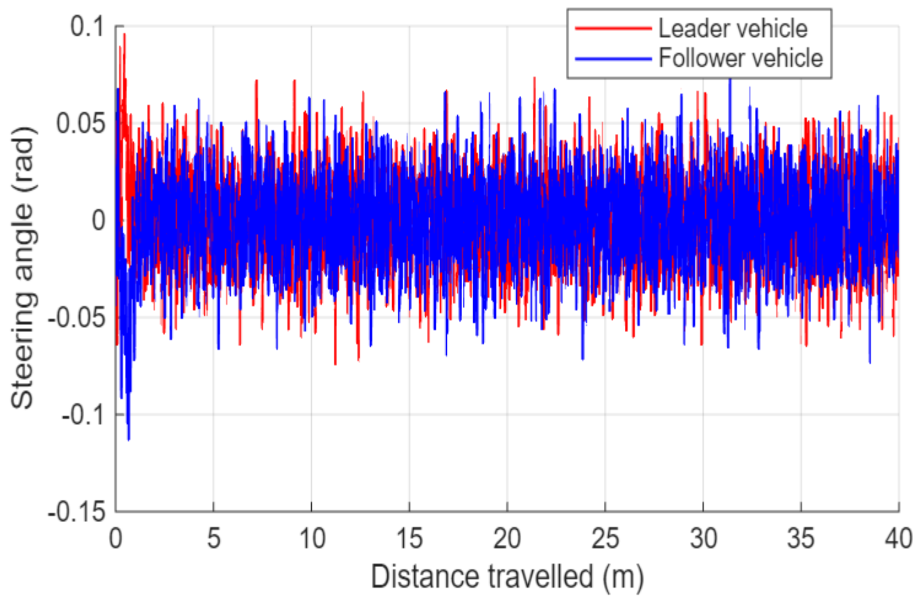

Figure A.21 Steering angle using the dynamic model on low-adhesion pathway

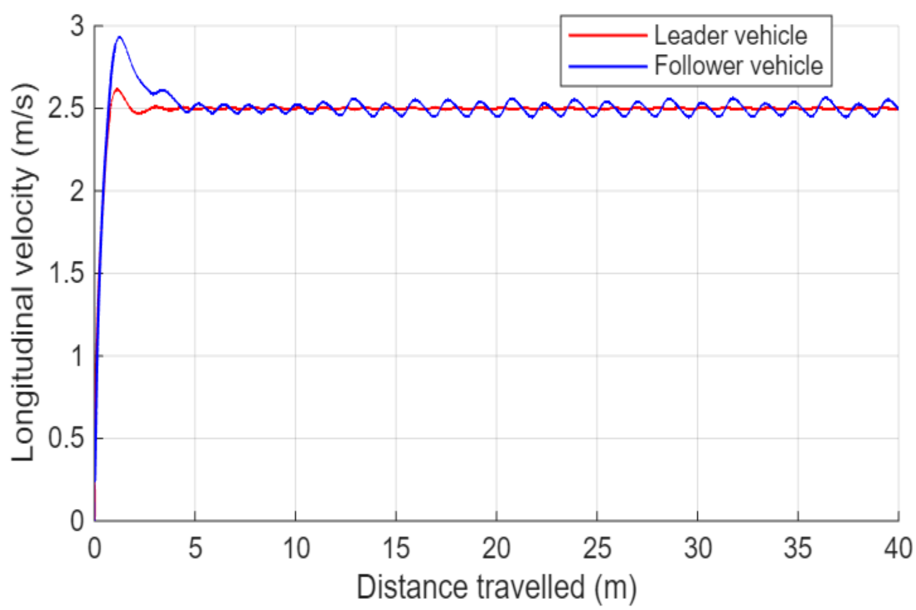

Figure A.22 Longitudinal velocity using the dynamic model on low-adhesion pathway

A.4.2.2 Kinematic Model

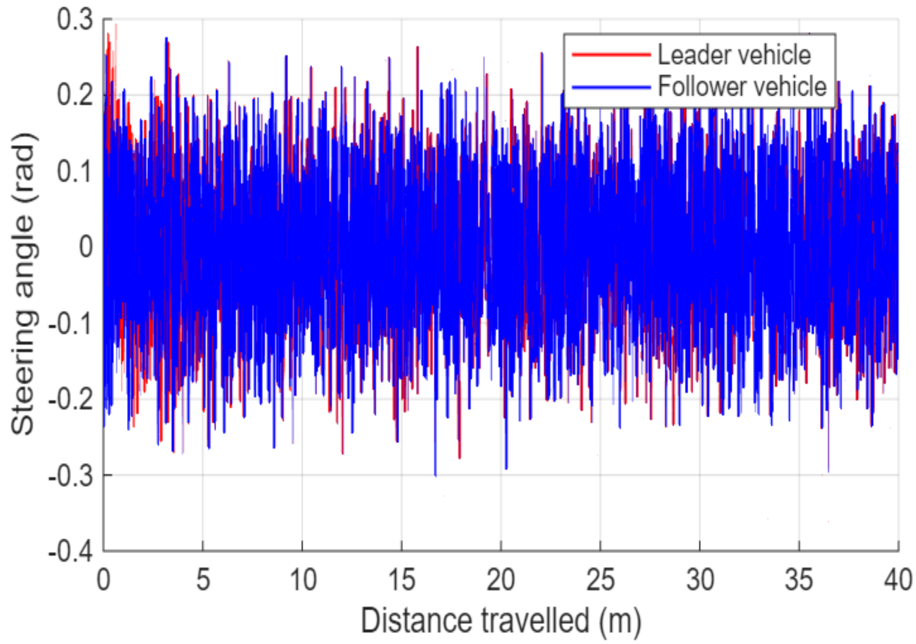

Figure A.23 Steering angle using the kinematic model on low-adhesion pathway

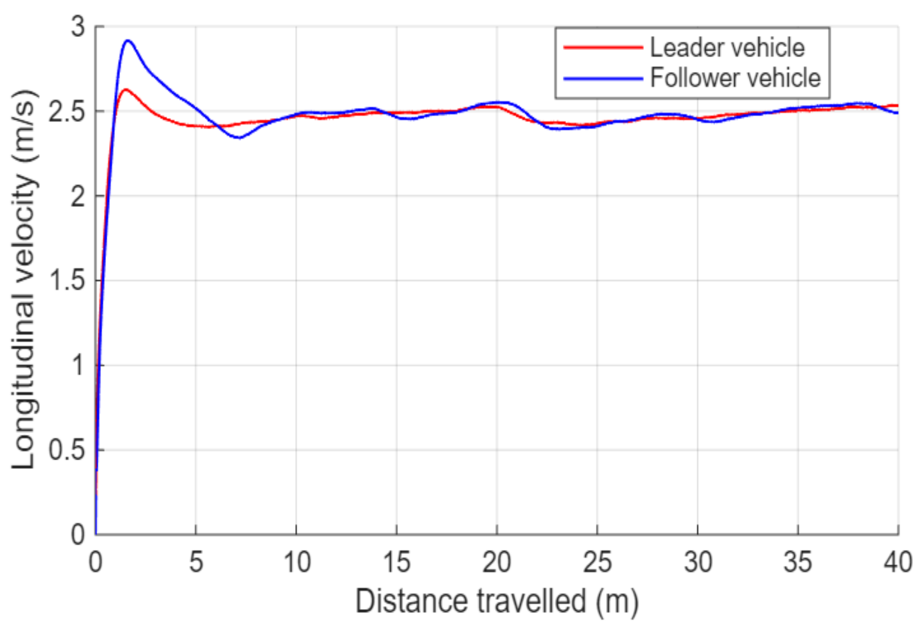

Figure A.24 Longitudinal velocity using the kinematic model on low-adhesion pathway

A.5 Different Target Speeds

A.5.1 High Speed

A.5.1.1 Dynamic Model

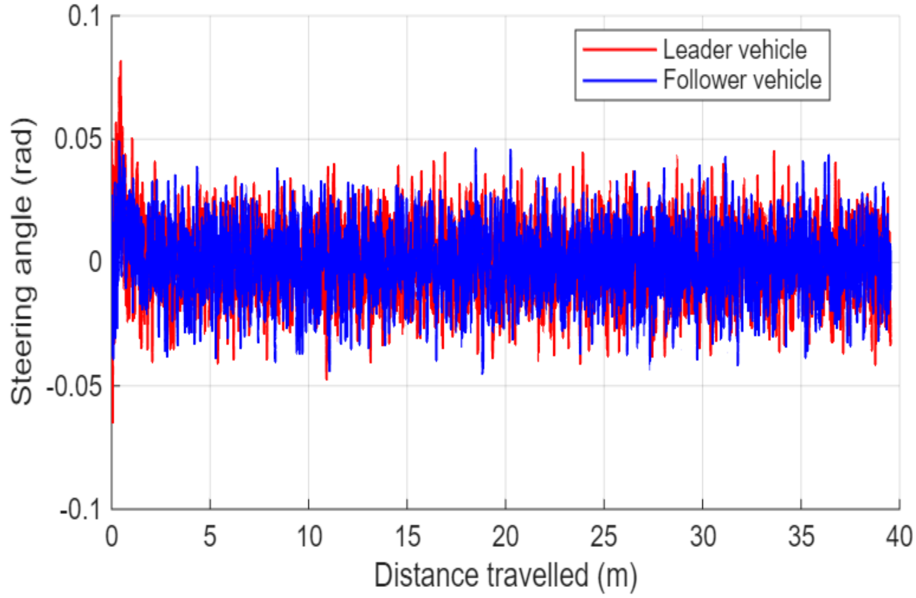

Figure A.25 Steering angle using the dynamic model at high speed

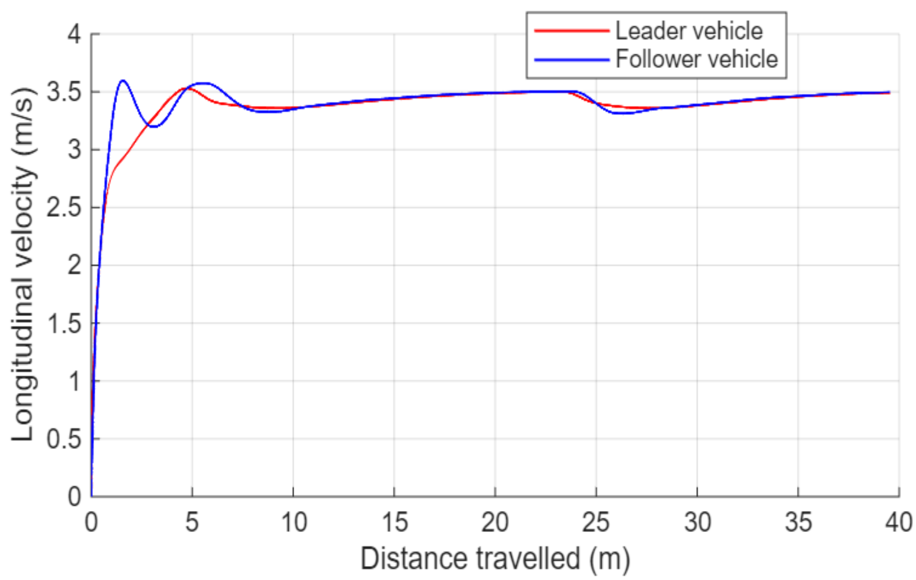

Figure A.26 Longitudinal velocity using the dynamic model at high speed

A.5.1.2 Kinematic Model

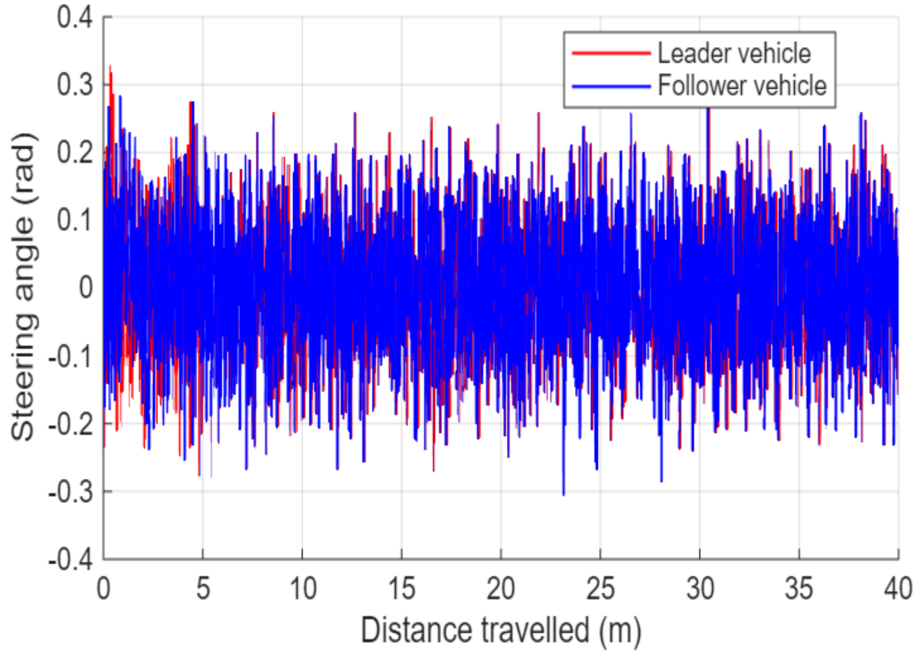

Figure A.27 Steering angle using the kinematic model at high speed

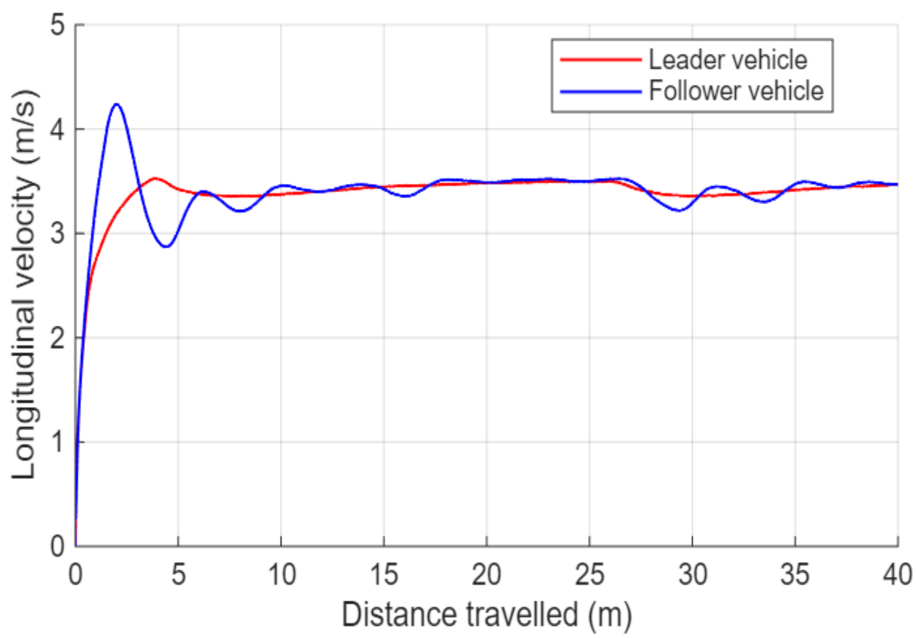

Figure A.28 Longitudinal velocity using the kinematic model at high speed

A.5.2 Low Speed

A.5.2.1 Dynamic Model

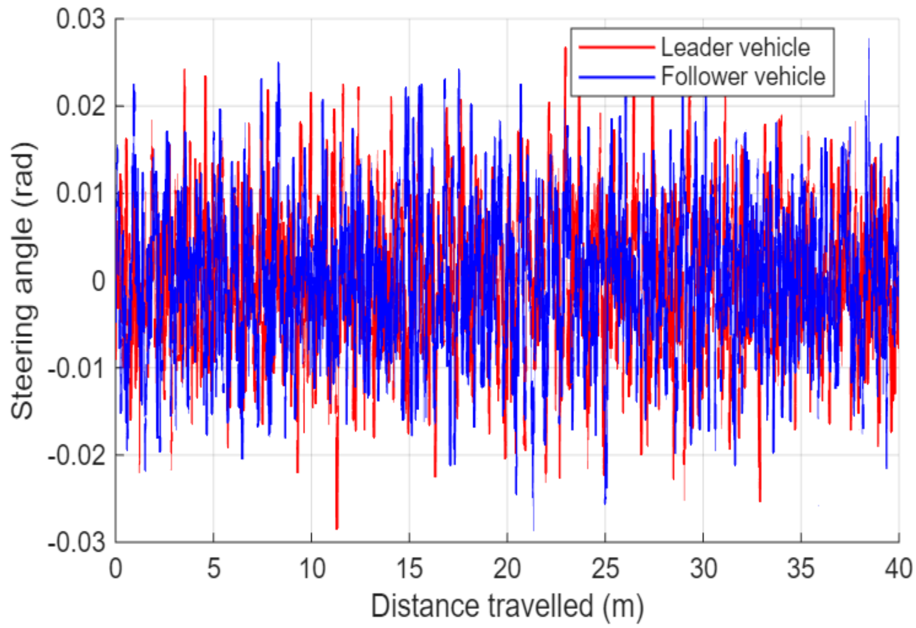

Figure A.29 Steering angle using the dynamic model at low speed

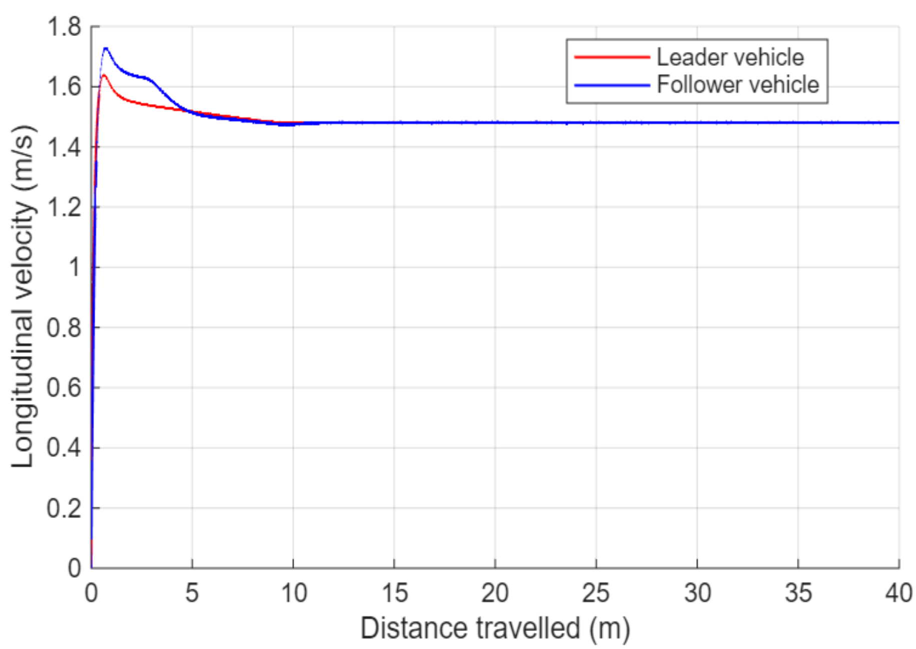

Figure A.30 Longitudinal velocity using the dynamic model at low speed

A.5.2.2 Kinematic Model

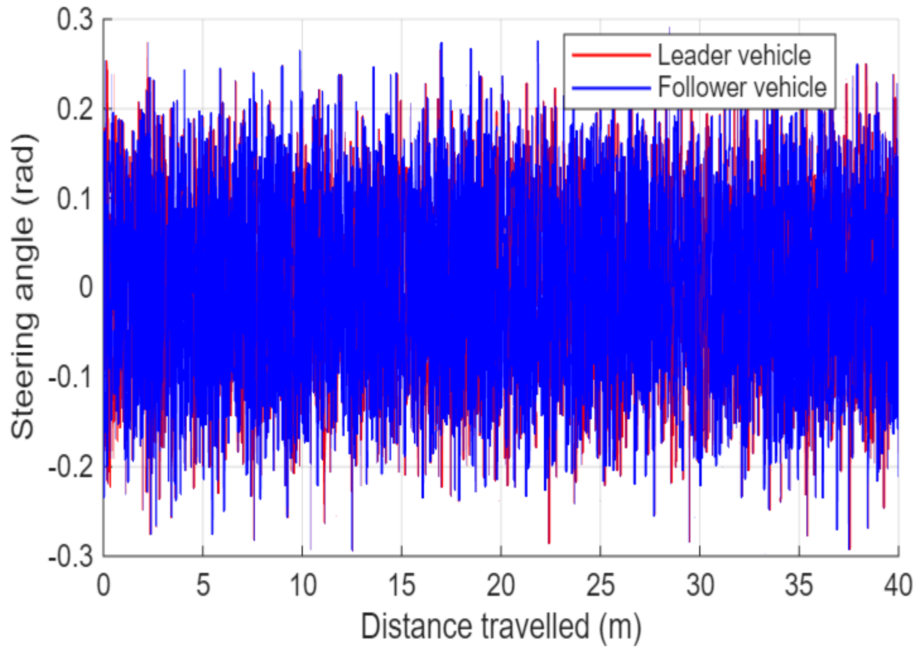

Figure A.31 Steering angle using the kinematic model at low speed

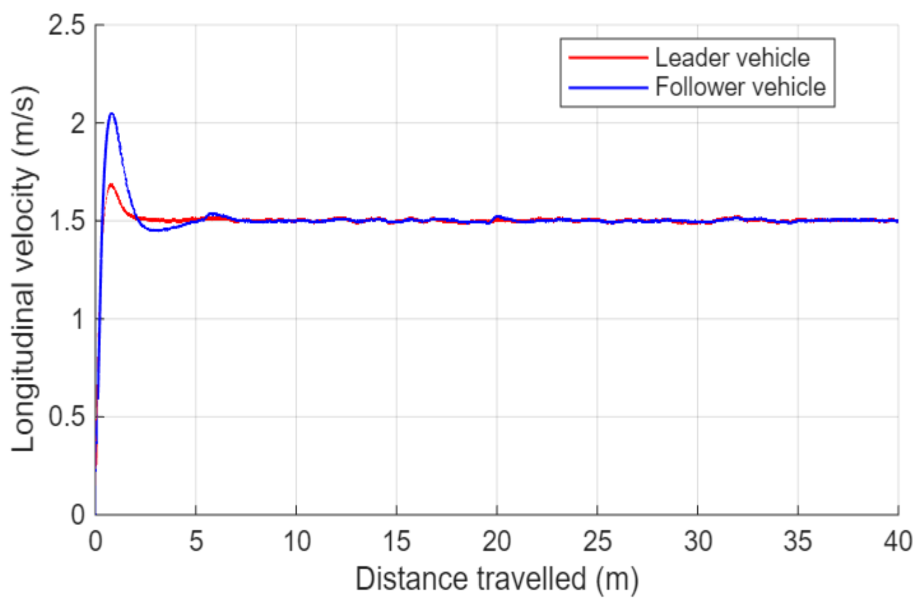

Figure A.32 Longitudinal velocity using the kinematic model at low speed

A.6 External Load on Truss

A.6.1 Dynamic Model

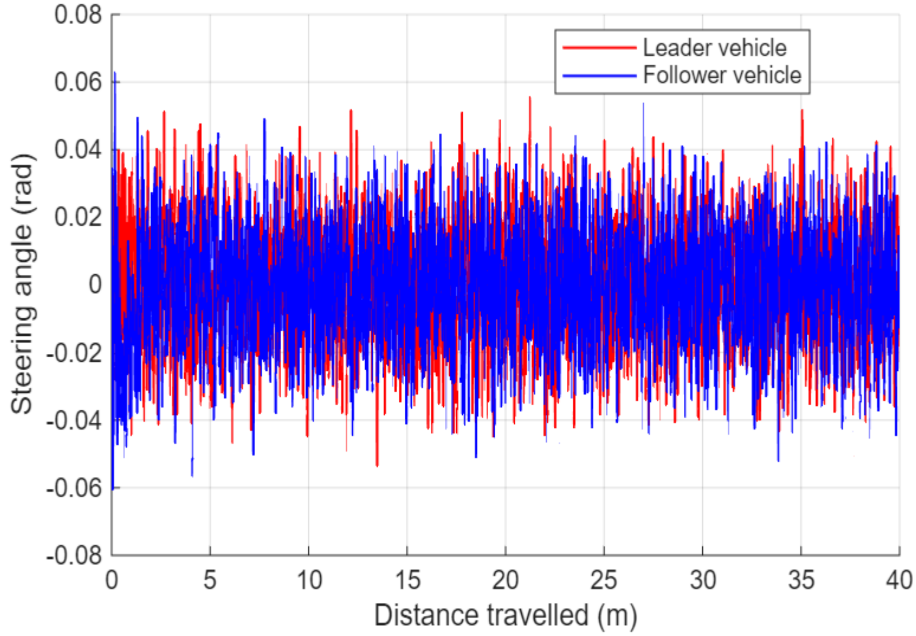

Figure A.33 Steering angle using the dynamic model with a large external load

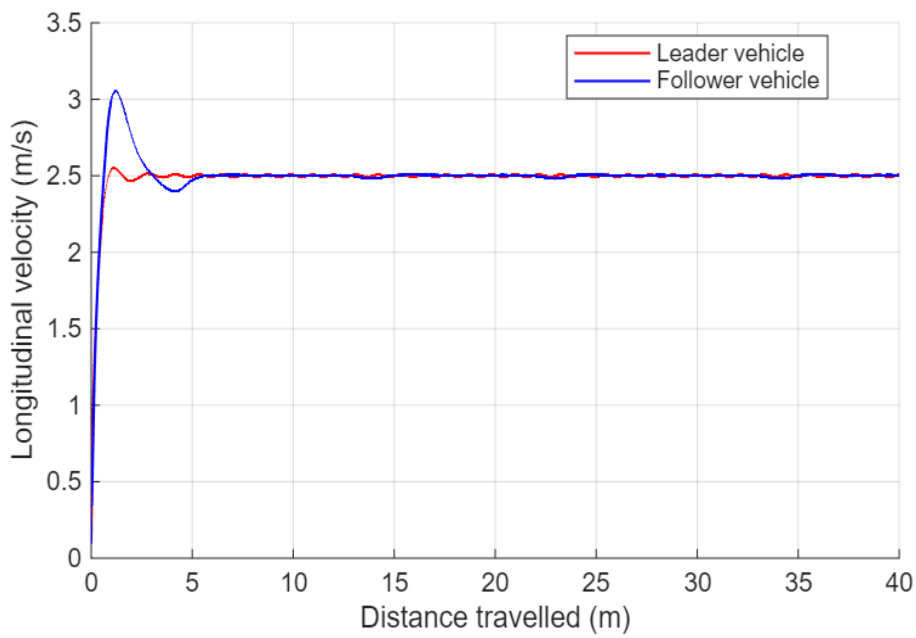

Figure A.34 Longitudinal velocity using the dynamic model with a large external load

A.6.2 Kinematic Model

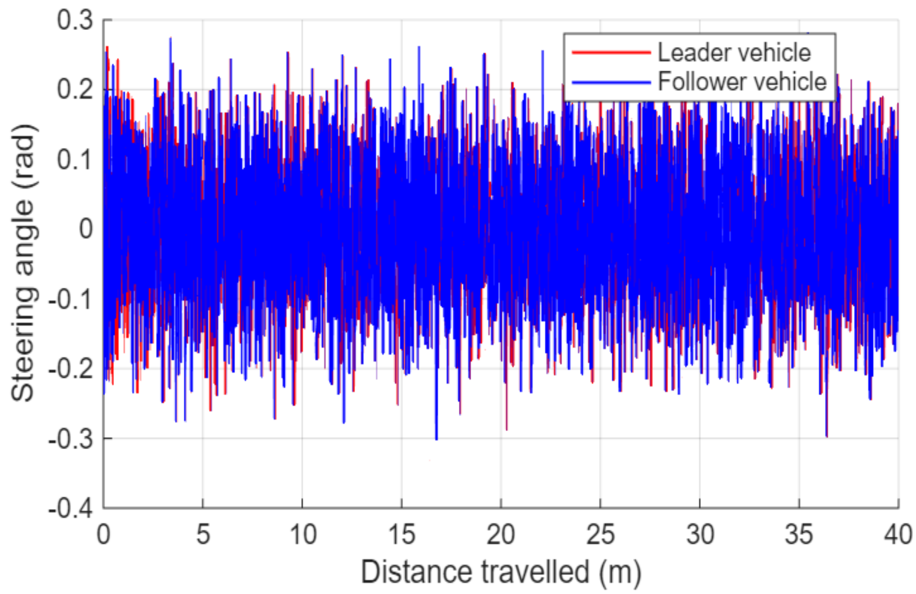

Figure A.35 Steering angle using the kinematic model with a large external load

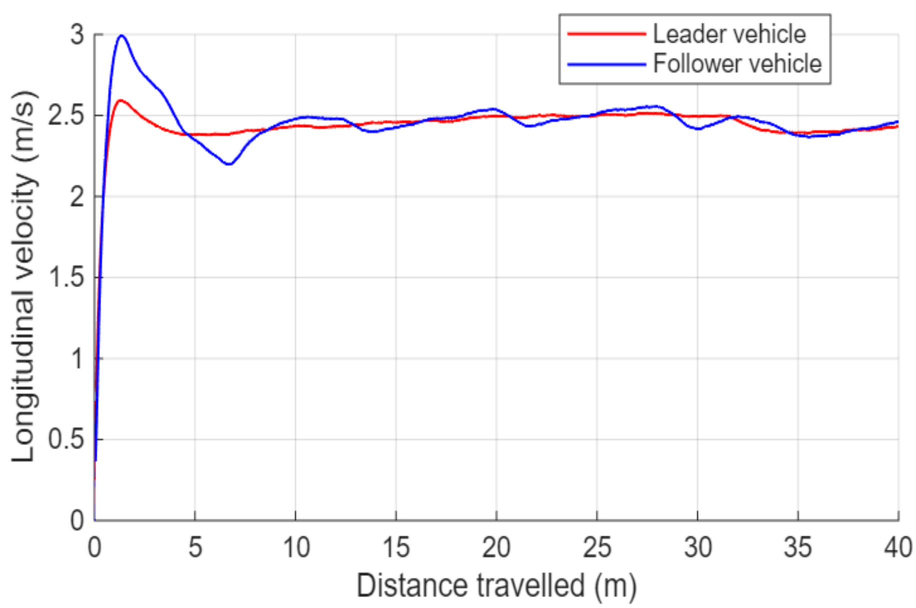

Figure A.36 Longitudinal velocity using the kinematic model with a large external load

A.7 Position of Implement on the Truss

A.7.1 Dynamic Model

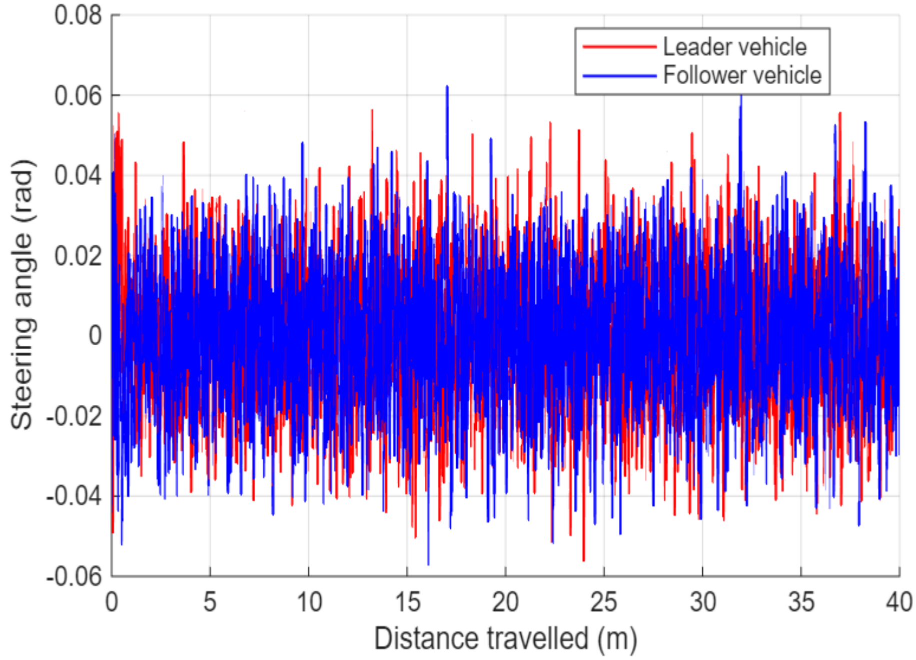

Figure A.37 Steering angle using the dynamic model for the follower-proximal configuration

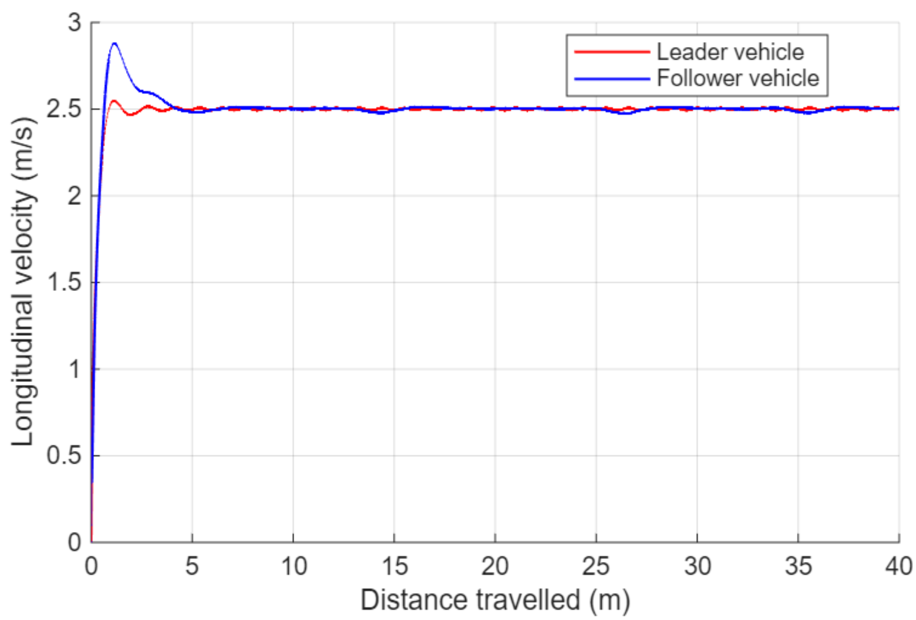

Figure A.38 Longitudinal velocity using the dynamic model for the follower-proximal configuration

A.7.2 Kinematic Model

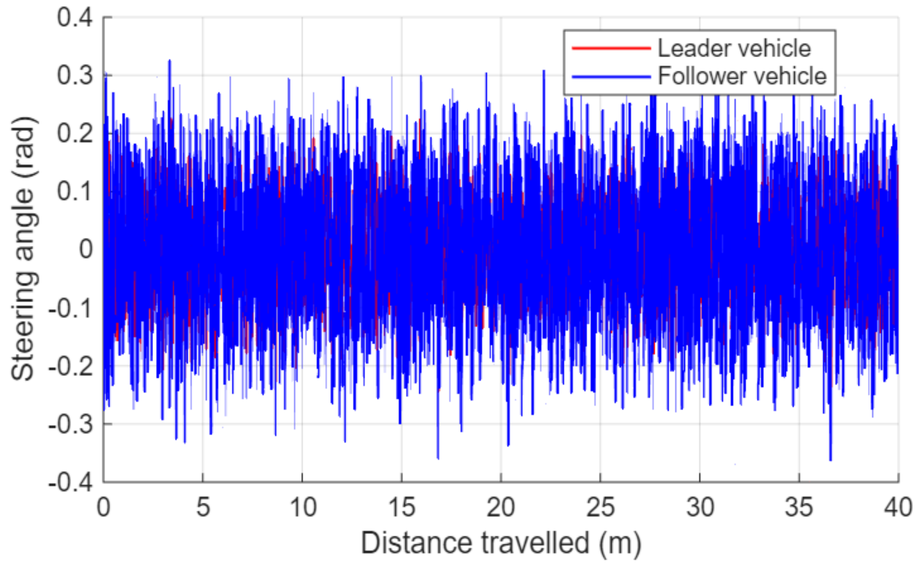

Figure A.39 Steering angle using the kinematic model for the follower-proximal configuration

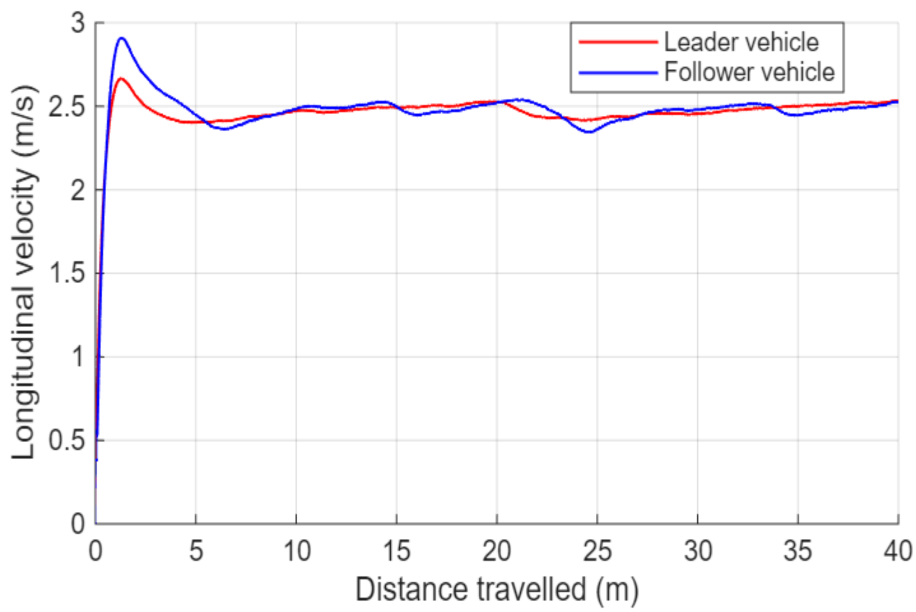

Figure A.40 Longitudinal velocity using the kinematic model for the follower-proximal configuration

A.8 Initial Offset Error

A.8.1 Large Initial Offset Error

A.8.1.1 Dynamic Model

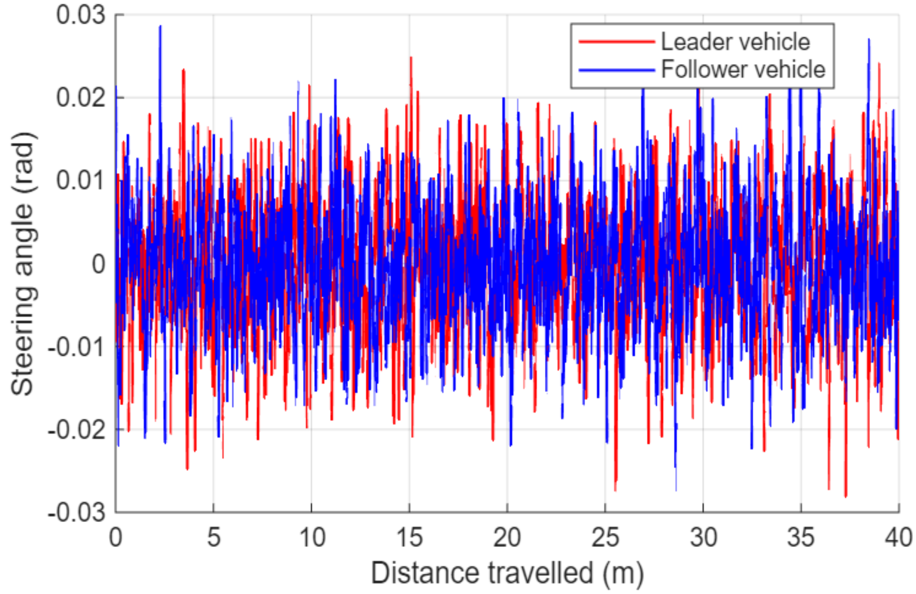

Figure A.41 Steering angle using the dynamic model with a large initial offset error

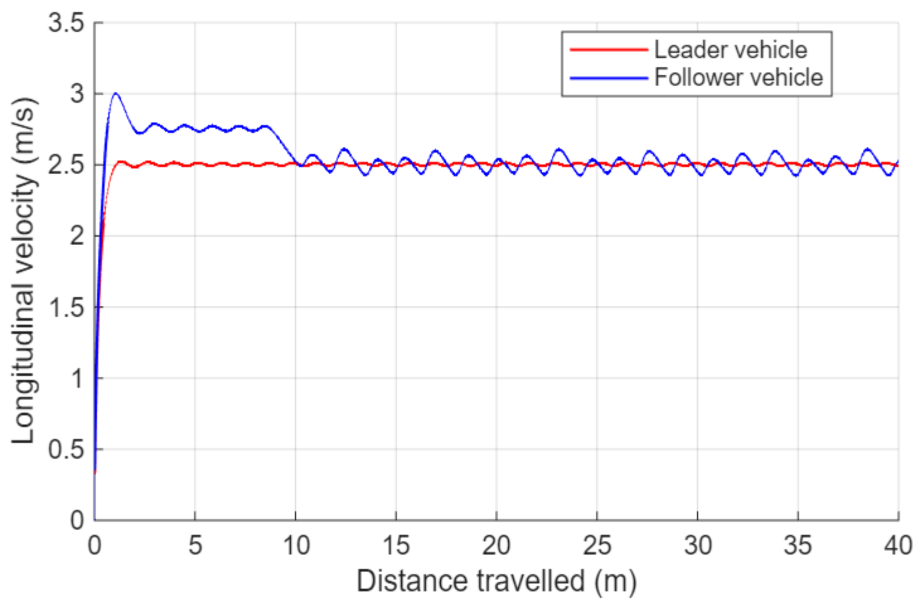

Figure A.42 Longitudinal velocity using the dynamic model with a large initial offset error

A.8.1.2 Kinematic Model

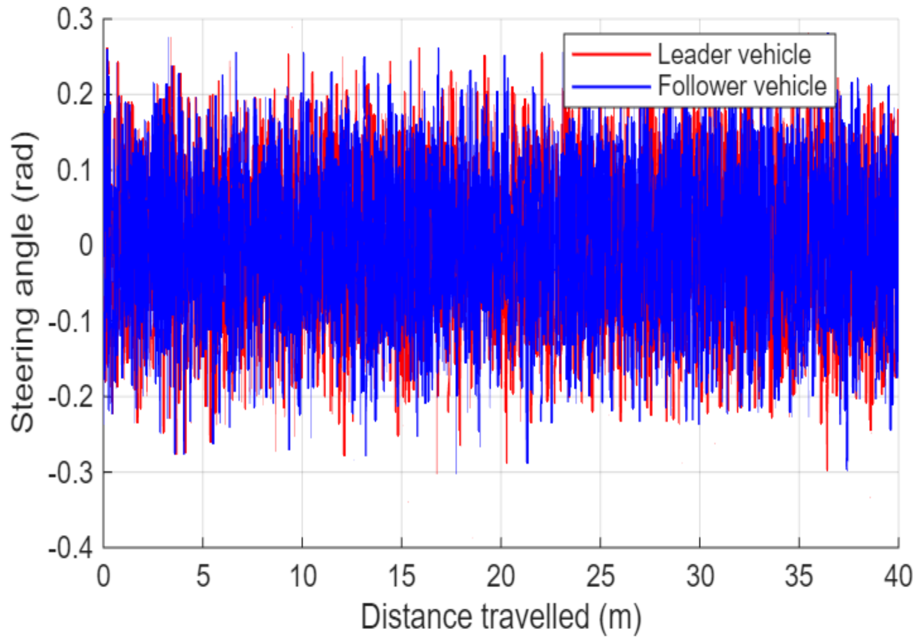

Figure A.43 Steering angle using the kinematic model with a large initial offset error

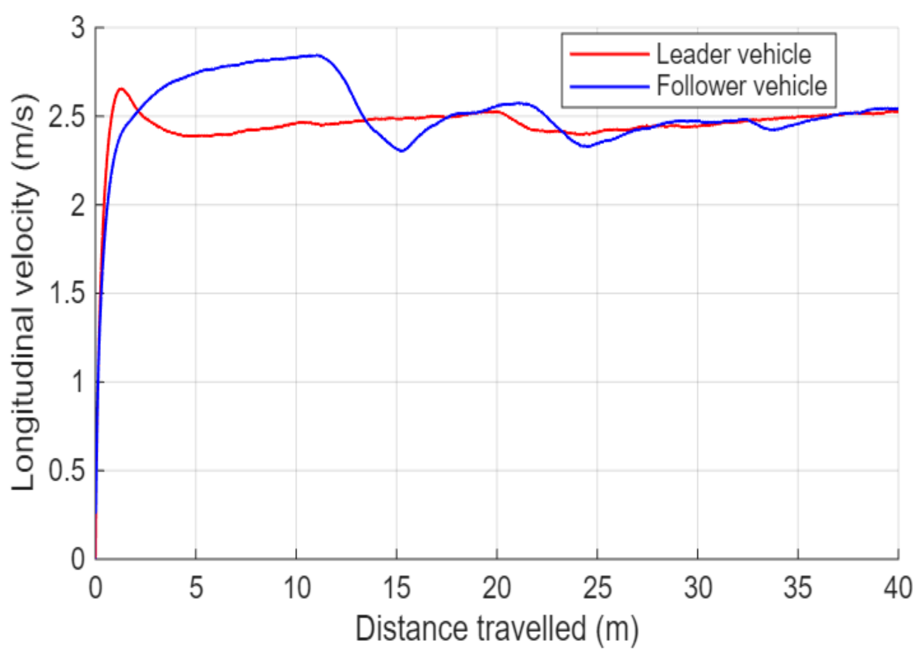

Figure A.44 Longitudinal velocity using the kinematic model with a large initial offset error

A.8.2 Small Initial Offset Error

A.8.2.1 Dynamic Model

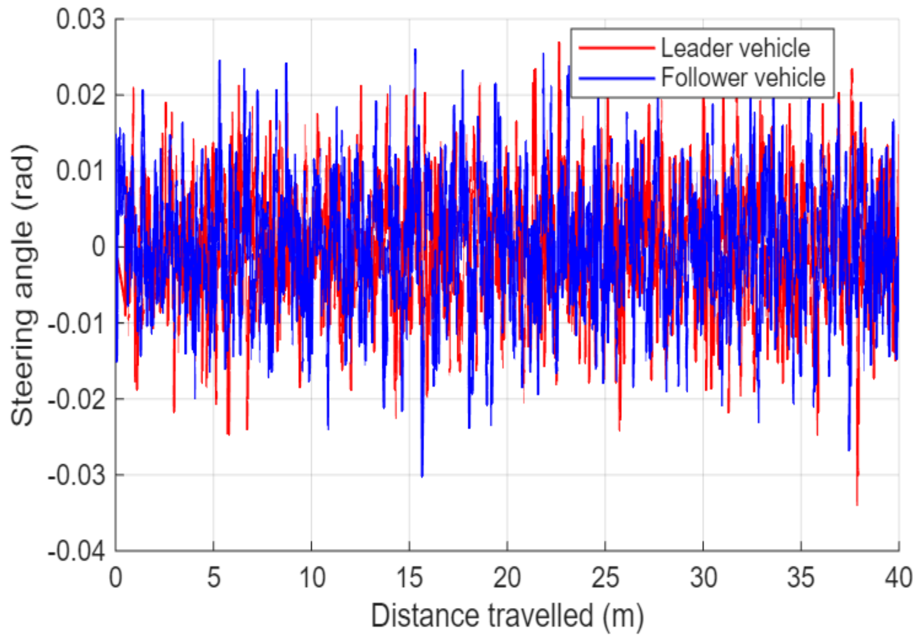

Figure A.45 Steering angle using the dynamic model with a small initial offset error

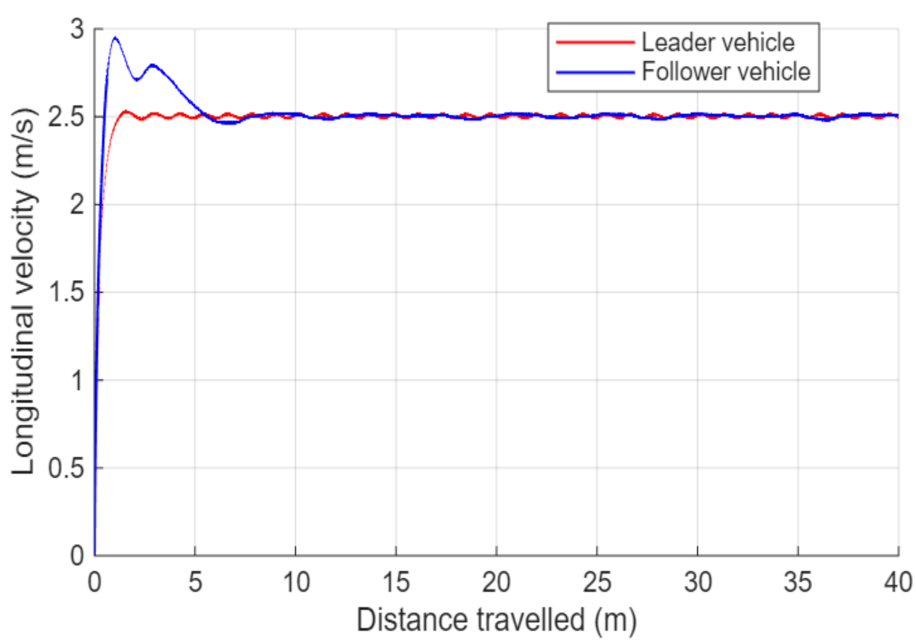

Figure A.46 Longitudinal velocity using the dynamic model with a small initial offset error

A.8.2.2 Kinematic Model

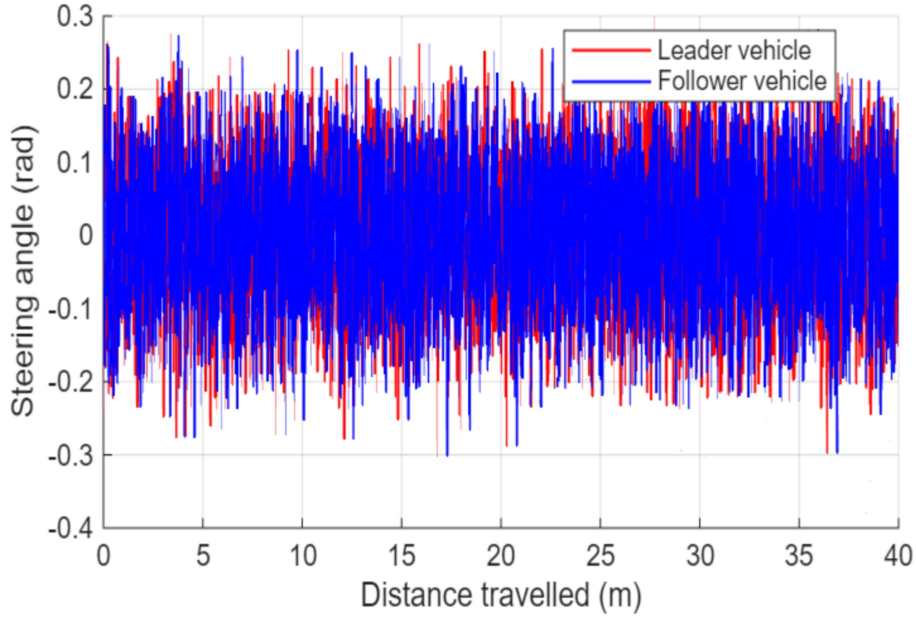

Figure A.47 Steering angle using the kinematic model with a small initial offset error

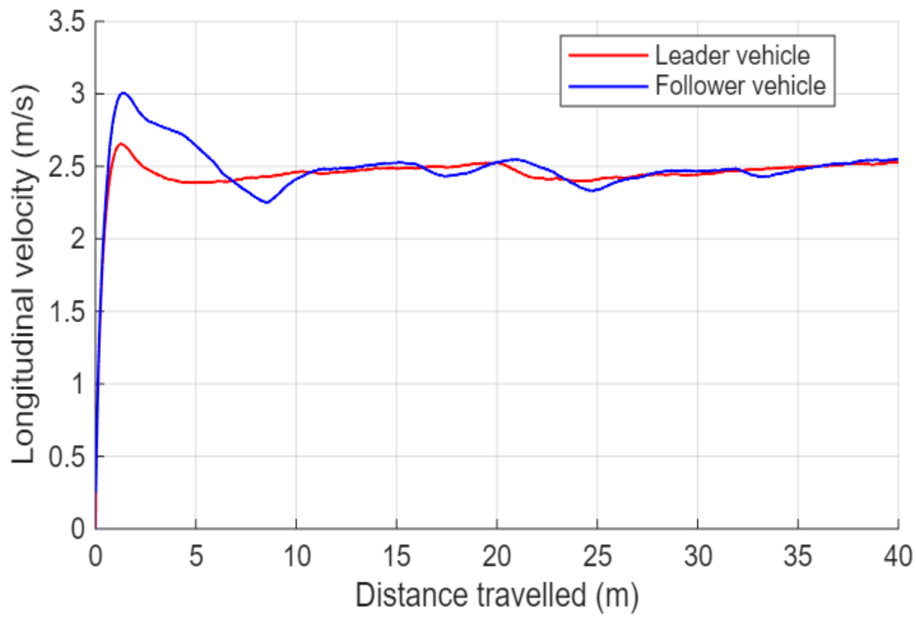

Figure A.48 Longitudinal velocity using the kinematic model with a small initial offset error

A.9 Additional Results for the Unified MPC

A.9.1 Curved Trajectory

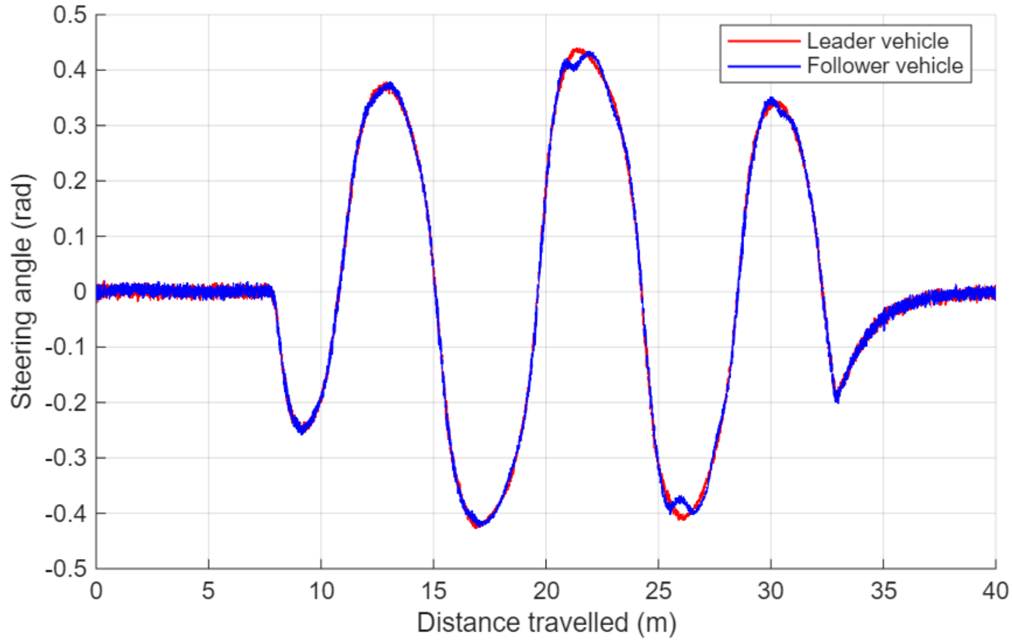

Figure A.49 Steering angle using the unified MPC for curved-trajectory tracking

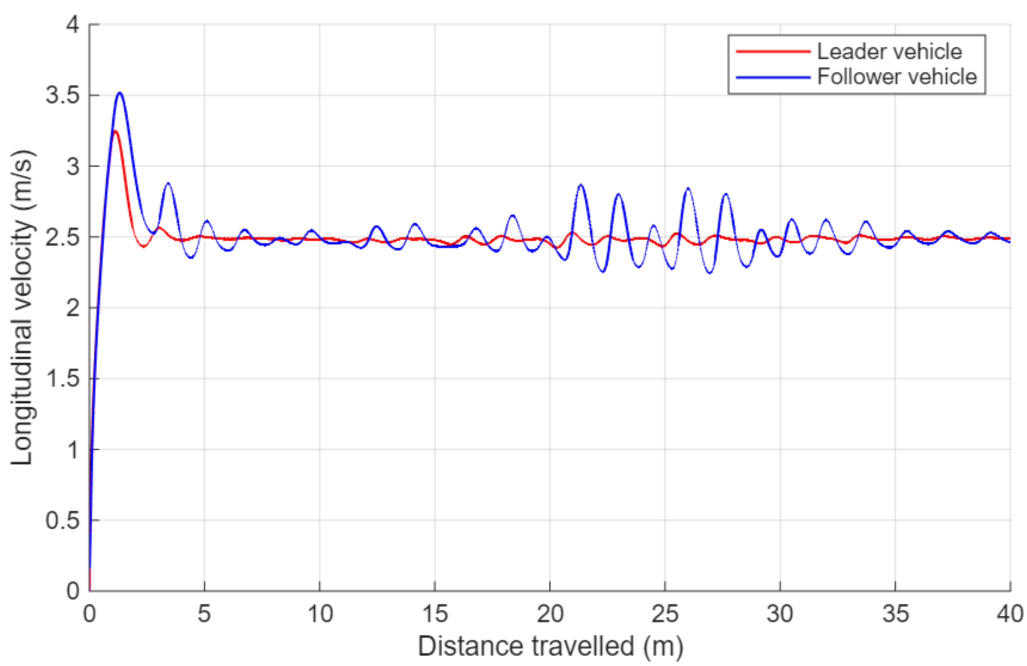

Figure A.50 Longitudinal velocity using the unified MPC for curved-trajectory tracking

A.9.2 High Speed

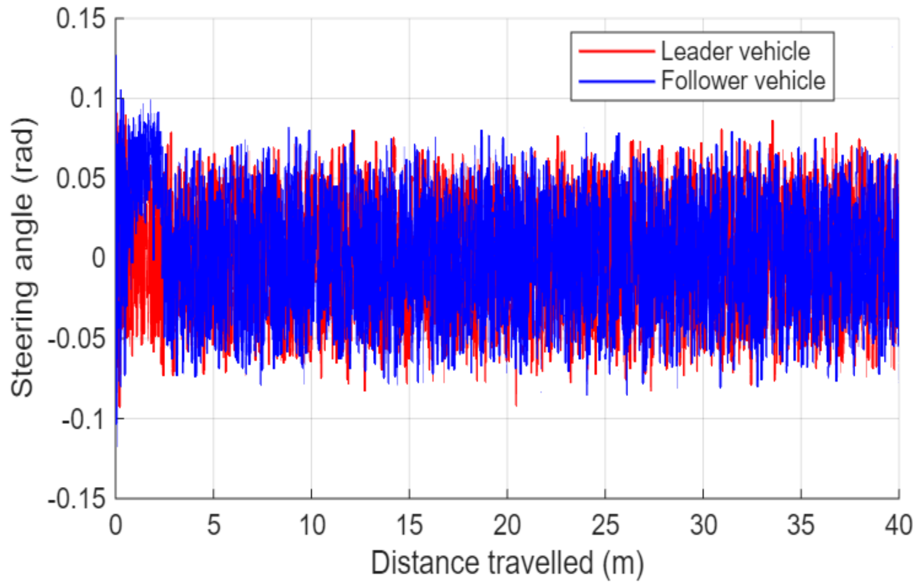

Figure A.51 Steering angle using the unified MPC at high speed

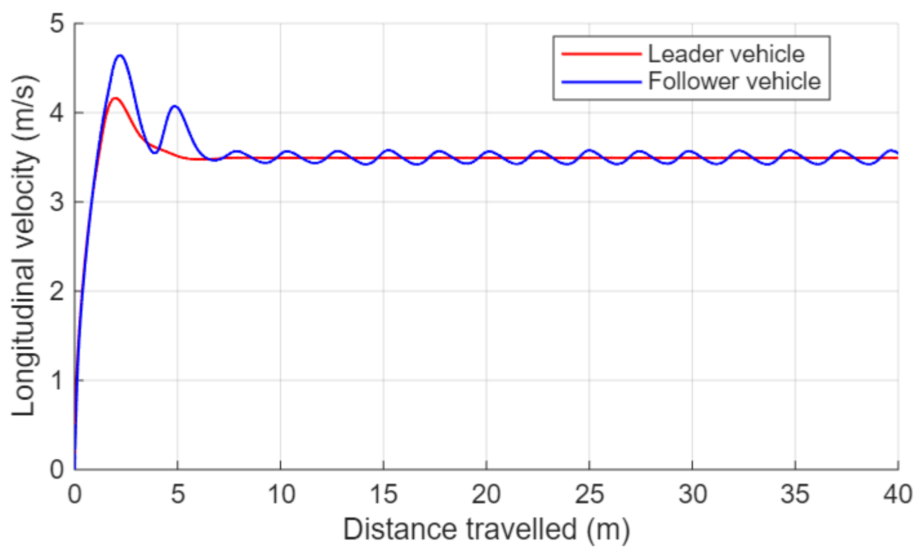

Figure A.52 Longitudinal velocity using the unified MPC at high speed

Appendix B
Additional Experimental Results

B.1 Single-Vehicle Path Following

To validate the control laws developed in Chapter 3, a single vehicle was tested on both straight-line and sinusoidal trajectories. The main performance metrics were lateral error and orientation error. Each condition was repeated twice to assess repeatability and reduce the influence of anomalous runs. All single-vehicle experiments were conducted on May 24, 2025. The May 24 session was run in dry conditions with light wind; no precipitation occurred during testing, and the pavement was dry and free of debris, so tire–surface friction was not reduced by moisture.

One representative trial for each condition is presented in this section, while the duplicate trials and supplementary results are provided in Sections B.1.3 and B.1.4.

B.1.1 Straight-Line Tracking

Table B.1 summarizes the initial and steady-state performance values for straight-line tracking.

Table B.1 Performance variables for single-vehicle straight-line tracking[a]

Description	Initial value	Steady-state value (Dynamic model)	Steady-state value (Kinematic model)
Longitudinal velocity (m/s)	0	0.97	0.97
Lateral error (m)	0.58	**±0.028**	±0.056
Orientation error (rad)	−0.024	±0.050	**±0.047**
Steering angle (rad)	−0.26	–	–

[a] Boldface: notably better than the other model.

The vehicle followed the straight-line reference path $y_1 = -1.6$ m. The initial conditions are: $x_1(0) = -4.83$ m, $y_1(0) = -1.02$ m, and $\theta_1(0) = -0.024$ rad. The reference line was placed 0.58 m from the vehicle's initial lateral position ($y_1(0) = -1.02$ m against the reference at $y_1 = -1.6$ m) so that each run began with a non-zero lateral error and the convergence of the controller to the path could be observed; a vehicle started on the reference line would have had only sensor noise to reject, which would not have tested the control law.

B.1.1.1 Dynamic Model

The control gains were configured as follows:

- Weighting parameters: $Q = [20\ 0;\ 0\ 42]$, $R = 30$
- Prediction horizon and control horizon: $N_p = 23$, $N_c = 10$

The main results are shown in Figure B.1 to Figure B.3.

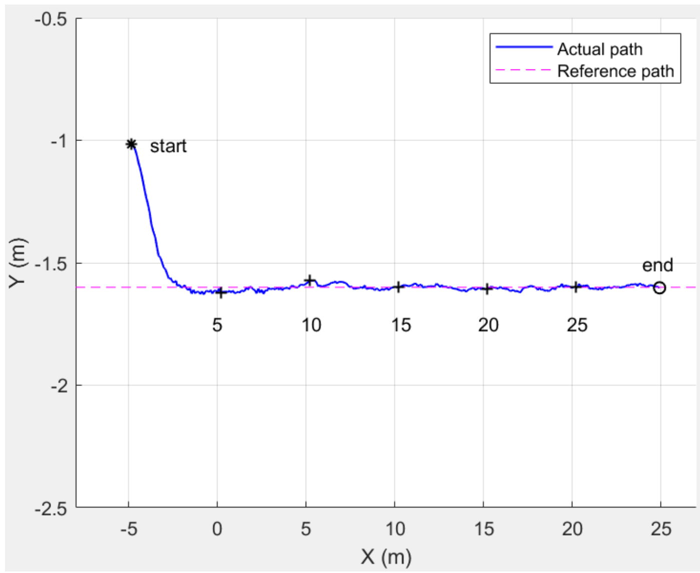

Figure B.1 Reference and actual paths for single-vehicle straight-line tracking using the dynamic model

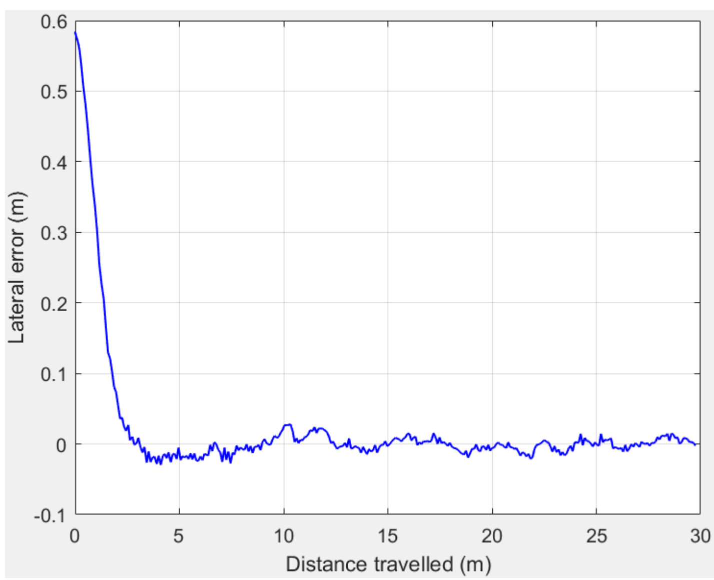

Figure B.2 Lateral error for single-vehicle straight-line tracking using the dynamic model

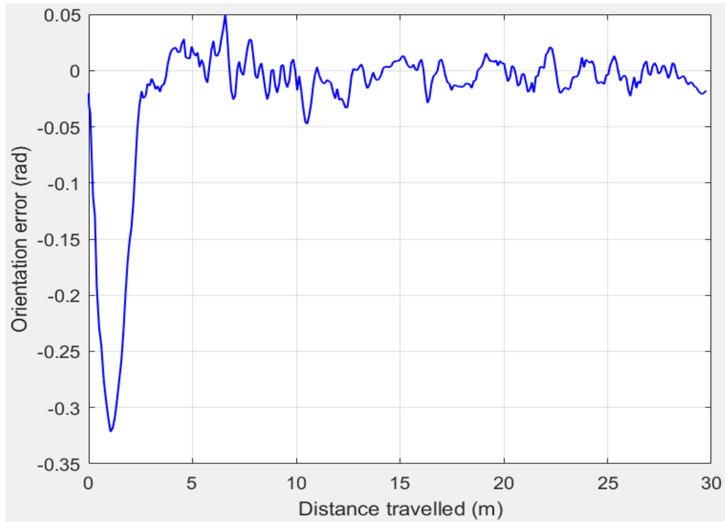

Figure B.3 Orientation error for single-vehicle straight-line tracking using the dynamic model

The IAE values were as follows:

- Lateral error $J_L = 0.898\ \mathrm{m}^2$
- Orientation error $J_\theta = 0.804$ rad·m

B.1.1.2 Kinematic Model

The control gains were configured as follows:

- Control gains: $k_1 = 2.2$, $k_2 = 1.21$

The results are shown in Figure B.4 to Figure B.6.

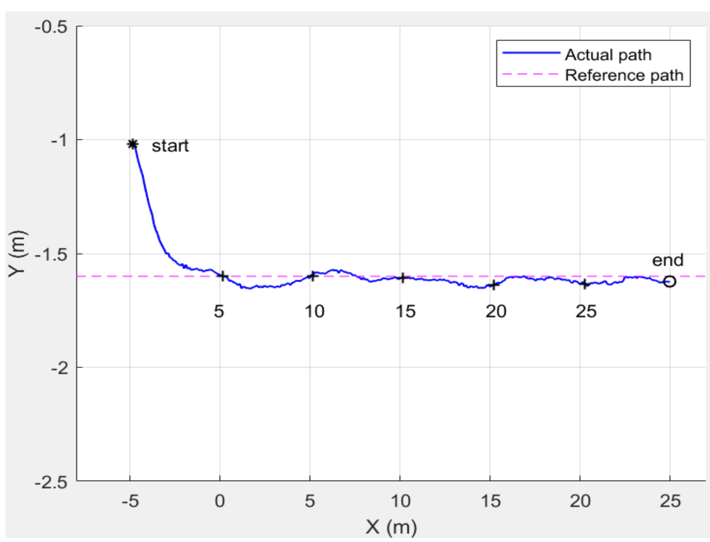

Figure B.4 Reference and actual paths for single-vehicle straight-line tracking using the kinematic model

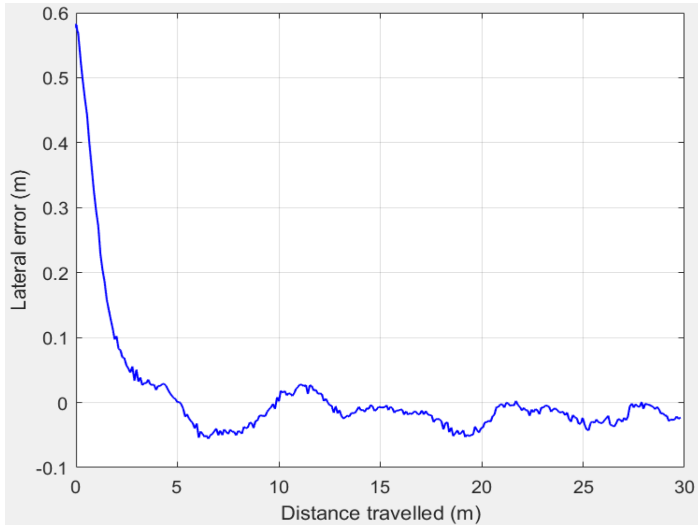

Figure B.5 Lateral error for single-vehicle straight-line tracking using the kinematic model

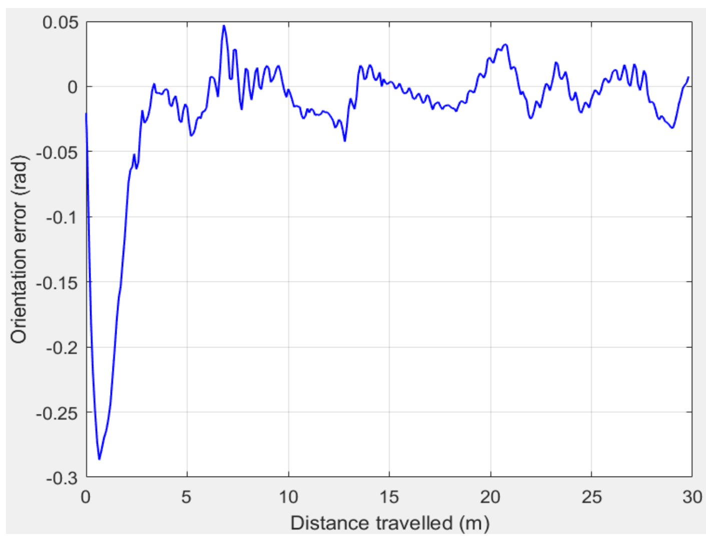

Figure B.6 Orientation error for single-vehicle straight-line tracking using the kinematic model

The IAE values were as follows:

- Lateral error $J_L = 1.27$ m^2
- Orientation error $J_\theta = 0.811$ rad·m

B.1.1.3 Experimental Results Comparison

The experimental trajectories for straight-line tracking using the dynamic and kinematic models are shown in Figure B.7.

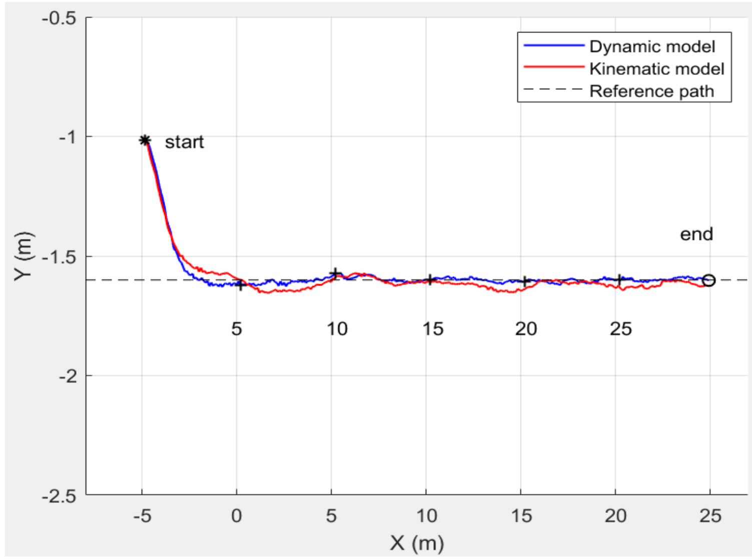

Figure B.7 Experimental trajectories based on dynamic and kinematic models of the single-vehicle straight-line tracking

From Section B.1.1, Table B.1, and Figure B.7, and assessed against the practical-significance thresholds of Section 5.3, both models reached steady state in lateral and orientation errors. The dynamic model reduced the steady-state lateral error by 50% (from $\pm$0.056 m to $\pm$0.028 m) compared with the kinematic model, a difference of 0.028 m that is nearly three times the 0.01 m threshold; both values are well within the $\pm$0.15 m bound. The steady-state orientation errors, $\pm$0.050 rad for the dynamic model and $\pm$0.047 rad for the kinematic model, differ by 0.003 rad, which is below the 0.0087 rad IMU threshold, so the two models are equivalent in steady-state heading on the straight path.

The dynamic model also yielded a 29% lower lateral error IAE (0.898 vs. 1.27 m^2), a difference of 0.37 m^2 that exceeds the 0.30 m^2 lateral IAE threshold and indicates smoother and more accurate straight-line tracking. The orientation error IAE was nearly identical for the two models (0.804 vs. 0.811 rad·m), a difference of 0.007 rad·m that is within measurement resolution. Overall, for single-vehicle straight-line tracking, the dynamic model provided practically better lateral path tracking than the kinematic model, with no resolvable difference in heading regulation.

B.1.2 Sinusoidal Trajectory Tracking

Table B.2 summarizes the initial and steady-state performance values for sinusoidal trajectory tracking.

Table B.2 Performance variables for single-vehicle sinusoidal trajectory tracking[a]

Description	Initial value	Steady-state value (Dynamic model)	Steady-state value (Kinematic model)
Longitudinal velocity (m/s)	0	0.97	0.97
Lateral error (m)	0.58	**±0.058**	±0.078
Orientation error (rad)	−0.069	±0.054	**±0.046**
Steering angle (rad)	−0.26	–	–

[a] Boldface: notably better than the other model.

The vehicle followed the sinusoidal reference path defined as

$$y_1 = 0.5 \cdot \sin\frac{\pi}{4} x_1 - 1.6 \tag{131}$$

The initial conditions were: $x_1(0) = -5.09$ m, $y_1(0) = -0.63$ m, and $\theta_1(0) = -0.29$ rad.

B.1.2.1 Dynamic Model

The control gains were configured as follows:

- Weighting parameters: $Q = [27\ 0;\ 0\ 36]$, $R = 100$
- Prediction horizon and control horizon: $N_p = 32$, $N_c = 15$

The results are shown in Figure B.8 to Figure B.10.

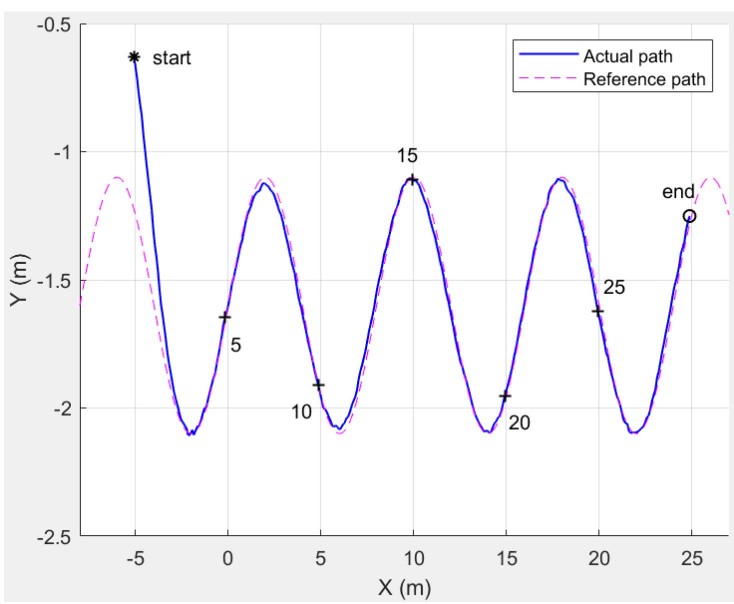

Figure B.8 Reference and actual paths for single-vehicle sinusoidal trajectory tracking using the dynamic model

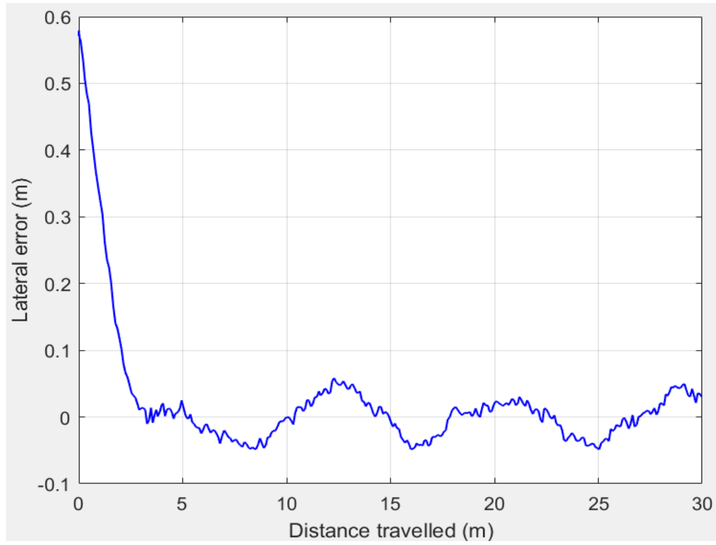

Figure B.9 Lateral error for single-vehicle sinusoidal trajectory tracking using the dynamic model

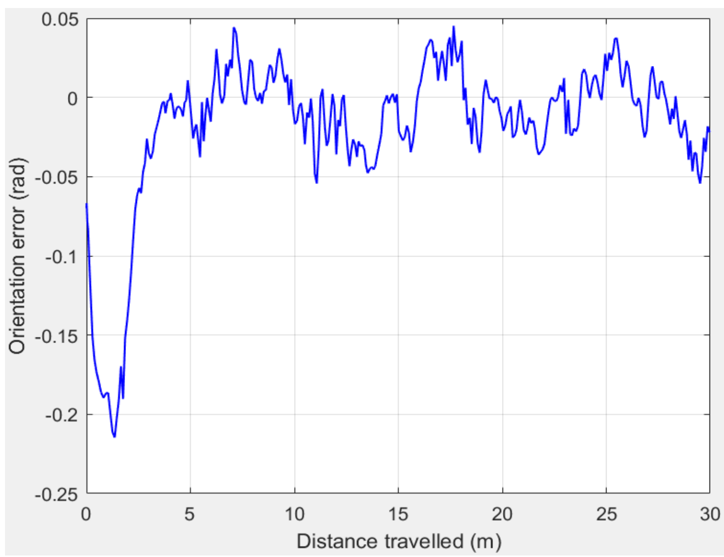

Figure B.10 Orientation error for single-vehicle sinusoidal trajectory tracking using the dynamic model

The IAE values were as follows:

- Lateral error $J_L = 1.33\ \mathrm{m}^2$
- Orientation error $J_\theta = 0.877$ rad·m

B.1.2.2 Kinematic Model

The control gains were configured as follows:

- Control gains: $k_1 = 1.8$, $k_2 = 0.81$.

The results are shown in Figure B.11 to Figure B.13.

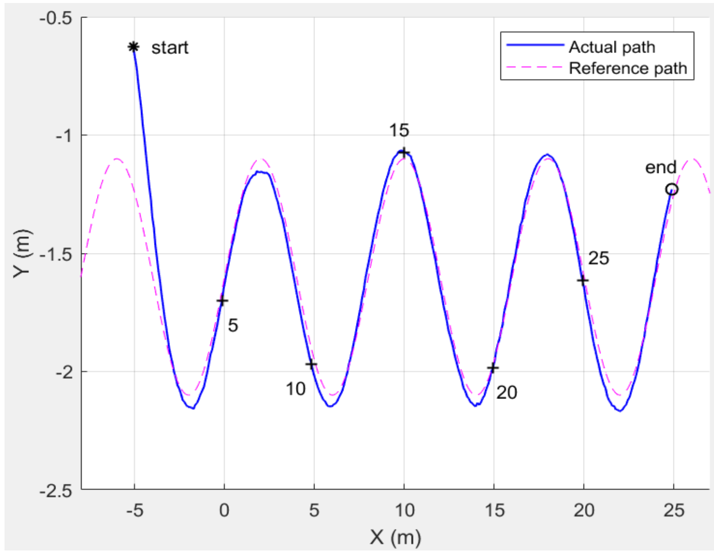

Figure B.11 Reference and actual paths for single-vehicle sinusoidal trajectory tracking using the kinematic model

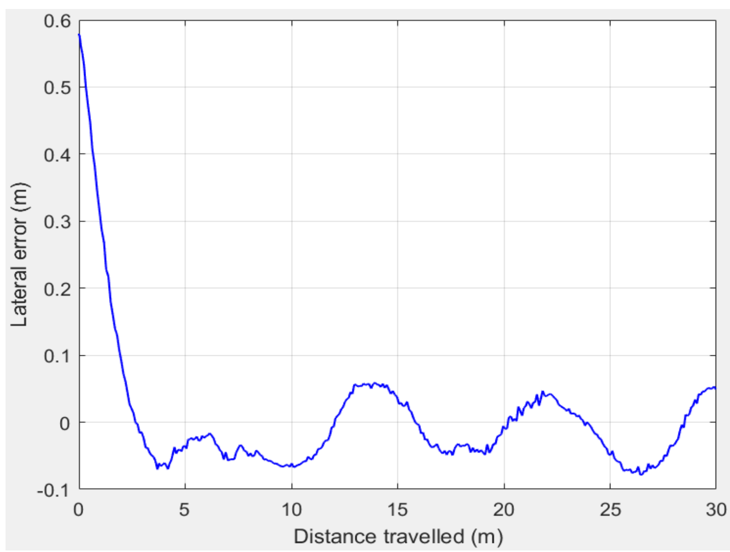

Figure B.12 Lateral error for single-vehicle sinusoidal trajectory tracking using the kinematic model

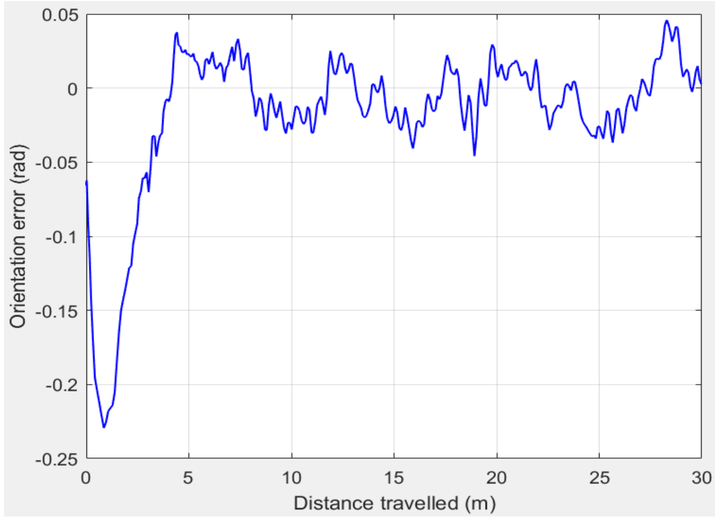

Figure B.13 Orientation error for single-vehicle sinusoidal trajectory tracking using the kinematic model

The IAE values were as follows:

- Lateral error $J_L = 1.73$ m^2
- Orientation error $J_\theta = 0.909$ rad·m

B.1.2.3 Experimental Results Comparison

The experimental trajectories for sinusoidal tracking using the dynamic and kinematic models are shown in Figure B.14.

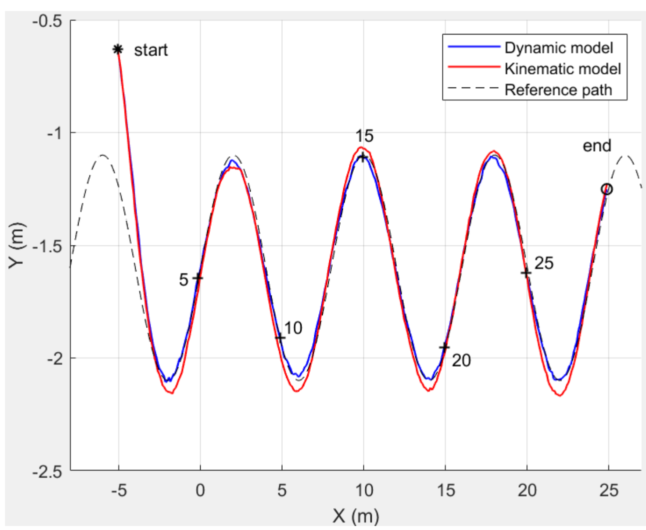

Figure B.14 Experimental trajectories based on dynamic and kinematic models of the single-vehicle sinusoidal trajectory tracking

From Section B.1.2, Table B.2 and Figure B.14, both models again converged to steady state. The dynamic model achieved a 26% lower steady-state lateral error (± 0.058 m vs. ± 0.078 m) than the kinematic model, a difference of 0.020 m that is twice the 0.01 m threshold; both values are within the ± 0.15 m bound. The steady-state orientation error was ± 0.054 rad for the dynamic model and ± 0.046 rad for the kinematic model; the 0.008 rad difference is at the 0.0087 rad IMU threshold and is not treated as a practically meaningful difference in either direction.

For the IAE metrics, the dynamic model reduced lateral error IAE by 23% (1.33 vs. 1.73 m²), a difference of 0.40 m² that exceeds the 0.30 m² lateral IAE threshold and demonstrates better adaptation to the changing curvature of the sinusoidal path. The orientation error IAE was 0.877 rad·m for the dynamic model and 0.909 rad·m for the kinematic model, a difference of 0.032 rad·m that is within measurement resolution. These results indicate that the dynamic model adapted more effectively to the sinusoidal path in lateral control, with heading regulation equivalent at the sensor level.

B.1.3 Supplementary Experimental Straight-Line Tracking

B.1.3.1 Dynamic Model

First set of supplementary experimental results (Finalized May 24, 2025).

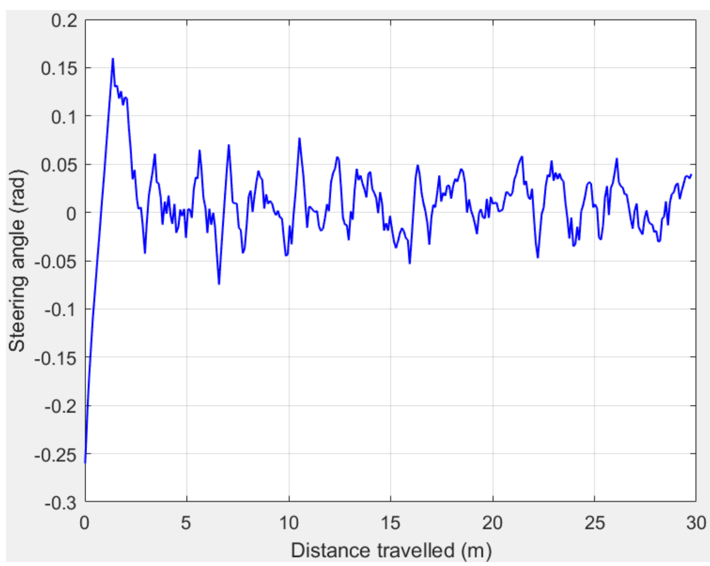

Figure B.15 Steering angle for single-vehicle straight-line tracking using the dynamic model

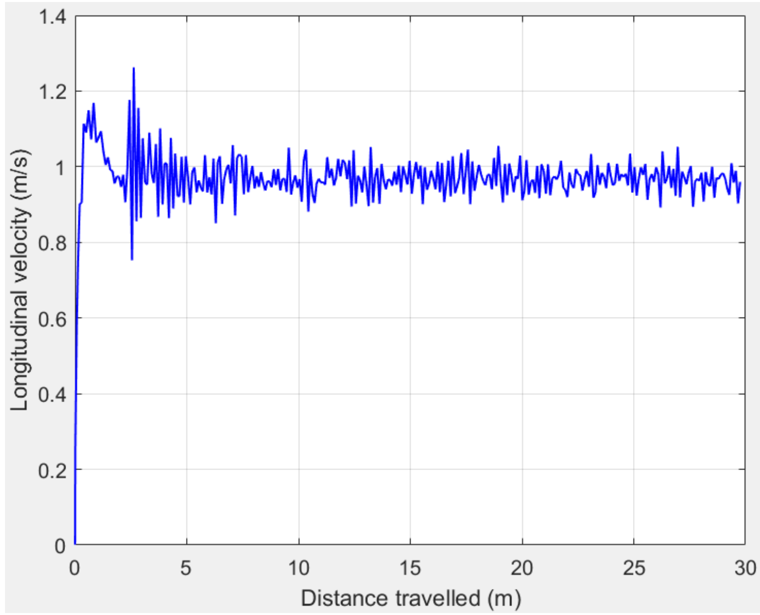

Figure B.16 Longitudinal velocity for single-vehicle straight-line tracking using the dynamic model

Second set of full experimental results (Finalized May 24, 2025).

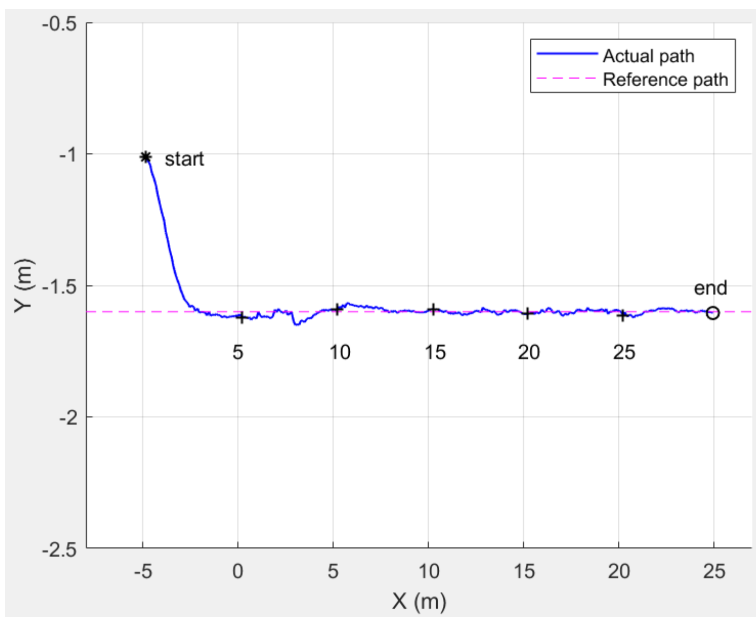

Figure B.17 Reference and actual paths for single-vehicle straight-line tracking using the dynamic model (second set)

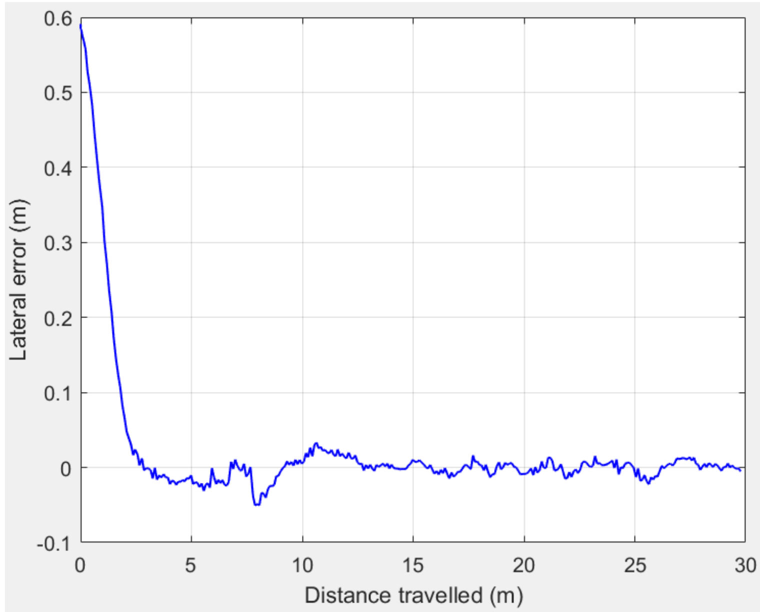

Figure B.18 Lateral error for single-vehicle straight-line tracking using the dynamic model (second set)

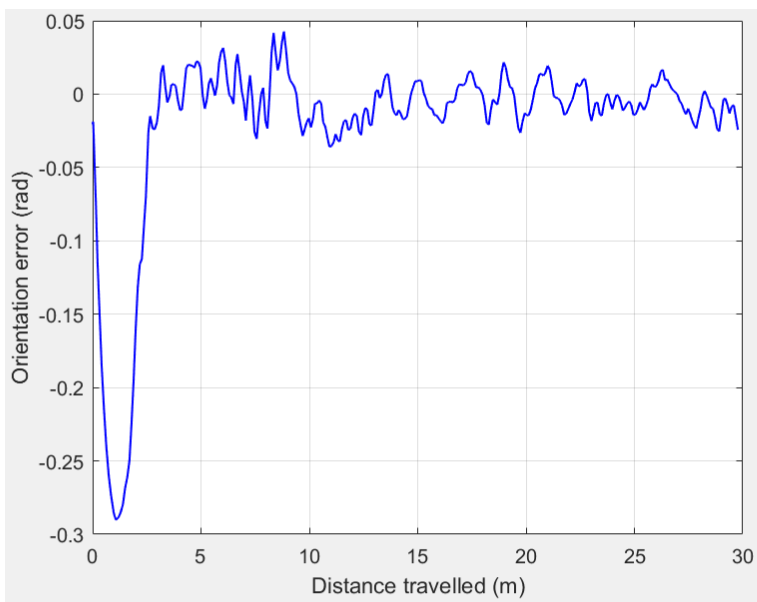

Figure B.19 Orientation error for single-vehicle straight-line tracking using the dynamic model (second set)

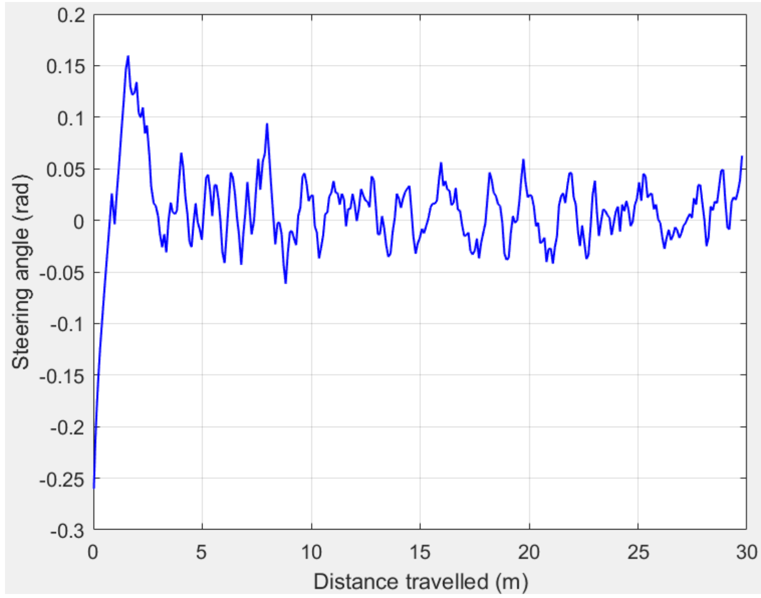

Figure B.20 Steering angle for single-vehicle straight-line tracking using the dynamic model (second set)

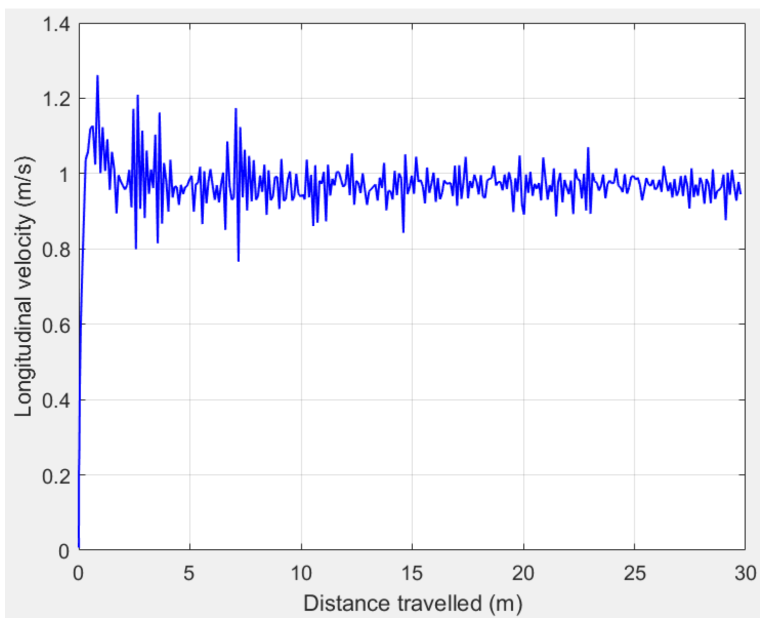

Figure B.21 Longitudinal velocity for single-vehicle straight-line tracking using the dynamic model (second set)

B.1.3.2 Kinematic Model

First set of supplementary experimental results (Finalized May 24, 2025).

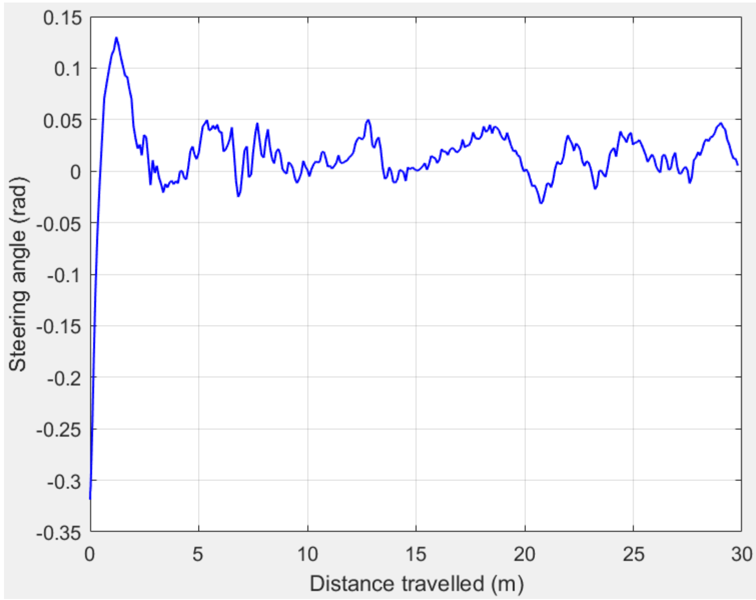

Figure B.22 Steering angle for single-vehicle straight-line tracking using the kinematic model

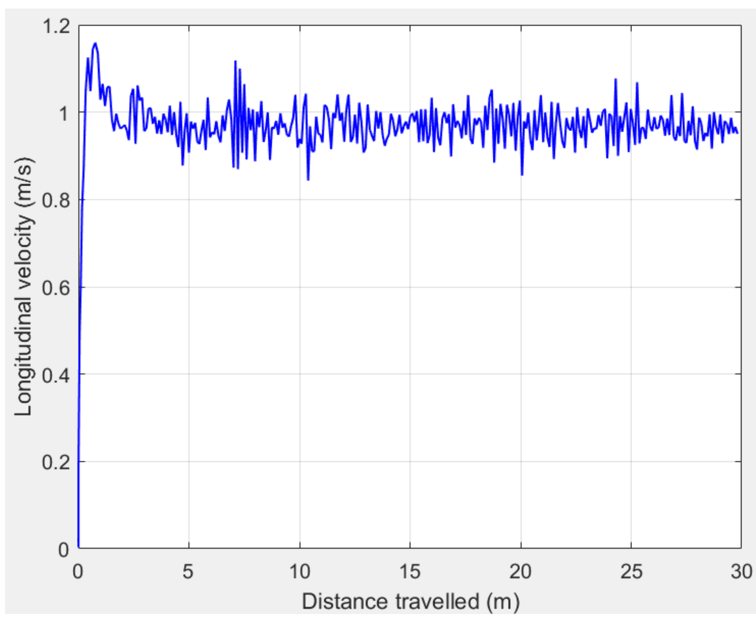

Figure B.23 Longitudinal velocity for single-vehicle straight-line tracking using the kinematic model

Second set of full experimental results (Finalized May 24, 2025).

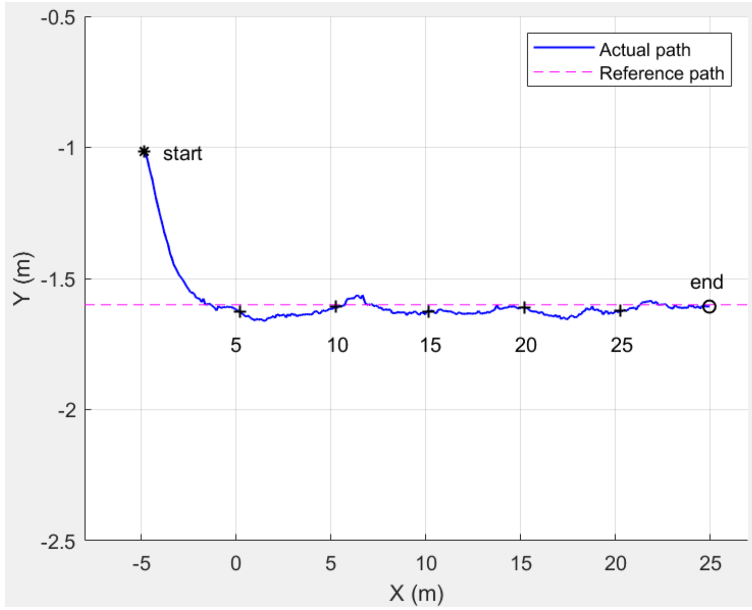

Figure B.24 Reference and actual paths for single-vehicle straight-line tracking using the kinematic model (second set)

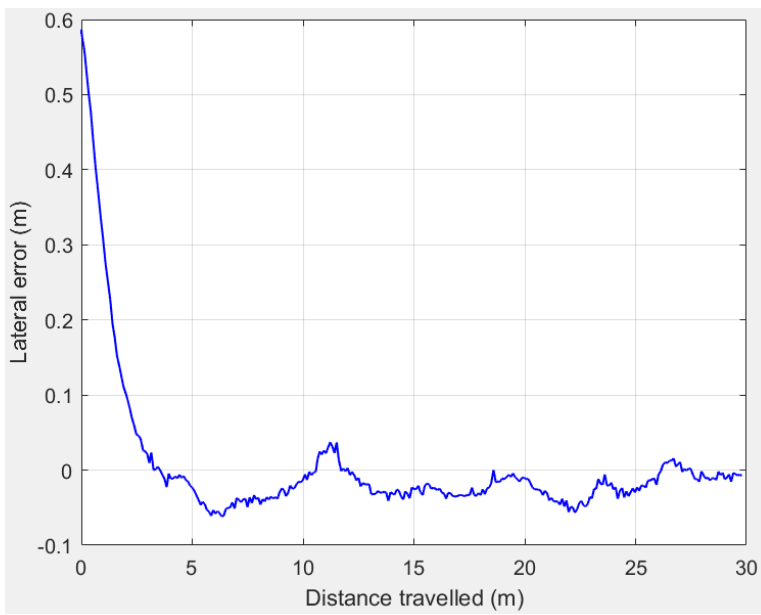

Figure B.25 Lateral error for single-vehicle straight-line tracking using the kinematic model (second set)

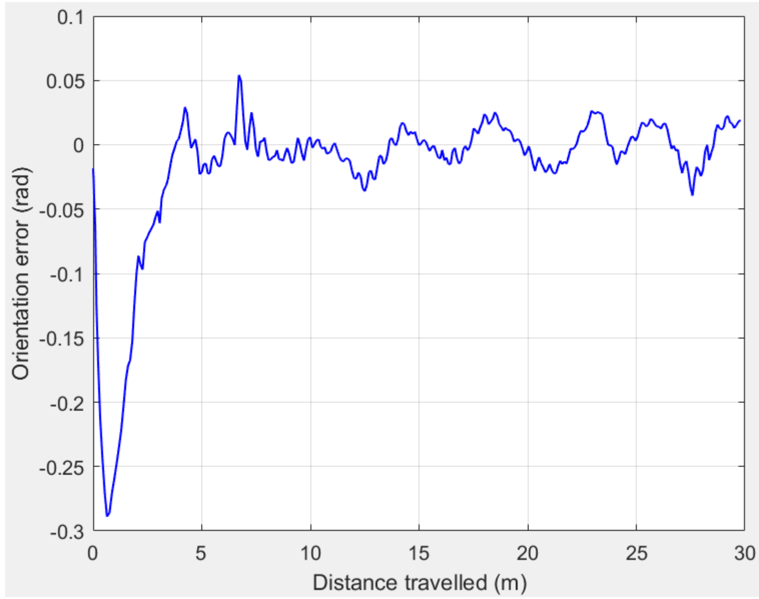

Figure B.26 Orientation error for single-vehicle straight-line tracking using the kinematic model (second set)

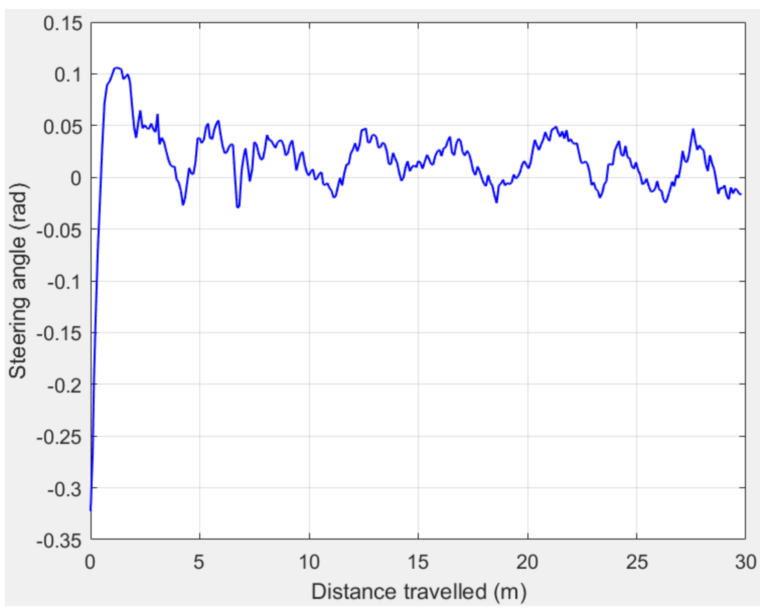

Figure B.27 Steering angle for single-vehicle straight-line tracking using the kinematic model (second set)

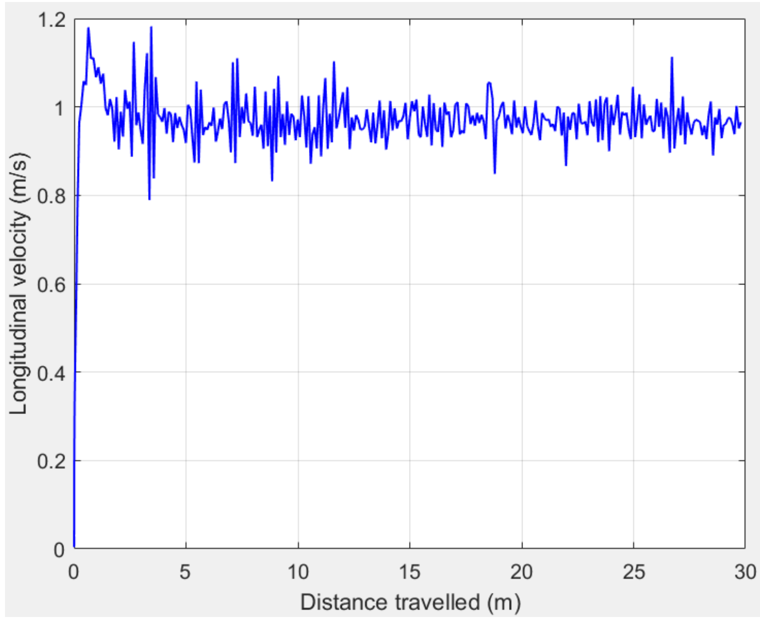

Figure B.28 Longitudinal velocity for single-vehicle straight-line tracking using the kinematic model (second set)

B.1.4 Supplementary Experimental Sinusoidal Trajectory Tracking

B.1.4.1 Dynamic Model

First set of supplementary experimental results (Finalized May 24, 2025).

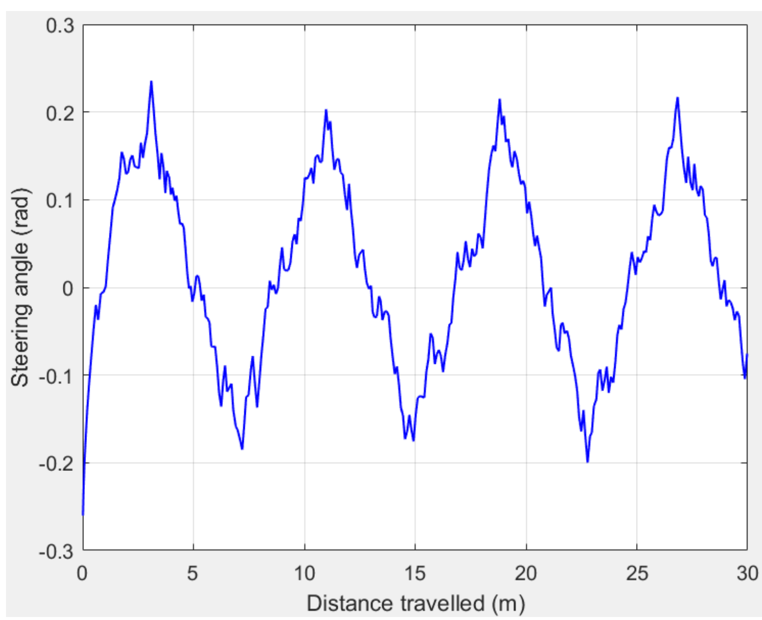

Figure B.29 Steering angle for single-vehicle sinusoidal trajectory tracking using the dynamic model

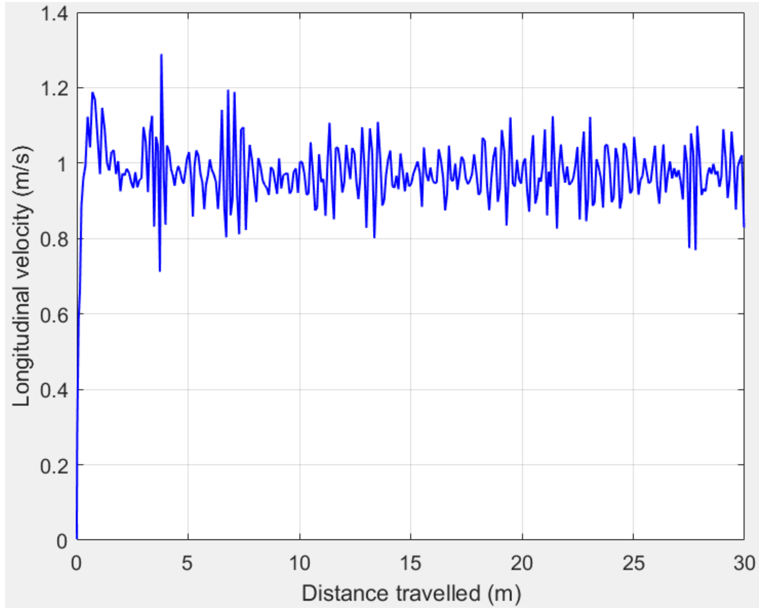

Figure B.30 Longitudinal velocity for single-vehicle sinusoidal trajectory tracking using the dynamic model

Second set of full experimental results (Finalized May 24, 2025).

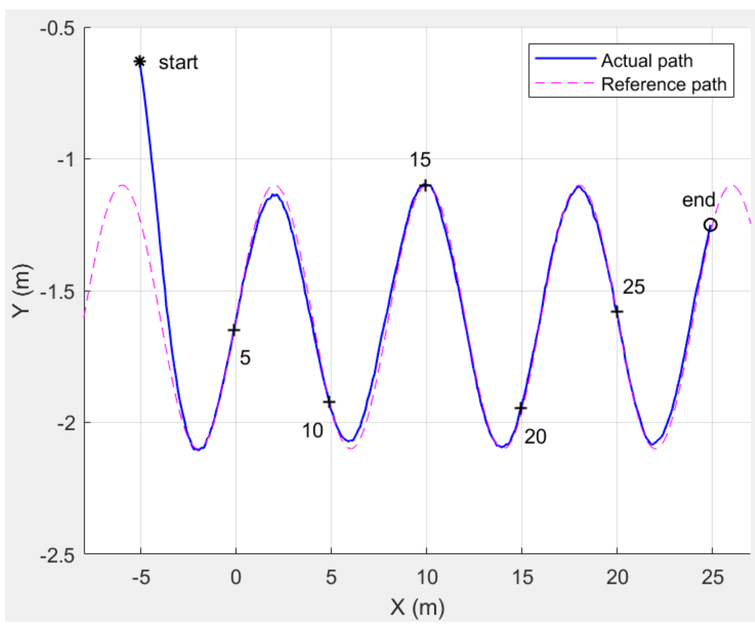

Figure B.31 Reference and actual paths for single-vehicle sinusoidal trajectory tracking using the dynamic model (second set)

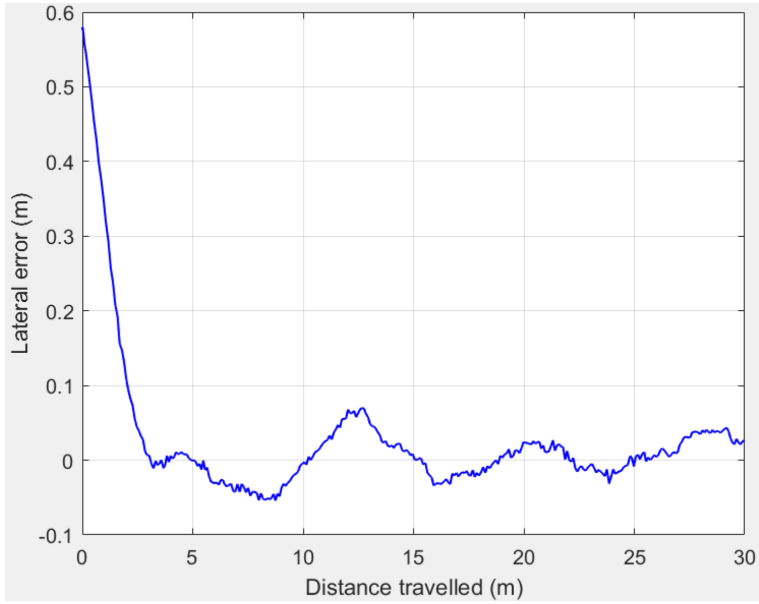

Figure B.32 Lateral error for single-vehicle sinusoidal trajectory tracking using the dynamic model (second set)

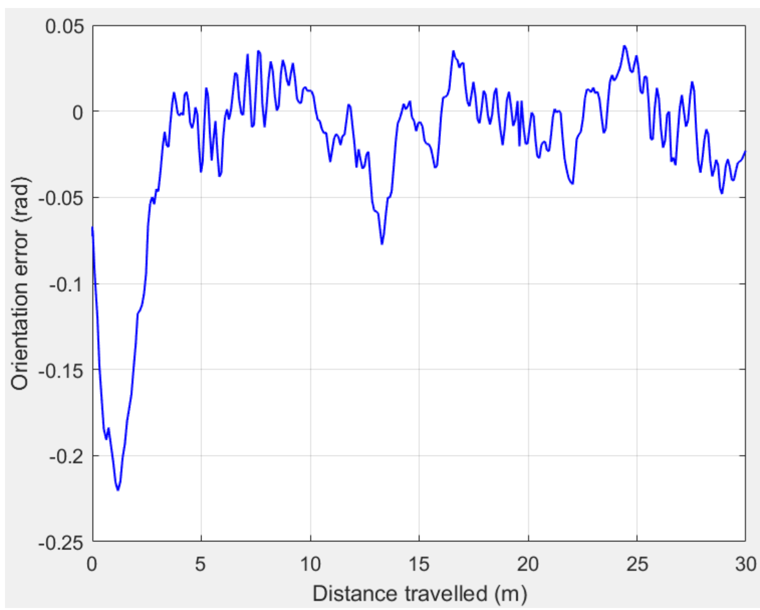

Figure B.33 Orientation error for single-vehicle sinusoidal trajectory tracking using the dynamic model (second set)

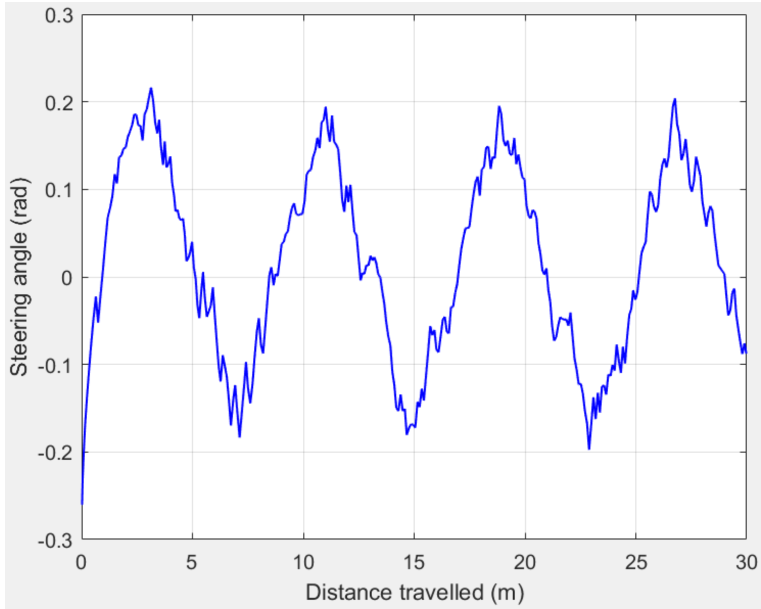

Figure B.34 Steering angle for single-vehicle sinusoidal trajectory tracking using the dynamic model (second set)

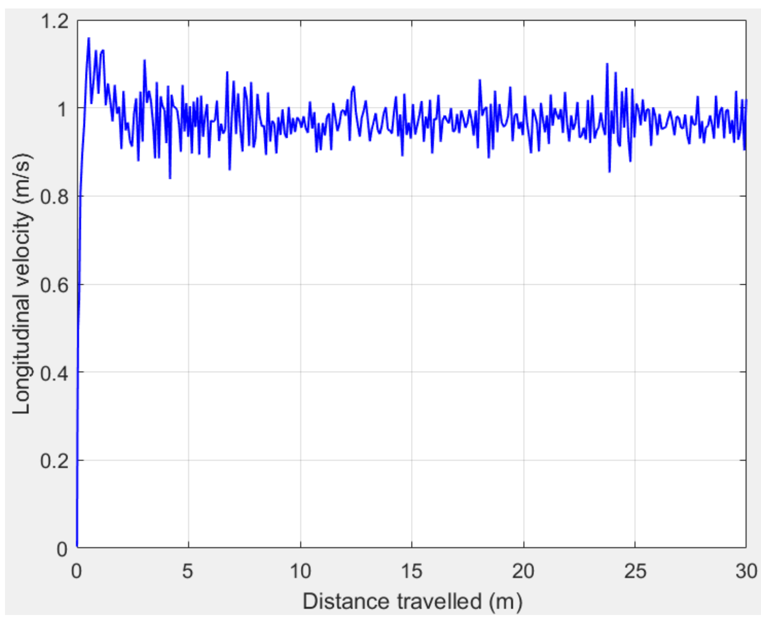

Figure B.35 Longitudinal velocity for single-vehicle sinusoidal trajectory tracking using the dynamic model (second set)

B.1.4.2 Kinematic Model

First set of supplementary experimental results (Finalized May 24, 2025).

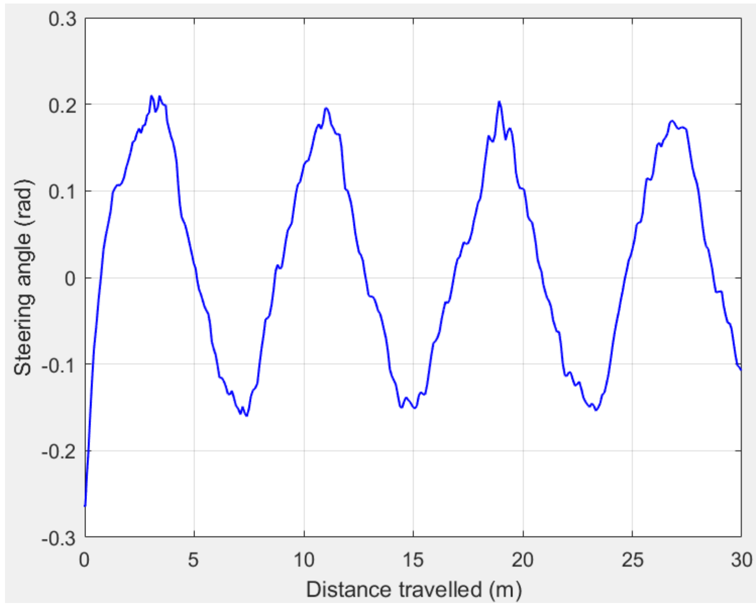

Figure B.36 Steering angle for single-vehicle sinusoidal trajectory tracking using the kinematic model

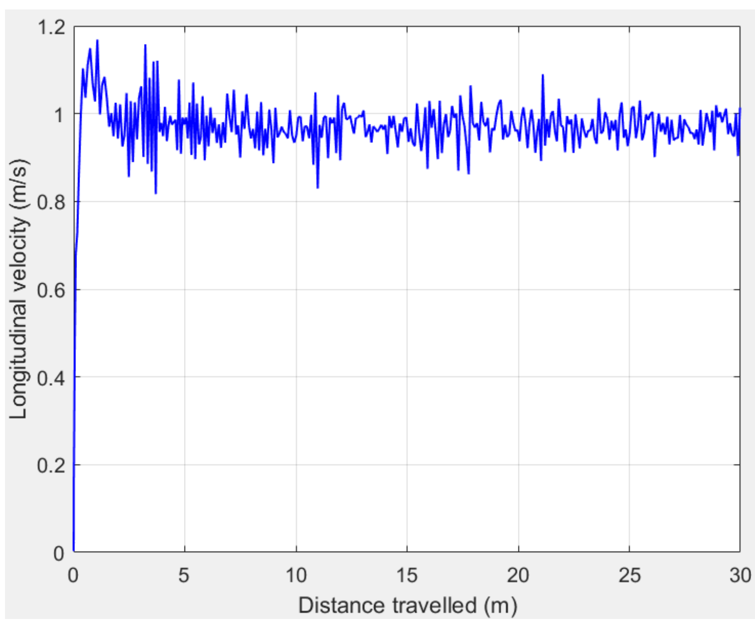

Figure B.37 Longitudinal velocity for single-vehicle sinusoidal trajectory tracking using the kinematic model

Second set of full experimental results (Finalized May 24, 2025).

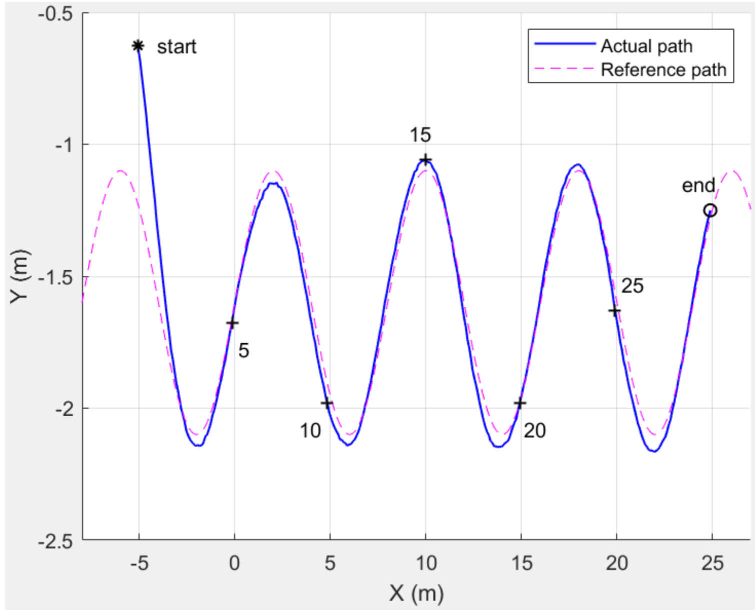

Figure B.38 Reference and actual paths for single-vehicle sinusoidal trajectory tracking using the kinematic model (second set)

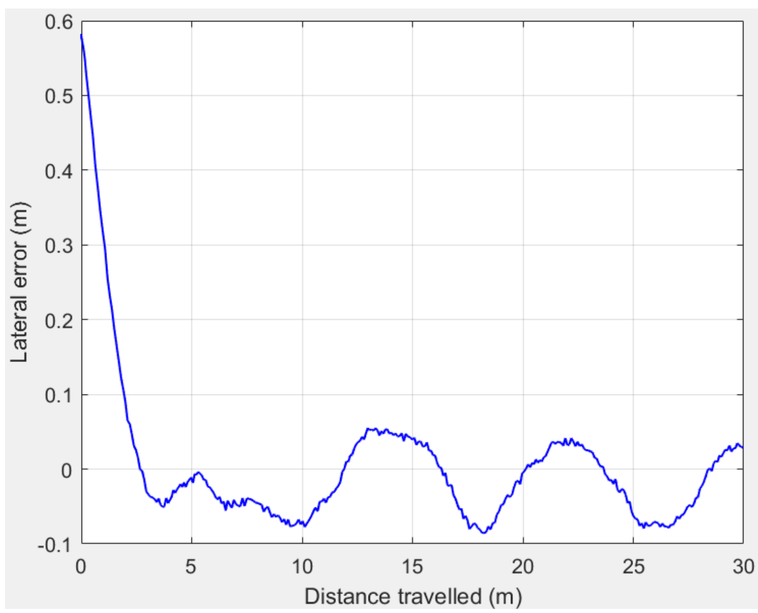

Figure B.39 Lateral error for single-vehicle sinusoidal trajectory tracking using the kinematic model (second set)

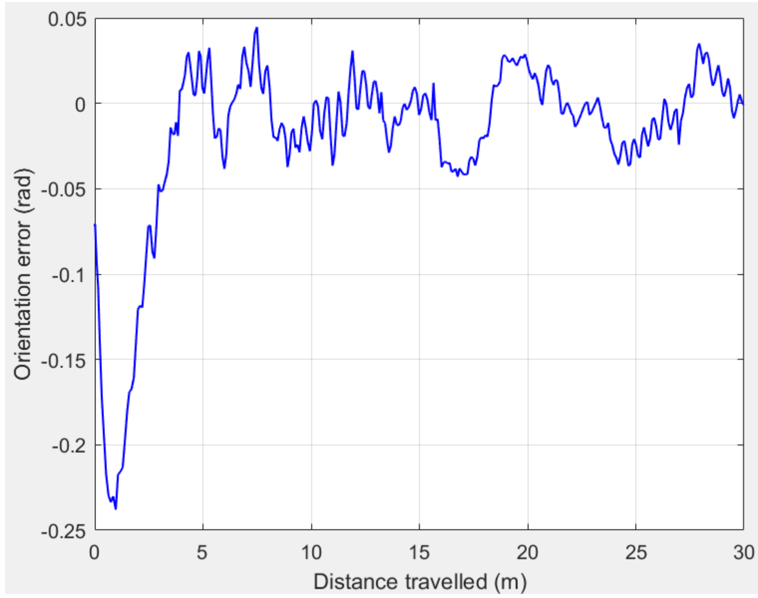

Figure B.40 Orientation error for single-vehicle sinusoidal trajectory tracking using the kinematic model (second set)

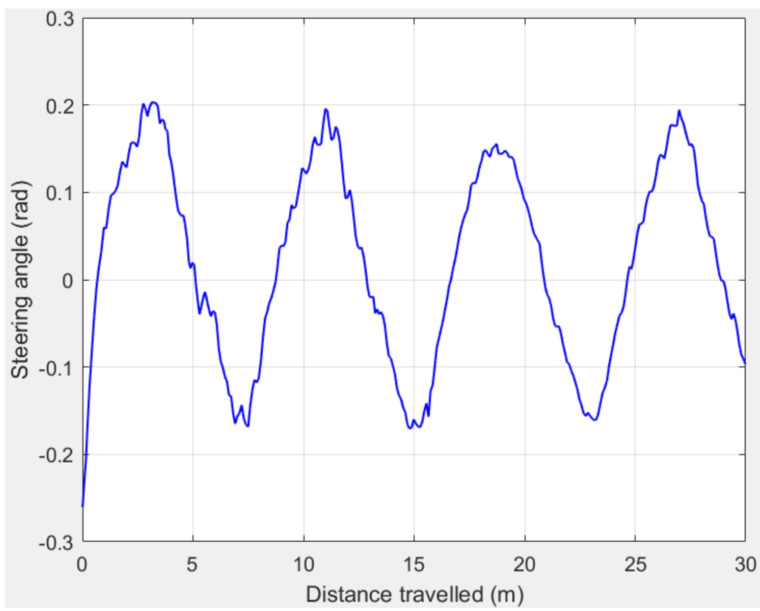

Figure B.41 Steering angle for single-vehicle sinusoidal trajectory tracking using the kinematic model (second set)

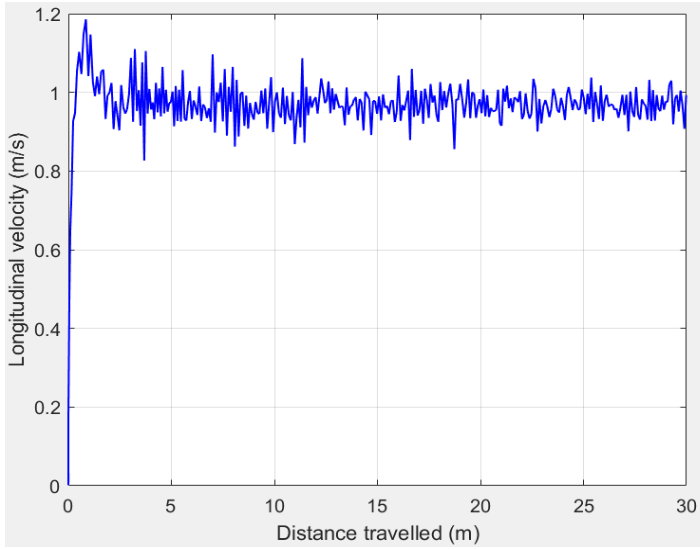

Figure B.42 Longitudinal velocity for single-vehicle sinusoidal trajectory tracking using the kinematic model (second set)

B.2 Two-Vehicle Cooperation

B.2.1 Straight-Line Tracking

B.2.1.1 Dynamic Model

First set of supplementary experimental results (Finalized June 6, 2025).

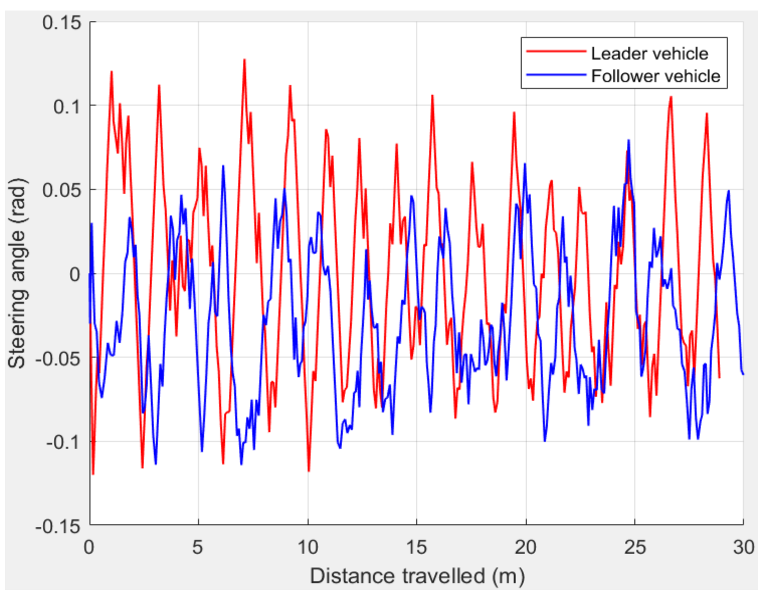

Figure B.43 Steering angle for two-vehicle straight-line tracking using the dynamic model

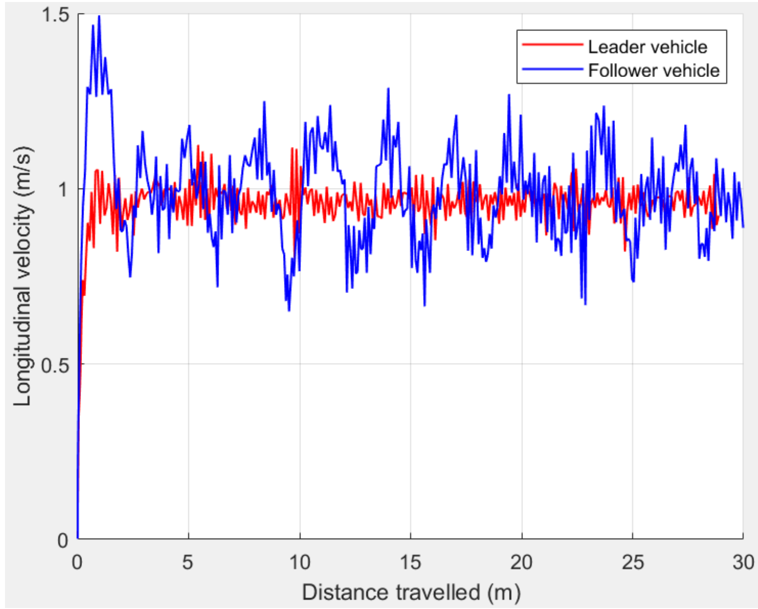

Figure B.44 Longitudinal velocity for two-vehicle straight-line tracking using the dynamic model

Second set of full experimental results (Finalized June 6, 2025).

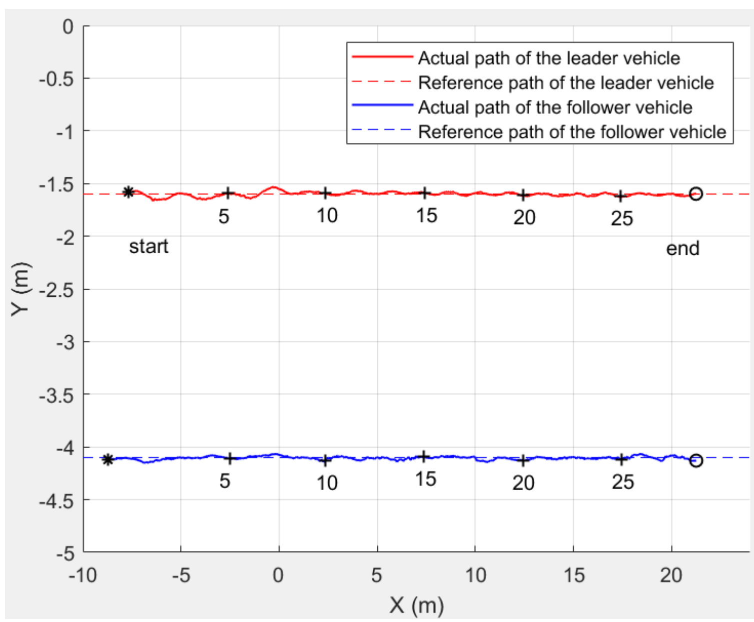

Figure B.45 Reference and actual paths for two-vehicle straight-line tracking using the dynamic model (second set)

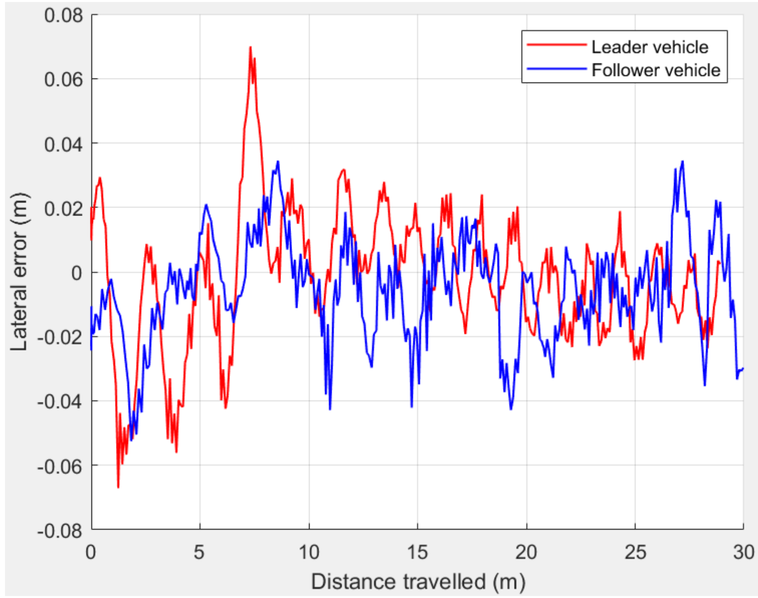

Figure B.46 Lateral error for two-vehicle straight-line tracking using the dynamic model (second set)

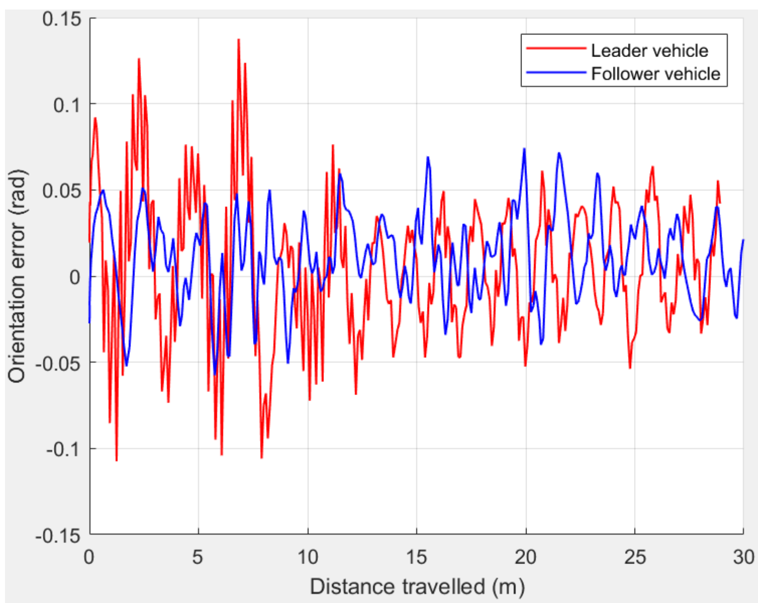

Figure B.47 Orientation error for two-vehicle straight-line tracking using the dynamic model (second set)

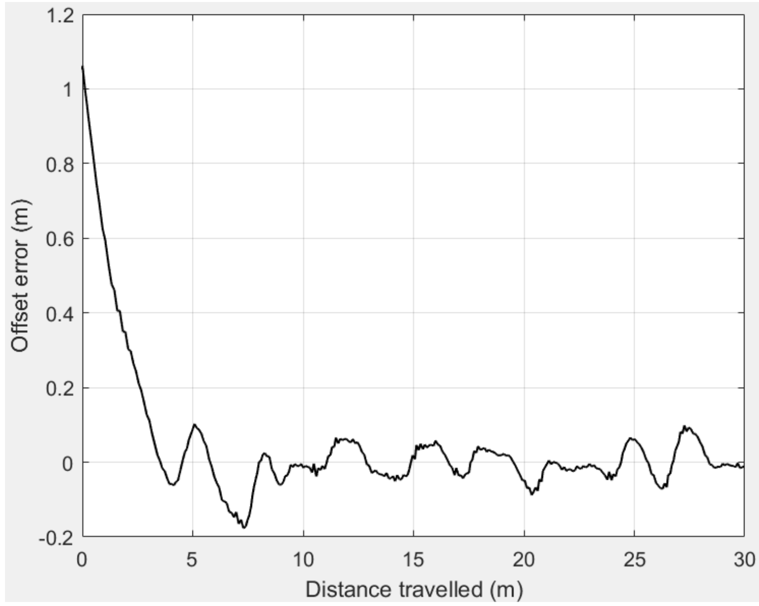

Figure B.48 Offset error for two-vehicle straight-line tracking using the dynamic model (second set)

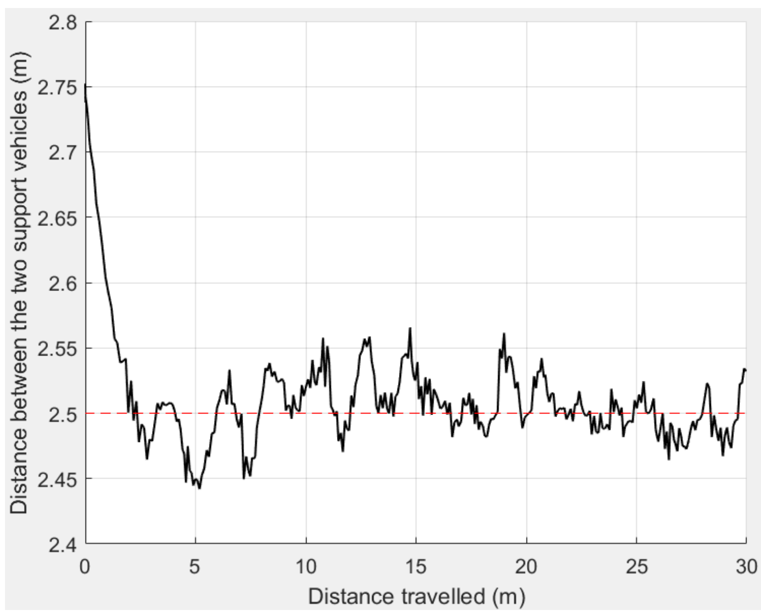

Figure B.49 Distance between the two support vehicles for two-vehicle straight-line tracking using the dynamic model (second set)

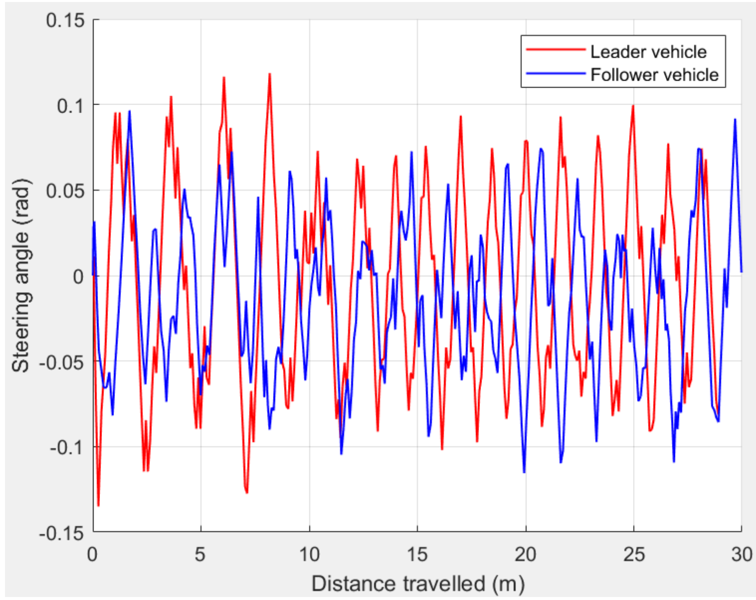

Figure B.50 Steering angle for two-vehicle straight-line tracking using the dynamic model (second set)

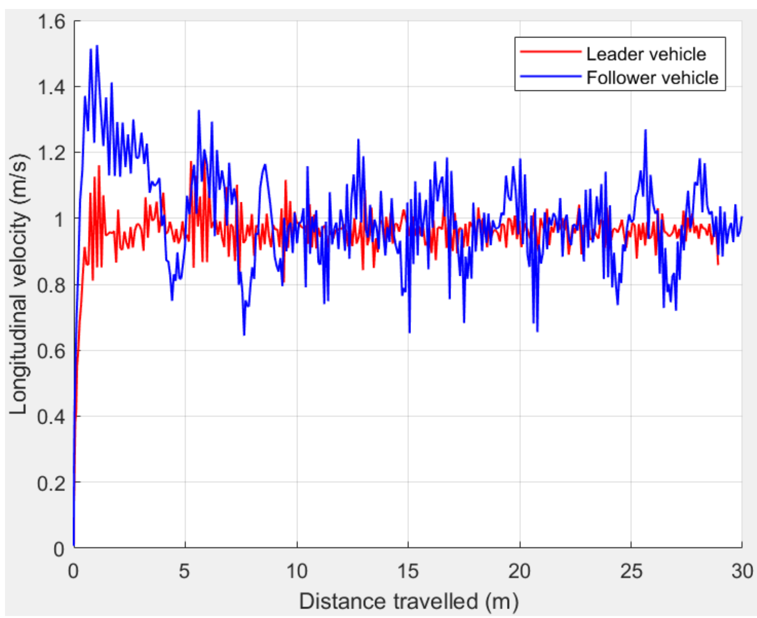

Figure B.51 Longitudinal velocity for two-vehicle straight-line tracking using the dynamic model (second set)

B.2.1.2 Kinematic Model

First set of supplementary experimental results (Finalized June 6, 2025).

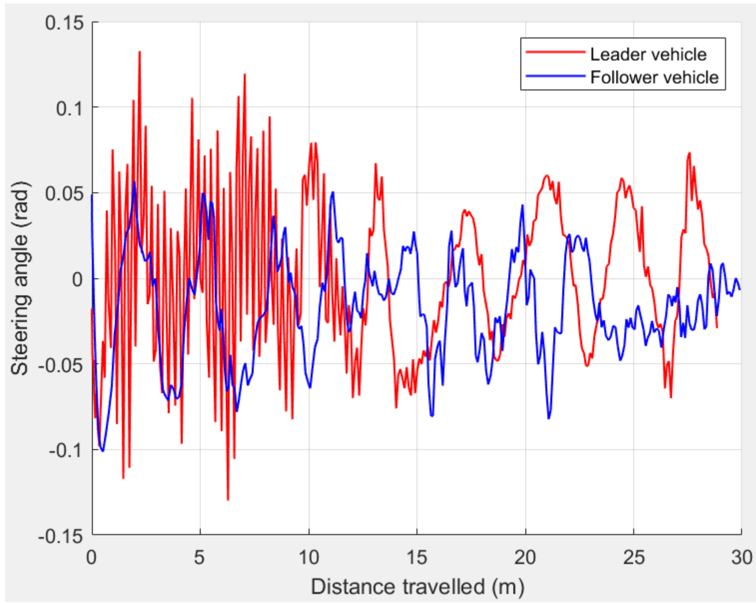

Figure B.52 Steering angle for two-vehicle straight-line tracking using the kinematic model

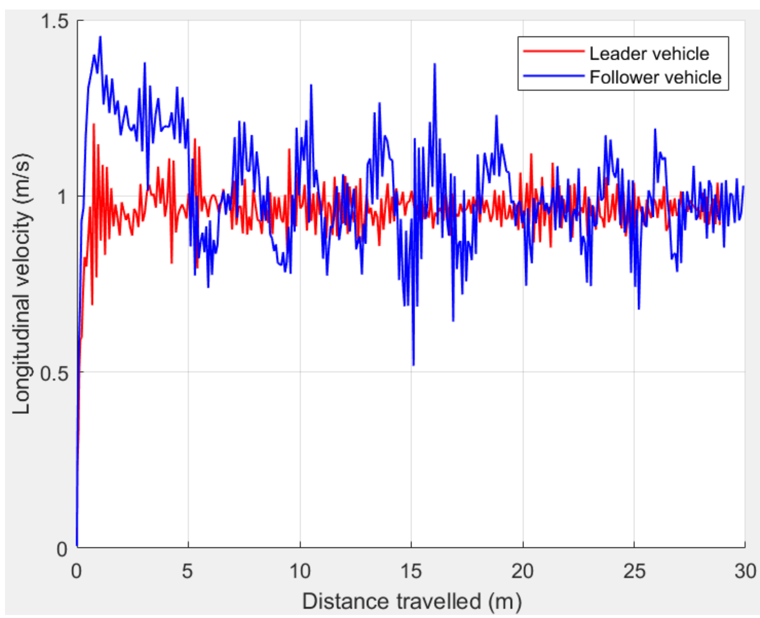

Figure B.53 Longitudinal velocity for two-vehicle straight-line tracking using the kinematic model

Second set of full experimental results (Finalized June 6, 2025).

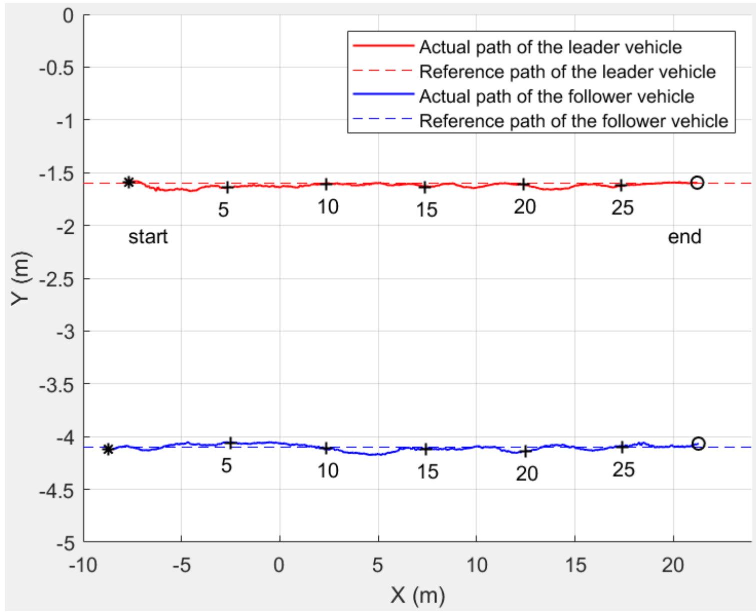

Figure B.54 Reference and actual paths for two-vehicle straight-line tracking using the kinematic model (second set)

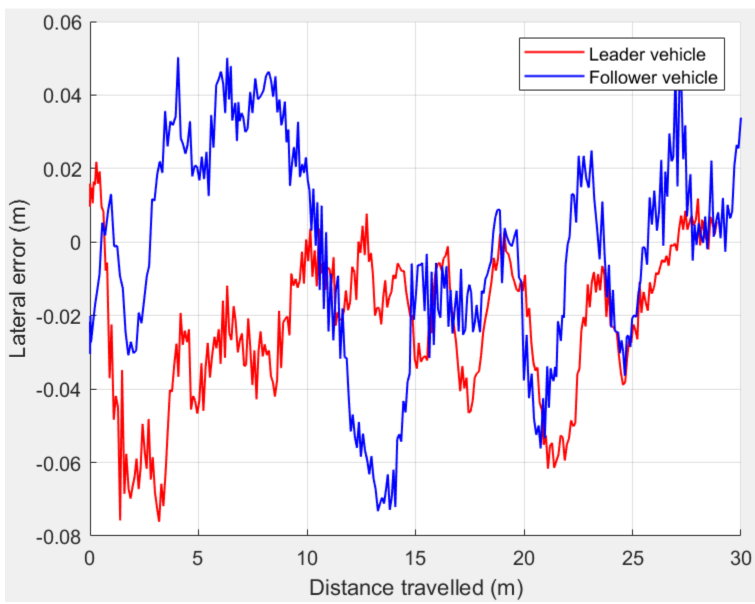

Figure B.55 Lateral error for two-vehicle straight-line tracking using the kinematic model (second set)

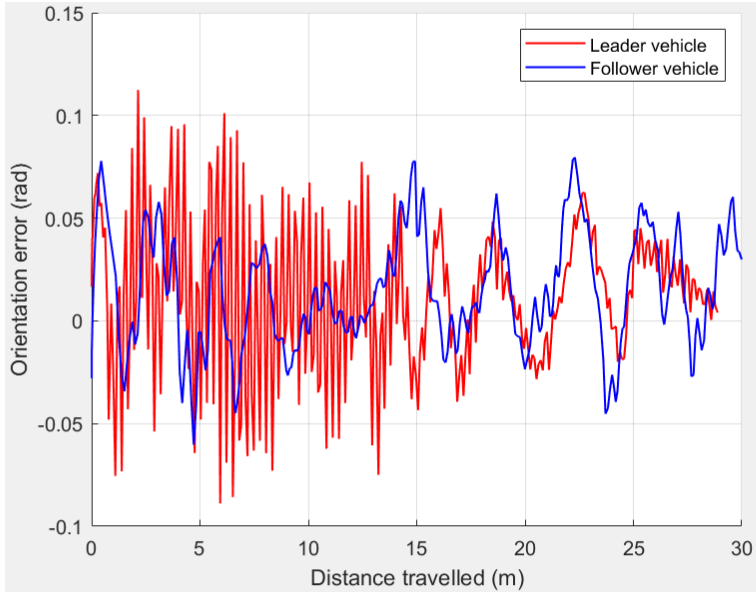

Figure B.56 Orientation error for two-vehicle straight-line tracking using the kinematic model (second set)

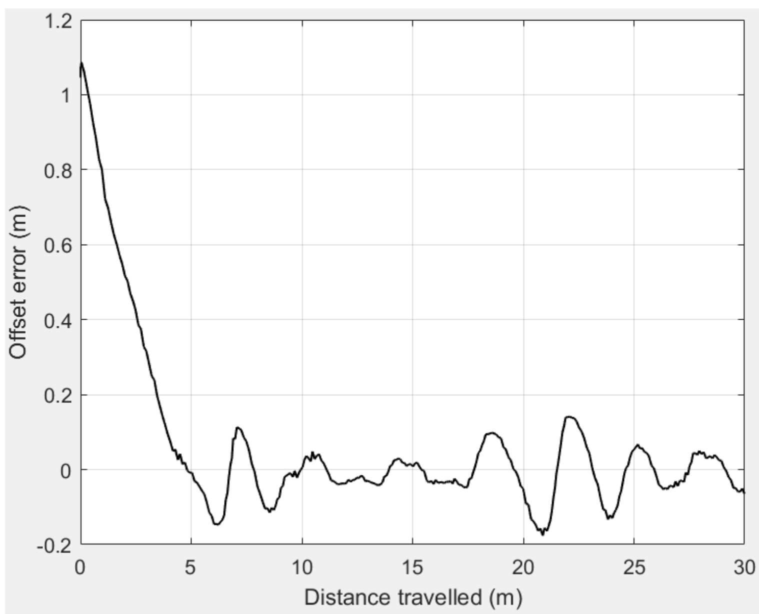

Figure B.57 Offset error for two-vehicle straight-line tracking using the kinematic model (second set)

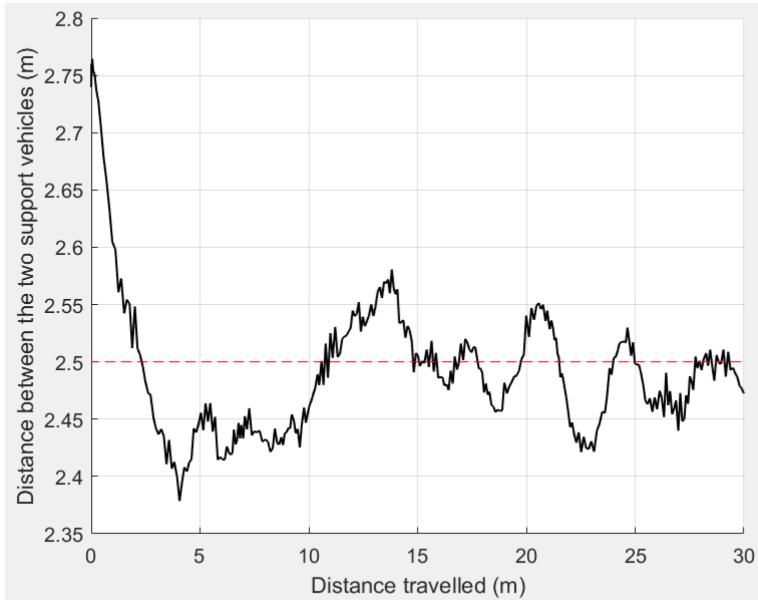

Figure B.58 Distance between the two support vehicles for two-vehicle straight-line tracking using the kinematic model (second set)

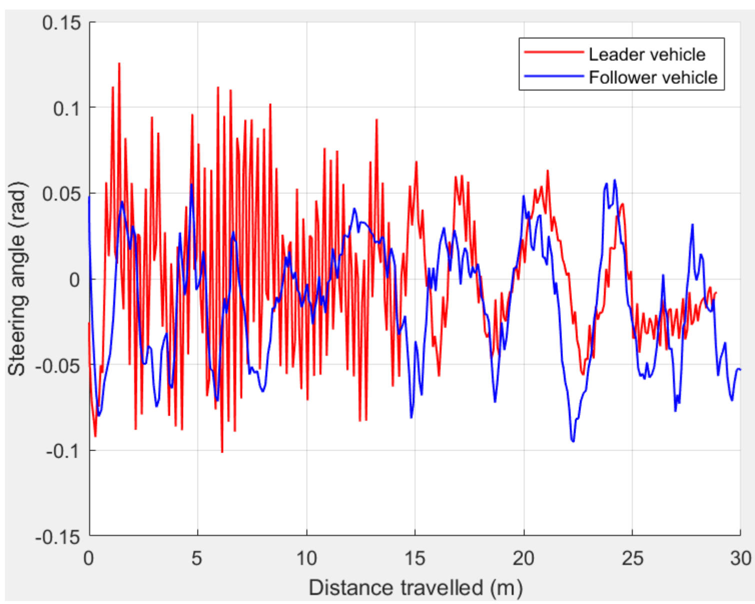

Figure B.59 Steering angle for two-vehicle straight-line tracking using the kinematic model (second set)

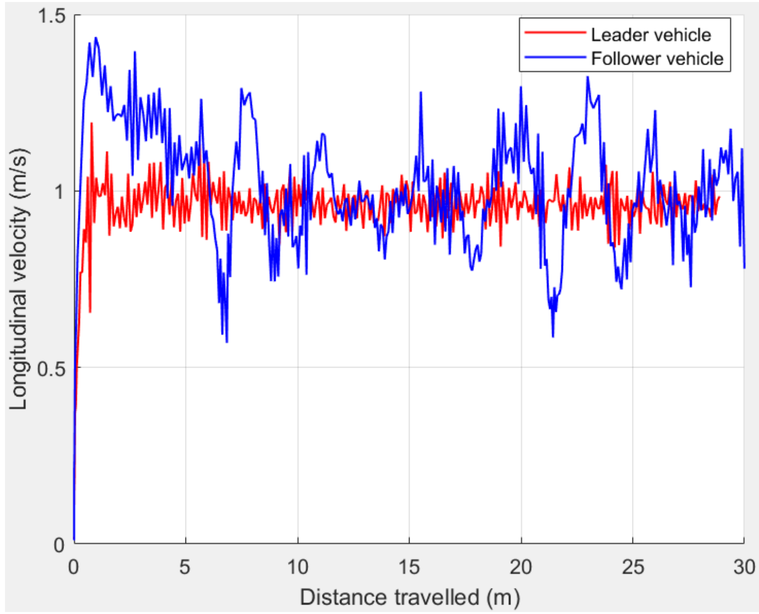

Figure B.60 Longitudinal velocity for two-vehicle straight-line tracking using the kinematic model (second set)

B.2.2 Sinusoidal Trajectory Tracking

B.2.2.1 Dynamic Model

First set of supplementary experimental results (Finalized June 7, 2025).

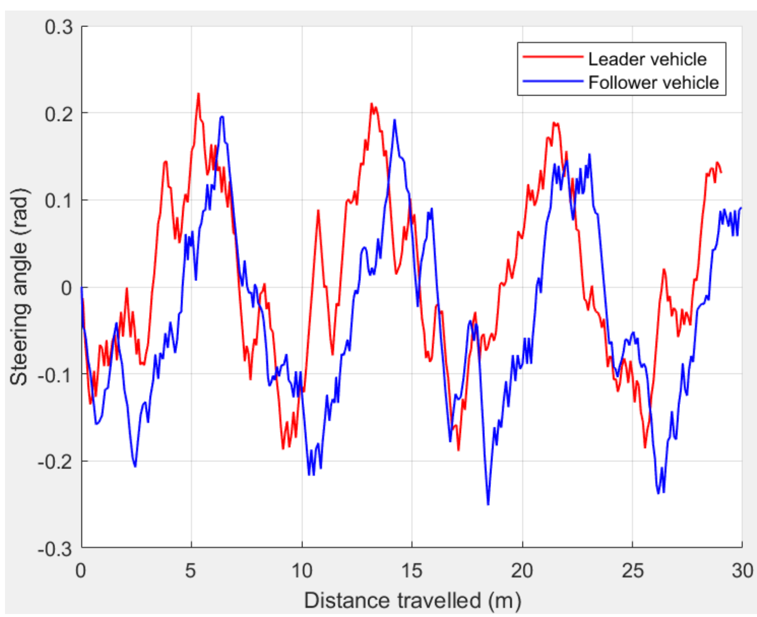

Figure B.61 Steering angle for two-vehicle sinusoidal trajectory tracking using the dynamic model

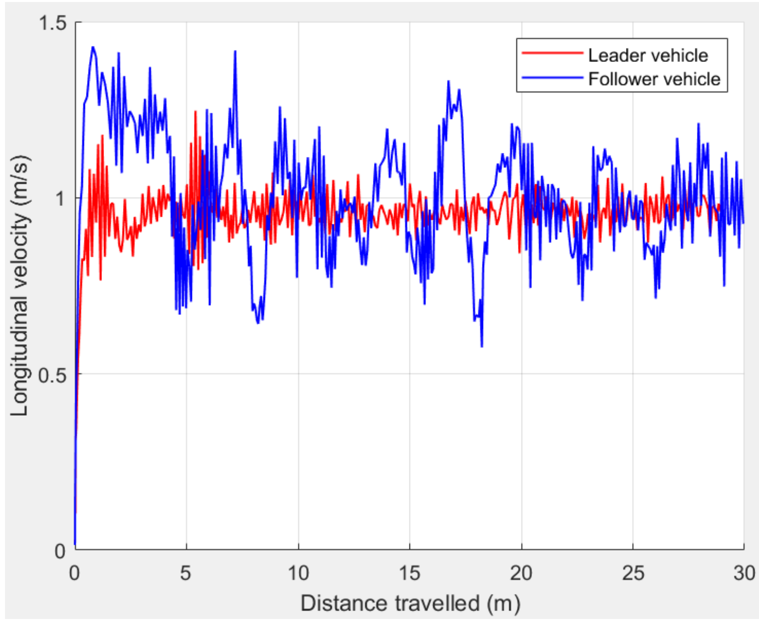

Figure B.62 Longitudinal velocity for two-vehicle sinusoidal trajectory tracking using the dynamic model

Second set of full experimental results (Finalized June 7, 2025).

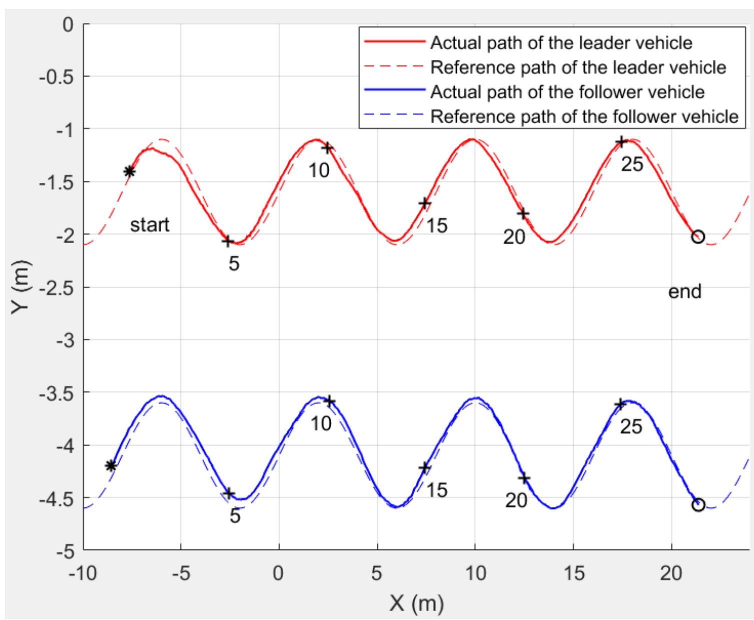

Figure B.63 Reference and actual paths for two-vehicle sinusoidal trajectory tracking using the dynamic model (second set)

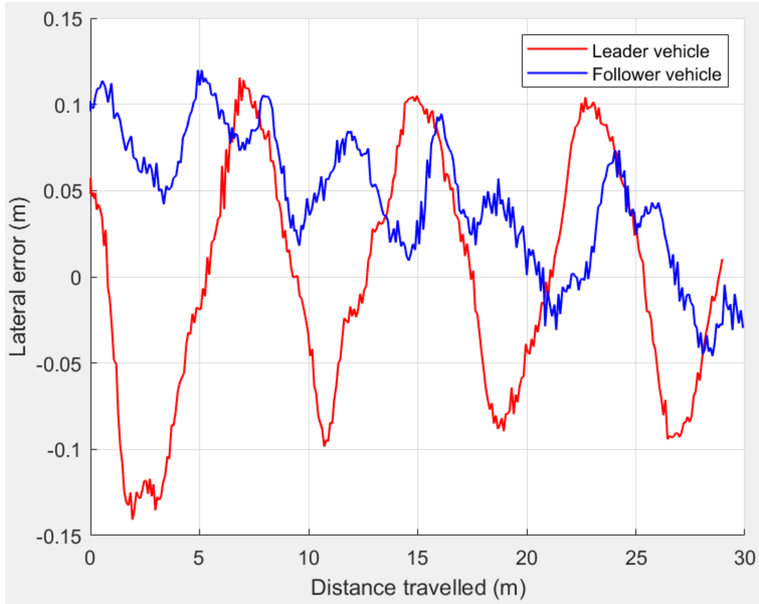

Figure B.64 Lateral error for two-vehicle sinusoidal trajectory tracking using the dynamic model (second set)

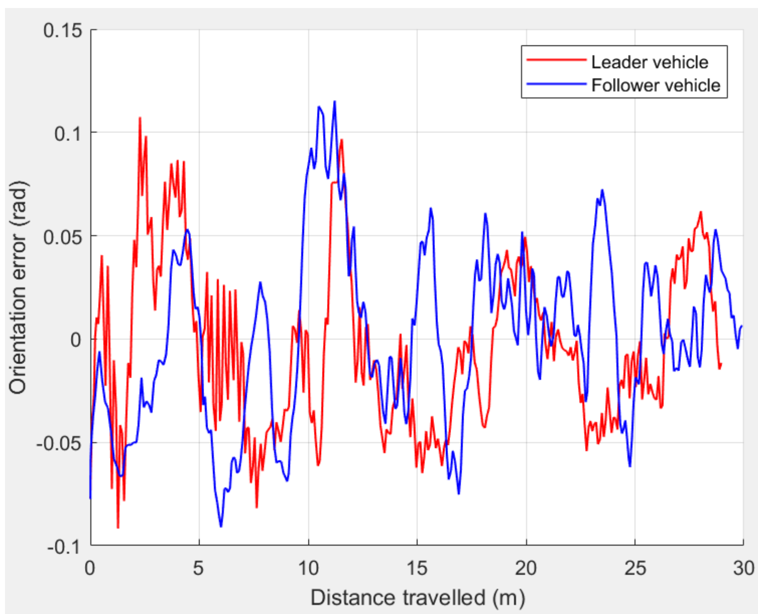

Figure B.65 Orientation error for two-vehicle sinusoidal trajectory tracking using the dynamic model (second set)

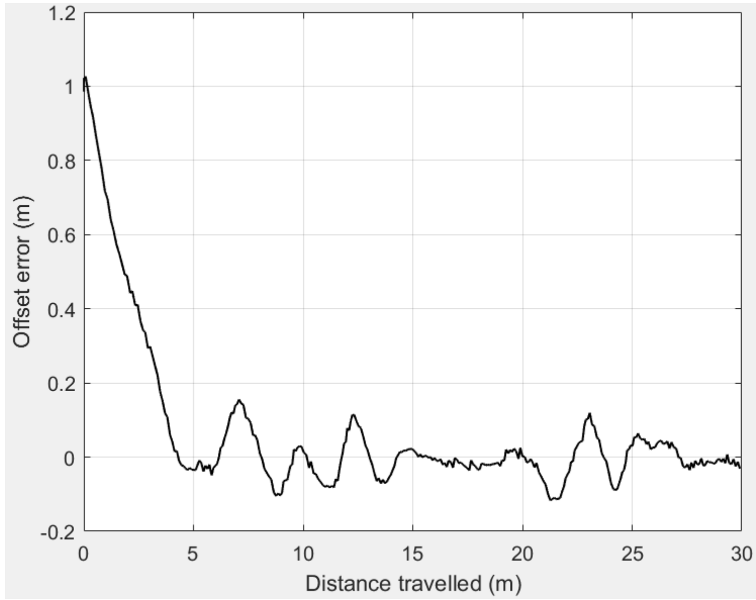

Figure B.66 Offset error for two-vehicle sinusoidal trajectory tracking using the dynamic model (second set)

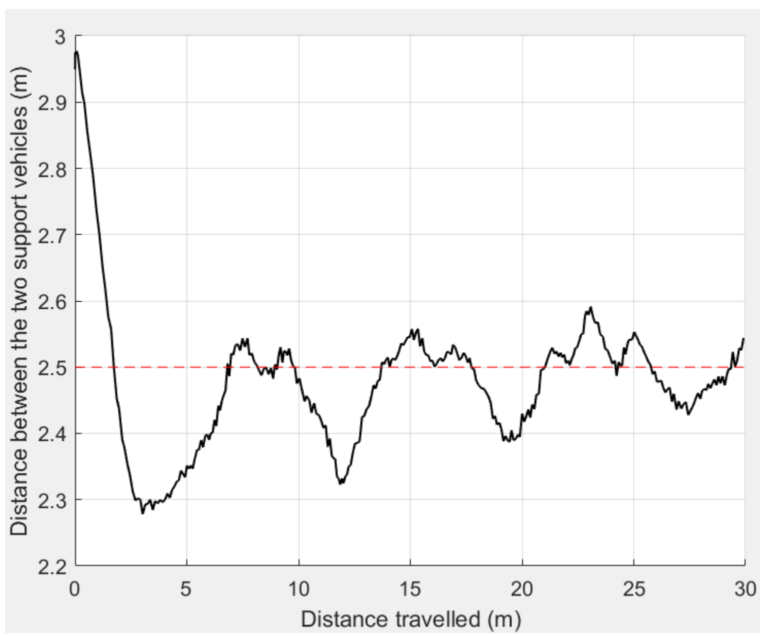

Figure B.67 Distance between the two support vehicles for two-vehicle sinusoidal trajectory tracking using the dynamic model (second set)

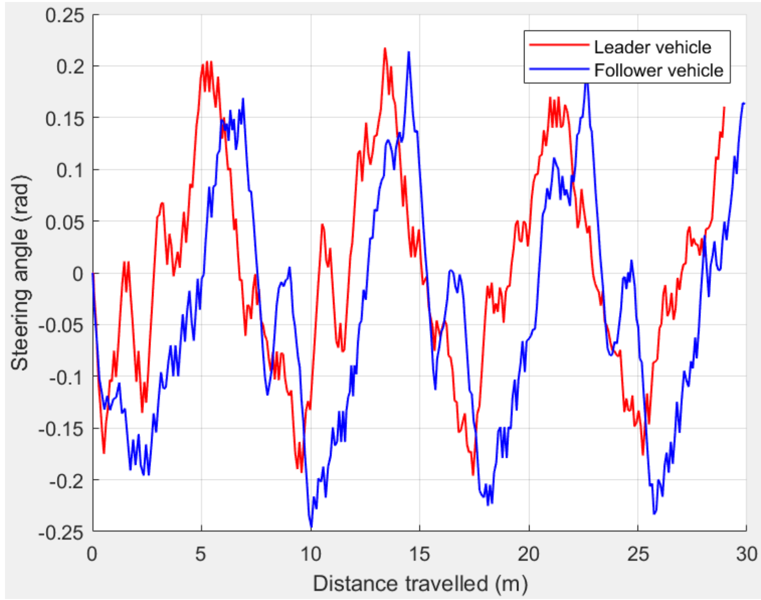

Figure B.68 Steering angle for two-vehicle sinusoidal trajectory tracking using the dynamic model (second set)

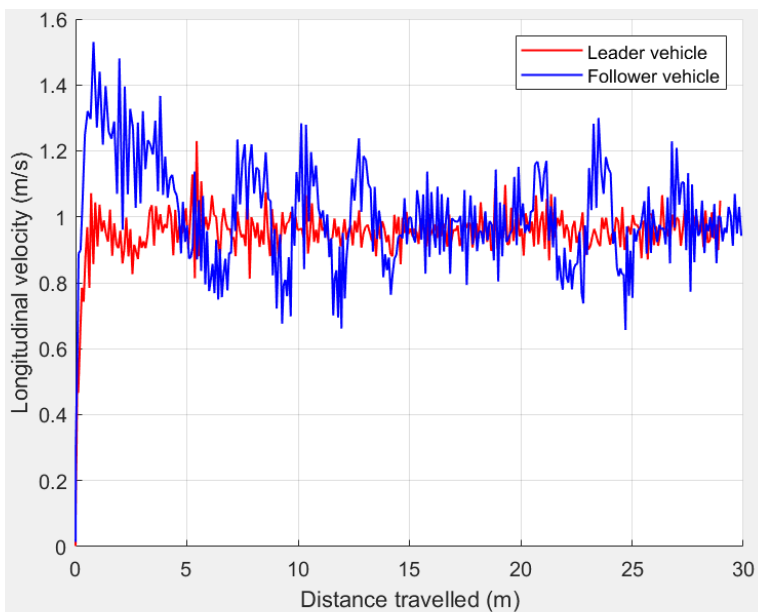

Figure B.69 Longitudinal velocity for two-vehicle sinusoidal trajectory tracking using the dynamic model (second set)

B.2.2.2 Kinematic Model

First set of supplementary experimental results (Finalized June 8, 2025).

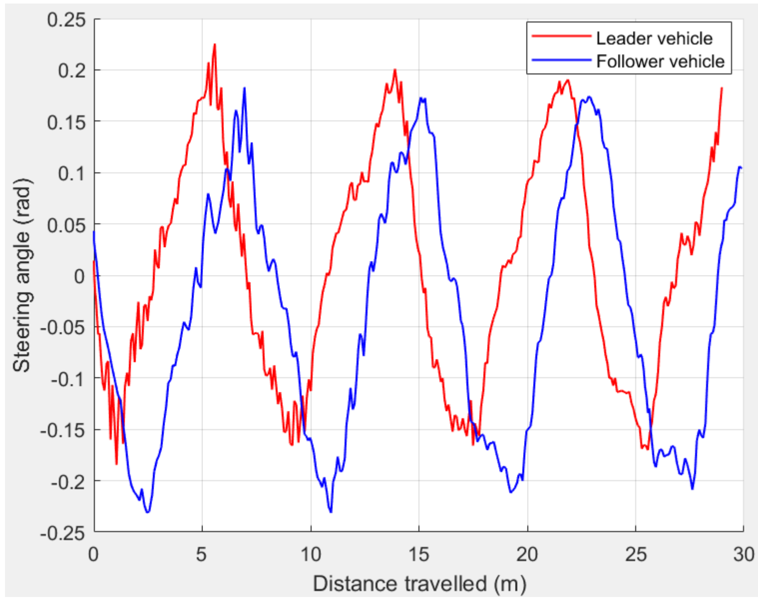

Figure B.70 Steering angle for two-vehicle sinusoidal trajectory tracking using the kinematic model

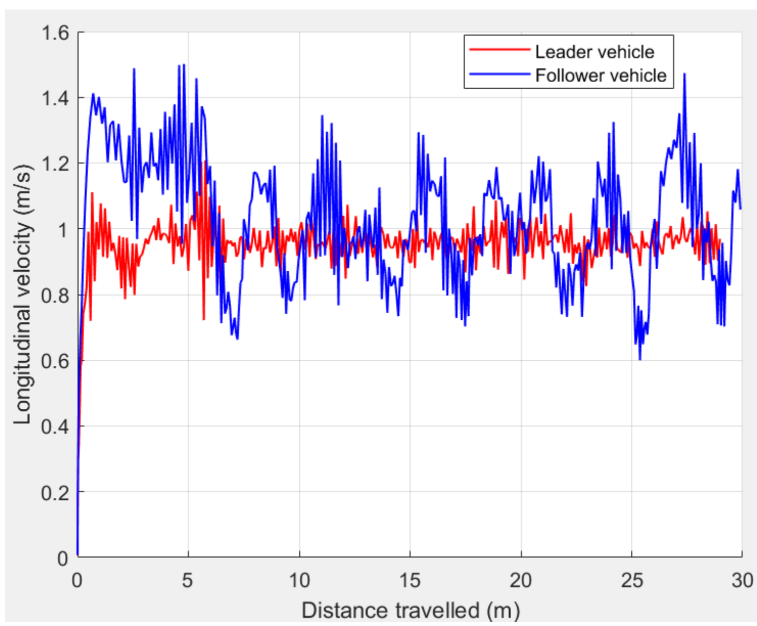

Figure B.71 Longitudinal velocity for two-vehicle sinusoidal trajectory tracking using the kinematic model

Second set of full experimental results (Finalized June 8, 2025).

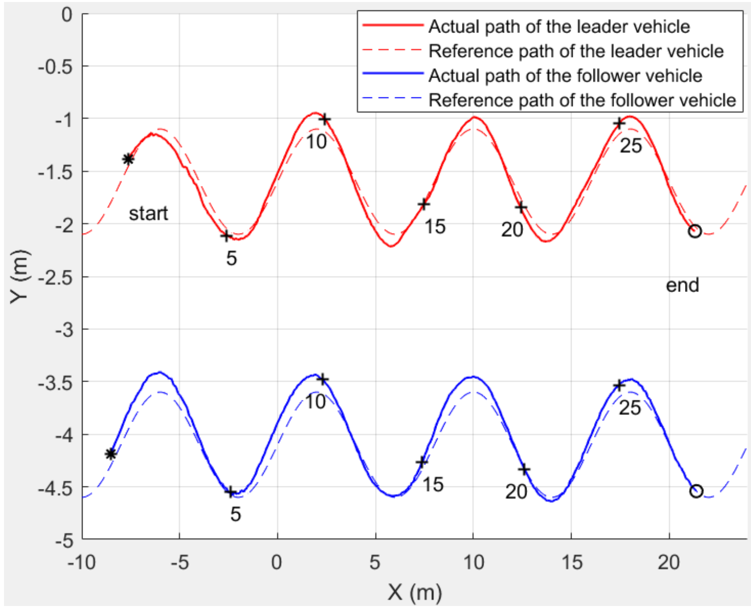

Figure B.72 Reference and actual paths for two-vehicle sinusoidal trajectory tracking using the kinematic model (second set)

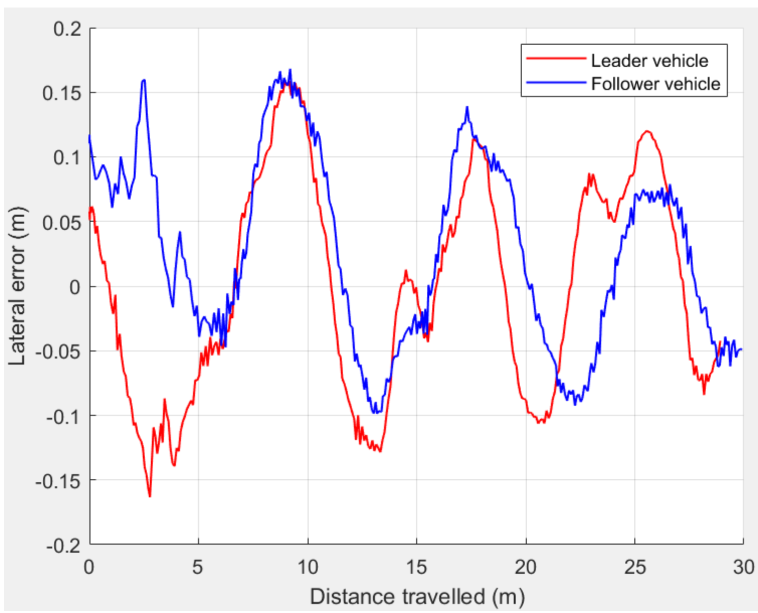

Figure B.73 Lateral error for two-vehicle sinusoidal trajectory tracking using the kinematic model (second set)

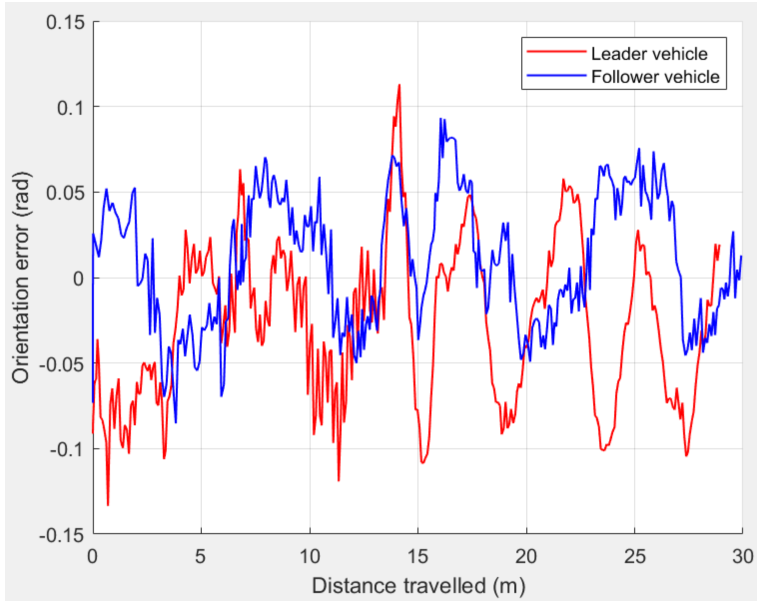

Figure B.74 Orientation error for two-vehicle sinusoidal trajectory tracking using the kinematic model (second set)

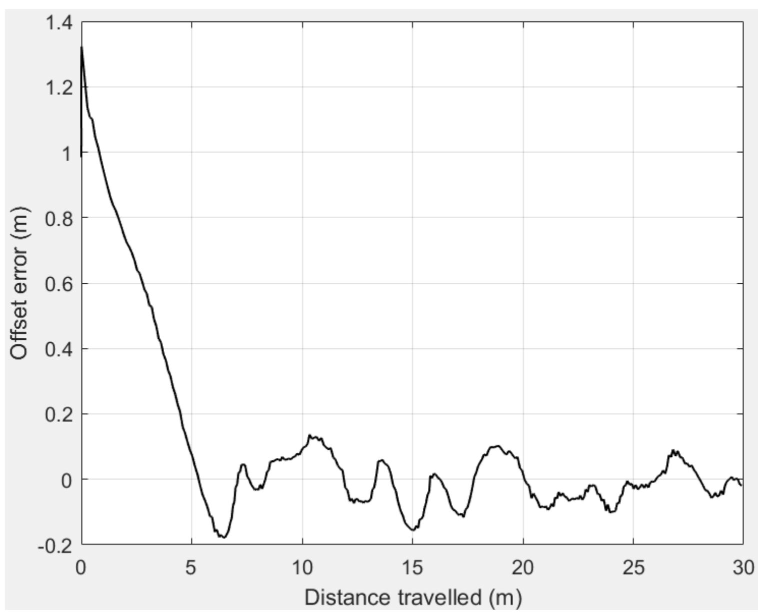

Figure B.75 Offset error for two-vehicle sinusoidal trajectory tracking using the kinematic model (second set)

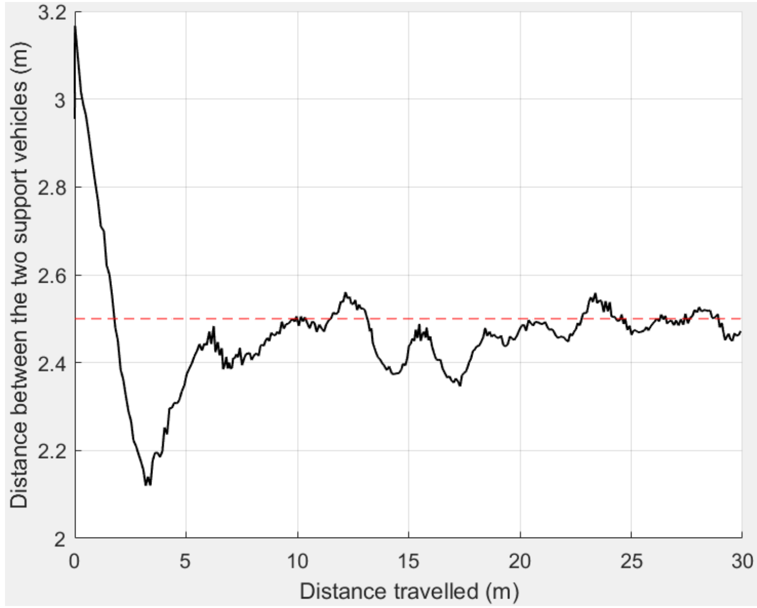

Figure B.76 Distance between the two support vehicles for two-vehicle sinusoidal trajectory tracking using the kinematic model (second set)

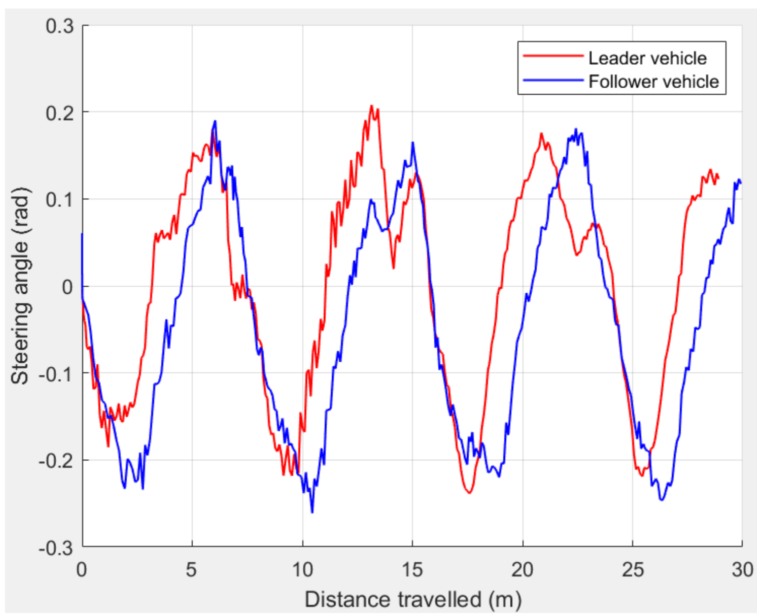

Figure B.77 Steering angle for two-vehicle sinusoidal trajectory tracking using the kinematic model (second set)

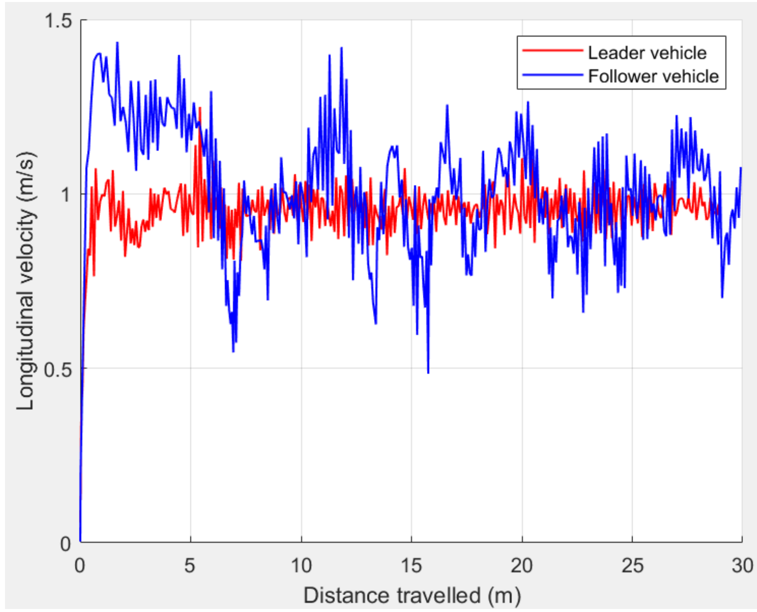

Figure B.78 Longitudinal velocity for two-vehicle sinusoidal trajectory tracking using the kinematic model (second set)